INDIRA GANDHI CENTRE FOR ATOMIC RESEARCH

2012

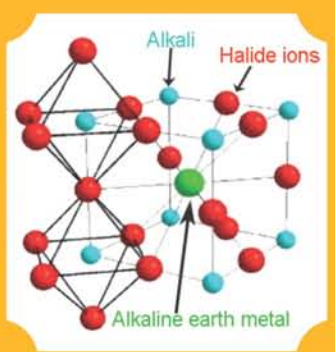

ANNUAL REPORT

सत्यमेव जयते

Government of India
Department of Atomic Energy
Indira Gandhi Centre for Atomic Research
Kalpakkam 603 102

IGCAR

2012

Indira Gandhi Centre for Atomic Research

ANNUAL REPORT

Government of India
Department of Atomic Energy
Indira Gandhi Centre for Atomic Research
Kalpakkam 603 102

“Actions today mould our tomorrows”

- Indira Gandhi

"…. The relative role of indigenous science & technology and foreign collaboration can be highlighted through an analogy.

Indigenous science and technology plays the part of an engine in an aircraft, while foreign collaboration can play the part of a booster.

A booster in the form of foreign collaboration can give a plane an assisted take-off, but it will be incapable of independent flight unless it is powered by engines of its own.

If Indian industry is to take-off and be capable of independent flight, it must be powered by science & technology based in the country …"

- Homi Jehangir Bhabha

".....There is a totality about modernisation, and in order to gain confidence, we must experiment with our resources even at the risk of failure. There is a need for a constant interplay between basic sciences, technology, industrial practice and management, if economic progress is to result from the activity undertaken"

- Vikram Sarabhai

Editorial Committee

Address for Correspondence
Dr. P.R. Vasudeva Rao
Chairman, Editorial Committee
Director, Chemistry Group
Indira Gandhi Centre for Atomic Research
Kalpakkam - 603 102

Phone : +91-44-2748 0229 / 0222
Fax : +91-44-2748 0222 / 0065
Email : vasu@igcar.gov.in
dcg@igcar.gov.in
Website : www.igcar.gov.in

Published by:
Scientific Information Resource Division
Resources Management Group
Indira Gandhi Centre for Atomic Research
Kalpakkam - 603 102

Contents

FRONT COVER

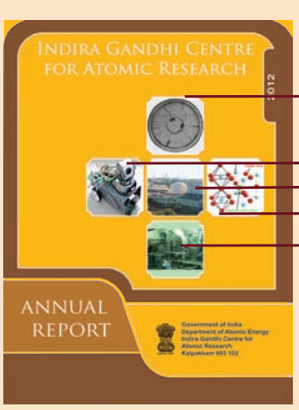

1. Photomosaic of MOX fuel pin cross-section at peak power location
2. Prototype vehicle used for testing wireless control system
3. Fast Breeder Test Reactor
4. Structure of mixed alkali halides
5. Vibro-packing and fuel pin welding

BACK COVER

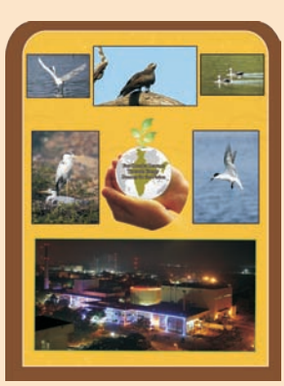

Flora and Fauna at Kalpakkam

Foreword

I am happy to share with you the Annual Report from IGCAR for 2012. This report highlights the achievements of the Centre in multidisciplinary areas of Science and Technology in the ambit of Fast Reactor and associated Closed Fuel Cycle Technologies interlaced with research in basic sciences.

Two irradiation campaigns have been completed in FBTR at its target power of 20.3 MWt. At the end of the 18th irradiation campaign, a series of experiments to understand the core physics such as the replacement worth experiment and reactor power were carried out. Irradiation of indigenously fabricated sodium bonded U-6%Zr metallic fuel has started in FBTR. Irradiation to study the behaviour of the sphere-pac fuel pin including segregation, if any and restructuring compared to a reference fuel pin containing MOX fuel has also been carried out in FBTR. As part of XI plan, the neutronic instrumentation system of KAMINI has been revamped with state-of-the-art instruments.

The construction of PFBR is in an advanced stage of completion. Qualification of the reactor components such as fuel handling machines, absorber rod drive mechanisms, sodium level probes, core flow monitoring mechanisms, eddy current based flow sensors and under sodium ultrasonic scanner and seismic test on shut down system have been carried out. The critical primary side components of inclined fuel transfer machine including primary ramp and primary tilting mechanism, have been qualified for reactor operation by in-sodium testing at reactor conditions. Towards design and manufacturing technology of future MOX reactors FBR 1 and 2, welded grid plate, inner vessel sector of single torus, large diameter bearings, tri-junction forgings for dome shaped roof slab and safety vessel sector integral with thermal insulation panels have been innovatively designed and manufactured indigenously. Reactor safety studies including large scale sodium fire with leak collection trays, simulation of post-accident scenarios with matching stimulants and steam leakage studies were completed by designing novel experiments. Identification of suitable site, design of core and plant characteristics or being undertaken towards the development of metal fuelled fast reactor. Eight reprocessing campaigns of mixed carbide spent fuel of FBTR have been successfully completed in CORAL. Modified designs of motor and control system of centrifugal extractors with improved operating performance of the plant have been utilized in CORAL. Process design to recycle the solvent and also reduce the waste volume of solvent, by an advanced distillation process has been validated. All the vital equipment and systems have been received at site for installation and commissioning of DFRP. Preparations for launching the Fast Reactor Fuel Cycle Facility Project have progressed well and the necessary site infrastructure has been created. It is expected that financial approval for the project would be available shortly.

Basic research relating to development of newer materials and methodologies included development of 9Cr oxide dispersion strengthened steel clad tubes in lengths up to four metres, improved D9 cladding material with different amounts of phosphorus and silicon, procedure joining AISI 304 SS pipes by A-TIG welding, for in-service inspection of reactor vessels of PFBR and reprocessing applications, GMR array sensor based magnetic flux leakage technique for non-destructive detection of defects, fabrication of irradiation capsules, development of Alumina coating on Inconel 600 rings for neutron detector chambers of FBRs, development of partially stabilised zirconia coatings on metallic and graphite substrates, fabrication of dissimilar joints by explosive cladding technique, India specific reduced activation ferritic-martensitic (INRAFM) steel for test blanket module of ITER, 304HCu stainless steel and Alloy 617 boiler tubes for advanced ultra supercritical thermal

power plants. Development of virtual reality system, 3D modeling and visualization of the fuel handling operation of the PFBR and FRFCF, modeling of all sub-systems and benchmark transients for operating training simulator, installation and commissioning of high performance computing cluster systems, R&D on intelligent human machine interface for plant monitoring and control are some of the significant areas of research being pursued as part of the electronics and instrumentation programme. Fabrication of MOX fuel pin by vibro compaction route, R&D on development of advanced separation schemes for actinide recovery, engineering scale studies on unit operations in pyroprocessing, development of thin film oxide semiconductor sensors, development of ion mobility spectrometer for explosive detection, thermochemical studies and thermophysical property measurements on several systems involving fuel and control rod materials such as U-Sn intermetallic compounds, boron compounds, uranium-neodymium mixed oxides etc., cesium loaded iron phosphate glasses, and tri-iso-amylphosphate (TiAP)-HNO_3 systems are some of the important activities completed in the domain of chemistry.

Radiation services to occupational workers have been further strengthened by upgrading the whole body counting facility and by standardizing the measurements with a phantom. The round robin exercise on atmospheric dispersion model validation has been successfully initiated with the participation of more than a dozen national institutes, universities and DAE units. The HEPA filter test facility has been accredited by NABL for the first time in any of the DAE units. Basic research in the areas relating to negative thermal expansion materials, superconducting materials, studies on nitrogen doped TiO_2 superhydrophyllic coatings, tribological properties of modified NiCrB coatings, studies on the stability of iron phosphate glasses, investigations on the formation of Y-Ti-O clusters in ODS alloys through Kinetic Monte Carlo simulations have been carried out. Repair of high purity germanium detectors has been successfully demonstrated. We are moving forward to use MCG and MEG for clinical studies.

Training School and Homi Bhabha National Institute are providing robust manpower for conducting the mission programmes. Collaborations have been furthered with eminent institutions. The service groups have worked towards providing better amenities, infrastructure, safety, medical facilities and better environment. Programmes aimed towards development of neighbourhood and creating awareness about our activities are progressing well.

I would like to compliment the editorial team steered by Dr. P. R. Vasudeva Rao and led by Dr. M. Sai Baba for bringing out this document with the traditional flavor and invigorating with modern design. I also appreciate colleagues from Resources Management Group, in particular Shri Gaddam Pentaiah and Shri K. Varathan for their contributions and efforts.

(S. C. Chetal)
Director, IGCAR

Mission of IGCAR

- *To conduct a broad based multidisciplinary programme of scientific research and advanced engineering development, directed towards the establishment of the technology of Sodium Cooled Fast Breeder Reactors (FBR) and associated fuel cycle facilities in the Country*
- *The development and applications of new and improved materials, techniques, equipment and systems for FBRs and*
- *To pursue basic research to achieve breakthroughs in fast reactor technology*

Vision

To be a Global Leader in Sodium cooled Fast Breeder Reactor and associated Fuel Cycle Technologies by 2020

Editorial

I have great pleasure in presenting the Annual Report of Indira Gandhi Centre for Atomic Research for the year 2012 as the Chairman of the Editorial Committee. Over the years, the annual report has continued to be an exercise in introspection and has at the same time, provided us a sense of pride about the diversity, complexity and depth of the R&D programmes at IGCAR. Successive Directors of the centre have emphasized the need to bring out the report in time and at the same time, incorporating the best of the results, articulated for wider readership. I take this opportunity to thank the editorial committee and Dr. M. Sai Baba in particular, for their dedicated efforts in meeting this requirement.

A reading of the annual reports for successive years would give a clear picture to the reader about the sustained level of excellence in the activities and the focus on the mission of the department. The format and layout of the report have been retained from the past issues. The articles have been specially prepared for the annual report and have gone through multiple stages of editing to ensure accuracy and readability and to provide a balanced picture on various programmes of the centre.

The articles are segregated into chapters to highlight the achievements with respect to FBTR, PFBR, R&D of FBRs, Fuel Cycle, Basic Research and Infrastructure. The flagship of the Centre, FBTR, has continued to operate successfully and has served as a test bed for irradiation of fuels and materials and for qualifying some of the equipment. The details of the irradiation campaigns taken up in FBTR and the revamping of the instrumentation of KAMINI are dealt with in the first Chapter. The construction of PFBR is at an advanced stage of completion and while IGCAR has completed all the R&D required for the construction and commissioning of PFBR, some other activities have continued, for providing more confidence in the design and also an insight into the operational issues. The post-irradiation examination of MOX fuel of PFBR irradiated in FBTR, in-sodium and seismic testing of critical components, development of innovative systems for under sodium viewing etc. are covered in Chapter II.

Chapter III deals with R&D towards future reactors including metal fuelled fast reactors. Topics covered include the design of reactor core and components for future reactors with emphasis on improved economics and safety. In line with the Department's emphasis on closed fuel cycle, a number of programmes are being pursued on the back end of the fast reactor fuel cycle and these are presented in Chapter IV. Chapter V contains an array of articles in basic research in the domains of science and engineering, most of them having direct applications to the mission programmes of the Centre. Chapter VI highlights the activities towards infrastructural development in 2012. Chapter VII provides a diary of significant events including seminars, workshops and eminent and popular lectures/colloquia and also showcases our achievements in the form of awards and honours.

The Editorial Committee sincerely thanks the authors who have contributed interesting articles highlighting the achievements. The committee is particularly thankful to Shri Gaddam Pentaiah and Shri K. Varathan of RMG, for their contributions towards expediting the publication. The Editorial Committee is indebted to Shri S. C. Chetal, Director IGCAR, whose outstanding leadership, guidance and emphasis on adherence to time schedules have spurred us to bring out this report in time and with quality.

(P.R. Vasudeva Rao)
Chairman, Editorial Committee
Director, Chemistry Group

Our New Director

Shri S. C. Chetal greets Dr. P. R. Vasudeva Rao
on his assumption of charge as Director, IGCAR

Dr. P. R. Vasudeva Rao, Distinguished Scientist and Director, Chemistry Group has taken over as Director, Indira Gandhi Centre for Atomic Research, with effect from February 1, 2013

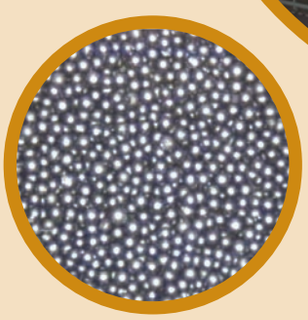

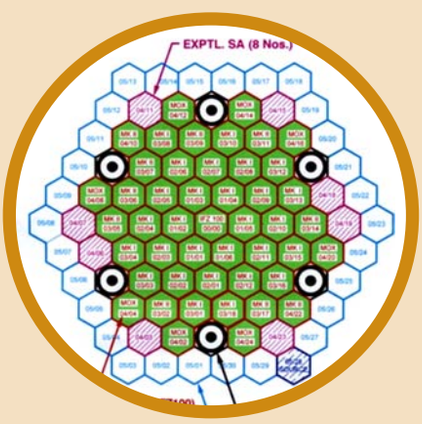

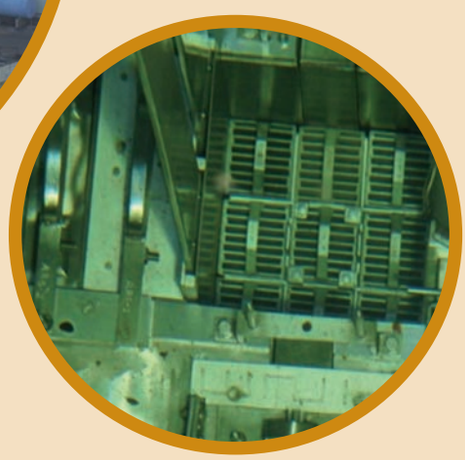

CHAPTER - I

Fast Breeder Test Reactor

I.1 Irradiation Mission of FBTR

FBTR has been operated in mission mode for experiments and irradiation during 2012. The 19th and 20th irradiation campaigns were completed with a maximum power of 20.3 MWt and producing 3.5 to 4 MWe (sufficient for feeding FBTR, RML and SGTF). Two campaigns were necessitated as one or more of the fuel subassembly (SA) attained its target burn-up i.e., 155 GWd/t for Mark-I and 100 GWd/t for Mark-II (Figure1). Table 1 and 2 gives the details of reactor operation and materials that were irradiated.

In order to further understand the causes for anomaly in the predicted shutdown margin noticed in the 16th irradiation campaign (December 2009), the following physics experiments were carried out at the end of the 18th campaign:

(a) Measurement of the replacement worth of fresh subassembly replacing burnt subassembly at the centre, 1st ring and 3rd ring. The deviation between calculated and the measured reactivity worth was found to be around 100 pcm which is attributable to effects not amenable to modeling in the reactor physics code. With this experiment, the reactivity anomaly observed in the 16th campaign was fully resolved.

(b) Reaction rate measurements of plutonium foil at the centre and third ring, together. Measured form factors were less than the calculated values, which implied that the peak linear power was smaller than the calculated value. For a given peak linear heat rating, the subassembly power is likely to be higher than the calculated value, by 6.1% at the centre and 0.4% at third ring.

These experiments involved six start-ups and criticalities for reactivity worth measurements and one for reaction rate measurement. The deviation in all these start-up experiments was within the stipulated margin. In all the three campaigns (18th, 19th and 20th) the reactor power and sodium temperatures were kept at more or less same to achieve same irradiation environment.

In the 19th and 20th campaigns, the materials that were irradiated in special subassemblies is indicated in Table1.

Testing of high temperature fission chamber meant for PFBR was carried out in the detector pit at a power level varying from criticality to 10 MWt.

Earlier, two design prototype detectors fabricated by BARC with 12 metres length of mineral insulated (MI) cables had been tested in APSARA shielding corner up to 853 K and a neutron flux of $7x10^7$ nv and the same detectors were also tested in FBTR upto 673 K, at a neutron flux of $8 x10^8$ nv and a gamma field of 70 kR/h. A neutron sensitivity of 0.12 cps/nv was measured. The technology was transferred to M/s. ECIL for fabrication of 40 detectors. A prototype high temperature fission chamber with 7 metres length of mineral insulated cables was tested at FBTR at room temperature in the neutron flux range $4x10^3$ nv (20 Wt) to $2x10^9$ nv (10 MWt).

Performance of the detector was satisfactory.

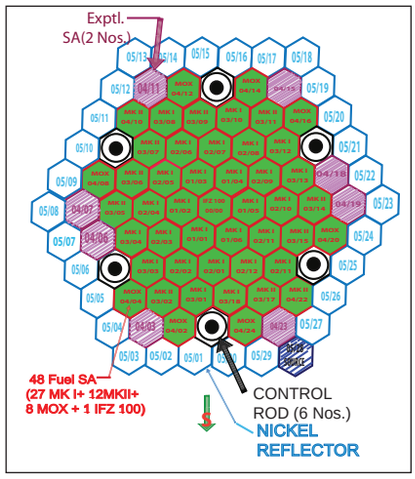

Fig. 1 *Core configuration of 20th irradiation campaign*

Table 1: Details of materials irradiated in special subassemblies

Location	Capsule	Remarks
04/03 and 04/15	Metallic fuel pin capsule (Natural U + Zr)	-
0406 and 05/13(04/18)*	SS 316LN impact & tensile specimens for low dose irradiation	The capsule at 05/13 was shifted to 04/18 in the 20th campaign
04/07	Ferro-boron	discharged after 20th campaign
04/19	Capsule with Yttria for ^{89}Sr production	
04/11 and 04/23	D9 material irradiation	Loaded in 14th campaign

Table 2: Details of reactor operation

Parameters	19th campaign	20th campaign
Reactor power	20.3 MWt	-
Reactor inlet / outlet Temperature	668 / 755 K	-
Central SA outlet temperature	808 K	-
Steam temperature	720 K	
Start of campaign	June 27, 2012	October 17, 2012
End of campaign	August 17, 2012	December 12, 2012
Energy generated	700 MWd /2.01 MU	633 MWd / 1.37 MU
Burn-up	100 GWd/t (One Mark-I SA)	155 GWd/t (Two Mark-I SA)

I.2 Physics Experiments at the End of 18th Irradiation Campaign

In the 16th irradiation campaign seven fuel subassemblies that had attained target burn-up of 155 GWd/t were replaced by fresh subassemblies. During start-up, large deviations were observed in critical heights with respect to predictions. These deviations were reconciled based on replacement worth measurement experiments. Reaction rate measurement by foil irradiation method experiment was also carried out. These experiments were carried out at the end of the 18th irradiation campaign.

The reactor physics code used in FBTR has provisions to include the effects of axial burn-up, isotopic changes and fission products to estimate reactor physics parameters like shutdown margin, linear power and total power in each subassembly. However axial expansion effect and bowing of burnt subassemblies cannot be modeled in the code due to complexities of these phenomena. Therefore, to validate the simulation code and to experimentally verify the above effects, replacement worth experiments were carried out.

Replacement worth experiments

The replacement worth experiment was performed at three locations (Figure 1) namely, Centre, first ring (01/01) and in third ring (03/08). In all these locations the same pair of subassemblies Mark-I (MK-I) with 144.5 GWd/t burn-up and Mark-I (new) with PHWR grade plutonium were used. The difference between the estimated worth and measured worth is the combined effect of bowing and axial expansion of burnt subassemblies.

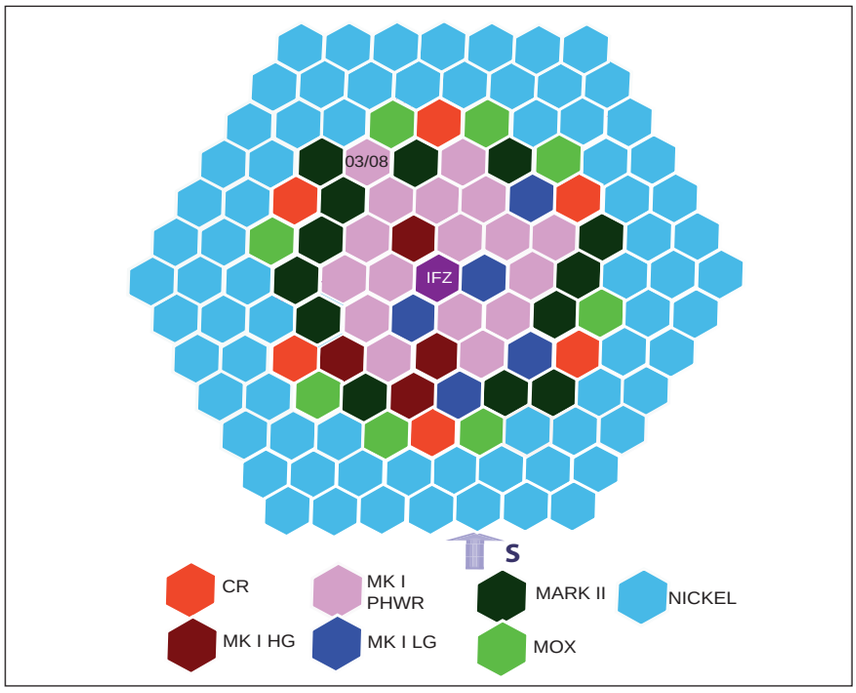

Fig. 1 *Core configuration during 18th irradiation campaign*

Measurement of worth of fresh Mark-I subassemblies replacing burnt Mark-I in first ring:

In the first experiment the burnt subassemblies at 01/01 was transferred to periphery and fresh Mark-I subassemblies were loaded in this position. The K_{eff} values were calculated for the core at

i) end of the core and

ii) after the fuel handling changes for this experiment.

The K_{eff} values were calculated at control rod height of 210 mm. The other parameters like shutdown margin and critical heights based on estimated control rod worth were computed. The reactor was started and critical heights were measured. K_{eff} at this critical height was computed. The difference between the K_{eff} value, at measured end of campaign critical heights and K_{eff} computed based on the measured critical heights was calculated. The deviation is found to be about 107 pcm.

Measurement of worth of fresh Mark-I subassemblies replacing burnt Mark-I in centre

This experiment was done in two steps.

Step 1**:** After the first experiment, the special subassemblies (IFZ 100) which were at centre (00/00) and the fresh subassemblies at first ring (01/01) were swapped. The critical heights were measured and K_{eff}, at this critical height, was computed.

Step 2: In this step, the fresh Mark-I at 00/00 was replaced by the burnt Mark-I from the periphery and the critical heights were measured. The difference in K_{eff} value, at measured critical heights, in step 1 and K_{eff} value at measured critical heights in step 2, which gives the worth of burnt subassemblies replacing fresh subassembly at 00/00 was found to be about 142 pcm.

Measurement of worth of fresh Mark-I subassemblies replacing burnt Mark-I subassemblies in third ring

This experiment was also done in two steps.

Step 1: In this step the Mark-I subassemblies at 03/08 location with 74.5 GWd/t burn-up and the Mark-I in 00/00 were swapped. Critical heights were measured and K_{eff} at this critical height was computed.

Step 2: In this step the burnt Mark-I at 03/08 was replaced by new Mark-I from the periphery and the critical heights were measured. K_{eff} at this critical height was computed. The difference of K_{eff} at critical heights at step 1 and step 2 of Experiment 3 was 104 pcm which gives the replacement worth of fresh Mark-I subassemblies in the third ring (03/08).

The deviation between the calculated and measured worth is found to be 100 to 112 pcm per subassembly. This is attributable to the effects which are not amenable to modeling in the reactor physics code. These effects include axial expansion of fissile stack, dilation and bowing of wrapper. These effects need structural deformation modeling by the core designers. Based on the current results, an approximate correction of 100 pcm per subassembly is required in predicting the critical height for fresh fuel replacing burnt subassemblies. Also the deviation in the calculation was very less whenever there were only internal transfers of subassemblies.

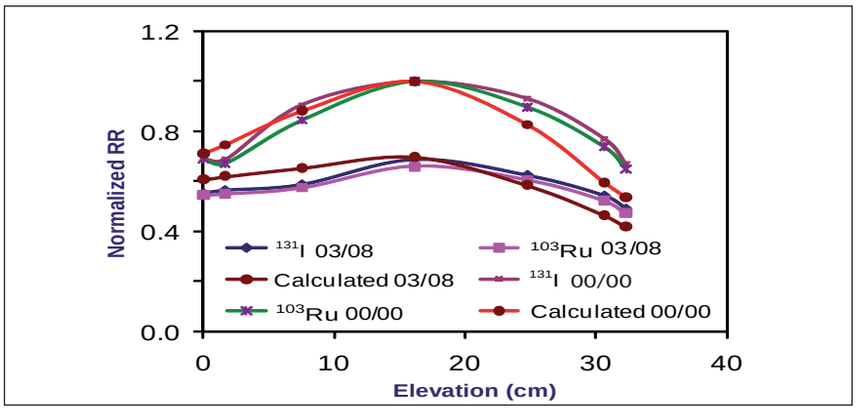

Fig. 2 *Measured and calculated activities at centre and third ring*

^{239}Pu reaction rate measurements

This experiment provides an independent estimate of reactor power. The reaction rates were measured in the 00/00 and 03/08 locations simultaneously.

Reaction rate distributions were obtained by irradiation of foils of fissile material. The fissile foils are made from 15 wt% PuO_2-ZrO_2 pellets clad with 2 micron thick nickel coating. Foils were loaded in foil holders and loaded in two capsules. The special subassemblies (ISZ-100) meant for the purpose was used to load two irradiation capsules (diameter 10/12 mm) carrying foils. The foil activation was carried out by four hour irradiation at a power level of 25 kW.

The calculated and measured activities are given in Figure 2.

At centre, the agreement between measured and calculated value is within ± 6% for ^{131}I and ± 9.3% for ^{103}Ru. At third ring the agreement is within ± 2.94% for ^{131}I and ± 1.54%, for ^{103}Ru. Measured form factors are slightly less than the calculated form factor and hence the peak linear power is smaller than the calculated linear power for given total power. For a given linear power the subassembly power is likely to be higher than the calculated value, by 6.1% at centre and 0.4% at third ring.

I.3 Fabrication of Sphere-pac Test Fuel Pins for Irradiation in FBTR

Sphere-pac fuel pins are prepared by vibrocompaction of microspheres of fuel. Since sol-gel process used in the fabrication of the fuel microspheres offers significant advantages over the conventional powder metallurgical processes used in the fabrication of pellets, efforts are underway at IGCAR in collaboration with Bhabha Atomic Research Centre, Mumbai in order to develop the sol-gel technology for the fabrication of fast reactor fuels. As a part of this endeavour, two sphere-pac fuel pins each containing coarse fraction of (U, Pu) MOX microspheres and fine fraction of UO_2 microspheres were fabricated for test irradiation in FBTR. The major objectives of this irradiation

campaign are to study the irradiation behaviour of the sphere-pac fuel pin including segregation, if any and restructuring as compared to a reference fuel pin containing MOX pellets.

The coarse MOX microspheres supplied by BARC were of 770±80 µm size and contained 53 % PuO_2, while the fine natural UO_2 microspheres were of 115±10 µm size (Figure 1) and were fabricated in IGCAR by using the jet-entrainment technique (Figure 2). This binary mixture was packed into a clad tube with typical dimensions of 5.7 mm ID and 531 mm length. As many as 75 runs were carried out for the production of UO_2 microspheres with the jet entrainment set-up, earlier, in order to optimize the process parameters viz., size of the nozzle, temperature of gelation, composition of the broth, washing routine as well as the conditions for calcination and sintering. The MOX as well as the UO_2 microspheres were checked for their physical integrity, dimensions and were found to conform to the desired chemical purity stipulated for the test irradiation in FBTR. Conditions for vibrocompaction also optimized.

A glove box train comprising facilities for handling the microspheres, vibrocompaction, end plug welding to fuel-pin and decontamination of the fuel pin was commissioned and qualified for handling MOX microspheres. This facility comprises of vacuum degassing set-up, weighing balance, sphere-transfer set-up (Figure 3), vibro-packing equipment, hardware loading station and an end-cap welding station (Figure 4).

The fuel pins after vibrocompaction of both fractions of microspheres (79% TD) and containing the hardware was held in the vertical position inside the welding chamber

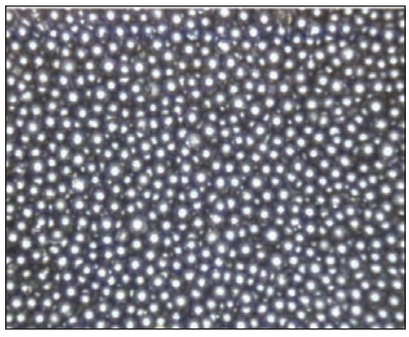

Fig. 1 *UO_2 microspheres*

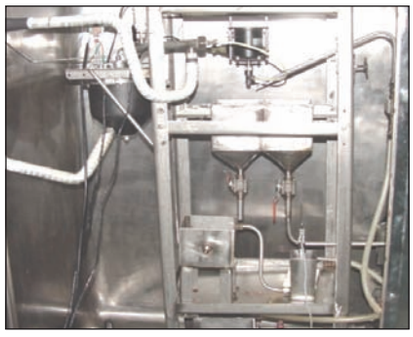

Fig. 2 *Jet-entrainment set-up*

and sealed with a helium pressure of 6.0-6.5 kg/cm^2 . The high helium pressure was selected to increase the thermal conductivity of the sphere-pac fuel column. The top end-plug was rammed on to the clad tube making an interference fit to seal the fuel pin maintained at high pressure. The end plug (AISI 316L) was press fit into the clad tube (D9) and welded in the (2G) position by autogenous pulsed TIG welding process. The adverse effects of elevated pressure of helium shielding gas during welding viz., onset of turbulence, arc instabilities, increased depth of penetration, narrow bead width and erosion of the tungsten electrode, were circumvented by optimizing the welding parameters. The welded fuel pin was decontaminated and subjected to quality control checks.

The welding procedure and fixture were qualified as per of the quality control protocols laid down for this process. These included visual examination, helium leak testing (10-15 MPa m^3/s max), X-radiography and metallography. The quality of the weld, pressure and purity of the plenum bond gas were ascertained with the help of tests performed on set-up and process test pins that were welded prior to the actual fuel pin welding. The MOX containing sphere-pac fuel pins were subjected to dimensional inspection, HLT and full length X-radiography in order to ascertain, the integrity of internals (Figure 5) as well as the weld joint. These quality control checks revealed that the pressure of helium was 6.1 kg/cm^2 with purity 98%, which are as per the specifications.

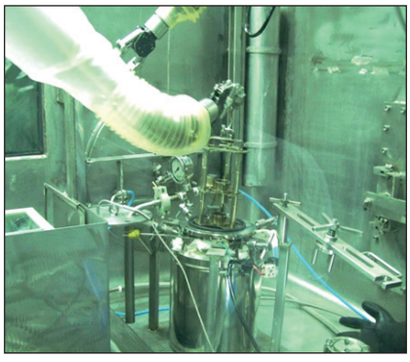

Fig. 3 *Sphere-handling facility*

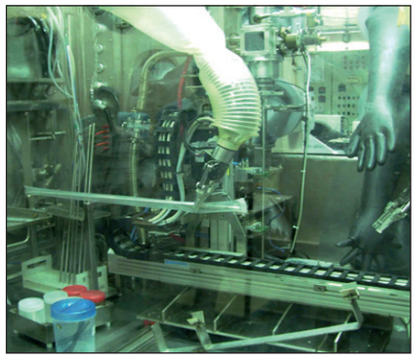

Fig. 4 *Vibro-packing and fuel pin welding*

Fig. 5 *X-radiography of the sphere-pac fuel pins*

The axial density profile was measured by using gamma scanning (attenuation) method in order to check if the plutonium distribution is uniform. The variation was within the acceptable value of ±1%. Earlier,it has been ascertained that uniformity of packing is not adversely affected by thermal cycling (Figure 6).

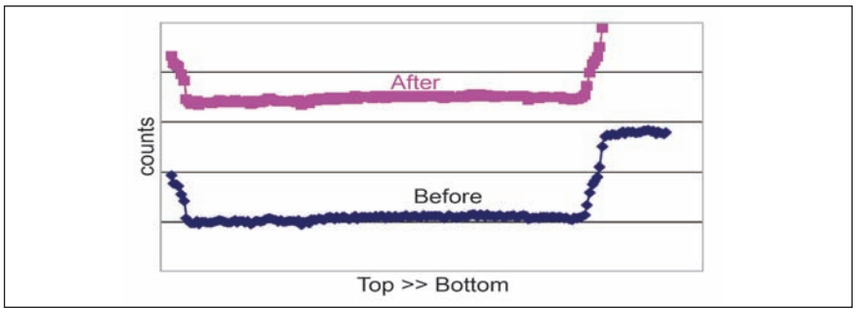

Fig. 6 *Axial density profile by gamma scanning before and after thermal cycling*

I.4 Failed Fuel Replacement in KAMINI Reactor

KAMINI is a 30 kW, ^{233}U fuelled research reactor. The reactor functions as a neutron source with a flux of 10^{12} n/cm^2/s at the core center. The reactor attained first criticality in October 1996 and nominal power of 30 kW in September 1997.

KAMINI uses plate type of fuel. Demineralized water is used as moderator, biological shield and coolant. Reflectors are made of beryllium oxide with Zircaloy-2 sheath. Cadmium is used as the absorber material in the safety control plates (SCP) provided for power control and shutdown of the reactor. Three beam tubes and three irradiation locations within the reactor tank facilitate neutron radiography of radioactive and non-radioactive objects, sample irradiation for neutron activation analysis, physics and shielding experiments. In addition there are two dry tube locations in the reactor tank for testing neutron detectors.

Nine rectangular fuel subassemblies are arranged in a 3x3 array. Each subassembly has eight flat plates of uranium aluminum alloy assembled in an aluminum casing to form the fuel subassemblies. Each fuel plate has a central meat section of 1 x 55 x 250 mm with 0.5 mm thick aluminum clad on both sides (Figure 1). A core cage is provided to arrest the movement of the subassemblies. The reflector modules are assembled around the core in a cubical arrangement for obtaining a fully reflected configuration (Figure 2). Adjustable reflector blocks (ARB) are provided for flexibility to alter the configuration in order to gain the required excess reactivity. In July 2008, the fission gas activity level in the reactor water started showing an increasing trend and was reaching the limit specified by the technical specifications (50 Bq/ml after 1 hour delay).

Based on investigation by an expert committee, it was decided to sample water from each subassembly through a sipping device and check for presence of fission gases and solid fission products. The sipped samples

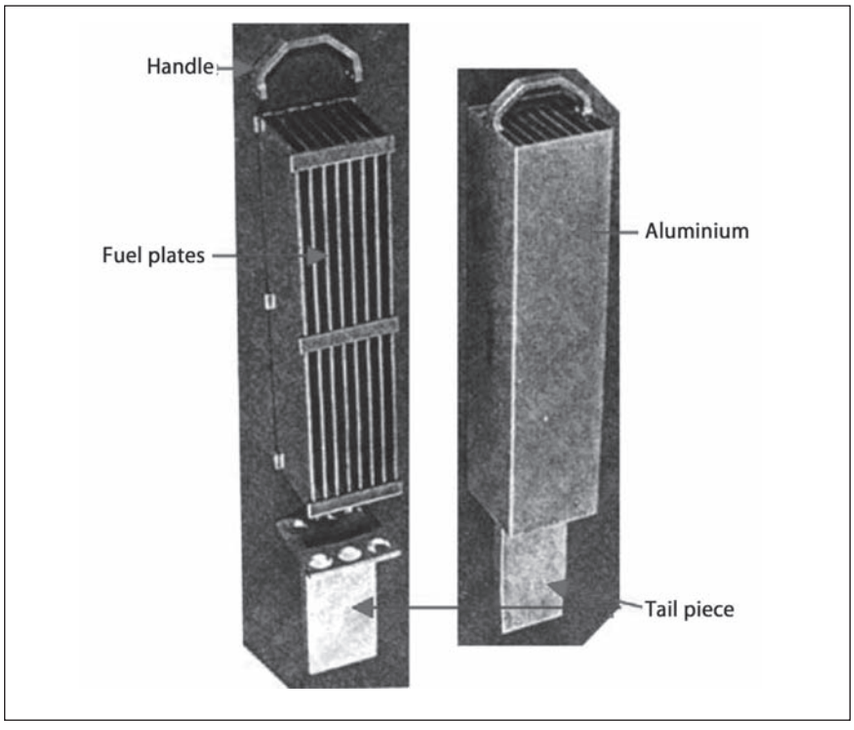

Fig. 1 *Fuel subassembly*

confirmed that radioactivity of fission product noble gases (FPNGs) at B1 position was about 13 times more compared to A3, which had the lowest radioactivity. Fuel subassemblies in location B2, C1 and C3 also showed 2-3 times more activity compared to A3. Though the exact cause of the release could not be ascertained, it was suspected to be due to the burn-up seen by the ^{233}U lodged in the subsurface of the clad. Absence of the iodine precursors indicated that the fission fragments were not liberated directly into the reactor tank water. Hence it was decided to replace the fuel subassembly in position B1 with a spare Pu-Al subassembly as envisaged in the design and its implications on reactor kinetics are covered in safety analysis. Since the worth of a Pu-Al subassembly is 2.8 mK lower than worth of ^{233}U-Al subassembly, even in the core periphery, additional ARB had to be added to compensate for the reactivity loss. These changes were carried out in May 2012, after review and clearance from safety authorities.

Pu-Al fuel subassembly was loaded in the vacant A3 position after shifting the subassembly in B1 position to storage location within the reactor tank. Both ARB-2 & ARB-3 were loaded in the core reflector position to compensate for the reactivity loss and provide sufficient excess reactivity for irradiating the samples for longer duration. Shielded fresh fuel transfer flask was used for handling the Pu-Al subassembly with radiological protection procedures under the supervision of a health physicist.

The combined worth of ARB-2 & ARB-3 and also worth of ARB-3 without ARB-2 in its position and excess reactivity was measured by making the reactor critical. The

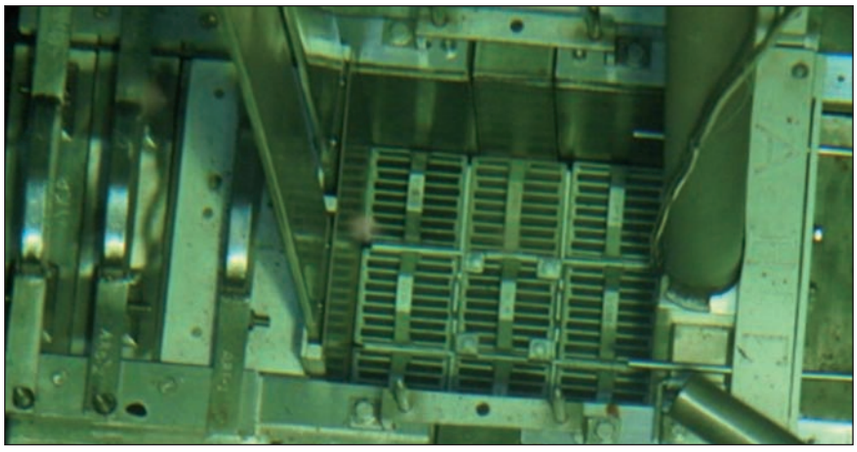

Fig. 2 *Reactor core*

water activity after removing the failed fuel has come down to one third of the water activity before replacement.

After replacing the failed U-Al fuel subassembly with Pu-Al subassembly and adding ARB-2 & ARB-3, the core excess reactivity was found to have reduced from 1.26 mK (measured worth before fuel handling) to 0.98 mK (measured after fuel handling). The Pu-Al subassembly replacing U-Al fuel assembly had a worth of 2.05 mK in KAMINI core as against 2.8 mK in position A3 measured in PURNIMA-III reactor. This could be attributed to burn-up seen by the U-Al subassembly. The measured worth of ARB-2 and ARB-3 in KAMINI is 1.546 and 0.342 mK as against the measured value of 2.5 and 0.8 mK respectively in PURNIMA. A difference of 1 mk was observed in the ARB-2 worth.

For investigating the cause, worth measurement of ARB-3 was carried out after shifting ARB-2 to storage location from the core. Subsequent criticality indicated a gain of around 0.9 mK and the same was confirmed by the repeat criticality.

For guiding the ARBs while lowering and positioning in the core, holes with stud arrangement are provided. A 4 mm projection is also provided at the bottom of ARBs for alignment with the slot on the top of module below ARBs. Improper alignment of the ARB can happen due to large gap between the hole and the studs in the supporting plate. This could affect the reflector position and also the water gap between the ARB-1 & ARB-2 and ARB-2 & ARB-3. It is inferred that the improper alignment of ARB-2, when it was loaded for the first time, could be the reason for the observed difference (1mK) in the worth of ARB-2 initially. After removing and reloading the ARB-2, the projection would have aligned in the slot properly. With this proper position of ARB-2, the reactivity worth of ARB-2 is almost matching with the worth measured in PURNIMA. During initial commissioning of KAMINI reactor, such change in core reactivity due to variation of water gaps between subassemblies and between the fuel assemblies and radial reflector had been observed. This change in reactivity is well below the technical specification limit of 110 pcm after handling core cage, fuel or reflector due to change in ARB's position. The reactor could be operated at rated power and for longer duration as sufficient excess reactivity is available for compensating the poisoning and coolant temperature rise.

The U-Al subassembly removed from position B1 will be shifted to Radio Metallurgical Laboratory hot cell for post irradiation examination.

I.5 Revamping of Neutronic Instrumentation System of KAMINI

Neutronic instrumentation system (NIS) is provided for monitoring the neutron flux from shutdown state to full power (30 kWt nominal) in KAMINI and to derive various parameters such as Log count-rate, Log power, Log-rate and Linear power for monitoring and for initiating safety action. NIS consists of two pulse channels for measuring start-up range flux and four DC channels for monitoring power-range flux. These detectors and channels have been in service since commissioning of KAMINI in 1996, a number of problems like high leakage current of detectors in the lower ranges, component failures, deterioration of PCBs, etc. were faced. Component obsolescence made it difficult to maintain these systems. Hence these systems were revamped with state-of-the-art instrumentation.

New detectors and processing electronics were procured.

The salient features of the new system are:

1. Detector, channel configurations and safety actions have been retained to ensure smooth transition with less additional wiring
2. Replacement of BCC detector of the pulse channels with fission counter
3. Uncompensated Ion chambers with mineral insulated cable, instead of soft-cables, for reliable connection between detectors and channels
4. Modular units for each function like power supply, amplification, trip etc. along with indications, test-point and online test facility to help in user-friendly maintenance
5. Additional Lin-P signal output from log-linear safety channels for monitoring channel discordance
6. Isolated 4-20 mA signal outputs for display and indicators
7. Functional and environmental qualification of all channels

Revamping of complete hardware was done in a phased manner. First, the uncompensated ion chambers (with soft cable) of all the four DC channels were replaced one-by-one with new detectors (with mineral insulated cable) housed in the dry tube assembly in the reactor (Figures 1 and 2). Test run was carried out with reactor operation before and after replacing the detectors. For each detector, the processing electronics channels were also replaced one-by-one.

Channel normalization was carried out wherever required. Linearity of the new detectors over the full power range was also evaluated.

In-situ calibration was carried out before keeping the channel in service to ensure healthiness of connections of trip channels.

Discordance monitoring

Since the on-line testing of the cable-continuity between the channels and the detector present in the old DC channels, was not satisfactory, it was dispensed with in the new nuclear channels and a computer-based Stand-alone discordance alarm system (SADAS) was designed, installed and commissioned for online monitoring of all the power-range nuclear channels of KAMINI, as suggested by SARCOP.

Fig. 1 *Detector with mineral insulated cable and connectors*

The replacement of all the four DC channels of KAMINI with new detectors and processing electronics was successfully completed and their performance during power runs was found to be satisfactory. The SADAS has proved to be a useful tool for ensuring the healthiness of these channels.

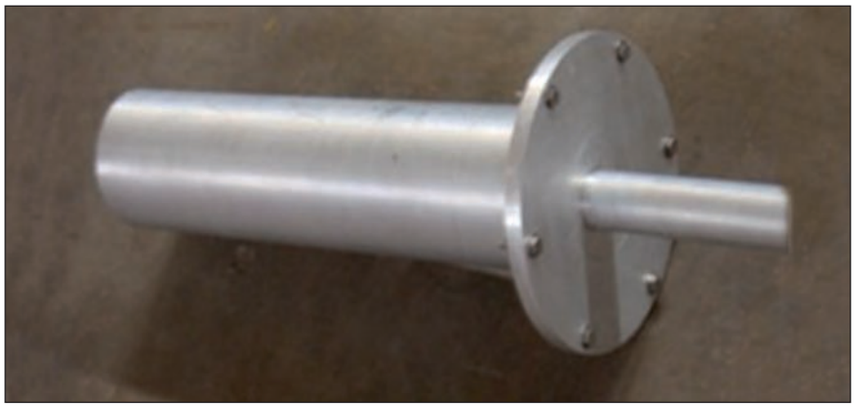

Fig. 2 *Ion chamber along with the dry tube*

CHAPTER - II

Prototype Fast Breeder Reactor

II.1 Construction Status of Prototype Fast Breeder Reactor

The entire civil structural work for nuclear island connected building had been completed (Figure 1). The construction of peripheral buildings surrounding nuclear island connected buildings, namely service water pump house, horton sphere, ventilation stack, diesel generator building and service building have also been completed.

Erection of major large diameter critical reactor components has been completed. 1751 out of 1758 numbers of core subassemblies and dummy fuel subassemblies have been loaded in the grid plate (Figure 2). Installation of large and small rotating plugs over the roof slab has been completed (Figure 3). With all reactor equipments in place, critical heavy density *in-situ* concreting in roof slab has been completed by maintaining the FME conditions without affecting the nuclear clean environment. Primary tilting mechanism and primary ramp, a part of inclined fuel transfer machine, has been fixed to grid plate. Erection of fuel handling equipment at various locations of fuel building is nearing completion. Pre-commissioning activities are in progress for the completed systems.

Erection of major long components commenced after elaborate planning and mock-ups and these include steam generators (Figure 4) and decay heat exchangers. All eight steam generators and four decay heat exchangers have been erected.

Commissioning of all the four numbers of emergency diesel generator from main control room (Figure 5), 230 KV gas insulated switchyard and 6.6 KV switchgear boards have been completed. All the three outgoing transmission lines from switchyard have been charged and connected to Southern Indian grid.

Erection of turbine equipments are nearing completion and all auxiliary equipments have been completed. Major heavy equipment like generator stator and rotor, live steam

Fig. 1 *Overall view of nuclear island connected buildings*

Fig. 2 *Inside view of reactor assembly with subassemblies loaded*

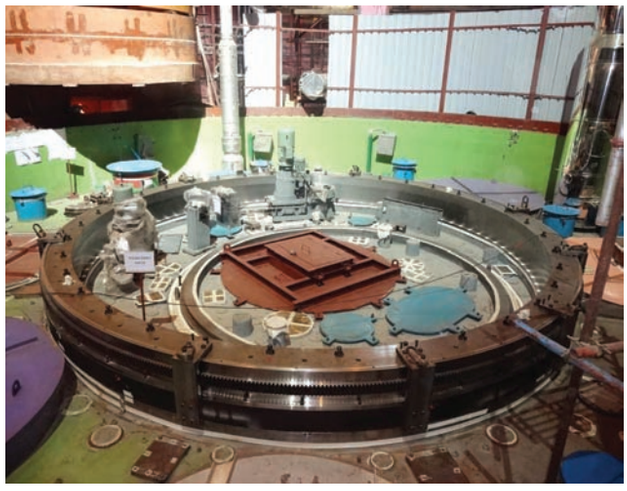

Fig. 3 *Large and small rotatable plug erected on roof slab*

re-heater, steam water separator lower and upper drum, three high, low and intermediate pressure turbine modules have been erected (Figure 6). Pre-commissioning works for the conventional auxiliary systems are in advanced stage of completion. Commissioning of de-mineralized water (Figure 7), raw water, normal service water and emergency service water systems have been completed.

The project has achieved an overall physical progress of 92.25% at the end of December 2012.

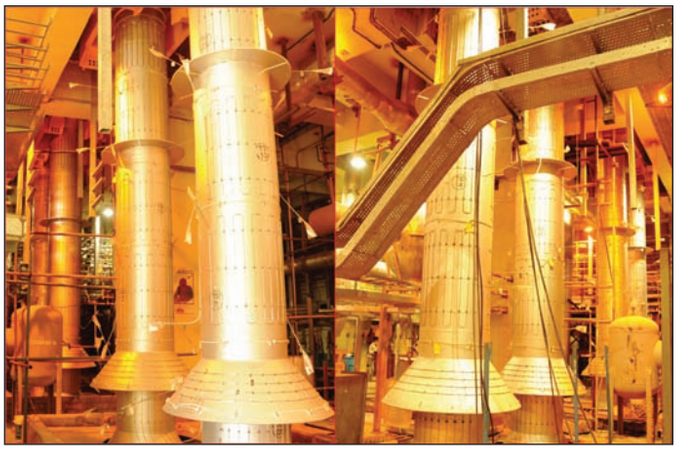

Fig. 4 *Steam generators erected in position*

Fig. 5 *Diesel generators in place*

Fig. 6 *Overall view of turbine floor*

Fig. 7 *Commissioning of de-mineralized water plant*

II.2 Microstructural Examination and Fission Gas Release Measurements on PFBR MOX Fuel Irradiated in FBTR to a Burn-up of 112 GWd/t

Comprehensive post irradiation examination has been carried out in the hot cells of Radiometallurgy Laboratory on PFBR MOX test fuel subassembly irradiated in FBTR at a peak linear heat rating of 450 W/cm up to a burn-up of 112 GWd/t. The fuel pin has annular MOX fuel pellets of composition $(U_{0.71}Pu_{0.29})O_2$ with enrichment of 53.5% U^{233}. D9 is used as the clad material. This report covers the results of microstructural examination and fission gas analysis (FGA) carried out as part of the performance assessment of the fuel.

Fission gas release behaviour gives valuable information on fuel performance. Fuel pins were punctured in a chamber, allowing the fission gas to expand into a pre-calibrated volume where the final equilibrated pressure was measured. Fission gas pressure was then calculated using the value of the internal volume (dead volume) of the fuel pin measured precisely from a separate experiment. The internal pressure ranges from 2.4 to 2.8 (± 0.1) MPa in the MOX fuel pins at ambient temperature (301 K).

The fission gas sample collected in a vial was analysed using a gas chromatograph with hydrogen as the carrier gas to arrive at the partial pressure of each gaseous fission product. The measured Xe/Kr ratio was found to be ~5.5 which is close to the yield ratio resulting from fission of U^{233}. Percentage of gas released was around 85%. The weight of the fuel pins, measured before and after puncturing the pins with a resolution of 0.1 mg was used to calculate the mass of fission gas and this allowed an independent confirmation of fission gas release.

Metallography was carried out on different axial locations of the fuel column on selected fuel pins. The fuel pin was impregnated with epoxy to immobilize the fuel column and also to prevent cracking and chipping of the pellets during sectioning. Transverse and longitudinal fuel-clad sections were extracted from the fuel pins at these axial locations using a custom built fuel pin cutting machine.

After remote sample preparation, the specimens were examined using optical microscope installed inside the hot cells. Replica of the metallographic specimens were extracted for preparing photomosaics of the fuel cross-sections and detailed measurements of clad OD and ID, pellet OD, fuel-clad gap and clad wall thickness. Typical photomosaics (Figures 1 and 2) prepared from replicas show fuel-clad gap at the peak power location. Fuel densification by the migration of porosities towards the central hole, resulting in an increase in its diameter to 2 mm from the nominal pre-irradiation value of 1.75 mm is clear. Fuel cross-sections at the top and bottom regions of the fuel column showed reduction in the central hole diameter and the fuel-clad gap.

Fuel pin sections where axial gamma scanning indicated localized peaks of ^{106}Ru revealed the presence of lustrous precipitates near the central hole which are inferred to be metallic fission products. Microstructural zones at different axial cross-sections indicated higher fuel temperatures at peak power location as evident from the columnar grain growth region. The metallographic cross-section at the locations where eddy current test showed defect indications revealed clad wall thinning due to fuel clad chemical interaction. The maximum clad wastage was found to be ~80 µm (Figure 3).

These results and the non-destructive tests carried out earlier show that the PFBR MOX test fuel subassembly irradiated in FBTR has performed well. The swelling and fission gas release are as expected. Fuel clad chemical interaction initiated internal clad wastage could be the life-limiting precursor at higher burn-ups.

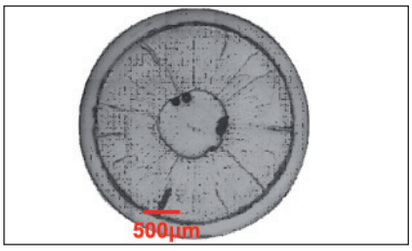

Fig. 1 *Photomosaic of MOX fuel pin cross-section at peak power location*

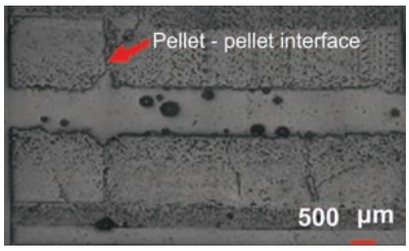

Fig. 2 *Longitudinal fuel pin section*

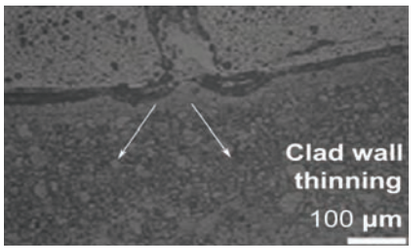

Fig. 3 *Clad wall thinning due to fuel clad chemical interaction*

II.3 Theoretical Predictions on Irradiation Behaviour of MOX Fuel Subassembly in FBTR

A test fuel subassembly consisting of 37 pins of PFBR type MOX fuel was irradiated in FBTR up to 112 GWd/t burn-up, to test the performance of PFBR fuel subassembly. The test fuel pin has a fuel column length of 240 mm with its top aligned with the top of Mark-1 active core. To assess the fuel performance, a blind code analysis was carried out using SATURN-FS1 code to study the irradiation behaviour of MOX fuel pin number 00/41 taken out of 37 pin bundle (Figure 1). The objectives of analysis is to find:

(1) Fission gas pressure and release

(2) Fuel pellet central hole diameter

(3) Fuel clad mechanical interaction and radial gap

(4) Clad and wrapper deformations

The results are discussed briefly as follows

Fission gas release

Estimated fission gas pressure inside fuel pin at the end of life is 2.5 MPa at 301 K temperature. This translates into fission gas release rate of about 75%. The variation of fission gas release along with various fission gas constituents with burn-up is shown in Figure 2.

Fuel pellet central hole

The central hole of fuel pellet at various axial levels from active core bottom at end of life is plotted in Figure 3. It is observed that the maximum pellet central hole diameter of 2.2 mm occurs at 57.5 mm from core bottom i.e., at maximum flux plane.

Clad outer diameter

The clad outer diameter at end of life at various axial levels from active core bottom is given in Figure 4. The maximum clad outer diameter of 6.65 mm, an increase of about 0.85%, seems to occur at 28 mm from core bottom. This is because, the swelling for D9 is predominant at lower temperature (673 K at 62 dpa) besides the irradiation creep being a strong function of swelling strain.

Wrapper deformation

Due to swelling and creep induced dilation of the wrapper, the width across flat of the hexcan changes along its length. The axial variation of wrapper width across flat at end of life due to void swelling and irradiation creep is shown in Figure 5. The available inter-subassembly gap is 0.75 mm whereas the maximum predicted dilation is 0.9 mm and this difference is attributed to the swelling correlation which predicted higher void swelling than the actual value which was confirmed by post irradiation examination.

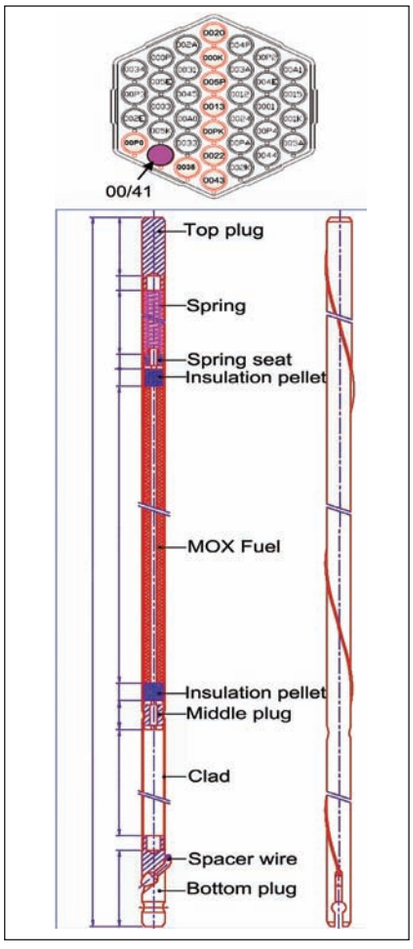

***Fig. 1** PFBR type MOX fuel pin irradiated in FBTR*

Other major observations

The maximum fuel pellet outer diameter increase occurs near

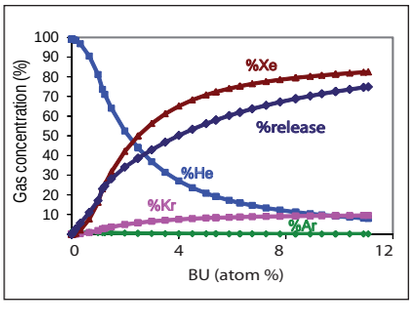

***Fig. 2** Fission gas release and gas composition*

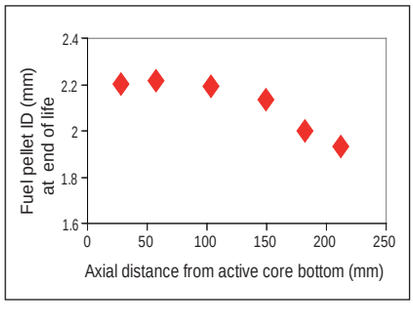

***Fig. 3** Axial variation of fuel pellet central hole at* end of life

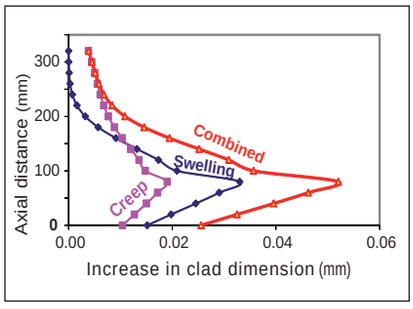

***Fig. 4** Axial variation of clad outer diameter at* end of life

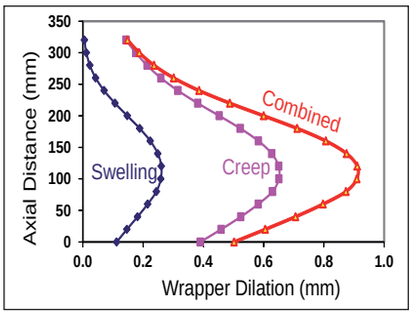

***Fig. 5** Axial variation of wrapper width across flat at end of life*

to active core top which is ~54 microns. Radial gap is present at end of life and hence, no fuel clad mechanical interaction all along the fuel pin length which is an important observation. The temperature distribution in the fuel pin at peak power location for beginning of life and end of life is calculated. It is inferred that the fuel central hole diameter has increased by ~27% at end of life and the fuel centre line temperature has reached 2565 K at end of life mainly due to the large gap drop because of fission gas dilution.

Currently, the code is being fine tuned taking into account the observations in the post irradiation examination. The analysis establishes the analytical capability of predicting the fuel performance.

II.4 Isothermal Testing of PFBR during Commissioning Stage: Objectives, Issues and Methodology

In PFBR, the liquid sodium would be preheated to 473 K and filled in primary and secondary sodium systems. After initial filling, it is essential to maintain the sodium temperature above 423 K throughout the primary and secondary systems in order to avoid freezing at any location. Before loading of fuel subassemblies, it is planned to perform isothermal testing of both primary and secondary sodium systems with the following objectives:

- Ascertaining functional behaviour of all the sodium systems at high temperature and nominal flow conditions.
- Verifying the performance of sodium components like sodium pumps, fuel handling systems, safety rod drive mechanisms, safety related auxiliary systems like hydrogen in sodium detection and hydrogen in argon detection systems, steam generator isolation valves, sodium dump, drain valves, etc.
- With increase in temperature, the impurity level in sodium will also increase which demands the service of sodium purification systems (both primary and secondary) before initial loading of fuel subassemblies.
- Also the performance of all the four safety grade decay heat removal systems with respect to the sodium temperature needs to be ascertained.

The isothermal testing is planned at 723 K for both primary and secondary sodium systems. As there is no other source to heat the primary and secondary sodium from initial filling condition (423-473 K) to 723 K, the strategy planned for heating is through operation of both primary sodium pumps and secondary sodium pumps at respective nominal speeds. By running the pumps, the frictional heat generated will heat the sodium and raise the temperature gradually. This strategy is also in-line with the experience from Phenix, Superphenix and other fast reactors.

As a commercial scale reactor from economy consideration, it is essential to complete the commissioning procedures in a short time and start power generation at the earliest. As isothermal testing is a part of commissioning activity, it is necessary to estimate the time required to bring the sodium systems to isothermal condition with the only available heat source namely through operation of sodium pumps.

Various heat losses from primary and secondary sodium systems to be considered during the heating operation are indicated schematically in Figure 1. Heat absorbed by sodium, structural materials and insulation are considered appropriately in the model as a function of temperature. The heat losses through biological shield cooling system, top shield cooling system, loss through decay heat removal systems (with dampers in fully closed condition), piping insulation, purification systems (both primary sodium initial purification and secondary sodium purification), loss through tube side of steam generators and pump mechanical seal cooling systems are also considered as function of temperature. Heat exchange between primary and secondary system through four intermediate heat exchangers immersed in primary sodium pool is modeled

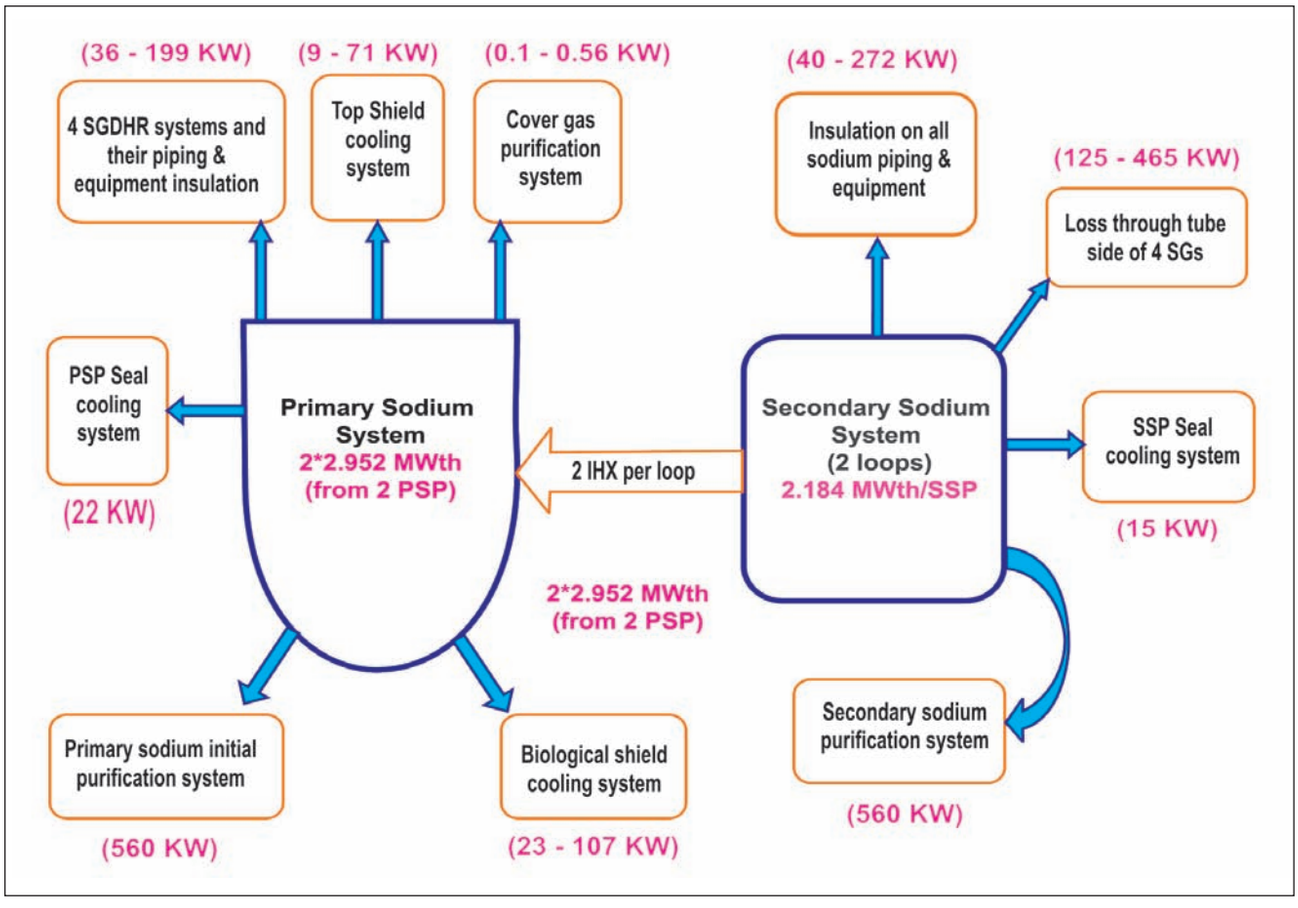

Fig. 1 *Flowchart of heat inputs and losses from primary and secondary systems*

appropriately by coupling the secondary sodium temperature with that of primary sodium.

The rate of heat loss through various systems as above are presented in Figures 2a and 2b as a functions of temperature of primary and secondary sodium systems respectively. The results of the study indicate that the secondary sodium system gets heated up faster than the primary system due to lower sodium inventory. Hence, there is simultaneous exchange of heat from both loops of secondary to primary through four intermediate heat exchangers immersed in the pool and the rate of heat transfer is presented in Figure 2. The heat loss from four safety grade decay heat removal systems (through insulation) is plotted in Figure 2a. The heat loss through cover gas purification system is insignificant (<0.5%) as compared to that from other systems.

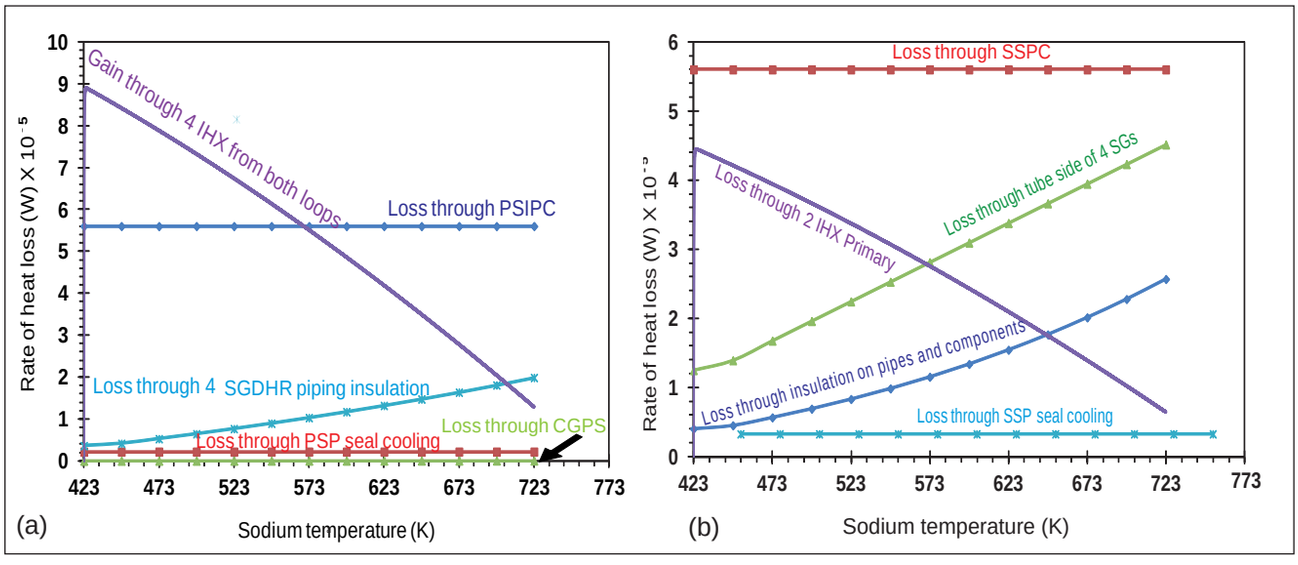

Fig. 2 *Rate of heat loss from (a) Primary and (b) Secondary system through various associated systems*

Considering various heat losses from the primary and secondary systems, temperature evolution in both primary and secondary sodium systems are predicted through a detailed in-house numerical computer program developed for this purpose. The results are given in Figure 3. It is considered that all primary sodium pumps and secondary sodium pumps are operated simultaneously at full power.

The total time duration for both primary and secondary sodium to reach 723 K from initial temperature of 423 K is estimated as 31.45 hours. The time duration to reach any intermediate temperature value can also be inferred from Figure 3. After attaining the isothermal condition (723 K), the operating speed of the pumps would be reduced to 315 rpm for primary sodium pumps and 767 rpm for secondary sodium pumps to maintain the isothermal temperature, accounting for the heat losses through various systems.

During heating operation, if any of the pumps (either primary sodium pump or secondary sodium pump) is tripped, the operation would be suspended and speed of remaining pumps would be reduced so that the heat losses in the system are compensated and the temperature would be maintained or reduced back to around 423/473 K at slower rate to meet the thermal stress limit in intermediate heat exchangers. The heating operation would be restarted, when the tripped pump is made available.

During commissioning, the performance test of safety grade decay heat removal system would be carried out with one loop at a time. During the test, heat loss from primary sodium through safety grade

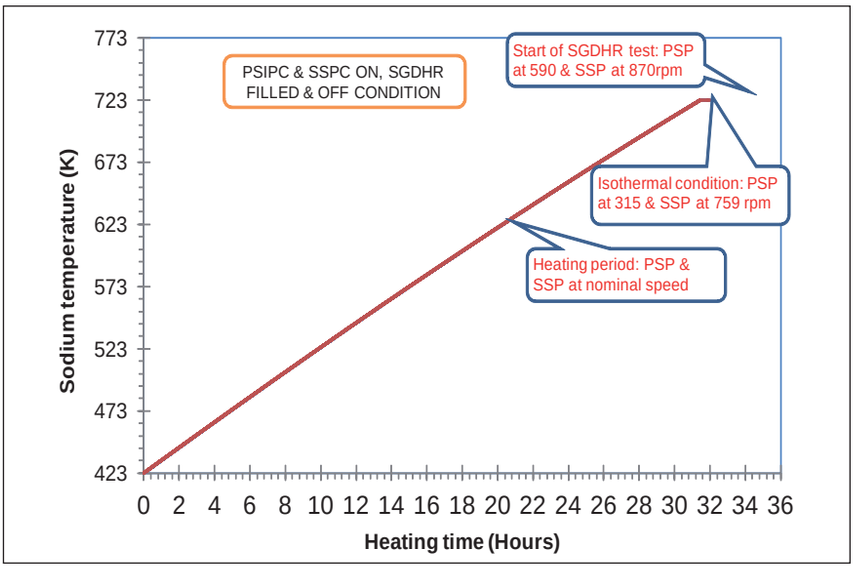

Fig. 3 *Evolution of temperature in primary and secondary sodium during the heating operation*

decay heat removal system via air heat exchanger with both dampers in full open condition is 6.24 MWt at 723 K. This additional heat loss from primary sodium system is planned to be compensated by increasing the speed of primary sodium pumps and secondary sodium pump (from earlier stabilized speed for the condition without operation of any safety grade decay heat removal system).

At 723 K, the total heat losses from primary sodium system is 0.98 MWth (excluding the safety grade decay heat removal under performance test) and the total heat loss from each secondary loop is 1.31 MWth. Hence, the total heat loss from primary and secondary loops together is 3.58 MWth. This study indicates that for compensating the total heat loss, the primary sodium pumps and secondary sodium pump are required to be operated at 590 and 870 rpm respectively.

The primary pump needs to be at the rated speed during testing of a safety grade decay heat removal system because, the rated power of two primary sodium pumps together is 5.90 MWth, which is lower than the heat loss through safety grade decay heat removal system being tested. Hence, the remaining and the other heat losses from primary system are compensated by increased speed of secondary pumps to 870 from 676 rpm which facilitate extra heat addition through the four intermediate heat exchangers. The rate of opening of damper and acceleration of primary sodium pumps and secondary sodium pumps should be synchronized such that the performance test can be conducted at essentially isothermal conditions.

During the test, in case the temperature drops below isothermal test condition of 723 K, the primary sodium initial purification circuit would be temporarily put off from service thereby keeping a check on temperature. Further, upper limit on the temperatures can be controlled by reducing the respective pump speeds.

This study has confirmed that through synchronized operation of both primary and secondary pumps in a controlled manner, the temperature of sodium systems could be raised to 723 K and all the isothermal testing can be carried out as envisaged for PFBR.

II.5 Thermal Hydraulics and Structural Mechanics Investigations of Primary Sodium Pump under Large Suction Re-circulation

In PFBR, two primary sodium pumps are operating in parallel to supply sodium to core at a flow rate of 7000 kg/s developing a head of 75 mlc. Hydraulic design of primary sodium pumps was finalized jointly by M/s. KBL-Pune and IGCAR after extensive experimental programme with 1:2.75 scale model studies at M/s. KBL. The testing programme included studies with different impeller-diffuser combinations to arrive at the preferred combination. Further, the preferred combination was specifically tested for cavitation behaviour by adopting paint erosion technique. After the model testing, full size primary sodium pumps have been manufactured by M/s. KBL-Pune and the performance of one of the impellers was tested in water. The test setup consists of a rectangular sump, stand pipe and pump assembly. The test included establishment of 'Head-Flow' curve also. At the end of 50 hours of testing, erosion marks have been observed on the pressure side of all the five blades. The reason for these marks could be either recirculation or non-uniform flow distribution at the impeller eye. It is also essential to understand the local pressure variations in the impeller. These features strongly depend on suction passage geometry. Further, the structural parts of the pump must be capable of withstanding flow induced vibration and transient thermal loadings possible during service of the pump in reactor. Towards these, detailed computational fluid dynamic studies have been carried out at our centre as well as Anna University and detailed structural mechanics studies have been carried out.

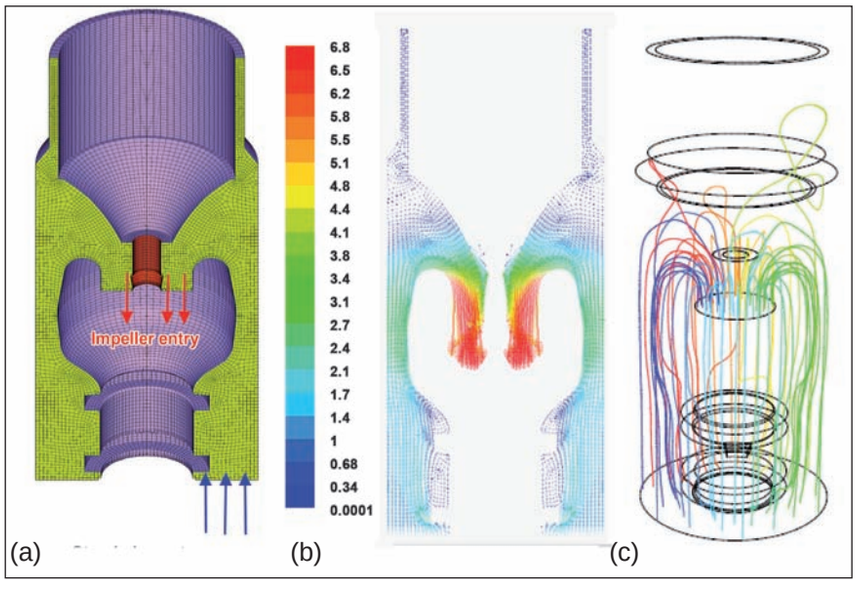

Fig. 1 *Investigation of flow hydraulics in suction passage (a) Stand pipe entry (b) Velocity pattern(m/s) and (c) Path lines*

Fluid mechanics studies

An integrated computational fluid dynamic analysis of test setup along with the pump is time consuming and computationally intensive. Hence, the analysis has been carried out by a decoupled approach, wherein

(1) Suction passage hydraulics,

(2) Impeller-diffuser hydraulics and

(3) Sump hydraulics are carried out independently.

The first set of investigations was carried out for the suction passage through which sodium flows towards the impeller (Figure 1). Based on 3-D analysis, it was noticed that the suction passage renders a non-uniform velocity field at the exit, where the flow takes a 180° turn before entering the impeller. In the experimental setup of the suction passage, a collar was provided to facilitate testing of the pump at different inclinations. A strong wake region was found to develop behind the collar which extended up to the impeller entry, with the associated flow non-uniformity in the entire suction passage. Detailed parametric studies have been carried out for the suction passage with different numbers of anti-vortex baffles attached to stand-pipe at various orientations with respect to the four webs of the pump. Also, the number of webs was increased from four to eight, in addition to varying the depth of the webs. Based on these studies and the conditions at testing site as well as in the plant, the following are recommended during testing:

- Eliminate the collar of the tilting mechanism in test passage
- Increase the number of webs to eight and extending the depth of the alternate webs.

The suggested modifications were found not to affect the requirement of net positive suction head significantly.

The impeller-diffuser hydraulics was

investigated for various combinations of flow and speed. The predicted axial velocity distribution at impeller entry shows that there is no suction recirculation at full speed and full flow conditions (Figure 2). Velocity distributions between impeller blades are found to be symmetric. As the flow progressed down by ~100 mm from the eye, axial velocity exhibited an upward flow close to the vanes on the pressure side. From the computational fluid dynamic simulations it was found that the pump develops 7.6 bar pressure head, which matched very well with test data. The pressure distribution at the tip of the vanes indicated low pressure zones in the wake of all the vanes, which could be sites for cavitation. Simulation of nominal condition of the pump did not show any bulk recirculation in impeller. Analysis was repeated for an operating condition of 20% flow at 100% speed. At this condition, the pump operates far away from the best efficiency point. The predicted axial velocity distribution at impeller entry for this condition is also depicted in Figure 2. It is clear that there is a strong suction recirculation within the impeller. The fluid flows into the impeller through the core region of the impeller eye while in the periphery it flows out of the impeller. Suction recirculation is the pertinent reason for blade erosion on the pressure side. Based on these studies, it is suggested that impeller should not be tested at low flow and high speed conditions during performance evaluation.

Detailed computational fluid dynamic analysis of water sump was carried out to quantify uniformity of flow entry to suction passage. It was found that the fluid completes multiple loops before entering the suction passage. This flow pattern is conducive for development of pre-swirls in the flow

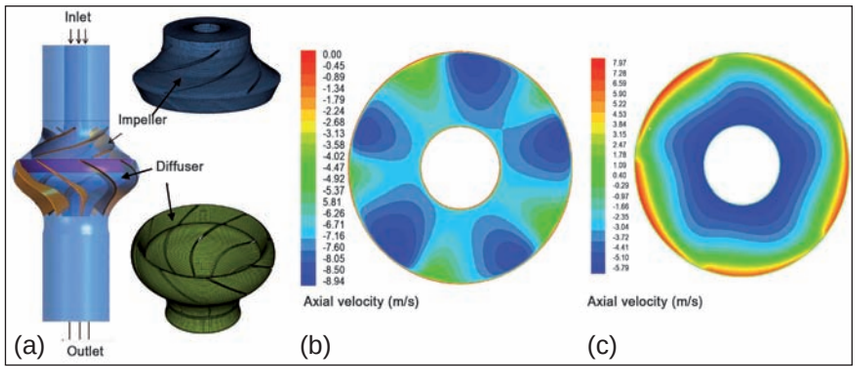

Fig. 2 *Investigation of flow hydraulics in impeller – (a) Diffuser assembly (b) At impeller eye 100 % speed & 100 % flow (negative velocity indicates flow is downwards without recirculation) and (c) At impeller eye 100 % speed & 20 % flow (positive velocity around periphery indicates flow is upwards with recirculation)*

that enters suction passage, which has to be avoided. Provision of a vertical porous plate in the sump before the suction passage was found to improve the sump flow.

Structural mechanics studies

From hydraulics studies it is found that the number of webs has to be increased from four to eight to improve flow uniformity. The extra four webs are welded with suction casing and these webs along with casing are subjected to stress analysis for mechanical as well as thermal loads. The stress due to mechanical load is primarily due to pressure difference between inner and outer surfaces of the pump casing which was found to be negligible. The outer surface of pump suction casing is in direct contact with cold pool sodium and during plant transients its temperature closely follows that of sodium. On the other hand, the inner surface of pump casing is not in contact with sodium. Due to this, large thermal stresses are induced during transients. The maximum thermal gradient determined for the event of 'loss of steam water system' is 40 K/min. Considering the weld all around the periphery of web in contact with casing slot, it is found that stresses are high, due to existence of thermal gradient in lower portion of web (Figure 3). To reduce the stress at weld location an innovative geometry is conceptualized in which the extra web portion inside the casing is removed in a curved profile (Figure 4) which avoids the existence of thermal gradient within the web. Secondly, a fillet is provided at all corners to reduce the stress values due to stress concentration. This optimized geometry has a reduced stress value meeting the design code limits.

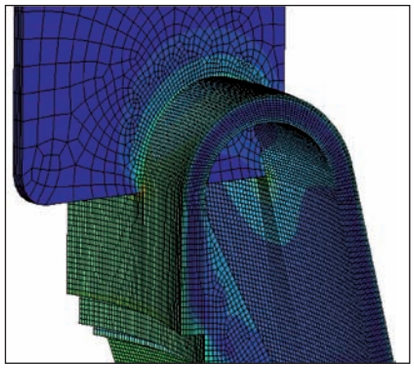

Fig. 3 *Instantaneous Von-Mises stress at web-casing junction during plant transient*

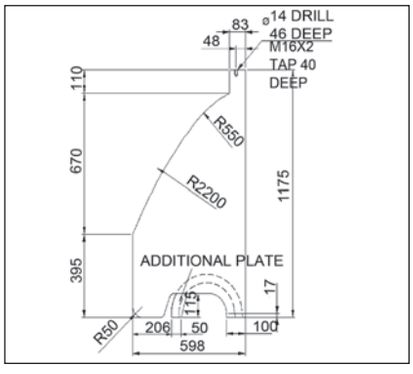

Fig. 4 *Improved web geometry*

II.6 Effect of Exhaust of Diesel Generators on Thermal Performance of Decay Heat Removal System under Extreme Wind Conditions

In the event of Class-IV power supply failure, the reactor is shutdown and the decay heat removal operation is carried out through a highly reliable and passive decay heat removal system known as safety grade decay heat removal system. This consists of four independent circuits, each with 8 MW heat removal capacity. Each circuit has one sodium to sodium decay heat exchanger and one sodium to air heat exchanger. An intermediate circuit connects the decay heat exchanger and air heat exchanger. All the flows in decay heat exchanger, intermediate circuit and air heat exchanger are by natural circulation. Decay heat exchanger transfers heat from hot pool to intermediate circuit and the air heat exchanger transfers the heat from intermediate circuit to the ambient air. The thermal center difference between decay heat exchanger and air heat exchanger drives the intermediate circuit flow and a tall stack provided above the air heat exchanger gives required driving force for the natural circulation of flow of air. In order to have high reliability for the safety grade decay heat removal system, diversity in the design of decay heat exchanger and air heat exchanger has been adopted. Two circuits (type A) have one design of decay heat exchanger and air heat exchanger in them and the other two (type B) have an alternate design concept for decay heat exchanger and air heat exchanger. Air heat exchanger-A is a serpentine tube type heat exchanger with single air inlet. Air heat exchanger-B is a vertical tube type heat exchanger with two air inlets. The air heat exchangers are located on the top of the steam generator building with their inlets at an elevation of +61 metres. There are two steam generator buildings in the plant, one on either side of reactor containment building. Steam generator building-1 (on the eastern side of reactor containment building) contains two safety grade decay heat removal loops, one of type-A and the other of type-B. Steam generator building-2 (on the western side of reactor containment building) also contains two safety grade decay heat removal loops, one of type-A and the other of type-B. There are two diesel generator buildings, one on both sides of reactor containment building and adjacent to each steam generator building. Each diesel generator building contains two diesel generators. Each diesel generator has a flue gas exhaust chimney with its exit window at an elevation same as air heat exchanger's air inlet window. Figure 1 shows the schematic arrangement of reactor containment building, steam generator building, air heat exchanger and the diesel generator exhaust chimneys. The distance between two adjacent chimneys is 9 metres. The crow flight distance between the diesel generator chimney's exit window and the inlet window of air heat exchanger's is 57 metres.

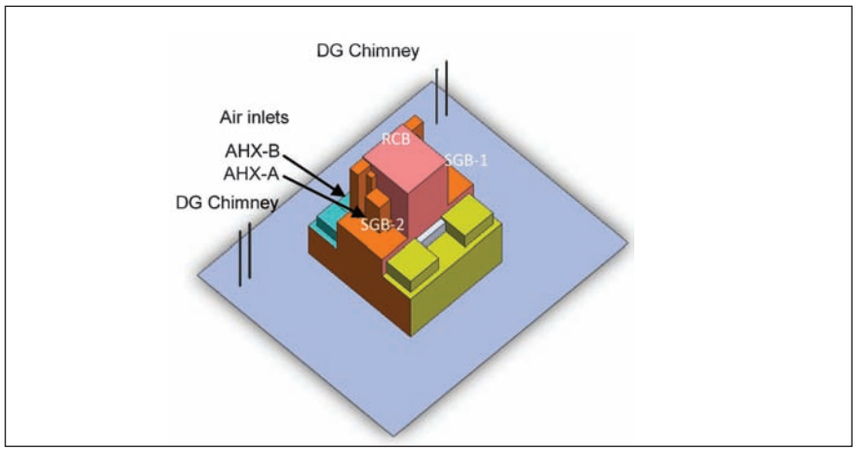

Fig. 1 *Layout of reactor containment building, steam generator building showing AHX and the DG exhaust*

Following Class-IV power failure, reactor SCRAM takes place based on pump speed reduction signal. The SCRAM signal trips the reactor and simultaneously the air heat exchanger's air dampers are opened automatically. Diesel generators also start automatically to cater emergency loads. The diesel generator exhaust flue gases come out of the chimney with a speed of 18 m/s and with a temperature of 653 K. If the wind speed and direction are in unfavorable condition, the flue gases may be carried towards air heat exchanger, increasing the ambient air temperature surrounding the air heat exchanger inlet. If the increase in the inlet temperature of air heat exchanger is significant, the heat removal capacity of air heat exchanger may deteriorate which is of safety

concern. Towards understanding the possibility of increase of air temperature adjacent to inlet of air heat exchanger due to the hot flue gas from diesel generator, a detailed 3-D computational fluid dynamic analysis has been carried out.

The computational domain includes the SG building, DG exhaust and ambient air between SG building and DG exhaust.

Both the DG exhausts are inlets to the computational domain. The air heat exchanger-A and air heat exchanger-B stacks are modeled with fixed mass outflow boundary condition at the top. Air inlet at 313 K is specified on two faces of the domain such that wind is directed towards air heat exchanger-B inlet.

Figure 2a shows the temperature distribution on the vertical plane in front of the SG building for the wind speed 25 km/h. It can be seen that the maximum temperature of air is at an elevation of 66 metres. The effect of wind speed on inlet temperature air heat exchanger has been studied in the range of 5-50 km/h. The estimated temperature rise in the ambient near the air inlet of air heat exchanger is shown in Figure 2b. It can be seen that for lower wind speeds the temperature increases with wind velocity but for higher wind speeds the temperature decreases.

For low wind speeds, the hot flue gas travels upwards due to buoyancy without affecting the inlet of air heat exchanger. At high wind speeds, the hot flue gas gets mixed well with ambient air leading to marginal change in the inlet temperature of air heat exchanger. However, at moderate wind speeds of about 25 km/h, the temperature increase is the maximum (8.4 K). Considering the increase in air inlet temperature, the heat removal capacity of air heat exchanger has been estimated. It is found that the capacity of air heat exchanger can reduce only by 0.2 MW/circuit.

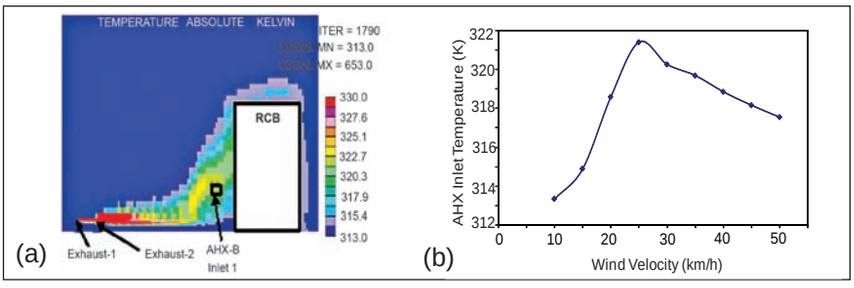

Fig. 2 (a) Air temperature field (K) in a vertical plane through DG exhaust and the AHX air inlet and (b) Air temperature at AHX inlet for various wind speeds

From the meteorological data for the year 2008 recorded at Kalpakkam site (Figure 3), It is seen that the unfavourable wind directions (ENE and WNW) occur for a duration of 12.8% in a year. The unfavourable wind speed magnitude of 6.94 m/s (25 km/h) occurs for a duration of 5.5% in a year. The unfavourable wind temperature (>313 K) occurs only for a duration of 0.4% in a year. From these data, it is clear that the probability of simultaneous occurrence of all these three together is very low. Further, during majority of the time, the wind speed is 7-18 km/h (2-5 m/s) and the ambient temperature is 297-303 K. For these conditions, the air inlet temperature of heat exchanger is predicted as 308 K.

Even if the temperature exceeds 313 K, the thermal hydraulic analysis indicates that the reduction in heat removal capacity of each safety grade decay heat removal circuit is very less. Further, since the safety grade decay heat removal circuits are kept over two SGBs, two safety grade decay heat removal loops (placed on same SGB) only see higher air inlet temperature due to particular wind speed and direction (which increases the temperature greater than 313 K) and the other two safety grade decay heat removal loops (placed in other SGB) will have the nominal ambient air temperature at their air inlet.

From the above studies, it is established that the present position of DG outlet need not be changed as it does not affect the heat removal capacity of safety grade decay heat removal circuits.

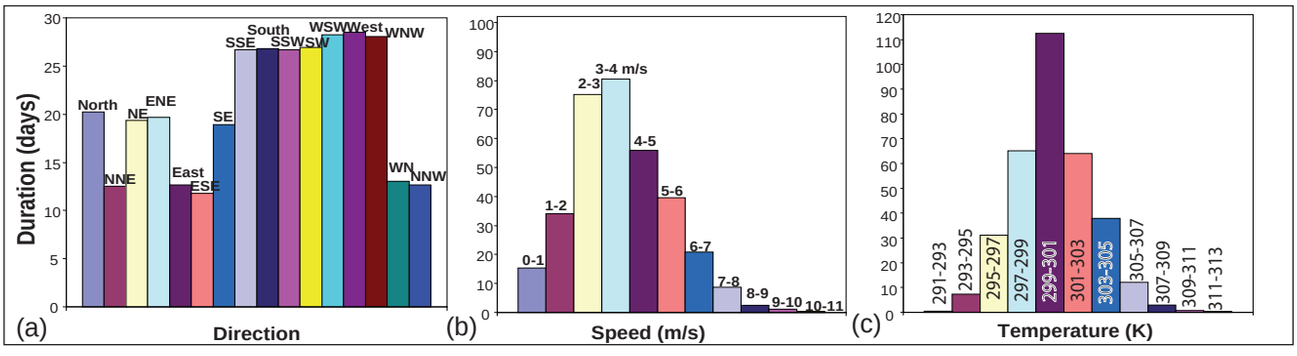

Fig. 3 Meteorological data on wind (a) Direction,(b) Speed and (c) Temperature for the year 2008

II.7 High Temperature Testing and Evaluation of Main Vessel - Roof Slab Weld Junction

Prototype Fast Breeder Reactor has three main heat transport circuits, viz. primary sodium circuit, secondary sodium circuit and steam-water system. The nuclear heat generated in the reactor core is removed by circulating primary sodium through the core. The primary sodium then transfers its heat to the secondary sodium through the intermediate heat exchanger. The entire reactor internals including core and primary sodium circuit are confined within the single vessel known as main vessel. Top shield consisting of roof slab and rotatable plug, provides biological and thermal shielding in the axial upward direction of the reactor and provides a leak tight barrier between cover gas and reactor containment building. Roof slab provides the support for all the components which enter into the reactor main vessel, heat exchangers, sodium pumps, fuel transfer machines etc.

Roof slab is erected and aligned with the main vessel. Main vessel and roof slab are expected to be concentric. Radial mismatch of 10 - 13 mm was observed during the weld fit up between the main vessel and roof slab. This mismatch is not uniform along the circumference of the vessel. This can be positive mismatch, negative mismatch and no mismatch condition as shown in Figure 1. In case of no mismatch condition, the stress induced due to the entire weight of primary sodium and other core internals will be membrane in nature. But in case of positive and negative mismatch conditions there will be bending stress in addition to the membrane stress. The magnitude of bending stress depends upon the offset between the main vessel and roof slab shell. In order to qualify this critical weld two sets of experimental and computational studies have been carried out. In the first set of studies, the main vessel-roof slab weld junction is analysed to understand the stress distribution along the surface of the junction. In the second set accelerated high temperature testing has been carried out to estimate the life of the weld junction.

Finite element modeling and experimental verification of main vessel-roof slab junction

A welded plate with the same material and having maximum weld deviation of 13 mm supplied by BHAVINI is used for the experiment. The plate has been further machined such that the maximum stress will act near the weld location. The shape and some of the important geometrical details of the experimental specimen are given in Figure 2. Thickness of the main vessel portion is 25 mm and the thickness of the roof slab shell is 30 mm. Both roof slab shell and main vessel are made of SS 316LN material. Strain gauges have been pasted at the critical locations to measure hoop and longitudinal strains at these locations.

Three dimensional numerical analysis of main vessel - roof slab offset geometry has been carried out using the finite element based ABAQUS software. Main vesselroof slab offset geometry has been modeled using 8-noded linear brick elements. One end of the geometry is fixed and concentrated downward force is applied at the other end. This gives an overall idea about the stress distribution along the surface of the geometry under the combined action of axial and bending loads. Based on the finite element model studies, it is found that the maximum Von-Mises stress of 129 MPa under the given loading condition acts

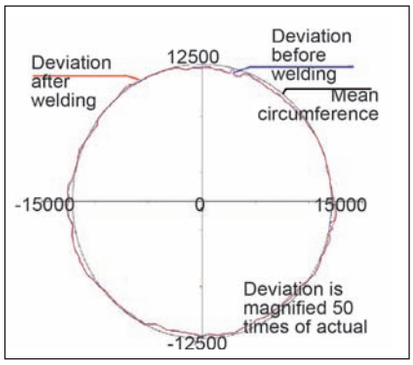

Fig. 1 Manufacturing deviation found at main vessel – roof slab joint before and after welding

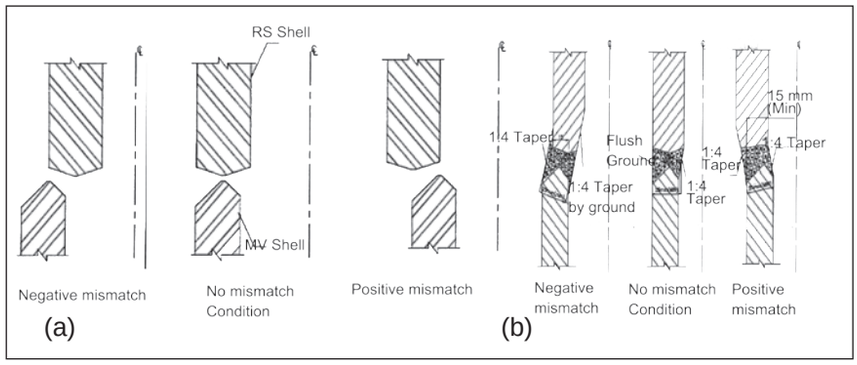

Fig. 2 Manufacturing deviation found during the weld fit-up between main vessel-roof slab shell joint (a) Before and (b) After welding

away from the weld location. Also, critical locations in the weld junction have been identified for fixing the strain gauges while conducting experiments.

Experimental and numerical values of hoop and longitudinal strains at the critical locations have been compared in Table 1. The experimental results are in good agreement with the numerical results. The minor deviation in the comparison is due to the deviation in identifying the similar location for comparison.

High temperature of weld junction

A high temperature creep strength test facility has been developed indigenously to test the main vessel-roof slab transition specimen for creep strength, which is depicted in Figure 3. The specimen has been loaded with a magnitude of four tonnes at its free end. The load applied is such that the state of stress acting in the test specimen is 10% more than that in the prototype main vessel roof slab shell joint. The load is applied by means of a hydraulic jack. This method of application of load simulates a constant stress condition throughout the experiment as in the prototype. In the prototype, the above junction will experience creep during decay heat removal condition. The maximum temperature at the main vessel-roof slab shell joint under decay heat removal condition is 773 K.

Table 1: Comparison of strain gauge data with FEM results

Location		Strain (FEM) - μ	Strain (Guage data) - μ
Hoop direction	SG-1	38.92	15.82
	SG-4	-72.70	-57.71
	SG-8	-103.8	-14.92
Longi-tudinal direc-tion	SG-2	-59.16	-19.40
	SG-3	284.00	296.40
	SG-7	460.28	348.23

Fig. 3 *Creep strength test facility*

The total duration of the decay heat removal condition (160 times) for the PFBR design life of 40 years is 16000 hours. The main vessel-roof slab shell joint specimen is tested at a temperature of 873 K to get quick result. Temperature for the accelerated experiment (873 K) has been derived based on Larson Miller parameter.

Experiment has been conducted at 873 K for a period of 900 hours and no crack was noticed at the end of the test. Considering there is a crack at the end of 900 hours, the rupture life of the specimen for the reactor operating conditon was found to be 838964 hours. Since, only a single specimen experimental result is avilable, additional factor of safety (4.6) has to be applied on the above life to take care of the statistical variation in the test results as per ASME Sec VIII Div.2 mandatory Appendix-6. To take care the variation in rupture life for the average to minimum value, additional factor of safety (3.85) has also been applied to the above rupture life. The net acceptable life of the junction has been determined to be 47372 hours.

Total hold time for the main vessel-roof slab joint at 773 K is only 16000 hours for the design life of 40 years. Thus, the allowable number of years in the creep life of the main vessel-roof slab joint under manufacturing deviation is computed to be 118 years.

The conclusions of these studies were instrumental in accepting the mismatch between the main vessel and roof slab shell.

II.8 Performance Testing of Transfer Arm in Sodium

Transfer arm is the in-vessel fuel handling machine of PFBR used for transferring of subassemblies within the core. Transfer arm (Figure 1) was designed by IGCAR and fabricated at M/s. L&T, Hazira. After shop floor testing, machine was assembled in Large Component Test Rig in Hall-III and 100 cycles of testing was carried out successfully. Then the machine was dismantled and reassembled in test vessel-5 by following the same procedure as planned in the reactor (Figure 2).

A modified grid plate arrangement is located inside the test vessel-5, supporting transfer pot and a cluster of seven subassemblies which simulates the core (Figure 3). Subassemblies are positioned inside the sleeves provided in the grid plate in hexagonal pattern where bowed subassembly is at the centre and remaining six straight subassemblies surround it. This is to simulate the smooth operation of the transfer arm even at the most unfavourable conditions. Transfer pot is positioned in the core such that for a 90 degree rotation of the transfer arm, the gripper subassembly travels from the core to transfer pot location. Transfer arm rests on the roof slab model at the top of test vessel. Elevation of the subassemblies and the transfer pot were maintained similar to the reactor conditions. To enhance the reliable functioning of the transfer arm, some design features were incorporated after air testing.

To achieve the single failure proof of gripper hoisting mechanism, new gear box system consisting of self locking type gear trains are provided. Additional gear box with electro magnetic brake is provided in the gripper hoisting mechanism.

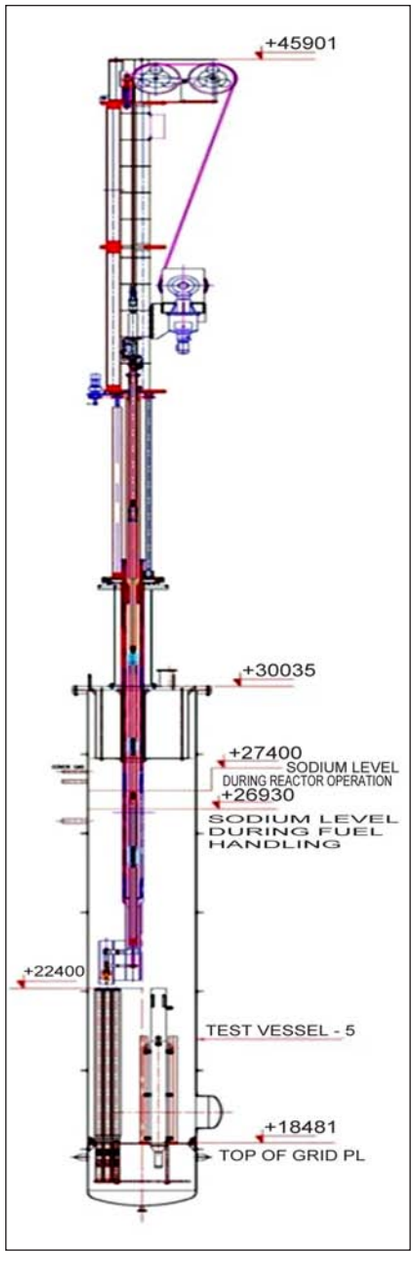

Fig. 1 *Schematic of transfer arm test setup*

Fig. 2 *Partially dismantled transfer arm*

Mechanical locking arrangements are incorporated for locking the gripper assembly for loaded transfer position and parking position. Additional sensors are deployed in the machine for improving the redundancy and better controlled operation of the instrumentation system.

A bellow was welded between the inner tube and outer tube of gripper hoisting mechanism. All pin joints

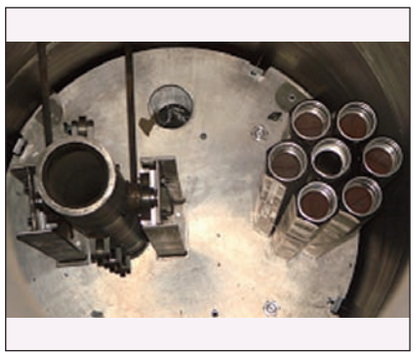

Fig. 3 *Cluster of subassemblies and transfer pot on grid plate*

of outer tube were seal welded. During testing, 600 mbar pressure by argon was maintained in between inner tube to outer tube for checking healthiness of the bellow.

One cycle of testing consists of transferring central subassembly from the core to transfer pot and vice versa. Operation of the transfer arm is carried out remotely through VME(versa modular european) based control console. Transfer arm consists of four operating mechanisms like gripper hoisting mechanism, guide tube hoisting mechanism, tranfer arm rotation mechanism and finger actuating mechanism. While testing, motor torque was continuously monitored. Testing is carried out in different conditions viz. air at room temperature, hot air, hot argon and sodium at 473 K. Hot air and hot argon testing were carried out at different temperatures like 333, 353, 373, 393, 423, 433 and 443 K.

During hot air testing at 433 K, while raising, a jerky motion in the gripper hoisting mechanism was observed at transfer pot location followed by tripping of motor due to high torque. This was due to mechanical locking of the foot of the subassembly with the bottom location of the transfer pot. Required design modifications were carried out in the foot of the subassembly and further testing were trouble free.

A total of 223 cycles of testing were carried out for the transfer arm, out of which 124, 33, 4 and 62 cycles of testing were carried out at room temperature, hot air, hot argon and sodium respectively.

The transfer arm was subjected to all conditions of operations and were found to be smooth. Motor torque required for the operation of all the mechanisms of transfer arm were within the acceptable limits. Torque required for raising the subassembly was measured by manual cranking and found to be 11 to 14 N-m. The operation of the transfer arm at 473 K after raising and lowering the sodium temperature to and from 673 K indicated need for a few modifications for smooth operation in the machine. The same is being addressed and meanwhile all other operations even after raising the sodium temperature to 823 K have been observed to be trouble free.

II.9 Design and Testing of Core Flow Monitoring Mechanisms I and II for Prototype Fast Breeder Reactor

In PFBR, subassemblies require different sodium flow based on their heat generation and position in the grid plate. This is achieved by providing suitable pressure drop devices at the bottom of each subassembly. There is a need for in-core flow measurement to ensure that each subassembly is receiving the required sodium flow. Core flow monitoring mechanism instrumented with eddy current flow meter is used for this measurement. PFBR has two core flow monitoring mechanisms, one for central canal and the other for observation port of small rotatable plug named core flow monitoring mechanisms I and II (Figure 1). Core flow monitoring mechanism-I measures high flows of fuel subassemblies and core flow monitoring mechanism-II measures low flows of blanket and storage subassemblies.

The upper part of core flow monitoring mechanism holds all the operating mechanisms, position sensors and motor while the lower part holds outer stationary tube and inner mobile assembly tube. Bottom end of mobile assembly is having a flow guide that contains eddy current flow meter. Sodium flow from subassembly outlet is made to pass around eddy current flow meter housed inside the flow tube. Eddy current flow meter mainly consists of three coils wound on a soft iron bobbin placed along the flow axis as shown in Figure 2. Central coil is called primary (P1) and secondary

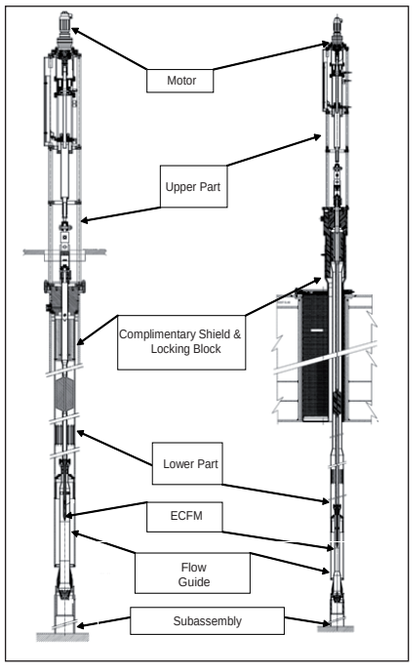

Fig. 1 *Core flow monitoring mechanisms 1 and 2 during flow measurement condition*

coils are placed symmetrically, one in upstream side of primary (S1) and the other in downstream side of primary (S2). All the three coils are encapsulated in stainless steel pocket. The primary coil is excited with a constant current sinusoidal source. The difference of voltages induced in the secondary coils is proportional to the sodium flow.

Both the mechanisms have common functional features.The upper parts are identical but lower parts have dimensional variation to suit respective locations as shown in Figure 3. The mechanisms can take a maximum misalignment of 22 mm with respect to subassembly. The mechanism is placed in respective positions and flow straightener connected to translation tube is lowered to sit on the subassembly head for flow measurement. It is raised then and by suitable rotation of small rotatable plug and large rotatable plug positioned on head of next subassembly and again the lowering operation is done to take measurement. This vertical travel is provided by means of a reduction geared reversible motor with a screw-nut mechanism. During flow measurement, a small downward force is applied to maintain leak tightness between subassembly and flow guide. Hydraulic experiments were carried out to determine the uncertainty in estimating the leakage flow and the hydraulic resistance in the flow guide region during core flow measurement. A 1:1 scale model study was carried out in water with Reynold's number simulation to determine the leakage flow, pressure drop and velocity in the sensor region. The test set-up for the experimental studies is shown in Figure 4. Experimental studies were carried out for core flow monitoring mechanisms I and II.

Figure 5 shows the percentage of flow through core flow monitoring mechanism I against the actual flow exiting from the subassembly. It can be seen from Figure 5 that the percentage flow through the core flow monitoring mechanism is 58.5%. The corresponding velocities in the sensor region for the different fuel zones vary from 0.76 to 1.32 m/s and the overall pressure drop in core flow monitoring mechanism for the fuel zones vary from 3.00 to 8.97 kPa. Similar results were obtained for core flow monitoring mechanism-II also.

The core flow monitoring mechanism I and II were manufactured by central workshop division successfully and their assembly and functional testing is in progress in Engineering Hall-III. Manufacture of eddy current flow meters for core flow monitoring mechanism I and II were completed. Manufacture and erection of test section for sodium calibration of eddy current flow meters is nearing completion at steam generator test facility and calibration studies will be taken up shortly.

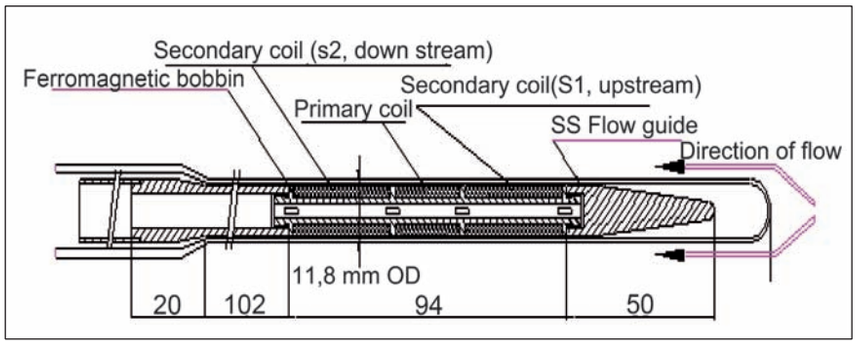

Fig. 2 *Eddy current flow meter*

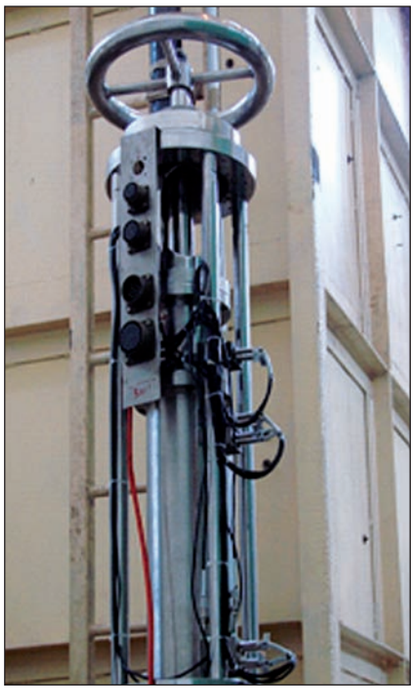

Fig. 3 *Upper part of core flow monitoring mechanism*

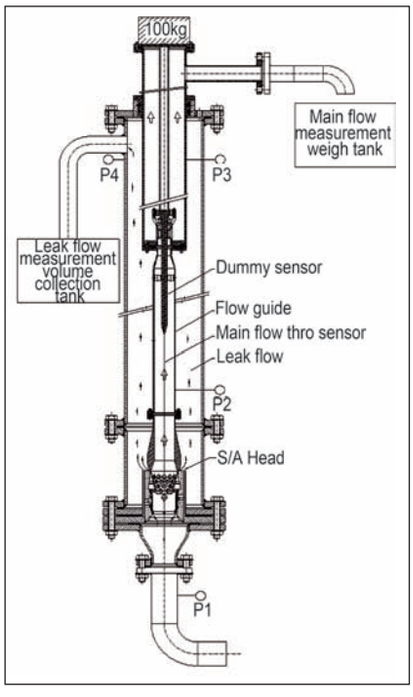

Fig. 4 *Experimental test setup*

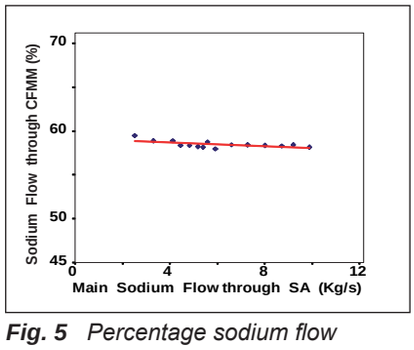

Fig. 5 *Percentage sodium flow through core flow monitoring mechanism 1*

II.10 Integrated Testing of Eddy Current Position Sensor with DSRDM

There are two independent shutdown systems in PFBR. Diverse safety rods (DSR) having B_4C absorber in conjunction with diverse safety rod drive mechanism (DSRDM) form second shut down system. Eddy current position sensor (ECPS) is being developed for measurement of drop time of diverse safety rods as well as confirmation of bottom most deposition of DSR. It is a sensor based on the principle of change of mutual inductance with insertion of DSR in the dashpot. The schematic of ECPS coils is shown in Figure 1. Performance of ECPS with regard to position detection of DSR in the bottom-most deposited condition has already been established by sodium testing. Demonstration of the integral performance of ECPS along with DSRDM and DSR is required before its adoption in reactor. In this regard, prototype DSR subassembly and lower part of prototype DSRDM were modified to incorporate ECPS coils. The schematic of location of these coils in DSRDM is shown in Figure 2.

ECPS has five coils, as shown in Figure 1, out of which one primary and two pick-up coils are placed just above the electromagnet of DSRDM. The secondary coil is placed in the sheath of DSR (Figure 2). The sensor coil is positioned near the dashpot location in the DSR sheath. The secondary and sensor coils form a closed loop by joining them in series and grounding both ends to the stainless steel sheath near dashpot location. The primary leads are terminated to flexible copper cables and routed out with the support of a flexible spring.

Testing of DSRDM (along with ECPS coils) and DSR has been carried out in the high bay of Engineering Hall III. Air testing on DSRDM was carried out in air test stand. Water was used as the working fluid of dashpot in air testing. ECPS coil voltages were recorded using data acquisition system.

In this testing, ECPS was tested in radially misaligned condition (which is the most frequent condition encountered in reactor) as well as with the axial misalignment up to 50 mm. The effect of radial misalignment on the performance of ECPS was already studied experimentally in static sodium testing. The axial misalignment was created by placing the electromagnet at different positions with respect to the DSR sheath. The readings were taken at axial misalignments of 0 to 50 mm between primary and

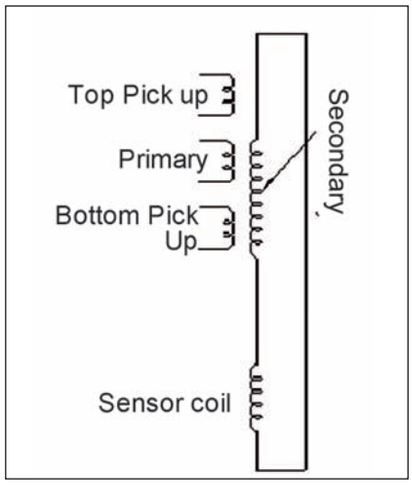

Fig. 1 *Schematic of eddy current position sensor*

secondary side coils of ECPS. Drop time measurement with acoustic sensors was also carried out to compare the results obtained with ECPS.

Primary winding of ECPS was energised with a constant current of

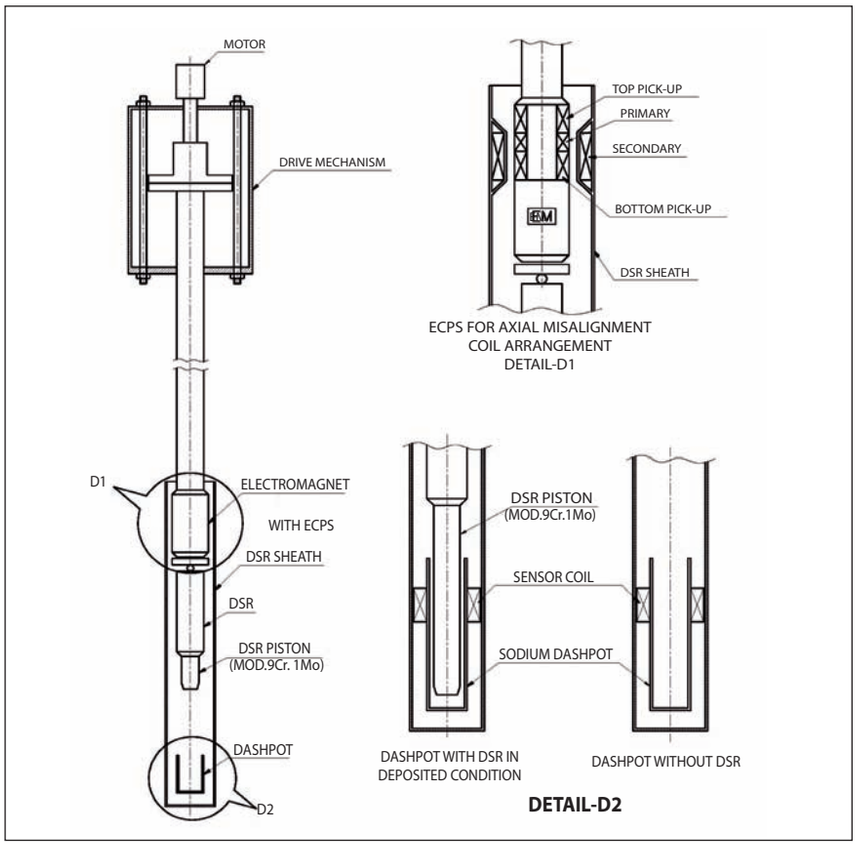

Fig. 2 *Location of eddy current position sensor coils in mechanism*

200 mA at 200 Hz and voltages of both the pick-ups were recorded for DSR deposited and not deposited conditions. From the plot of the pick-up voltages, the free fall time of DSR was calculated. The typical variation of pick-up voltage with insertion of DSR in the dashpot is shown in Figure 3. From Figure 3 the free fall time (i.e. the time the DSR takes to reach the bottom coil location after the SCRAM command) is measured. During testing acoustic sensors were also used for measurement of drop time and both the sensors yield almost identical values of DSR free fall time.

The integrated testing of eddy current position sensor with DSRDM has proved the DSR position detection in the dashpot and the free fall time measurement capabilities of ECPS. The testing was carried out with radial misalignment of 6 mm and with axial misalignment of 0 to 50 mm. These are the conditions which the sensor is likely to undergo in reactor and the present testing has demonstrated the successful working of sensor under all the tested conditions.

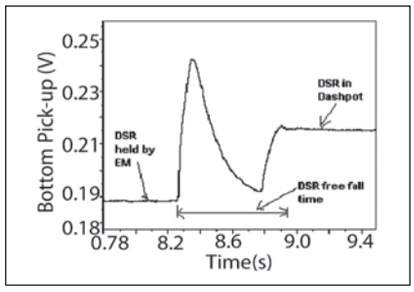

Fig. 3 *Measurement of diverse safety rods free fall time from eddy current position sensor pick-up voltage variation*

II.11 Qualification of Inclined Fuel Transfer Machine Chain by Testing and Analysis

In Prototype Fast Breeder Reactor, transfer of subassemblies between reactor and fuel building is carried out by inclined fuel transfer machine (IFTM) as shown in Figure 1. The hoisting mechanism of IFTM uses a dual welded link chain for hoisting the transfer pot carrying spent/fresh subassembly from/to the main vessel. Integrity of the chain is very important to avoid free fall of the pot carrying spent subassemblies into the vessel and consequent damage to the reactor. The chain made up of SS 304L was manufactured at M/s Indian Chains Pvt Ltd., Kolkata. The chain passed all the specified load tests. However, the surface of links indicated some minor notch-like-defects during liquid penetrant inspection. Hence, it is felt that there is a need to qualify the chain by testing under cyclic loading followed by break load to ascertain the life of the chain.

Two specimens, in which more surface defects found during the inspection, have been selected for testing and each specimen has three links. Special supporting fixtures were designed and integrated in the fatigue test facility at Structural Mechanics Laboratory. The representative chains were subjected to a fatigue load cycle varying from 1.5 (maximum) to 0.2 tonnes (minimum) for the qualification. Based on ASME mandatory Appendix-6 experimental procedure, the number of cycles

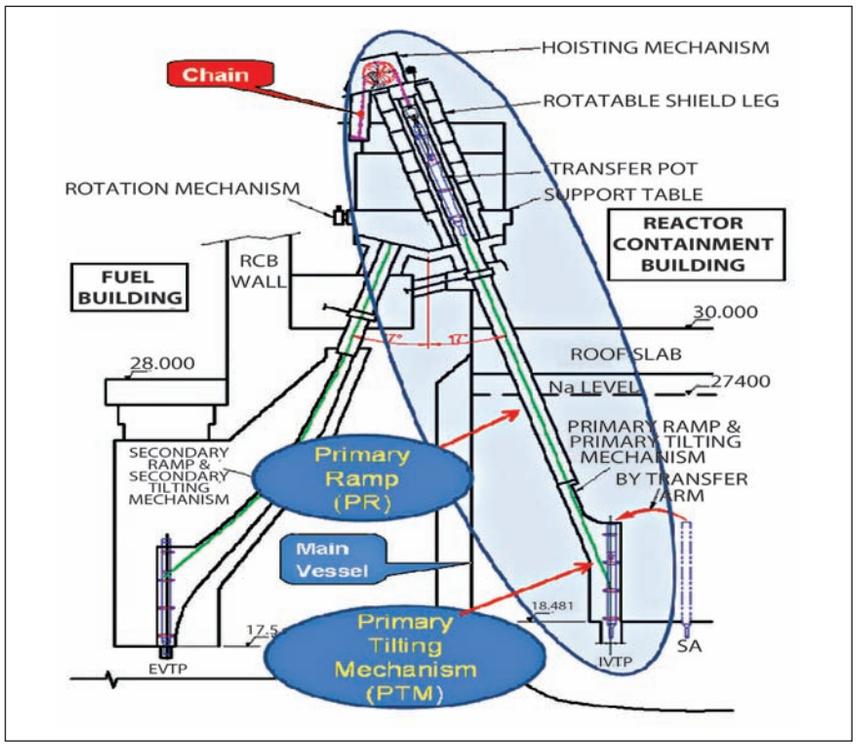

Fig. 1 *Schematic of inclined fuel transfer machine*

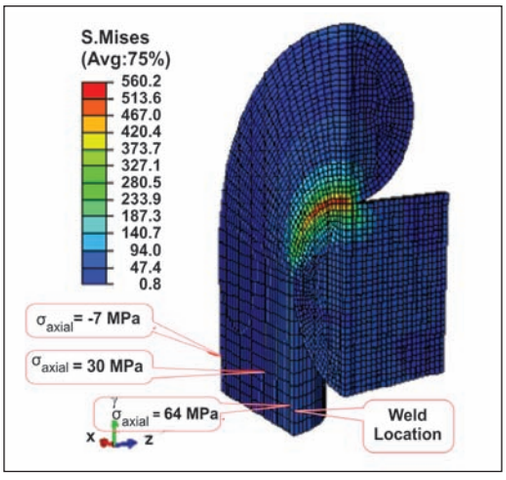

Fig. 2 Von-Mises stress distribution under tensile loading

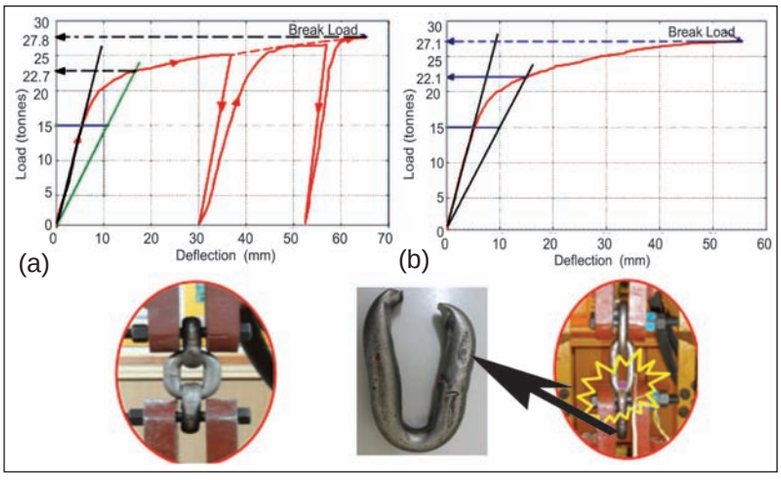

Fig. 3 Load-deflection diagram under break load testing (a) Specimen-1 (b) Specimen-2

required to qualify the chain for two specimen testing is 96470.

Finite element analysis of the 1/4th symmetric sector of the chain indicated that the nominal membrane stress is 30 MPa and that of the axial stress is 64 MPa at the inner surface and -7 MPa at the outer surface (Figure 2). The maximum stress intensity is found in the contact portion between two links. Hence, the defects in the weld may not be a concern for the structural integrity of the chain.

Qualification criteria for the IFTM chain assembly based on the testing is given below:

- Chain specimen shall be checked by liquid penetrant inspection before and after the fatigue loading so that the growth of the initial surface defects shall not be significant
- Individual chain links shall be articulated freely after fatigue testing
- After completion of fatigue testing, breaking load has to be ascertained.

Both the specimens have been subjected to the required fatigue loading as per the acceptance requirements. Break load testings have been completed for both the specimens soon after the fatigue test. The load deflection diagrams for both the specimens are presented in Figure 3. The first specimen was tested with the combination of loading and unloading. The load deflection diagram indicated that the breaking load observed based on testing for the first specimen is 27.8 tonnes and that of the second specimen is 27.1 tonnes. Higher breaking load for the first specimen is due to the hardening mechanism involved while loading and unloading during testing. The collapse load computed as per the ASME double slope method is lower than that of the experimental results. Since the breaking load of the chain is very high in comparison to the maximum possible service load of the chain (5 tonnes), it is established that sufficient margin is available for the safety of the manufactured IFTM chain.

Thus, based on tests and evaluation, it is demonstrated that the minor manufacturing deviations observed on the surface of the chains are acceptable. This approach has also indicated higher factor of safety on the load carrying capacity as well as fatigue endurance. This investigation is important to ensure that PFBR project does not get affected.

II.12 In Sodium Performance Testing of Primary Ramp and Primary Tilting Mechanism

Inclined fuel transfer machine (IFTM) is the ex-vessel fuel handling machine of PFBR. IFTM is used for charging fresh subassemblies into the reactor and to remove the spent subassemblies from the core. Primary ramp and primary tilting mechanism are the critical primary side components

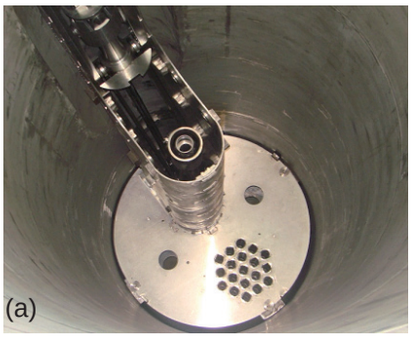

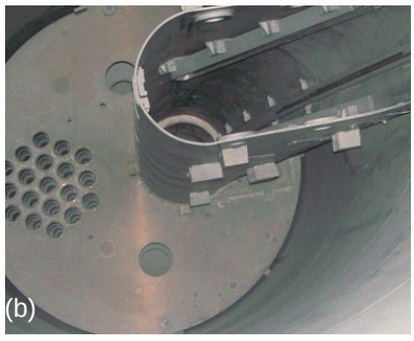

Fig. 1 Primary tilting mechanism (a) With transfer pot inside the test vessel-2 and (b) Inside test vessel-2 after sodium cleaning

of the IFTM located inside the reactor. Fabrication and testing of primary ramp and primary tilting mechanism were carried out to facilitate its installation in the reactor thereby, matching with the assembly sequence of reactor components.

Primary ramp and primary tilting mechanism were fabricated by M/s MTAR Technologies, Hyderabad. After completion of shop floor testing, performance testing was carried out in test vessel-2 (TV-2) of large component test rig (Figures 1a, 1b and 2) along with gate valve, ramp extension piece, transfer pot and simplified drive system with control console. Testing was carried out in stages viz. in air at room temperature, in hot air and in sodium at 473 K which is the fuel handling temperature of PFBR.

One hundred cycles of testing were carried out at room temperature and the overall performance of the system was satisfactory. Leak testing and inerting of the system followed by reduction in the moisture and oxygen levels to acceptable levels were carried out prior to high temperature testing.

Hot air tests were carried out for 24 cycles at different temperatures of 338, 368, 383, 398 and 423 K respectively. Current drawn by the motor and torque values were well within the acceptable limits. The operation of the transfer pot was trouble free and the system was found to be performing smoothly.

In sodium functional testing was carried out at 473 K. The effect of reactor operation at the rated temperature of 820 K on the aerosol deposition in cold regions like gate valve was also simulated by means of two dwell period tests each of 150 hours duration at 820 K. The dwell periods were interspersed between the cyclic tests. The system was tested for a total of 510 cycles in sodium. The performance of the system was good. Maximum current drawn by the motor was within 4.5 A. Measured values of torque were within 14 to 19 N-m.

After completion of testing, sodium in test vessel-2 was drained and vessel cooled to 333 K. Test vessel-2 was isolated from Large Component Test Rig and connected to a system for sodium removal using water vapour-CO_2 process. The cleaning process was very effective. A total of 3 kg of sticking sodium from the components and vessel surfaces was removed by this method. The value obtained experimentally (from H_2 monitoring during the process) was close to that obtained by estimation. The time taken for vapour phase reaction was 85 hours. The vapour phase reaction was followed by water wash using fine spray followed by washing in demineralised water (Figures 3a and 3b).

Fig. 2 Primary ramp

After cleaning and drying, quality assurance checks were carried out on primary ramp and primary tilting mechanism. Visual examination of the primary ramp and primary tilting mechanism and rollers and liquid penetrant examination of the weld between the primary ramp and primary tilting mechanism body and base plate and all accessible portion of the rails in primary ramp and primary tilting mechanism confirmed the healthiness of the system. Primary ramp and primary tilting mechanism was packed and despatched to BHAVINI.

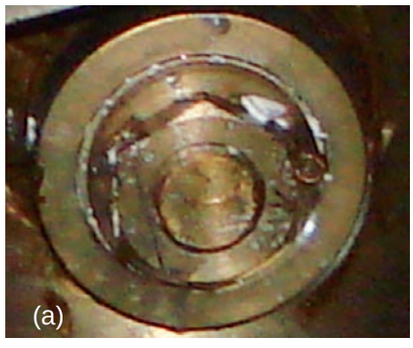

Fig. 3 Bearing assembly of transfer pot rollers (a) Before (b) After cleaning

II.13 Experiments in SGTF: Plugged Tube Operation of Steam Generator and Assessment of Hydrogen Flux across Steam Generator Tubes

Once through steam generator of Fast Breeder Reactor (FBR) carries high pressure water/steam in the tubes and low pressure sodium in the shell. In case of a tube leak in steam generator, the leaking tube will be isolated by plugging at both ends and power operation will be resumed. This results in deviation in temperature distribution in the affected and nearby tubes and associated stresses.

The test steam generator test facility in (Figure 1) is a 19 tube model of the 547 tube steam generator of PFBR.

Study of the effects of operating the steam generator with a single tube plugged was carried out in steam generator test facility by plugging a healthy tube. Experiment was carried out for four tubes at different orientations at around the nominal power of 5.5 MWt. It was observed that the individual tube outlet steam temperature readjusted in such a way that the tube in the vicinity of plugged tube delivered comparatively hot steam and the tubes away from the plugged tube delivered comparatively cold steam. Experimental results indicate that a single tube plugging does not significantly add to thermo-mechanical loading on steam generator tubes. These observations are in agreement with the analytical predictions.

The material of construction of PFBR steam generator is modified 9Cr-1Mo and the same material is used for the model steam generator test facility steam generator also. In secondary sodium system of sodium cooled fast reactor the major impurity in sodium is hydrogen, formed due to water/steam side corrosion in steam generator.

$$3Fe(s)+4H_2O\,(l/g) \rightarrow Fe_3O_4(s)+4H_2\,(g)$$

Hydrogen, produced in the water side, as a result of the reaction permeates through the ferritic tube wall to the sodium side, where hydrogen activity is less. The mass flux of hydrogen, permeating into secondary sodium, is important in the design of the secondary sodium cold trap (CT). Hydrogen flux depends on steam generator tube thickness, tube material, operating temperature and feed water chemistry and hence, it is specific for a sodium cooled fast reactor. Experiments were carried out in steam generator test facility to assess the hydrogen flux in a Mod 9Cr-1Mo steam generator. It is observed that the flux increases with power level (Figure 2). The steady state flux at rated power obtained is 1.25×10^{-7} gH/m^2.s, which is on lower side when compared to the reported steady state flux of 1.8 to 2.2×10^{-7} gH/m^2.s for 2.25Cr-1Mo material.

The experiments were repeated and found that the flux values are consistent. Experiments were also performed during transient conditions such as, start up after a long shutdown, steam generator

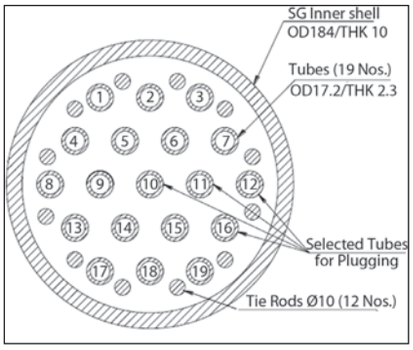

Fig. 1 *Tubes in steam generator of steam generator test facility*

operation after flow instability experiments etc. During flow instability tests, steam generator is subjected to cyclic thermal stress due to fluctuating water/steam flow resulting in temperature cycling. Such a cyclic stress could form cracks and discontinuities in magnetite layer on the tube inner wall. Figure 3 shows two cases at 1.1 MW wherein case-1 is a steady flow condition and case-2 is soon after a flow instability test.

Higher rate of hydrogen flux in case-2 is due to the discontinuities in the magnetite layer caused by thermal cycling. It was also observed that though the initial flux at start up after a long shut down is as high as 3.094×10^{-7} at 5.5 MW, it stabilizes to a lower steady state value in 1-2 days time.

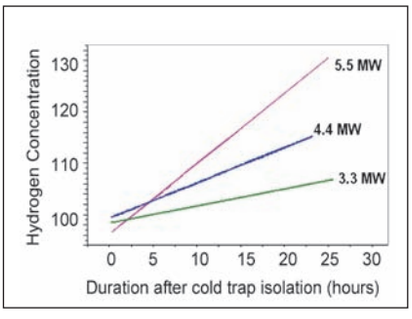

Fig. 2 *Variation of hydrogen flux with power*

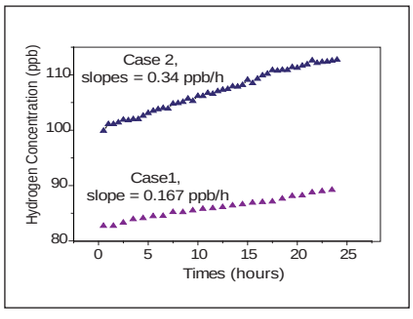

Fig. 3 *Two different cases at 1.1 MW*

II.14 Reassessment of the Heat Transfer Performance of Steam Generator in SGTF

The steam generator in steam generator test facility is of 5.5 MWt capacity. The ninteen tube steam generator has tubes of 23 m heat transfer length and is similar to the steam generator of PFBR in all respects except in number of tubes. Figure 1 shows the schematic of steam generator test facility.

Heat transfer performance of the 5.5 MWt capacity model steam generator was tested in steam generator test facility earlier (June 2007). During testing, the steam generator was operated with the nominal sodium flow of 104.5 m^3/h and with the nominal feed water flow rate of 8820 kg/h with a feed water inlet temperature of 507 K. Sodium temperature of 789.5 K at steam generator inlet was sufficient to transfer 5.5 MW from sodium to water for producing the steam at 17.2 MPa pressure and 766 K temperature.

After the first phase heat transfer experiments in June 2007, the steam generator was subjected to endurance testing at nominal pressure and temperature conditions. Many steady state and transient experiments were also conducted with the model steam generator.

Reassessment of the heat transfer performance of the steam generator by experiments was performed after about 10000 hours of steam generator operation.

To produce steam at 766.5 K at 17.14 MPa pressure with a heat transfer of 5.502 MW the sodium flow of 105.9 m^3/h was required with 791.5 K inlet temperature. The sodium inlet temperature to produce the steam at nominal conditions was two degrees more during reassessment compared to the first phase of experiments. Both the times the experiments were repeated many times and the thermocouples used to measure the temperature were calibrated. Hence, the increase in the requirement of sodium inlet temperature is on account of the reduction of heat transfer capability of the steam generator due to continued service. The reduction in the heat transfer capability of the steam generator as expected is on account of the scale formation inside the tubes and the fouling resistance considered for the thermal design of steam generator is 0.2×10^{-4} m^2K/W.

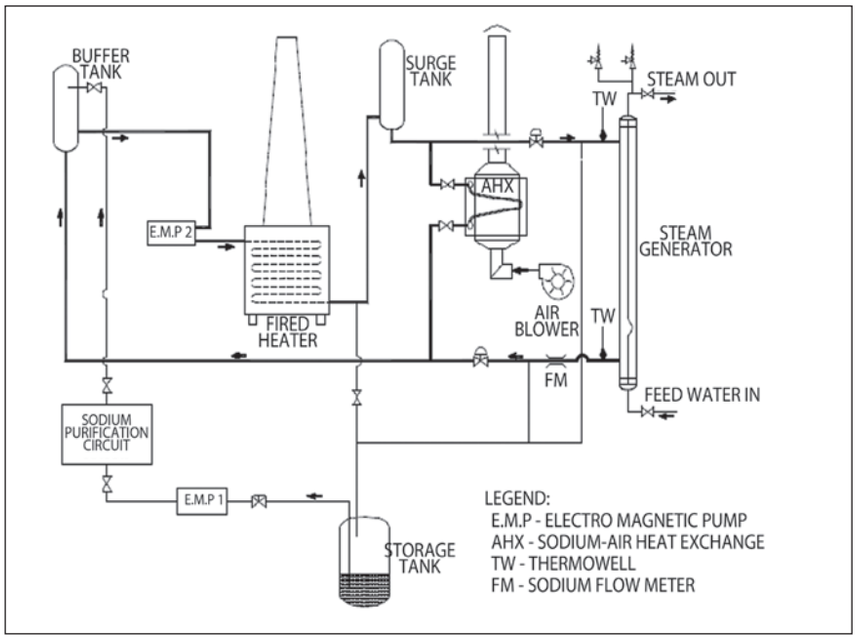

Fig .1 *Schematic of steam generator test facility sodium system*

The variation in wall thickness from the design value can influence the heat transfer performance of the steam generator. Hence, for assessing the heat transfer area

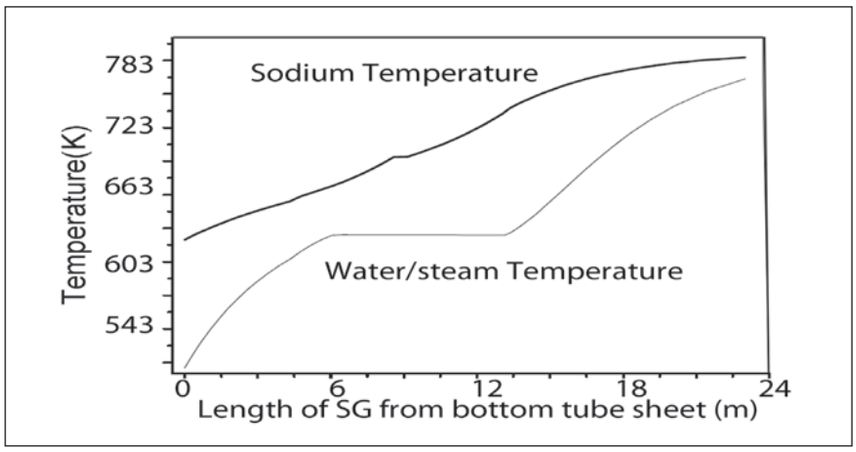

Fig. 2 *Temperature profile of sodium and water/steam in steam generator*

margin in steam generator the actual wall thickness of the tubes is to be considered. An investigation of the steam generator tube dimensions was conducted to determine the actual dimensions of the steam generator tubes used in the model steam generator tested in SGTF. This was done with the samples of tubes from the same lot of tubes from which tubes were used for manufacturing of model steam generator. The average tube dimensions estimated from the survey is found to vary by around 14% from the specification.

Experiments were conducted to determine the deviation of the single phase heat transfer coefficient U_{eco} from the theoretically estimated values. During the experiments the steam generator outlet water condition was kept at 313 K sub cooled to ensure the absence of sub cooled nucleate boiling in steam generator tubes. The water flow through the steam generator was varied from 25 - 40% of the rated water flow and sodium flow was varied from 14 - 20% of the rated flow.

From the experimental results, it was estimated that the theoretical calculations using the one dimensional computer code DESOPT under predicts heat transfer coefficients in the economizer region U_{eco} by 3%. The estimated average tube dimensions obtained from the investigation was used for the calculations.

Using the experimentally obtained parameters from the first phase of experiments and estimated 3% in the prediction of U_{eco}, it is assessed that the heat transfer coefficient in the boiling zone, U_{bio}, was over predicted by an average value of 20%. With these experimentally estimated correction factors on overall heat transfer coefficients, the tube length required for steam at 766K with nominal process parameters is calculated with DESPOT. Heat transfer length required for a fresh tube was estimated as 20 metres and the tube length required with an additional design basis scaling resistance is 20.8 metres. Hence according to the first phase of experiments the steam generator with 23 metres heat transfer length will have 13% of its area as margin. After the formation of the design basis scaling the margin in area will reduce to 9.6%.The temperature profile of sodium and water/steam in steam generator is shown in Figure 2.

II.15 Challenges in Manufacture of Stroke Limiting Device for Travel Control in CSRDM – PFBR

Stroke limiting device is a passive safety feature in PFBR. In order to enhance the overall reliability of the reactor shut down system (in addition to fast acting shutdown systems namely CSRDM and DSRDM) this stroke limiting device was developed. This assembly consists of precisely machined components namely ring gear assembly, shaft with splines, shaft housing, swing arm, connecting link, guide way, coupling shaft, plunger, spindle, bush, support plate, motor mount base plate etc, as shown in Figure 1.

Motor mount base plate made of carbon steel material has unique features with intricate profiles and high degree of geometrical and dimensional tolerances. The machining of the intricate contours requires meticulous planning and use of special purpose machines. The overall size of base plate was OD 338 mm and length 14 mm. The criticality in machining of motor mount base plate was eccentric bore machining of different diameters on different pitch circle diameters with intricate profile of various depths. Special tools and fixtures were designed and dedicated part program were developed to carry out machining of profiles. Spur gears and internal/ external splines of different sizes, spindles were precisely machined using special purpose machines and subsequently heat treatment was carried out. The precisely machined components of stroke limiting device were successfully machined and assembled as shown in Figure 2.

Fig. 1 *Machined components for stroke limiting device*

Fig. 2 *Stroke limiting device assembly*

II.16 Fabrication of Ultrasonic Transducers for Under Sodium Ultrasonic Scanner of Prototype Fast Breeder Reactor

An under sodium ultrasonic scanner has been developed for PFBR to detect protrusion, growth and bowing of the fuel subassemblies before every fuel handling operation. The high temperature and sodium-compatible ultrasonic transducers, which can work in liquid sodium, have been developed in-house for use in the scanner. Under sodium ultrasonic scanner has been utilized for two purposes in the Fast Breeder Reactor. The first one is to detect any fuel subassembly projecting from its original location which may hinder the fuel-handling operation. It is called the side viewing operation. Side viewing system scans in lateral direction and detects protrusion of any fuel subassemblies up to last row in the core. Side viewing transducer with frequency of 1 MHz is used for this purpose.

The second purpose is to locate the tops of the core subassemblies located directly underneath the scanner for the safe positioning of the scanner inside the reactor. It is called downward viewing operation. Downward viewing transducer (Figure 1a) with frequency of 5 MHz is used for this application. Downward viewing system scans vertically downwards in the in-vessel transfer port, locates the fuel subassemblies and parks the scanner.

Transducer housing is made of nickel to facilitate transducer wetting with sodium at 453 K. There are three side viewing transducers (Figure 1b) and seven downward viewing transducers (including three redundant downward viewing transducers) used in the PFBR scanner.

Fabrication of transducers

Fourteen transducers (five side viewing transducers and nine downward viewing transducers) were fabricated by soldering PZT crystal to the transducer diaphragm using solder alloy with melting point of 493 K. After assembling the transducers with insulator, spring and contact plate, mineral-insulated cable centre conductor was brazed to the contact plate. Subsequently the mineral-insulated cable was welded to the transducer housing. Inconel wire was used for welding. Functionality of the transducer was checked after each stage of welding. Helium leak test was carried out for all the transducers as a part of reactor qualification. All the transducers are placed inside the pressure vessel and the vessel was pressurized and maintained with helium at 1 kg/cm^2 for four hours. After removing from the vessel all the transducer weld joints were checked for a vacuum level of 10^{-8} Pa m^3/sec.

Endurance testing of transducers in sodium

Prior to mounting in the scanner, ten transducers required for the PFBR scanner along with four spare transducers were tested in sodium. Before sodium testing, all the transducers are tested in water individually and the pulse echo output waveform was recorded for each transducer. Then all the transducers are put together and immersed in sodium at 453 K for 150 hours in the sodium test vessel. The transducers were removed after the test and sodium cleaning was carried out. The transducers were then tested in water to confirm the performance and the pulse echo output waveform was recorded. These values were comparable with the performance observed before testing in sodium.

The ultrasonic transducers were also qualified for gamma irradiation test for five years of transducer life time in reactor. The transducers which were developed and qualified are mounted in the transducer holder (Figure 2) of under sodium ultrasonic scanner of PFBR.

Fig. 1 *(a) Downward and (b)Side viewing transducers*

Fig. 2 *PFBR scanner transducer holder with transducers*

II.17 Thermal Hydraulic Investigation of Extended Station Blackout Event

Fukushima event is a major accident in the nuclear reactor history. Despite the fact that all the reactors in that area tripped automatically due to earthquake and the power reduced to residual level, the event transformed to a major accident due to the inability of the system to remove decay heat under prolonged complete power failure situation. Following this accident, the nuclear community had a critical relook into various safety aspects of the reactors. One of the important criteria that emerged as an outcome is to meet all design safety limits even under complete power failure.

Following a station blackout, the reactor is shutdown and the decay heat is to be removed to maintain integrity of the core and primary components. In PFBR two diverse paths have been provided for decay heat removal :

(i) Decay heat removal through steam-water system, which is known as the operation grade decay heat removal system and

(ii) Decay heat removal through safety grade decay heat removal system

During complete power failure, operation grade decay heat removal system cannot be operated and decay heat is removed through safety grade decay heat removal system, which comprises four physically independent circuits each of 8 MW capacity. Each circuit consists of one decay heat exchanger (DHX) and one air heat exchanger coupled by an intermediate sodium circuit. The sizing of air stack and layout of

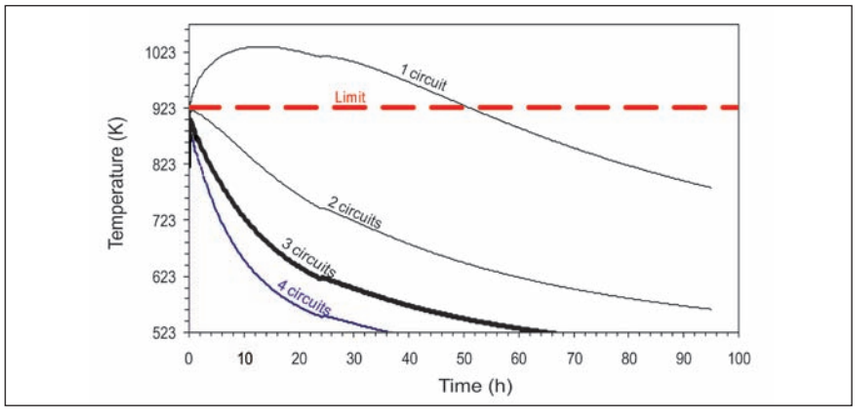

Fig. 1 *Evolution of hot pool temperature following complete power failure and main vessel leak*

safety grade decay heat removal circuit components is fixed to ensure adequate decay heat removal by natural convection flow of air, intermediate sodium and primary sodium. In order to have control over the heat removal by safety grade decay heat removal system, air dampers are provided at the inlet (2 nos.) and at the outlet (2 nos.) of each air heat exchanger. During normal reactor operation these dampers are in crack open position and in case of reactor SCRAM they are fully opened. The damper control is of 'fail-safe' design, i.e., on control power failure both pneumatic and electrical portions of the dampers will be opened. In the case of power failure to the electrically operated damper, the damper will remain 'stay-put'.

Following station blackout, the secondary sodium circuits and steam/water system become unavailable. The primary sodium pumps can run at 15% speed on pony motors for four hours on battery power. But, in the case of a complete power failure event, both the primary sodium pumps will also become unavailable and the decay heat generated in the core is removed by natural circulation of primary sodium. During the onset of natural convection, the core outlet temperature increases. But due to large thermal inertia of the sodium pools, the decay heat generated in the core is absorbed by the sodium pools without much increase in pool temperatures. Further, the long term system temperatures depend on the rate of heat removal from the hot pool which depends on the number of safety grade decay heat removal circuits deployed. Studies have been carried out to find the minimum number of safety grade decay heat removal circuits required to keep the system temperatures within acceptable limits under complete power failure event.

Complete power failure along with main vessel leak

In this study, it is assumed that following a severe earthquake there is a complete power failure and also there is a leak in main vessel. The consequences of this event have been analyzed using the thermal hydraulic system code DHDYN, where the reactor is shutdown on SCRAM signal and decay heat is removed by natural

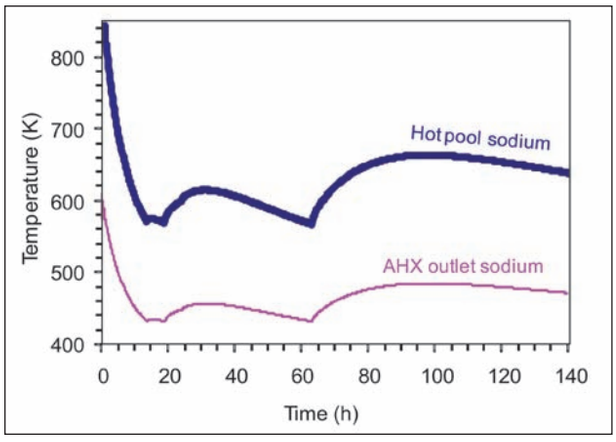

Fig. 2 Evolution of sodium temperature during sequential closing of air heat exchanger dampers

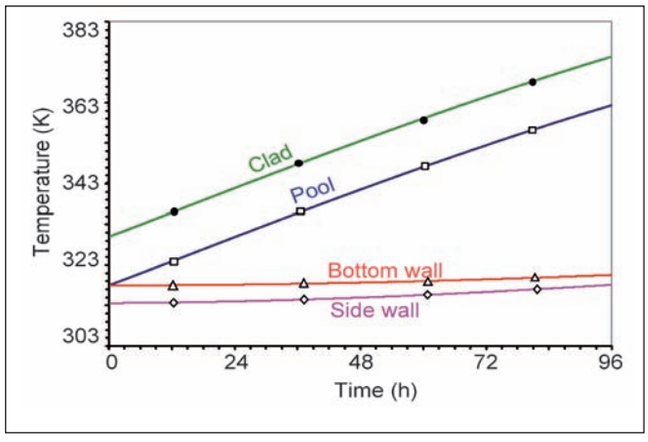

Fig. 3 Temperature evolution in various parts of spent fuel storage bay

circulation. As a result of main vessel leak, sodium level in hot pool drops by 1.34 metres and consequently, decay heat removal capacity reduces. Parametric studies have been carried out by varying the number of safety grade decay heat removal system circuits deployed on demand. Figure 1 shows the evolution of hot pool temperature as a function of number of circuits. It can be seen that with one circuit, the maximum hot pool temperature is 1032 K at 13 hours. With two circuits, this value reduces to 918 K which is less than category 4 design safety limit of 923 K and it takes only 30 hours for the temperature to drop to 723 K. By this study, it is demonstrated that even under main vessel leak condition, the hot pool temperature can be maintained below the design safety limit with two safety grade decay heat removal system circuits deployed.

Safety grade decay heat removal system operating strategy

During long term decay heat removal operation following station blackout, the circuit temperatures come down gradually. It is essential to maintain the intermediate circuit sodium temperature above its freezing point to keep the decay heat removal system in healthy condition. The intermediate circuits are provided with line heaters that are powered only by class IV power supply. Hence, they are not available to heat the sodium circuit if required. In order to avoid the risk of sodium freezing it is necessary to close the air heat exchanger dampers as and when required to reduce the heat loss.

Various operating strategies have been investigated by using the thermal hydraulic code DHDYN and finally a strategy with sequential closing of dampers has been selected. In this strategy, when the sodium outlet temperature of air heat exchanger reduces to below 433 K, dampers of one of the operating safety grade decay heat removal system are closed. This reduces the decay heat removal rate. The sodium outlet temperature of the air heat exchanger increases initially and then reduces after some time. Again when the sodium outlet temperature of the air heat exchanger reduces below 433 K, another set of dampers of one of the operating air heat exchanger are closed. Figure 2 shows the evolution of hot pool sodium temperature and sodium outlet temperature of air heat exchanger. It can be seen that the dampers of first, second and third air heat exchangers need to be closed at 15, 23 and 70 hours respectively. After this, only one circuit is used for decay heat removal operation. Adopting this strategy the decay heat removal operation can be continued for more than ten days even under complete power failure condition without any risk of sodium freezing.

Spent fuel storage bay

Spent subassemblies are stored under water in the spent fuel storage bay (SFSB) before they are transported to reprocessing plant. SFSB consists of two distinct rectangular pools filled with water such that subassemblies are submerged by 4.5 metres. The pool is surrounded by a concrete wall of 1.7 metres thickness. Dedicated water cooling circuit is provided to remove the decay heat generated by subassemblies stored in it. In case of a station blackout event, the cooling circuit along with the ventilation system which maintains the fuel building air temperature and relative humidity will be lost. Fuel building gets isolated due to the fail safe position of dampers. In this situation, pool water and the air in fuel building gets heated up. However, there will not be any pressurization of the building since the building is not 100% leak-tight. Transient thermal analysis of SFSB has been carried out for complete power failure

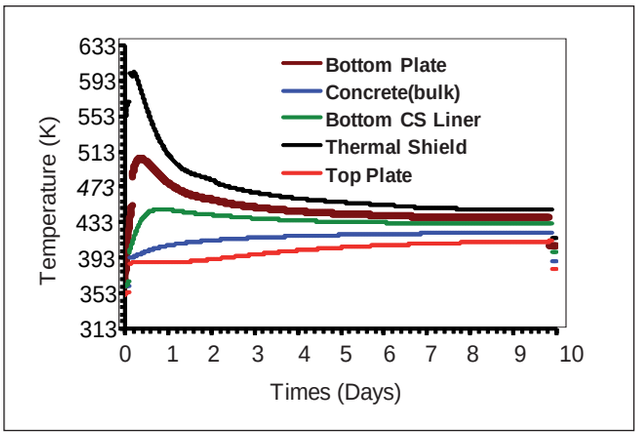

Fig. 4 *Temperature evolution in various parts of reactor vault*

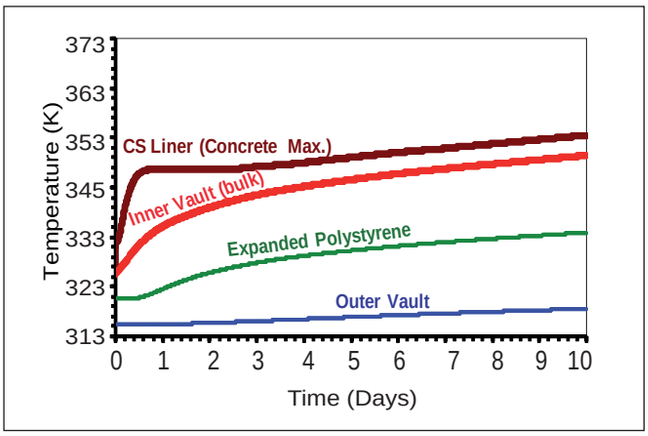

Fig. 5 *Temperature evolution of various parts of roof slab*

event under emergency core unloaded condition (a condition with maximum decay power). Heat transfer by convection, radiation and evaporation are considered in this analysis. Figure 3 shows the temperature evolution of various parts. It is seen that the clad temperature reaches boiling point of water after four days and after that pool level drops at the rate of 210 mm/day. With this rate of evaporation, the subassembly will be in submerged condition for more than twenty days. The study indicates that adequate time is available for planning emergency operation.

Reactor vault

During normal operation, the reactor vault is cooled by a dedicated water cooling system operated on class IV and III power supplies. During complete power failure situation, the vault cooling is not available and hence, the vault temperatures rise gradually. Evolution of reactor vault temperature has been predicted by thermal analysis considering the transient temperature variation of primary sodium temperature as boundary condition. Figure 4 depicts evolution of vault temperature at various parts. It is seen that the inner vault maximum and bulk temperatures are only 376 and 371.4 K respectively. Similarly, the outer vault maximum and bulk temperatures are 349 and 325 K respectively. These values are much less than the permissible temperature limits demonstrating that power supply to reactor vault cooling system is not required at least for ten days. This is due to the large thermal inertia of two metres thick concrete vault and thermal insulation fixed to safety vessel.

Roof slab

During normal operation, roof slab is cooled by a dedicated air cooling system operated by class IV and class III power supplies. During complete power failure, cooling to roof slab is lost and its temperature rises. Figure 5 shows temperature evolution in various parts of roof slab predicted by thermal analysis. It is seen that the temperature of the seals (same as top plate temperature) reaches a maximum value of only 413 K at the end of 10^{th} day. The maximum temperature attained by shielding concrete is only 453 K. These are well within the corresponding acceptable limits.

II.18 Linear and Non-Linear Stability Analysis of Prototype Fast Breeder Reactor

One of the important factors determining the operational safety of nuclear reactors is their inherent stability characteristics. In this context, sodium-cooled fast reactors are generally considered to be more stable compared to light water reactors. The sign, magnitude and rate of change of reactivity feedbacks determine the stability of reactor power against various forms of disturbances. For PFBR, doppler and fuel expansion and core radial expansion feedbacks are negative while steel and sodium expansion are positive. The negative components have considerably higher magnitude compared to positive components, which is desirable from the stability requirement.

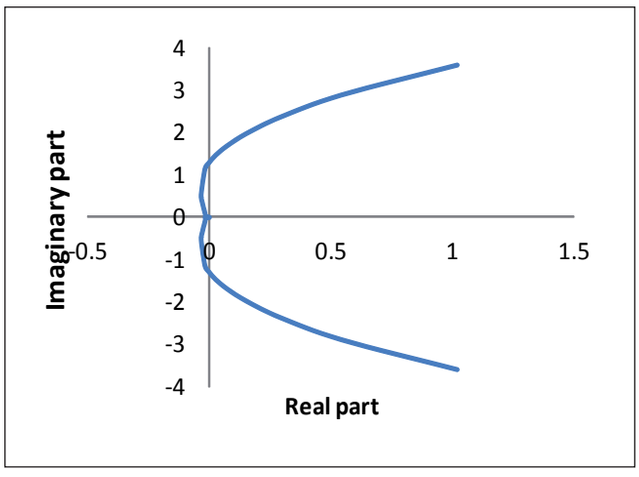

Fig. 1 *Nyquist plot for PFBR*

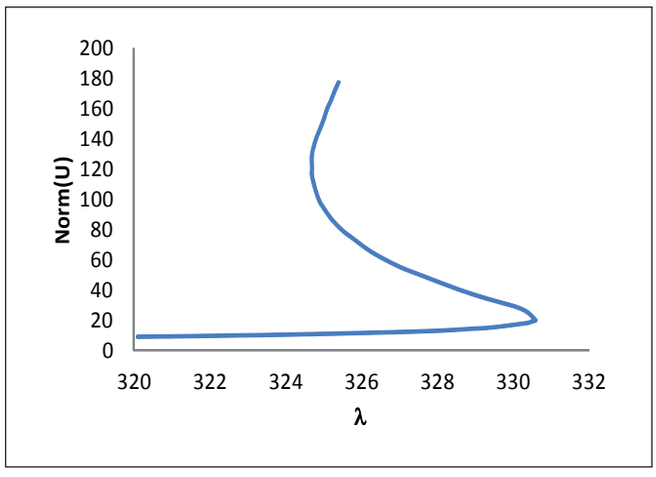

Fig. 2 *Solution diagram with two limit points*

The approach used for establishing the stability depends on the type of reactor under study. Simple linear stability analysis would be adequate for example, for small and medium sodium cooled fast reactors , which can be qualitatively considered as milder non-linear system compared to pressurized water reactors. This is due to strong neutronic coupling, good negative feedback coefficients and absence of fission product poison effects. For strongly non-linear systems, linearized analysis would not be adequate to capture or rule out some of the complex behaviours attributed to them, like existence of multiple equilibrium points, sensitivity to initial conditions and issues of global stability.

The method of linear stability analysis is the frequency domain approach, where, reactor power transfer functions are constructed from linearized point kinetics and heat transfer equations. The stability of the reactor is ensured when the static power coefficient is negative (-0.7 pcm/MWt) and the Nyquist plot of open loop transfer function does not encircle (-1, 0) point in complex plane (Nyquist criterion) as shown in Figure 1. The time constant of dynamic power coefficient is 3 seconds, a small enough value to ensure quick feedback. In PFBR there are no instabilities due to xenon oscillation and moderator boron reactivity effects. Also, there is no coolant boiling during operation. So, linear stability analysis is mostly adequate.

Non linear stability analysis is also being pursued to establish global stability of the reactor. Non linear stability analysis of PFBR has been initiated by considering a one group space dependent non-linear reactor dynamics equation with fuel, steel and coolant temperature feedback. The model has a parameter λ and three constants which depend on temperature coefficients of fuel, coolant and concentrations of boron and xenon.

By the method of continuation of solutions to the governing non-linear equations, a suitable function of power is plotted with λ as the variable. From the solution diagram (shown in Figure 2 for pressurized water reactors) regions giving multiple solutions can be easily identified. For PFBR case (Figure 3) the allowed solution is unique. It is concluded from the numerical and analytical study that PFBR is globally stable subjected to the constraints of the model. Further study is being done with distributed reactivity coefficients.

The stability of PFBR has also been established by studying power evolution due to large perturbations. Reactivity perturbations of 0.1 to 1$ and flow perturbation of 10% were introduced for one second duration at 100, 40 and 20% power. The power is stabilised in a few seconds without any oscillations, confirming stability. An illustration of perturbation of 0.5 $ is shown in Figure 4. Sinusoidal reactivity perturbations of 0.5 $ at 10, 1, 0.1 and 0.01 Hz were also studied. The reactor is found to be stable even when only Doppler feedback is considered.

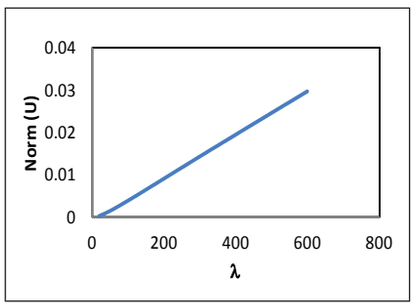

Fig. 3 *Single stable solution applicable for FBR operating regime*

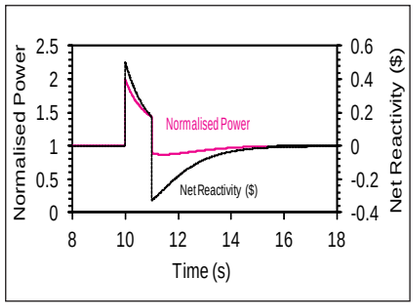

Fig. 4 *Net reactivity and normalised power with time. Full power and flow, Δρ = 0.5$*

II.19 Seismic Qualification of Control and Safety Rod Drive Mechanism

Full scale prototypes of control and safety rod drive mechanism and control and safety rod have been manufactured and extensively tested for their performance and endurance in air as well as in sodium at IGCAR. These testing have qualified them for normal operation in reactor. However, as per the safety criteria, seismic qualification has to be demonstrated by testing. As a part of the seismic qualification, control and safety rod drive mechanism along with control and safety rod have been successfully tested for operation base earthquake. During testing, full insertion of control and safety rod within the stipulated time and healthy functionality of control and safety rod drive mechanism have been demonstrated.

A dedicated facility for conducting the seismic testing of tall and slim Absorber Rod Drive Mechanisms (ARDMs) has been constructed at the Dynamic Research Laboratory of Structural Engineering Research Center (SERC), Chennai.This facility is mainly a concrete structure (reaction wall) having 14 metres height; six metres of the structure is below the ground level and 8 metres above the ground level (Figure 1).Three rigid support structures have been designed, fabricated and erected. These act as a rigid interface between reaction wall and control and safety rod drive mechanism/control and safety rod subassembly mechanism (~12 metres length) and grid plate sleeve was supported on uni-axial sliding facility, which in turn was mounted on rigid support structure. Three actuators with maximum displacement of ±50 mm and maximum capacity of five tonnes were used to shake the mechanism at three locations namely control plug top level, grid plate level and bottom level of hexagonal subassembly. Experiments have been conducted to measure the natural frequency of individual components and coupled system. The experimental results were compared with that of theoretical simulations and found to be satisfactory.

On receiving the SCRAM signal, the electro-magnet is de-energized and the mobile assembly of control and safety rod drive mechanism along with control and safety rod is released to fall under gravity. At the end of free fall travel of 835 mm, the mobile assembly is decelerated by an oil dashpot for the remaining 250 mm travel. The free fall time is the most important parameter as the negative reactivity added during this travel of control and safety rod ensures shutdown of the reactor with sufficient margin.

Full scale prototypes of control and safety rod drive mechanism and control and safety rod were subjected to seismic excitations at room temperature and the drop with seismic excitation was done at six different delay times from the start

Fig. 1 *Seismic qualification test setup for CSRDM*

of seismic excitation and SCRAM signal. The maximum drop time was recorded when electromagnet was de-energised at five seconds after the starting of seismic excitation. There was an increase of 50 milliseconds when compared to the normal drop (Figure 2). Apart from drop time, strain, displacement and acceleration were also measured. All the results obtained were very much within the acceptable limits.

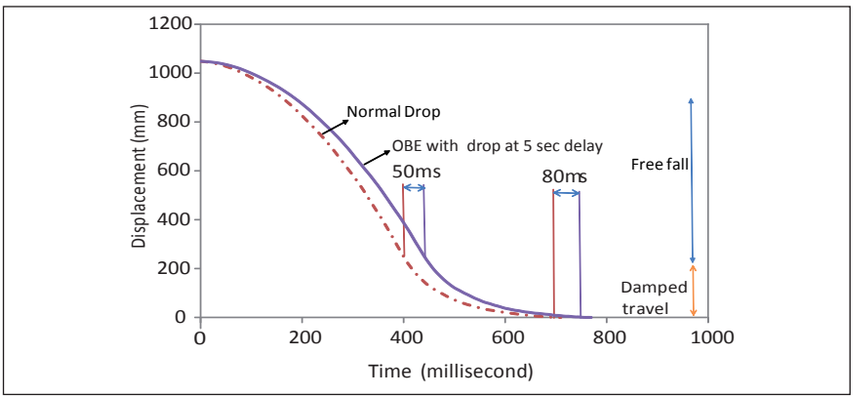

Fig. 2 *Effect of seismic excitation on drop time*

II.20 Seismic Qualification of Non-conventional Systems by Analysis and Testing

Seismic design philosophy adopted for the structures, systems and components of nuclear power plants, ensures the structural integrity and functional requirements for all the components for smooth operation and safety of the nuclear power plants under earthquake loading conditions. Seismic design of nuclear power plants in general follows a dual design criteria in which the systems and components are designed for two levels of earthquakes, viz. operating basis earthquake and safe shutdown earthquake. Seismic design is performed by analysis and/or testing. Seismic design of PFBR is carried out based on detailed analyses and testing. The methodology adopted for the seismic qualification of some of the critical components other than the reactor assembly and piping systems are discussed here.

Seismic qualification of control panels

Control panels are the most critical systems of the nuclear power plants, and they control the entire operation of the reactor including the safety actions such as shutdown of the reactor under any extreme undesirable events. Earthquake is one of the most severe loading conditions for which the functional and structural integrity of the panels must be demonstrated beyond any ambiguity. Since it is difficult to demonstrate the functionality of the control panels which consists many relays, switches, computers etc. by analysis, qualification by shake table experiments are performed for all the panels in PFBR. Here the floor vibrations at the support location of the panels

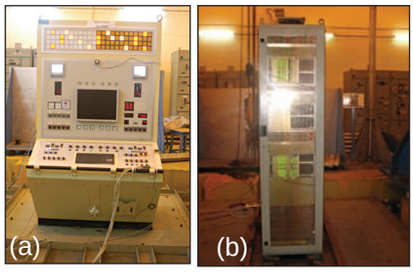

Fig. 1 Seismic qualification of panels for PFBR (a) Main control room panel and (b) LCC panel

are generated by the seismic vibration analysis of the nuclear interconnected building (NICB) by using simulated earthquake ground motions corresponding to operating basis earthquake and safe shutdown earthquake conditions. The floor vibration in the form of floor response spectra is fed to the shake table to simulate the floor vibrations at the support location of the panels. The panels are mounted on the shake table simulating the actual mounting condition in the reactor and tests are carried out with the panel in energized condition for five numbers of operating basis earthquake and one safe shutdown earthquake as per the IEEE-344 guide lines for the qualification of electrical/electronic equipments. Figure 1 shows the seismic qualification experiments performed for the main control room panels, using ten tonnes shake table at structural mechanics laboratory. Similar tests were performed for all the critical panels for PFBR. For seismic qualification of the logic circuit components like relays, contactors, limit switches etc., which are part of several control panels and logic circuits at different locations, a novel approach has been followed based on combination of analysis and experiments where the excitation at

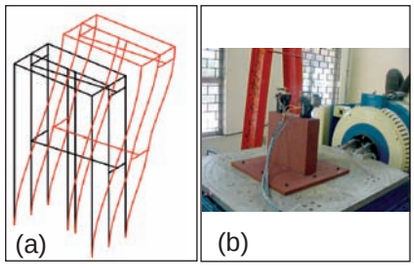

Fig. 2 Seismic qualification of logic devices (a) Finite element analysis of control room panel and (b) Testing of relays

the support location of these small components are generated from the detailed finite element analyses of the control panels which houses these components. The response acceleration time histories at the support location of the components obtained from the time history analysis of the panels are fed to the shake table and components are qualified by mounting them on a specially designed support structure, simulating actual mounting condition and the structure in turn is bolted to the shake table for testing. This methodology has been successfully adopted for the seismic qualification of logic circuit components of FBTR (Figure 2) as a part of the seismic reevaluation program of FBTR and for the seismic qualification of the logic circuit components of control and safety rod drive mechanism and diverse safety mechanism of PFBR.

Seismic qualification of sodium valves and isolation valves

Flow control valves, dampers and isolation valves in nuclear power plants form another group of non conventional critical systems, because of their special design features, which is warranted due to the system and operating requirements. Most of the sodium

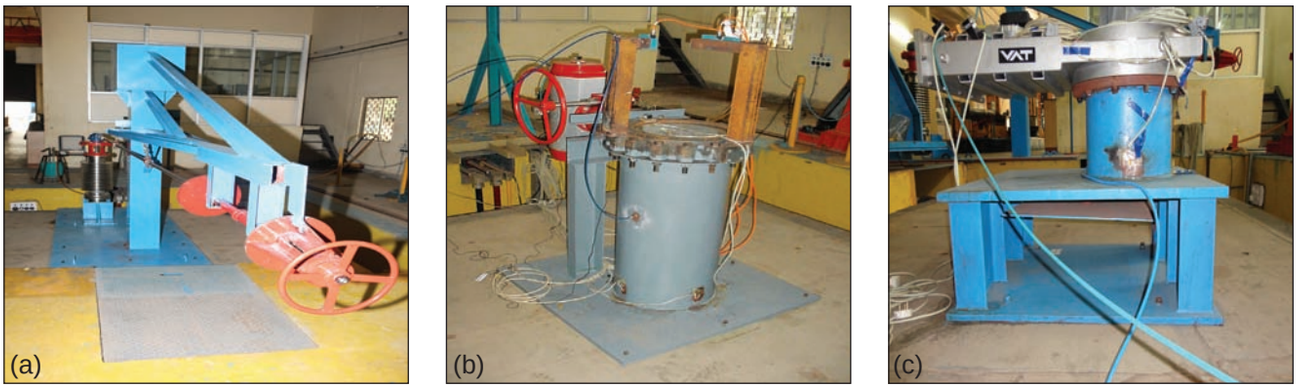

Fig. 3 *Seismic qualification of valves: (a) Extended stem valve, (b) Reactor containment building damper of FBTR and (c) Isolation valve*

valves in fast reactor heat transport systems are characterized by large diameter body with fins and extended stem, which are supported at multiple locations. During an earthquake event, these valves experience differential support motion through the multiple support points. To qualify the component for this condition, multiple support excitations need to be created in the shake table in a conservative manner using specially designed support structure. The support structures used for qualification of extended stem valves are designed by detailed finite element analysis to ensure that, the support motions are reproduced conservatively during testing. Figure 3a shows the setup used for the seismic testing of a typical extended stem sodium valve. In this experiment, the leak tightness of the valve is ensured by pressurising the fluid at one side of the valve using a pressurizing system and monitoring the pressure during and after the seismic tests. Similar tests were conducted for RCB isolation damper for FBTR and isolation valves for fuel transfer cells of PFBR as shown in Figures 3b and 3c respectively.

Seismic qualification of safety vessel insulation panel

Safety vessel thermal insulation panel of PFBR is performing the important function of limiting the heat flux to the reactor vault and thereby keeping the vault temperature below the acceptable limit. These panels are mounted on the outer surface of the safety vessel using studs. The integrity of these panels has to be ensured during an earthquake, even with the extreme event of main vessel leak. The integrity of the panels is demonstrated by shake table tests. The support excitations for the tests are generated by the seismic analysis of the reactor assembly along with safety vessel under various scenarios including the leaked condition of the main vessel. The setup used for the qualification test is shown Figure 4.

Seismic qualification of electrical systems

Electrical systems of nuclear power plants, whose functionality cannot be ensured by detailed analysis, are qualified by shake table testing. Here, the required response spectra used for the testing are generated from detailed analyses of the structures, where these components are mounted, using general purpose finite element codes such as CAST3M. Spectrum compatible time histories are generated for the shake table testing such that the test response spectrum envelopes the required response spectra, meeting the IEEE-344 criteria for the input excitation. Electrical components such as lighting system, electrical penetration assembly and battery banks have been tested by specially designed mounting structures and the functional requirements and structural integrity are ensured by performing the tests for operating basis earthquake and SSE conditions. Figure 5 shows the testing of the lighting system for PFBR containment building. Similar tests were conducted for all the safety related electrical systems of PFBR to demonstrate the functional and structural integrity requirements under seismic loading.

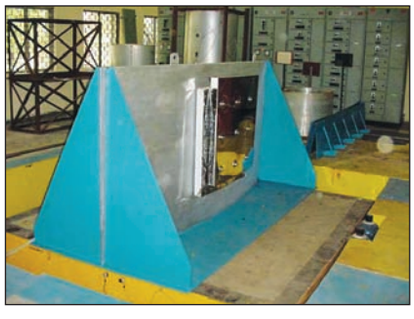

Fig. 4 *Seismic qualification of safety vessel insulation panel*

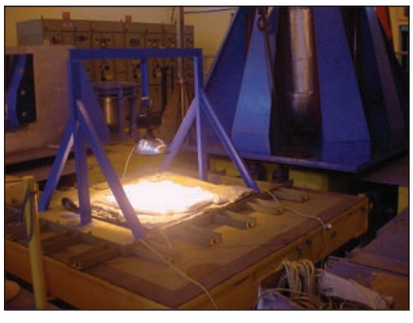

Fig. 5 *Seismic qualification of RCB lighting system for PFBR*

II.21 Sodium Calibration of Prototype Fast Breeder Reactor Mutual Inductance Level Probes

Mutual inductance type continuous and discrete level probes are used for monitoring sodium level in primary and secondary sodium circuits of PFBR. These level probes have been manufactured by industry as per IGCAR design and required calibration in sodium before installation in PFBR. There are twenty nine mutual inductance type continuous and discontinuous level probes each of length varying from 0.66 to 9.6 metres. These probes were brought to FRTG and calibrated in sodium at the operating temperature range of 453-823 K. During calibration, the continuous level sensors are characterized to find out the operating frequency and the resistance to be connected across secondary winding for temperature compensation. For discrete level probes, no level and full level readings at two extreme operating temperatures were measured to fix the threshold for level appearance or disappearance in the electronics.

The sodium calibration of these level probes was done in test vessel-1 in Hall-III, FRTG. In order to facilitate calibration of mutual inductance level probes in sodium in test vessel-1 of large component test rig, modifications were done in the sodium loop and a new flange was also fabricated. The flange was designed such that all the probes can be immersed completely in sodium. Provision was made in top flange by providing more pockets to test more than one level probe at a time as shown in Figure1.

Calibration of continuous level probes (Figure 2) involved measurement of secondary output voltages when the probe was fully surrounded by sodium and when the surrounding sodium was fully drained at different frequencies and at the maximum and minimum temperatures. These readings were used to calculate the value of temperature compensating resistor (Figure 3). Thereafter, readings were once again taken with temperature compensating resistor connected across the secondary but at fixed frequency. All the 29 continuous level probes were characterized.

Fig. 1 *Calibration set-up for level probes*

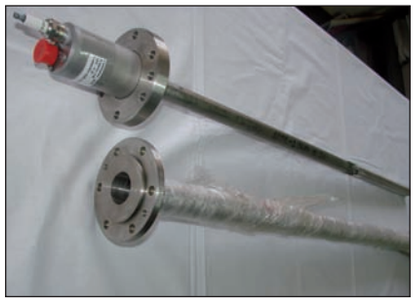

Fig. 2 *Continuous level probe with pocket*

For discrete level probes, the operating frequency was fixed at 2.5 kHz and values of secondary voltage with and without sodium at the maximum and minimum operating temperature need to be determined. For determining this, the primary current to the probe was adjusted to 100 mA and frequency was set at 2.50 kHz. Sodium was filled in the vessel so that all the sensing elements were immersed in sodium and the sodium temperature was maintained at 453 K. Each secondary output was measured at 453 K and at maximum operating temperature with and without sodium. For discrete level probe electronics, the sensor secondary output voltage with sodium at maximum operating temperature and without sodium at minimum operating temperature were fed to the electronics and the threshold (average of the secondary voltage without sodium at minimum temperature and with sodium at maximum temperature, Figure 4) was set in the electronics for level indication. After calibration, all these probes with the external resistance connected across the secondary terminal were sent to BHAVINI.

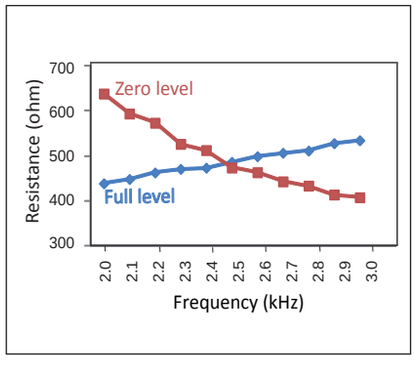

Fig. 3 *A typical resistance vs frequency curve for obtaining R_{ext}*

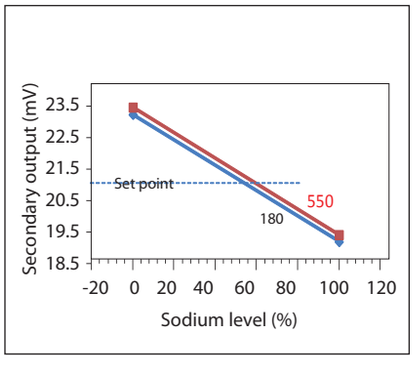

Fig. 4 *Setting up of threshold (set point) in discrete level probe*

II.22 Development of Displacement Method for Electromagnet Response Time Measurement in Control and Safety Rod Drive Mechanism

Control and safety rod drive mechanism and control and safety rod (CSR) form part of first shutdown system of PFBR. The main functions of control and safety rod drive mechanism are to facilitate start-up, power control, controlled shut down and SCRAM the reactor under abnormal conditions. During normal operation, mobile assembly of control and safety rod drive mechanism is held by an electromagnet located at the top of control and safety rod drive mechanism. On receiving the SCRAM signal, electromagnet is de-energised and the mobile assembly of control and safety rod drive mechanism along with control and safety rod is released to fall under gravity. There is a finite delay in the start of movement of control and safety rod even after receiving the SCRAM signal on account of electromagnet response time. As the negative reactivity addition commences only after control and safety rod starts moving down into the core, the electromagnet response time is an important safety parameter, which has to be measured during each SCRAM. As per the technical specifications of the plant the maximum allowable response time is 100 milliseconds.

Generally, current decay method is used for measuring electromagnet response time. In this technique, current decay through the electromagnet coil after de-energisation is indirectly measured and is used for electromagnet response time measurement. A typical electromagnet response time curve is shown in Figure 1. The first peak corresponds to SCRAM initiation and second peak corresponds to mobile assembly detachment. Thus, the time interval between the first and second peaks is the electromagnet response time.

However, a need to develop a simplified alternative method is felt on account of difficulties in implementing the current decay method in PFBR. An alternate method called displacement method has been developed, wherein the electromagnet response time is estimated from the displacement characteristics of mobile assembly during SCRAM. Inbuilt potentiometer records the displacement characteristics of mobile assembly. In this technique, the time instant of detachment of mobile assembly alone is obtained from displacement versus time curve measured from potentiometer signal during SCRAM action. The time instant of initiation of SCRAM action is taken directly from the corresponding SCRAM signal.

An ideal displacement versus time curve during SCRAM action is shown in Figure 2. Displacement is expressed in terms of potentiometer output. Initially the curve is flat because the mobile assembly is held stationary by the electromagnet. When the electromagnet is de-energised mobile assembly starts moving, but with some time delay due to electromagnet response time. Mobile assembly moves with uniform acceleration till the end of free fall and the corresponding portion of the curve is parabolic. In displacement method, two criteria viz. negative slope criterion and back calculation criterion are proposed for identifying the exact time instant of mobile assembly detachment. In negative slope criterion, the time instant at which the slope of the displacement

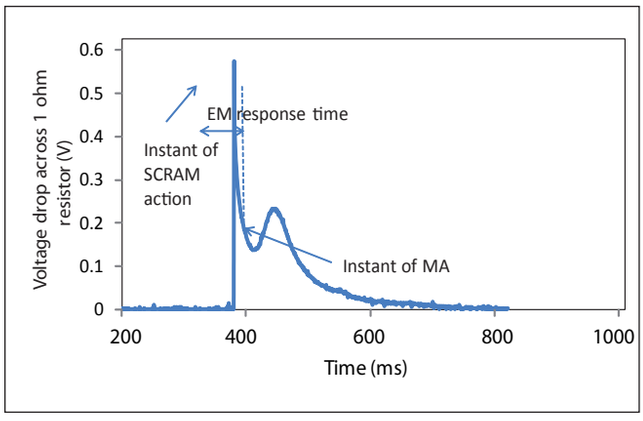

Fig. 1 A typical EM response curve of current decay method

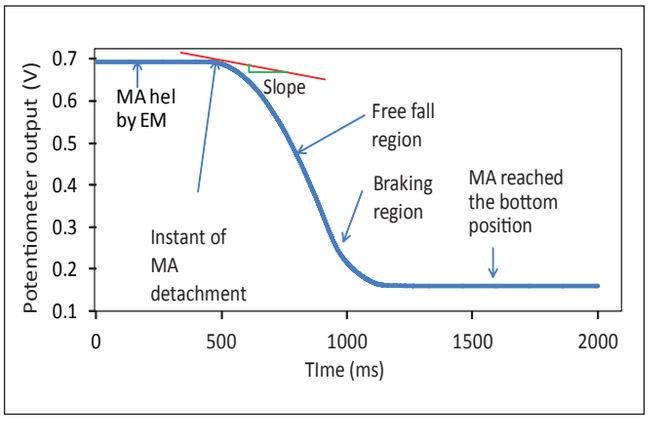

Fig. 2 Displacement versus time curve of displacement method

curve turns negative from zero, as marked in Figure 2, is the instant of mobile assembly detachment.

In back calculation criterion, instant of mobile assembly detachment is identified as follows:

- The distance travelled by mobile assembly(s), from its SCRAM position (position before initiation of SCRAM) is estimated from the potentiometer reading at a given instant of time, 't'.
- The time required for moving the above distance is calculated using

$$t = \sqrt{\frac{2 * s}{a}}$$

  where, t = time required to travel *'s'* distance with *'a'* uniform acceleration
- The instant of detachment is equal to (T-t)

Negative slope criterion is very simple to implement and accurate at high data sampling rates only, whereas back calculation criterion is relatively complex and accurate even at low sampling rates.

Qualification of displacement method encompasses three stages, viz. feasibility study in off-line mode, online testing with control and safety rod drive mechanism and integrated testing with associated hardware and software.

In feasibility study performance of displacement method was validated with current decay method as reference. For this purpose, unconditioned potentiometer data and decay current data stored during performance testing of control and safety rod drive mechanism were utilised. But those signals were found to contain noise such as small random fluctuations around the actual value and spikes at few instances. Hence, the potentiometer signal was subjected to signal processing to reduce the noise and make it suitable for extraction of information regarding instant of electromagnet detachment. Among many kinds of digital filters available, median filter was chosen for this application owing to its excellent spike noise removal and smoothening properties. A new scheme of median filtering specific to this application termed as 'Multi-pass recursive median filter with variable window' was developed. The performance of the filter was validated against standard filters. Considering high sampling rates employed in acquiring potentiometer data, negative slope criterion was used during feasibility study. Instant of mobile assembly detachment values obtained from the displacement method and from the current decay method are presented in Table 1. Good agreement of the results could be seen which demonstrates the feasibility of displacement method.

During the second stage of testing, (i.e. online testing with control and safety rod drive mechanism) potentiometer data was sampled at a low rate of 30 Hz (same as the rate of data acquisition in control and safety rod drive mechanism - real time computer of PFBR) as opposed to high frequency sampling done in feasibility study. It was found that the low sampling rate affected the accuracy of displacement method with negative slope criterion. Hence, instant of mobile assembly detachment was estimated with back calculation criterion. Testing was carried out with electromagnet set current and drop height as parameters. Table 2 shows the results obtained with different set currents and Table 3 shows the results obtained with different drop heights. Good agreement between the current decay method and the displacement method with back calculation criterion could be observed.

Necessary hardware and software changes for implementation of displacement method in PFBR are being carried out currently. After these modifications, integrated testing for qualification of displacement method for PFBR would be taken up.

Table 1: Negative slope criterion

Drop height (mm)	Time instant of EM detachment (ms)	
	Current Decay	Displace-ment
300	844	843
400	596	589
500	585	591
600	456	446
700	1051	1059
1085	823	825

Table 2: Back calculation criterion (Drop height = 500 mm)

Set current (A)	Instant of detachment (ms)	
	Displace-ment	Current decay
0.6	1153.9	1159
0.8	1205.0	1210
0.8	1279.4	1282

Table 3: Back calculation criterion (Set Current = 0.8 A)

Drop height (mm)	Instant of detachment (ms)	
	Displace-ment	Current decay
300	1075.1	1080
500	1205.0	1210
500	1279.4	1282
700	1272.8	1283

II.23 Qualification of I&C Components of Failed Fuel Location Module

Function of Failed Fuel Location Module is to identify the fuel subassembly with failed pin after getting indication from bulk delayed neutron detectors. The mode of detection is by monitoring the presence of delayed neutrons in the sodium coming out of fuel subassembly. Sodium sampling tubes are positioned above the top of each fuel subassembly and the other ends of the sampling tubes are connected to the base plate of the selector valve of function of failed fuel location module. Sodium, coming out of fuel subassembly, passes through the sampling tube to the selector valve that selectively permits sodium from any particular fuel subassembly.

Other end of the selector valve is connected to a DC conduction pump that sucks sodium from the sampling line and sends to a capacity, which is situated above the top of the control plug. Specially designed power supply (4 V, 2500 A) is provided on the top of the control plug. This feeds DC conduction pump (DCCP). The capacity can hold 200 cc of sample sodium. Sodium returns from the capacity to the hot pool through a permanent magnet flow meter. Neutron detector block is provided around function of failed fuel location module housing at the level of sodium capacity.

The detector signal is used to determine the neutron flux due to the presence of delayed neutrons. Moderator is provided to thermalize the neutrons. Boron coated counters are used for monitoring the delayed neutrons.

Positional drive system

Drive shaft of the selector valve is rotated by a positional drive system(Figure 1) with an encoder. Rotation of the selector valve permits sequential monitoring of each fuel subassembly outlet for the presence of delayed neutrons due to the failure of fuel pin. The maximum allowable positioning error to avoid intermixing of sodium from the adjacent holes in the selector valve while sampling sodium from a particular location is 1.25^{o}. The inaccuracies in positioning are caused by the specified manufacturing tolerances, the nominal clearances between stationary and rotating parts and the angle of twist of the rotating parts. Special care has been taken to control these inaccuracies. The allowable error in the positional drive system is 10 arc-minutes. The system needs to work at 343 K.

Testing and qualification

Positional accuracy and referencing are performed at various speeds and loads. Additional referencing encoder and torque sensor were provided for testing. Burn in was performed at 343 K for 168 hours followed by environmental tests and EMI/EMC. After successful testing by above methods, seismic tests were performed. The floor response spectra for this test is taken as the response spectrum at roof slab location of PFBR. The results during burn in at 343 K, 1.5 rpm speed and 66 Nm torque were given in Table 1.

Fig. 1 *Positional drive system for failed fuel location module*

To ascertain the complete life of the motor, accelerated life test has been performed on the motor with continuous acquisition of position accuracy data at 373 K for 5 days.

Table 1: Results of burn in experiment

Parameter	Before burn in			After burn in		
	Set Angle	Angle reached	Accuracy	Set Angle	Angle reached	Accuracy
Angle	10.91	10.92	0.01 ^{o}	10.91	10.92	0.01 ^{o}
Angle	174.55	174.54	0.01 ^{o}	174.55	174.54	0.00 ^{o}
Angle	207.27	207.27	0.00 ^{o}	207.27	207.26	0.01 ^{o}
Angle	278.18	278.18	0.00 ^{o}	278.18	278.18	0.00 ^{o}
Angle	354.55	354.55	0.00 ^{o}	354.55	354.54	0.01 ^{o}

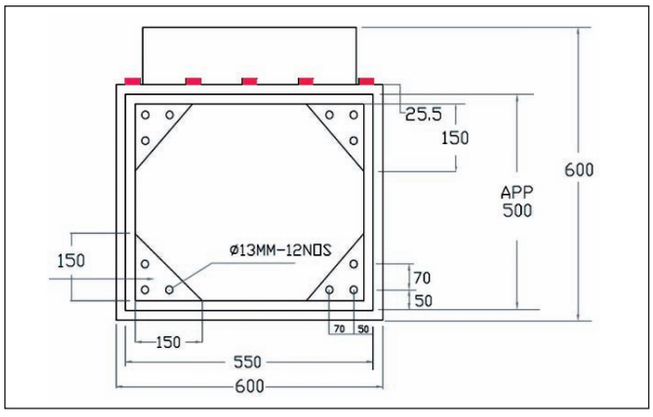

Fig. 2 *Original support structure of power supply unit*

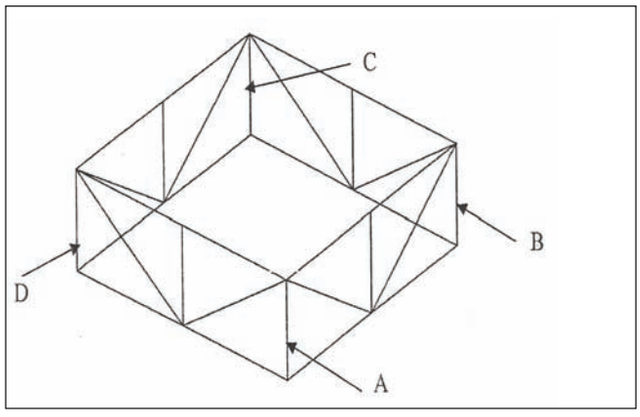

Fig. 3 *Base frame showing reinforcement locations*

DC conduction pump power supply

The power supply unit consists of fifteen pluggable power modules, each of 4 V/200 A, paralleled, one control module and an input section. With this arrangement any faulty power module can be taken out of the system after switching OFF its MCB, without disturbing the system operation (with reduced current).

Sixteen modules and a input section are housed in a cabinet having size of 600 mm (W) x 2000 mm (working height)x600 mm (D). The input to the system is 415 V ± 10% , 3 phase, 4 wire AC, 50 Hz, ± 4%. The output is 0-4 V DC/0-2500 A. The over all control is through front panel controls/ RS232-485 interface.

The power supply is SMPS based unit developed by M/s Digitronics, Pune. The rack consists of fifteen units of 4 V/200 A (Model A0800-14) power modules and one control module. Each unit has 1 power train. The input section consists of EMI Filter, inrush limiting rectifier, PFC MOSFET, diode and choke to deliver 4V DC. The same PCB houses power supplies for fans, control and logic circuits.

Each power train works on full bridge rectifier principle using power transformer and chokes. Adequate heat sinking is provided for switching devices, rectifier and bridges. Forced air is used to cool the heat sinks (air flow sideways). Control module has micro controller board having micro controller section, PWM controller, current shunt amplifier and RS232/RS485 isolated communication section. Control box which is at the bottom of the rack includes 20*4 character backlit LCD display, rotary encoder, function/ control buttons and nine LEDs for status monitoring.

Line/load tests, ripple, remote control tests and 168 hours burn in are performed on the power supply. After the successful testing of these, the power supply was subjected to environmental tests such as dry cold, dry heat, temperature cycling and damp heat cycle tests at test labs in ETDC, Pune. EMI/EMC tests are also conducted on the panel after the successful environmental testing. The tests include conductive and radiative emission-susceptibility tests and surge tests. Functional and structural integrity of the power supply unit of DC conduction pump of failed fuel location module has been demonstrated by shake table experiments in energized condition using ten tonnes shake table at IGCAR for one operation base earthquake.

The required response spectra for the test is taken as the response spectrum at roof slab location of PFBR. The original panel supporting structure (Figure 2) has been reinforced by ISA 50 angles (Figure 3) to strengthen the panel-support structure connection at the four corners. Responses have been measured by strain gauges and accelerometers kept at various locations of the panel. During the testing, abnormal vibrations are observed on the panel sheets. Hence, it is recommended to stiffen these sheets to reduce the vibration and the same was implemented in all the other units (Seismic test results are given in Table 2).

The detailed inspections carried out during and after seismic test demonstrated the healthiness of the panel during and after seismic qualification tests.

Table 2: Seismic test results

	Before seismic test			After seismic test		
Parameter	Load end	Local display	Remote	Load end	Local display	Remote
Voltage (V)	3.97	3.98	3.99	3.96	3.99	3.98
Current (A)	2498	2497	2493	2497	2494	2493
Ripple (mV)	14	---------	---------	15	---------	---------

II.24 Design and Development of Safety Critical Eddy Current Flow Meter Electronics

In PFBR, two pumps are used in the primary circuit. In case of an event of rupture of the main pipe, a category-4 event, the heat removal from the core will be severly affected, which leads to increase in the temperature of the clad and fuel. In order to prevent the temperature from reaching the design safety limits, protection to the plant is provided by selecting pressure drop across the primary pump as a SCRAM parameter. Alarm is initiated when pressure drop across the pump falls below 98% of the nominal value and safety action is initiated when pressure drop across the pump falls below 95% of the nominal value.

An eddy current based flow sensor is used for this purpose. The sensor is installed in the bypass line. The sensor consists of a primary coil, excited by a constant sinusoidal current of 200 mA (±5 mA) at 400 Hz (±2 Hz) and two secondary coils. The pressure drop is derived from the difference of the voltages induced in the secondary coils.

To ensure safety and high availability (minimize spurious trips) of the reactor, triple modular redundancy was employed. Hence, for each pump, three independent sensors and signal processing electronics are provided. The major constraints in the design of the signal processing electronics is that it has to deal with a low level signal wherein 40 mV corresponds to 100% of the process value in the presence of a large common mode voltage with an accuracy of 0.5% and initiate safety action within a stipulated time of 300 ms. Further, a stable sinsusoidal current source is necessary to ensure good sensitivity.

The signal processing electronics shown in Figure 1 consists of five major modules viz. transmitter module, which generates a stable sinusoidal voltage, power amplifier module, which converts the sinusoidal voltage to a current and drive the primary coil of the sensor, receiver module, which processes the secondary coil voltages and evaluates the difference (which is a measure of pressure drop) Delta-H module, which computes the pressure drop and initiates alarm and safety action on demand, and flow module, which computes the flow.

Modular design approach was adopted for the signal processing electronics to ensure adequate cooling and ease of maintainability. A single 6U module holder houses the signal processing electronics for a single channel for both the primary pumps.

The design of the system was carried out in accordance with safety design guide D-10 by incorporating failsafe design features against postulated failures like failure of excitation, sensor secondary cables open, failure of clock, failure of power supplies, failure of computation of pressure drop and flow, irrational set points and voltage difference in the secondary coils out of bounds. Further, on-demand testability was also provided for surveillance purposes to ensure the healthiness of the blocks, which are not covered by on-line diagnostics.

Functional testing of the signal processing electronics with sensor as shown in Figure 2 was completed. Further, it has also undergone environmental qualification testing as per IS-9000 standard successfully.

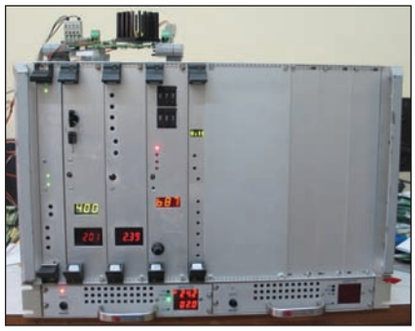

Fig. 1 *Eddy current flow meter signal processing electronics channel*

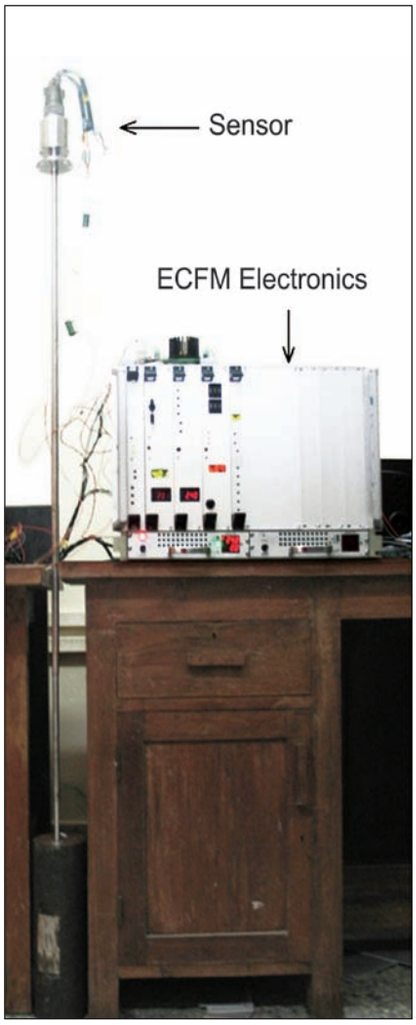

Fig. 2 *Functional testing of eddy current flow meter electronics with sensor*

II.25 Risk Cost Optimization for Safety Grade Decay Heat Removal System of PFBR using Genetic Algorithm

Safety critical systems play a vital role in the safe operation of nuclear power plants. Hence, they must be always available. Periodic activities like surveillance tests and preventive maintenance are carried out on components of standby safety systems of nuclear plants to improve their availability and thereby reduce the risk associated with their failure. Such activities incur costs owing to the manpower required, number of tests to be conducted, testing costs etc. For economical operation of nuclear power plants it is required that minimum cost be involved while ensuring the safety of the plant. So, we need to schedule the tests on various components such that the total testing cost of system and system availability are optimum. Optimization of cost versus risk and finding the best testing strategy in Fast Reactor domain is done on the safety grade decay heat removal system of Prototype Fast Breeder Reactor using genetic algorithm.

Problem formulation

The schedule for surveillance tests on safety grade decay heat removal system of PFBR has to be optimized. The influence on unavailability by surveillance testing is shown in Figure 1.

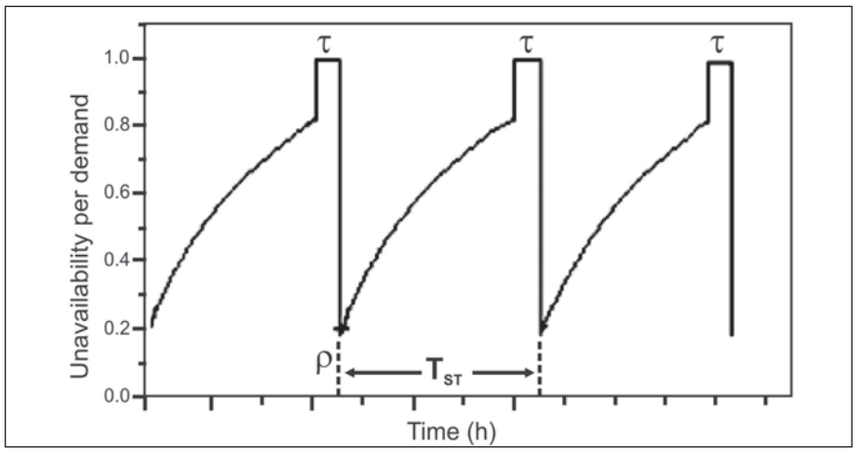

Fig. 1 *Influence on the unavailablity on demand considering surveillance testing*

Unavailability and cost are functions of test interval and reliability parameters. The list of symbols used to represent reliability parameters and their meanings are given in Table 1. The value for these reliability parameters were taken from the probabilistic safety analysis (PSA) report of PFBR. The unavailability equation used is given in Equation-1 of Table 2 where $u_i(x)$ represents unavailability of component 'i' that depends on the vector of decision variable x.

Total unavailability is found from the cutset equations obtained from the fault tree analysis. The probability of top event (i.e.) system failure is found by adding the minimal cutsets (minimal way in which system can fail). Hence, system unavailability is sum of 'j' number of minimal cut sets and the product 'k' extends to the number of basic events in the j^{th} cut set as given in equation-2 of Table 2. u_{jk} represents the unavailability associated with the basic event k belonging to minimal

Table 1: Reliability parameters

Symbol	Meaning
T_i	Surveillance test interval
t	Mean time to test
λ	Standby failure rate
T_R	Mean time to repair
C_{ht}	Surveillance testing cost per hour
C_{hr}	Cost of repair per hour
d	Demands/year
T_m	Mission time

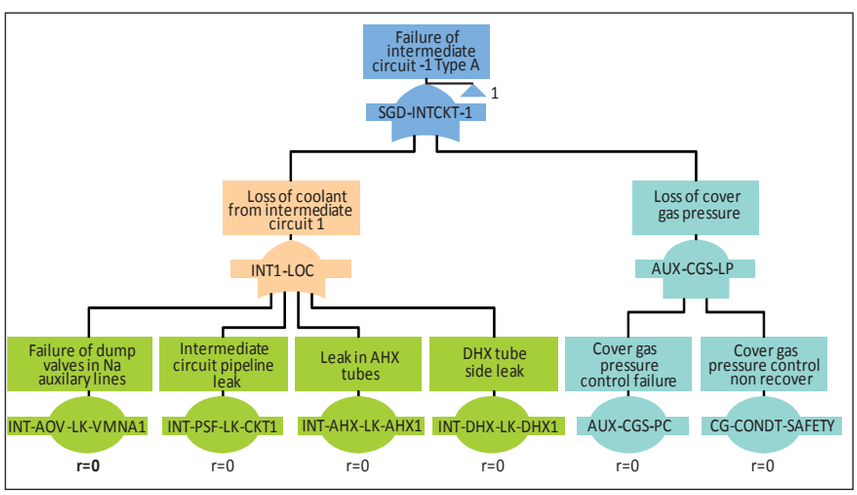

Fig. 2 *Fault tree for failure in one loop of safety grade decay heat removal system*

cut set number j. The cost model is established as given in equation-3 of Table 2.

The total yearly cost of the system having i number of components is the sum of cost of testing individual components and is as given in equation-4 in Table 2.

The top event for safety grade decay heat removal 'S' is the unavailability of safety grade decay heat removal system to remove decay heat in 4/4 failure mode. The fault trees were developed using immediate cause approach. The fault trees are constructed and analyzed using the software ISOGRAPH. A partial fault tree for the loss of safety grade decay heat removal is shown in Figure 2. The total number of components to be tested is ten.

There are about two hundred minimal cutsets obtained from the fault tree analysis of which three cutsets are listed below:

1. INT-AHX-LK-T11.INT-DHX-LK-T12.INT-PSF-LK-CKT3.INT-AOV-LK-VMNA4

2. INT-AHX-LK-T11.INT-DHX-LK-T12.INT-PSF-LK-CKT3.AUX-CGS-PC4.CG-CONDT-SAFETY

3. INT-AHX-LK-T11.INT-DHX-LK-T12.INT-PSF-LK-CKT3.INT-PSF-LK-CKT4

Hence , the system unavailability equation will be:

U(x) = u(INT-AHX-LK-T11). u(INT-DHX-LK-T12).u(INT-PSF-LK-CKT3). u(INT-AOV-LK-VMNA4) +u(INT-AHX-LK-T11).u(INT-DHX-LK-T12).u(INT-PSF-LK-CKT3).u(AUX-CGS-PC4).u(CG-CONDT-SAFETY) +u(INT-AHX-LK-T11) . u(INT-DHX-LK-T12) . u(INT-PSF-LK-CKT3) . u(INT-PSF-LK-CKT4) + …

Genetic algorithm for optimization

The problem of risk-cost optimization for safety grade decay heat removal has a large search space and involves a multimodal domain where multiple solutions are possible. For locating the global best solution in such cases, metaheuristic approaches are suited and hence, we employ genetic algorithm for this study.

Test interval is the decision variable; unavailability and cost are functions of test interval. One is objective function and the other is constraint. The problem is solved using genetic algorithm for two cases:

i. Keeping the cost as objective function to be minimized and unavailability as constraint given as Equation-5 and 6 of Table 2.

ii. Keeping the unavailability as objective function to be minimized and cost as constraint given as Equation-7 and 8 of Table 2.

The presence of constraints in this optimization make it difficult for a normal genetic algorithm technique to give precise result, hence, some improvements like penalization are implemented. An object oriented genetic algorithm library is developed in C++ and the test interval optimization for safety grade decay heat removal system is achieved using this library.

A genetic algorithm applied successfully in the test interval optimization problem. The optimal test interval for carrying out surveillance testing of the various components of safety grade decay heat removal system of PFBR in the most economical way is found without affecting plant safety. The results for cost minimization are given in Table 3. The yearly cost of surveillance is estimated to be 30 lakh rupees.

Table 2: Equations

Sl. No	Equation
1	$u_i(x)=\lambda(T_i/2+T_R)+(1-e^{-\lambda T_m})$
2	$U(x)=\sum_j \prod_k u_{jk}(x)$
3	$c_i(x)=\frac{t}{T_i}C_{ht}+\lambda T_R C_{hr}$
4	$C(x)=\sum_i c_i(x)$
5	$Min(\sum_{i=1}^{n} c_i(x))$
6	$U(x) \le MaxRisk$
7	$Min(U(x))$
8	$\sum_{i=1}^{n} c_i(x) \le MaxCost$

Table 3: The results for cost minimization (Cost Min, Risk Constraint = 5E-07)

Auxiliary circuit Cover Gas Pressure Control Failure (AUX-CGS-PC)	124 days
Intermediate circuit dump valve leak external(INT-AOV-LK-VMNA)	2 weeks
Intermediate circuit pipeline leak (INT-PSF-LK)	1 year
Primary Heat Transport - Pump Failure (PHT-PUMP-FR)	1 day
Primary Heat Transport - Main Motor Failure (PHT-MM-F)	6 days
Primary Heat Transport - Pony Motor Failure (PHT-PM-F)	4 days
Leak in AHX tubes-type1 (INT-AHX-LK-T1)	36 days
Leak in AHX tubes-type2 (INT-AHX-LK-T2)	38 days
DHX tube side leak-type1 (INT-DHX-LK-T1)	1 year
DHX tube side leak-type2 (INT-DHX-LK-T2)	269 days

II.26 3D Simulation of Fuel Handling System Operations for PFBR Training Simulator - KALBR-SIM

The full scope replica operator training simulator provides an efficient platform for imparting training for nuclear power plant operators. The incidents due to human errors related to fuel handling system in yester years has led to extended period of reactor shutdown, which is a costly affair. Hence, it has become essential to incorporate fuel handling simulator for training the operators to enhance the skill level. It is highly essential that the operator knows the interlocks and the controls for carrying out the fuel handling operations efficiently. Keeping this in mind, the simulator for fuel handling system has been designed, developed and implemented in-house. It forms a part of PFBR operator training simulator named KALBR-SIM (KALpakkam Breeder Reactor SIMulator).

Fuel handling system, one of the important sub-systems of PFBR consists of in-vessel and ex-vessel subassembly handling. In-vessel core handling involves transfer arm, large rotatable plug and small rotatable plug operations. Ex-vessel fuel handling involves inclined fuel transfer machine, rotatable shield leg, gate valves etc.

The development of fuel handling system modeling started with a detailed study and understanding of the system through design, operation notes and relevant drawings. A scope document was prepared covering, the components to be modeled, the related logics, controls and transients/malfunctions. Based on this, data collection was carried out using various resources like control notes, design notes, panel/console drawings, general assembly drawings, annunciation window legend drawings and periodic interaction with design experts. After thorough understanding of the system, a conceptual design was carried out followed by a detailed design. Fuel handling system modeling involves three basic modules namely process, logic and virtual panel models. The development of process model involves 3D models of components like transfer arm, IFTM etc. and animating them. The 3D models and animation were developed in-house using platform independent C++ code with Open GL based application programming interfaces. The process modeling application outline includes C++ headers and computer aided three-dimensional interactive application (CATIA) models. Some of the complex 3D models were inherited from CATIA models. The other 3D models that were necessary for the successful operation of the fuel handling system simulator were developed in C++ using triangle strip set and mesh application programming interfaces. Figures 1 and 2 show 3D models of fuel handling.

A top level window was created for visualization of the application.

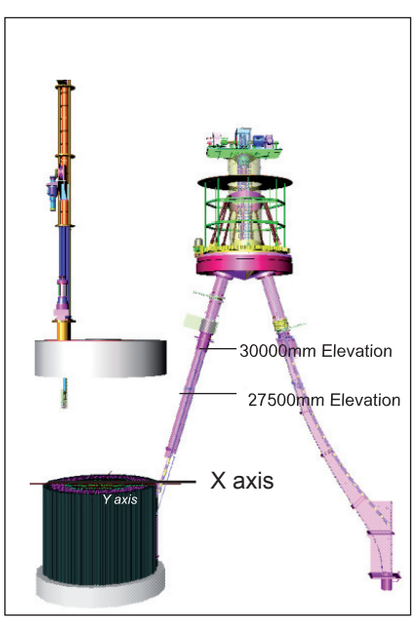

Fig. 1 *Core, transfer arm and Inclined fuel transfer machine models*

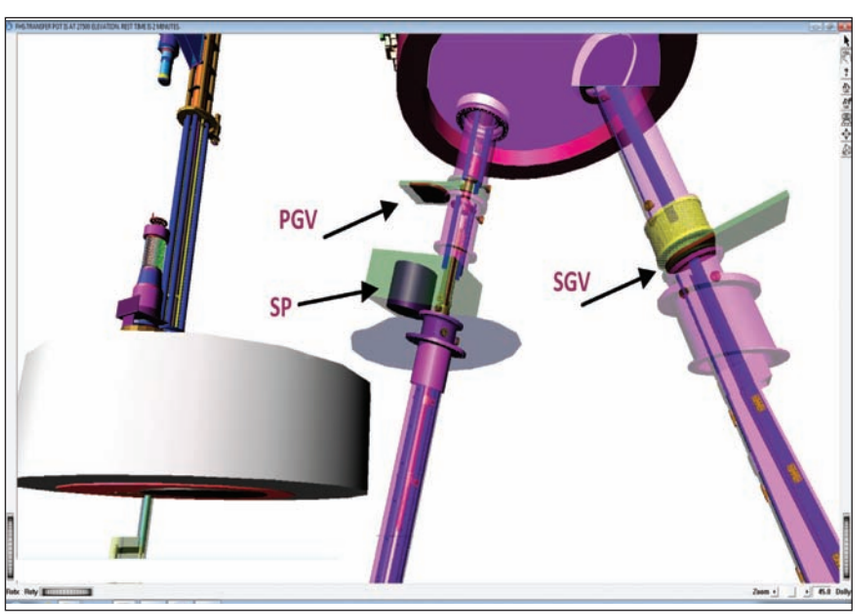

Fig. 2 *Primary (PGV), secondary (SGV) gate valves and shield plug (SP)*

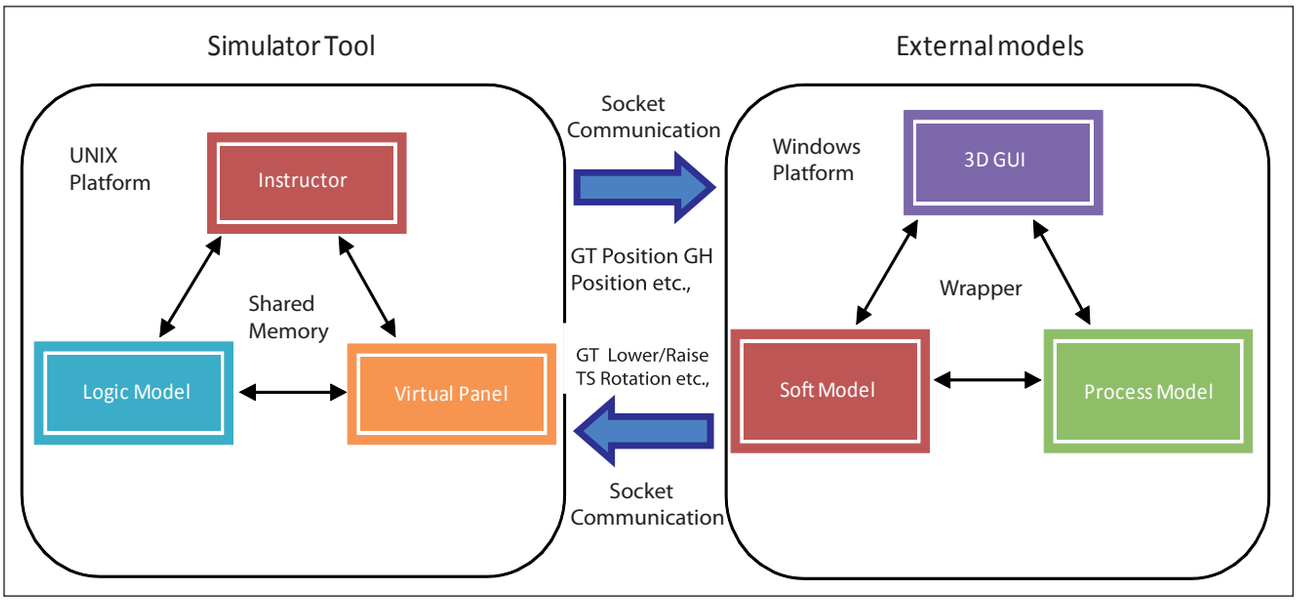

Fig. 3 *Integration of fuel handling system*

A user interface for interacting with GUI was also designed. This gives soft inputs to the system. After initialization of all variables used, OpenGL drawing area and render area were designed so as to create a scene graph. A viewer was also created which contains lights, cameras and interactivity to the scene graph. This viewer was then configured and made visible and event loop was triggered. A module was written to handle events, engines, multi-threading etc. The operators need to control the in-vessel and ex-vessel fuel handling operation from control room hardware panel as well as through soft panels containing the control buttons. Hence, a soft panel GUI was developed using Java. The panel was designed for both computer guided and manual operations. The relevant buttons alone are enabled during fuel handling and rehearsal operation.

The controls and interlocks are programmed using C and integrated into the simulation software environment. Handling control hardware panels were modeled using a commercial off-the-shelf (COTS) graphics tool. The virtual panel replicating the hardware panel has four control panels and four consoles. The process models were tested independently and then integrated with the simulator and tested. User datagram protocol (UDP) socket based multi-threaded framework based on client/server architecture for cross-platform data communication was used in full scope replica PFBR operator training simulator. A WinSock application was written in VC++ in windows platform. A UDP socket was created and bound with port address of simulator server which resided in UNIX platform. Send and receive functions were written at either end and successful communication was established and tested. Figure 3 shows the integration of simulator tool with external models for fuel handling system.

Malfunctions pertaining to fuel handling system were also modeled successfully. On selection of malfunctions from instructor station malfunction list, the corresponding alarm and message get activated. The operator will be unable to proceed with the operation once a malfunction is encountered. The operator has to either switch over to manual mode and safely terminate the operation or wait for the next instruction.

The final integrated models of fuel handling system consisting of handling control room panels and consoles-1 and 2 were demonstrated to local validation committee. The rehearsal operation followed by fuel handling movement operation was simulated and demonstrated in handling control room panel 1 & 2 and console 1& 2. Both computer guided and manual mode operations were also demonstrated. The malfunctions associated with fuel handling system viz. RSL stuck at parking position, primary gate valve failing to open, secondary gate valve failing to open, shield plug fails to open, neutronic counts high, guide tube (GT) stuck at parking position, gripper hoist(GH) stuck at parking position, top structure (TP) stuck at zero position and finally gripper fingers failing to open were also demonstrated.

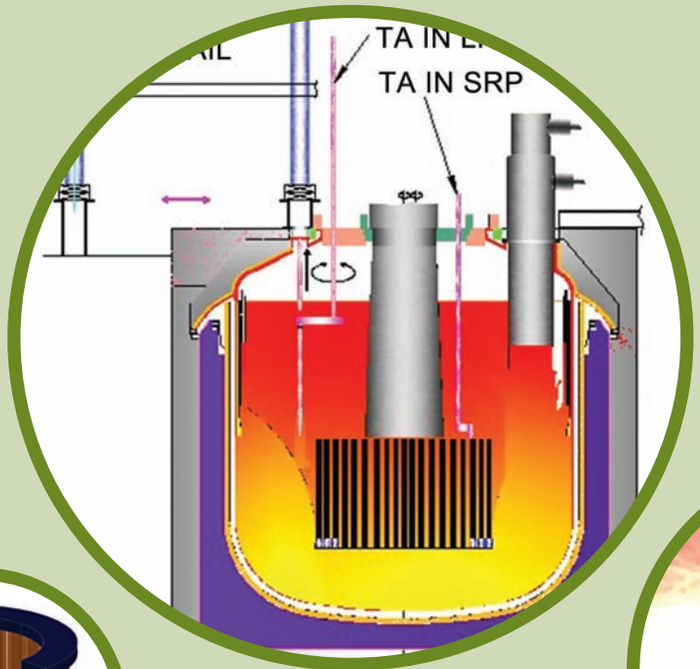

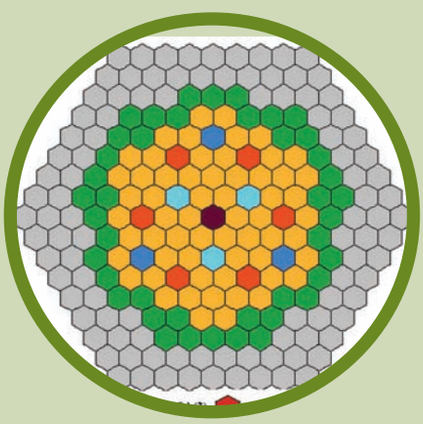

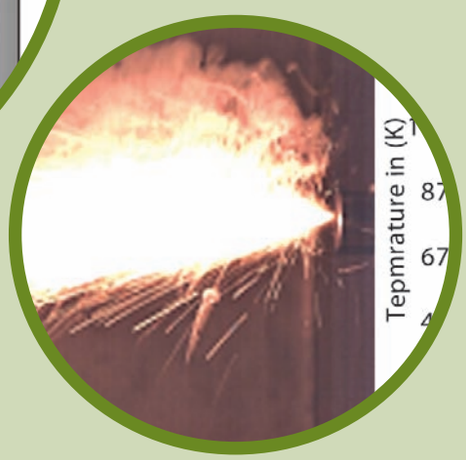

CHAPTER - III

Research & Development for FBRs

III.1 Design Confirmation of Innovative Features of Reactor Assembly by Analysis

The commercial fast breeder reactor (CFBR) is the future 500 MWe reactor which is envisaged to have a twin-unit concept. Design and construction experiences from PFBR helped the Centre to achieve an optimized design for CFBR with enhanced safety. Components where innovative modifications are proposed include control plug (CP), inner vessel, main vessel, grid plate, sodium header, number of primary pipes and roof slab.

The bottom part of inner vessel will be a single torus to enhance buckling strength. The single torus can affect the thermal hydraulics of hot pool. Since the control plug is integrated with small rotatable plug, it is possible to increase the diameter of control plug at the bottom to facilitate monitoring of all the sodium temperatures of the fuel and blanket subassembly, towards enhancing safety. The shape of the control plug can influence free surface velocity that in-turn affects gas entrainment. Hence, detailed hot pool thermal hydraulics have been studied for three different control plug shapes, viz., cylindrical, cylindrical with hemispherical core cover plate and conical. Mixing in hot pool, velocity distribution around intermediate heat exchanger and free surface sodium velocity were found to be favorable with the proposed shapes of the inner vessel and control plug. The porosity, length and position of the anti-stratification skirt attached to the bottom of the control plug have been finalized to avoid thermal stratification in the hot pool. The free surface sodium velocity is found to be acceptable with the introduction of an annular anti-gas entrainment baffle attached to the inner vessel. The size and location of this passive baffle have been finalized. The computational mesh and pool temperatures without anti-stratification skirt and with the skirt are depicted in Figure 1.

The temperature distribution on the vessel has been predicted by a conjugate heat transfer analysis with porous body model for the core and is depicted in Figure 2. It is seen that the absolute temperature and the radial as well as axial temperature gradients in the vessel are within acceptable limits. Size of main vessel as well as the radial gaps between the thermal baffles and main vessel have been reduced in CFBR. This is possible due to the close manufacturing tolerance achieved in PFBR. Further, since economy is one of the objectives, it is necessary to optimize the flow rate to main vessel cooling system, considering the revised part load operation strategy. Two and three dimensional thermal hydraulic analyses of the main vessel cooling system have been carried out for nominal and one coolant pipe rupture conditions. It is seen that a coolant flow rate of 200 kg/s at full power is adequate, which is 50% of the PFBR value. The ovality of ± 15 mm in the shells is acceptable from circumferential temperature variation in main vessel. Further, jet breaker plates of width 860 mm, located at 200 mm above the cooling pipes (24 Nos.) render a fairly uniform flow and temperature fields. The predicted main vessel temperature under full power condition is depicted in Figure 3 for a 180° sector.

Sodium from each primary pump enters a spherical header, where it branches into multiple streams to enter the grid plate. The header is spherical in shape to have a compact layout and avoid interference of primary pipes with intermediate heat exchangers. The number of primary pipes in commercial fast breeder reactor is four per header to enhance the safety against a primary pipe rupture event. With

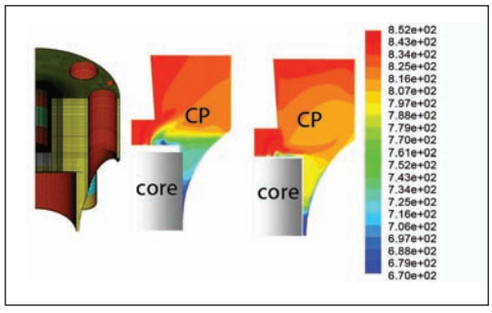

Fig. 1 *Temperature field (K) in hot pool with conical control plug: CFD mesh (left), without skirt (middle), with skirt (right)*

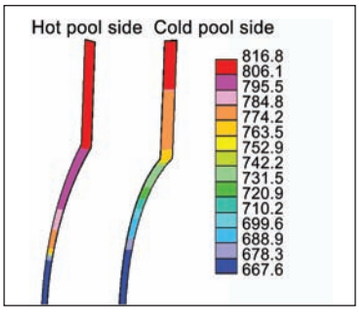

Fig. 2 *Steady state temperature (K) distribution in inner vessel*

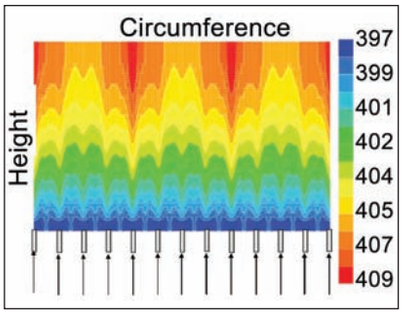

Fig. 3 *Main vessel temperature (°C) in a 180° sector during full power*

four pipes, all the pipes do not have identical lengths and bent radii. As a result there could be flow maldistribution among the pipes.

Further, proper flow guiding devices inside the spherical header is essential to reduce the pressure loss in the assembly. From computational fluid dynamics studies the optimum baffle configuration, which can significantly reduce the pressure loss in the header, has been identified. With this baffle, the flow maldistribution among the pipes only ±5%. Figure 4 shows the header with four pipes, pressure distribution in a vertical plane in the basic header with large scale low pressure zone with recirculation and the same in a header with optimized baffle configuration.

With four primary pipes per header, the diameter of primary pipe is reduced from 600 (in PFBR) to 420 mm (in CFBR). It may also be noted that with the reduction in diameter of pipes, the structural integrity of pipes improves. During the event of primary pipe rupture, sodium supplied by the pumps bypasses the core through the ruptured path back to the cold pool and the core flow rapidly decreases, with the associated increases in sodium and clad temperatures. From plant dynamic studies it is found that the core flow is 57% of the nominal value. The maximum values of clad hotspot and average sodium hotspot temperatures reached are 340 and 194 K lower than the corresponding design safety limits, even without any safety action. Evolution of clad hotspot temperature with SCRAM by second parameter is shown in Figure 5. Results for the two pipe configuration are also shown in the same figure, wherein it is clear that there is no risk of bulk/local sodium boiling during the event. Due to the selection of four primary pipes, there is significant improvement in the margins of various core temperatures.

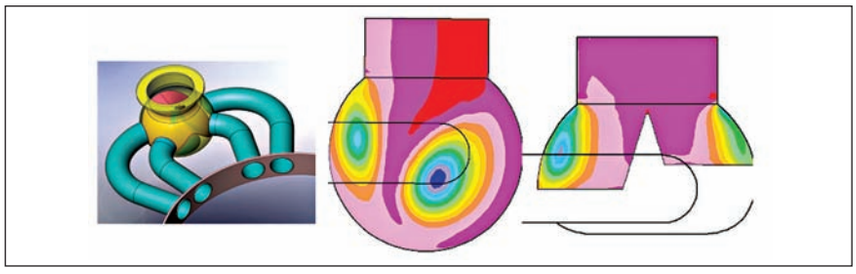

Fig. 4 *Pressure distribution in spherical header: header (Left), hasic header (middle) and header with internal baffle (right)*

In the case of PFBR the roof slab is a large box type structure with many penetrations, which posed difficulties during manufacturing, in particular due to laminar tearing. Alternatively, taking the advantages of higher load carrying capacity with reduced thickness, a dome shaped roof slab is conceived for commercial fast breeder reactor. An integrated 3-dimensional thermal hydraulic analysis of the top shield, triple point and reactor vault has been carried out (Figure 6). The study reveals that with one thermal shield below the roof slab, the concrete temperature around main vessel and safety vessel support embedment can be contained within the permissible limit by providing a dedicated cooling pipe network with reduced pipe pitch. Further, the heat flux on the roof slab with the modified geometry is found to be 1300 W/m^2 which is an important parameter for the design of jet coding system for top shield, is only ~10% higher than that of PFBR.

Thus, the thermal hydraulics feasibility of innovative modifications for commercial fast breeder reactor and quantification of their benefits in terms of safety and economy have been confirmed.

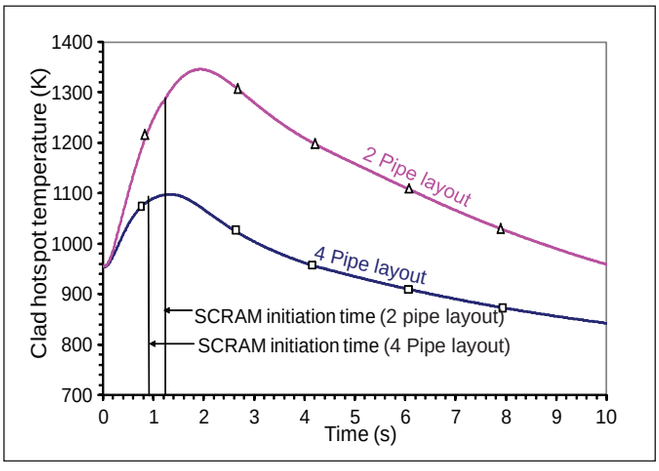

Fig. 5 *Evolution of clad hotspot temperature during a primary pipe rupture event*

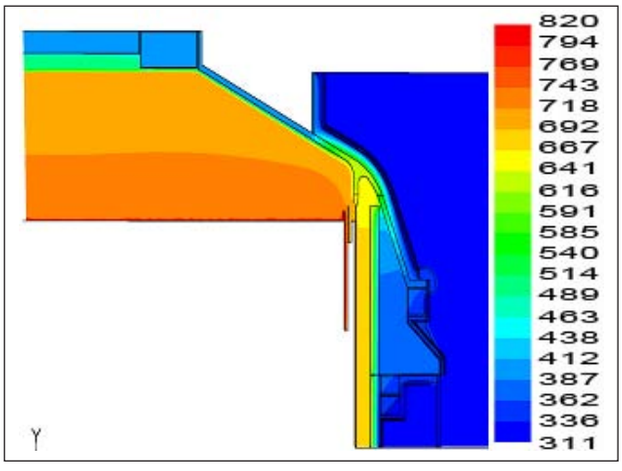

Fig. 6 *Temperature distribution (K) in top shield and reactor vault during full power*

III.2 Technology Development of Components for Innovative CFBR Reactor Assembly

Many innovative design and safety features are incorporated in reactor assembly in addition to the proven concepts towards development of components for PFBR.

In reactor assembly of commercial fast breeder reactor, eight primary pipes with reduced size are provided (compared to four in PFBR) to increase core safety margin in case of one pipe rupture event. Due to the increase in number and reduction in size of the primary pipes, the grid plate height is reduced. Also, in grid plate, sleeves are provided only for subassemblies that require forced cooling and for few rows of shielding subassemblies. For other shielding subassemblies, spigots are provided on top plate. With this arrangement the diameters of grid plate shell and bottom plate are reduced. Taking advantage of the indigenously available advanced welding technology, fully welded concept is adopted for grid plate, thereby totally avoiding unnecessary leakage in grid plate.

The shape of inner vessel is optimised with reduced upper shell diameter and double curvature single toroidal redan, which results in higher buckling strength and reduced thickness and hence reduced weight.

Roof slab has been conceptualised with dome-shape structure resting on a conical skirt, which is under compression, supporting the entire reactor assembly. At the junction of roof slab with main vessel and skirt support, a tri-junction ring forging is provided. These features enhance the reliability of the support for the reactor assembly.

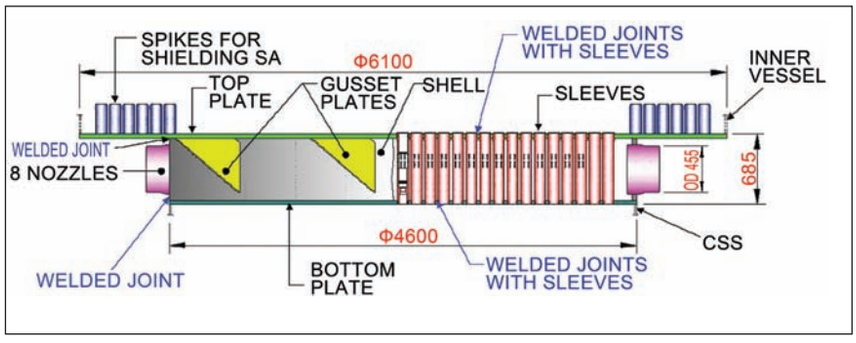

Fig. 1 *Sectional view of welded grid plate*

The material of construction of these components is austenitic stainless steel (Type 316LN/304L) and the components have fully welded box-type shell structure. A comprehensive technology development exercise was undertaken for the manufacture of welded grid plate, single toroidal inner vessel sector and tri-junction ring sector forging to finalise the design, to demonstrate the manufacturing feasibilities and to reduce the duration of manufacture of components for the reactor assembly.

For technology development of welded grid plate (Figure 1), a full size component having selected number of sleeves and spikes was manufactured (Figures 2 and 3). During the process of development, various technical challenges had to be faced. The successful resolution of them resulted in fine tuning of the design. Manufacturing procedures were evolved during the course of development based on numerous mock-up and trials. Some of them are related to

(a) Innovative joint configuration for shell-plate weld eliminating the need for welding and grinding inside the box structure with limited space between top and bottom plates

(b) Sleeve-plate and spike-plate weld joint configurations

(c) Procedures for various heat treatments and machining of the individual parts and assembly

(d) Suitable distortion control measures

(f) Procedure for measuring the verticality of sleeves

Fig. 2 *Box structure (in inverted position) after assembly of top and bottom plates and shells*

Fig. 3 *Final machining of spikes on assembly of welded grid plate*

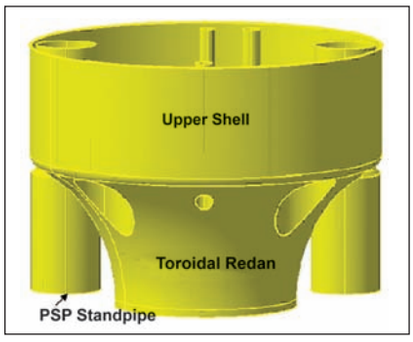

Fig. 4 *3-D model of inner vessel*

Fig. 5 *Forming of toricone of inner vessel sector using die and punch*

Fig. 6 *Profile measurement of inner vessel sector using swing arm arrangement*

(g) Procedure for examination of sleeve-plate joints etc.

For the technology development of inner vessel (Figure 4), a sector of doubly curved toricone with a portion of upper cylindrical shell was manufactured. The major activities involved are the development of suitable die and punch, pressing the job and inspection of the profile. Weight of the die and punch made of carbon steel, is around 22 tonnes. Pressing of the toricone was carried out gradually on 4000 tonnes capacity press (Figure 5). A number of trials and mock-up were carried out, first on carbon steel and then on stainless steel blanks. After each trial, the dimensions achieved were reviewed and based on the feedback, the profiles of die and punch were suitably modified. The finalised die and punch were used for pressing the actual job. The dimensional inspection was carried out using the conventional swing arm template/local templates and ECDS methods (Figure 6). The achieved profile of the toricone satisfies the design requirements.

To enhance the reliability of dome shaped roof slab, it is proposed to use a forged piece at the tri-junction joint of main vessel, roof slab and roof slab support shell (Figure 7). The major challenge in the realization of dome shaped roof slab is ensuring the indigenous supplier base for the critical tri-junction forging in stainless steel which is ~12 metres in diameter having an overall cross sectional dimension of ~500 x 500 mm.

The indigenous technology development of the tri-junction forging (in the form of 30° sectors) was undertaken and the same was completed successfully (Figure 8) after overcoming several challenges. One of the major challenges faced is incomplete filling of material within the cavities of the dies (Figure 9). This was resolved by adopting pre-forming of the ingot to favourable shape with external means and then feeding the pre-formed shape to the forging hammer. This process of finalisation involved many brainstorming discussions with the industry. Another major challenge faced was ultrasonic examination of complex shaped tri-junction. This was overcome by identifying multiple locations for scanning with shear wave and normal wave probes parallely. One MHz probes were used at locations where depth of material is very high.

The successful completion of technology development activities undertaken for three major reactor assembly components such as welded grid plate, single toroidal inner vessel and tri-junction forging of dome shaped roof slab has demonstrated the manufacturing feasibilities and given confidence for the design improvements incorporated in the reactor assembly components of CFBR.

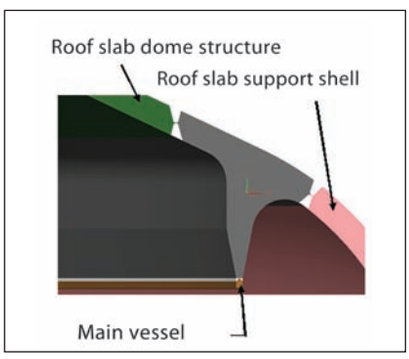

Fig. 7 *Tri-junction of roof slab, main vessel and support shell*

Fig. 8 *View of forged tri-junction sectors*

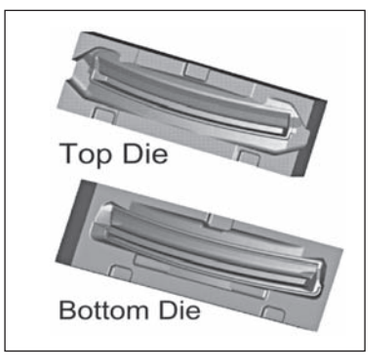

Fig. 9 *3D view of forging dies*

III.3 A Concept of Fuel Handling System for Twin Units of CFBR

Fuel handling system of fast breeder reactor is a potential area for capital cost reduction. Fuel handling system operations are carried out under reactor shutdown conditions and reduction of fuel handling time will improve the capacity factor. Being twin units and with very low utilization of fuel handling equipment in FBRs due to off-line refuelling, there is a merit to study and implement sharing of fuel handling facilities to the extent possible without compromising safety between the twin units. PFBR design and construction experience has given valuable inputs towards design simplifications and improvements.

Figure 1 shows the fuel handling scheme for CFBR as compared to PFBR. For in-vessel handling, two rotatable plugs along with two offset arm type machines, one in small rotatable plug (SRP) similar to the present transfer arm of PFBR (reach = 572.5 mm) and the other additional machine in large rotatable plug (LRP) with a reach of 1322.5 mm is arrived at. The in-vessel handling machines are provided separately for each reactor unit. The in-vessel transfer post is located in inner vessel at a distance of 4115 mm from the core centre from considerations of location of corresponding discharge port in roof slab and ensuring adequate submersion of subassembly during in-vessel transfer to ensure removal of decay heat.

For CFBR, the inclined fuel transfer machine is replaced with a simple shielded flask moving on a carriage similar to FBTR. The flask transfers subassemblies discharged through the discharge port in roof slab to the fuel transfer cell in fuel building. Flask transfer also enhances the capability to handle subassembly with higher decay power.

For the twin units, considering the requirement of sharing of component handling equipment, a common fuel building housing fresh and spent fuel handling equipment with the fuel transfer cell linking both the reactor containment buildings is provided. A separate but common decontamination building, housing all special handling equipment is provided in between the two reactor containment buildings. A unique twin reactor layout for the nuclear island connected buildings layout has been arrived at and is shown in Figure 2.

The major saving in cost is due to sharing of fuel handling equipment between the twin units. The savings in material consumption is expected to be ~46%. The research and development efforts required for realizing the above economical benefits has also been identified. The above efforts are expected to significantly improve the economics and safety of future sodium cooled fast reactors.

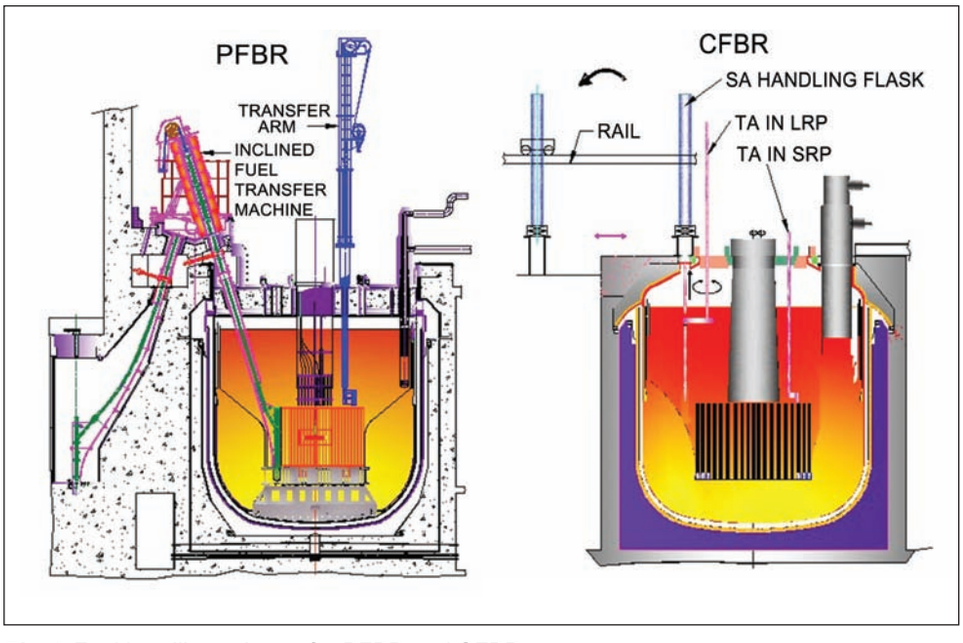

Fig. 1 *Fuel handling scheme for PFBR and CFBR*

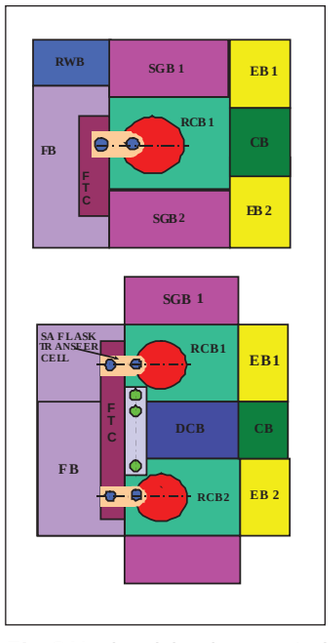

Fig. 2 *Nuclear island connected buildings layout – PFBR versus CFBR*

III.4 Advanced Fuel Cladding and Wrapper Materials-Characterization, Performance Evaluation and Joining Technique

Economic feasibility of fast reactors can be achieved with extended fuel burn-up and lower doubling time. The burn-up is largely controlled by the resistance of the fuel cladding and wrapper materials to void swelling and creep. For the 500 MWe Prototype Fast Breeder Reactor (PFBR) with mixed $(U,Pu)O_2$ (MOX) fuel, alloy D9 is chosen for fuel cladding and wrapper. To improve the burn-up further, a modified version of alloy D9, named as indian fast reactor advanced cladding-1 (IFAC-1), has been developed with optimized titanium, phosphorous and silicon contents.

Creep resistance of inherently void swelling resistant 9Cr-ferritic-martensitic steel has been improved with the dispersion of nano-size yttria particles, to develop oxide dispersion strengthened steel cladding tubes with long-term creep strength, for increased burn-up. Development of modified 9Cr-1Mo steel cladding tubes and 9Cr-1Mo steel wrapper for future metallic fuel reactors with reduced doubling time is taken up. Several aspects of the fuel cladding tubes including microstructural stability, irradiation performance and weldability with end plug in alloy D9; characterization of yittria dispersoid in oxide dispersion strengthened steel and mechanical properties of modified 9Cr-1Mo cladding tube are presented.

Performance evaluation of D9 clad and wrapper irradiated to 60 dpa in FBTR

Using FBTR as test bed, a 37 pin subassembly with MOX fuel of PFBR composition and 20% CW alloy D9 as cladding and wrapper material was irradiated to a burn-up of 112 GWd/t. The maximum displacement damage in alloy D9 clad and wrapper corresponded to 60 dpa (displacement per atom) and the irradiation temperature varied from 673 to 823 K along the fuel column. The irradiation performance of alloy D9 was assessed through remote measurements of post-irradiation swelling and mechanical properties in the hot cells on samples extracted from cladding and wrapper.

The swelling values of alloy D9 cladding (max: 2%) and wrapper (max: 0.2%) at 60 dpa obtained from immersion density measurements confirmed that the alloy D9 swells much less compared to SS 316 at similar displacement damages (Figure 1). Also, the increase in dimensions of the alloy D9 was marginal compared to those for SS 316 cladding and wrapper at similar dpa.

The tensile properties showed a hardening effect with decrease in ductility (Figures 2a and 2b). For low irradiation temperatures around 673-723 K (lower portion of fuel column), there was a significant increase in yield strength (YS) and ultimate tensile strength (UTS) with a decrease in uniform elongation. The hardening effects were more prominent in alloy D9 wrapper compared to cladding due to its relatively lower operating temperatures at the same axial location. The extent of hardening decreased in both cladding and wrapper as the irradiation temperature increased beyond 723-753 K and the ductility loss was also less severe at these high temperature locations.

The post-irradiation examinations revealed that alloy D9 clad/wrapper

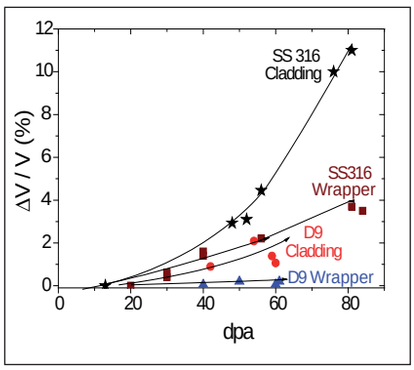

Fig. 1 Comparison of the swelling behavior of D9 clad and wrapper with SS 316

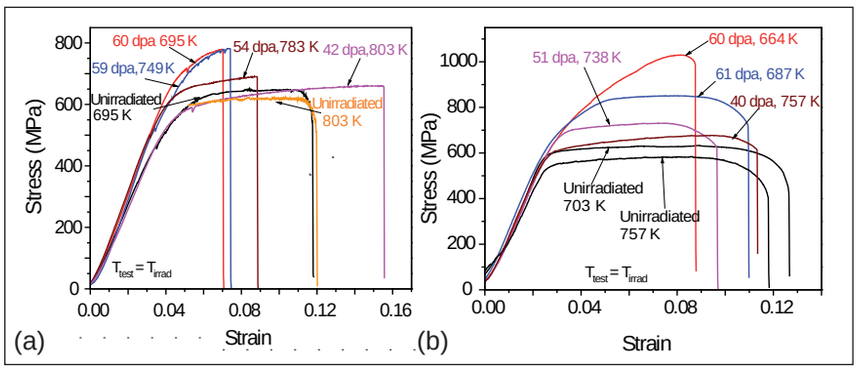

Fig. 2 Stress-strain curves of irradiated alloy D9 (a) Cladding and (b) Wrapper

had performed satisfactorily with respect to enhanced swelling resistance and retention of mechanical properties at a displacement damage of 60 dpa achieved in FBTR.

Thermal ageing behaviour of improved D9 alloys

Alloy D9 with better void swelling resistance and microstructural stability with appropriate modifications of Ni and Cr content and Ti additions has been developed. While Ti precipitates as nanoscale carbides and helps in void swelling resistance, trace alloying additions of Si and P would be effective only if retained in solution.

Alloy D9 has been developed with different P (0.025 and 0.04 wt.%-low P and high P) and Si (0.75 and 1 wt%-low Si and high Si) with a fixed Ti:C ratio. These alloys were thermally aged at 873 and 973 K for one and two years in order to establish

(i) The optimum alloy composition which retains the strength and

(ii) The precipitate evolution that may deplete the trace elements from the matrix.

The hardness of all these alloys increased (Figure 3), due to precipitation of nano size 'MC' type carbides. At 973 K, the extent of hardening is lower and continued ageing leads to a reduction in hardness. Formation of Cr rich

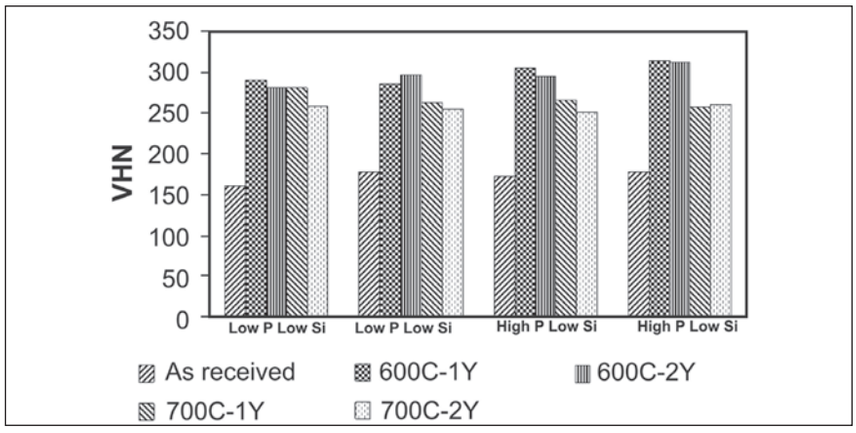

Fig. 3 *Hardness as a function of thermal ageing (Microhardness/100 g load)*

carbides and intermetallics deplete the solid solution strengthening elements like Cr, Mo, Ti, Si from the matrix, lowering the hardness. However, none of the alloys showed any segregation of phosphorus. As the effectiveness of elements like Si and P can be achieved only if they are retained in solution, among the four alloys that were studied, the low Si high P alloy is recommended as the optimum choice for further detailed study. This alloy has been identified as IFAC-1.

Dispersoid characteristics in a Fe-Y_2O_3 model oxide dispersion strengthened alloy during mechanical milling

Oxide dispersion strengthened ferritic martensitic steel is being developed as a future structural material for sodium-cooled fast reactors mainly because of its exceptional high temperature creep strength and excellent void swelling resistance. During synthesis of this alloy by mechanical alloying, the oxides may dissolve and later re-precipitate during the consolidation process. A clear knowledge of this phenomenon is necessary to control the size and distribution of dispersoids in the oxide dispersion strengthened steel matrix which decide its strength. To facilitate this, a non-dilute model oxide dispersion strengthened alloy, namely, Fe-15 wt% Y_2O_3 powder was synthesized by ball milling using indigenous nano-yttria powder. The alloy powder was milled for various milling times from 10 to 60 hours in inert atmosphere. The powder was characterized by XRD and electron microscopy techniques both prior to and after milling (Figures 4a, 4b and 4c). The starting size of the Fe powders was 50-150 µm while that of the yttria powder was 20-40 nm. When subjected to mechanical milling for various durations, both Fe and yttria

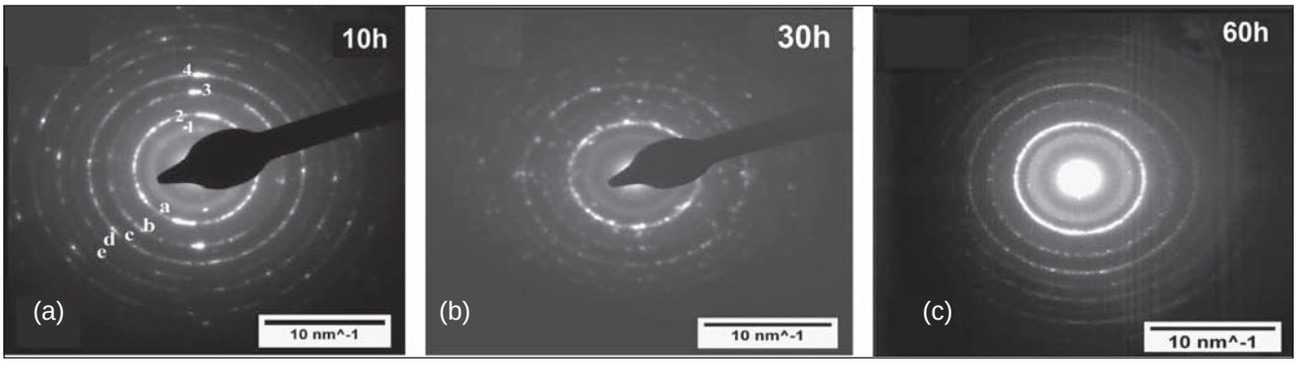

Fig. 4 *Selected area diffraction pattern for powders milled at (a) 10 hours (1 to 4 indicate the diffraction from yttria crystallites, a to e represent those from ferrite crystallites), (b) 30 hours and (c) 60 hours*

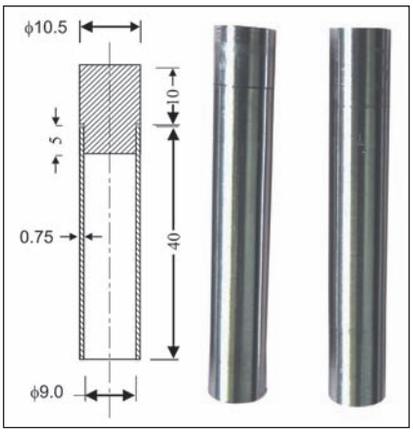

Fig. 5 *Tube and plug configuration and the machined components*

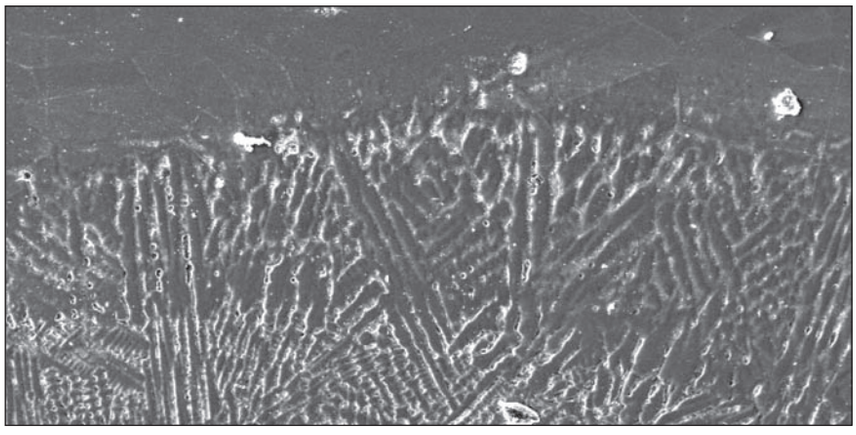

Fig. 6 *SEM photograph of the joint showing no crack/porosity*

crystallites were refined to 5-10 nm. The electron diffraction pattern of the 10 hours milled powder showed a ring pattern for polycrystalline Fe as well as yttria. However, with increase in milling time, the integrated diffraction corresponding to Y_2O_3 (411) became broad and diffused indicating a gradual loss of crystallinity. This result is also supported by XRD.

Development of D9-D9 weld joints

It is proposed to irradiate fast reactor core structural material specimens of current and future interest in FBTR to dose levels of upto 100 dpa. Cold worked alloy D9 is the preferred irradiation capsule material to withstand the high dose levels envisaged. During fabrication of the irradiation capsule, alloy D9 tubes are to be welded to alloy D9 plugs to make partitions to load the specimens. It is known that austenitic stainless steel with decreased Cr_{eq} / Ni_{eq} like alloy D9 is highly susceptible for solidification cracking during welding. An experimental programme has been pursued to develop defect-free welds and standardise the weld parameters. Alloy D9 tubes and plugs were machined from cold worked D9 rods (Figure 5).

The weld parameters have been standardised by trials and six joints have been made. The weld beads appeared shiny and smooth with uniform solidification. All the weld joints were leak tight as indicated by helium leak test. Radiography with 145 kV source strength X-ray machine using shape correction block fabricated for this test indicated no significant defect in the weld joints. Scanning electron microscopy of a longitudinal section revealed no internal defects such as crack or porosity (Figure 6) at the interface or weld zone.

The weld joints were then subjected to a few thermal cycles to simulate the effect of temperature changes from operating to shutdown conditions of the reactor. No surface crack was observed at room temperature on the three samples encapsulated in quartz tubes with a low-pressure argon environment and exposed to 873 K for 100 hours. No defect was found in the samples by helium leak test or X-radiography after three subsequent thermal cycles from 873 to 473 K. The results indicate the successful development of alloy D9 cladding tube with alloy D9 end plug weld joints for the intended use.

Mechanical properties of modified 9Cr-1Mo steel clad tube for metal fuel fast reactor

In advanced fast reactors with metallic fuel, modified 9Cr-1Mo steel has been envisaged as cladding material in view of its adequate creep strength at the relatively low operating temperature.

Tensile and creep properties of modified 9Cr-1Mo steel cladding tubes of size 6.6 mm outer diameter and 0.45 mm wall thickness developed at IGCAR were assessed. The results were compared with modified 9Cr-1Mo steel tubes, which are used for steam generators in fast reactors. The developed modified 9Cr-1Mo cladding tube has tensile strength comparable to that of National Institute of Material Science, Japan (NIMS) tube especially at higher temperatures of interest. The creep strengths of modified 9Cr-1Mo steel clad tubes are well above the RCC-MR maximum allowable stress and minimum creep rupture stress and compare well with those for the steam generator tubes and NIMS tubes. (Figure 7).

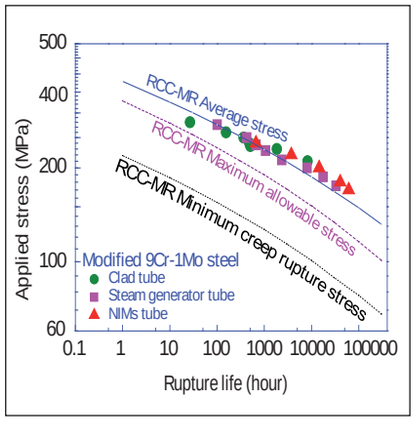

Fig. 7 *Creep strengths of tubes fabricated at our Centre*

III.5 Resisting Stress for Constitutive Analysis of Hot Deformation in Modified 9Cr-1Mo (P91) Steel

Simulation of metal forming processes using finite element analysis requires accurate description of the flow behaviour in terms of suitable constitutive equations. Constitutive analysis is performed on modified 9Cr-1Mo (P91) steel by invoking resisting stress for dislocation motion. True stress-true plastic strain data obtained from isothermal hot compression tests on P91 steel over a wide range of strain rate (0.001-100 s^{-1}), temperature (1173-1373 K) and strain (0.1-0.5) were analysed in terms of resisting stress. A new procedure called 'Y-Transition' method was developed for evaluating resisting stress and for predicting the flow behaviour. Incorporating the resisting stress a suitable strain dependent constitutive rate equation is developed for predicting the flow behaviour of P91 steel.

Flow stress data obtained at different strains (0.1-0.5 at steps of 0.05) were found to follow the Dorn power-law equation with distinct low and high stress regimes. The ordinate corresponding to the intersection of the straight lines for low stress and high stress regime in the power–law plot was designated as 'Y-Transition'. The average values of n_1 = 5.12, n_2 = 10.46 and Y-Transition = 8.71×10^{-7}; where n_1 and n_2 are the stress exponents for low stress and high stress regime, respectively. Figure 1 shows the typical linear

$$(\dot{\varepsilon}kT / D_L Gb)^{1/5}$$

plot of versus σ/G to determine resisting stress σ_R at strain of 0.3. In this plot relating flow stress σ and strain rate $\dot{\varepsilon}$, D_L is the lattice diffusivity, G is the shear modulus at temperature T, A is a dimensionless constant, k is the Boltzman constant and b is the Burger's vector. The normalized values of threshold stress (σ_H/G) and transition stress (σ_T/G) were determined as shown in Figure 1. It was observed that at low stresses, (σ_R/G)= K(σ/G) and (σ_R/G) approaches a constant threshold stress (σ_R/G= σ_H/G) in the high stress regime. The proportionality constant K was evaluated as K = σ_H/σ_T. The criterion of average value of 'Y-Transition'=8.71×10^{-7} was used for demarcating low and high stress regimes at all strains and for determining (σ_T/G), (σ_H/G) and K at various strains.

Rationalisation of flow behaviour in terms of effective stress is shown in Figure 2 for a typical strain of 0.3. At strain of 0.3, K = 0.7309 and (σ_H/G) = 0.002976. The slope of the line gives n_0, while A_0 is obtained from the intercept and these were evaluated at various strains. The flow behaviour was found to follow the constitutive rate equation in terms of effective stress. The prediction of flow stress was carried out by employing the values of constitutive parameters, viz. A_0, n_0, K and (σ_H/G) obtained at various strains. The successful prediction of flow stresses is demonstrated in Figure 3 with R = 0.99 and average absolute relative error AARE of 6.62% revealing the good predictability of the developed constitutive rate equation in terms of resisting stress for P91 steel.

The above analysis could be integrated with numerical modeling tools for simulating metal forming processes.

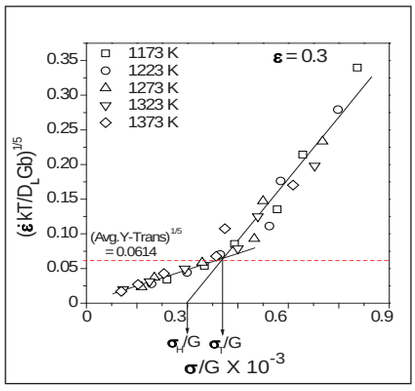

Fig. 1 Determination of transition and threshold stress at strain of 0.3

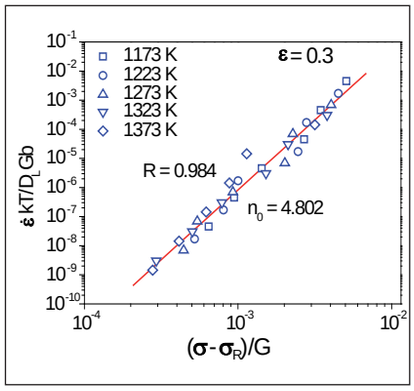

Fig. 2 Rationalisation in terms of effective stress for strain of 0.3

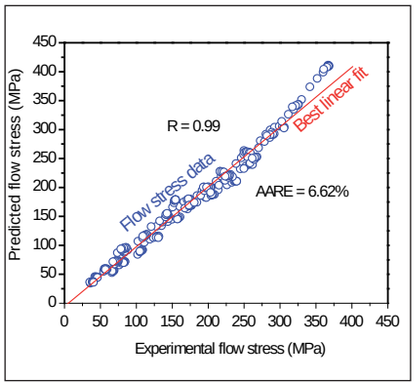

Fig. 3 Prediction of flow behaviour for the strain range 0.1-0.5

III.6 Experimental and Modeling Studies on Long Term Behaviour of G91 Material

The long term behaviour of base metal and welds of modified 9Cr-1Mo steel (P91) has been evaluated. Effect of long term ageing on the fracture behaviour in ductile-brittle transition regime has been studied. Use of ultrasonic imaging to characterise type-IV cracking in weldments has been examined. The effect of multiaxial state of stress on creep rupture behaviour was studied. Also, use of continuum damage mechanics(CDM) approach for creep life prediction is demonstrated.

Effect of thermal ageing on dynamic reference temperature (T_0^{dy})

P91 steel has potential application as wrapper material in FBRs, where it will be exposed to temperatures of 673-873 K along with irradiation. Both thermal ageing and irradiation result in micro-structural changes leading to degradation in mechanical properties. Increase in ductile brittle transition temperature (DBTT) is a matter of concern for fuel handling operations. It is required to understand the individual contributions of thermal and irradiation effects. Hence, the effect of thermal ageing on the ductile to brittle transition temperature behaviour has been assessed for P91 steel using the dynamic (conservative) reference temperature (T_0^{dy}) approach. The steel in normalized and tempered (NT) condition and subsequently cold worked to 5, 10 and 15% were subjected to thermal ageing at 873 and 923 K for 5000 and 10000 hours. For the NT and all the cold worked levels, thermal ageing at 923 K for 10000 hours resulted in a drastic increase (353-363 K) in T_0^{dy}. A moderate increase of 293-298 K was observed for the NT steel aged at 873 K for 5000 hours and for the 10% cold worked steel aged at 873 K for 10000 hours.

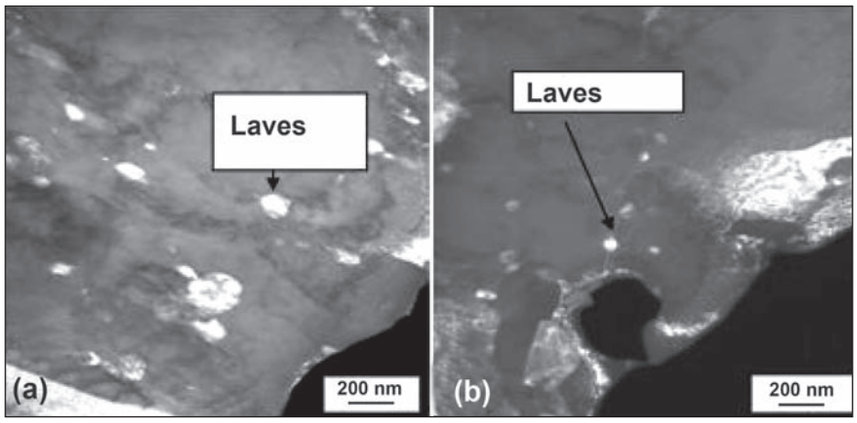

Fig. 1 *Dark field images of P91 steel thermally aged for 10000 hours at (a) 923 K and (b) 873 K revealing the laves phase globules along grain boundaries*

Detailed TEM study of the embrittled materials aged at 923 K/10000 hours and 873 K/10000 hours has indicated presence of hexagonal laves phase of $Fe_2(Mo,Nb)$ type with different size and spatial distributions. The size of the Laves phase globules was found to be > 200 nm for the steel aged at 923 K/10000 hours, and 20-100 nm for the steel aged at 873 K/10000 hours (Figures 1a and 1b). The increase in the T_0^{dy} is attributed to the embrittling effect of a network of laves phase precipitates along the grain boundaries, with the size of the laves phase globules deciding the degree of embrittlement.

Creep life prediction of grade 91 steel using CDM approach

The creep behaviour in terms of creep strain-time and rupture life of grade 91 steel in both low and high stress regimes has been successfully predicted using kinetic creep law envisaged in CDM approach proposed by Dyson and McLean. In this CDM approach, microstructural damage evolution rates are coupled with kinetic creep law containing microstructural parameters in order to account for the overall creep damage and prediction of creep curves. In the first instance, damage caused by decrease in dislocation density resulting in coarsening of dislocation networks and subgrains together with coarsening of precipitates has been considered. The coarsening of precipitates has been taken mainly as the average of the two main constituents, i.e., the $M_{23}C_6$ and MX precipitates in the analysis. Using in-house developed numerical algorithm, the optimisation of material data has been carried out by means of experimental short term creep strain-time curve at 110 and 140 MPa for MGC heat (NIMS data) of grade 91 steel. By using optimised data set, extrapolation and prediction of creep strain-time curves have been carried out. While the prediction was good for short term (high stress of 110 and 140 MPa) tests, the

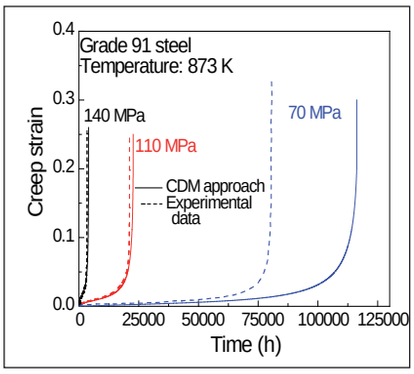

Fig. 2 Creep strain–time data for 140, 110 and 70 MPa at 873 K and predictions using the first analysis

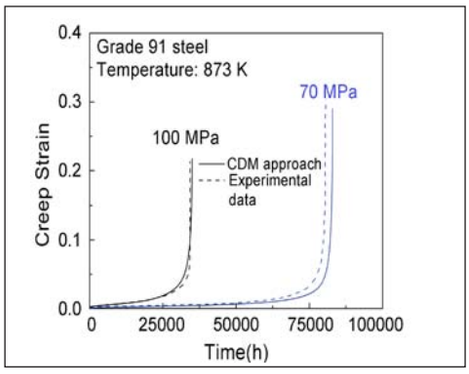

Fig. 3 Creep strain–time data for 100 and 70 MPa at 873 K and predictions using the refined analysis

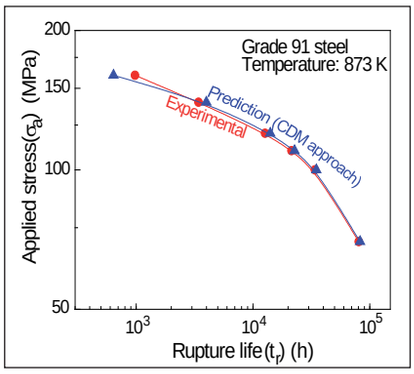

Fig. 4 Comparison of experimental values of rupture life with those predicted using refined analysis

difference between experimental and predicted creep curves for long-term (low stress ~70 MPa) tests was considerably higher. Therefore, the analysis was refined by suitably incorporating the variations of number density of precipitates with time caused by the coarsening of $M_{23}C_6$ and loss of MX precipitates due to conversion of MX into Z-phase to obtain creep strain-time curves in the long-term creep regime (Figure 2). Apart from these, the decrease in solid solution strengthening caused by depletion of Mo due to the formation and growth of laves phase, Fe_2Mo was also included. Following these modifications in the kinetic creep law, a good agreement between experimental and predicted creep strain-time curves was obtained in the long-term creep regime as shown in Figure 3 for 100 and 70 MPa. Excellent match was obtained between the predicted and experimental rupture lives in both low and high stress regimes (Figure 4).

Multiaxial stress response of G91 steel under creep condition

The effect of multiaxial state of stress on creep rupture behaviour of modified 9Cr-1Mo steel has been studied by introducing U-notch of different acuity in the creep test specimen of 5 mm gauge diameter. The notch acuity (ratio of notch plane diameter to notch root radius) is varied from 1 to 20 keeping the specimen diameter to notch plane diameter ratio fixed at 1.67. The different notch acuitys introduce elastic stress concentration factors (ESCF) in the range 1 to 3.4. Creep rupture life increased in presence of notch indicating notch strengthening for this material. The rupture life increased rapidly with increase in notch acuity and saturated at higher notch acuity, as indicated in Figure 5 .

Finite element analysis of stress distribution across the notch during creep exposure has been carried out. Norton's creep law relating the steady state creep rate, $\acute{\varepsilon}_s$ with applied stress, σ ($\acute{\varepsilon}_s = A\sigma^n$, where $\acute{\varepsilon}_s$ is in h^{-1}, σ is in MPa; A and n are constants) was used as a constitutive material model for the analysis. The elastic modulus was assumed to be 200 GPa and constant 'A' was selected to give a steady state creep rate of 10^{-5} s^{-1} at 230 MPa for a given value of 'n'. The calculations were carried out for 'n' values ranging from 1 to 10. The element size was reduced at and close to the notch root and elastic analysis was used to ensure that the mesh configuration was sufficiently refined near the notch root to predict the theoretical ESCF at the notch root. A tri-axial state of stress develops around the notch during creep deformation. The stresses redistribute across the notch plane and saturate during steady state creep deformation. Figure 6 shows the variation of maximum principal stress around the notch with creep exposure for notch acuity of two.

The stress redistribution in the notch plane causes the peak stress at the notch root to decrease and that at the centre of the specimen to increase. The extent of increase

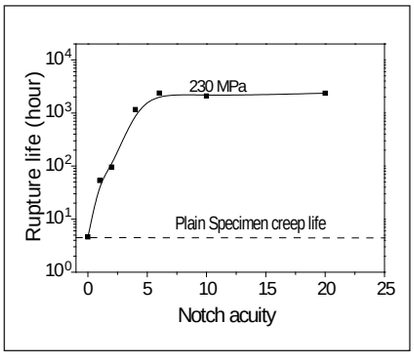

Fig. 5 Effect of triaxial state of stress (notch acuity) on creep rupture behaviour of Mod.9Cr-1Mo steel at 873 K

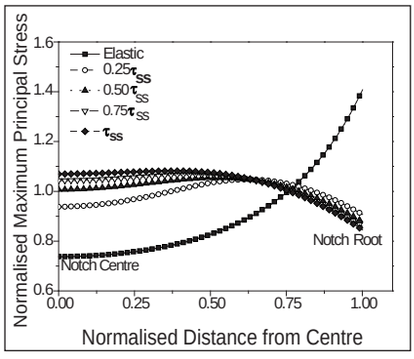

Fig. 6 Normalized maximum principal stress across the notch plane as a function of creep exposure time for notch acuity = 2 (τss : time to reach stationary state)

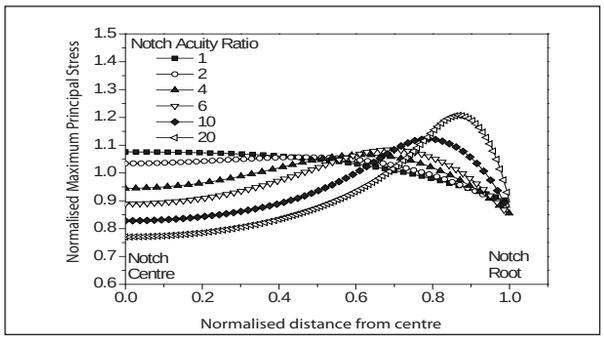

Fig. 7 Variation of normalized maximum principal stress across the notch plane as a function of notch acuity (n = 7)

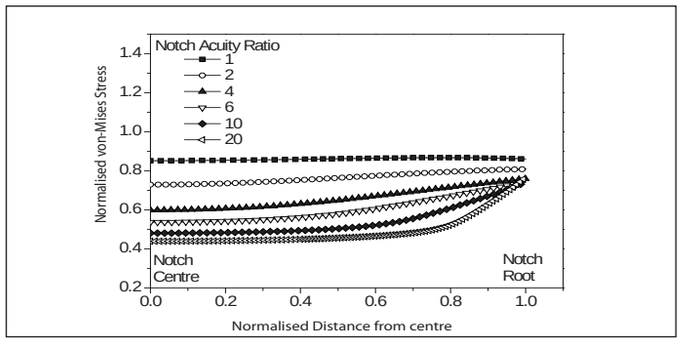

Fig. 8 Variation of normalized von-Mises stress across the notch plane as a function of notch acuity (n = 7)

in stationary stress at the centre decreased with increase in notch acuity and with creep exposure time. The maximum of principal stress increased and shifted from centre to near notch root with the increase in notch acuity (Figure 7). The von-mises stress did not change appreciably across the notch plane for relatively shallow notches, while for relatively sharp notches, it increased gradually at the notch root (Figure 8). The von-mises stress remained below the net stress for all the notch acuity conditions investigated, leading to notch strengthening in the material and increase in creep rupture life of the steel.

Ultrasonic imaging of type-IV cracking in G91 steel weldment

Operational experience from the usage of G91 steel weldment at high temperature shows that failures are due to type-IV cracking in heat affected zone near the base metal in intercritical/fine grained heat affected zone. Since initiation of type-IV damage occurs internally, and cannot be detected using surface techniques, an ultrasonic imaging based methodology is developed for early detection of type-IV cracking in G91 steel weldments.

Various rectangular cross sectional specimens with weld in the centre of the gauge region were subjected to creep at 923 K and 50 MPa for different durations. Ultrasonic C-scan imaging has been carried out across the weld line in the creep tested specimens in two perpendicular sections of the weldments. The ultrasonic velocity was minimum (time of flight, t_f maximum) in the weld region and it increased in the heat affected zone to reach the maximum (t_f minimum) in the parent metal (Figure 9).

Hence, the heat affected zones could be differentiated from the weld and the parent metals based on the velocity or in-turn the time of arrival of the back-wall echo.

In the samples crept for durations up to 1011 hours (~24% ε_f ; ε_f = failure strain), no localized damage were observed (Figure 10). However, in the samples crept for more than 1992 hours (~51% ε_f), very high attenuation was observed in one or both sides of the welds in the heat affected zones (loss of signals in Figure 10. In figure, arrows indicate loss of signal in HAZ due to type-IV cracking). The location of high attenuation is identified to be towards the parent metal i.e., in the intercritical/fine grained heat affected zone which is typical for the type-IV cracking. The occurrence of the type-IV cracking is clearly evident in form of high backscatter noise in the heat affected zones (Figure 11). This clearly demonstrates that ultrasonic measurements can be used for detection and imaging of type-IV damage in ferritic steel weldments, even when the damage is still confined internally and no change is observed on the surface.

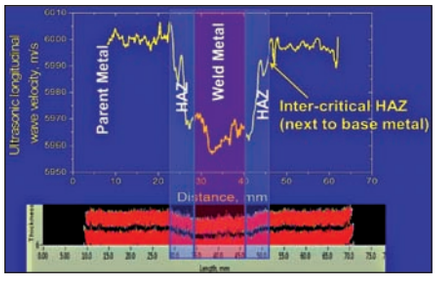

Fig. 9 Ultrasonic velocity and a B-scan image generated for the first back-wall echo in the weld in PWHT condition

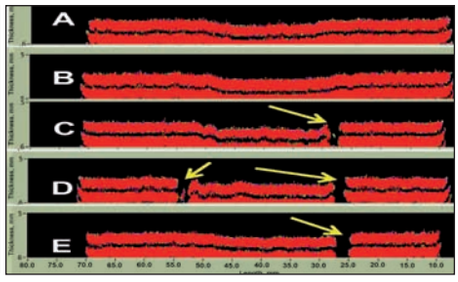

Fig. 10 *Ultrasonic B-scan images of the back-wall echoes across a weld crept at 923 K/50 MPa for (A) 527 h (ε =13% ε_f) (B) 1011 h (ε=24%ε_f) (C) 1992 h (ε=51% ε_f), (D) 2351 h (ε=76% ε_f), (E) 2762 h (ε=75% ε_f).*

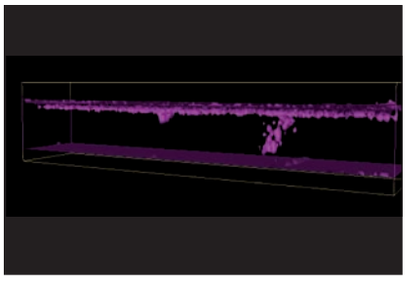

Fig. 11 *3D image generated using ultrasonic signals for the sample crept for 2351 hours*

III.7 Experimental Simulation of Parametric Instability of Liquid Free Levels Subjected to Seismic Excitations

When liquid filled containers are disturbed, the free surface of the liquid undergoes oscillations, which is referred as sloshing. It is an important phenomenon of relevance in seismic design of nuclear systems having partially filled tanks/vessels. The free-surface exhibits many interesting characteristics under vertical excitation of the container. The response of the free surface under harmonic vertical excitation is governed by the famous Mathieu equation. The solution of Mathieu equation may be stable, periodic or unstable depending on the system parameters, i.e., frequency ω_v and amplitude a_v of external excitation, and system's natural frequency ω_n. For some combinations of frequency and amplitude of the forcing excitation, the response of the free surface is unbounded, i.e., amplitude increases exponentially leading to parametric instability, while for other combinations the response is bounded. The stability of the Mathieu equation can be shown by stability charts. The stability chart of non-dimensional Mathieu equation developed using harmonic balance method is shown in Figure 1.

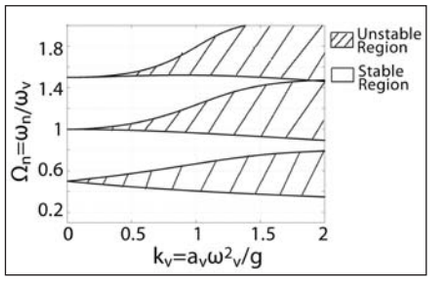

Fig. 1 *Stability chart of Mathieu equation for dynamic stability of free-surface under vertical excitation (right)*

Fig. 2 *Experimental setup to analyse dynamic stability of free-surface*

Benchmark shake table tests are conducted in Structural Mechanics Laboratory, to analyze the dynamic stability of sloshing in large size (1.2x1x1 metre) rectangular containers. One side of the tank was made of acrylic glass to enable visualization of slosh waves by high speed photography. The experimental setup is shown in Figure 2. A sine sweep test is conducted first to calculate the slosh natural frequencies and the measured frequencies are compared with analytical values in Table 1. A close match between the analytical and experimental data validates the idealization of the model and instrumentation. Following this, the container is excited with different frequencies and amplitudes covering both the stable and unstable regions of the stability chart (Figure 1). Figure 3 shows the response of free-surface for excitation parameters in stable and unstable regions.

Figure 3(a) shows the response of the free-surface when the external excitation frequency is 0.8 times the

Table1: Experimental and analytical slosh natural frequencies

Mode f_{mn}	Experiment Hz	Analytical Hz
f_{10}	0.7324	0.7724
f_{01}	0.8544	0.8634
f_{11}	-	1.0060
f_{20}	1.0986	1.1385
f_{02}	1.4648	1.2489
f_{22}	-	1.4255
f_{30}	-	1.3969
f_{03}	1.70898	1.5303
f_{33}	-	1.7460

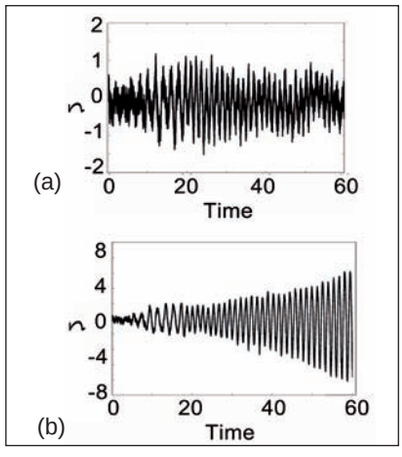

Fig. 3 *(a) Stable response, ω_v = 0.5634 Hz, a_v = 0.02g; (b) Unstable response, ω_v = 1.4648 Hz, a_v = 0.2g*

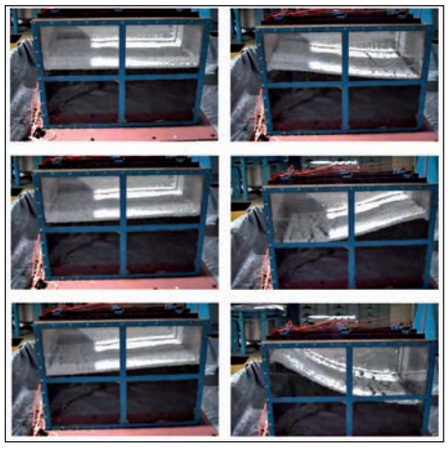

Fig. 4 *Snapshots of the free-surface at various instants depicting instability*

fundamental slosh frequency, with amplitude 0.002 g (stable region). Figure 3(b) shows the response when the external excitation frequency is twice the fundamental slosh frequency with amplitude of 0.2 g (unstable region). It shows an exponential increase in amplitude of the free-surface wave, which is typical of parametric instability. Figure 4 shows the snapshots of the experiment at various instants when the free-surface is unstable.

This benchmark exercise brought out the importance of the study of the instability liquid free surface under base excitation which is of special interest to sodium cooled pool type fast reactors, where the possibility of setting up unstable sloshing of the liquid free surface of the sodium pool in large diameter main vessel cannot be ruled out under seismic excitations. The numerical simulations carried out at our Centre to study the parametric instability of sodium free surface of reactor assembly of PFBR, ensured that under seismic excitation, response of sodium free surface is bounded. To validate the numerical simulation, it is planned to conduct experiments on 1/8th scale model of main vessel using multi-axial shake table facility at structural mechanics laboratory.

III.8 Commissioning of Innovative Test Facilities for Studies on Sodium Safety

Sodium has been chosen as a coolant due to its excellent heat transfer and favourable nuclear properties. Even though sodium is unanimous choice as a coolant in India and many other countries where fast reactor programme is pursued, its high chemical reactivity sometimes poses safety issue, which has to be addressed for safe operation of SFR. Hence, small and large scale experimental test facilities are erected and commissioned for conducting various studies for enhancing sodium safety.

An experimental facility named MINI MINA is set up for conducting experiments with small sodium inventories (2-5 g). The test facility consists of a vertical quartz viewing cylinder with stainless steel end plates as shown in Figure 1. The bottom plate has a provision for supporting sodium holdup vessel and entry of injection nozzle for generating the spray. The interaction chamber is highly instrumented with thermocouples, thermal imaging, high speed imaging, transient pressure measurement and gas analysis.

Series of experiments were carried out to study single sodium droplet burning, particle distribution during sodium spray fire, effect of sodium fire on performance of fire retardant low smoke cable, effect of oxygen concentration in sodium burning and sodium concrete interaction. Figure 1 shows some of the images of the experiments carried out.

A medium scale sodium fire facility, MINA is setup to conduct studies with sodium upto few kilograms. The MINA facility has a rectangular test chamber of size 5.6 × 5.4 × 4.6 m (139 m^3 volume) which can withstand pressure of 4 bar at 773 K temperature. A sodium loop with necessary tanks, valves, heaters, related instrumentation and cover gas system supplies required sodium to the test chamber. A leak tight door and four view ports meant for viewing/video-graphing and thermal imaging are also provided for the test chamber. Gas and wall temperatures of the chamber are

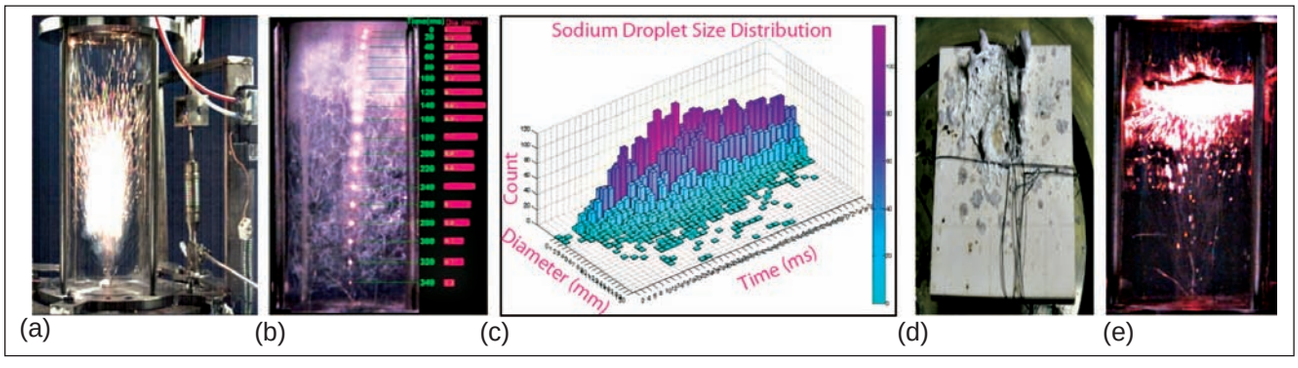

Fig. 1 *(a) Sodium spray fire (b)Droplet combustion (c) Droplet size distribution (d) Sodium concrete and (e) Sodium cable fire interaction*

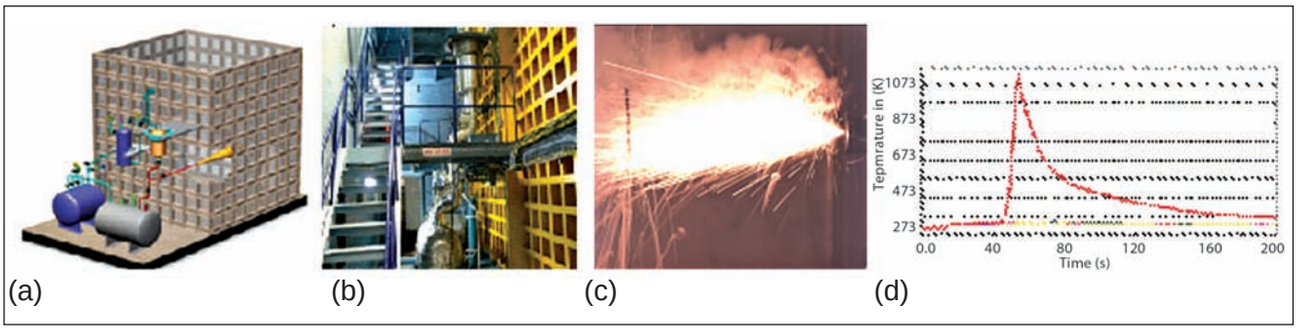

Fig. 2 *(a) MINA test chamber (b) MINA sodium loop (c) Spray fire scenario and (d) Temperature around the spray*

measured at 25 locations using K-type thermocouples during the experiment. A strain gauge type pressure transducer is installed to measure the gas pressure inside the hall. A sodium spray fire test was carried out earlier by burning 2 kg sodium and spatial temperature distribution and pressure build up in the test chamber were obtained. A schematic of the MINA facility, spray fire experiment and temperature distribution near the spray are shown in Figure 2.

The sodium-cable fire facility is an integrated experimental facility which has been designed and setup, to investigate different scenarios of sodium fire, core disruptive accident resultant sodium fire and resultant cable fire (i.e., as secondary fire) on top shield platform and sodium aerosol dispersion studies in the confinement. Core disruptive accident resultant sodium fire is simulated by ejecting sodium through eighty one numbers of small nozzles arranged in a circle as shown in Figure 3. The facility is also meant for studying the effect of sodium fire on the integrity of important safety grade components like decay heat exchanger piping, etc. held in the top shield platform of PFBR containment building. Figure 3 shows sodium-cable fire test facility.

Sodium fire experimental facility has been set up to study sodium spray fire, pool fire and combined fires to assess the consequences like pressure rise and temperature rise. Recently qualification of leak collection tray of PFBR was carried out in sodium fire experimental facility. The qualification system of leak collection tray consists of a drain system with fusible plug assembly and a dump tank where the leaked sodium is collected and stored as shown in Figure 4. The leak collection tray has a sloping cover of 800 mm length, 400 mm width and sodium holdup vessel of 700 mm length, 300 mm width and 340 mm depth. Two pipes of 30 mm diameter are provided from sloping cover tray into the holdup vessel for draining the sodium. The holdup vessel has a volume of 60 litres and provided with two 2" size drain pipes which are connected to a 4" size header and dump tank with fusible plug assembly. The sodium system consists of sodium supply tank with 500 litres volume with necessary heaters and instrumentation.

The tank bottom is provided with a release nozzle with 11 mm inner diameter to form 1 cm^2 leak area simulating a possible sodium pipe leak as per leak before break theory. The nozzle is provided with a release system rupture disc, which will open up under rated pressure. The concrete test chamber has volume of 570 m^3 (9x6x10.5 metres height) and has provisions for air/ inert gas injection, exhaust and instrumentation. The design pressure of the chamber is 50 kPa. The chamber is also provided with pressure relief system which consists of a pressure relief valve set at 40 kPa and a rupture disc with burst pressure of 48 kPa. The pressure relief system is designed assuming a pessimistic scenario of 500 kg sodium fire on entire flooring of the test chamber. The sodium supply tank is provided with heaters, thermocouples and discrete level probes. Temperatures are also monitored at fusible plug of the tank bottom, leak collection tray

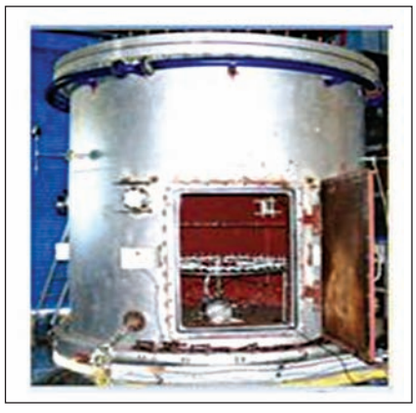

Fig. 3 *Sodium – cable fire test chamber*

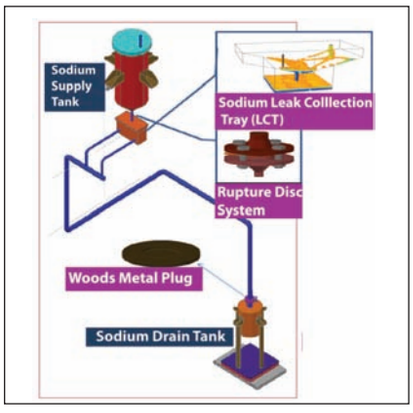

Fig. 4 *Leak collection tray test setup*

sloping cover, holdup vessel, drain header, isolation plug and drain tank. Two dedicated video cameras are employed for monitoring the scenario.

In qualification test about 100 kg of liquid sodium at 673 K was allowed to leak though an opening of 1 cm^2 area in to the leak collection tray for about 120 seconds. The test indicated that provision of a vent hole near fusible plug will improve the performance of the leak collection tray system.

An experimental setup was designed and erected for understanding small sodium leaks in sodium systems through a small opening. The setup consists of a stainless steel sodium holdup vessel designed for five bar pressure at 873 K, with a small release hole of 0.3 mm at the bottom. The vessel can accommodate 50 g of solid sodium and is provided with a heater furnace system for preheating it to the required temperature. The vessel is also connected to argon pressurization system. A collection pan with online weight measurement system is provided below the vessel in an enclosure. The enclosure consists of inert gas supply, oxygen monitoring systems for maintaining inert atmosphere to prevent the sodium burning.

Main objectives of the facility are

1. To measure sodium leak rates at different conditions and compare with theoretical predictions
2. To understand self plugging of the hole due to sodium and its oxide
3. To establish conditions for unplugging.

Few experiments were conducted with 25 g of sodium, which is released at different pressures for different experiments. In few cases self plugging of the hole was observed after partial release of sodium. Few more experiments are being done to establish the conditions for plugging/unplugging and for a design feedback on the detectable leak rate.

Small and large test facilities are commissioned towards sodium fire study. This will facilitate in development of containment code and enhanced safety of the sodium cooled fast reactor.

III.9 Indigenous Development of Electric Penetration Assemblies

In any nuclear power plant it is essential to maintain the leak tightness of reactor containment building and hence all the penetrations made in the walls including that of cables that cross the wall boundary are required to maintain the leak tightness. The power, control and instrumentation cables entering reactor containment building may pass the leakage of air borne radioactivity through stranded conductors, space between the cores, armour etc. Hence, electric penetration assemblies are used to prevent any leakage through cable passage.

In PHWR, research and test reactors in India as of now electric penetrations are made at site wherein cables with multi-strands in the conductor cores are provided with strand sealing arrangement using moulds. The outer sheath, inner sheath and armour of cable are removed for the specified portion and fixed inside the cable penetration mould tube. The individual cores of cables are exposed and separated out by inserting PVC wedge between them and resin is filled into the space between cores. In this type of site fabricated penetrations online leakage monitoring is not available.

In Koodankulam project and in PFBR prefabricated tested factory assembled modular electric penetration assemblies are used. These assemblies are double sealed and are internally pressurized for leakage monitoring in all possible leak paths. The modular type serves the purpose for easy replacement and maintenance. These assemblies are inserted within nozzles which are embedded in the concrete wall of containment building and are welded on the nozzles.

As of now these assemblies are manufactured by 'Conax Buffalo Corporation' (USA), 'IST-Auxitrol' (France), and 'Elox-Prom' (Russia), 'SCHOTT' (Germany). In a reactor plant, the average requirement of electrical penetration assembly is around 100 numbers having roughly ten feed through. In order to reduce the import of large number of high price items it was decided to go for indigenous development of electrical penetration assembly.

Electrical penetration assembly (Table 1) developed in house consists of stainless steel assembly and flanges, copper conductors, modular penetration pipes, baffle plates and ferrule fittings. The flanges are welded to the container on both the ends. The modular penetration pipes are fitted to the assembly using ferrule fittings at the ends of flanges and baffle plate supports the modular penetration pipes inside the pipe. The modular penetration pipe consists of Kapton insulated copper conductor(s)/rod(s) inside the pipe with 200 mm long longitudinal araldite insulation cum seal on the both ends. The space between the copper rod(s) and the tube and copper rods are maintained inside the modular penetration pipe with teflon disc. A pressure gauge connection is used for filling the inner space of the electrical penetration assembly and modular penetration pipe with dry air/dry nitrogen and continuous monitoring of pressure reading inside electrical penetration assembly .

Electrical penetration assembly specifications

Sealant fills the radial gap between copper conductors and modular penetration pipe to provide leak tightness. As the copper conductors carrying high currents and voltages are in direct contact with the sealant material, it requires a good electrical insulator and its operating temperatures must be from 293 to 373 K.

As the electrical penetration assembly is exposed to very high gamma radiation dose at the time of core disruptive accident, the sealant must have good radiation resistance. The material used for modular penetration pipes is stainless steel and for conductors is copper, therefore the sealant must have high value of lap shear strength for stainless steel to stainless steel joints as well as copper to copper joints so that the joint between the sealant and stainless steel as well as copper and sealant is able to withstand significant shear stress. The sealant has to be filled inside 25 and 50 NB modular penetration pipes without any voids and the radial width of the gap is of the order of few millimetres. Therefore the material must have low viscosity before curing. The modular penetration pipes are used in 48 V DC, 230 V AC, and 415 V AC systems, therefore sealant must have high dielectric strength and very high volume resistivity/insulation resistance.

Significant differential thermal expansion in copper/sealant/ stainless steel may result in the failure of the stainless steel-sealant or sealant-copper joint, therefore the value of coefficient of thermal expansion of stainless steel, copper and sealant must not differ by a large value.

There are two types of polymers which give good physical, electrical and mechanical properties at high temperature operations required by electrical penetration assembly-thermosetting resins (epoxy adhesives) and thermoplastics. Polysulfone is thermoplastic which has operating temperature of 173 to 423 K with excellent properties in its operating range and its properties degrade at temperatures more than 423 K. Araldite is a thermosetting resin and when mixed with a catalyst (hardener) makes an epoxy with good properties. It has excellent properties at higher temperatures i.e., more than 373 K but as the temperature drops, the properties start degrading. Due to difficulties in handling of polysulfone, high temperature Araldite was selected as sealant material.

Table 1: Electrical Penetration Assembly Specifications

S.No.	Parameter	Value
i	Insulation material for modular penetration pipe	Araldite (mixed with hardener in ratio 5:2)
ii	Stopper material between insulation –air gap for modular penetration pipe	Teflon
iii	Electrical insulation resistance for each modular penetration pipe at 1000 V DC for 1 minute (before and after high voltage test)	-
	Conductor to conductor	> 500 MΩ
	Conductor to pipe	> 500 MΩ
iv	Leakage current at 1600 V AC for 1 minute	-
	Conductor to conductor	< 0.1 mA
	Conductor to pipe	< 0.1 mA
v.	Pressure hold for air space between two Araldite fillings inside modular penetration pipe	2 bar for seven days
vi.	Conductor material	Copper (wrapped with insulation tape)
vii.	Modular penetration pipe fitting with electrical penetration assembly container	Stainless steel ferrule
viii.	Pressure Hold for EPA container	2 bar for 7 days

Vibration method and IR value

Radiography was carried out on a prototype modular penetration pipe to evaluate araldite filling compactness inside modular penetration pipe. The radiograph showed voids and irregularities in the Araldite filling. Experiments with Araldite also showed that heating Araldite converts it into a solid. Therefore, vibration technique was adopted using a vibrating bowl feeder (VIBRO) and using this setup, trial pouring was done and the pouring was successful to give a good packing density.

In order to improve the sealing insulation resistance the material of stopper disc was changed from Hylam to Teflon and finally a good insulation resistance value of more than 1000 MΩ between conductors to pipe was achieved. The high voltage test followed by IR value test and pressure hold test on the manufactured modular penetration pipe was successful.

Qualification tests for electrical penetration assembly

The following tests were carried out for qualifying the indigenously developed electrical penetration assemblies as per IEEE 317-1983 - IEEE standard for electric penetration assemblies in containment structures for nuclear power generating stations

Insulation resistance test

1000 V DC is applied between adjacent conductors and between pipe and conductors and insulation resistance measured for qualification of this test is greater than 1000 MΩ. This test was carried out before and after high voltage test to ensure no breakdown in Araldite.

High voltage test

Each modular penetration pipe was tested against high voltage of 1600 V, 50 Hz AC for one minute. The high voltage test was carried between adjacent conductors and conductors to pipe. The leakage current observed during this qualification test was less than 1 mA.

Fig. 1 *Manufactured electrical penetration assembly*

Fig. 2 *Electrical penetration assembly with pressure gauge*

Pressure hold test (Figures 1 and 2)

Each electrical penetration assembly and modular penetration pipe was tested for leak tightness by pressurizing the modular penetration pipes and electrical penetration assemblies. Pressure of 2 bar was applied in the space between two Araldite fillings for checking against leak tightness. The duration of this test was seven days and at the end of seven days no reduction in pressure was observed.

Seismic qualification

The electrical penetration assemblies were seismically tested in shake table and all functional tests were successfully carried out, after this test.

Effect of humidity on electrical penetration assembly while storage

The value of insulation resistance was found to be less than 20 MΩ between conductor to conductor and less than 10 MΩ between conductors to pipe after three months of storage for all modular penetration pipes. The effects of humidity on IR value were observed by testing a representative modular penetration pipe inside environmental chamber and IR tests were carried out at various relative humidity values and temperatures (Figure 3). It was found that the modular penetration pipes regain their insulation resistance value of greater than 1 GΩ at 30% relative humidity inside the chamber.

Hence, it was decided to fill the space between the end seals of modular penetration pipe with dry nitrogen during storage and use. Two numbers of electrical penetration assemblies with Araldite as sealant were manufactured and qualification tests were performed successfully. It is planned to manufacture electrical penetration assemblies with polysulfone as sealant in future and compare the performance.

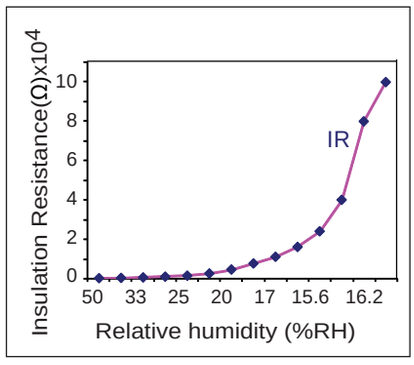

Fig. 3 *Insulation resistance as a function of humidity*

III.10 Indigenous Design and Development of Cold Crucible for Molten Fuel Coolant Interaction Studies

Melting of fuel and other structural materials in the reactor core of Sodium cooled Fast Reactor (SFR) may occur under extremely unlikely events that cause the imbalance between the heat generation and heat removal in the core. The thermal interactions resulting from the physical contact between high temperature molten core materials with relatively low temperature liquid sodium could lead to rapid heat transfer from the fuel to the sodium. It is called the molten fuel coolant interaction. The consequence of this interaction is a rapid pressure rise due to the sodium boiling and this could result in large scale vapor explosion. Subsequent important safety related issues are the coolability (i.e., decay heat removal) and recriticality aspects of the core debris that has been formed during molten fuel coolant interaction. Assessment of these issues requires the knowledge on the fragmentation and relocation behaviour of molten core material, size, shape and heat transfer characteristics of the debris heap formed. For this purpose, it is necessary to simulate molten fuel coolant interaction phenomena experimentally with molten prototypic reactor materials (like SS, U and UO_2). In order to carry out the experimental studies on the molten fuel coolant interaction phenomena under hypothetical core meltdown accident scenario in sodium cooled fast reactor, it is required to generate a molten pool of the corium which is a mixture of fuel and structural material. But it is very difficult to melt and handle the molten materials since the melting temperatures of the fast reactor core materials are very high. For conducting out-of-pile experiments that simulate the molten fuel-coolant interaction phenomenon, cold crucible induction melting (CCIM) technique has been adapted to prepare the molten corium in sodium fuel interaction (SOFI) facility.

Cold crucible induction melting is an inductive heating of a material by an alternating electromagnetic field in a water/oil cooled container known as “cold crucible” (Figure 1). Heating is accomplished by Ohmic losses caused by eddy currents induced in the charge. The design parameters of induction melting such as current that passes through the induction coil, the frequency of the current, the design of the crucible and coil, and charge filling level in the crucible play an important role in the heating process. The experimental evaluation of some of these parameters, such as the design of the crucible, applied current, and frequency, is complicated because it is necessary to consider different crucible geometries and different induction generators. Numerical modeling of the various processes occurring in induction heating is a way to easily understand the influence of these parameters and to reduce the expenditure on experimental works.

The physical phenomena taking place in induction heating are highly complex and strongly inter-related. The magnetic field generated by the coil creates induced currents in the charge. These induced currents heat the material by Joule heating. Once the charge temperature increases, its material

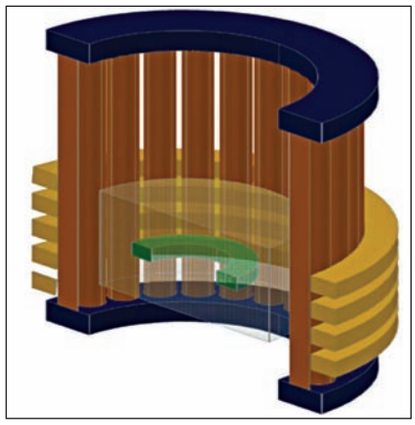

Fig. 1 *Schematic of cold crucible*

properties will change varying the values of the induced currents and the temperature distribution in the charge. The temperature dependent variation of the material properties will be different for different materials. Understanding the effect of temperature dependent material properties on the heating behavior is essential for designing an efficient induction heating system.

In order to understand the influence of different parameters on the induction heating process of a material, a 2-D axi-symmetric model, with integration of harmonic electromagnetic and transient thermal phenomena, has been developed using a finite element based commercial software. As the fast reactor core is comprised of materials like uranium (U, in metal fueled SFR), uranium dioxide (UO_2, in oxide fueled SFR) and stainless steel (SS 316L, as core structural material), the induction heating behavior of these materials up to their melting point has been studied using the model. The effect of temperature-dependent material properties such as electrical resistivity, thermal conductivity, specific heat and density of these materials on the heating

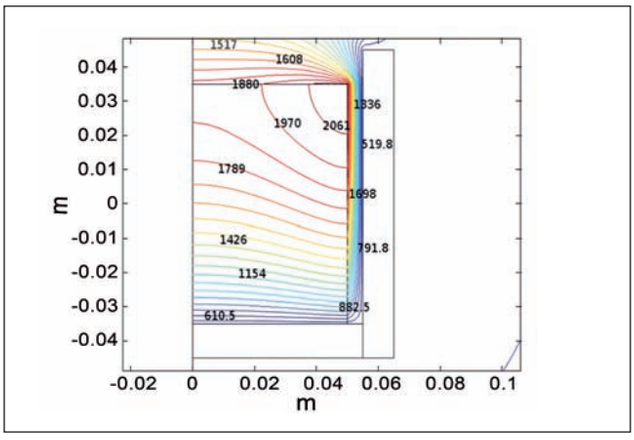

Fig. 2 *Temperature distribution at 900 s (for stainless steel with 2.5 kA and 3 kHz)*

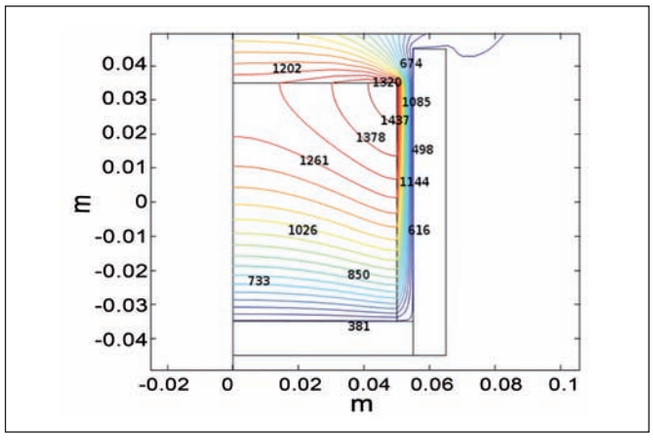

Fig. 3 *Temperature distribution at 900s (for U with 2.5 kA and 3 kHz)*

behavior has been investigated by incorporating these properties in the model. The model starts with the evaluation of electromagnetic field for calculating the total Joule heat generated by the eddy current.

This heat source is used in the heat transfer governing equation for evaluating the temperature and based on this temperature, the material properties are evaluated for further electromagnetic analysis.

A cold crucible of laboratory scale dimensions (size 130 mm OD and 110 mm ID) has been chosen for the present analysis. The diameter of the charge is taken as 100 mm and its height is 70 mm. A four-turn, 140 mm internal diameter and 80 mm height cylindrical copper coil, made of a square copper tube [12×12 mm], is used as induction coil. The same geometrical conditions are considered for the analysis of heating behavior of the three materials to understand the influence of different material properties on the heating behavior and to identify the appropriate values of the input parameters required for the efficient melting of these materials.

The materials uranium and SS 316L are both good electrical conductors. The optimal frequency of the coil current required for efficient heating of these materials for chosen size is in the order of one kilo Hertz (kHz). Figures 2-3 illustrate the simulation results for the temperature distribution in SS 316L and uranium, where they reached their melting points with low frequency currents (2.5 kA with 3 kHz). It can be observed from Figures 2 and 3 that the temperature rise in SS 316L is relatively faster compared to that in uranium. This is due to the fact that the thermal inertia of uranium increases suddenly above 600 K compared to that of stainless steel under almost constant electromagnetic power density.

As the electrical conductivity of UO_2 is very small, the optimal frequency of current required on the induction coil for efficient heating of UO_2 is in the order of hundreds of kHz to mega Hertz (MHz). The analysis has been carried out with the same input coil current of 2.5 kA but with different frequencies. The melting temperature of UO_2 (3150 K) attained in 900 seconds time with applied coil current intensity of 2.5 kA with a frequency of 300 kHz (Figure 4).

A high frequency power source along with a susceptor (i.e., a metallic material) inside the charge material is generally used to initiate the melt in the low conducting ceramic materials. A tungsten metal ring of square cross section [10×10 mm] has been used as a susceptor and considered at the geometric center of the UO_2 charge. The analysis has been carried out with the input coil current of 2.5 kA at different frequencies. It is observed that UO_2 charge has reached melting temperature in 900 seconds under applied coil current of 2.5 kA with 37 kHz frequency. From this it is understood that the UO_2 (ceramic) charge can be easily melted at

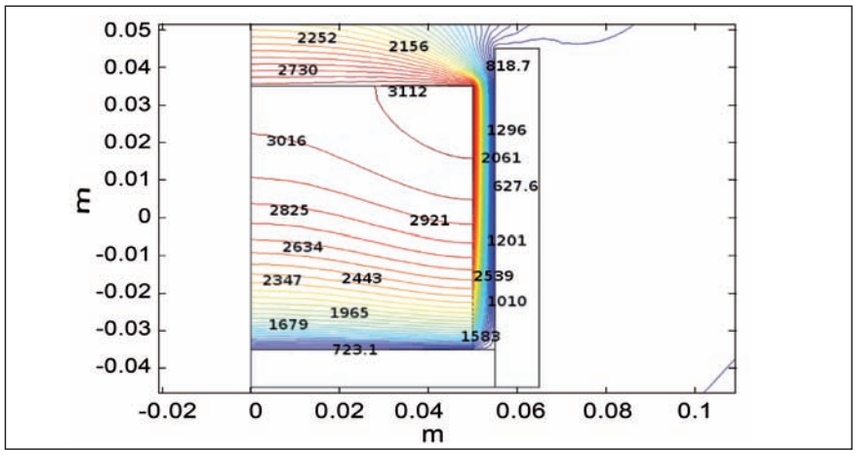

Fig. 4 *Temperature distribution at 900 seconds (for UO_2 with 2.5 kA & 300 kHz)*

relatively lower frequencies by using a susceptor.

Analysis results indicate that the material properties and their temperature dependency will have substantial influence on the induction heating behavior of these materials. So, it is necessary to consider the temperature dependent behavior of the cold crucible induction melting system while choosing the input conditions for efficient operation. The model developed is used to optimize the cold crucible induction melting system being used for conducting the molten fuel coolant interaction experiments.

The cold crucible as well as the induction coil has to be provided with a cooling medium to maintain them at low temperatures for assuring the integrity at brazed joints. A heat transfer fluid 'Therminol' is chosen as cooling medium instead of water to avoid water source near sodium system. The induction coil is cooled by circulating therminol in a closed loop with a pump and a compact oil chiller. Whereas, the cold crucible reinforced with copper tubes is cooled by a separate loop.

The loop consists of an stainless steel oil tank, rotary gear pump, oil heat exchanger, inlet and outlet pipelines for flowing the oil. The oil heat exchanger is a shell and tube type heat exchanger with oil on shell side and chill water on the tube side. The oil exiting from the heat exchanger is circulated through the cold crucible by a bypass line from the main pipeline. The chilled water is circulated by an independent loop with air cooled water chiller, which acts as a final heat sink. Isolative valves and pressure gauges are provided at the desired locations like pump outlet, oil tank etc. Required oil flow rate in the crucible is maintained by manipulating valves in the bypass loop and main pipeline. The theminol temperatures in the crucible, coil circuits are maintained well below 323 K by adjusting the flow.

In addition to the oil cooling circuits a gas cooling system is also employed. In this system inert gas is injected externally onto the cold crucible through two specially designed headers with many nozzles to provide external cooling. Inert gas flooding will also aid to prevent any fire during accidental oil leak or melt leakage though the crucible walls.

III.11 Sodium Aerosol Characteristics in Cover Gas Region of SILVERINA Loop

In the normal operation of sodium cooled fast reactor, evaporation of sodium from the hot pool surface and subsequent condensation results in the formation of sodium aerosol within the cover gas space. Sodium aerosols play an important role in heat transfer from the sodium pool surface to the roof top plug and aerosol deposition on cooler surface. The deposited aerosols may hinder the rotational movement of rotating plug. In the reactor design, necessary care has been taken to account for the heat and mass transfer phenomena. At this juncture, it is utmost important to know the aerosol concentration and droplet size distribution in order to predict effectively the heat and mass transfer phenomena, which may get changed due to interaction of thermal radiation with aerosols and mass transfer due to condensation of aerosols. It is also to be considered that sodium aerosol properties would get modify due to

(i) Temperature difference between the sodium pool surface and the bottom of the roof top plug

(ii) Possible enhanced coagulation of sodium aerosols upon interaction with gamma radiation, resulting increase in sizes.

Hence, it is proposed to carry out the experiments to characterize the size distribution and mass concentration of sodium aerosols in the cover gas region by adopting suitable procedures. Experiments are planned to be conducted in two phases. In the first phase, the experiments are being conducted in SILVERINA Loop. In the second phase it is planned to conduct experiments in FBTR. Here, drawing the sodium metal aerosols into the collector without exposing them to the environment, and analyzing them using off-line technique is a challenging aspect.

SILVERINA loop

SILVERINA sodium loop was constructed and commissioned at Engineering Hall-I to conduct various experiments related to PFBR and general Sodium Technology. This is a dynamic sodium loop with an electromagnetic pump and consists of three test pots namely test pot-1(TP-1), test pot-2 (TP-2) and test pot-3(TP-3), cold trap, plugging indicator, sodium sampler, heater

vessel, interconnecting pipe lines, bellows sealed valves, flow meters and cover gas circuit. Sodium is filled in to the loop from a storage tank with a sodium hold up to capacity of 1300 kg. The experiments are conducted in test pot-1.

Aerosol sampling

The integrated view of TP-1 and Aerosol Sampling System is shown in Figure 1. The aerosol sampling system consists of

(a) Aerosol sampling tube
(b) Aerosol sampling bottle,
(c) Line Heaters and controller and
(d) Aerosol flow controlling device.

The sampling bottle is filled with paraffin oil(~700 ml) and maintained at ambient temperature. The aerosol sample laden cover gas is made to pass through the bottle so that condensation of sodium vapour and solidification of aerosol particle would occur as the cover gas enters into the paraffin oil. The residence time of the cover gas is increased due to baffle arrangement (Figure 1 sample collection bottle), which ensures that all sodium aerosols get trapped from the cover gas before it goes out of the bottle. Besides, the cover gas coming out the sampling bottle-1 is made to pass through sampling bottle-2 so as to remove aerosols escaped, if any, from the first bottle. After isolating the bottles from the system the sampling bottles are taken for analyzing the samples. The size distribution of sodium aerosols is determined by using mastersizer (M/s Malvern Instruments, UK). The instrument measures the particle size distribution (sodium aerosol) hovered in a liquid dispersant (paraffin oil) by using ensemble diffraction technique. The scattered intensity and angle with respect to background measurement (without aerosol) gives the number concentration and particle size distribution. The measurement of sodium aerosols mass concentration

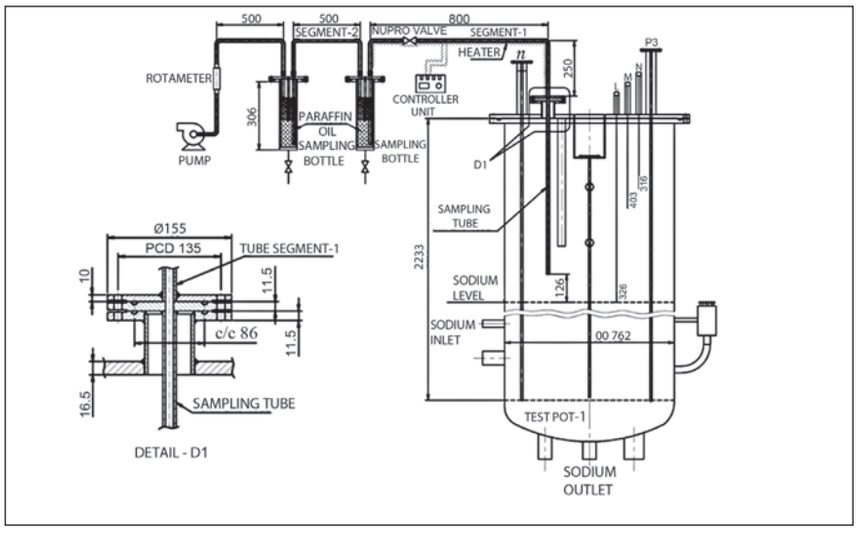

Fig. 1 *SILVERINA loop and sodium aerosol sampling system*

is carried out by conductivity method using the instrument conductometer (M/s Metrohm, 856 conductivity module, Switzerland). The mass of sodium aerosols trapped in the liquid paraffin is measured by transferring them into a water medium (to become NaOH) and measuring the change in conductivity of the NaOH solution. Sodium mass concentration is estimated by using a pre-established calibration graph between changes in conductivity vs concentration of NaOH.

To begin with experiments are conducted by inserting a sampling tube upto the middle level (415 mm from the top). Sodium cover gas height is 825 mm from the top of the TP-1. The pressure of cover gas region is kept 0.35 bar. The sampling line temperature is kept at 383 K. The quantity of paraffin oil taken in each bottle is 700 ml. The sampling flow rate is 2 lpm and sampling time is 15 minutes. After sampling, the paraffin oil is analyzed and the aerosol size distribution is found to vary from 1 to 12 µm with MMD around 4 µm (σ_g = 1.5) (Figure 2). The mass concentration of sodium aerosols is found to vary from 1 to 9.56 g/m^3. The sampling is also carried out at bottom level of the cover gas region (715 mm from the top) by inserting another tube. At a pool temperature of 673 K, the aerosol mass concentration is found to be higher near the pool (2.45 g/m^3) than at the middle (1.02 g/m^3) of the cover gas height.

It is observed that, measurable concentration was observed only from 623 K onwards and it increases with increase of pool temperature i.e., difference in temperature between pool and roof top. It is also observed that concentration of sodium aerosols is more near the pool surface than at the middle level of the cover gas space and it behaves as the mist which hinders the visibility of the core. The measured concentration and particle size distribution values are found to be in accordance with the literature value. Further experiments are being planned to complete the measurement in bottom level and top level and modeling the characteristics of aerosols using C-GAS code.

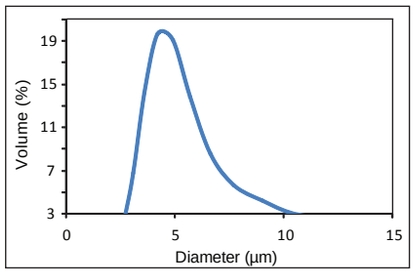

Fig. 2 *Sodium aerosol (metal vapour) size distribution*

III.12 Operation of Creep and Fatigue Loops for Conducting In-sodium Creep and Pin-On-Disc Tribometer Experiments

The creep and fatigue loops of in-sodium test facility (INSOT) are being operated to study and evaluate the mechanical properties of PFBR component materials in dynamic sodium at high temperature.

In-sodium creep experiments

The creep loop has four test chambers which are operated for conducting creep rupture experiments of PFBR component materials in dynamic sodium. The loop has been operated at temperatures of 873 K in six test campaigns from 2006. In the earlier test campaigns creep rupture tests at different stress levels on SS 316L(N) base material at 873 K have been successfully completed. The sixth test campaign of creep experiments was started in June 2012 with four numbers of creep experiments at 873 K on Mod 9Cr-1Mo base metal in test sections TS-2A, TS-2B, TS-3A and TS-3B. The creep loop has been in continuous operation at 873 K till the final experiment reached 2872 hours. The test parameters of the creep experiments in sodium of the sixth test campaign are summarised in Table 1. Periodic loop surveillance such as temperature monitoring, leak detection, level detection, dump valves, control logics of electro magnetic pumps, immersion heaters, class-I, II and III power supply systems have been periodically carried out as per the technical specification requirements for effective and safe operation of the loop in conducting this high temperature creep experiment campaign. The purity of the loop sodium was maintained consistently at reactor grade by continuous on-line purification. The cold point temperature of the cold trap was maintained at 393±5 K. Periodic weekly plugging runs were conducted to monitor the oxygen level and which was maintained less than 2 ppm. The sodium flow velocity around the test specimen in the test chamber was maintained at 2.5 ms^{-1}.

The performance of the sodium purification system, heat exchangers, immersion heaters, electromagnetic pumps and programmable logic controller based SCADA instrumentation system were excellent and this is the key factor in ensuring loop availability for conducting the long term creep experiments. Twenty numbers of creep experiments at 873 K have been completed till date.

In-sodium pin-on-disc tribometer experiments in fatigue loop

The commissioning activities of the pin-on-disc tribometer [PODT] (Figure 1) test section in fatigue loop of INSOT facility were systematically carried out for safe operation of the new test section at 573 K. The system parameters like sodium flow rate (0.3 m^3h^{-1}), sodium purity, sodium temperature (573 K) and sodium level in test vessel were monitored and maintained to meet the test requirements. PODT was operated and the performance of various mechanisms and control panel were checked. Subsequently in January 2012, the first trial experiment was conducted at 573 K on SS 304L (pin and disc material). After completion of the PODT at 573 K, the loop modifications were carried out and made ready for high temperature operation at 823 K.

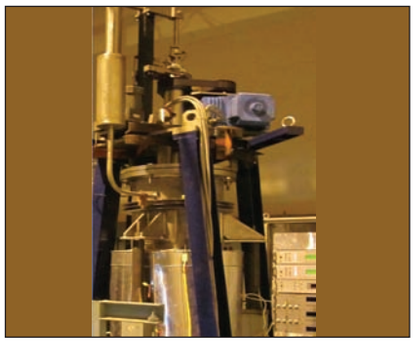

Fig. 1 *Pin-on-disc tribometer at site*

In October 2012, the fatigue loop was operated at 573 K and the loop temperature was raised to the test temperature of 823 K in steps and stabilized. PODT was checked for working at 823 K. After loop purification, the first high temperature PODT experiment at 823 K was successfully carried out on SS 304L (pin and disc material).

The performance of the indigenously developed tribometer in high temperature sodium was very good. In November 2012, another high temperature experiment was carried out successfully on a different material combination of Nimonic-80A disc and SS 316L pins.

Table 1: Test Parameters for Creep experiment conducted on Mod. 9Cr-1Mo Base Material at T= 873 K

Test section	Applied Stress [MPa]	Elongation [mm]	Test duration [hours]	Date of Completion
TS2A	150	4.381	340	30.06.12
TS2B	140	4.075	396	02.07.12
TS3A	135	4.374	1356	11.08.12
TS3B	130	5.75	2872	21.10.12

III.13 Self Wastage and Impingement Wastage Experiments on Steam Generator Tube Material Specimens in SOWART

The tube wall of a steam generator separates liquid sodium from high pressure water/steam. An accidental leakage of water into sodium causes sodium water reaction leading to damage of the leaking tube itself (self wastage) and damage on its adjacent tube (impingement wastage). Experimental studies are going on in SOWART to study the wastage phenomenon. Experiments are carried out in a test section called impingement wastage test section which houses two tubes; one leak tube/injector having a leak and a target tube of 9Cr-1Mo. The leak is oriented towards the centre line of the target tube. Once steam is admitted to the injector, it leaks to form a sodium water reaction jet that impinges on the target tube producing wastage. Impingement wastage test section has acoustic wave guide rods oriented around.

Impingement wastage experiments 8 and 9 were carried out. Experiment-8 was performed with a nickel leak simulator having a pinhole. It produced wastage of 0.8 mm depth on the target tube (Figure 1a). During experiment-9, target tube was fully punctured (Figure 1b). It was with a Mod 9Cr-1Mo leak tube with 100 mg/s leak rate. Over all, relative wastage resistance of Mod 9Cr-1Mo was found to be about two.

Self wastage experiments were conducted in SOWART with sodium at 723 K. Specimens with pin holes and fatigue cracks were tried. Three experiments were carried out in the year with Mod 9Cr-1Mo leak simulators having a fatigue crack/pinhole. Experiment-7 was with a fatigue crack but it did not open up even after waiting for 12 hours. Experiment-8 was with a pinhole and ended up with critical enlargement of leak simulator (Figure 1c). Experiment-9 was with a fatigue crack that was full opened, after 10 hours of dormant period. Full opening of leak simulators caused impurity addition in loop, which required long time for purification. The results of the experiments are being analyzed.

Presently, impingement wastage experiments according to IGCAR-CEA implementing agreement on experimental studies and code calculations on impingement wastage for 9Cr-1Mo steam generator tubes are being carried out. Two of the experiments were carried out till date. CEA had supplied 9Cr-1Mo tubes, of 15 mm outer dia, 2.2 mm wall thickness, to fabricate leak simulator/injector and target tubes. A piece of the tube, sized to 160 mm length, was used for manufacturing the injector. It was locally thinned down and a 0.1 mm pinhole was made by mechanical drilling. The injector along with a target tube assembly was fixed in impingement wastage test section of SOWART. Sodium water reaction occurred during both of the tests. During test-1, there was no impingement wastage found on the target tube, as predicted by PROPANA code by CEA. There was no appreciable self wastage. During test-2 both impingement wastage and self wastage occurred (Figure 1d). The depth of the wastage is being analyzed.

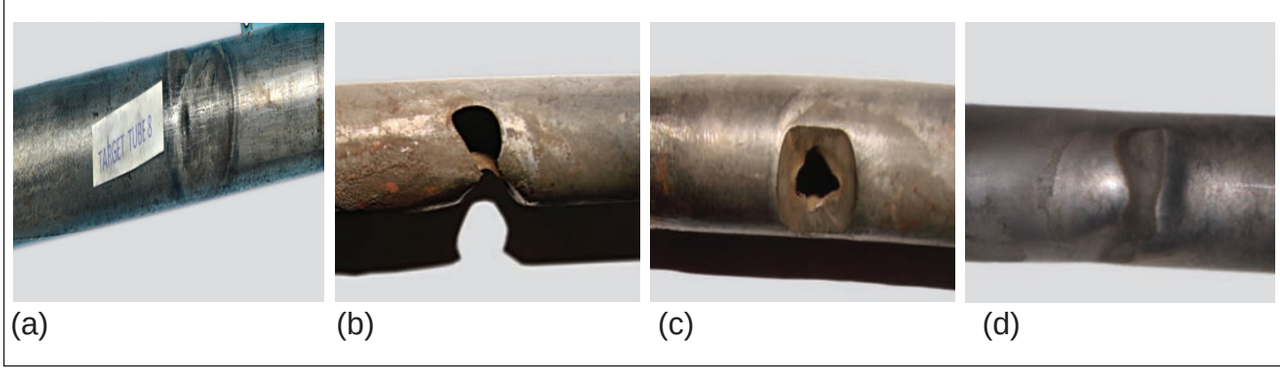

Fig. 1 *(a) Target tube experiment-8 (b) Target tube experiment-9 (c) Self wastage experiment-8 and (d) Impingement wastage occurred to CEA tube*

III.14 Novel Method for the Removal of Manganese from Fast Reactor Radioactive Liquid Effluent using Reticulated Vitreous Carbon

During the operation of fast reactors, components get wetted by sodium. In addition, due to activity transport, radionuclides get transported and deposited on various primary components of the reactor. Sodium cleaning and decontamination of fast reactor components is essential prior to maintenance or during their final disposal. Large volumes of radioactive liquid waste are generated as a result of sodium cleaning by water based process followed by chemical decontamination using a mixture containing sulphuric and phosphoric acids. In a majority of fast reactors, components such as pumps and intermediate heat exchangers get contaminated mainly due to the activated corrosion product ^{54}Mn. Hence, high concentration of ^{54}Mn is encountered in liquid waste in addition to other radionuclides such as ^{60}Co, ^{59}Fe etc. It is essential that the acidic and radioactive liquid waste be treated to reduce the radioactivity prior to interim storage and transportation to waste management facility for final disposal. With the objective to reduce the volume of secondary waste and to concentrate the active nuclides in solid matrix, an electrochemical method using electrodeposition technique was developed.

This novel technique competes with traditional methods of effluent treatment such as precipitation and ion exchange. The traditional methods demand large space in the decontamination facility housed in the reactor containment building and increase the cost of construction. Electrodeposition of manganese species from a mixture of sulphuric and phosphoric acid medium has not been reported in the literature. Hence the feasibility of removal of manganese ions from sulpho-phosphoric acid medium was studied in the present work. Reticulated vitreous carbon was used as the electrode material as it is chemically resistant in the acidic medium in addition to other properties such as porosity, relatively large void volume, high surface area, rigid structure, low resistance to fluid flow etc.

Experiments were carried out for the removal of manganese from simulated solution containing 0.15 M H_2SO_4, 0.46 M H_3PO_4 (pH 1.6) and known quantities of manganese species. Cyclic voltammetry (CV) was used to define the potential region of manganese. Electrodeposition was carried out in static mode using reticulated vitreous carbon as the working electrode, plutonium as the counter electrode and standard calomel electrode (SCE) as the reference electrode. Manganese ions were deposited at +1.2 V on reticulated vitreous carbon using chronoamperometry. After electrodeposition for seven hours, the surface was characterized using scanning electron microscopy and energy dispersive X-ray analysis. The first layer of reticulated vitreous carbon are seen and surface concentration of Mn was found to be 4.5 wt.%.

As reticulated vitreous carbon provided appreciable deposition efficiency when electrodeposition was attempted under flowing conditions, experiments were carried out using a flow through cell. The schematic and photograph of the flow through cell experimental set up are shown in Figures 1 and 2 respectively. Metal ions from the inactive simulated solution are deposited at the inner surface of the porous electrode as the electrolyte is percolated through the cell.

Electrodeposition was carried out with initial concentrations of a few hundreds of ppm in a flow through cell. Surface deposition was quantified using energy dispersive X-ray analysis and was found to be 6-8 wt.% of manganese along with O and P. The progress of the electrodeposition was followed as a function of time by taking aliquots of sample solution and analysing for manganese

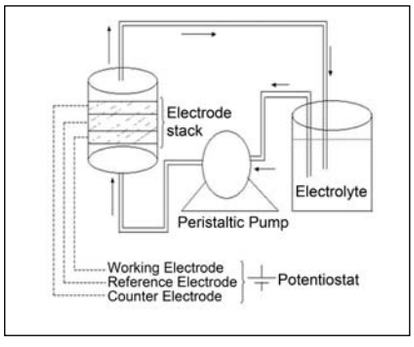

Fig. 1 *Schematic of flow through cell*

Fig. 2 *Experimental set up of flow through cell*

concentration by atomic absorption spectroscopy and comparing it with the initial concentration. Figure 3 shows the reduction in manganese concentration analysed by atomic absorption spectroscopy in simulated effluent solution containing 100 ppm of manganese.

In order to increase the efficiency of electrodeposition, parametric studies were carried out as a function of pore size of reticulated vitreous carbon, pH and temperature of the electrolyte. It was observed that a maximum efficiency of 90% could be achieved using 60 pores per square inch reticulated vitreous carbon, at 323 K and at a pH of 1.6.

This study demonstrates a new method for fast reactor effluent decontamination based on electrodeposition technique. The ease of operation and requirement of minimum space of this method makes it more advantageous than other conventional methods such as precipitation and ion exchange. In this method radioactivity is concentrated on a solid matrix such as reticulated vitreous carbon which has a large surface area.

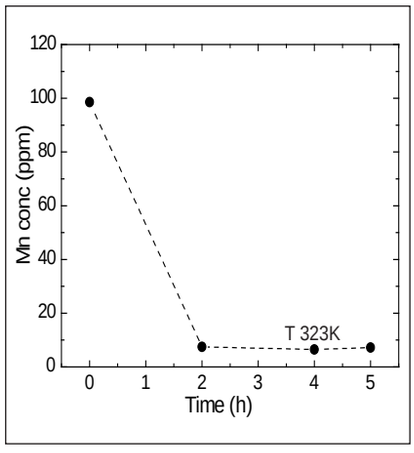

***Fig. 3** Atomic absorption spectroscopy analysis of simulated effluent during electrodeposition at 323 K as a function of time*

III.15 Radionuclide Trap Studies for Removal of ^{54}Mn from Primary Sodium of Fast Reactors

Owing to the high neutron flux encountered in the core of fast reactors, a large number of activated corrosion products such as ^{54}Mn, ^{60}Co, ^{59}Fe, and ^{51}Cr are produced from structural and clad materials. These nuclides gradually get released into the coolant stream as a result of corrosion by liquid sodium. In addition to this, in the event of a fuel pin failure, volatile fission products such as ^{137}Cs, ^{134}Cs, ^{131}I etc. are released steadily into the coolant. Due to the activity transport occurring in the reactor circuits, these radionuclides are transported and get deposited at various locations of primary coolant circuits. Since most of these nuclides are fairly long-lived and possess relatively high gamma energies, they pose problems during regular operation and maintenance of the reactor system, resulting in long plant shutdown time and demanding high radiation shielding requirements. In addition, these radionuclides pose problem in disposal of liquid effluent generated during decontamination/decommissioning stage.

One of the methods of minimizing the radioactivity burden caused by these nuclides is to develop suitable radionuclide trap materials to concentrate and contain them at suitable locations in the reactor systems. Development of such trapping materials would contribute to a great extent towards successful disposal of these nuclides at a later date. Data from the operating fast reactors indicate that Ni is a promising material for trapping ^{54}Mn ($t_{1/2}$ = 312 d and γ energy = 834 keV) which is one of radionuclides causing activity burden. Experiments carried out in earlier research reactors revealed that Ni foil is effective in trapping ^{54}Mn from sodium. Large pressure drop across the trap was experienced when Ni foil was used. In order to minimize the pressure drop in the reactor circuit and to provide large surface for the deposition of Mn, Ni foam with high surface and large porosity has been proposed as candidate material for trapping ^{54}Mn from the primary sodium circuits of fast breeder test reactor and prototype fast breeder reactor (as part of CFBR R&D activities). In addition, Ni foam possesses unique features such as exceptional uniformity, lightweight, intrinsic strength, corrosion resistance, good electrical and thermal conductivity. Experiments were carried out at IGCAR to understand the deposition mechanism of Mn on Ni foam.

Experiments were conducted in a static sodium system. Ni foam and foil samples of known weight were immersed in liquid sodium containing a known quantity of Mn powder at 673 and 773 K for different duration of time ranging from 100-1000 hours.

After equilibration, Ni foam and foil samples were taken out after 100,

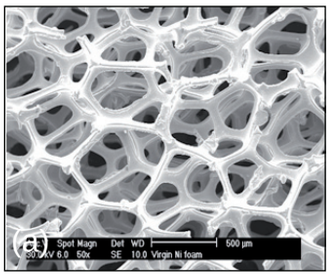

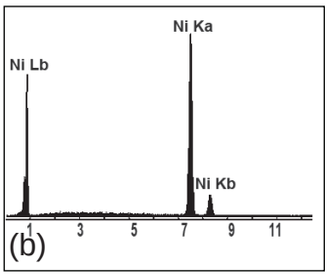

Fig. 1 *(a) Secondary electron image and (b) EDS spectrum of virgin Ni foam*

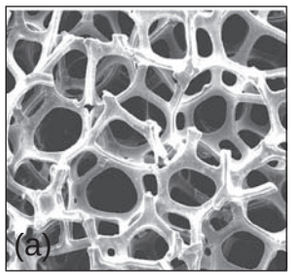

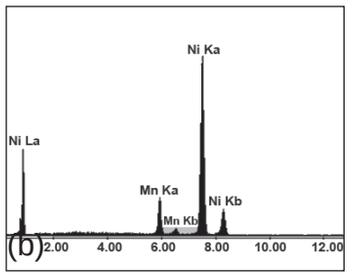

Fig. 2 *(a) Secondary electron image and (b) EDS spectrum of Ni foam exposed to sodium at 773 K for 1000 h*

250, 500, 750 and 1000 hours. The surface of the specimens was characterized using scanning electron microscope and energy depressive X-ray analysis. The bulk concentration of Mn in foam and foil was analyzed by wet chemical method using atomic absorption spectrophotometer. The properties of Ni foam and foil used for this experimental work is given in Table 1.

Scanning electron microscope image and energy depressive X-ray spectra of the virgin Ni foam and the one exposed to sodium containing Mn at 773 K for 1000 hours are shown in Figures 1 and 2 respectively. It is observed that there is no appreciable change in the morphology of the Ni foam exposed to sodium (Figure 2a) compared to virgin foam (Figure 1a). This, in turn, indicates that the mechanical properties are retained even after sodium exposure. EDS spectra as shown in Figure 2(b) shows indication of Mn deposition on Ni surface. X-ray elemental mapping of Mn on Ni foam and foil, shows uniform deposition of Mn on the surface of both Ni foam and foil. Bulk and surface concentrations of Mn in Ni foam and foil as a function of time are shown in Figures 3(a) and 3(b) respectively. It is observed that bulk concentrations of Mn in Ni foam are almost twice higher than those in foil samples. This indicates deposition of Mn in all the layers of the Ni foam compared to its distribution on the surface of Ni foil.

In order to understand the corrosion of Ni foam in flowing sodium, samples were exposed to a dynamic sodium system in radioactive sodium chemistry loop at 773 K for 1000 hours. The corrosion rate from weight loss measurement was estimated and found to be 0.83 mpy. In addition, it was observed that there is no change in surface morphology of Ni foam after sodium exposure. These results indicate that Ni foam is highly compatible in sodium. In addition, the estimation of Mn in Ni foam was carried out using an instrumental neutron activation analysis (INAA). INAA analysis of Ni foam showed around 700 ppm of manganese. INAA analysis of Ni foam exposed to Na at 673 K in static system without any intentional addition of Mn showed 4 ppm of Mn. In the above experiments the source of Mn is the dissolved metal impurity in Na from the material of construction of the experimental set up. These results indicate that Ni is able to trap even traces of Mn impurity in Na.

A portion of the sample exposed to Na at 773 K was analysed by atomic absorption spectrophotometer and INAA. There is good agreement between the values obtained from atomic absorption spectrophotometer and INAA too. Results from these analyses indicate that the concentration of Mn in Ni foam was increasing with the exposure time in Na. From these results, it can be estimated that 1 g Ni foam can trap 4.18×10^{-2} g of Mn which is equivalent to 320 Ci while 1g Ni foil can trap Mn equivalent to 190 Ci. This indicates that Ni foam has higher capacity for trapping Mn than that of Ni foil.

From this study, it is concluded that, Ni foam is highly compatible in sodium and also shows higher trapping efficiency for Mn compared to Ni foil due to is high surface area. In addition, its highly porous structure minimizes the pressure drop across the trap.

Table 1: The properties of Ni foam and foil

	Ni foam	Ni Foil
Purity	99.9%	99.9%
Pores per square inch	110	-
Density	0.2 g/cc	-
Porosity	97.5%	-
Pore size	200 µm	-
Thickness	1.8 mm	0.15 mm

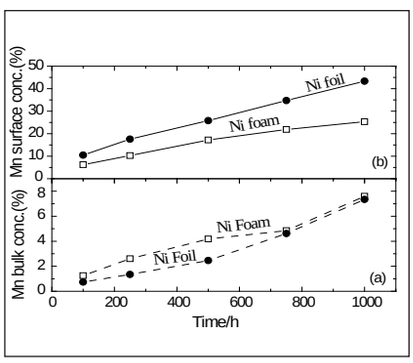

Fig. 3 *(a) Mn bulk concentration(%) and (b) Mn surface concentration (%) trapped in Ni foam and foil as a function of time*

III.16 Calibration of Semiconductor based Hydrogen Sensor for Argon Cover Gas in Engineering Sodium Facility

For continuous monitoring of trace levels of hydrogen in the argon cover gas over liquid sodium, a thin film based sensor using tin oxide was installed in tandem with the thermal conductivity detector (TCD) based system with nickel diffuser during December 2006 in sodium water reaction test facility (SOWART). The detection limit of TCD based system is ~30 vppm. Tin oxide based sensor was integrated with the TCD based system with a view to extend the capability of hydrogen detection in argon down to 1 vppm.

In the present experiments, tin oxide sensor was calibrated on-site by introducing known quantities of hydrogen (gas phase injections and typical concentration range was 8 to 110 vppm) after by-passing it from TCD based sensor system. Performance of the sensors was tested by injecting low (calculated) quantities of hydrogen through sodium (hydrogen injection section). The hydrogen injected will travel through sodium and escape to the cover gas plenum in the expansion tank. The temperature of sodium in the entire loop including the expansion tank was maintained at about 523 K, which would ensure minimum dissolution of hydrogen in sodium. The nickel coil diffuser was maintained at 773 K to ensure the diffusivity of hydrogen from cover gas to the argon stream flowing through the diffuser. Two campaigns of experiments were planned and carried out. In the first, 5 to 50 vppm of hydrogen (in argon) was used in the experiments. In the second campaign, experiments were carried out between 40 and 100 vppm of hydrogen (in argon). The background level hydrogen in argon cover gas was maintained less than 1 vppm in all these experiments.

Typical response exhibited by sensor-1 for 5 vppm (in argon) injection of hydrogen through sodium at 523 K is shown in Figure 1. A change of 26 mV in signal was observed for this concentration. Figure 2 shows the typical synchronous response transients exhibited by tin oxide (sensor-2) and TCD based sensors towards 60 vppm (in argon) injection of hydrogen through sodium. The change in signal is ~180 mV. TCD based sensor system also showed a change of about 35 mV (corresponds to 35 vppm of hydrogen).

Figure 3 shows the comparison of gas phase calibration results with those of hydrogen injection through sodium by tin oxide based sensor-2. A close match in the signal exhibited by the sensor for both the studies is observed. It also further confirms that the hydrogen concentrations realized in argon cover gas are nearly same either when introduced through sodium or gas phase. However, the sensor output is not linear in the hydrogen concentration range of present studies. As observed in the graph, for 20 vppm change in hydrogen concentration, the typical change in sensor output is 200 mV. The change in sensor output is 500 and 600 mV for 60 and 80 vppm change respectively.

These experimental studies and the results demonstrate the usefulness of tin oxide based sensor for monitoring low levels of hydrogen in argon cover gas during low power operating conditions of the reactor.

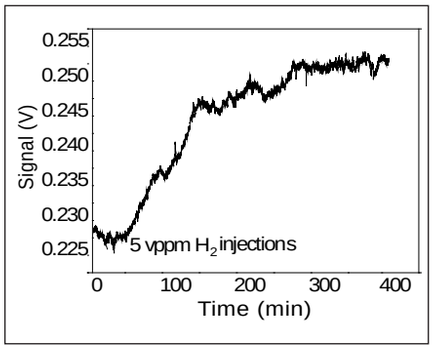

Fig. 1 Response characteristics of tin oxide based sensor (sensor-1)

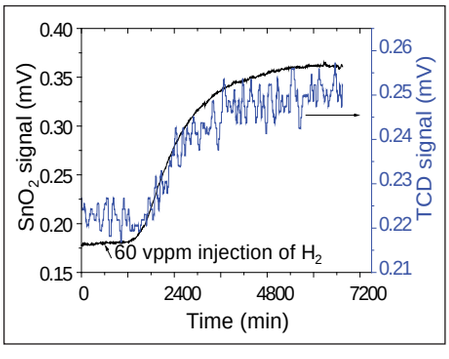

Fig. 2 Synchronous response transients exhibited by tin oxide (sensor-2 and TCD based sensors for 60 vppm injection of hydrogen

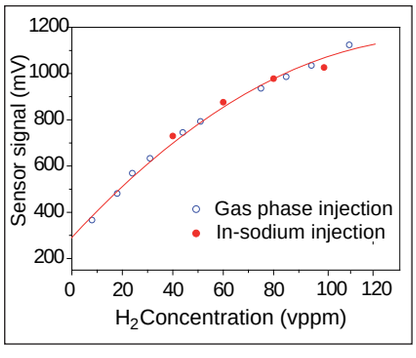

Fig. 3 Calibration traces shown by tin oxide based sensor (sensor-2) for in-sodium and gas phase hydrogen injections carried out in SOWART

III.17 Acoustic Leak Detection Studies in SGTF Steam Generator

In PFBR, sodium in the secondary circuit is circulated through once through steam generator to produce superheated steam at 172 bar pressure. It is an important requirement from safety and economic considerations to detect water/steam leaks in steam generator tubes at the incipient stage. Presently, sensors based on hydrogen concentration in sodium and argon cover gas are being used for detecting water/steam leaks from tube side to sodium in the shell side. These detectors are sensitive enough to detect even micro leaks but with response time of about 2-3 minutes. It is possible to detect a leak of 1 g/s of water/steam into sodium within one second by the acoustic leak detection technique. Instantaneous response is the advantage of acoustic technique and it is also effective in detecting developing leaks and leak into stagnant sodium around thermal baffles in steam generator. Localization of leak is also possible with acoustic technique by suitably keeping the sensors on various points on the steam generator shell.

Experiments were conducted in 5.6 MWt steam generator in steam generator test facility for studying background noise present during different operating power levels. Ten waveguides instrumented with accelerometers were welded on steam generator shell along the length of the steam generator, to collect the acoustic signals (Figure 1). In leak simulation studies, argon gas was injected at 20-100 bar through an orifice of 0.5 mm into shell side sodium. The acoustic signals from six accelerometers after amplification and filteration were recorded on a high speed digital instrumentation tape recorder.

In an operating steam generator, sodium flow, water/steam flow, and boiling noise along with the noise from adjacent machinery contribute to background noise. When water/steam at high pressure leaks into sodium, acoustic noise will be generated whose signal strength is much lower than that of background noise. The signal-to-noise ratio (S/N) of leak signal is reported to be around -17 dB in case of a water/steam leak of 1 g/s.

Development of advanced signal processing techniques is necessary to distinguish the acoustic leak signals from the background noise. Wavelet detailed coefficients variance technique is analyzed with the experiment data. In this, discrete wavelet transform with

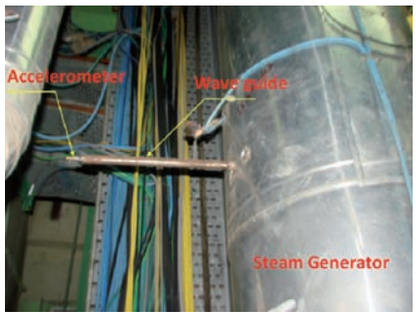

Fig. 1 *A typical waveguide position on the SG*

seven levels of decomposition using Daubechies-04 wavelet is used to analyze the time signal. The variance of the level-4 wavelet detailed coefficients is used as feature to detect the onset of leak. The results of analysis for different power levels of steam generator are shown in Figure 2.

Algorithms for leak detection was developed and tested with data from SGTF and steam to sodium injection studies in sodium water reaction test facility. An online acoustic leak detection system with programmable national instruments analog input modules and PXI embedded controller for real time signal processing on LabVIEW platform was developed and is under operation at SGTF to monitor acoustic signals and also store data during argon injection studies for off-line signal analysis.

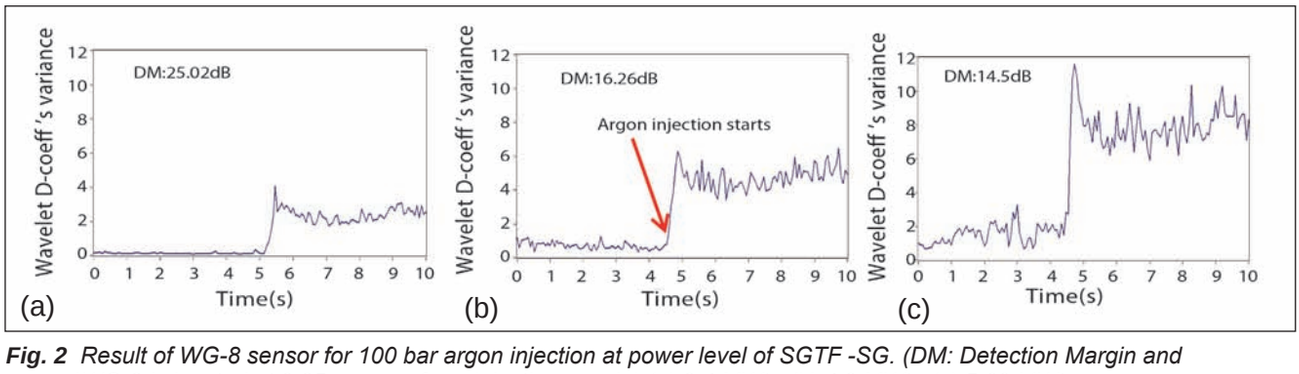

Fig. 2 *Result of WG-8 sensor for 100 bar argon injection at power level of SGTF -SG. (DM: Detection Margin and *WG-8 is located at 9.85 m away from injection nozzle) (a) 3.4 MWt, (b) 4.3 MWt, (c) 5.60 MWt*

III.18 Metal Fuel Test Reactor: Objectives and Core Design Options

Fast reactors based on metal fuel are essential for the rapid growth of nuclear energy due to their capability of high breeding and low doubling time. Towards this, a comprehensive program for developing fast reactor technology based on metal fuel with closed fuel cycle has been started in India. Construction of a Metal Fuel Test Reactor (MFTR) at IGCAR has been planned to enable full-scale experimental testing of fuel subassemblies before launching commercial metal FBRs. With the availability of MFTR, it is possible to experimentally validate various core physics design parameters. It is also possible to demonstrate the safety of metal FBRs by carrying out several reactor safety experiments similar to that carried out in other world reactors. MFTR would have a co-located pyro-reprocessing plant to demonstrate closure of the fuel cycle. The discharged fuel from MFTR will be recycled after reprocessing and fuel fabrication. MFTR will also be used to produce radio isotopes for medical applications and also for the development of materials. Provisions are made in the design for irradiation experiments towards validation of new fuel and structural materials, capable of achieving higher burn-up and doses. Subsequent to FBTR, this facility would form the back bone of all R&D activities related to irradiation at IGCAR.

Preliminary physics design of a reference MFTR core is performed with ERANOS 2.1 system such that this core satisfies the design requirements of:

(a) Minimum reactor thermal power
(b) Relatively low critical mass for plutonium
(c) Marginal breeder to meet its own fuel requirement
(d) Peak linear heat rating of 450 W/cm at all time of irradiation
(e) Single fuel enrichment
(f) Hexcan size and clad diameter same as that of PFBR
(g) Fuel column height of 1000 mm (h) Peak burn-up of 150 GWd/t
(i) Six control and safety rods and 3 diverse safety rods
(j) Three experimental locations and
(k) Special experimental central assembly. With above requirements, reactor power of 320 MWt is arrived at. Sodium bonded fuel pin design is used for this study. Ternary fuel U-Pu-6%Zr is used.

Physics Design

An optimum core is arrived at with sixty fuel and forty two radial blanket subassemblies. The central location is reserved for a special assembly with hundred and eighty fuel pins to be utilized for irradiation experiments besides three other experimental locations in the fourth ring. There are six control and safety rods and three diverse safety rods. There are 102 steel reflector subassemblies made of 316 LN steel. MFTR core is shown in Figure 1. Based on peak linear heat rating requirement of 450 W/cm, Pu enrichment is optimized to be 21%. The excess reactivity of the core is computed by taking into account the reactivity loses during reactor operation-loss due to

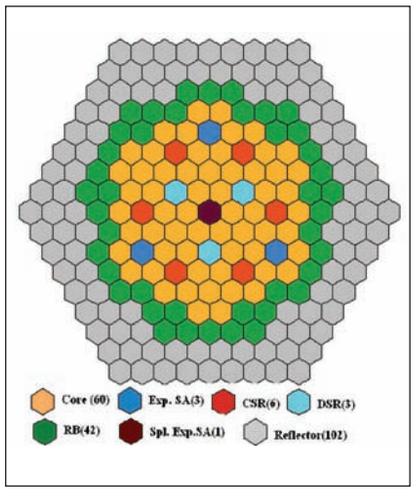

Fig. 1 *Metal fuel test reactor core*

temperature and power rise, due to burn-up besides excess margin provided for the core. The required value of multiplication factor at the hot state is estimated to be 1.0866 and the computed value for this optimized MFTR core (after adding transport theory correction) is 1.0827. Burn-up loss of reactivity for one cycle (300 days) of operation is estimated to be 3785 pcm. Maximum subassembly power at the centre is 6.7 MWt and in the first ring it is 7.7 MWt. The subassembly power at the core boundary is about 3 MWt. The design is such that the central special assembly has peak linear heat rating of 445 W/cm, while subassemblies in the first has peak linear heat rating of 438 W/cm. Similarly, an optimum cycle length of 300 effective full power days (400 calendar days with 75% load factor) is arrived at for achieving peak burn-up of 150 GWd/t. Computed breeding ratio is 1.12. Average neutron flux at the central subassembly is 4.5×10^{15} n/cm^2-s, whereas it is about 1.7×10^{15} n/cm^2-s at the core boundary. The flux levels

at the experimental locations are ~2x10^{15} n/cm^2-s. Total plutonium and depleted uranium requirements for initial core loading is 940 kg and 12.8 tonnes respectively.

Engineering Design

Engineering design involves sizing of fuel pin satisfying the given set of conditions.

Design criteria

- Fuel centre temperature with all uncertainties shall not exceed its melting point at 115% of the operating power [Over Power Margin (OPM)-15%].
- Clad inside temperature shall be less than 923 K under hotspot condition.
- Sodium temperature shall be less than its boiling point.
- Cumulative damage fraction limit is restricted to 0.25.

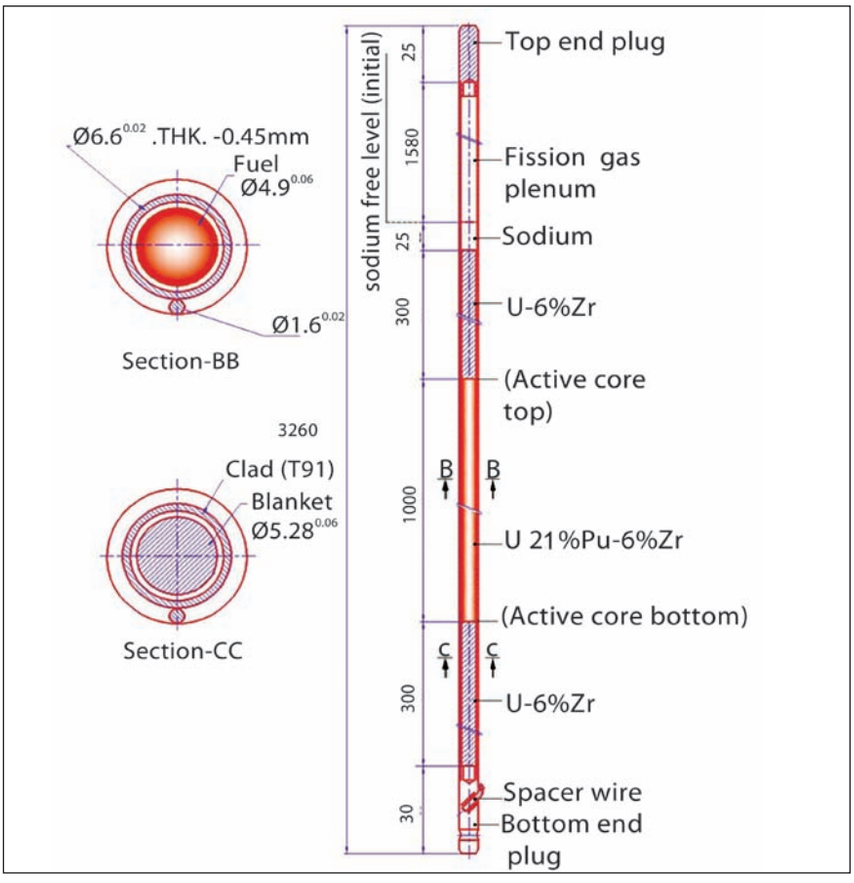

***Fig. 2** MFTR sodium bonded metallic fuel pin*

Design requirements

Design shall be such that the fuel shall always remain covered with sodium during its life and the fission gas plenum length shall be sufficient to accommodate fuel swelling and sodium expelled for the target burn-up.

Fuel pin sizing

Based on available infrastructure, the diameter of fuel pin is maintained at 6.6 mm with thickness of 0.45 mm. To avoid lower temperature eutectic between fuel and the clad, modified 9Cr-1Mo, T91 steel is selected as the clad material.

U-21Pu-6Zr fuel smeared density is kept at 75% theoretical density to avoid fuel clad mechanical interaction and to allow sodium infiltration into the fuel which helps in increasing the thermal conductivity of fuel.

The fuel slug diameter is 4.90±0.06 mm. The active core length is 1000 mm. Since the commercial MFBRs are likely to have 1 metre length active core, it is decided to test its behavior and fabrication feasibility in MFTR.

To study the breeding potential, U-6Zr, blanket slug with smeared density of 85% TD is provided on either side of fuel column to a length of 300 mm each. A typical fuel pin is shown in Figure 2. Top plenum is provided for 1600 mm based on the 100 GWd/t burn-up, satisfying cumulative damage fraction limit of 0.25, in addition to 25 mm of initial filled sodium resulting in plenum to fuel length ratio of 1.6:1. Fuel pin length is ~ 3260 mm. 217 pins would be arranged in a triangular pitch inside Hexcan made of modified 9Cr-1Mo (T91) material with width across flat of 131.3 and thickness 3.2 mm.

Characteristics of MFTR core are summarized in Table 1.

Table 1: Summary of MFTR core characteristics

Parameters	Value
Power (MWt)	320
Fuel	U-Pu-6% Zr alloy
Fuel density (g/cc)	17.1 at 20
No. of enrichment (s)	1
Pu enrichment (%)	21
Fuel pin diameter (mm)	6.6 mm
No. of fuel pins per subassembly	217
Cycle length (days)	300
No. of fuel subassembly	60
No. of blanket subassembly	42
No. of control & safety rod /diverse safety rods	6/3
B_4C enrichment	To be optimized
No. of reflector subassembly	102
No. of experimental locations	4
Breeding ratio	1.12
Average core centre flux	4.5x10^{15} n/cm^2-s

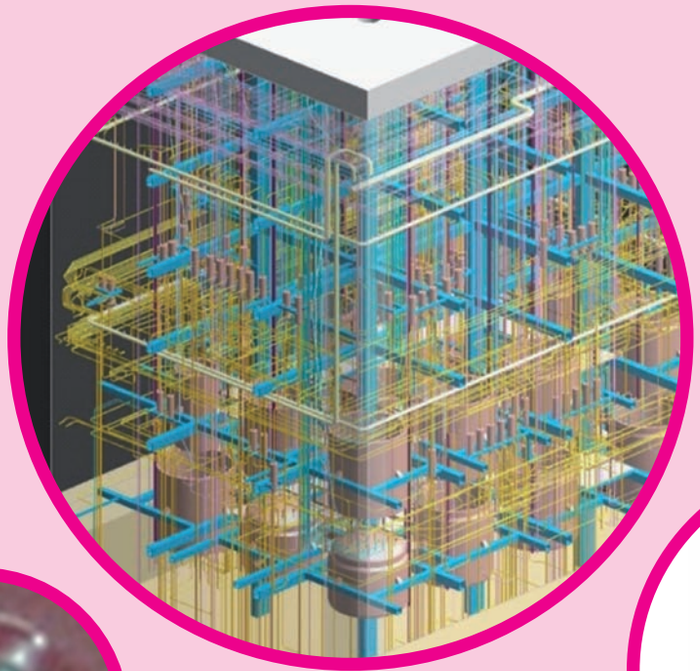

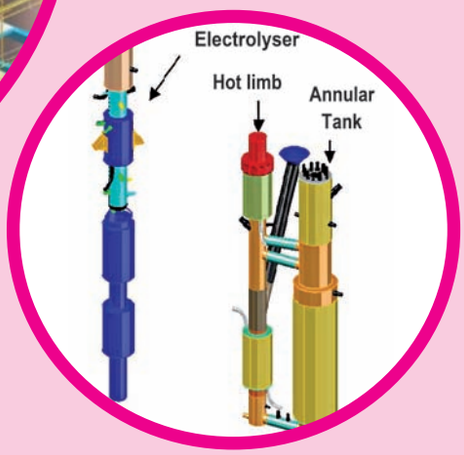

CHAPTER - IV

Fuel Cycle

IV.1 Fast Reactor Fuel Cycle Facility

Design of the Fast Reactor Fuel Cycle Facility (FRFCF) to close the fuel cycle of Prototype Fast Breeder Reactor has been completed. The work is being piloted by Indira Gandhi Centre for Atomic Research with technical support from Bhabha Atomic Research Centre and Nuclear Fuel Complex. Approval of Atomic Energy Regulatory Board for the site of FRFCF (Figure 1) has been obtained. Preparatory project for development of site infrastructure and engineering of FRFCF has been completed. Basic infrastructure like approach roads, construction power supply system, workshop, storage and construction office space has been created at the site to reduce the lead time required to commence the construction work, once the financial sanction for FRFCF project is available. First stage review of the preliminary safety analysis report by project design safety committee for FRFCF has been completed and the committee has recommended to AERB to issue consent for construction of FRFCF. Detailed project report for FRFCF has been approved by Atomic Energy Commission. Process of obtaining approval of cabinet for the project is in progress. Construction work on the project is expected to commence in 2013.

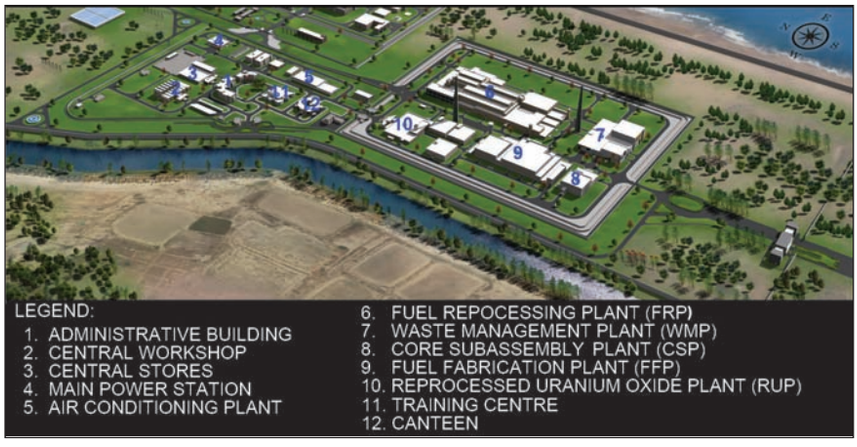

***Fig. 1** Perspective view of the Fast Reactor Fuel Cycle Facility*

IV.2 Design of Fuel Reprocessing Plant in Fast Reactor Fuel Cycle Facility

The spent fuel from PFBR is proposed to be reprocessed at the Fast Reactor Fuel Cycle Facility (FRFCF), to be set up at Kalpakkam, to recover plutonium and uranium for recycling.

The process flow sheet of fuel reprocessing plant is based on the operating experience of processing spent mixed carbide fuel of FBTR in the pilot plant CORAL. The major processing steps are dismantling of fuel subassemblies, chopping of fuel pins, dissolution in nitric acid medium, co-decontamination, partitioning, plutonium and uranium purification solvent extraction cycles and plutonium and uranium reconversion operations. The layout of fuel reprocessing plant was designed considering remote operation and maintenance philosophy.

Fuel reprocessing plant is designed with five floor levels that range from -10.5 to +20 m RL in seven functional blocks. Head end block of fuel reprocessing plant consists of separate lines for processing fuel subassembly, radial subassembly and post-irradiation examination of failed subassemblies. Laser dismantling technique, which was demonstrated for dismantling FBTR fuel assemblies, will be adopted for fuel and radial subassemblies. The design of the chopper envisages multi-pin chopping due to slender nature of fuel pins. Titanium will be the material of construction for dissolver, instead of conventional 304L grade stainless steel, due to highly corrosive nature of the solvent. Ti-SS 304L dissimilar welding technique has been developed for integrating dissolver with rest of the plant made of SS 304L. Buffer cell with material transfer ports is provided for transfer of hulls and solid wastes arising out of dismantling operations to minimize the extent of α contamination.

Plutonium process block consists of separate concrete cells for

co-decontamination, partitioning, plutonium purification cycles, plutonium recovery from raffinate and solvent wash. Uranium process block consists of concrete cells for uranium purification, uranium recovery from raffinate, solvent wash and uranium product evaporation. Evaporation block consists of concrete cells for raffinate, waste and solvent wash waste evaporation. Each evaporator is kept in an isolated concrete cubicle to enable maintenance. Short residence time centrifugal extractors will be deployed for plutonium rich solution processing to minimize the solvent damage. Mixer-settlers are used for solvent wash. All the remote operations are done using master slave manipulators (MSM) and in-cell cranes with specially designed tools. In the uranium section, pulse columns are employed for the uranium purification and diluent wash. Sampling cells and analytical cells are distributed across the processing sections in such a way that piping for taking representative samples is minimized. The high active/medium active liquid samples collected in a sampling cell are analyzed *in-situ* in the analytical cell. Low active samples are analyzed in the active analytical laboratory after transporting the sample bottles using pneumatic conveyer. The cut away view of a sampling cell is shown in Figure 1. Solid waste transfer cells are integrated with the contactor cells/sampling cells for collection of solid wastes and disposal. Provision is made for assaying the solid wastes before transferring them to the waste management plant.

The process flow diagram, piping and instrumentation diagrams and equipment layouts have been finalized. Owing to high density piping involved in process cells and waste tank farm (WTF), 3D modeling of piping was adopted to avoid interferences. View of the in-cell piping in a typical process cell of FRP is shown in Figure 2. Provisions are made in the layout of the plutonium reconversion facility for adopting automation of plutonium reconversion process. Manual intervention in the uranium reconversion facility that converts uranyl nitrate solution into uranium oxide powder is minimized by deploying rotary equipment such as precipitator, vacuum pan filter, vertical rotary tray drier and rotary calciner. The technology developed at the Nuclear Fuel Complex is adopted in this section of fuel reprocessing plant.

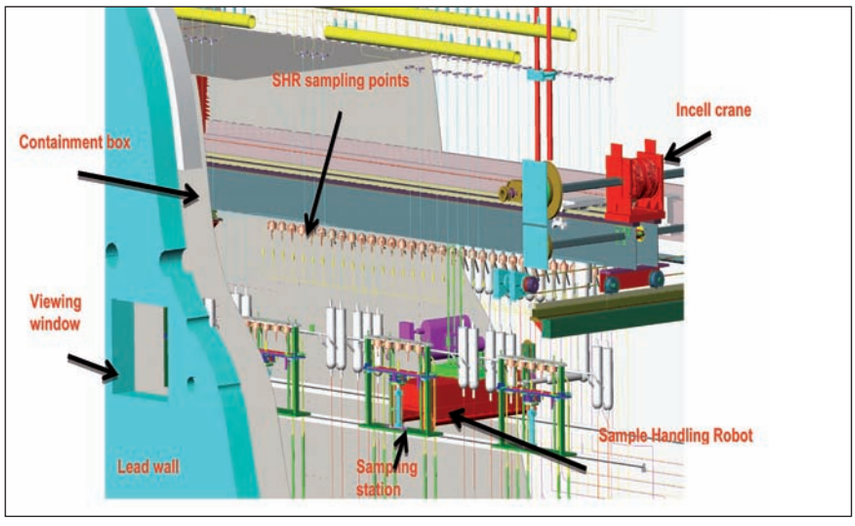

Fig. 1 *Incell view of sampling cell*

Provisions are made in the WTF layout for collection of samples for carrying out studies related to actinide recovery from HLW and for in-service inspection(ISI) of tanks. Provisions have also been made for *in-situ* estimation of plutonium inventory in plutonium cells and for ISI of dissolver, evaporators, floors of process cells and area below containment boxes.

Structural integrity of various safety related tanks, equipment and their supports, in-cell piping, supporting structures of ducts and piping and special equipment like glove boxes, reconversion boxes, fume hoods and cell doors has been ensured by analysis as per the relevant codes and standards.

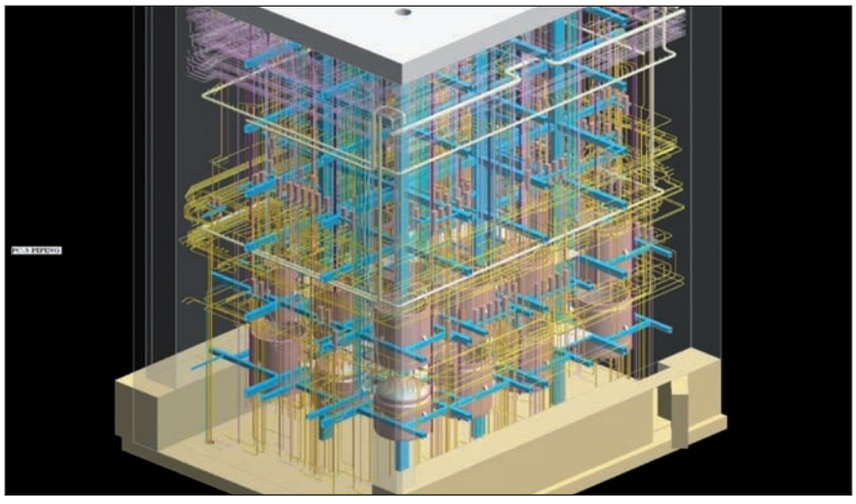

Fig. 2 *Schematic view of in-cell piping in a typical process cell of fuel reprocessing plant*

IV.3 Development of Modified Solvent Extraction Flow Sheet for Short Cooled FBR Fuels

The basic PUREX flow sheet for solvent extraction for FBR spent fuel reprocessing needs to be modified to meet the challenges of plutonium recovery, limitations in the loading of plutonium due to limited organic concentration and increased decontamination factors required for specific fission products. Two of the major fission products, zirconium and ruthenium play an important role in limiting the decontamination of products in this process because of their reasonably high distribution ratios and the complex nature of extraction behaviour. The fact that they behave quite opposite with respect to acidities, makes it difficult to achieve the required separation. Hence, issues with respect to zirconium and ruthenium are to be carefully addressed.

Considering the difficulty in removing the fission products especially zirconium and ruthenium, a single extraction cycle is a difficult proposition. A flow sheet with dual scrub, one for removing ruthenium which requires higher acidity and the other for removing zirconium (with a lower acidity) has been formulated. Because of the dual scrub, there is a challenge of refluxing of plutonium which might lead to third phase formation due to the lower solubility of the plutonium complex in the organic phase. This is a safety related issue since there is a risk of criticality due to high concentrations of plutonium.

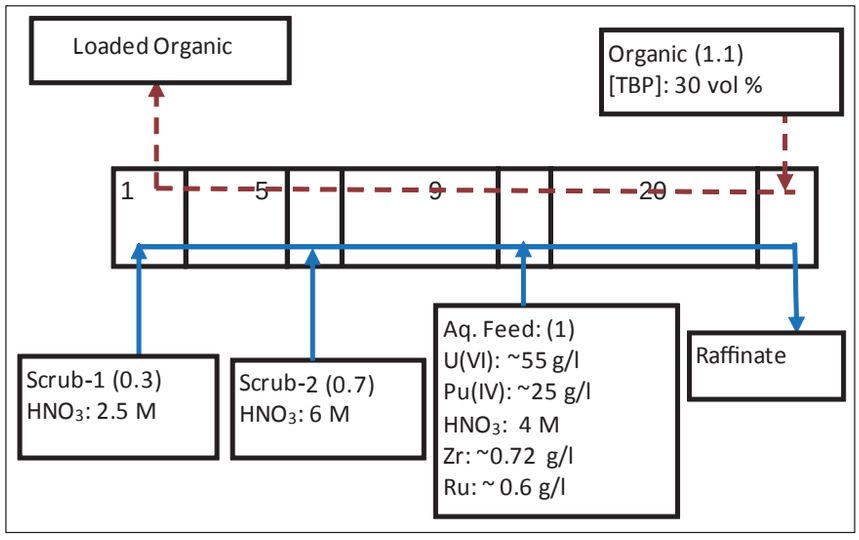

***Fig. 1** Proposed purification flow sheet*

Formulation of flow sheet

Solvent extraction flow sheet for purification and separation of uranium and plutonium is formulated based on PUSEP (version-2) computer code. Typical concentrations of FBR spent fuels are taken as feed inputs. The allowable product contamination due to zirconium and ruthenium are derived based on the concentration of radioactive species of zirconium and ruthenium. Typical decontamination factors required are of the order of 10^5 for both ruthenium and zirconium. The flow sheet design also involves consideration of issues such as third phase formation due to excessive plutonium loading in the solvent, polymerization of plutonium owing to low acidity and capability to demonstrate the safe operation with possible upsets of flow rates of various streams. The

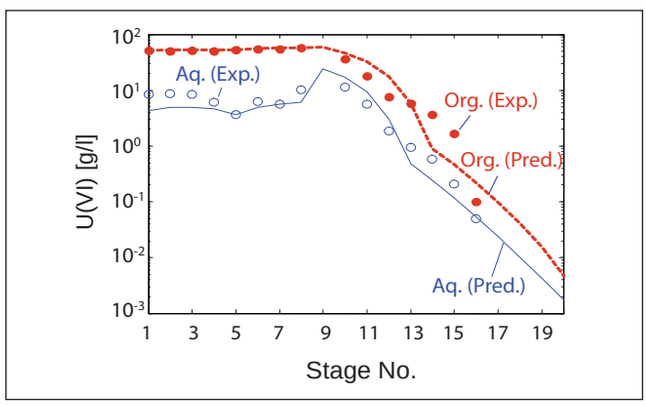

***Fig. 2** Uranium concentration profile (extraction cycle)*

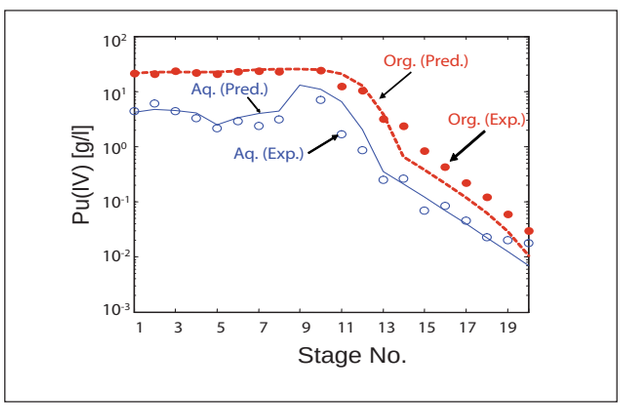

***Fig. 3** Plutonium concentration profile (extraction cycle)*

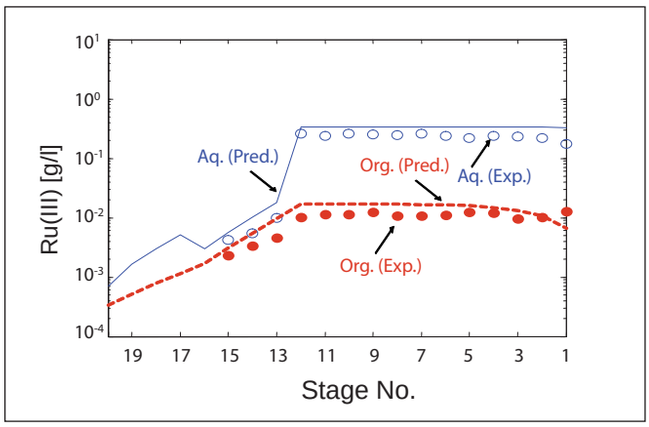

Fig. 4 Comparison of experimental and calculated profile of ruthenium in stages of mixer settler

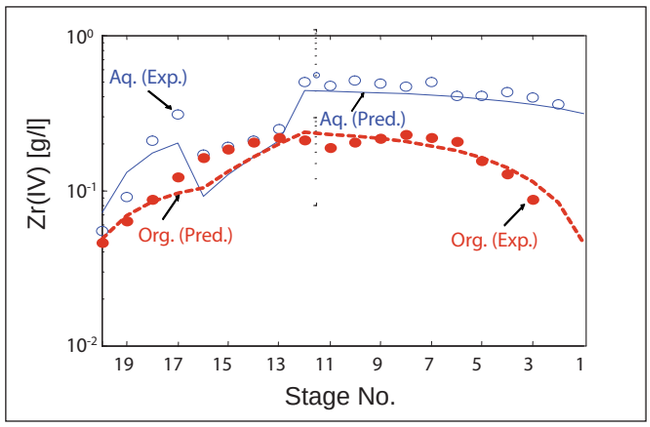

Fig. 5 Comparison of experimental and calculated profile of zirconium in stages of mixer settler

purification flow sheet should meet the following specific requirements:

(a) The organic extract shall not contain fission product activity especially that of zirconium and ruthenium more than 1 µCi/kg for uranium and 25 mCi/kg for plutonium

(b) The recovery of uranium and plutonium shall be better than 99.9% even during possible upset of operating conditions

(c) Plutonium concentration in the solvent in any of the stages, even during the postulated upset operating conditions, shall be less than safe limiting maximum concentration and

(d) Plutonium contamination in the uranium product should be less than 0.4 ppm.

Choice of acidity of feed solution

Though Pu(IV) has a maximum distribution ratio at about 6 M acidity, 4 M is considered as optimal feed acidity taking into consideration that zirconium extraction increases with increase in acidity.

Choice of the solvent loading

Though organic can be loaded as much as possible to maximize the decontamination factors, the amount loaded will be limited by the solubility of plutonium complex in the solvent. Though limited organic concentration can be taken as 45 g/l, an upper limit of 35 g/l is considered as safe concentration to take care of any upset condition.

Design of scrub section

The distribution coefficient of ruthenium goes through a peak (between 0.5 to 0.75 M aqueous acid) and then decreases as a function of acidity. Hence, dual scrub with one scrub at a high acidity of 6 M (for effective removal of ruthenium) and another scrub with lower acidity of 3 M (for effective removal of zirconium) are proposed. Considering 35 g/l as the safe limiting concentration of plutonium with possible variations in the flow rates, steady-state concentration profiles of plutonium were predicted with the simulation code in order to check whether this maximum concentration of plutonium in any of the stage can exceed limited organic concentration during off-normal conditions. Experiments were conducted with the proposed flow sheet (Figure 1) in a 20-stage mixer-settler. Experimental and calculated profiles are shown in Figures 2 to 5. The proposed flow sheet was found to meet the desired objective which can be implemented for the solvent extraction of uranium and plutonium in fast reactor spent fuel reprocessing.

IV.4 Extraction Behaviour of Zirconium in Fast Breeder Reactor Fuel Reprocessing

In the most widely used PUREX process for the reprocessing of irradiated fuel, uranium and plutonium are co-extracted into the organic solvent tri-butyl phosphate (TBP) diluted with hydrocarbon in the first extraction cycle, while most of the fission products remain in the aqueous phase (raffinate). However, the two fission product elements, zirconium and ruthenium play an important role in limiting the decontamination of products because, the extraction behaviour of zirconium and ruthenium are

complex and they behave quite opposite with respect to acidities, making it difficult to achieve the required separation. Generally, the distribution coefficient of zirconium (D_{Zr}) increases with acidity while for ruthenium, it decreases. The difficulties are more pronounced for the fast reactor spent fuels where the concentrations of these FPs are high. A necessary prerequisite for any realistic simulation of counter-current extraction in the PUREX process is a reliable relation for the prediction of distribution coefficients of the species involved. Although a number of models of distribution coefficients for PUREX system have been reported in the literature, they do not include zirconium. Hence, it was felt necessary to develop distribution coefficient correlations for zirconium as applicable to the fast reactor fuel composition. Extraction data of zirconium in various concentrations of HNO_3 (2.5-6 M) in the presence of uranium were measured in Reprocessing Group in order to validate model equations. The measured values of D_{Zr} will serve as database for the development of solvent extraction code for modeling and simulating process flow sheets. A thermodynamic model has been developed for the extraction of zirconium by tri-butyl phosphate. The model equations are based on chemical mass action principles in which the effect of metal complexation and activity coefficients are considered. The model works well in predicting the extraction of zirconium by tri-butyl phosphate at various nitric acid concentrations. The influence of concentration of nitric acid and uranium on the extraction behaviour of zirconium was also analysed.

Table 1: The Equations governing the extraction equilibrium and corresponding constants in terms of activities and activity coefficients

S.No.	Governing equations	The equilibrium constants
1	$H^+ + NO_3^- + TBP \Leftrightarrow TBP \bullet HNO_3$	$K^*_{H1} = K_{H1}\frac{\gamma_{TBP_f}}{\gamma_{TBP\cdot HNO_3}} = \frac{[TBP \bullet HNO_3]}{[H^+][NO_3^-]\cdot\gamma_{12}^2[TBP_f]}$
2	$H^+ + NO_3^- + 2TBP \Leftrightarrow (TBP)_2 \bullet HNO_3$	$K^*_{H2} = K_{H2}\frac{\gamma^2_{TBP_f}}{\gamma_{(TBP)_2\cdot HNO_3}} = \frac{[(TBP)_2 \bullet HNO_3]}{[H^+][NO_3^-].\gamma_{12}^2.[TBP_f]^2}$
3	$H^+ + NO_3^- + TBP \bullet HNO_3 \Leftrightarrow TBP \bullet 2HNO_3$	$K^*_{H3} = K_{H1}K_{H3}\frac{\gamma_{TBP_f}}{\gamma_{TBP\cdot 2HNO_3}} = \frac{[TBP \bullet 2HNO_3]}{[H^+]^2[NO_3^-]^2.\gamma_{12}^4.[TBP_f]}$
4	$Zr^{4+} + 4NO_3^- + 2TBP \Leftrightarrow Zr(NO_3)_4 \bullet 2TBP$	$K^*_{Zr} = K_{Zr}\frac{\gamma^2_{TBP_f}}{\gamma_{Zr(NO_3)_4\cdot 2TBP}} = \frac{[Zr(NO_3)_4 \bullet 2TBP]}{[Zr^{4+}][NO_3^-]^4.\gamma_{12}^4.[TBP_f]^2}$
5	$UO_2^{2+} + 2NO_3^- + 2TBP \Leftrightarrow UO_2(NO_3)_2 \bullet 2TBP$	$K^*_U = K_U\frac{\gamma^2_{TBP_f}}{\gamma_{UO_2(NO_3)_2\cdot 2TBP}} = \frac{[UO_2(NO_3)_2 \bullet 2TBP]}{[UO_2^{2+}][NO_3^-]^2\gamma_{12}^3.[TBP_f]^2}$

The extraction model developed is intended for incorporation in computer code PUSEP developed for the analysis of PUREX flow sheet of FBR fuel reprocessing. One of the important factors in the modeling of extraction of metals is the calculation of free extractant concentration available for the metal complexation. Since, nitric acid and uranium are both extracted by TBP, their contributions should also be considered in the development of model equation. The K_D relations were derived from the extraction equilibria of the components; the governing equations for the extractable species are given in Table 1.

Distribution coefficient of zirconium is given by the equation,

$$D_{Zr} = \frac{[Zr(NO_3)_4 \bullet 2TBP]}{[Zr^{4+}]} = K^*_{Zr}[NO_3^-]^4.\gamma_{12}^4.[TBP_f]^2$$

The equation for the estimation of γ_{12} was determined by a least-square method using the experimental data reported in literature. The values of equilibrium constants for the extraction of zirconium were determined by non-linear regression analysis of Equations 1 to 5 of Table 1 using the experimental data from literature and the data generated at our laboratory. The calculated and experimental extraction isotherms of nitric acid, zirconium and zirconium in different concentrations of uranium are shown in Figures 1 to 3 respectively. Figure 2 reveals that D_{Zr} increases with HNO_3 concentration whereas it decreases with increase in uranium concentration.

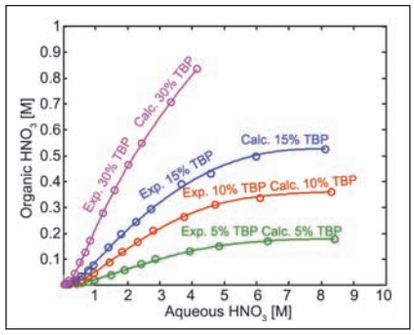

Fig. 1 *Extraction isotherms of nitric acid for 5, 10, 15 and 30 vol% TBP*

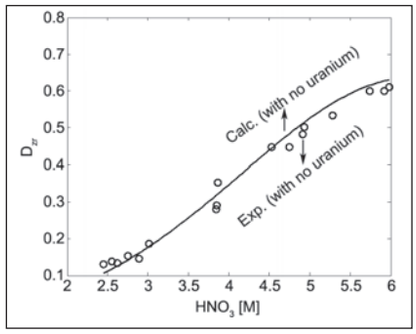

Fig. 2 *Distribution coefficient for zirconium against nitric acid concentration*

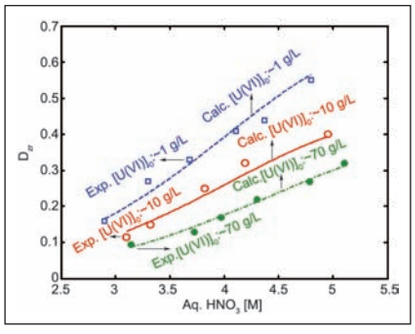

Fig. 3 *Effect of uranium on the extractability of zirconium*

IV.5 Design and Development of Electrolytic Dissolver for Demonstration Fast Reactor Fuel Reprocessing Plant

In the Demonstration Fast Reactor Fuel Reprocessing Plant (DFRP) the mixed carbide as well as the oxide fuels will be reprocessed. For dissolving the 44% PuO_2 - 56% UO_2 MOX fuel, electro-oxidative dissolution technique (EODT) using Ce(III)/Ce(IV) redox intermediate is envisaged for complete dissolution of the fuel. Owing to the presence of highly concentrated nitric acid and hence, the corrosive oxidative environment in the dissolver cell, titanium grade-2 was chosen as the material of construction for the dissolver. The choice is mainly due to the corrosion resistance of titanium, easy availability, fabrication expertise and adequate experience in the fabrication of dissimilar joints. A thermo-syphon type titanium dissolver had been developed and deployed at the pilot plant CORAL, for the dissolution of Pu-rich mixed carbide fuel of FBTR. Spent carbide fuel of FBTR with burn up varying from 25 to 155 GWd/t was successfully dissolved in this dissolver and reprocessed in CORAL facility. Based on the vast experience gained over a decade of successful operation of CORAL dissolver, a modified electrolytic dissolver was designed for the dissolution of Pu-rich mixed oxide/carbide fuel of FBTR at DFRP. The salient features of this equipment are removable type basket for hull transfer, hull agitation arrangement to reduce plutonium loss and air sparger to aid better circulation. The dissolver and electrolyser units (Figure 1) have been separated as individual equipment with appropriate piping arrangement for circulation through air-lift, making the electrolyser operation amenable for not only dissolution but also in electro-chemical conditioning. The critical components were machined from rounds to have weld configuration amenable for NDT, so that guaranteed life of the unit can be realised. The equipment is designed in such a way that the basket and electrode are amenable for remote operation and maintenance. To minimise the corrosion rate of weldment an indigenously developed Ti-5%Ta-1.8%Nb filler wire was used. Several innovative techniques were adopted while fabricating and inspection of the components meeting the stringent technical requirements. The functional test is also conducted for the electrolytic dissolver. A monolithic reaction bonded silicon nitride (RBSN) tube of length 600 mm for the purpose of separating the anode and cathode compartments of the electrolyser was fabricated and Pt-10% Ir electrodes of the geometry shown in Figure 2 were designed to withstand the highly corrosive environment. Ti/SS 304L explosive cladded dissimilar couples were developed to connect the titanium dissolver to the rest of the plant equipment made of SS 304L. The physical properties of dissimilar couples were validated for dissolver application and dissimilar ingots were manufactured using pulsed TIG welding with controlled heat input. The titanium dissolver and electrolyser with associated piping systems are being installed in DFRP.

Fig. 1 *Photograph of electrolyser and dissolver*

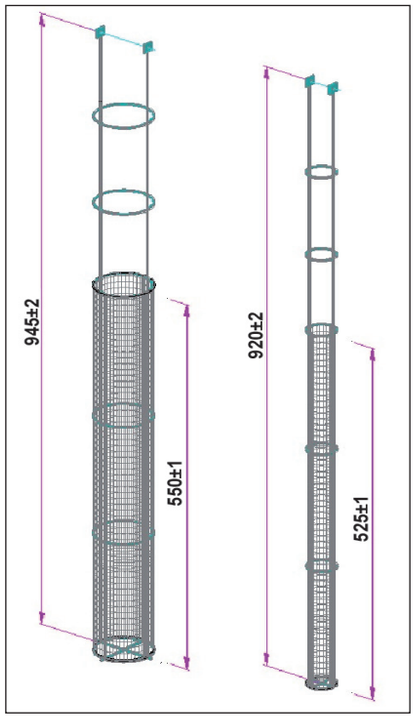

Fig. 2 *Anode and cathode of electrolyser*

IV.6 Modeling of Pu(VI) Distribution Equilibria in 30% TBP Based PUREX Process Conditions

Hexavalent plutonium (PuO_2^{2+}) is an important non-key species in the PUREX process. A significant quantity of Pu(VI) is generated initially during the dissolution of the irradiated high Pu content fuel of fast reactors. Even though extractability of Pu(VI) is considerably lower than Pu(IV) in TBP based PUREX systems, there is a risk of loss of valuable Pu to aqueous raffinate waste leading to subsequent extra operation for recovery and rework. A feed conditioning step to convert Pu(VI) to Pu(IV) is usually employed in the high Pu flow sheets. TBP based Pu(VI) extraction operations have been discussed in classical as well as contemporary literature.

For 30% TBP solvent, Pu(VI) extraction data reported by us earlier were combined with the archival data in the literature and an extraction model was developed based on the analysis of reported data. In the literature, from the slope analysis of earlier results, the solvation number for Pu(VI) in TBP systems was reported as 2. The experimental data reported by Sajun et al. was processed and an average value of 1.71 was obtained by numerical analysis. The reason for this behaviour may be attributed to the likely speciation of Pu(VI) in the organic solutions as solvates of varying compositional structures instead of the fixed formula $PuO_2(NO_3)_2.2TBP$. In the present case, two major compositional parameters considered are aqueous phase acidity and organic phase loading. Aqueous phase acid concentration affects equilibrium constant, K by altering aqueous phase ionic strength. Organic phase loading (in this case represented by organic uranium concentration) is a measure of driving force available for mass transfer from aqueous to organic phase. The experimental data reported by Codding et al. and Kumar et al. for Pu(VI) extraction by 30% TBP solvent were analyzed and a polynomial model with R^2 value of 0.987 was developed. Mean deviation and standard deviation were 0.54 and 10.76% respectively. A reasonably good agreement was observed. Figure 1 shows the variation of Pu(VI) distribution coefficient with the aqueous acidity at varying levels of organic loading. The notable observation from Figure 1 is that there is a reasonable agreement between the classical Pu(VI) extraction data of Codding et al. and contemporary data of Kumar et al. at nearly zero organic loading and at acidity levels below 2 M.

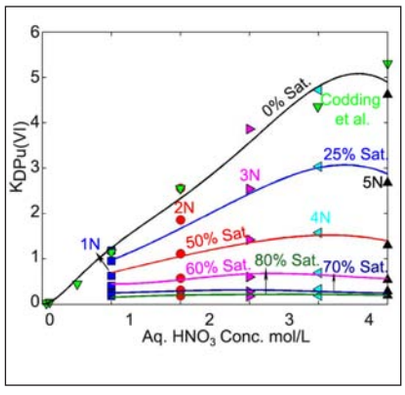

Fig. 1 *Variation of Pu(VI) distribution coefficients with aqueous acidity; experimental data for 1-5 M acidity were used from literature*

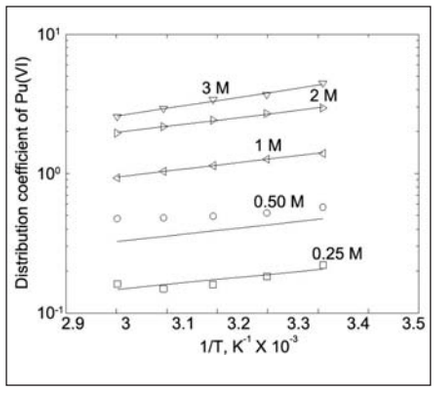

Fig. 2 *Comparison plot for temperature dependency of Pu(VI) distribution coefficients in 30%TBP; experimental data of Sajun et al. were used in this study*

Temperature dependence of Pu(VI) distribution coefficients

Arrhenius type temperature dependency was assumed for the distribution coefficients of Pu(VI) in 30% TBP-nitric acid system. Experimental data reported by Sajun et al. were used in this study. The slopes and intercepts of Arrhenius plots (1/T versus ln K_D) were found to be continuous functions of aqueous acidities. The slopes of Arrhenius lines for different acidities could be correlated as a third order function in aqueous acidity. The back-calculated distribution coefficients had a mean deviation of - 4.5% and a standard deviation of 10.2% for temperature dependency. The parity plot is shown in Figure 2. Except the data for 0.5 M aqueous acidity, all other comparisons were satisfactory. There was a small offset in the data of 0.5 M aqueous acidity and all other data points followed the behaviour predicted by the model.

The developed model is being integrated with the in-house developed computer code SIMPSEX (SIMulation Program for Solvent EXtraction) for the analysis and simulation of high plutonium flow sheets for reprocessing FBR fuel.

IV.7 Direct Dissolution and *in-situ* Extraction of UO_2 Pellet in Organic Solutions

Supercritical fluid assisted solvent extraction (SCFE) is an established technique for the separation of many solutes of industrial importance. The basic problem with SCFE process is remote operation at very high pressures inside hot cells and it is coupled with complex maintenance.

Recently, direct dissolution of UO_2 and *in-situ* extraction of uranium was tried at ambient pressures in Reprocessing Group. In a series of experiments, a gram level dissolution of UO_2 was carried out with TBP-HNO_3 complex at 333 K and at ambient pressures without the use of supercritical CO_2.

Dissolution of fuel pellet fragments

About one gram of UO_2 was added to 15 ml of the equilibrated TBP-HNO_3 complex in a beaker. Temperature was maintained within the range of 333 ± 10 K by controlling the rate of heating. The solution was agitated by a magnetic stirrer to avoid dead zone inside the beaker. Dissolution time was observed visually and final solution was analysed for uranium concentration. After six hours of experimental run, the solution was allowed to cool to room temperature (~300 K) and the U(VI) concentration was analyzed by Davies-Gray method. The results are given in Table 1.

Parametric dissolution study

Three different solvate compositions were investigated for evaluating the dissolution performance in nearly identical operating conditions. The assumed composition was $TBP(HNO_3)_x(H_2O)_y$. The current study correlates the dependency of dissolution and rate constant with the complex composition as the solubility of the complex varies with x and y.

Table 1: Details of a gram-level experiment

Parameter	Value
Initial aqueous acidity	15.5 M
Organic to aqueous phase ratio	1
Equilibrated organic acidity	4.63 M
Weight of UO_2	0.9152 g
Organic U(VI) concentration	50.745 g/l
Uranium recovery*	94.4%
*Assuming pellet assay as 100% UO_2	

It was concluded that UO_2 pellet can be efficiently dissolved and *in-situ* extracted by a complex formed by saturation of 100% TBP with 15.5 M nitric acid as shown in Table 2. The dissolution rates as well as total dissolution were found to be a strong function of solvate composition. For effective dissolution, there were requirements of a minimum organic acidity and a minimum amount of water, dissolved in organic phase. For intact UO_2 pellet (weighing about ~15 g), nearly complete dissolution by organic adduct at atmospheric pressure in a reasonable time was observed when these constraints were met. This process for direct dissolution of UO_2 in $TBP(HNO_3)_x(H_2O)_y$ complex does not require supercritical pressures. Further studies in this regard are in progress.

Table 2: Experimental results and related data for direct dissolution and in-situ extraction by different $TBP.(HNO_3)_x.(H_2O)_y$ complexes at T= 333-343 K and P=1 bar (Case I: Organic Solvate Composition 1, Case II: Organic Solvate Composition 2 and Case III: Organic Solvate Composition 3)

Attribute	Case I	Case II	Case III
Initial nitric acid concentration for equilibration (M)	8	15.5	15.5
A/O ratio during equilibration	1	0.4	1
Organic acidity (M)	2.64	3.20	4.63
Initial weight of UO_2 pellet (g)	17.6200	13.3737	15.8329
Total time of dissolution (hours)	74	101	10
Final solution volume (ml)	310	116	150
Conc. of uranium in solution (g/l)	19.654	51.982	92.122
Density of solution at 298.15 K (g/ml)	1.0725	1.0974	1.1755
% Dissolution	39.2	51.2	99.0
Solvate composition* $TBP.(HNO_3)_x(H_2O)_y$	x= 0.72 ; y= 0.38	x= 0.88 ; y= 0.30	x= 1.27 ; y= 0.27
Rate Constant (min^{-1})	0.0058	0.0069	0.3768
*Water content estimated by gravimetric analysis			

IV.8 Separation of U(VI) and Pu(IV) from Trivalent Lanthanides and Americium using Tri-isoamyl Phosphate

Tri-isoamyl phosphate (TiAP) has received considerable attention in the recent past as an alternate extractant to tri-n-butyl phosphate (TBP) for fast reactor fuel reprocessing applications. Counter-current solvent extraction runs have been carried out under various conditions to develop a suitable flow sheet for fast reactor fuel reprocessing using 1.1 M TiAP/ heavy normal paraffin (HNP) as the solvent. In the current study, the solvent used in the earlier runs has been recycled to perform continuous mixer-settler runs for the demonstration of the bulk separation of U(VI) and Pu(IV) from Am(III) and trivalent lanthanides such as La(III), Pr(III), Nd(III), Sm(III) and Eu(III) as fission product representatives.

A solution containing ~30 g/l of plutonium, ~70 g/l of uranium, ~0.53 mg/ml of Am(III) and ~1.6 mg/ml of lanthanides in 4 M HNO_3 was used as the aqueous feed. TiAP based spent solvent (1.1 M in HNP) was regenerated by washing with 5 M NaOH solution followed by water wash. The mixer-settler used for this study was a 16-stage equipment with a hold up volume of ~640 ml (Figure 1). An amplitude of 100-150 mm in the pulse probe (id=6 mm) at frequency of 30 cycles/min were maintained in all runs. The outlet organic and aqueous streams were collected from 1st and 16th settlers, respectively. The organic and aqueous stage samples were collected from settlers after the attainment of steady state in all the runs. Stage samples were analyzed for nitric acid and metal ions by using suitable analytical methods.

Fig. 1 *Mixer-settler used for flow sheet development study*

The flow sheet scheme adopted for the separation is shown in Figure 2. The first run comprising

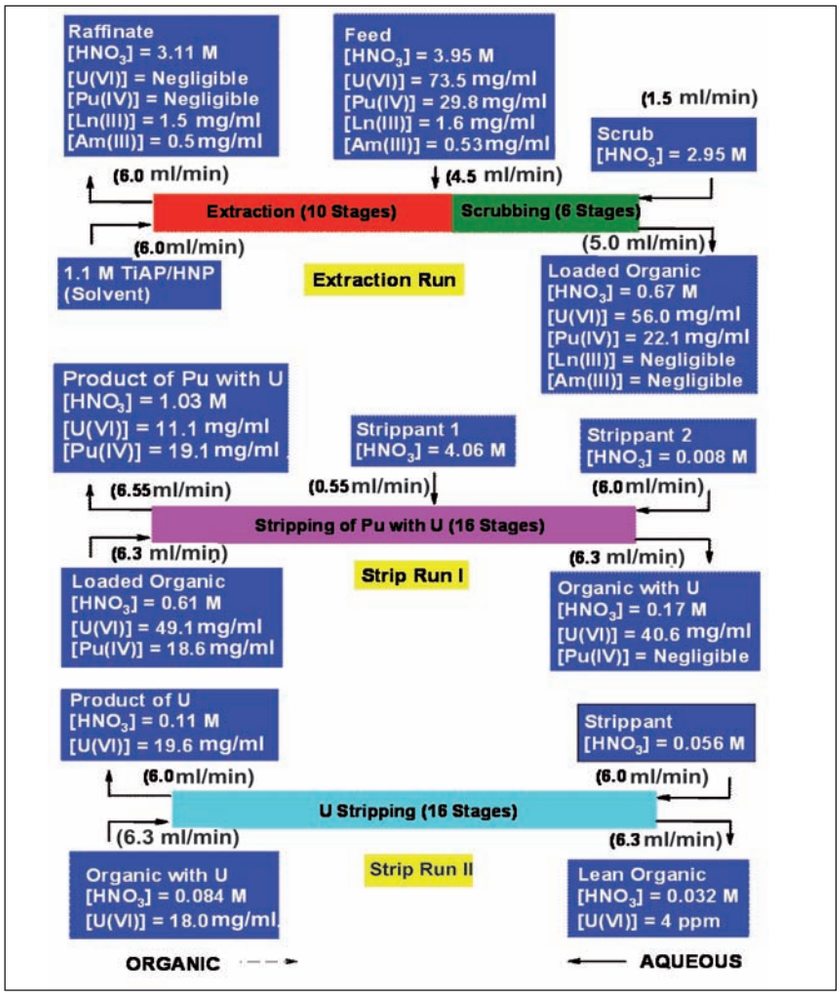

Fig. 2 *Flow sheet (Outlet samples: The steady state samples; Inlet loaded organic streams in strip runs: The solutions collected from the beginning to the end of the respective previous run)*

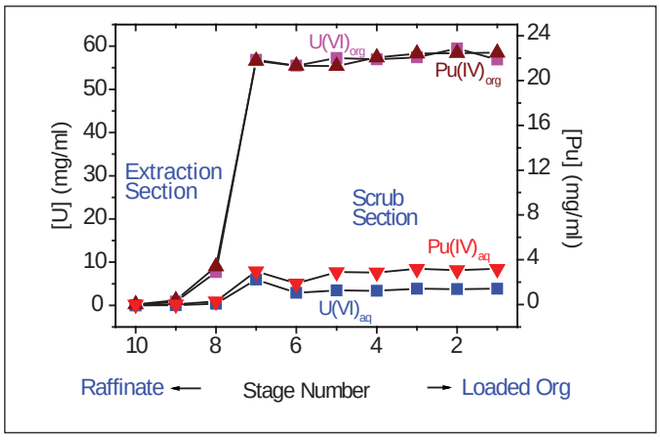

***Fig. 3** Stage profiles for the extraction of U(VI) and Pu(IV)in the extraction run*

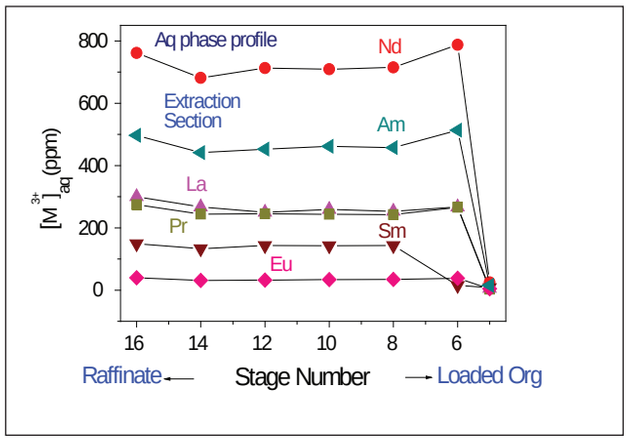

***Fig. 4** Stage profiles for Ln(III) and Am(III) in aqueous phase in the extraction run*

ten stages for extraction and six stages for scrubbing was performed for the separation of U(VI) and Pu(IV) from Ln(III) and Am(III). The other two were runs for stripping of the extracted metal ions from loaded organic phase. The stage profile data shown in Figure 3 indicate that only 3-4 stages are required for the extraction of U(VI) and Pu(IV) with negligible loss of heavy metals into raffinate. The concentration of Am(III) and lanthanides in loaded organic phase was below the detection limit. The stage profiles for Ln(III) and Am(III) in aqueous phase for the extraction run are shown in Figure 4. Results indicate that concentration of Ln(III) and Am(III) in the aqueous phase at various stages of the extraction section is comparable which in turn indicates that Ln(III) and Am(III) are not extracted by TiAP and the Ln(III) and Am(III) from 5th stage to 1st stage in the scrub section is negligible.

Subsequently, the extracted heavy metals were transferred from the organic phase to aqueous phase by carrying out Strip Run-I and Strip Run-II. The stage profile data shown in Figure 5 for Strip Run-I indicate that entire amount of Pu(IV) along with a fraction of U(VI) was stripped from the loaded organic with 4M and 0.01M HNO_3 solutions. The remaining fraction of U(VI) retained in the organic outlet stream of the Strip Run-I was stripped by Strip Run-II with a negligible loss of U(VI) in the lean organic stream (4 ppm) using 0.056 M HNO_3 as the strippant. Stage profile data for Strip Run-II are shown in Figure 6. In general, reasonably good trend for the distribution of nitric acid and metal ions in the organic and aqueous phases as well as excellent mass balance were obtained in all runs. Results indicate that high fission product decontamination factors can be achieved in fast reactor fuel reprocessing with 1.1 M TiAP/HNP as the solvent which can also be recycled. However, additional experiments with irradiated TiAP based solvent and U-Pu feed solutions spiked with dissolver solution of spent fuel from FBTR are also planned before the actual testing of TiAP in the reprocessing plants.

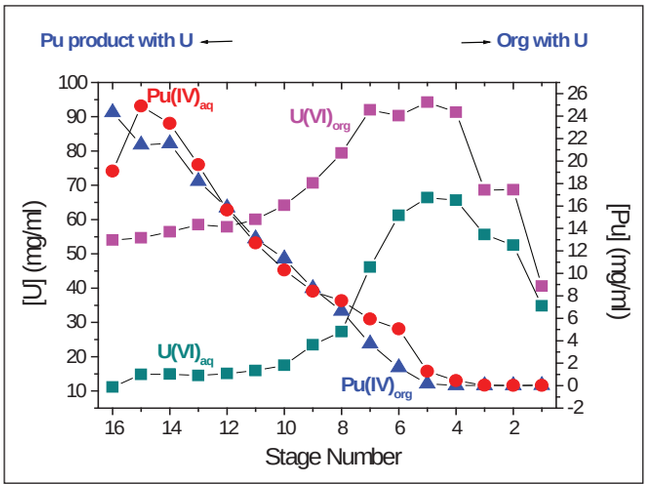

***Fig. 5** Stage profiles for U(VI) and Pu(IV) in the Strip Run-I*

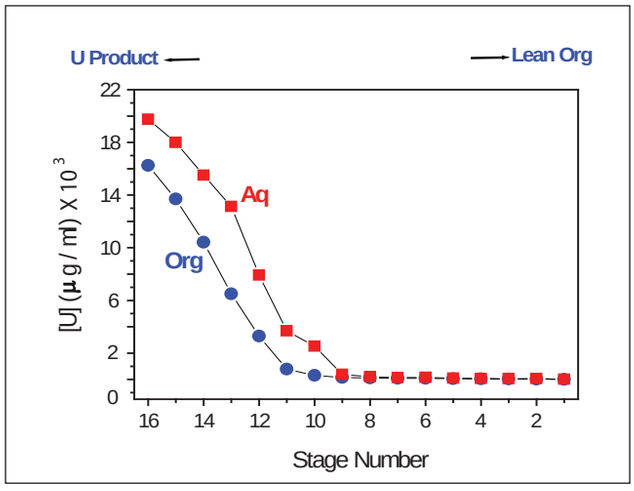

***Fig. 6** Stage profiles for U(VI) in Strip Run-II*

IV.9 Separation of Ruthenium from Simulated High Level Liquid Waste by Electro-oxidation

High level liquid waste comprising of the fission products in a solution of 4 molar nitric acid, is generated after the separation of uranium and plutonium from spent fuels of fast breeder reactors by solvent extraction. Ruthenium (Ru) is one of the troublesome fission products because of its relatively high abundance, long lived radiotoxic isotopes (^{103}Ru, $t_{1/2}$= 39.26 days and ^{106}Ru, $t_{1/2}$ = 373.59 days) and its existence in the oxidation states ranging from 0 to 8. Owing to the large number of complexes of Ru in HNO_3 medium as well as the high volatility of RuO_4, problems are encountered not only during the dissolution and solvent extraction but also in the treatment of high level liquid waste for disposal. In the nuclear waste management and disposal operations, Ru gets oxidized to highly volatile radiotoxic $^{103}RuO_4$ and $^{106}RuO_4$ which on contact with the cooler surface of the container decompose to a non-volatile black deposit of RuO_2, resulting in an increase in the radiation dose of the plant. Hence, it is desirable to separate Ru from the waste solution prior to waste processing. In the present study, Ru separation could be achieved by electro-oxidation of ruthenium nitrosyl nitrate, $Ru(NO)(NO_3)_3$ solution as well as from simulated high level liquid waste using cerium as the redox intermediate catalyst in divided as well as undivided cell configurations and the percentage level of separation of Ru was compared under different experimental conditions. Since Ce is one of the fission products, its use as the redox catalyst will neither call for any change in the vitrification process nor would add significantly to the waste volume as the quantities added are not high.

Standard solutions of $Ru(NO)(NO_3)_3$ containing 160 ppm of Ru (the concentration of Ru in high level liquid waste) in 1, 2 and 4 molar nitric acid were prepared by diluting the commercially available $Ru(NO)(NO_3)_3$ solution. Pt electroplated Ti mesh and Pt plated Ti gauze of surface area 150 and 20 cm^2 respectively were used as anode and cathode. 500 ml of $RuNO(NO_3)_3$ or simulated high level liquid waste solution prepared in 1, 2 or 4 molar HNO_3 was taken in the cell and electrolysis was performed with the anodic current density (J_A) of 10 or 20 mA/cm^2 at 313 K as well as at 333 K with and without cerous/ceric redox couple. The RuO_4 vapour generated due to the oxidation of Ru at the anode was trapped in a gas wash bottle containing 8M HNO_3. Concentration of Ru was determined by ICP-OES analysis.

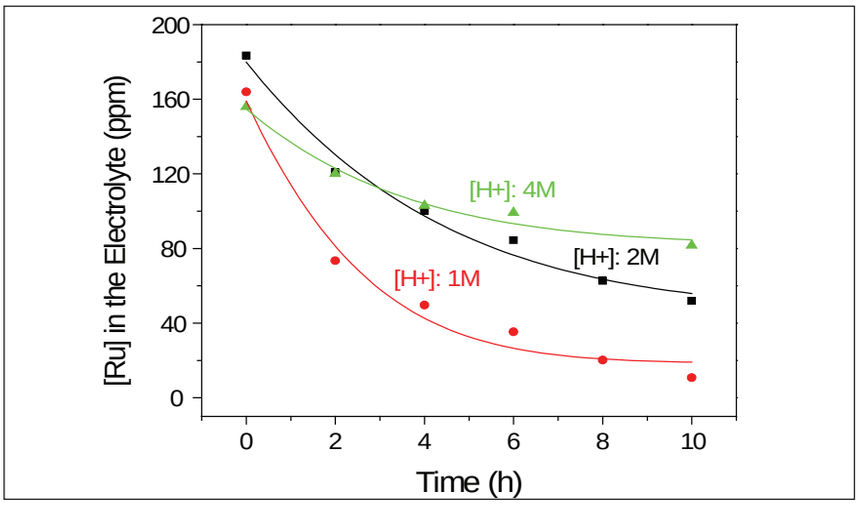

***Fig. 1** Dependence of acidity on the electro-oxidation of Ru from $Ru(NO)(NO_3)_3$ solution*

Effect of acidity on the separation of ruthenium

Preliminary experiments on the separation of Ru by electrolysing $RuNO(NO_3)_3$ solution in 4 molar HNO_3 at the J_A value of 10 mA/cm^2, without cerous ions and in the presence of 0.01 molar $Ce(NO_3)_3$ revealed the amount of Ru oxidized to be insignificant even at 333 K and after six hours of electrolysis, whereas substantial quantity of Ru could be separated in the presence of 0.02 and 0.04 molar $Ce(NO_3)_3$. Further, the RuO_4 vapour produced by electro-oxidation of Ru was observed to get deposited as black RuO_2(s) on the outer surface of the diaphragm tube and recovering Ru by trapping in 8 M HNO_3 could not be accomplished. Hence, subsequent separation experiments were carried out in undivided electrolytic cell in the presence of Ce. The percentage separation of Ru from $RuNO(NO_3)_3$ solution in 4 molar HNO_3 was determined to be only 24 and 36% after six hours of electrolysis in the presence of 0.04 M $Ce(NO_3)_3$ at the J_A values

10 and 20 mA/cm^2 respectively. Experiments conducted at lower acidities for longer duration at 308 and 318 K resulted in better separation yield and the results are shown in Figure 1. With 0.04 molar cerous ions, separation of Ru increased from 48 to 72 and to 93% when the nitric acid concentration was decreased from 4 to 2 and to 1 molar respectively after ten hours of electrolysis at a current density of 20 mA/cm^2. The decrease in the percentage separation of Ru with increase in acid concentration could be due to the formation of various ruthenium nitrosyl complexes at different acidities. It is reported that the higher concentration of nitrous acid at higher acidity replaces the weakly bound NO_3^- groups by the more nucleophilic NO_2^- groups. During electrolysis, HNO_3 is reduced to HNO_2 at the cathode and the proportion of HNO_2 to HNO_3 increases with increasing acidity, thereby increasing the proportion of nitrato-nitro complexes and the percentage of Ru(NO) mono nitro complex has its maximum concentration of 50% in 4 molar acid solution. As the nitrito complex is more stable, it is difficult to oxidize the metal to RuO_4.

Effect of concentration of cerous ions, current density and temperature

As evidenced from Figure 2, the separation of Ru increased with increase in J_A and temperature when electro-oxidation was carried out for 10 hours. The various experimental conditions and the percentage separation of Ru from $RuNO(NO_3)_3$ solution of acidity 1 molar are listed in Table 1. It is observed that the separation of Ru increased from 81 to 93% by increasing J_A from 10 to 20 mA/cm^2 and temperature from 313 to 318 K, in the presence of 0.04 molar cerous nitrate. Nevertheless, the same amount of Ru could be separated with 0.02 molar Ce also under identical experimental conditions. Maximum separation could also be accomplished with a lower concentration of Ce and J_A by conducting electro-oxidation at slightly higher temperatures.

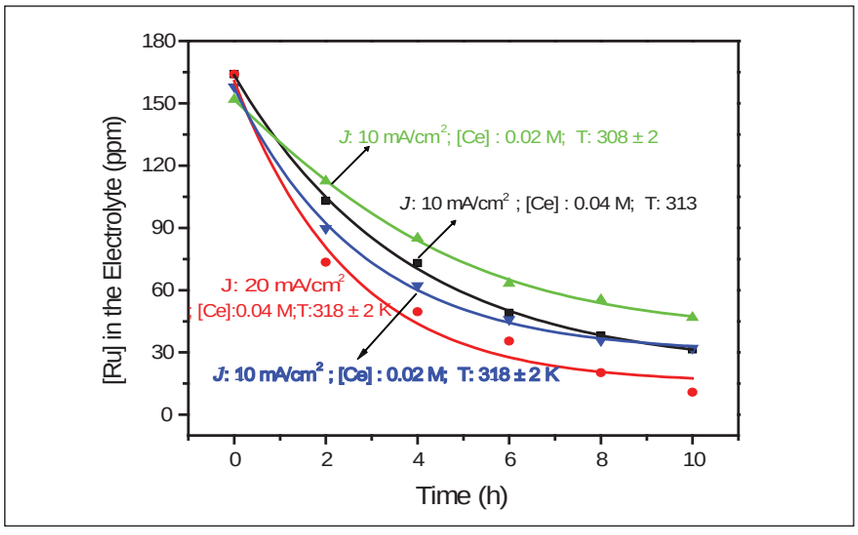

***Fig. 2** Influence of the concentration of Ce, J_A and temperature on the separation of Ru*

Separation of Ru from simulated high level liquid waste

Separation of Ru from simulated high level liquid waste in 4 and 1 molar acidity by electro-oxidation was conducted under various experimental conditions. Separation of about 21% only was possible after 10 hours of electrolysis from simulated high level liquid waste in 4 molar HNO_3 at the J_A value of 10 mA/cm^2 in the presence of 0.04 molar of Ce and this value increased to 47% when the acidity was reduced to 1 molar under the experimental conditions. Increasing J_A to 20 mA/cm^2 could enhance the separation of Ru from simulated high level liquid waste in 1 molar nitric acid to about 54% in the presence of 0.04 molar cerium at 318 K. Compared to the quantitative separation of 95% of Ru from $RuNO(NO_3)_3$ solution, the value of 54% obtained from the simulated liquid waste is very low. Since the noble metal palladium present in simulated high level liquid waste would have interfered in the electro-oxidation of Ru, the percentage separation was less. Apparently, the large amount of nitrite ions in the waste also could have contributed to the reduction in the percentage separation of Ru. To eliminate the interference of nitrite ions (produced at the cathode) in the oxidation reaction of Ru at the anode, a divided cell with glass frit as the diaphragm requires to be designed. As electro-oxidation method does not introduce corrosive metallic ions in the waste and as it is a simple and safe process, it can be adopted in the reprocessing plants for the removal of ruthenium.

Table 1: Percentage separation of Ru from $RuNO(NO_3)_3$ solution of acidity 1 molar

Current density (mA/cm^2)	Temp. (K) ± 2	[Ce] (M)	% Separation after 10 hours
10	313	0.04	81
20	318	0.04	93
10	308	0.02	69
10	318	0.02	80
20	318	0.02	95

IV.10 Development and Demonstration of Lanthanide-Actinide Separation from CMPO-raffinate

Partitioning and transmutation of minor actinides present in high-level liquid waste is considered as a viable method for the safe management of high-level liquid waste. Recently, a method for partitioning of minor actinides from fast reactor (FR) high-active waste (HAW) by using a solvent composed of 0.2 M n-octyl(phenyl)-N, N-diisobutylcarbamoylmethyl-phosphine oxide (CMPO)-1.2 M tri-n-butylphosphate (TBP) in n-dodecane (n-DD) was developed and subsequently demonstrated in a mixer-settler with FR-HAW (155 GWd/t). The trivalents were quantitatively extracted in six contacts and recovered back using a stripping formulation composed of 0.1 M citric acid and 0.1 M nitric acid. Therefore, the product obtained from the mixer-settler run was a solution of trivalent lanthanides and actinides present in 0.1 M citric acid medium. Consequently, this solution acts as a feed for mutual separation of lanthanides and actinides.

The separation of lanthanides(III) from actinides(III) or vice versa is a challenging task due to the similarity in chemical and extraction behaviour of 4f- and 5f- elements. Several methods based on phosphorous and amidic extractants have been proposed for the mutual separation of actinides and lanthanides. However, a method based on bis(2-ethylhexyl)diglycolamic acid (HDEHDGA) as extractant and diethylenetriamine pentaacetic acid (DTPA) as aqueous complexing agent for mutual separation was developed. The structure of HDEHDGA is shown in Figure 1.

The diglycolamic acid is an acid derivative of alkyl-3-oxapentane,

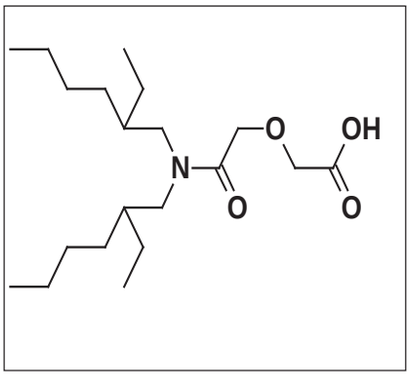

Fig. 1 *Structure of HDEHDGA*

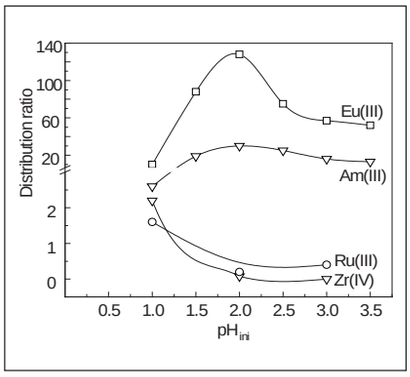

Fig. 2 *Variation in the distribution ratios of Eu(III), Am(III), Zr(IV) and Ru(III)*

emerging as a promising candidate for lanthanide-actinide (Ln-An) separation. Unlike the other reagents in-use, the diglycolamic acids are made up of CHON-atoms and they are completely miscible with n-dodecane.

The extraction behavior of Am(III) and Eu(III) in a solution of 0.1 M HDEHDGA/n-DD as a function of pH was studied from an aqueous phase containing 0.1 M citric acid spiked with ^{241}Am(III) or $^{(152+154)}$Eu(III) tracer. The results are shown in Figure 2. It is observed that the distribution ratios of Eu(III) and Am(III) increases with increase of pH, reach a maximum value at pH 2, followed by decrease in distribution values. The extraction of Eu(III) is always higher than Am(III) at all pH values, which is characteristic to the diglycolamides and diglycolamic acid extractants. It is also observed that the distribution ratio of ^{106}Ru(III) and ^{95}Zr(IV) are quite low and they decrease with increase of pH.

The conditions needed for the selective stripping of Am(III) from the loaded organic medium were optimized using citric acid and pH. The experiments involved equilibration of loaded organic phase (containing Eu(III) and Am(III)) with aqueous solution containing 0.01 M DTPA and citric acid at pH 3. This procedure was repeated until Am(III) was completely stripped to aqueous phase. The results indicated that the number of contacts needed for stripping of Am(III) and Eu(III) decreased with increasing concentration of citric acid. At 0.025 M citric acid concentration, Am(III) was recovered quantitatively in seven contacts. However, this was accompanied by 63% stripping of Eu(III). To minimize the stripping of Eu(III), the pH of the aqueous phase was decreased from pH 3 at a constant citric acid and DTPA concentration of 0.025 and 0.01 M respectively. Studies indicated that Am(III) could be back extracted quantitatively from the loaded organic phase with negligible contamination of Eu(III) using the aqueous solution composed of 0.01 M DTPA-0.025 M citric acid at a pH of 1.5. Therefore, a stripping formulation composed of 0.01 M DTPA-0.025 M citric acid at pH 1.5 was proposed for the back-extraction of Am(III) from the loaded organic phase, 0.1 M HDEHDGA/n-DD, in a mixer-settler run.

Mixer-settler studies with simulated waste

Based on the optimized conditions indicated above for extraction and stripping, a counter-current run was performed using a 20-stage ejector mixer-settler. In this study, the radioactive tracers $^{(152+154)}$Eu(III) and ^{241}Am(III) were used as lanthanide and actinide representatives respectively. The summary of the results is as follows: the Eu(III) exhibiting higher distribution ratio than Am(III) was extracted quantitatively in two stages. Complete extraction of Am(III) is achieved in ~3-4 stages. The radioactivity remaining in the raffinate was determined to be negligible. The loaded organic phase was collected and stripping of Am(III) from the organic phase was performed using 0.01M DTPA-0.025 M citric acid at pH 1.5. Stage sample analysis revealed that the quantity of Am(III) remaining in the organic phase decreased with increase in number of stages. After twenty stages of stripping, only 4% of Am(III) was retained in organic phase, indicating the recovery of Am(III) into aqueous phase was 96%. About 98% of Eu(III) was retained in the organic phase in all stages of the mixer-settler and only ~2% of Eu(III) was stripped to aqueous phase after twenty stages. The measurement of radioactivity of Am(III) and Eu(III) in lean organic and aqueous product also confirmed that the contamination of Eu(III) in Am(III) product was less than 2%, whereas the contamination of Am(III) in the organic phase was ~4%.

Ln-An separation with real-waste (CMPO raffinate obtained from minor actinide partitioning run)

The typical composition of a CMPO raffinate obtained after minor actinide partitioning of high active waste (155 GWd/t) is shown in Table 1. For batch and mixer-settler studies, the radioactive isotopes ^{154}Eu(III) (1274 keV) and ^{241}Am(III) (alpha active) were used as lanthanide and actinide representatives respectively, for assay. Initially, the batch experiments were performed with the real waste. The experiments involved extraction of lanthanides and actinides in a solution of 0.1 M HDEHDGA in n-DD and stripping using 0.01 M DTPA + 0.025 M citric acid at pH of 1.5. The extraction results confirmed that >99% of Am(III) and Ln(III) were extracted in to organic phase and about 90% Am(III) alone was recovered in to aqueous phase within 10-12 contacts during stripping.

Based on the above results, lanthanide-actinide separation was performed using a 16-stage mixer-settler installed in hot-cell (Figure 3). The feed solution was the aqueous product obtained after minor actinide partitioning. This solution was directly fed in to a mixer-settler for extraction. The extraction of Am(III) and Eu(III) in 0.1 M HDEHDGA/n-DD was quantitative in 1-2 stages. The extraction of ruthenium was negligible. The organic phase was collected and subjected to stripping using 0.01 DTPA + 0.025 M citric acid at pH 1.5. After the run, analysis of organic phase showed the presence of about 95% of lanthanides (based on Eu(III) analysis) and about 25-30% of Am(III). Similarly the analysis of aqueous phase showed the presence of about 70-75% Am(III) with <5% Ln(III). These results are in-line with simulated studies described above using 20-stage mixer-settler. Lower separation (~70%) achieved with actual waste could be attributed to the employment of 16-stage mixer settler in hot cell, as compared to a 20-stage mixer settler for simulated studies. Nevertheless, our results with simulated and real wastes demonstrate the possibility of separating actinides from lanthanides using HDEHDGA. It is worthwhile to mention here that the studies were demonstrated for the first time with a CHON based ligand, soluble in the nuclear diluent, n-DD, for Ln-An separation and with real FBR waste.

Table 1: Radioactivity of some radionuclides present in the feed for lanthanide-actinide separation. pH of the solution measured to be 1.7

Radionuclide	Activity/ µCi/ml
^{154}Eu	10.0
^{144}Ce	14.0
^{241}Am	24.0
^{106}Ru	7.5

Fig. 3 *16-Stage mixer-settler for lanthanide-actinide separation in hot-cell*

IV.11 Electrorefining Studies on U-Zr Alloy and Plutonium

Chopping of U-6Zr allloy rods in T-91 tubes using single pin chopper and electrorefining of uranium-6 wt% zirconium alloy were carried out in the engineering scale inactive demonstration facility. The electrolyte salt which had been used in an earlier run of uranium electrorefining was used for this study. Initially, $CdCl_2$ and U^{4+} in the LiCl-KCl-UCl_3 electrolyte were reduced by equilibrating with uranium metal. The salt was analysed by cyclic voltammetric technique after equilibration of the salt with uranium metal and the absence of Cd^{2+} ions in the salt was confirmed. The electrorefiner crucible contained 5 kg of cadmium pool at the bottom of the cell, overlying ~13 kg of LiCl-KCl-5.5 wt% UCl_3 (Figure 1) electrolyte salt. U-Zr alloy in perforated basket as anode and 21/4 Cr-1Mo rod as cathode were used in electrorefining.

The cell was operated at 773 K. Provision was made to record cyclic voltammogram in the electrorefiner to monitor the ionic species during the course of electrorefining. The cathode and anode potentials of the electrorefiner were monitored independently using two reference electrodes (1 wt% AgCl (in LiCl-KCl)/Ag) - one placed close to the anode and the other close to the cathode. Electrorefining was carried out in galvanostatic mode. Current of 5-9 A was maintained between cathode and anode during various campaigns depending upon the amount of U-Zr alloy present at the anode basket. U-Zr alloy of 1006 grams was added in the anode basket in three lots. The potential between the cathode and reference electrode ranged between –1.5 to –1.6 V when sufficient amount of U-Zr was present in the anode basket. It was observed that the potential between the cathode and reference electrode shifted to less cathodic potential as and when the U-Zr alloy at the anode got depleted. Similarly the potential between anode and reference electrode ranged between –1.2 to –1 V and the potential shifted to more anodic potential as and when the U-Zr alloy at the anode got depleted. About 1184 grams uranium metal occluded with salt was recovered on the cathode (Figure 2). The occluded salt amounts to about 18% of the cathode deposit. About 343 A hours current was passed in all. Current efficiency of the process was calculated after deducting the weight of the salt in the cathode deposit and was found to be about 87%.

Fig. 1 *LiCl-KCl-UCl_3 electrolyte salt in crucible*

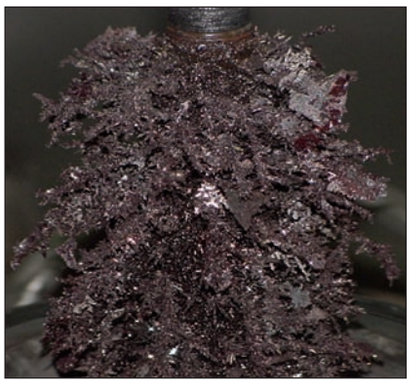

Fig. 2 *Uranium deposit on the solid cathode with occluded salt*

Cathode deposit obtained from each campaign of the U-Zr electrorefining run was heated in the graphite assembly at about 1000 K under vacuum to distill off the occluded salt. The deposit (Figure 3) was then melted in an induction furnace to consolidate the uranium metal ingot. Uranium metal ingot (Figure 4) of around 500 g was made by melting distilled cathode deposit from six campaigns.

The electrolyte salt was analysed for uranium, zirconium, cadmium and for impurities like Fe, Cr, Ni and Ag. Uranium was analysed by Davis and Gray method based on potentiometric titration. The results showed that the concentration of

Fig. 3 *Uranium deposit after distillation of salt*

Fig. 4 *Uranium metal ingot*

uranium in the electrolyte remained constant throughout the run and the concentration of UCl_3 in the electrolyte was 5.5 wt%. Zirconium was estimated without extracting uranium by ICP-MS. The amount of zirconium in the salt was < 0.01%. However, zirconium was found to get deposited along with uranium in some campaigns where the amount of U-Zr alloy in the anode basket was less. Cd, Fe, Cr, Ni and Ag in the electrolyte were analysed by atomic absorption spectrometer. The impurities were < 0.001% in the salt.

The separation factor for zirconium with respect to uranium in the uranium deposit at the cathode was found to vary in different U-Zr electrorefining campaigns. For the first six campaigns the separation factor ranged between 1000-4000 and for campaigns 8-10 the separation factor was 4-8.

Studies on electrorefining of plutonium

The electrorefining of plutonium was carried out in an inert atmosphere active glove box to determine the separation factors of La and Ce with respect to the electrodeposited plutonium. The LiCl-KCl eutectic was initially equilibrated with about 10 gram of plutonium metal at 773 K for four hours under stirring conditions. The salt (Figure 5) was sampled for measuring the concentration of plutonium. Consequently, about 300 and 150 mg of Ce and La respectively were added in the anode basket and equilibrated for four hours at 773 K.

Fig. 5 *$PuCl_3$-LiCl-KCl salt*

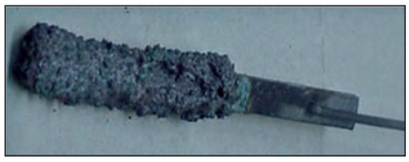

Fig. 6 *Plutonium deposit with occluded salt on tantalum sheet*

The salt was sampled for estimation of La and Ce prior to electrorefining of plutonium. The concentration of lanthanum and cerium in the melt before and after electrorefining was determined by HPLC. There was no change in the concentration of La and Ce in the salt samples before and after electrorefining experiments.

The electrorefining of plutonium was carried out at 773 K in constant current mode for about six hours on a tantalum sheet. The plutonium electro deposit (Figure 6) with occluded salt cover was subsequently taken in an alumina crucible and melted at 1053 K for two hours. A few globules of plutonium metal (Figure 7) were obtained after breaking the salt cover.

Plutonium metal sample was dissolved in concentrated HCl and evaporated to near dryness. An aliquot was re-dissolved in HIBA medium and injected into HPLC for the detection of lanthanides.

Electrochemical behaviour of Pu(III) was studied at 748-823 K in LiCl-KCl eutectic by using the transient electrochemical methods: cyclic voltammetry (CV) (Figure 8) chronopotentiometry (CP) (Figure 9) and impedance spectroscopy.

All the electrochemical experiments were carried out with tantalum rod and sheet as working electrode, high density graphite rod as a counter and Ag/AgCl as reference electrode. The results showed that reduction of Pu(III)/Pu occurs via a single step three electron transfer quasi-reversible process. The reduction potential for Pu(III)/Pu(0) redox couple at 773 K in LiCl-KCl eutectic has been determined with reference to Ag/AgCl electrode. Diffusion coefficients calculated from CV and CP methods are found to be in the range of 10^{-5}. The values are in agreement with that reported in literature. Heterogeneous rate constant (K_s) for Pu(III)/plutonium process as calculated and Matsuda-Ayabe criteria was applied to interpret the reduction process.

Fig. 7 *Plutonium metal globules*

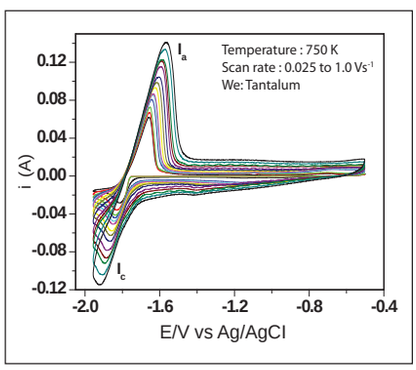

Fig. 8 *Cyclic voltammogram of $PuCl_3$ in LiCl-KCl. Conc. of $PuCl_3$: 2.25 x 10^{-4} mol. cm^{-3}*

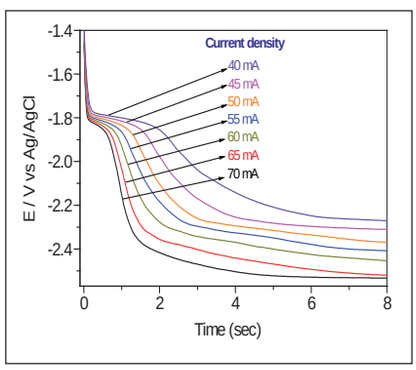

Fig. 9 *Chronopotentiogram of $PuCl_3$ in LiCl-KCl at various current densities at T=773 K; Conc. of $PuCl_3$: 2.25 x 10^{-4} mol. cm^{-3}*

IV.12 Studies on Dissimilar Joints of Ti-Ta-Nb Alloy and Zircaloy-4 with SS 304 for Reprocessing Applications

The materials selection for FBR spent fuel reprocessing plants is based on their corrosion resistance in boiling concentrated HNO_3. Ti-5Ta-1.8Nb alloy (Ti-Ta-Nb) and Zircaloy-4 (Zr-4) are candidate materials for the electrolytic dissolvers. Propensity for formation of brittle and corroding intermetallics at the weld interface prohibits the use of fusion welding process for joining Ti-Ta-Nb or Zr-4 with 304L austenitic stainless steel (SS), the structural material for the remaining plant. Hence, Ti-Ta-Nb and Zr-4 have been joined with 304L SS by explosive cladding, a solid state welding process and their performance assessed.

Dissimilar joint Ti-Ta-Nb/304L SS

The joint between Ti-Ta-Nb and stainless steel showed a wavy interface with few shrinkage cavities and pockets of molten and solidified metal. Overall increase in the hardness of the weld was observed with a high hardness of ~400 VHN very near the interface on stainless steel side of the joint. Intermetallic phases could not be detected within the resolution limit of EPMA and XRD. Formation of metastable fcc phase in Ti-Ta-Nb clad and martensite in stainless steel base plate, indicated deformation-induced phase transformation due to high impact collision during explosive cladding.

Explosive clads passed ultrasonic test revealing debonding only towards the edges of the plates. To quantify the bond strength of explosive clads, tensile, bend and shear tests were carried out. Bend angle in the longitudinal direction was 110º whereas only 5º was obtained in the transverse direction. Shear strength of the clad was in the range 293-450 MPa.

Further, corrosion resistance of the explosive clads was assessed in vapour, liquid and condensate phases of 11.5 M boiling HNO_3. Corrosion in both vapour and condensate was found to be <1 mpy whereas in liquid it was ~3 mpy. Higher corrosion rate in liquid phase was understood from severe intergranular corrosion of stainless steel (Figure 1). Formation of reaction zones and intermetallic phases at the interface during heat treatment at 873-1073 K established that stress relieving should be carried out at temperatures < 873 K.

Dissimilar joint Zr-4/304L SS

In any dissimilar joint, corrosion activity is maximum at the interface. Monitoring such activity in micro scale helps in identifying corroding sites, eliminating them during the development of dissimilar joints. Scanning electro-chemical microscopy, a powerful technique for obtaining spatially resolved electrochemical activity information from surfaces at micrometer scale was employed to study Zr-4/304L SS joint in HNO_3.

Figure 2a shows Zr-4/304L SS explosive clad interface exhibiting a wavy pattern, a characteristic feature of explosive clads. Local rise in temperature at the interface due to the severe plastic work and shock wave, favoured the formation of $Fe_{75}Zr_{20}Cr_5$ type intermetallics.

Figure 2b shows the scanning electro-chemical microscopy tip approach curves obtained on both 304L SS and Zr-4. Current and the

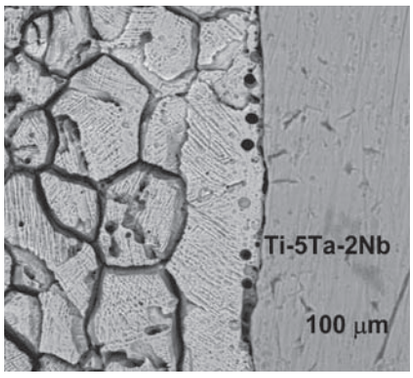

***Fig. 1** Microstructure of the explosive clad exposed to liquid phase of HNO_3*

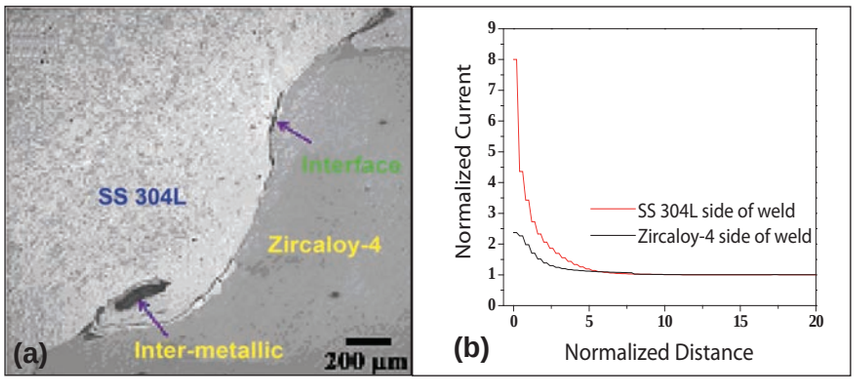

***Fig. 2** (a) SEM micrograph of Zr-4/304L SS explosive weld (b)* Scanning electro-chemical microscopy *tip approach curve on 304L SS and Zr-4 side of the weld in 11.5 M HNO–*

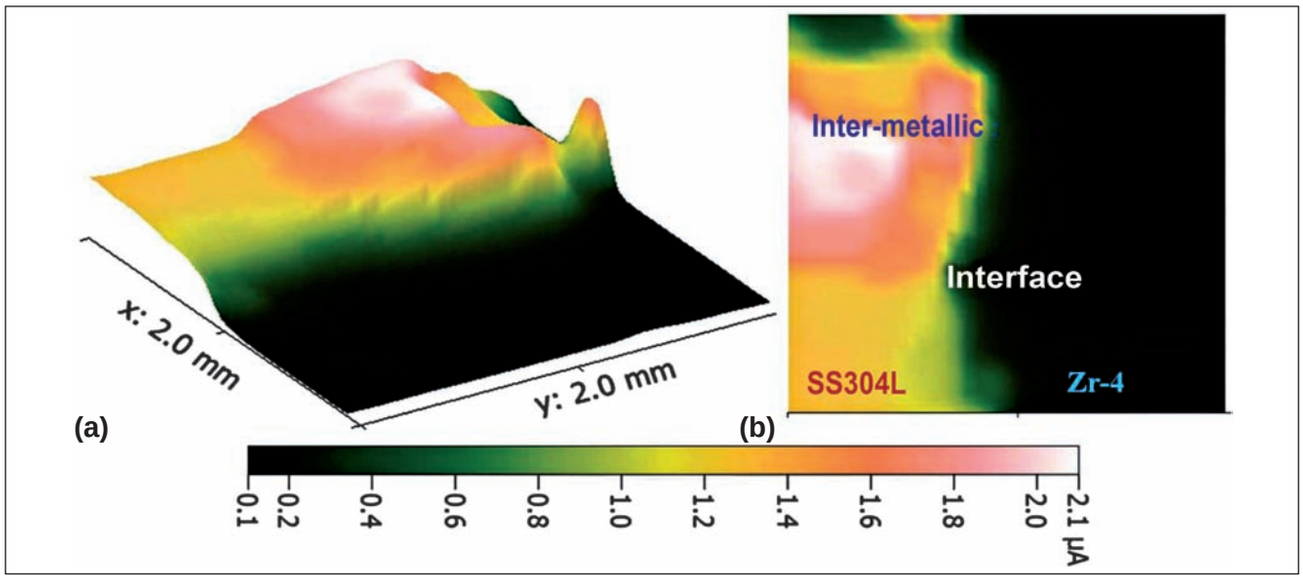

Fig. 3 *(a) 3D and (b) 2D images revealing EC activity in Zr-4/304L SS weld*

distance were normalized by the limiting tip current (when tip was far away from substrate) and tip diameter respectively. As scanning electro-chemical microscopy tip approached the substrate, an increase in tip current was noticed for both 304L SS and Zr-4 indicating positive feedback. Near the substrate, in the tip-substrate gap, nitrous acid reacts with the dissolved oxygen to yield nitric acid ($2HNO_2 + O_2 \rightarrow 2HNO_3$) facilitating electron transfer reaction. However, higher current observed on 304L SS side indicated higher electrochemical activity.

In concentrated HNO_3, it is known that 304L SS is in active state. Corrosion products from 304L SS such as Fe(III) ions catalyze reduction reaction of nitric acid to form higher concentration of nitrous acid. Thus, more electron transfer reaction takes place which leads to higher tip current for 304L SS. In contrast, in Zr-4, catalyzing the reduction reaction of nitric acid is not feasible due to the formation of stable ZrO_2 passive film.

Figures 3a and 3b are three and two dimensional scanning electro-chemical microscopy maps revealing electrochemical activity in Zr-4/304L SS dissimilar weld. It was observed from the figures that the tip monitored high current 'i' value of 1.2-1.6 µA corresponding to 304L SS (shown as yellow colour). When the tip encountered Zr-4 region (dark green colour), the tip 'i' rapidly decreased to 0.1-0.2 µA indicating that Zr-4 was in passive state. An intermediate activity was observed at the interface region as shown in light green colour with the 'i' value of 0.4-0.8 µA. In Figure 3b, a distinct higher activity region is revealed in orange-white colour with 'i' value of 1.8-2.1 µA. This higher surface reactivity is attributed to preferential dissolution of intermetallic phases and active corrosion at the weld interface.

While conventional electrochemical activity techniques will average the electrochemical activities masking contribution from local corrosion phenomena, scanning electro-chemical microscopy maps are found to be effective in revealing active and passive behaviour of 304L SS and Zr-4 in dissimilar welds.

IV.13 Corrosion Behaviour of Container and Electrode Materials for Pyrochemical Reprocessing Exposed to Molten LiCl-KCl Salt

Spent metallic fuel from future fast breeder reactors will be reprocessed through pyrochemical route involving eutectic mixture of LiCl-KCl molten salt medium. Low and high density graphite, glassy carbon and pyrolytic graphite are candidate materials for containers and electrodes in pyrochemical

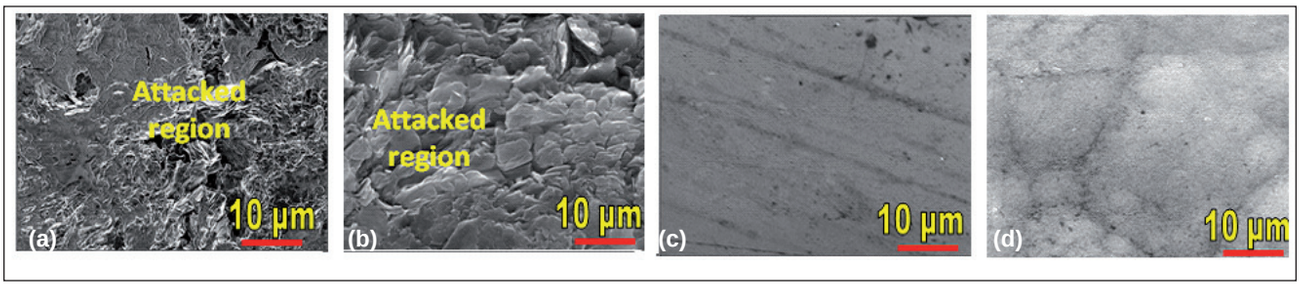

Fig. 1 *SEM micrographs of corrosion tested carbon allotropes in LiCl-KCl salt at 873 K for 2000 hours (a)* Low density graphite *(b)* High density graphite*(c) GC (d)* Pyrolytic graphite

reprocessing, mainly due to the ease in fabricability, mechanical integrity at high temperatures, thermal shock resistance and high inertness towards chlorine. Thus, it is important to understand the interaction of these container and electrode materials with molten salt at high temperatures.

Corrosion behaviour of the above mentioned graphite and carbon materials in molten LiCl-KCl electrolyte medium at 873 K for 2000 hours under ultra high purity argon atmosphere was investigated. The structural and microstructural changes after exposure to molten chloride salt were investigated by weight change, scanning electron microscopy, atomic force microscopy, X-ray diffraction and Laser Raman spectroscopy. Visual examination after 2000 hours of exposure to LiCl-KCl salt revealed the formation of pores and uniform attack on the surfaces of low and high density graphites. The shiny and mirror like appearance of as-received Glassy carbon was lost after corrosion test; however, the surface was observed to retain its non-porous nature. The corrosion tested pyrolytic graphite surface appeared the same as that of as-received pyrolytic graphite. Glassy carbon and pyrolytic graphite showed insignificant weight loss whereas low density graphite and high density graphite gained weight of about 0.188 and 0.034% respectively after exposure to LiCl-KCl salt. This indicates that molten salt can easily penetrate into the pores of low and high density graphite compared to glassy carbon and pyrolytic graphite. The surface morphology of corrosion tested low density graphite, high density graphite, glassy carbon and pyrolytic graphite are shown in Figures 1a to 1d respectively. The microstructure of as-received low density and high density graphite revealed pores, defects and small cracks, through which the molten salt could have penetrated into the interior, causing either loss of material or absorption of salt (Figures 1a and 1b). As-received glassy carbon surface exhibited a columnar morphology which on exposure to LiCl-KCl salt changed to smooth surface (Figure 1c) and the corrosion attack was insignificant. The density of glassy carbon was quite low since it contained small (a few nm) closed pores. The salt particles could not penetrate into glassy carbon owing to the absence of open porosity. Pyrolytic graphite immersed in molten LiCl-KCl salt for 2000 hours did not show any evidence of degradation and attack (Figure 1d). As pyrolytic graphite is prepared by the thick deposition of carbon on graphite substrate by cracking hydrocarbons at temperatures above 2200 K, the material becomes dense and devoid of pores and impurity elements like hydrogen in its structure, which led to lower corrosion rate than glassy carbon, high and low density graphite. The results indicate that the penetration of molten salt into carbon materials can be prevented by using impermeable graphite grades like glassy carbon and pyrolytic graphite. The degradation of graphite depends on the degree of structural disorder, surface uniformity, preparation method and density of the material.

The atomic force microscopy (AFM) studies revealed that the difference in surface roughness values before and after corrosion test was maximum for low density graphite and minimum in the case of pyrolytic graphite sample. The deposition of salt particles on the surfaces of low and high density graphite resulted in more roughness. XRD data did not show any phase change and formation of new compound after the corrosion test. Raman studies confirmed slight increase in disorder induced by molten salt, in the carbon materials. The integrated intensity (ID/IG) and bandwidth were higher for low density graphite than that for other graphite/carbon materials, indicating higher disorder in low density graphite. The corrosion results obtained from this study showed that the resistance of graphite materials to molten LiCl-KCl salt under ultra high purity argon atmosphere is in the order, pyrolytic graphite greater than glassy carbon greater than high density graphite which is greater than low density graphite.

IV.14 Corrosion Behaviour of Mock-up Zircaloy Dissolver

For qualifying Zircaloy-4 as a candidate material for dissolver in the aqueous processing of spent fuels of Fast Breeder Reactors in future reprocessing plants, long term corrosion testing of thermo-siphon based mock-up Zircaloy dissolver vessel using simulated dissolver solution was initiated. To reduce the acid makeup, the dissolver off-gas line was connected to a vent-pot through a down draft condenser. To maintain negative pressure of around 3" water column, an air ejector was provided. Heating pad was wound over the right limb of the dissolver and temperature at liquid and vapour phase is measured using mineral insulated 'T' type thermocouples. A PID controller was provided for controlling the process liquid temperature at 383 K. Liquid level, density and pressure inside the dissolver are monitored using air purge method. Back pressure is measured using smart differential pressure transmitters. The picture of the dissolver is shown in Figure 1. Calculated quantities of metal oxides or nitrates to simulate the concentration of dissolver solution corresponding to the composition of fission products and corrosion products envisaged in FBTR Mark-I fuel which had undergone a burn up of 150 GWd/t and after a cooling period of one year were dissolved in 11.5 M nitric acid and 13.5 l of this solution was used for the experiment. Vanadium salt was used to simulate plutonium ions.

Apart from qualifying Zircaloy-4 dissolver vessel, several other candidate materials (Table 1) are evaluated for their corrosion behaviour in the simulated dissolver environment. A PTFE(polytetrafluoroethylene) sample holder was designed and fabricated to accommodate the test coupons such that they are exposed to the vapour (358 K) and liquid phases (383 K) of the simulated dissolver solution. The corrosion rates were calculated based on the weight loss of the coupons after 100, 250 and 500 hours of operation. Corrosion rates in liquid and vapour phase for commercially pure (CP)-Ti, Ti-5Ta-1.8Nb, Zirconium-702 and Zircaloy-4 were insignificant, both in as-received and weld conditions. However, high corrosion rates were obtained for the dissimilar welds of SS 304L with CP-Ti and Zircaloy-4. Typical values calculated for the corrosion rate of CP-Ti + SS 304L dissimilar weld after 500 hours of exposure were 7.57 and 3.74 mm/y in the liquid and vapour phases respectively. After 500 hours testing, SEM investigations of the corrosion coupons revealed an un-affected surface morphology for CP-Ti, Ti-5Ta-1.8Nb, Zirconium-702 and Zircaloy-4 indicating the high corrosion resistance in dissolver environment due to the formation of corresponding protective passive film. The SEM images (Figure 2) confirmed that Zircaloy-4 shows no sign of corrosion damage while severe corrosion was observed along the interface and the SS 304L side of the dissimilar weld. Further testing up to 1000 hours is in progress. Long term corrosion data under plant simulated condition will be obtained through 10,000 hours of operation. The obtained data will be used to model and to predict the life time of Zircaloy component and the candidate materials.

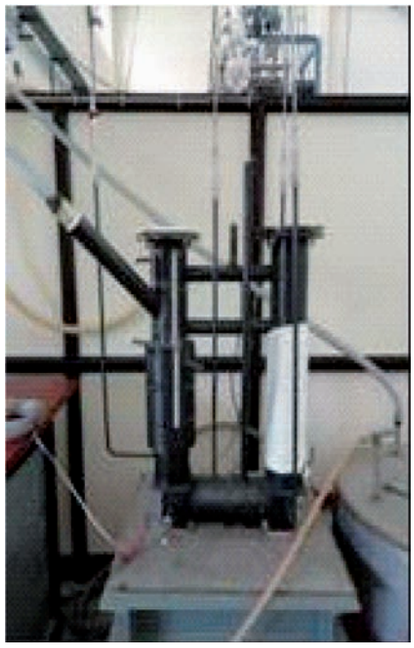

Fig. 1 *Zircaloy dissolver set up*

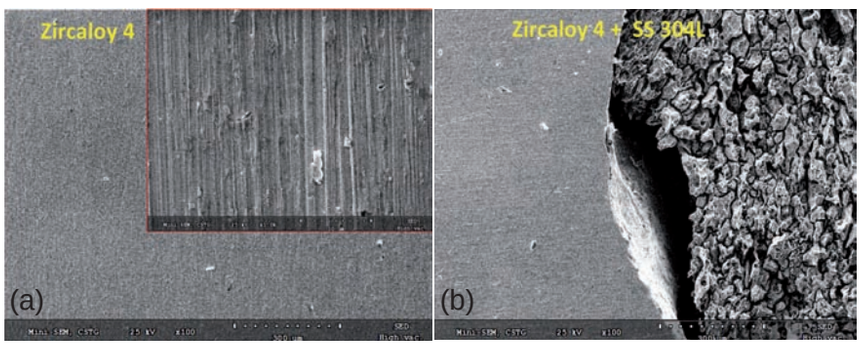

Fig. 2 *(a) Zircaloy-4 and (b) Dissimilar weld with SS 304L subjected to the liquid phase of the simulated dissolver solution for 500 hours*

IV.15 Development of Remote Handling and Inspection Tools for Reprocessing Facilities

Remote handling and in-service inspection (ISI) have become indispensible tools in the nuclear fuel reprocessing facilities. Periodic inspection is essential to monitor the health of critical equipment in fuel reprocessing plants. Customised remote handling tools enable the operation of critical activities in reprocessing plants. Some of the developments towards the remote handling and inspection tools for reprocessing plants are presented.

Three-axis scanner for in-service inspection of DFRP dissolver vessel

Dissolver vessel is a critical equipment, used for the dissolution of spent fuel in the Demonstration Fast Reactor Fuel Reprocessing Plant (DFRP). The hot limb of the dissolver vessel is subjected to corrosion-induced degradation due to nitric acid environment and hence, periodic inspection is essential. Design and development of a prototype three-axis scanner has been taken up for the remote in-service inspection of dissolver of DFRP. Experience garnered from the development of in-service inspection device for the inspection of CORAL dissolver has been effectively used for this purpose.

The dissolver essentially consists of three cylindrical limbs, about 1.5 metres high, with branched connectors stemming out at various points. The cylindrical limbs are the annular tank (A), hot limb (B) and cold limb (electrolyser-C) as shown in Figure 1. Both the hot and cold limbs are to be inspected periodically using visual and ultrasonic NDE(non destructive examination) techniques. The dissolver is located in the cell as shown in Figure 2.

In order to perform testing and validation of the scanner, a mock-up dissolver vessel in SS 304L was fabricated. The internal diameter of the vessel is Ø102 mm with flange of diameter Ø122 mm at the top. The thickness of the vessel is 10 mm. Though the dissolver is located within the work-envelope of the master-slave manipulator and the in-cell crane, lack of in-service inspection-specific ports dictated that the device should be permanently positioned inside the cell. Moreover, a conceptually apt design should allow the inspection gadget to be separated from the main in-service inspection device for storage within a lead-shielded chamber inside the dissolver cell.

The geometry and arrangement of the dissolver naturally gave rise to the design of the gadget with the capability of covering a cylindrical work-space. Considering the operation under remote conditions, the device is designed with three major degrees of freedom-along the three-axis for scanning the inner surface of the vessel.

In this three-axis scanner, the primary motion along the length of the vessel (Z-axis) provides the measurements at various depths. A chain and sprocket mechanism driven by an AC servo motor lowers a helical pulley block along the 'Z' axis in a rectilinear manner. This makes it capable of covering a distance of 1550 mm along this direction. A spin along the 'Z' axis provides the azimuth rotation (θ) enabling the NDE probe to cover the full circumference at a particular depth. This motion, with a full range of 360º, is actuated by an AC servo motor with a wire rope on a capstan pulley. A similar AC servo motor actuates the probe elevation (α) providing the tilt to the NDE probe in the vertical plane, with a range of ±90º. The motors have been kept away on the vessel top and modularity has been incorporated in the design by separating the drive and motor for the 'Z' axis.

The position feedback is provided by underwater compatible and

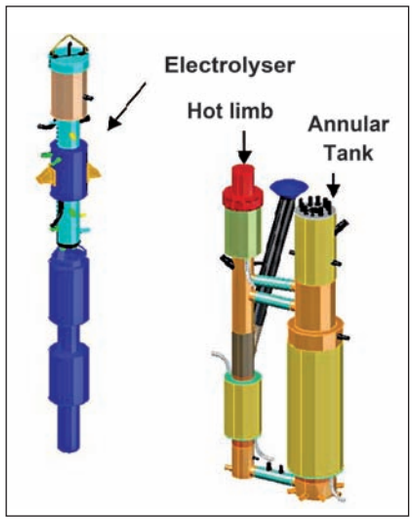

Fig. 1 *DFRP dissolver*

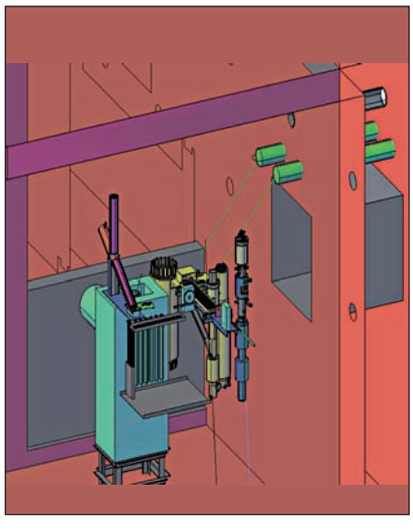

Fig. 2 *Dissolver cell layout in DFRP*

Fig. 3 Various modules of the 3-Axis scanner

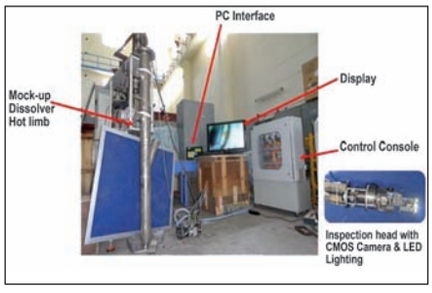

Fig. 4 Mock-up dissolver vessel mounted with the 3-Axis scanner

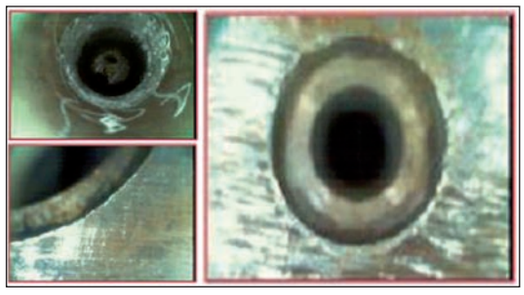

Fig. 5 Images acquired during the mock-up trials

magnetic type non-contact sensors for all axes. A PC-based user-interface has been provided to operate and monitor the device through the motion controller. The various modules of the three-axis scanner are shown in Figure 3.

In addition to visual examination, the scanner has been designed to conduct immersion ultrasonic examination for detecting the wall thinning. Hence, experiments were conducted using the inspection head of the scanner under water in order to check the performance, since water is used as the couplant. The integrated assembly of the three-axis scanner during the visual examination trials using a camera on the mock-up dissolver vessel is shown in Figure 4 with the control console and the user-interface. A 1/3" CMOS camera having a horizontal scan resolution of 380 lines has been used for the visual examination. In the initial trials, tests in the mock-up vessel have been sucessful.

Figure 5 shows the internal surface (radial view) and the axial view images acquired by the camera during the trial runs. The various ports and the boundaries in the mock up dissolver vessel could be clearly seen.

The three-axis scanner for the DFRP dissolver vessel has been demonstrated as an effective device for conducting the remote ISI of the DFRP dissolver. A series of tests using ultrasonic technique is underway to consolidate the test procedures using the mock-up dissolver prior to deployment at site.

Remote handling tools

Two major developments currently underway for reprocessing facilities are the servo manipulator and the power manipulator. The servo manipulator is designed with a load capacity of about 15 kg. The major distinct advantage in this case is that the use of the servo manipulator eliminates the penetrations required in the hot-cell. Since the electrical leads traverse across the cells, there is leak-tightness. Another significant device is the power manipulator for handling higher loads of about 25 kg. This is being developed for in-cell handling of the metallic fuel cycle programme.

Tomographic detection of choked material in centrifugal extractor

For non-destructive detection of choked materials in the centrifugal extractor bowl of reprocessing plants, computed tomography technique has been developed after simulations by inserting copper and stainless steel wires of 0.5 and 1.0 mm diameter. Using 200 kV-1 mA X-ray source, X-ray detector (127 microns pixel pitch) and fourier back projection algorithm, the data from 180 projections obtained in steps of one degree were analyzed and reconstructed slices were obtained to reliably detect the choked materials with good sensitivity, as shown in Figure 6.

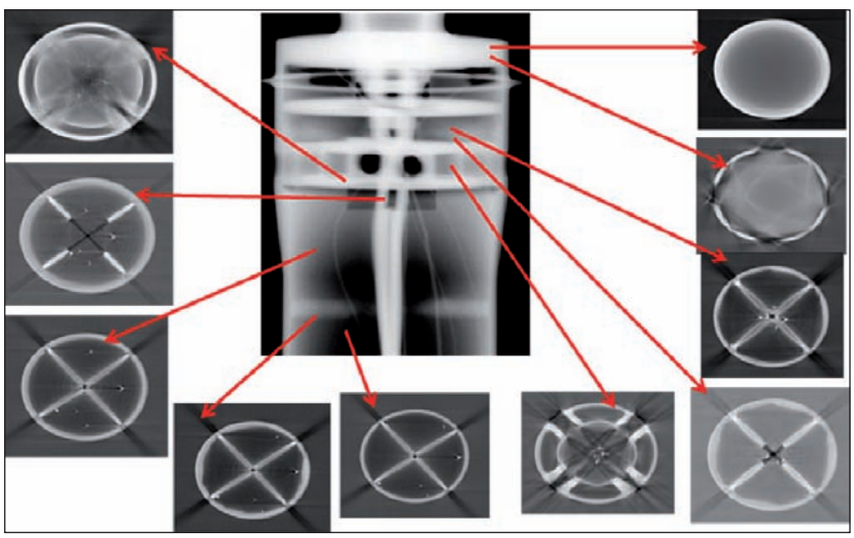

Fig. 6 Reconstructed tomographic slices at various locations on the centrifugal extractor bowl (white dots show the locations of the wire i.e. choked material)

IV.16 An Innovative Pulsating Sensor Based Level Sensing Device for Demonstration of Fuel Reprocessing Plant

A novel approach has been adopted to design a high resolution, high precision dielectric based level sensing device for continuous monitoring of liquid level in a ~2 metres storage tank containing de-mineralized (DM) water in Demonstration Fast Reactor Fuel Reprocessing Plant.

The choice of appropriate level sensor for a dedicated application depends on various factors such as nature of liquid, types of measurement-continuous or discrete, influence of surrounding environment on level measurement, quality of data obtained (precision, accuracy, response time, resolution), easy way of calibration or calibration check during continuous prolonged use, easy maintenance etc., besides transmission of data either through wire or wireless. Considering these aspects, a laboratory made setup which showed excellent performance, is deployed in designing such level sensing device.

The principle of the proposed technique involves introduction of a uniform stainless steel pipe of appropriate length and diameter into the storage vessel from the top whose level measurement is required. The other end of the pipe is placed very close to the bottom of storage vessel. A flexible hose connects upper end of pipe to one arm (wide arm) of a specially designed manometer using leak proof connector. The other arm (narrow arm) is opened to atmosphere. The sensor assembly constitutes a multiple number of mirror polished stainless steel plates of suitable dimensions separated with uniform gap forming parallel plate capacitor assembly. The manometer is partly filled with low volatile mineral oil. Hence, the capacitance of the sensor assembly is governed by two dielectric media (oil and air). The capacitive assembly forms a part of a specially designed logic gate oscillator (LGO) which is powered by 5 V DC. With increase in liquid level in the storage vessel some quantity of liquid enters inside the pipe by replacing trapped air inside it. This results in a pressure difference between both arms of manometer. This pressure difference (expressed in mm oil level) is proportional to the hydrostatic head of water in the tank; hence, it is a linear function of the water level in tank. During level measurement there is a change in oil level in the sensing arm which results in minor increase in the capacitance due to change in overall dielectric permeability of the media following the change in ratio of oil and air in the sensing arm. This results in appreciable shift in output pulse frequency of logic gate oscillator. In laboratory, a calibration test facility has been constructed and using this, the relation between frequency and liquid level was determined. The relation between pulse frequency and water level, presented in equation 1, is established by suitable calibration of the level probe.

$$l = a*f2 + b*f + c \text{ ------ (1)},$$

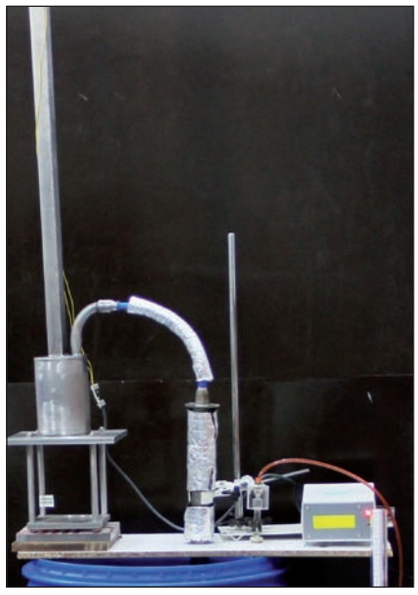

Fig. 1 *Experimental facility for level measurement using innovative sensor*

R-square : 0.99965 Where l = level (mm), f = frequency (kHz), a = 4.4109, b = -3.8528e2 and c = 8.329e3. Results obtained from the laboratory level measurement set up showed excellent precision (< 1% RSD) and resolution < 8 mm. The photograph of the experimental facility used for laboratory investigation is shown in Figure 1.

Further work is in progress towards construction of actual level probe with dedicated instrument which will be used in the storage vessel of Demonstration of Fuel Reprocessing Plant. In the plant a calibration test facility is under construction. During calibration check the level sensor assembly has to be removed from the storage tank and fixed onto the calibration test facility. The proposed level sensor can also be used for continuous measurement of liquid level in any type of liquid either conducting or non-conducting type.

IV.17 Development of PLC Based Control System for Demonstration Fast Reactor Fuel Reprocessing Plant

Design

The architecture for programmable logic controller (PLC) based system for control and data acquisition is given in Figure 1. The PLC for DFRP has hot standby redundant CPU. The two CPUs of the PLC are kept in panels at two different locations. This PLC is connected with safety grade M (medium risk events), L (low risk events) and non safety (NS) signals. The classification of events has been done considering the frequency of occurrence of events and its consequence. The instrumentation is in line with AERB/NPP-PHWR/SG/D10 and D20 for nuclear power plants as there is no classification available for reprocessing plants. The total number of Inputs/Outputs (I/Os) connected to the PLC are 2600 which includes 550 digital inputs, 1400 digital outputs (with external relays) and 650 analog inputs of 4-20 mA type. The reliability of this control and data acquisition system is improved by the presence of redundancy in (a) PLC CPU and power supply (b) I/O servers (c) remote input output (RIO) and ethernet communication link. The availability of interlocks for safety grade M variables is by diverse hardware (PLC and hardwired logics implemented through alarm trip units).

Remote input output architecture

RIO architecture is used for PLC based control system. The field instruments are connected to RIO drops and each RIO drop has a local processor possessing capability to communicate with the PLC CPU through redundant RIO communication link. RIO drops communicate with the CPU of the PLC through the RIO head end processor available in the PLC CPU rack. The RIO drop rack also has analog and digital input and output modules. Twenty RIO drops have been distributed in three locations (close to field instruments). The redundant servers get the information from the modbus over TCP/IP over ethernet modules installed in PLC CPU rack.

Detailed engineering

Detailed engineering was done taking into account of ventilation, air circulation, environmental, EMI/EMC, seismic categorization

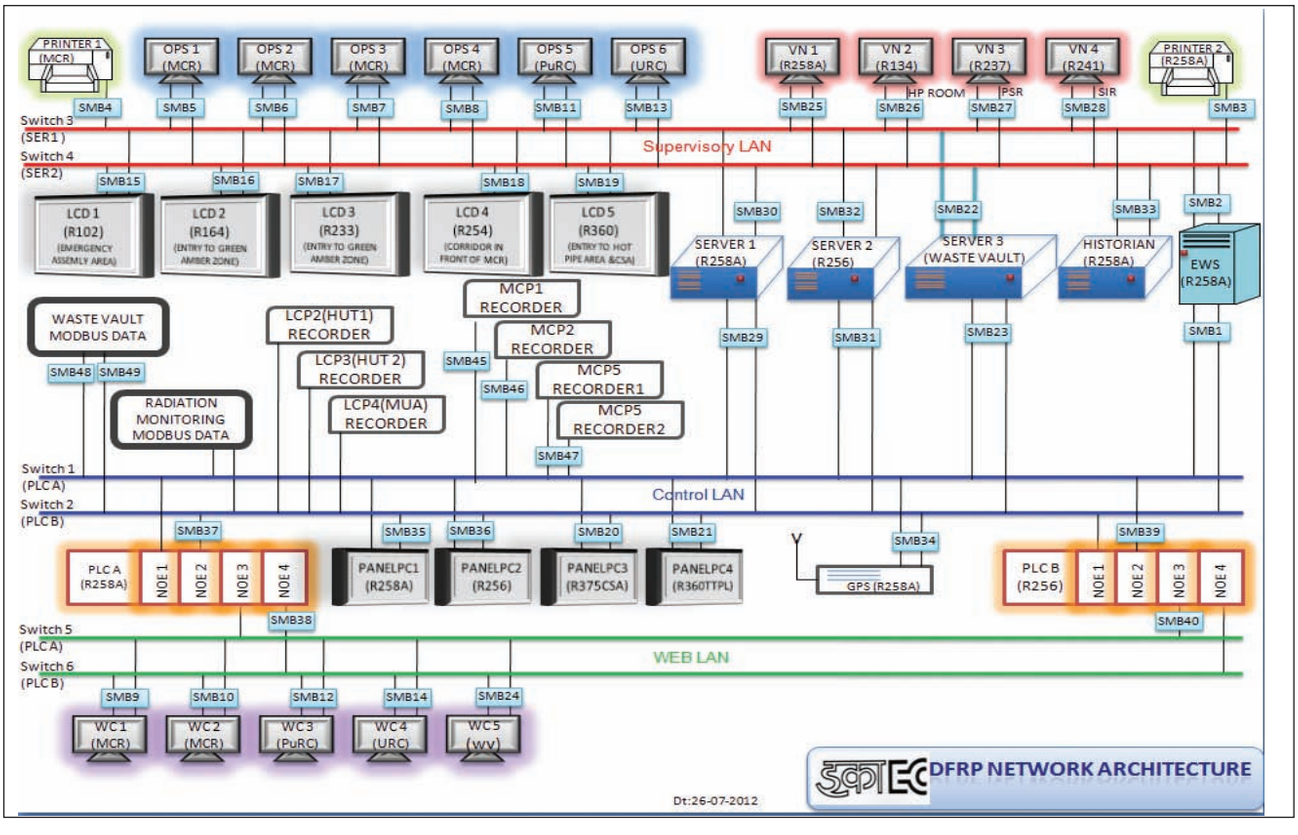

Fig. 1 *Architecture for PLC based system for control and data acquisition*

and other relevant aspects. The panels were engineered in accordance with the principles governing good human engineering and ergonomic design. The main control panels and consoles of DFRP are shown in Figure 2. The detailed documents were prepared as part of the design to successful commissioning of control and instrumentation system.

Fig. 2 *Main control panel and consoles of DFRP*

Functions of components of PLC based control system

SCADA servers and operator stations: Information from the PLC is communicated to the two (primary and standby) rack type servers through the control LAN at two different locations. The information from the primary server is provided to the operator stations through the supervisory LAN. The server computers have SCADA server software loaded in them. The operator stations are SCADA clients.

Historian server stores the data only in case of deviation or changes in the state of I/O signals in a database and periodically archives information in a removable storage media.

Engineering station for application software download into (a) PLC through the control LAN, (b) SCADA operator stations through the supervisory LAN and (c) redundant servers through either the control or supervisory LAN. Software downloading is done from the engineering station once the modified application software has been tested in simulator PLC and SCADA system.

Diagnostic system and web clients: The diagnostic station in server room continuously monitors the healthiness of the network components of the PLC based SCADA system. Five web clients at different locations get the information from the PLC web server modules through the web LAN.

Intelligent displays with built-in PC and panel PCs: Five intelligent displays with built in PC get information from the SCADA server through the supervisory LAN and are fixed one per floor at the entrance of operating area in that floor, for the user to get a glance of the radiation dose in the area of his work. Five panel PCs at the RIO panels in different locations of DFRP get the information from the PLC web server modules through the web LAN and give the status of signals pertaining to inputs and outputs connected to a particular RIO panel.

GPS time server is connected to the servers through the control LAN and is for synchronization with reference clock and distribution of time to network components.

Radiation data on VGR and supplementary monitoring room: The ethernet output of radiation monitors is connected to the redundant servers for data acquisition and monitoring. The ethernet output of some radiation monitors are also connected as ethernet input to multichannel paperless recorder in RADAS panel in MCR. A supplementary monitoring station (with server capability) is located in waste vault control room from which safety grade H, M and L signals can be monitored when the main control room (MCR) becomes inhabitable. Similarly, information from waste vault is made available in DFRP main control room through fiber optic link.

PLC and SCADA simulator system is used for the development and modification of PLC and SCADA application programs. The programs are then downloaded into the main system through the engineering station.

Commissioning

Commissioning of PLC based control system involved (a) Calibration of DP and ultrasonic level transmitters for the measurement of level of liquid, density and tank pressure, (b) Safety ground G1, shield ground G2, and signal ground G3 verification, (c) Configuring multichannel paperless video graphic recorders (VGR), alarm trip units (ATU), signal isolators and temperature transmitters, (d) Continuity testing of wiring and network testing, (e) Loop checking of analog and digital signals, (f) Testing of hardwired interlocks (involved bypassing of interlocks in PLC), (g) Commissioning test and (h) Documentation.

IV.18 Design and Implementation of a Wireless Control System for a Remote Vehicle Using TCP/IP Protocol

In a reprocessing plant, the radioactive waste generated after the fuel is reprocessed, is stored in specialized tanks inside the underground waste vault. Periodic inspection of the waste vault is required to ensure the leak tightness of the tanks. Visual inspection is carried out remotely with the help of a wired robotic vehicle installed with a camera. The vehicle moves through the specially laid out tracks inside the waste vault.

The total inspection volume increases as the capacity of the reprocessing plant increases. The paths of the remote vehicle in this scenario becomes so complex that it is not possible to use a wired vehicle for inspection as it leads to the entanglement of wires. Wireless based control system and video streaming are very useful in this particular scenario. Video streaming of visual data requires very high bandwidth. Out of several available wireless transmission protocols, TCP/IP based wireless protocol is found to be most suitable. Wireless 802.11 b/g standard supports bandwidth up to 54 Mbps and is suitable for video streaming.

The wireless control system primarily consists of two units, control system with wireless camera deployed on the mobile vehicle and graphical user interface. Figure 1 shows the wireless control system overview. It consists of PIC 18F based embedded system with motor drivers, Wi-Fi module-Wiz610Wi and a wireless camera. All modules are interconnected by means of a wireless router. Wi-Fi modules are interfaced to the serial lines of the microcontroller and it acts as a protocol translator i.e., from Wi-Fi to serial and vice-versa. Wi-Fi router acts as a central station for receiving and transmitting the packets. A GUI has been developed using VB 6.0 compiler for issuing the control commands to the wireless control system and is shown in Figure 2a. Commands reach the Wi-Fi router first and are redirected to the Wi-Fi module. Wi-Fi module converts the frame into the serial protocol format and microcontroller reads it through its serial interface. Command is interpreted and vehicle is actuated using motor drivers. It is tested with a prototype vehicle as shown in Figure 2b. Command and acknowledgment are encrypted using dynamic keys with RC4 encryption for enhanced security and transmitted. Obstacle sensing and dual acknowledgment provide collision-free travel and deterministic communication. All features are implemented using a custom protocol. It encapsulates encryption keys and sensor data in to the command/acknowledgment frame. Differential algorithm is used to steer the vehicle in curved paths.

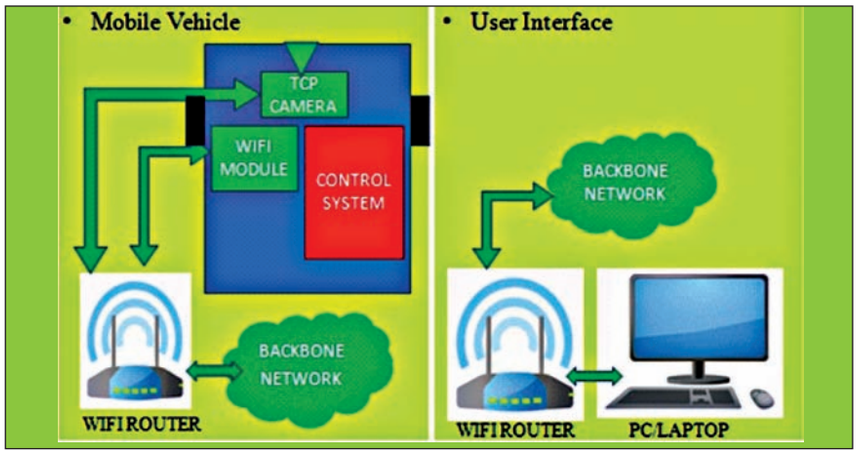

Fig. 1 *Wireless control system overview*

The developed wireless control system has been successfully tested with the help of a prototype vehicle. Commands sent from GUI and live video streaming have been received with good quality. Various motion profiles like left, right, straight and curved were tested and verified.

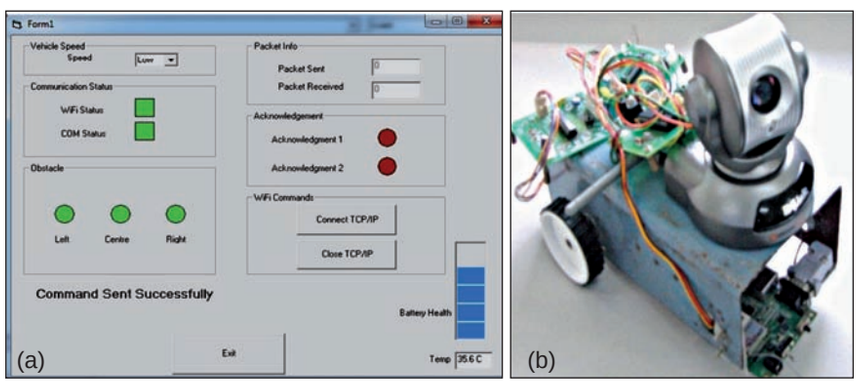

Fig. 2 *Wireless control system (a) Graphical user interface developed in VB and (b) Prototype vehicle used for testing*

IV.19 Recovery of Plutonium from Polymeric Waste Matrix using Supercritical Fluid Extraction

Supercritical fluid extraction (SFE) method has emerged as a useful technique in the recent past for the extraction and recovery of various metal ions from diverse waste matrices.

Removal of various long lived radionuclides from waste matrices is of major concern in nuclear industry. Various organic materials such as polymers, rubbers and cellulose, widely used in nuclear industry and research facilities are prone to be contaminated with radioactive materials. SFE is an alternative and attractive technique for recovery of actinides from such waste matrices.

The polymeric waste generated from radioactive laboratory typically includes radioactive contaminated gloves, PVC, neoprene etc. An extensive investigation was carried out at our laboratory for the extraction and recovery of plutonium from these matrices using SFE.

Initial studies were carried out on the extraction and recovery of simulated plutonium waste from polymeric matrices such as neoprene, PVC and surgical gloves using modified Sc-CO_2. Subsequently, the recovery of plutonium from an actual polymeric matrix was demonstrated using Sc-CO_2 modified with n-octyl(phenyl)-N,N-diisobutylcarbamoylmethylphosphine oxide (CMPO). In the method development studies, SFE experiments were carried out in a 1ml extraction vessel and the methods were evolved for the complete removal of plutonium from actual polymeric matrix. The entire waste was then processed using a 0.1 litre capacity extraction vessel and recovery of plutonium was demonstrated from the polymeric PVC waste matrix. The SFE system employed for these studies consists of two reciprocating pumps one for pumping carbon dioxide and the other pump for the co-solvent (modifier), a constant temperature oven and a backpressure regulator. The SFE system was set-up in a glove box incorporating certain modifications for handling high pressures and radioactive materials. A secondary vessel accommodated the primary extraction vessel to contain any accidental pressure release during the extraction.

The PVC matrix containing plutonium was cut into small piece and was loaded in to a 1 ml capacity extraction vessel and SFE was carried out using Sc-CO_2 modified with CMPO/methanol under the typical experimental conditions viz. pressure: 250 bar and temperature:50^{o}C. An extraction period of about 1-2 hours was used. The extract was collected in isopropanol medium for the assay of plutonium. Subsequently, the actual waste, i.e., polymeric waste with plutonium were loaded in a 0.1 litre (11 cm height x 4 cm dia) capacity extraction vessel and SFE was carried out in several batches for the recovery of plutonium from polymeric matrix. In a typical batch, approximately 50 grams of PVC waste was loaded in a 0.1 litre scale extraction vessel for the recovery of plutonium. Longer extraction periods were employed when samples were processed from a 0.1 litre capacity vessel as Sc-CO_2 throughput was not adequate for its geometry i.e. number of CO_2 changes per unit time was less compared to the one observed with 1 ml vessel. The organic compounds added as additives in neoprene, surgical gloves and PVC were co-extracted during SFE of actinides from these matrices.

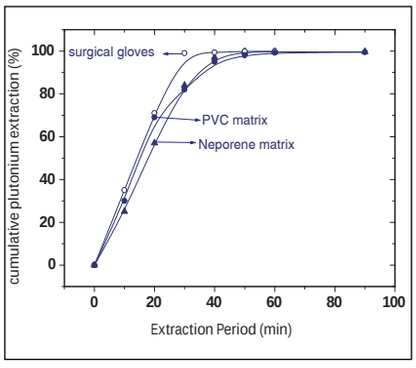

***Fig. 1** Recovery of plutonium from simulated polymeric waste matrices*

The results on the extraction and recovery of plutonium (both Pu(IV) /Pu(III)) from simulated PVC matrix is shown in Figure 1 (As shown in figure sample: plutonium nitrate (~10 µg Pu equivalent) dried on neoprene/ surgical glove/PVC in fumehood for 240 hours prior to SFE. Waste matrix was placed in a 1 ml extraction vessel. Experiments: Sc-CO_2: 3ml/min; modifier flow rate: 0.1ml/min; P: 250 bar; Temperature: 50^{o}C. Modifier composition: 5 g CMPO + 1.83 ml concentrated HNO_3 made up to 100 ml in methanol.) A highest recovery of about 99.9% was observed using Sc-CO_2 modified with CMPO in methanol at 50^{o}C. The extraction efficiency was found to vary from 97 to 99.9% (ten independent SFE experiments) during the course of these studies. The extraction profiles indicated that major portion of plutonium was removed and extracted in about 30-45 minutes itself. Similarly, near complete extraction and recovery of plutonium from simulated waste matrices, i.e. neoprene

matrix (96±3.5%, six independent experiments) and surgical glove matrix (95 ± 4.6%, six independent experiments) was demonstrated.

A typical extraction profile for recovery of plutonium from actual waste i.e. PVC matrix is shown in the Figure 2 (Sample: Plutonium in PVC matrix; Experiments: Sc-CO_2 : 3ml/min; modifier flow rate: CMPO/methanol (5 g CMPO+1.83 ml concentrated HNO_3 made up to 100 ml in methanol) 0.1ml/min; P: 250 bar; Temperature: 50°C. Extraction essel capacity: 0.1 litre). The extraction was continued till the presence of plutonium in the extract.

For the recovery of plutonium from polymeric matrices, CMPO was chosen compared to ligands such as TBP, TTA and acetyl acetone as it gave better extraction efficiency during recovery of plutonium from cellulose matrix. Nitric acid was sprinkled on to the polymeric matrices to convert plutonium in to its soluble species for its complete extraction.

The preliminary studies have established that the SFE technique provided faster, cleaner and better efficient extractions and recoveries of plutonium with minimum generation of secondary solvent waste. These studies also

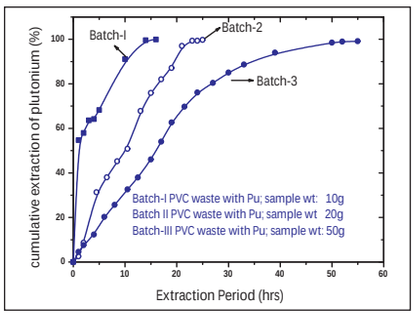

***Fig. 2** Supercritical fluid extraction and recovery of plutonium from actual PVC waste matrix*

demonstrated the feasibility of recovery of actinides from various waste matrices in a preparative scale facility which is an attractive feature for processing of large amount of radioactive wastes.

IV.20 Assay of Actinide Mixtures in Solution by K-edge Densitometry

Nondestructive assay (NDA) methods based on gamma and neutron emissions are used to characterize the spent fuel solutions in reprocessing plants. However, these measurements require corrections based on geometry and material properties and incomplete knowledge of these quantities can lead to large uncertainties in the results. One of the methods that can provide an accurate measurement of concentration in solutions is X-ray K-edge densitometry. This can be used for spent fuel solutions having high dose levels. A system has been recently commissioned at the Radiochemistry Laboratory, IGCAR for this purpose.

K-absorption edge densitometry utilizes the sharp, discontinuous structure in the photon absorption probability of elements as a function of energy. The sharp rise in this absorption probability at a particular well-defined energy is known as the edge of the element. By contrast, for elements other than the element of interest, the photon absorption probability near the edge energy region is quite smooth and varies very little in the vicinity of the edge. The experimental measurement of actinide concentration involves the determination of the degree of absorption of the gamma photon on either side of the absorption edge of the element of interest. The K-edge appears at 109.7 keV for thorium, 115.6 keV for uranium and 121.8 keV for plutonium. The K-edge and the L_{III} absorption edges have been used in the assay of special nuclear materials.

The transmission of photons at energy just lower than the absorption edge of a solution where the path length is x can be written as

$$Ln(T_L) = -(\mu_s^L \rho_s + \mu_m^L \rho_m)x \qquad (1)$$

Where, *L* denotes the lower energy side of the edge, subscripts *s* and *m* refer to the measured element and the matrix respectively. A similar expression can be written for the transmission just above the upper edge i.e. for T_U and using both expressions the concentration of the species of interest, ρ_s , is given as

$$\rho_s = \frac{1}{\Delta\mu x} Ln\left(\frac{T_L}{T_U}\right) + \rho_m\left(\frac{\Delta\mu_m}{\Delta\mu}\right) \qquad (2)$$

The $\Delta\mu_m$ in the second term is zero as X-ray continuum is being used in these estimations and hence the expression for concentration reduces to

$$\rho_s = \frac{1}{\Delta\mu x} Ln\left(\frac{T_L}{T_U}\right) \qquad (3)$$

A 220 kV, 10 mA X-ray generator was used to generate the continuum required for this work. The X-ray continuum was suitably tailored by means of filters and the collimated X-rays were allowed to be incident on the sample solution contained in a sample container with a path length of

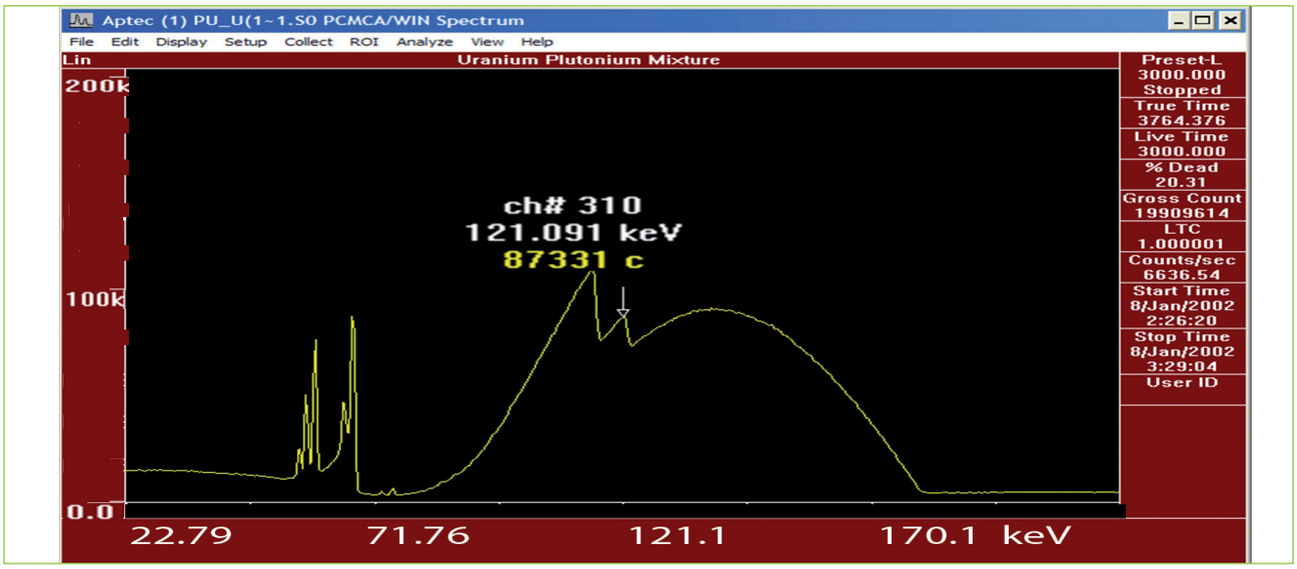

Fig. 1 *Spectrum showing the K-edge absorption by thorium and uranium*

22.1 mm. The X-rays after traversing through the solution were allowed to impinge on a well shielded low energy photon spectrometer (area 500 mm^2, resolution 520 eV at 122 keV) through a tungsten collimator of 2 mm diameter to ensure that only radiation that had passed through the sample was seen and all scattered radiation were cut off. The preamplifier output was connected to a 8 K MCA card with onboard amplifier and ADC. The system was first used to assay mixtures of thorium and uranium with the thorium concentration varying from 8 to 90 $mg.ml^{-1}$ and the uranium concentration varying from 91 to 12 $mg.ml^{-1}$.

Analysis of actinide mixtures containing plutonium require additional precautionary measures. The solutions were placed in a polypropylene vial of 22 mm diameter. This vial was placed concentrically inside another polypropylene container having 36 mm diameter. Thus, the actinide solution was residing inside a doubly sealed container and the solution could be used in the K-edge experimental set-up. Mixtures of plutonium and uranium solutions with the plutonium concentration varying from 12 to 34 $mg.ml^{-1}$ and the uranium concentration varying from 80 to 57 $mg.ml^{-1}$ were analyzed and the results are shown in Table 2. The mixtures were obtained by diluting a high concentration plutonium solution by adding uranium solution having a concentration of 99 $mg.ml^{-1}$ to get the required concentrations of uranium and plutonium in the mixtures. All measurements were carried out of an operating voltage of the X-ray tube maintained at 180 kV at a current of 1 mA and the counting time was fixed as 3000 seconds. A typical spectrum obtained for uranium-plutonium mixture solution with the present setup is shown in Figure 1.

The number of photons transmitted through the sample in the few channels on the lower energy side

Table 1: Results of assay of thorium uranium mixtures

Thorium			Uranium		
Concentration ($mg.ml^{-1}$)		Δρ/ρ	Concentration ($mg.ml^{-1}$)		Δρ/ρ
Actual	Experimental		Actual	Experimental	
86.31	87.34	0.012	9.90	11.95	0.21
76.72	76.84	0.002	19.81	19.35	-0.02
57.54	57.14	-0.007	39.61	41.03	0.04
47.95	45.59	-0.05	49.52	47.23	-0.05
19.18	18.30	-0.04	79.22	80.04	0.01
9.59	8.45	-0.11	89.13	91.04	0.02

Table 2: Results of assay of uranium plutonium mixtures

Uranium			Plutonium		
Concentration ($mg.ml^{-1}$)		Δρ/ρ	Concentration ($mg.ml^{-1}$)		Δρ/ρ
Actual	Experimental		Actual	Experimental	
56.59	57.46	0.02	11.64	11.80	0.01
66.02	66.84	0.01	13.58	13.54	-0.003
66.02	66.88	0.01	27.16	27.94	0.03
74.27	75.07	0.01	20.37	20.65	0.01
79.22	79.84	0.01	16.30	15.80	-0.03

of the edge were used and a plot of ln(ln(1/T)) against ln(Energy) was constructed. The best-fitted line obtained using the least square fit formula is extrapolated to the absorption edge of uranuim to determine the transmission at the absorption edge i.e. T_L. In a similar fashion, a few channels on the higher energy side of the edge are used for extrapolation and determining the transmission at the adsorption edge i.e. T_U. The ratio of the number of photons transmitted T_L / T_U is the jump ratio of the element of interest. The jump ratio for uranium and plutonium are calculated and the concentrations are obtained using the equation (2).

The results of the analysis of thorium -uranium mixtures are shown in Table 1 and of uranium-plutonium mixtures in Table 2.

It can be seen from these tables, that the error ranges upto about ±3% against the internationally accepted value of about ±1%. This is attributed to small variations in the path length as the positioning of the vial could not be reproduced very accurately. This resulted in the variation in the path length as the vial used was circular. A variation of 1 mm in the path length would lead to an error of about 5% as the vial diameter was 22 mm.

IV.21 Studies on the Thermal Decomposition of the System TiAP-HNO_3

Tri-isoamyl phosphate (TiAP) is an attractive alternative to TBP, with near similar extraction behaviour and physical properties but much lower aqueous phase solubility and does not form third phase during the extraction of Pu(IV). In addition to the solubilised extractant inadvertent entrainment of the extractants into the aqueous streams is a concern during the evaporation operations as the extractants come into contact with high nitric acid concentrations and metal nitrates. Studies on the development of TiAP as an extractant for fast reactor fuel reporocessing are underway and the results of studies carried out on the thermal decomposition behaviour of TiAP-HNO_3 systems, employing an adiabatic reaction calorimeter in air ambience, under closed and open conditions, are reported here.

The systems studied were, neat TiAP, nitric acid-solvates viz., TiAP·1.1HNO_3 and TiAP·2.2HNO_3, nitric acid-solvates with sodium nitrite and uranyl nitrate, solutions of TiAP in n-dodecane (n-DD) and solutions of TiAP in 2,2,4,6,6 pentamethyl heptane (PMH) with nitric acid. The samples were heated from room temperature either to the decomposition temperature of the sample or 773 K (the maximum limit of the calorimeter) in steps of 10 K in heat-wait-search mode.

Nitric acid solvates, TiAP·1.1HNO_3 and TiAP·2.2HNO_3, were prepared by equilibration using neat TiAP and 8 and 15.6 M nitric acid. The organic phase was subsequently separated and characterized for its acidity by titration with 0.1 M sodium hydroxide solution with phenolphthalein as the indicator. Required aliquots (2 ml) of the acid-solvates were taken for calorimetric investigations.

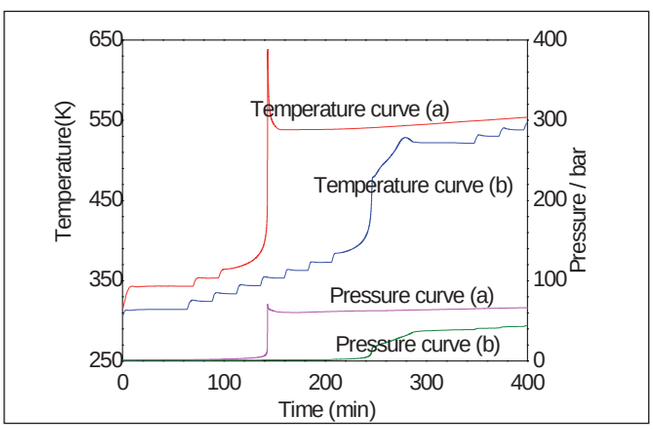

Fig. 1 Decomposition of nitric acid solvates of TiAP (a) TiAP·2.2HNO_3 (b) TiAP·1.1HNO_3

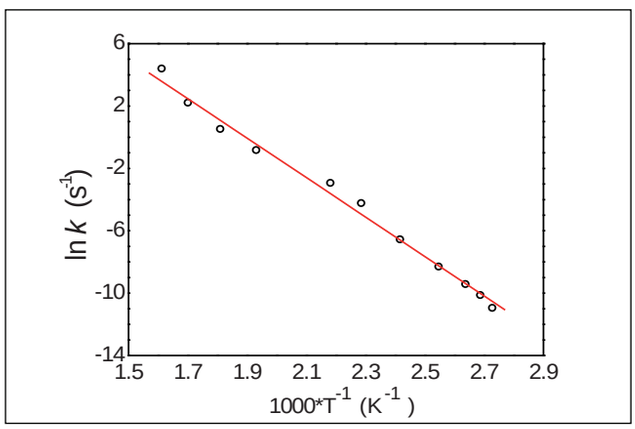

Fig. 2 Arrhenius plot for the decomposition of acid-solvate TiAP•2.2HNO_3

Solutions of 1.1 M TiAP/n-DD and 1.1 M TiAP/PMH were prepared by diluting neat TiAP with the respective diluents. Solution of 1.1M TiAP in n-DD was equilibrated with 8 M nitric acid as described above and an aliquot of the organic phase containing the acid-solvate with or without the addition of metal salt was used for calorimetric measurements. Neat TiAP was found to be stable up to 535 K and decomposed above this temperature. The acid solvates, TiAP·1.1HNO_3 and TiAP·2.2HNO_3 were found to decompose exothermically at 384 and 365 K respectively (shown in the Figure 1) with high rise in temperature and pressure, generating gases such as N_2O, CO_2 and CO and a blackish residue. These products are expected to be formed owing to the presence of amyl group in the phosphate and nitric acid. The amount of nitric acid present in the acid solvate strongly influences the decomposition behaviour of TiAP.

Heat capacities of acid-solvates at constant pressure have been measured in the temperature range 305-340 K by differential scanning calorimeter. These values were used for deriving the enthalpy of decomposition of acid solvates as given in Equation 1.

$$\Delta H_r = C_p \times \Delta T_{ad} \times \Phi \qquad (1)$$

where ΔHr is the enthalpy change of a reaction, Cp is the heat capacity of reactant, ΔT_{ad}, the adiabatic temperature rise and Φ, the phi-factor. The phi-factor is defined by the following expression.

$$\Phi = 1 + \frac{(mC_P)_C}{(mC_P)_S} \qquad (2)$$

where $(mC_p)_c$ and $(mC_p)_s$ are the thermal mass of the sample container and sample respectively.

Enthalpy change for the decomposition of acid solvates TiAP·1.1HNO_3 and TiAP·2.2HNO_3 were found to be -465.1±2.4 and -937.0±6.2 kJ mol^{-1}, respectively.

The rate constant for an exothermic reaction can be obtained by the following expression.

$$k = \frac{\frac{dT}{dt}}{(T_f - T_i)\left(\frac{T_f - T}{T_f - T_i}\right)^n} \qquad (3)$$

where *k* is the rate constant, *n* is the order of the reaction, *dT/dt* is the rate of temperature rise. T_i, T_f and *T* are the temperatures at initial, final and any time *t* of the exothermic region.

The decomposition of acid-solvates followed first order kinetics. Logarithmic dependence of the rate constant with reciprocal temperature is shown in Figure 2 for the decomposition of TiAP·2.2HNO_3. Similar plot was made for the decomposition of TiAP·1.1HNO_3. Activation energy and pre-exponential factor for the decomposition of acid-solvates derived from the slope and intercept were found to be 132.9±1.1 kJmol^{-1} and 5.5×10^{13} s^{-1} respectively for TiAP·1.1HNO_3 and 105.2±0.7 kJmol^{-1} and $2.6\times10^{10}$$s^{-1}$ respectively for TiAP·2.2HNO_3. Addition of metal salts such as sodium nitrite and uranyl nitrate in the form of aqueous solutions do not seem to alter significantly the onset temperature for the decomposition of acid-solvate, TiAP·1.1HNO_3 from 384 K, similar to the phenomenon exhibited by TBP·1.1HNO_3 system.

Decomposition behaviour of acid solvate TiAP·1.1HNO_3 in air under open condition showed three exotherms at 383, 435 and 519 K. The first one at 383 K was due to the decomposition of acid-solvate TiAP·1.1HNO_3. However the decomposition in the open system did not go to completion due to the possible formation of nitric acid-water azeotrope, the boiling of which resulted in a plateau around 393 K for a time period of ~70 min. The heat-wait-search operation continued further till the second exotherm initiated at 435 K, which was again due to the decomposition of remnant TiAP·1.1HNO_3. The temperature rise for both the first and second decompositions was around 140 K in the open system, which was comparable to the temperature rise of 168 K observed in closed condition depicted in Figure 1. Similarly TiAP·2.2HNO_3 exhibited exotherms initiating at 376, 455 and 519 K. The explanations given above are also valid for the decomposition of TiAP·2.2HNO_3.

The third exothermic event initiated at 520 K was due to the decomposition of left over unreacted TiAP vapour, which was similar to the decomposition pattern observed for the neat TiAP.

Solutions of 1.1 M TiAP/n-DD did not exhibit any accelerated decomposition with 4 M HNO_3 due to the lower concentration of TiAP and nitric acid present in those systems. However, the solution with 15.6 M HNO_3 showed an accelerated decomposition with an activation energy of 124.0±0.9 kJmol^{-1} due to higher amount of nitric acid. The solution of 1.1 M TiAP/PMH also exhibited a similar decomposition behaviour with an activation energy of 135.5±1.4 kJmol^{-1}. However, the solution 1.1 M TiAP/PMH decomposed at higher temperatures in all the cases studied under similar conditions compared to the diluent n-DD. These studies indicated that it is safer to use branched diluents to reduce the severity of runaway reactions.

In comparison to TBP, neat TiAP performs better with respect to thermal stability as well as aqueous solubility. However, the acid solvate of TiAP was found to be less stable compared to that of TBP acid solvate.

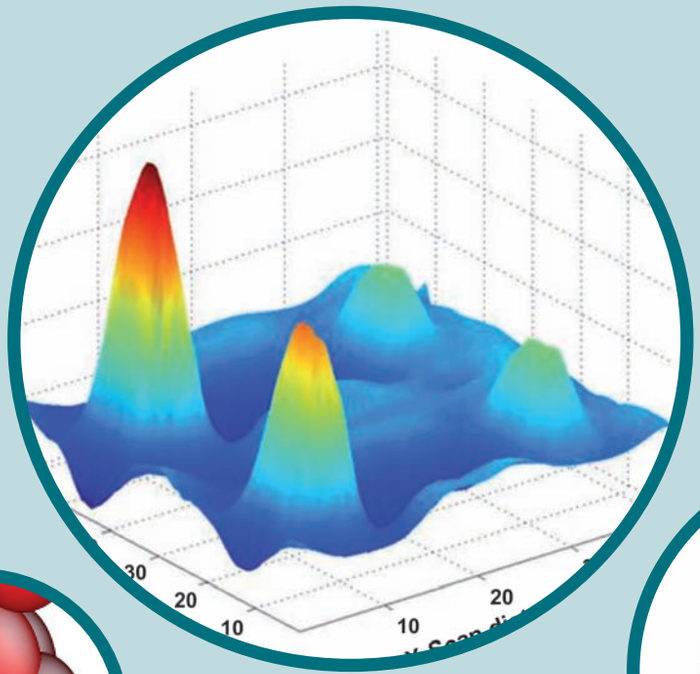

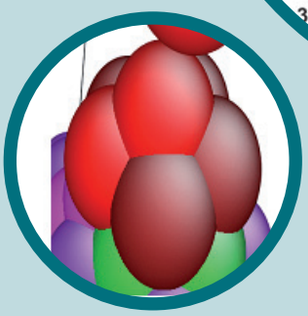

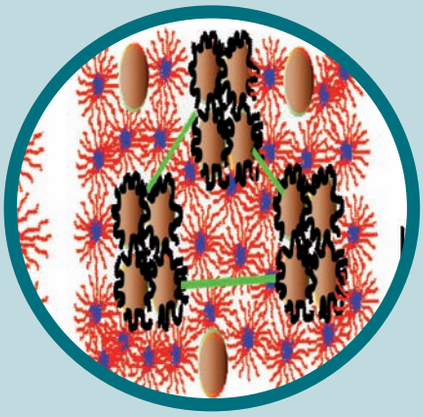

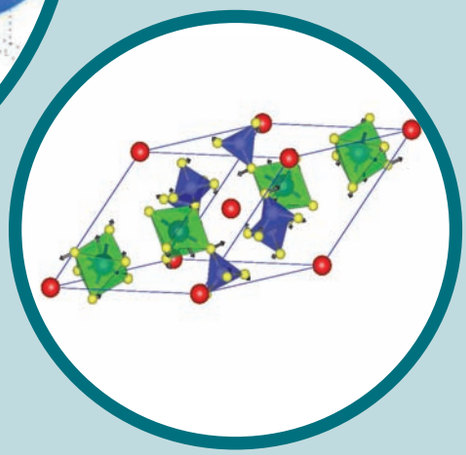

CHAPTER - V

Basic Research

V.1 Development of 304HCu SS and Alloy 617 Tubes including Joining Technologies for Advanced Ultra Super Critical Thermal Power Plants

Under a national mission for collaborative development of advanced ultra super critical (AUSC) technology for coal-fired thermal power plant, IGCAR, BHEL and NTPC have jointly signed a memorandum of understanding in 2011. The aim of this project is to indigenously develop materials, fabrication technologies, design and to build an 800 MW AUSC plant, which will be operated at a steam pressure of 300 bar and a temperature of 973K. The thermal efficiency of AUSC boiler is expected to increase from 35 to 46%, reducing CO_2 and green house gases significantly per unit of electricity produced. With the promotion of steam parameters to AUSC level, high temperature materials with improved creep strength, steam corrosion and oxidation resistance such as advanced austenitic heat resistant steels and Ni-base superalloys are required. In fact the research and development of these high quality materials has become a key factor for AUSC technology.

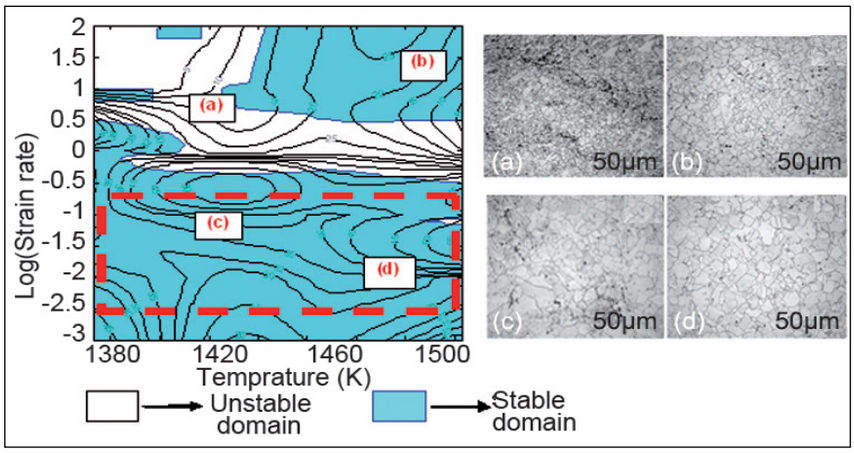

Fig. 1 *Domains of processing map for alloy 617 and corresponding microstructures at (a) 1423 K and 1 s^{-1}, (b) 1473K and 10 s^{-1}, (c) 1423 K and 0.1 s^{-1} and (d) 1473 K and 0.1 s^{-1}*

Indigenous development of 304HCu SS and alloy 617 tubes

Austenitic stainless steel 304HCu and nickel base Alloy 617 are the candidate materials for AUSC plants. For the first time in India, the indigenous development of 304HCu SS seamless tubes (52 mm OD, 9.5 mm WT) and Alloy 617 seamless tubes (52 mm OD, 11.9 mm WT) has been taken up in collaboration with industrial partners, MIDHANI and NFC. Based on the comprehensive survey of international literature and codes, specifications for 304HCu SS and Alloy 617 tubes were prepared, with controlled chemistry and grain size to ensure minimum scatter in mechanical properties, better weldability and balanced creep strength and low cycle fatigue life.

The selection of proper routes for melting, temperatures for hot-forging, hot-extrusion, cold-pilgering, temperature and time for the intermediate heat treatment and final heat treatment are all crucial to control the size and volume fraction of primary carbides or carbo-nitrides and consequently for meeting the required mechanical properties and microstructure. The melting practices, metal forming (forging, extrusion, pilgering) parameters, and heat treatment schedules followed are different for 304HCu SS and alloy 617. Billets and tubes were subjected to solution annealing treatment during intermediate forging and post-extrusion processes for homogenization of chemistry and controlling the size and volume fractions of primary carbides and carbo-nitrides. To ensure the quality, a detailed characterization of the 304HCu SS and Alloy 617 tubes were carried out in each stage of manufacturing by studying the microstructures (grain size, precipitates morphology and distribution) and hardness measurement across the tube thickness. Based on these characterizations after each of the fabrication process steps and by carrying out systematic laboratory-based heat treatment studies, the intermediate and final heat treatment schedules (temperature and time) were optimized and implemented during tube production. In order to find the optimum strain rate and temperature for hot extrusion of Alloy 617 and 304HCu SS, studies on hot workability of these two materials were carried out. For this, uniaxial compression tests at constant true strain rates of 0.01, 0.1, 1, 10 and 50 s^{-1} were performed using Gleeble Thermo-Mechanical Simulator in the temperature range of 1373-1523 K for Alloy 617 and 1130-1520 K for 304HCu SS. All the specimens were given 50% deformation after which they were

quenched in water to freeze the microstructure (Figure 1). The experimental load-stroke data were converted to true stress–true plastic strain curves using the standard procedure. These data were used to develop processing maps on the basis of Dynamic Materials Model (DMM). The domains of processing maps were validated using the microstructures obtained from extensive optical metallography of the specimens tested at the above conditions. The processing map and the microstructures corresponding to various domains for Alloy 617. Based on analysis of the processing map, microstructural investigations and activation energy variation, two suitable hot-working domains were identified for the Alloy 617. The first one occurs at 1350-1423 K and strain rate of 0.001-0.05 s^{-1}, whereas the second one occurs at 1323-1473 K and strain rate of 3-50 s^{-1}. However, only one domain was indentified for 304HCu which occurs at 1473-1523 K and strain rate of 1-50s^{-1}. These studies enabled successful production of 304HCu SS and Alloy 617 tubes meeting international standards. Production of 74 metres of Indigenous 304HCu SS tubes and 34 metres of Alloy 617 tubes have been produced, meeting the chemistry, tensile properties and NDT requirements as per the specifications (Tables 1 and 2).

The SEM-EBSD analysis of 304HCu SS and Alloy 617 tubes has shown random texture which is preferable. The Alloy 617 tube produced is almost free from inclusions. Table 3 shows the Charpy V-notch impact toughness of Indigenous Alloy 617 and 304HCu SS tubes for two different notch orientations. For Alloy 617 tube, standard specimens (55×10×10 mm with 2 mm deep V-notch) were used, whereas for 304HCu SS tubes, sub-size specimens (55×5×5 with 1 mm deep V-notch) were used as 304HCu SS tube wall thickness is 9.5 mm. The equivalent full size impact toughness for 304HCu SS was calculated by the empirical formula; $C_v(full)=K*C_v$ (sub) with K=8 and the same is given in Table 3.

Welding technology

The objectives are to qualify the welding consumables and development of welding procedures for similar and dissimilar welding of 304HCu SS and Alloy 617 tubes. The welding development started with preparation of specifications of filler wires for gas tungsten arc welding. For welding of 304HCu SS, as various codes and standards do not specify welding consumables for this relatively new material, based on literature survey and our own experience, three different consumables, viz. ERNiCrCoMo-1 (Inconel 617), ERNiCrMo-3 (Inconel 625) and ER304HCu were considered for welding procedure development using gas tungsten arc welding process. ER304HCu available in market in recent times is developed by M/s. Bohler with higher Ni and Mn compared to

Table 1: Chemistry and mechanical properties of indigenous 304HCu SS seamless tube

Elements	C	Mn	P	S	Si	Ni	Cr	Cu	Nb	N	B	Al	Fe
Wt.%	0.10	0.89	<0.01	0.006	0.21	9.3	17.2	2.9	0.47	0.094	0.003	0.0035	Bal.
Tensile properties		UTS (MPa)	YS (MPa)		UTS (MPa)				% Elongation			Hardness	
Specified		590 minimum	235 minimum		590 minimum				35			95 HRB maximum	
Product Analysis		-	284		633				43.5			95	

Table 2: Chemistry and mechanical properties of indigenous Alloy 617 seamless tube

Chemical Composition									Tensile Properties		
Element	Cr	Fe	Mn	Mo	Co	Al	C	Cu		Specified	Typical
Wt.%	22.1	0.12	<0.01	9.4	11.6	1.2	0.06	<0.01	YS (MPa)	240	339.2
Element	B	Si	S	N	Ti	Nb	V	Ni	UTS (MPa)	665	812.5
Wt.%	0.0036	<0.01	0.001	0.005	0.4	<0.02	<0.05	Bal.	% Elongation	35	59

Table 3. Charpy V-notch impact toughness of indigenous 304HCu SS and Alloy 617 tubes

Materials ⇨ / No. of Tests ⇩	Alloy 617 Tube (Charpy energy-Joules)		304HCu SS Tube (Charpy energy-Joules)			
	Circumferential direction	Radial direction	Circumferential direction		Radial direction	
	Full size specimen (10x10x 55 mm)		Sub-size (5x5x55mm)	Eqvt. Cv (Full size)	Sub-size (5x5x 55mm)	Eqvt. Cv (Full size)
Test 1	327	271	34	272	35	280
Test 2	328	274	33	264	34	272
Test 3	246	265	35	280	34	272

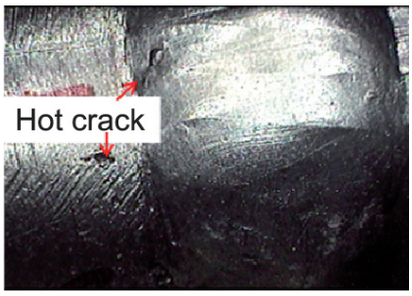

Fig. 2 *Typical hot crack in weld joint*

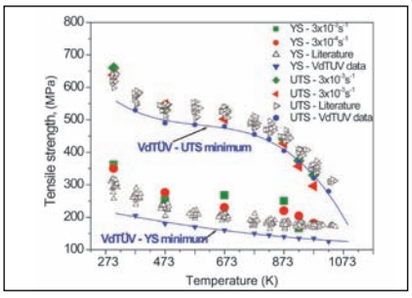

Fig. 3 *Variation of tensile strength of 304HCu steel with test temperature*

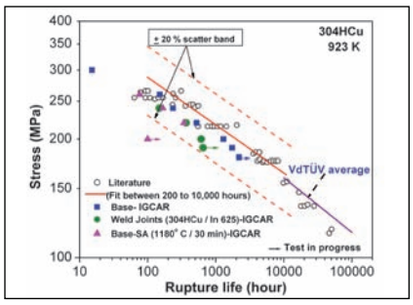

Fig. 4 *Variation of creep rupture life with applied stress of 304HCu steel at 923 K*

304HCu base materials. For gas tungsten arc welding of Alloy 617, and for dissimilar welding of 304HCu SS to Alloy 617, ERNiCrCoMo-1 consumable has been selected. Indigenous development of ER304HCu and ERNiCrCoMo-1 consumables were completed at M/s. MIDHANI, Hyderabad as per the specifications. Imported filler wires with various sizes in all the three grades were used for comparison purpose.

Initial welding procedure qualification (WPQ) was carried out for Indigenous 304HCu SS tubes using two consumables ERNiCrCoMo-1 and ERNiCrMo-3 by gas tungsten arc welding process. Two joints of mock-up welds were prepared using the above filler wires with a single 'V' groove (70°) to optimize the welding parameters for welding procedure specification (WPS). Weld defects like root crack, hot crack and crater crack were observed during the initial trials due to sluggishness in fluidity of nickel base consumables ERNiCrCoMo-1 and ERNiCrMo-3. Typical appearance of hot crack observed during the initial trials is shown in Figure 2. These problems were overcome by suitably altering the weld joint design and optimisation of heat input. After optimisation of weld parameters, actual weld procedure qualification joints in each category followed by production of 10 joints using each filler wire have been completed and are qualified by liquid penetrant examination (LPE) and radiography. Table 4 shows the transverse tensile properties of the WPQ weld joints of indigenous 304HCu SS tubes for the two consumables ERNiCrCoMo-1 and ERNiCrMo-3. Both types of weld joints failed in base material with sufficient ductility. Bend test results indicated that the joints have adequate soundness as per standards. WPQ for other combinations of base materials and filler wires as mentioned earlier are in progress.

Tensile and creep properties of indigenous 304HCu SS tube and weld joints

The variation of tensile strength of indigenous 304HCu SS tubes with temperature is shown in Figure 3 and compared with those of the internationally reported values. The yield strength of the developed steel is higher than that reported in literature at all the test temperatures. The ultimate tensile strength of the steel is comparable to the internationally reported values at all the temperatures except at higher test temperatures where values are close to the minimum values.

The variation of creep rupture life at different applied stresses for indigenous 304HCu SS tubes at 923 K is shown in Figure 4 and is compared with those of the international reported data. The indigenously developed 304HCu SS tube have creep rupture strength within the ± 20 % scatter band and is close to the lower scatter band. Weld joints of this steel welded using ERNiCrMo-3 consumable possess lower creep rupture strength than that of the base metal. Failure of the joint fabricated by TIG welding process employing ERNiCrMo-3 consumable, creep fractured at 923 K and 200 MPa (rupture life 610 hours) occurred at the base steel close to the weld fusion line (Figure 5).

Table 4: Tensile properties of indigenous 304HCU SS tube base material and weld joints

Materials/Weld Joints		YS (MPa)	UTS (MPa)	Elongation (%)	Failure Location
304HCu SS Base Material		311	635	41.5	Not applicable
304HCu SS Weld Joints	ERNiCrMo-3	436	699	47.0	Base Metal
	ERNiCrCoMo-1	424	651	38.5	

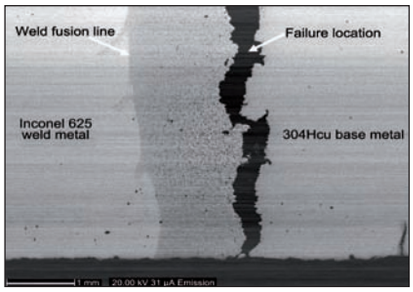

Fig. 5 *Creep failure location in 304HCu SS weld joint*

V.2 Beneficial effects of Dynamic Strain Ageing under Load-Controlled Cycling: Fatigue Crack Growth and Ratcheting

Dynamic strain ageing exerts a strong influence on various parameters describing the mechanical response of many engineering alloys. Since this phenomenon is related to the interaction of moving dislocations with diffusing solute atoms, its effects are limited to certain ranges of temperatures (T) and strain rates ($\dot{\varepsilon}$). Caution is exercised for the design of components operating in the dynamic strain ageing regime, since dynamic strain ageing is generally considered detrimental to the mechanical behaviour. However, contradicting reports on the effect of dynamic strain ageing on the fatigue resistance are available in the literature. Two instances of beneficial influence of dynamic strain ageing on the material behaviour under cyclic loading conditions are presented.

Fatigue crack growth behaviour of modified 9Cr-1Mo steel.

The fatigue crack growth resistance of modified 9Cr-1Mo steel was found to increase with temperature (T) in the dynamic strain ageing regime. In the Paris regime, fatigue crack growth rates (da/dN) decreased as a function of T for various levels of $\Delta K_{eff}/E$ (Figure 1). Effective stress intensity factor (ΔK_{eff}) is normalized by elastic modulus (E) to account for the possible influence of T-dependence of E on the fatigue crack growth behaviour. Notwithstanding the scatter, it is clear that as T increases from 300 to 723 K, da/dN decreases; the magnitude of decrease depends on $\Delta K_{eff}/E$. Above 723 K, an expected increase in da/dN indicating reduced fatigue resistance is observed. Also, the effective fatigue crack growth threshold $\Delta K_{eff,th}$ remained nearly constant at ~ 3 MPa.m$^{1/2}$ from 300 to 623 K, increased steeply to 5 MPa.m$^{1/2}$ from 623 to 723 K and then decreased with further increase in T. It has been observed that work hardening rate (θ) increases in the dynamic strain ageing regime for this material (θ/E increases from 40 to 60). The effect of θ on the fatigue damage accumulation is clear from Figure 2, which shows higher plasticity and hysteresis loop energy for low θ condition under load (stress)-controlled situation. The reverse is true for displacement (strain)-control.

Further, the mechanism of dynamic strain ageing has been identified by estimating the activation energy (Q) for the process. The T-dependence of effective crack tip strain rate can be expressed as,

$$\dot{\varepsilon}_{tip,eff} = Ae^{-Q/R_gT}$$

where A is a constant, R_g is the gas constant and T is in K. Q values estimated for 623-723 K for different da/dN values were in the range 55-80 kJ/mol (Figure 3) which is same as that for carbon diffusion in ferritic steels (47-90 kJ/mol) suggesting that dynamic strain ageing, controlled by interstitial diffusion is responsible for the T-dependent changes in fatigue crack growth behaviour observed in the present study.

Ratcheting behaviour of 316LN SS

Ratcheting is the progressive directional accumulation of deformation due to asymmetric loading in structures. In sodium cooled fast reactors (SFRs), high amount of strain accumulation due to ratcheting can appreciably thin down structural components in the primary sodium circuit. Therefore, ratcheting is one of the prime considerations in the design of piping components. Since the operating temperature of SFRs (~820 K) encompasses the dynamic strain ageing regime for 316LN austenitic stainless steel, it is essential to investigate the manifestations of dynamic strain ageing in ratcheting. The influence of dynamic strain ageing on the ratcheting behavior of the above steel was investigated as a function of mean stress (σ_m), stress amplitude (σ_a) and temperature. dynamic strain ageing offers a high resistance to deformation due to locking of mobile dislocations by the solute atoms. As a result, cycle by cycle

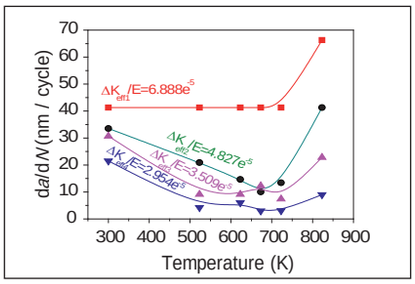

Fig. 1 *Cyclic rack growth rate as a function of temperature for different levels of $\Delta K_{eff}/E$*

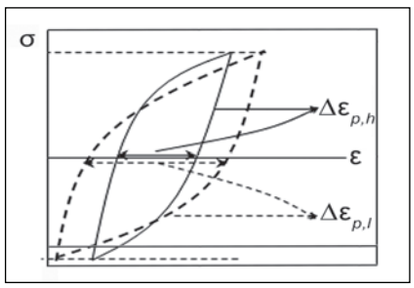

Fig. 2 *Schematic hysteresis loops under stress controlled fatigue. $\Delta\varepsilon_p$,h : high θ , $\Delta\varepsilon_p$,l : low θ*

strain accumulation was observed to be very slow, thus extending the life of the material. Test results obtained under different combinations of σ_m- σ_a were analyzed at 823 K, in order to arrive at a map delineating different deformation regimes occurring in presence of dynamic strain ageing viz. Ratcheting (continuous accumulation of strain), strain burst (sudden avalanche of strain) and elastic shakedown (fully elastic deformation). The ratio of mean stress and stress amplitude (σ_m/σ_a) plotted as a function of hysteresis energy (loop area) showed that, at a critical value of this ratio, there is a transition from ratcheting to elastic shakedown (Figure 4). Since elastic shakedown occurring under the influence of dynamic strain ageing is a desirable condition in the design of structural components against ratcheting, (σ_m/σ_a) ratio beyond the critical value will ensure that shakedown will prevail.

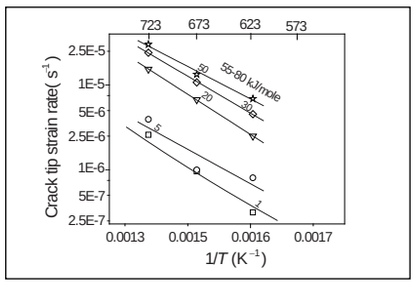

Fig. 3 T-dependence of crack tip strain rates for various da/dN values in the DSA range 623-723 K

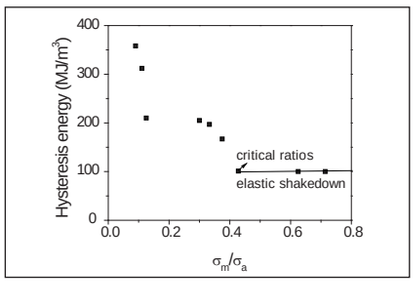

Fig. 4 Variation of hysteresis energy with σ_m/σ_a showing transition from ratcheting to elastic shakedown at 823 K

V.3 Molecular Dynamics Simulation of Deformation and Fracture Behaviour of bcc-Iron and Copper Single Crystals under Tensile Loading

Molecular dynamics simulation of mechanical behaviour of materials is of significant interest to researchers in the fields of nano-mechanics and in multi-scale modelling. molecular dynamics simulation provides valuable insights into operative deformation and damage mechanisms, as formation of lattice defects and cracks and their movement under different loading conditions can be visualized and correlated with observed mechanical response. molecular dynamics simulations of tensile behaviour of initially defect-free single crystals of Fe (bcc) and Cu (fcc) with suitable interatomic potentials have been carried out. LAMMPS software package with rectangular simulation box containing about 30000 atoms is used. The specimen was periodic only in z [001] direction, which was also the loading direction. NVE (where number of particles, volume and energy are fixed) ensemble was employed with pressure control by Berendsden Barostat and temperature control by velocity rescaling method. Tensile deformation on Cu has been simulated at 10 K with a strain rate of 1×10^9 s^{-1}, whereas single crystal iron was investigated in the temperature range 10-900 K with strain rates of 5×10^8, 5×10^9 and 5×10^{10} s^{-1}. A few simulations were also carried out under adiabatic conditions.

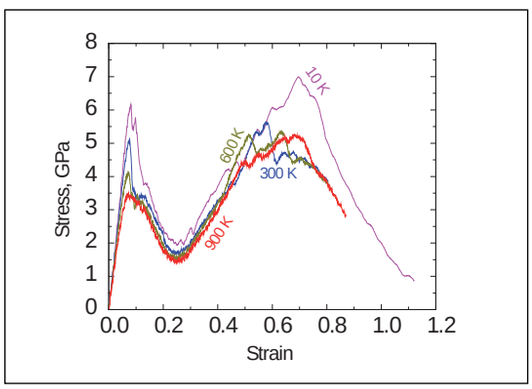

Fig. 1 Tensile behaviour of single crystal bcc iron

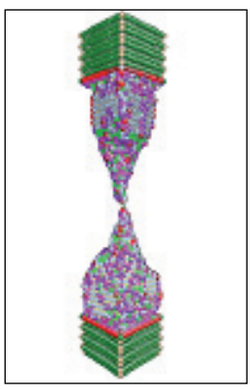

Fig. 2 Necking in single crystal of iron

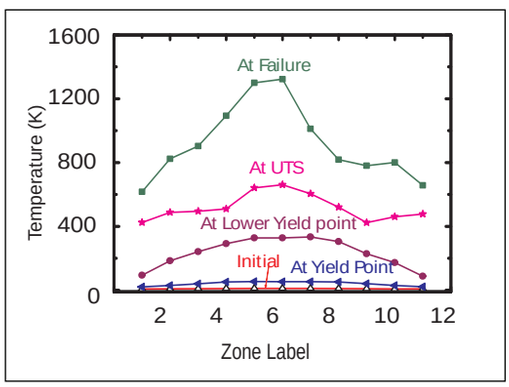

Fig. 3 Temperature distribution along the specimen under adiabatic conditions

The stress-strain response in Fe was characterised by a rapid increase in stress to a peak value followed by significant stress drop (Figure 1). The drop in stress was attributed to initiation of dislocations and due to phase transformation from bcc to fcc (14%). The stress thereafter increased up to ultimate tensile strength. Beyond ultimate tensile strength, development and growth of necking (Figure 2) resulted in rapid decrease in flow stress with strain. Yield strength and ultimate tensile strength are found to decrease with increase in temperature and decrease in strain rate. Under adiabatic conditions, temperature across the specimen increased with plastic deformation and showed a peak in the region where necking would initiate (Figure 3).

Tensile behaviour of single crystal Cu was characterized by sharp rise in stress in elastic regime followed by significant drop on dislocation nucleation (Figure 4). Half dislocation loops are observed to initiate from surface at the onset of yielding and propagate into the specimen on further straining (Figure 5a). The dislocation density was estimated from the images as total dislocation line length/volume. An important outcome of this simulation is that the variation in dislocation density with strain could be correlated with the tensile stress-strain response (Figure 4). The material invariably failed by necking and an interesting observation is that pentagonal arrangement of copper atoms was seen in the necked region (Figure 5b). It is planned to extend the molecular dynamics simulation studies to binary and ternary systems with larger system sizes and with detailed investigation on microstructural evolution.

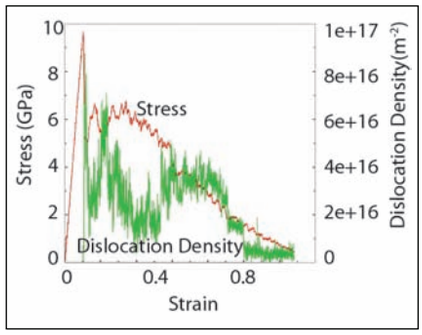

Fig. 4 *Tensile behaviour of copper superimposed with dislocation density*

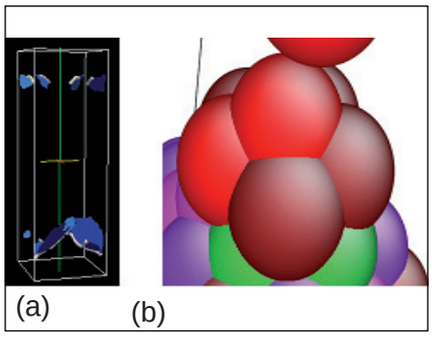

Fig. 5 *In copper (a) Half dislocation loops initiate on the surface at the onset of yielding and (b) Pentagonal arrangement of atoms in the neck*

V.4 Acoustic Emission and Thermography Studies during Hydrotesting of Stainless Steel Pressure Vessels with Artificial Defects

Nondestructive evaluation techniques are useful for structural integrity assessment as well as condition monitoring of operating components. On-line monitoring of pressure vessels during hydrotesting using acoustic emission and Infrared thermography enable detection of deformation as well as damage to the vessel under pressure and detection of growing defects, if any. Acoustic emission technique is based on the generation of transient elastic waves by rapid release of energy from localized sources in materials and is useful for detection of dynamic changes taking place in the component, while infrared thermography technique maps the temperature change on the surface of the component due to energy release during deformation and crack growth.

Cylindrical pressure vessels were fabricated from AISI type 304 austenitic stainless steel pipe (250 Niobium and schedule 10). Both the ends of the pipes were closed with sheets (3 mm thickness) of the same material. At one end of the vessel, defects (diameter 40 mm) of different depths (1.8 mm, 2.2 mm and 2.5 mm). were machined in the center of the closure sheet, in order to initiate failure during hydrotesting. A non-conducting rubber sheet was used to cover the closure end of the vessels containing the defects to prevent water entering in to the defect region. Figures 1a and 1b show the photograph and thermal image of one of the vessels.

Hydrotesting of the vessel was carried out upto failure. The acoustic emission signals generated during the hydrotesting were recorded using a 150 kHz resonant sensor. Simultaneously infrared thermography imaging was carried out using an infrared camera.

During the hydrotest, pressure was increased continuously

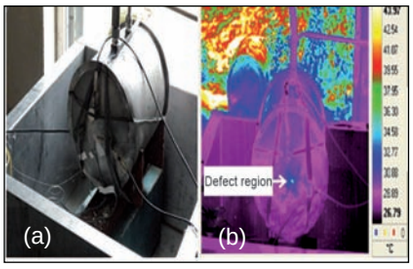

Fig. 1 (a) Photograph and (b) Thermal image of the vessel with defect depth 2.5 mm

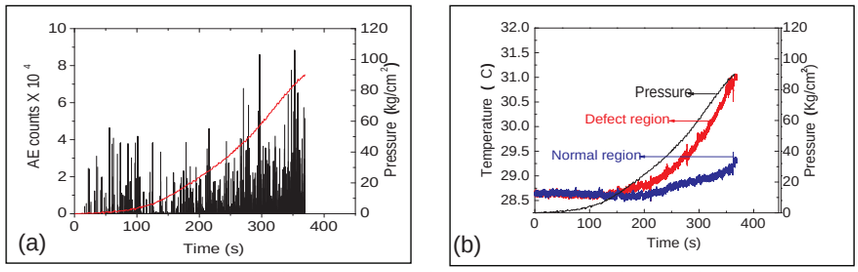

Fig. 2 (a) Acoustic emission counts and pressure versus time and (b) Temperature rise and pressure versus time for defect depth of 2.2 mm

with time. Figure 2a shows the applied pressure and the acoustic emission counts generated during the hydrotest for the vessel with 2.2 mm deep defect. The variation in pressure and temperature rise as a function of time is shown in Figure 2b. It can be seen from Figure 2a that acoustic emission signals are generated from the beginning of the pressurization and the acoustic emission counts increase with time. The acoustic emission signals generated are attributed to the occurrence of deformation in the vessel due to increase in the pressure. The acoustic emission generated is also due to localized deformation in the defect region and initiation and growth of cracks leading to final leakage.

It can be seen from Figure 2b that the temperature in the defect region as well as in the surrounding normal regions increase with time as expected. The temperature rise during hydrotesting of the vessel is attributed to the deformation occurring during the pressurization process. Nevertheless, the temperature rise in the defect region is much higher as compared to that in the normal region, particularly beyond 25 kg/cm^2. The acoustic emission total count also increases at higher rate beyond this (Figure 2a). This can be attributed to the localized deformation and crack growth in the defect region which releases higher amount of thermal energy, compared to the surrounding regions as well as acoustic emission.

It can also be seen that the rise in temperature is higher for the vessel with deep defect. These results assume importance for structural integrity assessment of pressure vessels where detection of more acoustic emission signals and associated rise in temperature can give an advance warning about an impending failure of operating vessels by nondestructive means.

V.5 Imaging NDE Techniques for Characterization of Inhomogeneous Plastic Deformation

Multi modal imaging non contact, nondestructive techniques like Infrared thermography (IRT) and Digital image correlation (DIC) have now been recognized as efficient tools for deformation characterization. These novel techniques have the capabilities of reflecting the microscopic dislocation activities by means of macroscopic thermal and strain fields evolutions. These techniques are to apply study Lüders band phenomenon - involving inhomogeneous plastic deformation which affects the surface quality of steel products produced during metal forming operations. Emphasis has been placed on studying the evolution of pre-yield plastic micro-strain and its influence on the nucleation and formation of Lüders band. It has been observed that in

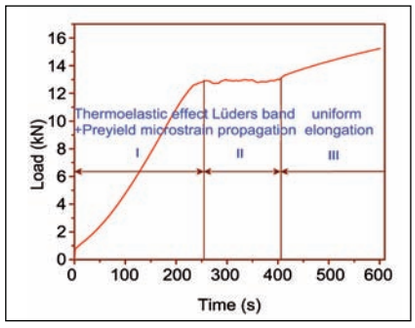

Fig. 1 Load variation with time obtained for the specimen of dimension 100x25x1.6 mm

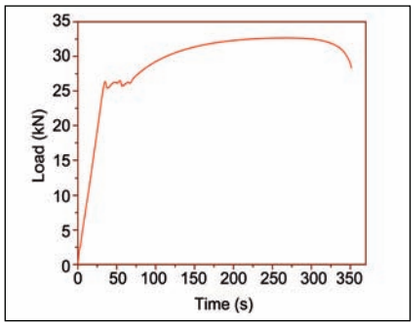

Fig. 2 Load variation with time obtained for the specimen of dimension 100 x 25 x 2.6 mm

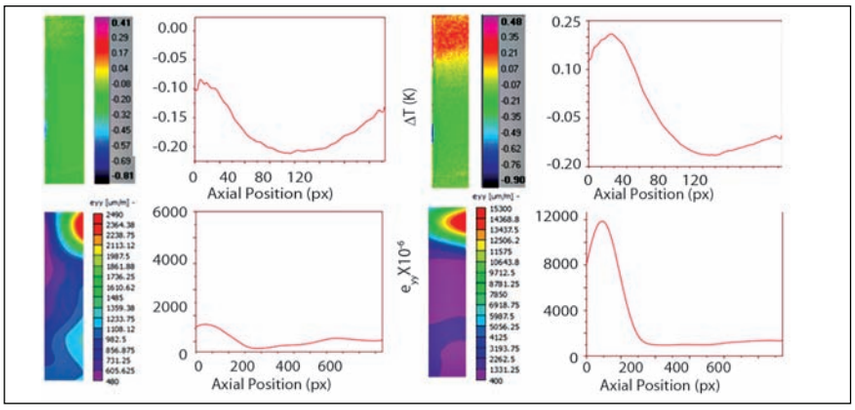

Fig. 3 *Thermal, strain fields and their axial profiles in the interval of 210-254 seconds*

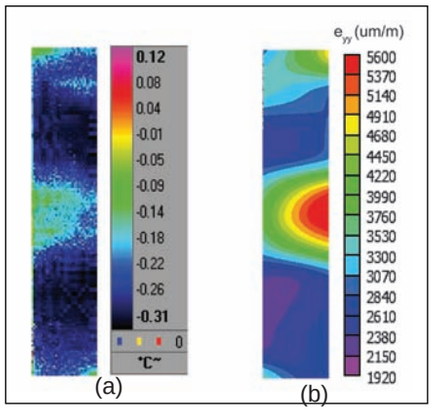

Fig. 4 *(a) Thermal and (b) Strain field at 35 seconds*

both thermal and optical images, the zone of formation of Lüders band is much before the macroscopic yield point which has significant industrial application for monitoring the safety of stressed components to take preventive action against plastic deformation of structural components. Influence of generation of pre-yield plastic microstrain on band nucleation and propagation in a welded material is also studied through associated thermal and strain field evolutions.

Studies on preyield plastic microstrain

The load variation with time obtained for the specimen of dimension 100x25x1.6mm deformed at 1.3x10^{-4}/s strain rate is presented graphically in Figure 1. Region I is where two phenomena namely thermoelastic effect and pre-yield microstrain occur. Region II characterizes propagation of Lüders band. In region III, uniform strain hardening along the gauge length takes place.

It is observed that after 200 seconds, temperature and strain increases in the upper end region which confirms the existence of non-uniform plastic deformation in the upper end region before the onset of macroscopic yield point (at 254 seconds) as shown in Figure 3. This shows that microstrain which fluctuates initially becomes stable on a local zone (fillet region) under the influence of stress concentration induced by gripping. This study also reveals the potential of these techniques in providing better visualization of the zone of band formation much ahead of the upper yield point (at 254 seconds).

Lüders deformation in welded mild steel

The load variation with time obtained for the specimen of dimension 100x25x2.6 mm which is tungsten inert gas welded at the centre and deformed at 8.3 x 10^{-4}/s strain rate is presented graphically in Figure 2. At 35 seconds corresponding to upper yield point it is found that pre-yield microstrain which fluctuates initially forms Lüders band at the centre of the gauge length in the weld zone and at the ends of the gauge length as shown by thermal and strain fields in Figures 4a and 4b. This is because of the stress concentration induced in these zones due to gripping and welding process.

Generally, in Lüders band deformation, at the end of load plateau band propagation (either single or two bands) will cover the entire gauge length. But in welded specimen it is found that at the end of load plateau corresponding to 67th second bands ceased to propagate in the weld zone as shown in Figure 5. This is because in welded mild steel, strength of the heat affected zone and weld zone is higher than that of the base metal and so stress required for yielding these zones is higher than that of base metal.

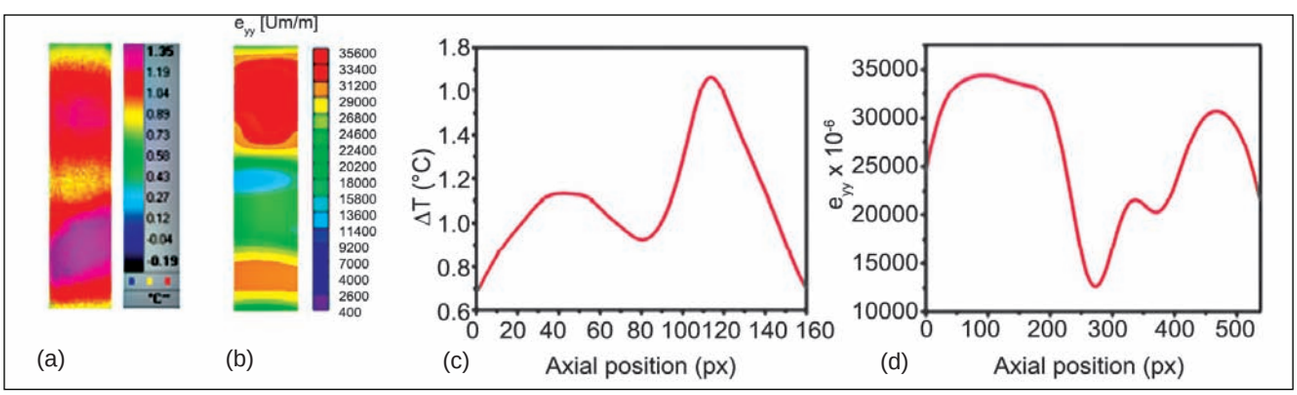

Fig. 5 *(a)Thermal, (b) strain fields and (c) and (d)their axial profiles at 67th second*

V.6 Immersion Ultrasonic Technique for Characterization of Delamination in Coatings

Electrodeless nickel deposition is widely used for developing nickel phosphorus and nickel boron (Ni-B) coatings Ni-B coatings are one of the most widely used in strategic industries due to its good corrosion, wear resistance and excellent hardness.

The inspection of coatings for coating thickness evaluation, thickness variation and debond detection is important before using them in field since if the coating thickness is not up to the desired level and if the coating to substrate adhesion is not good, it will lead to failure of the system. Most of the inspection for coating thickness measurement and adhesion quality inspection involves destructive testing (Metallography). Non destructive testing methods are promising tools for coating thickness and debond evaluation due to their ability to inspect nondestructively. Ultrasonic testing is the most widely used nondestructive testing method to determine the quality of coatings due to following reasons:

- Uniform coupling
- Spherical, cylindrical and linear focusing either with phased array or with concave acoustic lenses which increases the sensitivity to smaller defects
- Use of very high frequencies which give reduced ultrasonic beam width and much higher resolution
- Inspection over uneven surfaces
- Ultra high resolution C-scan imaging
- Large area mapping and
- Inspection of complex geometries.

In the present work we discuss the inspection of Ni-B coatings on AISI 316 L SS plate with coating thickness 75 µm for debond detection using Ultrasonic immersion technique. The substrate thickness was 3.6 mm.

The immersion ultrasonic experimental set up is shown in Figure 1. The scanning system used for the experiment was specifically designed and fabricated. Number of stages in manipulators available in this system is 5 (X, Y, Z, α, and θ); for scanning planar and cylindrical objects. Maximum scanning distance possible in X and Y axes is 500 mm and that in Z axis is 250 mm, scanning angles possible in α and θ stages is ±360° with lead screw accuracy 0.02 mm per 300 mm and traverse speed 50 mm/s. Ultrasonic transducer used for scanning was 5 MHz spherically focused immersion probe of 9 mm diameter from M/s Panametrics. The transducer was excited by PR5900 pulsar-receiver from M/s Olympus through a double shielded microdot cable.

Preliminary studies were carried out on a 3 mm thick austenitic stainless steel plate of dimensions 150×100×3.54 mm. On this plate several circular notches of different diameter at various depths were fabricated by EDM method. Minimum material thickness over the notches was 230 µm. All the notches were made on the same face of the plate. This plate has been immersed in DM water and immersion scanning has been carried out over the plate by keeping the circular notches opposite to the scanning side. Scanning resolution given was 0.2×0.2 mm. A particular C-scan image of this plate is shown in Figure 2a. With this experimental set up, Ni-B coated (coating thickness 75 µm) specimens have been subjected to immersion ultrasonics. The coated side was kept at the top (facing the transducer) during scanning.

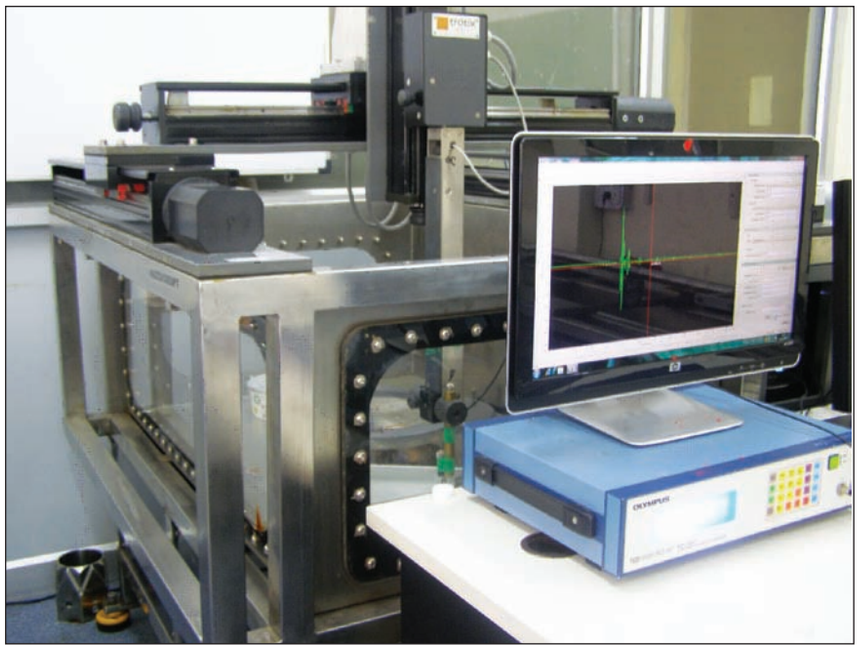

Fig. 1 *Immersion ultrasonics experimental set up*

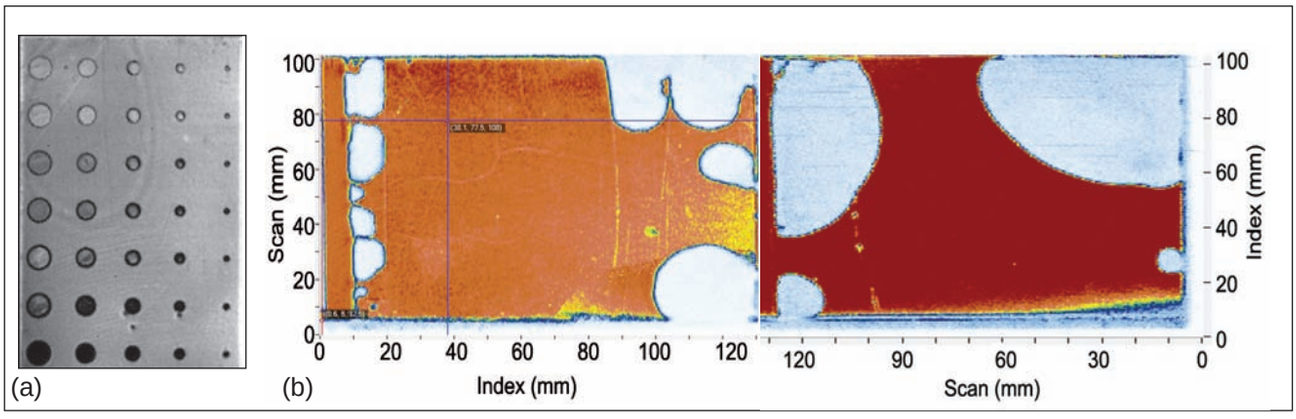

Fig. 2 *C-scan image of (a) SS plate with circular notches and (b) Ni-B coated plates indicating delamination*

The C-scan image is shown in Figure 2b. The light colored region is due to the lack of back wall reflection which is caused by the debonding.

In conclusion, it is demonstraed that immersion ultrasonic testing can be used to find out the debonding accurately. Since this technique is a non-contact one, this can be applied on irregular geometries as well as on the surfaces which are not even.

V.7 The Role of Magnetic Contribution on Influencing the Stability of Fe-Cr Alloys: A Calorimetric Investigation

The Fe-Cr binary system forms one of cornerstones of ferrous metallurgy. Over the years, this system has been subjected to extensive experimental investigations and a vast database with regard to high temperature phase equilibria, s-phase precipitation and γ/α phase boundary, have been accumulated. For long, this database served as the resource base for many critical assessments and modelling of phase diagram, including low temperature equilibria, that is below 750 K.

It is only in the past decade, careful small angle neutron scattering experiments have suggested a serious revision of less than 1000 K phase equilibria to be mandatory, in that about 8 to 10 wt.% Cr has been found to dissolve in α-Fe disordered terminal bcc solid solution phase. Further, for compositions in the range 9-12 wt.% Cr, the stable state of the alloy is actually α' (Fe-rich bcc)+α" (Cr-rich bcc) two phase mixture. The α'/α" miscibility gap is crossed at about 923 to 973 K for compositions of 9-12 wt.% Cr. It is interesting to recall that this composition range lies in the domain of interest of nuclear grade ferritic steels.

On the theoretical front, numerous first principles/density functional theory calculations on phase stability have supported these experimental findings rather broadly and further added that it is Fe-Cr magnetic interaction which favour short range magnetic ordering that confers extra stability by the way of providing a small negative contribution to formation enthalpy. Since then, very few calorimetry experiments have been performed to quantify the various contributions to the thermodynamic stability of Fe-Cr alloys. It is amidst this scenario, that a research initiative has been launched to investigate the thermodynamics of Fe rich Fe-Cr alloys by calorimetry. The following is brief summary of the major findings on Fe-20 wt.% Cr alloy.

Small two gram buttons have been prepared from high pure starting material (99.995 %) by arc-melting, followed by five hours-annealing at 1423 K. The X-ray diffraction, optical microscopy and scanning electron microscopy/energy dispersive X-ray spectrometer analyses have attested to the presence of $\alpha'+\alpha$" two phase mixture. The slow (3 K/min) heating differential scanning calorimetry (DSC) scan (Figure 1) has revealed the presence of three distinct features:

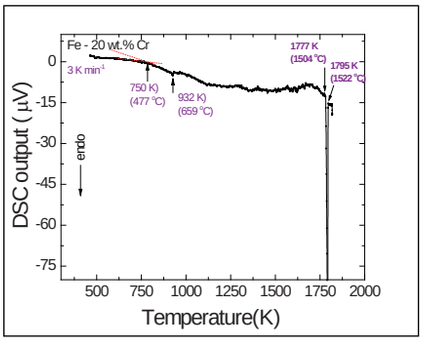

Fig. 1 *Slow scan DSC trace of Fe-20 wt.% Cr alloy*

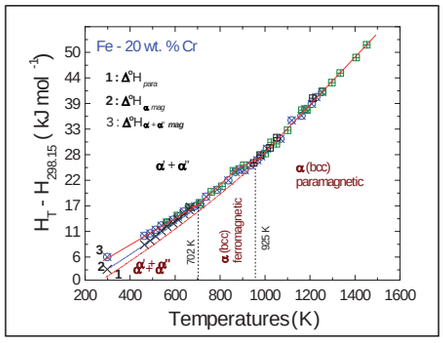

Fig. 2 *Enthalpy increment variation with temperature for Fe-20 wt.% Cr alloy*

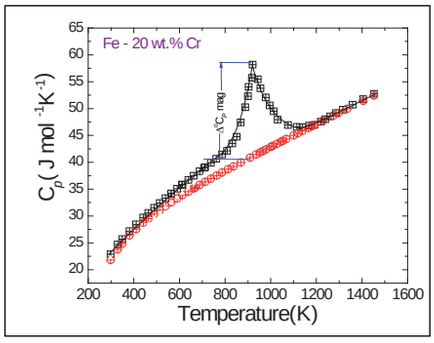

Fig. 3 *Specific heat variation with temperature showing both magnetic and nonmagnetic contribution*

(i) at about 750 K, the α'+α" two phase mixture begins to enter into the single phase a domain, which of course is not complete for kinetic reasons; (ii) the onset of ferro to paramagnetic transition of the a phase at about 932 K, which is followed by melting at 1777 K.

The isothermal inverse drop calorimetry measurements of enthalpy increment (H_T-$H_{298.15}$), performed over the temperature range 400-1473 K (Figure 2) have quantified the enthalpy effects accompanying both the α'+α"→α reaction and $\alpha^{ferro} \rightarrow \alpha^{para}$ transition at T_c. The deconvolution of the enthalpy data carried out by standard theoretical procedures further yielded the specific heat (C_p) variation, due both to magnetic and nonmagnetic contributions as a function of temperature (Figure 3).

It is clear that C_p^{mag} makes a substantial contribution to the overall stability. Further studies on quantifying the effect of Cr-concentration are currently underway.

V.8 Thermochemistry of Systems Involving Fuel and Control Rod Materials

Gibbs energy of formation of U-Sn intermetallic compounds

Gibbs energies of formation of the intermetallic compounds, USn_3, U_3Sn_7, USn_2 and USn were determined by using four different high temperature molten salt galvanic cells of the type: U(s)// UCl_3 in LiCl-KCl (eutectic)//U-Sn alloy, where pure uranium was used as one of the electrodes and a two phase alloy of uranium and tin as the other. The two phase alloys used in four cells as the electrodes were <USn_3> + {Sn}, <U_3Sn_7 + USn_3>, <USn_2 + U_3Sn_7> and <USn+USn_2>, respectively. The Gibbs energies of formation of USn_3, U_3Sn_7, USn_2 and USn with respect to α-U and liquid Sn, in the temperature range 682-905 K, were computed from the measured emf values. The present Gibbs energy of formation of USn_3 is found to be in very good agreement with the data of Y Johnson et al. obtained by using the molten salt emf method. However, the values obtained by vapor pressure method by Alcock and Grieveson were more positive than the rest (Figure 1). Their values are plausibly in error owing to the inaccuracies arising from the experimental procedure or due to the uncertainties in the auxiliary data employed in arriving at the values of the vapor pressure or both.

Ours are the first experimental data for the Gibbs energy of formation for U_3Sn_7, USn_2 and USn. The enthalpies of formation of USn_3, U_3Sn_7, USn_2 and USn calculated from the measured emf values at the mean temperature $\Delta_f G°(Usn_3)$ of measurement

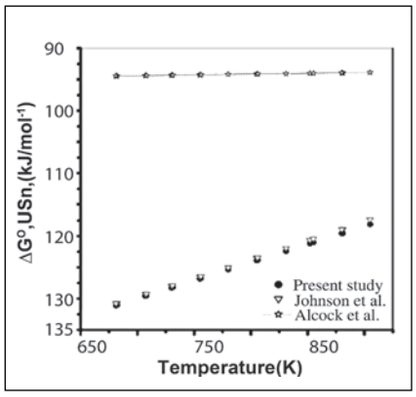

Fig. 1 *Temperature dependence of Gibbs energy of formation of USn_3*

are –172.8, –527.8, –174.9 and –176.9 kJ mol^{-1} whereas the values computed using Miedema's model are –132.09, –393.6 –129.83 and –110.62 kJ mol^{-1} respectively. Though the trends in the two sets of enthalpy data as a function of Sn concentration are similar, the Miedema's values are less exothermic. It is known that Miedema's values are based on assumption of regular solution whereas U-Sn system shows more negative deviation from ideality.

The partial molar excess Gibbs energy of uranium in the saturated solution of tin computed from our studies are in good agreement with the values reported by Johnson et al. in the temperature range 500-800 K.

Gibbs energy of formation of intermetallic compounds with respect to α-U and liquid Sn in the temperature range 682-905 K are given below:

$$\Delta_f G^\circ (USn_3)(kJmol^{-1}) = -172.8 + 0.061T(K)$$

$$\Delta_f G^\circ (U_3Sn_7)(kJmol^{-1}) = -527.8 + 0.200T(K)$$

$$\Delta_f G^\circ (USn_2)(kJmol^{-1}) = -174.9 + 0.073T(K)$$

$$\Delta_f G^\circ (USn)(kJmol^{-1}) = -176.9 + 0.064T(K)$$

Reaction of B, B_2O_3 and B_4C with Na_2CO_3

A thermogravimetric study of reaction of sodium carbonate with elemental boron, B_2O_3 and B_4C was conducted under flowing argon. The reaction products were further subjected to transpiration thermogravimetric measurements. Some residues were subjected to Knudsen effusion mass spectrometry and thermal ionisation mass spectrometry as well. The present study is a sequel to two previous experimental observations related to:

1) Steep fall in vacuum in thermal ionisation mass spectrometry when the filaments containing the mixture of Na_2CO_3 and B (or H_3BO_3 or B_4C) were being heated to measure the boron isotope ratios; and
2) The detection of $Na_2BO_2^+$ as the only boron containing positive ion in thermal ionisation mass spectrometry, at variance with the Knudsen effusion mass spectrometry results on $NaBO_2$(s) which showed $NaBO_2^+$ as the principal ion, originating from the major species $NaBO_2$(g) and $Na_2BO_2^+$ as a much less intense ion, originating from the minor species $(NaBO_2)_2$ (g).

The thermograms recorded over (B+Na_2CO_3), (B_2O_3+Na_2CO_3) and (B_4C+Na_2CO_3) mixtures consistently revealed onset of chemical decomposition of Na_2CO_3 at temperatures much lower than the temperatures at which pure Na_2CO_3 would undergo thermal decomposition. The results of the transpiration thermogravimetric measurements were in accord with those reported for $NaBO_2$, indicating that the reactions were complete. The mass spectrometric examination of the residues from transpiration thermogravimetric measurements re-affirmed the predominance of $NaBO_2^+$ in Knudsen effusion mass spectrometry and $Na_2BO_2^+$ in thermal ionisation mass spectrometry leading to the inference that even in thermal ionisation mass spectrometry, it is only the monomeric species $NaBO_2$(g) that yields Na^+ as well as $Na_2BO_2^+$, by through two processes that occur on the filament surface: $NaBO_2 \rightarrow Na^+(BO_2)^-$ and $NaBO_2 + Na^+ \rightarrow Na_2BO_2^+$. The essential inferences from the results of thermogravimetric measurements can be summarized as follows: formation of sodium borates under flowing argon occur in all the above cases at T ≤ 973 K, evidently facilitated by the onset of chemical decomposition of Na_2CO_3 at temperatures where the normal decomposition pressure of Na_2CO_3 is ≤ 2 x 10^{-5} Pa; the reaction involving boron (be it as element or B_4C) at different stages is dictated by the magnitude of the effects of two reactions, one involving oxidation of B (or B_4C) and the other involving chemical decomposition of Na_2CO_3 presumably by B_2O_3 which has its onset at ~873 ± 50 K and the two reactions act in tandem towards the eventual formation of sodium borates.

Thermophysical properties of uranium-neodymium mixed oxides

Rare earths constitute a significant fraction of the fission products in the irradiated oxide fuel. The major component among these is Nd (Fission yield = 20 at. %). Rare earth oxides form substitutional solid solutions with UO_2. Knowledge of the solubility of these oxides, as well as the thermophysical properties such as heat capacity and thermal expansion are useful in understanding the in-pile behaviour of the fuel. As part of the investigations, the system U-Nd-O was investigated recently. The solid solutions $(U_{1-y}\ Nd_y)O_{2\pm x}$ with values of y ranging from 0.2 to 0.85 were prepared by the citrate gel-combustion route and sintered at 1873 K. The room temperature X-ray diffraction patterns of these solid solutions are shown in Figure 2. It is evident from the latter that those samples with Nd fractions (y) between 0.2 and 0.8 comprised a solid solution with the well-crystallized fluorite structure, whereas additional hexagonal Neodymium oxide lines (HXN) were visible for y>0.80. Therefore, it can be inferred that the solubility limit of $NdO_{1.5}$ in uranium oxide lies between the y values of 0.80 and

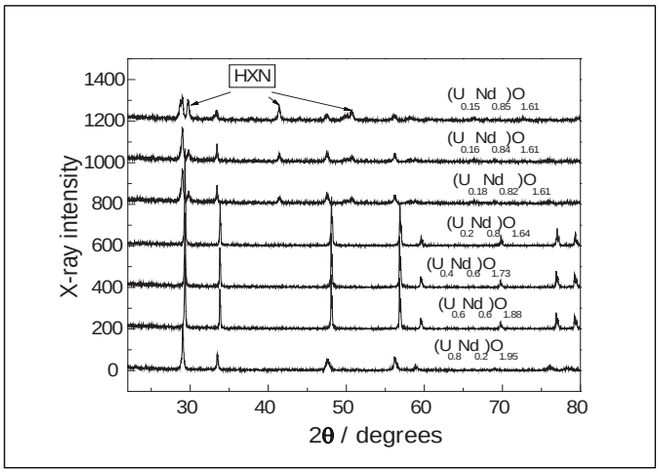

Fig. 2 *Room temperature patterns of $(U_{1-y}\ Nd_y)O_{2\pm x}$*

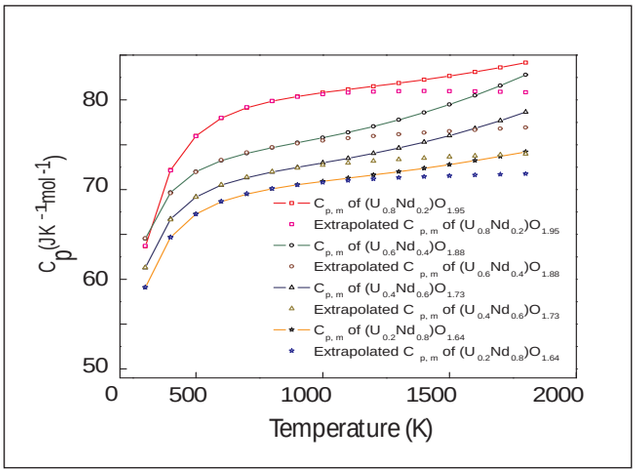

Fig. 3 *Temperature dependence of the heat capacity of $(U_{1-y}\ Nd_y)O_{2\pm x}$*

0.82. Measurements on the lattice thermal expansion of $(U_{1-y}\ Nd_y)O_{2\pm x}$ (y=0.2, 0.4, 0.6, 0.8) were carried out by using high temperature X-ray diffraction in the temperature range 298-1973 K. The coefficient of thermal expansion (α_m) in this temperature range for $(U_{1-y}\ Nd_y)O_{2\pm x}$ (y=0.2, 0.4, 0.6, 0.8) were found to be 16.46, 16.64, 16.79, 16.89×10^{-6} K^{-1} respectively . It is evident that α_m increases with the Nd content in the solid solution. This is commensurate with the progressive displacement of the strong U^{4+}- O^{2-} bond with Nd^{3+}- O^{2-} bond with a diminished magnitude of bond strength. This in turn leads to an enhancement of the anharmonicity in the lattice vibrations leading to a higher thermal expansion.

Heat capacity and enthalpy increment of $(U_{1-y}\ Nd_y)O_{2\pm x}$ (y=0.2, 0.4, 0.6, 0.8) were measured by using DSC and drop calorimeter in the temperature range 298-800K and 800-1800 K respectively. Heat capacity data in the temperature range 800-1800 K were computed from the measured values of enthalpy increments. These values are plotted together in Figure 3 which reveals an anomalous increase in the heat capacity with temperature in the temperature range 900-1000 K. This was attributed to the ease of formation of the Frenkel defect pair in the UO_2 lattice due to the incorporation of an aliovalent cation, viz., Nd^{3+}. The enthalpy of defect formation was estimated to be 1.03 to 1.05 eV from the excess heat capacity values.

V.9 Application of Pulsating Sensors

Conductivity monitoring technique to study chemical speciation-application to reaction of Na_2SiO_3 and HCl

Some of our recent investigations on application of chemical speciation to study reaction of Na_2SiO_3 and HCl using conductometric titration approach have been presented in this report.

A fixed volume of standard sodium silicate solution [concentration varies from 1 to 20 ppm (mg/l SiO_2)] was taken in a 25 ml beaker. A vertical Teflon conductivity probe with a pair of Pt electrodes used as sensing electrodes was placed inside the solution. The reactant was added to the analyte in steps of small volume of addition under continuous stirred condition. The change in conductivity and volume of addition of titrant were monitored online using two different channels. The online titration plot thus generated in each case was analysed to give information of different species formed during titration.

Figure 1 shows a typical online titration plot obtained during titration of 20 ppm SiO_2 against 0.1 N HCl. Sudden decrease in conductivity in region 1 (channel-4 of Figure 1) is due to replacement of highly conducting OH^- ion, formed due to hydrolysis of a part of Na_2SiO_3 as indicated below, by less conducting chloride ion refer (Equation 1). The major

unhydrolysed Na_2SiO_3 undergoes following two steps reaction refer (Equations 2 and 3).

These two steps reaction are supported by the following conductivity shift as shown in regions 2 and 3 of the online titration plot. The slope change with small decrease in conductivity in that region is attributed due to replacement of silicate ion by Cl^- and $HSiO_3^-$ ion, the sum of molar conductance of Cl^- and $HSiO_3^-$ being slightly less than that of SiO_3^{2-}. The increase in conductivity at region 3 is due to replacement of less conducting $HSiO_3^-$ ion by relatively more conducting chloride ion.

When concentration of Na_2SiO_3 falls to 1 ppm SiO_2 level the pattern of conductivity plot is entirely different which indicates that the reactant reacts with the analyte in different way. Before the onset of titration a part of sodium silicate undergoes hydrolysis and rest reacts with dissolved carbon dioxide present in the sample as represented in Equations 4 and 5 (Table 1).

Initial decrease in conductivity in region 1 is due to replacement of more conducting OH^- ion by less conducting Cl^- ion. The increase in conductivity in region-2 is due to replacement of $HSiO_3^-$ (generated from reactions 4 and 5) by relatively more conducting Cl^- ion (refer Equation 6 in Table 1). Further change in slope associated with increase in conductivity in region 3 is due to replacement of HCO_3^- (refer Equation 7 in Table 1) by more conducting Cl^- ion.

Sharp increase in conductivity in region 4 is due to build up of unreacted HCl. When titration is carried out in argon flushed condition the bicarbonate region does not appear which shows the absence of dissolved carbon dioxide in the sample.

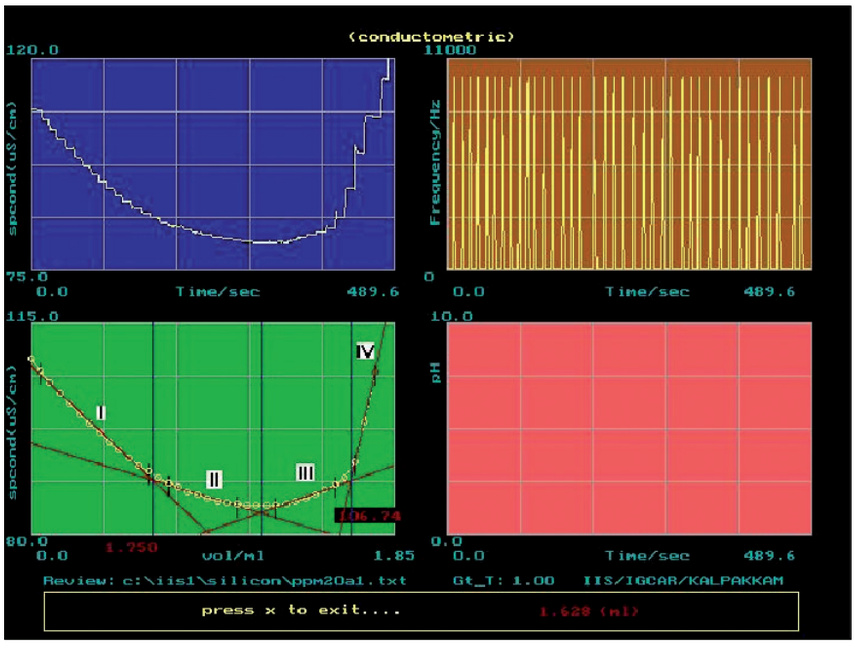

Fig. 1 *An online titration plot obtained during titration of 20 ppm SiO_2 against 0.1 N HCl*

From this investigation, it is interesting to note that with a simple approach it is possible to explore quantitative information of chemical species in a composite sample matrix. It also provides excellent information regarding various stages of chemical reactions present in a composite system. There is further scope of using this finding to look for a simple analytical technique for assay of silica.

Studies on oscillating chemical reaction using pulsating sensor

Unlike other chemical reactions, the oscillatory chemical reaction is a highly complex and far from equilibrium dynamic system which attracted attention of researchers. In this type of reactions, a specific reaction intermediate species plays vital role. The oscillation in the concentration of intermediate product arises till the system remains far from equilibrium. The most important criteria for this kind of chemical oscillator are:

(i) It should be far from equilibrium which implies that the change in free energy must be large and negative

(ii) It should contain at least one autocatalytic step or alternatively cross catalytic steps between two steps and

(iii) There should be at least two steady states under the initial condition.

In oscillatory chemical reaction periodic or cyclic changes in the concentration of some of the intermediates occur which can be monitored by change in colour or other physical parameters, e.g. redox potential, pH, absorbance etc. Hence, in order to characterize chemical oscillating reactions several analytical techniques viz. potentiometry, spectrophotometry, chemiluminescence and spectrofluorometry etc. were used depending upon the nature of systems being investigated. High resolution and fast response redox potential monitoring device using pulsating sensor based instrumentation developed in IGCAR has been deployed to characterize a halogen free oscillating chemical reaction (Cu(II)-catalyzed-H_2O_2-KSCN-

NaOH) in a much simpler way. Special attention has been focused to enhance the speed of the reaction by considerably reducing the period of oscillation by normalizing the temperature and flow rate of reactants. Finally, the oscillatory chemical reaction has been deployed for rapid assay of chemicals using analyte pulse perturbation technique. In this work, following analyte pulse perturbation technique, we demonstrated rapid assay of hydrazine and uranium in aqueous solutions at trace levels using Cu(II)-catalyzed-H_2O_2-KSCN-NaOH oscillatory system. Probably for the first time we identified two new candidates viz. hydrazine and U(VI) which perturb oscillation in Cu(II) catalyzed-H_2O_2-KSCN-NaOH oscillatory reaction system.

A laboratory designed glass CSTR (continuous stirred tank reactor) bath of capacity ~ 20 ml, covered with a water recirculation jacket coupled with a high precision constant temperature bath with accuracy ± 0.1ºC was used to carry out experiments on oscillating reaction. A multichannel peristaltic pump was used to deliver three reactants to drain reaction product continuously at desired flow rates. Thus, the concentrations of all reagents were maintained constant throughout the experimental campaign. The solution in the bath was made homogeneous with a magnetic stirrer. A Hamilton micro syringe was used to dispense the perturbing analyte into the oscillating reaction system. A Pt-SCE (Saturated Calomel Electrode) couple was used and online change in pulse frequency which is directly related to emf during reaction was monitored online. The experimental setup is shown in Figure 2.

After getting online plots (time versus potential) at several constant temperatures and flow rates experiments were conducted

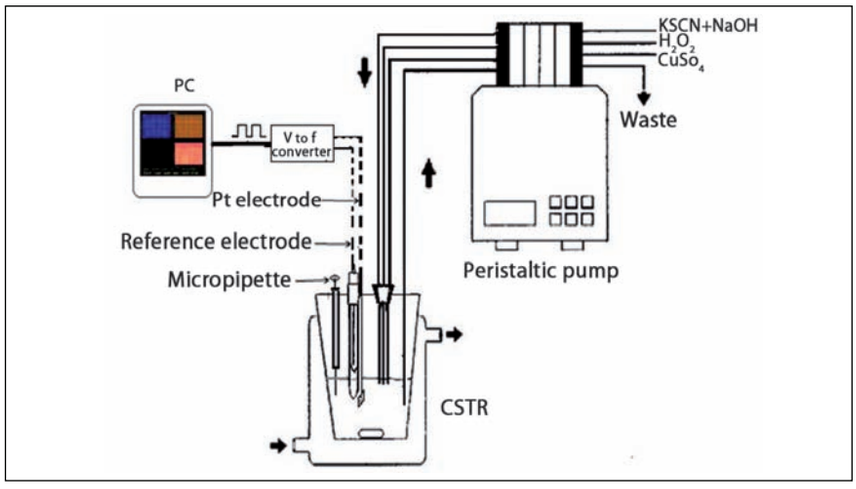

Fig. 2 *Experimental setup for oscillatory chemical reaction*

to see pulse perturbations in Cu(II)-catalysed-peroxide –thiocynate system using standard hydrazine and uranium solutions. Figures 3 and 4 show pulse perturbation peaks in the above OCR using uranium and hydrazine at different concentrations respectively. Usually perturbation of oscillation occurs when the added analyte interacts with the intermediate products of the reaction by its redox or chelating properties. Thus, feedback loops in oscillatory chemical reaction, the presence of which is important for oscillatory chemical reaction, are disturbed which ultimately result in perturbation. When hydrazine is added to this oscillatory system, it reacts with Cu^{2+} in alkaline medium as shown in Equation 8 of Table 1 .

Therefore, concentration of Cu^{2+} in the system becomes less and thus, positive feedback loop of this oscillatory reaction system is hindered. This may result in decrease in amplitude and period of oscillation. Similarly, in case of uranium, hydroperoxyl radical $HO_2^{\bullet}$ which is formed as an intermediate species in Cu(II)-catalyzed –KSCN-H_2O_2-NaOH oscillating reaction plays a vital role in maintaining negative feedback loop by destroying superoxyl Cu (I) complex is shown in Equation 9 of Table 1 .

Uranium metal ion (UO_2^{2+}) reacts with $HO_2^{\bullet}$ radical to form a stable radical complex [U(VI)- $HO_2^{\bullet}$]. Hence, due to deficiency of $HO_2^{\bullet}$ oscillation will be affected to some extent resulting in perturbation of oscillation peak. Calibration plots based on three independent measurements have been prepared in uranium and hydrazine assay at 3.2 - 31.1 µM and 14-110 µM of N_2H_4 concentrations level respectively. About 40-45 samples per hour

Table 1: List of reactions

S.No.	Equations
1	$Na_2SiO_3+H_2O \rightarrow NaOH+H_2SiO_3$
2	$Na_2SiO_3 + HCl \rightarrow NaCl + NaHSiO_3$
3	$NaHSiO_3 +HCl \rightarrow NaCl+H_2O+SiO_2$
4	$Na_2SiO_3 + H_2O \rightarrow NaOH + NaHSiO_3$
5	$Na_2SiO_3 + H_2O + CO_2 \rightarrow NaHCO_3 + NaHSiO_3$
6	$NaHSiO_3 + HCl \rightarrow NaCl + H_2O + SiO_2$
7	$NaHCO_3 + HCl \rightarrow NaCl + H_2O + CO_2$
8	$Cu^{2+} + 2N_2H_4 + 2OH^- = Cu \downarrow + N_2 + 2NH_3 + 2H_2O$
9	$Cu(I)\text{-}HO_2^+ + nSCN^- \rightarrow Cu(I)\ (SCN^-)_n + HO_2^{\bullet}$

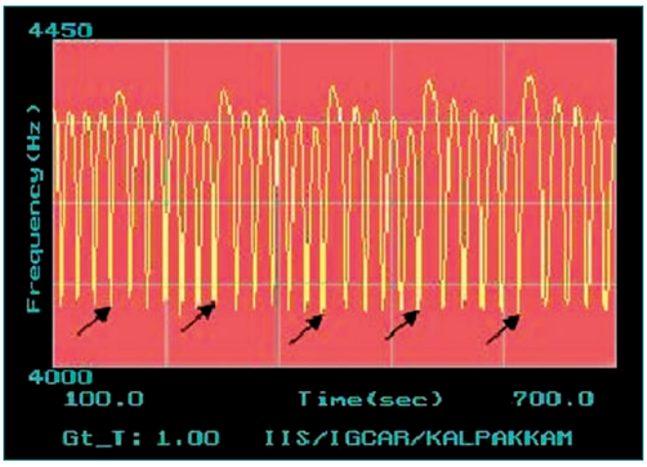

Fig. 3 *Pulse perturbation peaks for Cu(II) catalysed-thiocyanate-peroxide OCR due to uranium*

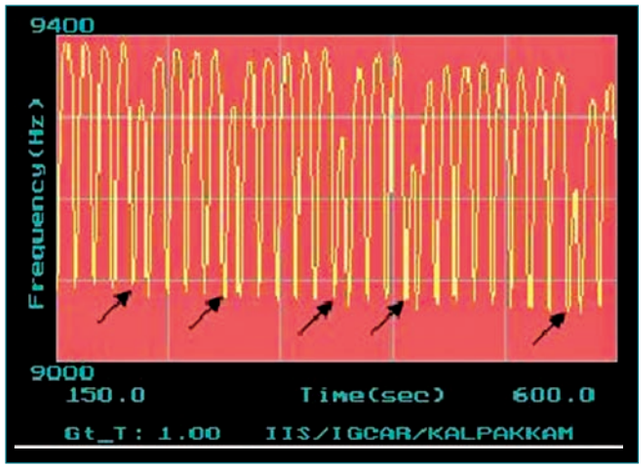

Fig. 4 *Pulse perturbation peaks for Cu(II) catalysed-thiocyanate-peroxide OCR due to hydrazine*

could be easily analysed by using this analyte pulse perturbation technique. Thus, there is enhanced scope to deploy these basic investigations towards development of rapid analytical techniques for industrial applications including nuclear applications using oscillatory chemical reaction as a platform.

V.10 Efficient Hydrogen Generation from Pt Loaded TiO_2 Nanotube Powders

Hydrogen, an effective energy carrier, is considered an alternative for reducing dependence on fossil fuels and environmental pollution. Hydrogen generation by photolytic splitting of water, being an environmentally friendly and economically viable process, has been considered as the best possible option. The principle behind photolysis of water using TiO_2 is that, when TiO_2 is in contact with water, the photo-excited conduction band electrons can reduce water to generate hydrogen, provided the conduction band level is more negative compared to H^+/H_2 reduction potential. Among the quasi one-dimensional nanostructures, nanotubes are preferred because of their high surface area. The photocatalytic efficiency of TiO_2 is limited due to the high recombination rate of photo generated electron-hole pairs. To resolve this issue and enhance the photocatalytic activity, deposition of noble metals (Pt, Au and Pd) and their chemical modification have been proposed. Since, the Fermi levels of the noble metals are lower than the TiO_2 conduction band, when loaded on to TiO_2, the photo excited TiO_2 electrons migrate towards the noble metal leaving behind the holes in the valence band, thereby reducing the electron-hole recombination rate and enhancing the photocatalytic efficiency. Among the noble metals, Pt has been found to be more effective and it acts as a catalyst for the hydrogen evolution, by reducing the activation energy for water reduction.

In the present study, anatase phase TiO_2 nanotubes having 7.53±1.53 nm internal diameter and ~25 micrometers length with a crystallite size of ~10 nm (Figure 1a) were fabricated by rapid break down anodization technique.

The Pt/TiO_2 photo catalysts corresponding to different weight percent of Pt were prepared by $NaBH_4$ reduction of TiO_2 dispersed H_2PtCl_6. The weight percentages of Pt deposited on TiO_2 was estimated assuming complete reduction of H_2PtCl_6 and Pt concentrations in nanotube powders were 1.25, 2.5, 5 and 10 wt%. TEM images of 1.25 and 5 wt% Pt loaded TiO_2 are shown in Figures 1b and 1c. From Figure1b it is clear that, at 1.25 wt% loading, the Pt particles are of very fine nature and well dispersed. Figure 1d shows the corresponding histogram for the particle size distribution. The mean diameter calculated by image analysis is 1.978±0.349 nm. Similar results

are obtained for 2.5 wt % Pt loaded samples.

The XRD pattern reveals that the photo catalysts corresponding to low Pt loadings (≤2.5 wt %) are of anatase phase. The chemisorbed surface areas of the as-prepared and Pt-loaded TiO_2 as well as the dispersion of Pt obtained from temperature programmed desorption reduction oxidation experiment showed decrease in chemisorbed surface areas and dispersion with increase in Pt loading from 1.25 to 10 wt%. Higher Pt loading led to agglomeration of particles resulting in reduction in active surface area. The photocatalytic hydrogen generation experiments were performed in a 150 ml quartz at 298±2 K. Two sets of measurements with different ultra voilet sources were made, (i) 120W (λ=380 nm) and (ii) 64 W (λ=254 nm). In a typical experiment, 20 mg of the photo catalyst (Pt/TiO_2) was suspended in 80 ml 1:3 ratio ethanol-water mixture and irradiated from the bottom of the reactor and the gas generated over the reaction mixture was analysed using a polymer electrolyte membrane based H_2 sensor (PEMHS). The typical signal of H_2 produced by photo dissociation of ethanol-water mixture, using 120 W source (λ=380 nm) PEMHS is shown in Figure 2a. Photo-induced H_2 generation was high at 1.25 and 2.5 wt% Pt loading, but decreased with further increase in Pt loading. At low Pt loading, the Pt nanoparticles (~2 nm) have a narrow size distribution and is homogeneously distributed (Figure 1). Hence, the available surface area is high and reduction of proton to hydrogen on Pt being a surface reaction, H_2 generation increases. If the active sites for H_2 generation are located at the Pt-TiO_2 interface rather than on isolated Pt and/or TiO_2 nanoparticles, a decrease in H_2 generation rate at higher Pt loading can be expected as further increase in Pt loading leads to agglomeration of Pt nanoparticles resulting in interface area shrinkage. This will manifest as a sharp drop in H_2 generation rate, as observed in the present study (Figure 2b). In addition, the reduced size of Pt particles brings its Fermi level to an optimal level with respect to conduction band level of TiO_2 facilitating enhanced electron harvesting. The hydrogen CSA of Pt/TiO_2, measured using temperature programmed desorption reduction oxidation technique, shows maximum value at 1.25 wt% Pt and a decrease thereafter. The highest photo catalytic activity observed (at 120 W, λ = 380 nm) is for 1.25 and 2.5 wt% Pt loaded TiO_2 samples and are 777.3 and 927.9 μ moles/hour/gram of Pt/TiO_2, respectively. Experiments carried out under similar conditions with 1.25 and 5 wt% of Pt loaded TiO_2 photo-catalysts, using 64 W UV source (λ = 254 nm) resulted in H_2 generation of 0.030 and 0.010 moles/hour/gram of Pt/TiO_2, respectively. From the results of the H_2 generation studies, the turn over frequency (TOF) of the Pt surface area was calculated as,

TOF = rate of H_2 generation (mole. s^{-1}) / moles of surface Pt atoms

The number of moles of surface Pt atoms was calculated from temperature programmed desorption reduction oxidation studies. Taking into account the complete reduction of $HPtCl_6$, the TOF values of Pt/TiO_2 corresponding to 1.25, 2.5, 3.75, 5, 7.5 and 10 wt% Pt loadings calculated from the results of H_2 generation studies carried out at 120 W (λ = 380 nm) radiation are 0.0035, 0.0035, 0.0011, 6.644×10^{-5}, 7.99×10^{-5} and 15.27×10^{-5} s^{-1},

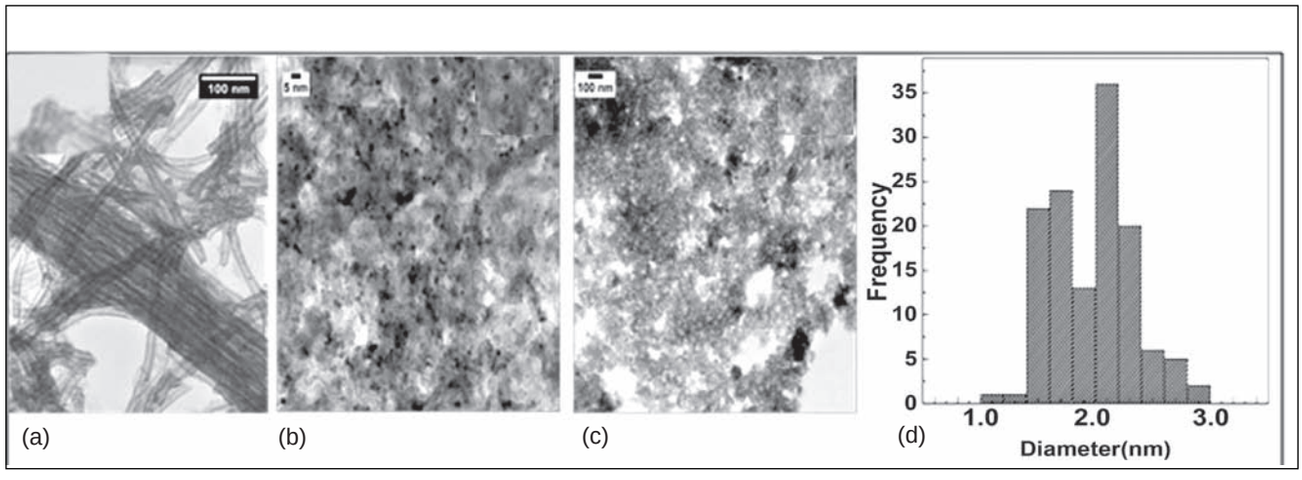

Fig. 1 *TEM image of the (a) TiO_2 nanotube powders synthesized by RBA technique, (b) 1.25wt% pf Pt loaded TiO_2, (c) 5 wt% Pt loaded TiO_2 and (d) the histogram of the particle size distribution of 1.25 wt% if Pt loaded TiO_2*

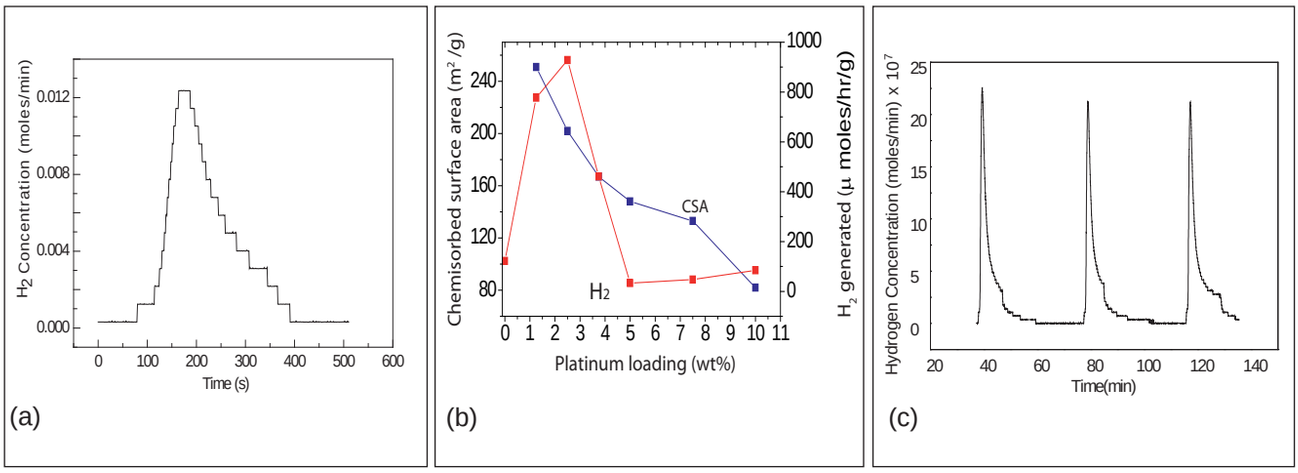

Fig. 2 *(a) The typical signal of H_2 produced by photo dissociation of ethanol - water mixture (b) Variation of CSA and H_2 production (at 120 W, λ = 380 nm) with Pt loading and (c) Signal from the hydrogen sensor revealing theconstant hydrogen generation rate from ethanol–water system by photocatalysis using 1.25 wt% Pt loaded TiO_2, at 120 W (λ = 380 nm)*

respectively. The decrease in TOF values with increase in Pt loading indicates changes in chemical environment of Pt atom. The Pt particle size obtained from the TEM studies, for 1.25 wt% Pt loading is 1.99 nm and the calculated dispersion value is 57%. The TOF value obtained using this dispersion is 0.0059 s^{-1}. Photo catalytic H_2 generation is also a function of incident light wave length. The TOF value for H_2 generation from 1.25 wt% Pt loaded TiO_2 suspensions irradiated using 64 W (λ = 254 nm) source was found to be 13.69 s^{-1}. In all the H_2 generation measurements, it was observed that the amount of H_2 produced for a given time of irradiation did not vary when repeated, using the same Pt/TiO_2-ethanol/water system (Figure 2c). The hydrogen generation rate of 0.030 moles/hour/g of Pt-TiO_2 obtained by us is one of the highest reported values.

V.11 Near Frictionless Surface of Diamond Thin Films

Use of materials for applications in micro and nano devices require development of thin films with high wear life and low friction coefficient, these requirements can only be met by developing advanced thin films architectures such as multilayers or nanocomposites with low surface energy. In so far as carbon based materials are concerned, various hybridization states in carbon constitute specific aspects for material designing of films with low friction coefficient. One of them is ultra nanocrystalline diamond (UNCD) film where the wide area grain boundaries contain amorphous carbon (a-C) with sp^2 hybridized bonding state. However, ultra nano grain with the size of less than 10 nm normally consists of sp^3 hybridized carbon bonding. Optimizing the grain size, morphology and sp^2 and sp^3 hybridized states form the basis for the design of low friction diamond film. However, friction coefficient of UNCD film is not low enough for efficient functioning of micronano devices. We report the significance of hydrogen plasma exposure on achieving control over desired chemical properties. Films with diamond nanowire architecture grown under optimized plasma chemistry exhibit exceptionally low friction behavior. Mechanism explaining the friction behavior of as-grown and hydrogen plasma treated diamond nanowire films is studied.

Diamond nanowire films were deposited on silicon substrates in N_2(94%)/CH_4(6%) plasma by microwave plasma enhanced chemical vapour deposition (MPECVD) technique with microwave power 1200 W and frequency of 2.45 GHz. The surface of the films was post treated by pure hydrogen plasma for 15 minutes at a pressure of 5 torr and microwave

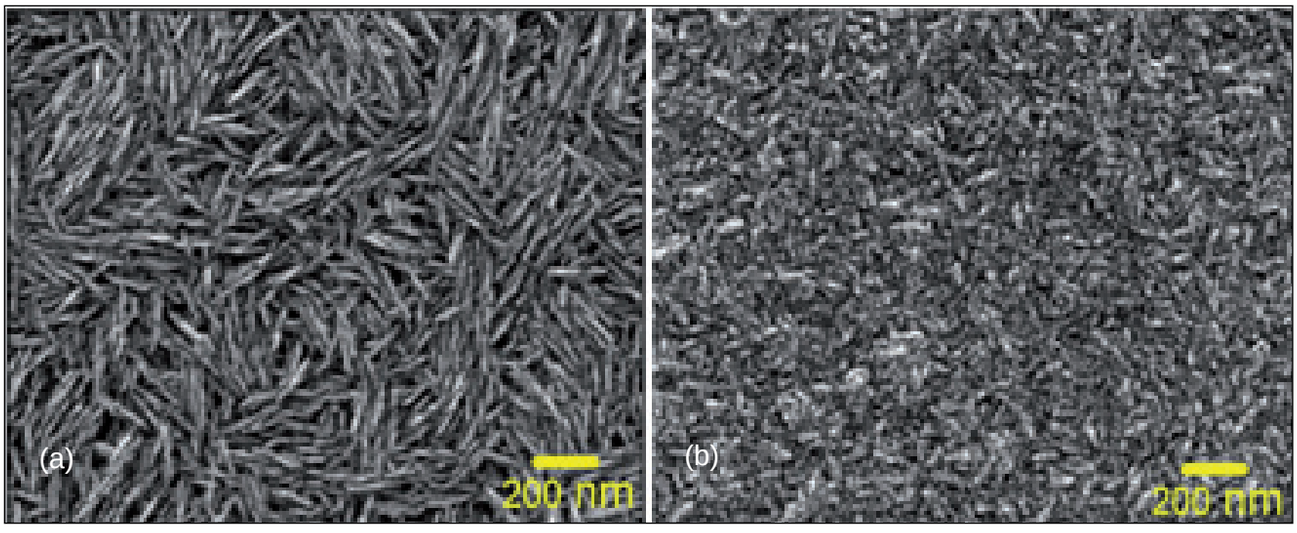

Fig. 1 *FESEM images of (a) As-grown DNW and (b) H_2 plasma treated DNW films*

power of 600 W. Contact angle (CA) of these films were measured by sessile drop method. Circular reciprocating mode of a ball on disk nano tribometer, was used to carry out tribological tests as a function of normal load. A contacting Al_2O_3 ball with 1.5 mm diameter was made to slide against the static films at a speed of 0.5 cm/s. Tribology experiments were conducted in ambient and humid atmospheric conditions at room temperature.

The top-view FESEM micrographs of as-grown and H_2-plasma treated diamond nanowire films indicate that films as grown (Figure 1a) possess highly dense and uniformly distributed wire-like granular microstructure, while the H_2-plasma treated diamond nanowire films have ultra-small size spherical grains (Figure 1b). The transition in the morphology by H_2 plasma treatment is due to the removal of carbon layer from the surface of as-grown diamond nanowire film. Raman spectra of these films are shown in Figure 2. Peaks designated as v_1, v_2 and v_3 correspond to trans-polyacetylene (t-PA) chains existing in grain boundaries. These peaks are the evidence for occurrence of nano-diamond phase. Broad band of D corresponds to first order T_{2g} symmetry of nano-diamond phase. The shift of this band at high frequency 1327 cm^{-1} in Figure 2b results in enhanced bond symmetry. In addition, decrease in FWHM of this band is associated with increased size of diamond grains that occur due to H_2 plasma treatment. The friction coefficient is high 0.22-0.28 in diamond nanowire film (Figure 3a) which is measured at various loading conditions. Value of friction coefficient in similar condition drastically diminishes to ~0.0001 in H_2 plasma treated diamond nanowire films (Figure 3b). For as-grown diamond nanowire film, the friction coefficient is mainly associated with large fraction of lubricated sp^2C-C bonded graphitic phases that exist in the grain boundaries. In the as-grown film, the friction coefficient is related to low surface energy which is evident from high contact angle of 152°. On the other hand,

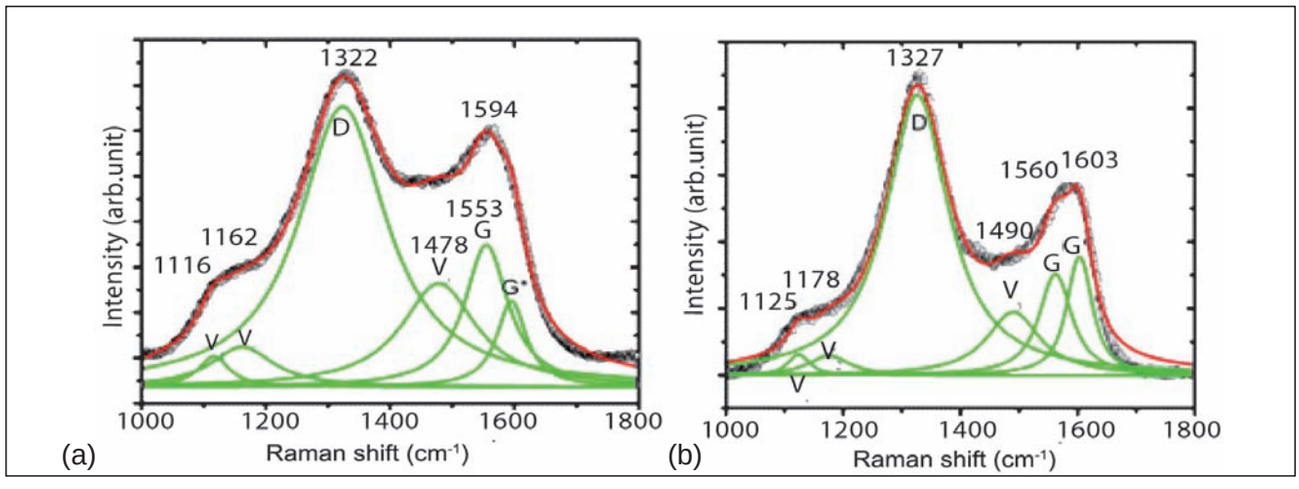

Fig. 2 *Raman spectra of (a) As-grown and (b) H_2 plasma treated DNW film*

the capability to adsorb the H_2O molecule is less because of high contact angle of as-grown diamond nanowire film. In this condition, mechanism of surface passivation during tribology test is limited as the adsorption of H_2O molecules is energetically unfavorable. Moreover, dissociation of H_2O molecules and formation of C-H and C-OH bonds are limited which do not sufficiently act to chemically passivate the uncompensated valence electron of C-C bonds. Therefore, the external passivation mechanism to compensate the dangling bonds is restricted. This is the primary reason which shows high friction coefficient in as-grown diamond nanowire film. In contrast, the surface passivation process becomes energetically favorable when H_2 and O_2 molecules are present on the surface. It is shown that the main effect of the adsorbate is to prevent the formation of covalent C-C bond across the diamond interface. The CA is lower 128° in H_2 treated diamond nanowire films where electrostatic attraction between the positively charged surface and the compensating water droplet is strong. In this condition, capability of the surface to "self-lubricate" by adsorbing water molecules into the diamond surface causes significant decline in the friction coefficient. The existence of H_2O molecules and adsorption capability of surface consisting of reservoir of chemical species which continuously saturate the carbon dangling bonds that originates at the sliding interface. With increase in normal load, the friction coefficient decreases as shown in Figure 3b. This generally happens due to graphitization of the sliding surface when sp^3 C-C phase transforms into sp^2 C-C phase. This transformation is related with dissociation of hydrogen molecules.

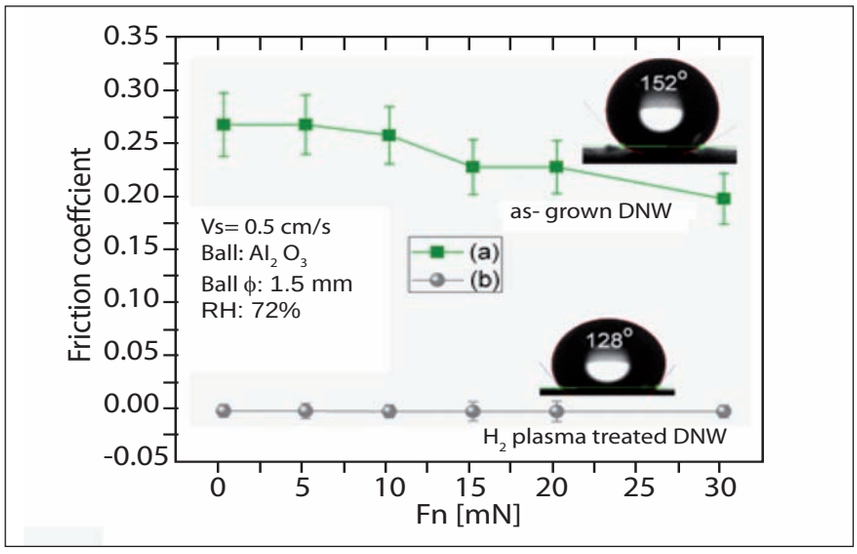

Fig. 3 *Friction coefficient versus normal load of (a) As-grown and (b) H_2 plasma treated DNW films*

V.12 Room Temperature H_2 Sensing using Functionalized GaN Nanotubes

Nanotubes with large surface areas have received considerable interest in wide range of applications pertaining to drug delivery, catalysis and chemical sensing. Considerable progress has been made towards controlled growth of GaN nanowires and improvising various functionality by suitable surface modification. There is only a few published work, however, on the growth of GaN nanotubes mostly employing template or using metal catalysts. A single-step growth process of square shaped wurtzite (wz) GaN nanotubes by a quasi-vapor-solid process is reported. A chemical route is used for the functionalization of GaN nanotubes with Pt nanoclusters of average diameter ~1.6 nm. The Pt nanoclusters help in the formation of localized Schottky barrier, which is involved in the sensing process. Catalytically enhanced dissociation of molecular H_2 has been shown to be detected at room temperature up to the lowest value of 25 ppm, as compared to those of other GaN systems. For the first time, We report a very low activation energy value of 29.4 meV, which will be useful in practical sensing of H_2 at room temperature without any application of bias voltage.

Nanotubes were synthesized at 1173 K using a hot walled chemical vapor deposition reactor on Au coated Si substrate with Ga (99.999%, Aldrich) as precursor and high purity NH_3 as

reacting gas with a flow rate of 10 sccm for two hours. The nanotubes were further functionalized with Pt nanoclusters using lysine [$HO_2CCH(NH_2)(CH_2)_4NH_2$] as a capping agent following standard hydroxylation process with necessary washing and subsequent drying in N_2 gas. The hydroxylated samples were treated with 1mM of lysine and subsequently by 1mM of $HPtCl_4$ under continuous stirring for 30 min along with freshly prepared 0.1 M $NaBH_4$ solution in order to achieve the desire Pt nanoclusters surrounding the nanotubes. The product was washed and dried in nitrogen gas. To remove lysine, Pt functionalized samples were heated at 573 K for 30 minutes. A buffer layer of 5 nm thick Cr followed by 80 nm thick Au films on inter-digitized electrodes of 1 mm spacing contact probes were made by sputtering for electrical measurements.

Figure 1 shows typical field emission scanning electron microscopic morphology of the control nanotubes. GaN nanotubes are homogeneously distributed throughout the substrate (Figure 1a). Typical length extends to several micrometers. The typical images of the Pt decorated GaN nanotubes are also shown in Figure 1b. Most of the nanotubes exhibit nearly square shaped cross-section with wall thickness of about ~10-15 nm and average side dimensions of nearly ~ 50 nm.

The structure of individual GaN nanotubes was studied by high resolution transmission electron microscope (HRTEM; Zeiss Libra 200) analysis. A typical tube like contrast is observed (Figure 2a). The areas close to the edge are appearing darker than the central zone. The Pt decorated nanotubes (Figure 2b) exhibit relatively rougher external surface, as compared to that for the pristine

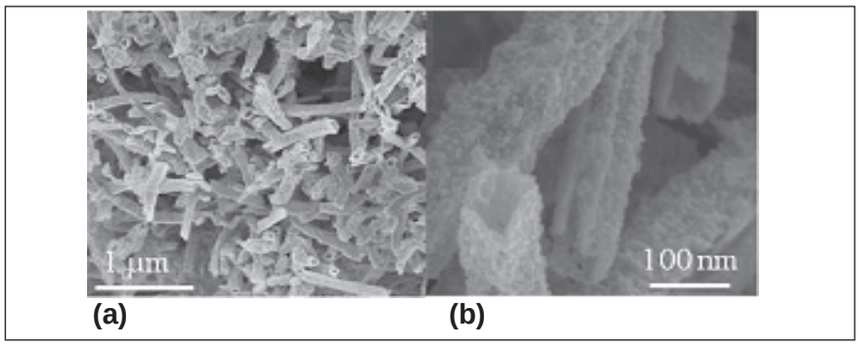

Fig. 1 *(a) Low and (b) High magnification FESEM images of nanotubes*

nanotubes (Figure 2a). A typical high resolution image reveals uniform distribution of Pt nanoclusters, with average diameter of ~1.6 nm, over GaN Nanotubes(Figure 2c). The nanoclusters are indexed to cubic Pt along with known d-spacing. The presence of wz-GaN is proven by selected area electron diffraction (SAED) pattern in the outset of Figures 2c and 2d shows the bright field image of Pt decorated nanotubes along with the corresponding dark field using <111> diffraction spot of the Pt nanoclusters.

The H_2 sensing using the Pt-decorated GaN nanotubes is investigated as a function of time over a range of 25-200 ppm H_2 in N_2 background in the temperature range of room temperature to 473 K (Figure 3a). At room temperature, a factor of ten in relative sensitivity is recorded for Pt decorated nanotubes as compared to that shown by control nanotubes. The relative sensitivities of H_2, however increase to 3.8 at 25 ppm and 10.8 at 100 ppm at 373 K (Figure 3b). We have

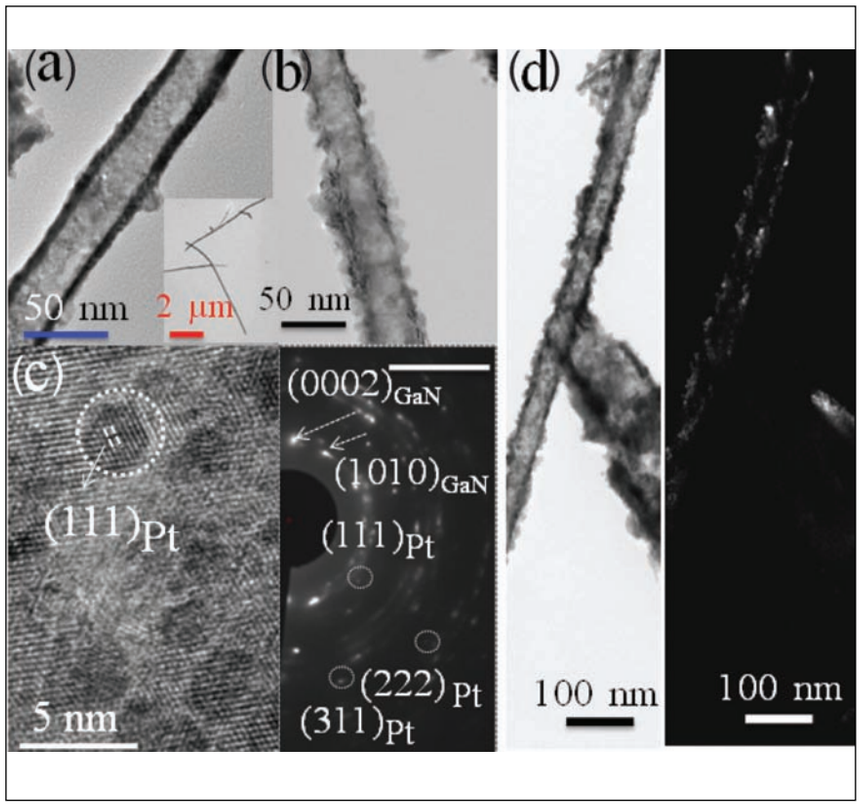

Fig. 2 *HRTEM studies of (a)Pristine and (b)Pt nanoclusters coated GaN Nanotubes. (c)High resolution images along with SAED pattern and (d) bright and dark field images of Pt nanoclusters on GaN Nanotubes*

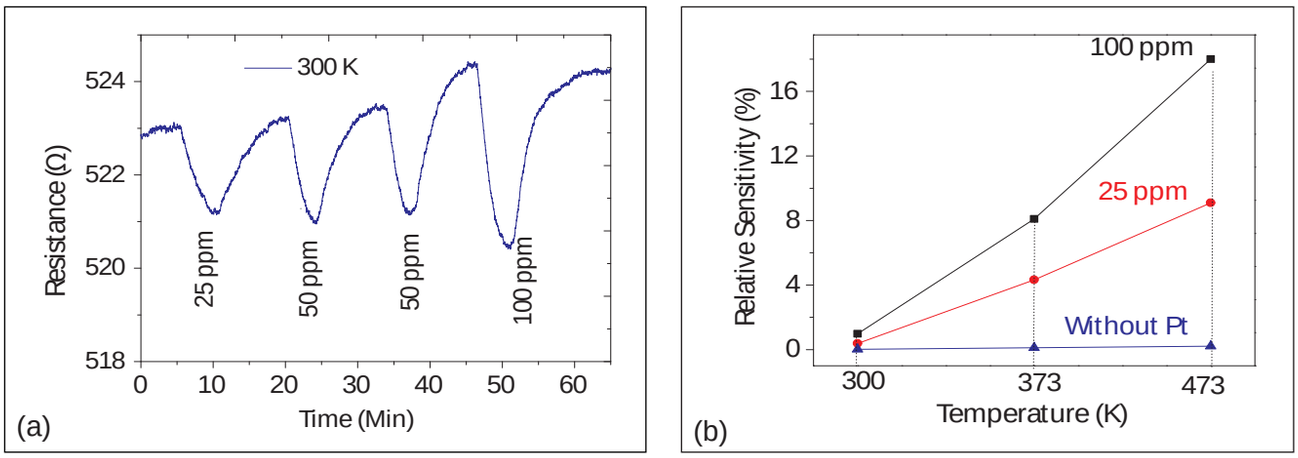

Fig. 3 *(a) Time dependent change in resistance of Pt decorated GaN Nanotubes at 300K (b) Relative sensitivity to H_2*

reported the lowest ever detection limit of 25 ppm of H_2 at room temperature using the nanotubes in the GaN system. An Arrhenius plot of the rate of change of sensitivity (S) in Pt-decorated nanotubes with temperature is used to calculate the adsorption activation energy of 29.4 meV (Figure 4), which is the lowest ever reported, as compared to other GaN systems. Encouraged with low value of activation energy in our system, we have further estimated a theoretical detection limit up to 1 ppb at room temperature from extrapolation of the measured values and considering a sufficiently low background noise (Figure 5). Low sensitivity of detection at room temperature (Figure 3b) should, however be considered before its use for all practical purpose.

It is well known that, Schottky barrier formed between the metal and semiconductor surface gets altered as a result of chemical reaction at the interface. In our study, the excess electrons, generated as a result of catalytic dissociation of H_2 on Pt active sites can surpass the Schottky barrier and travel through the metal conduction band contributing to the conduction process resulting in the decrease of resistance at Pt-decorated GaN nanotubes interface. The low activation energy of Pt and GaN nanotubes interface enhance the catalytic dissociation of H_2 through a non-adiabatic energy transfer route leading to a high value of sensitivity. The fact that such a H_2 sensor has an advantage over others with sensing elements being effectively integrated with GaN based electronics is leading to further miniaturization.

Thus, we have reported the growth of wz-GaN nanotubes with regular square facets using CVD technique. These nanotubes have been functionalized with Pt nanoclusters for exhibiting noble catalytic properties. We report here a H_2 induced increase in the conductivity for the lowest value of 25 ppm level at room temperature for the Pt-decorated GaN Nanotubes surfaces, as compared to other GaN systems with a very low activation energy value of 29.4 meV. A theoretical detection limit up to 1 ppb of H_2 is estimated. This study will be extremely useful for developing H_2 sensor device with low power application, in emergency cases, as detection of H_2 is very important in the nuclear reactor assembly.

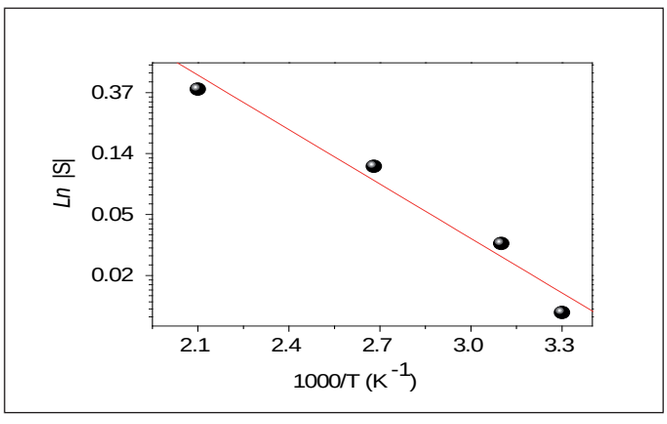

Fig. 4 *Arrhenius plot of ln |S| ~ 1/T*

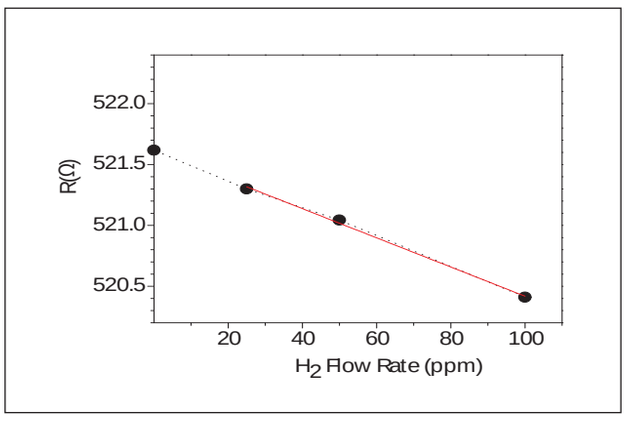

Fig. 5 *H_2 Sensing limit extrapolated to ppb level*

V.13 Thermal Expansion and Specific Heat of Cesium Loaded Iron Phosphate Glasses

The high level waste arising from fast reactors require an alternate glass matrix since some of the elements are poorly soluble in borosilicate glass. Among the non-borosilicate glasses, iron phosphate glass has been demonstrated as a potential matrix for the immobilization of waste that are not compatible with borosilicate glass. Iron phosphate glass can also be used for the immobilization of certain oxides like Cs_2O, Cr_2O_3, UO_2, Bi_2O_3 and MoO_3. Understanding the thermophysical properties of cesium loaded glass is essential prior to loading ^{137}Cs in iron phosphate glass matrix.

Experiments were conducted to understand the thermal behaviour of iron phosphate glass and the effect of Cs_2O loading on its high temperature behavior up to 700 K. In addition to thermal expansion by dilatometry, heat capacity of the cesium loaded glasses were determined using Differential Scanning Calorimetry up to 700 K. Enthalpy increment was computed from the fitted heat capacity curves. Isoperibol drop calorimetry was used for the direct determination of the enthalpy increments of the glasses in the temperature range 373 to 723 K. Heat capacity was computed using the fitted enthalpy increment data and compared with those from DSC measurements.

The glasses under present study were labeled iron phosphate glass, IP9C1, IP8C2, IP7C3, IP6C4 and IP5C5 depending on the composition as shown in Table 1. The sample code IP stands for iron phosphate and C stands for cesium.

Thermal expansion studies were carried out by using a home-built push rod dilatometer in air up to 700 K at a heating rate of 2 K/min using LVDT sensor and quartz push rod. Specimen temperature was measured by a chromel-alumel thermocouple placed very near the specimen. High density thoria pellets were used as standards. The percentage linear thermal expansion of iron phosphate glass and cesium loaded iron phosphate glass are shown in Figure 1. The thermal expansion behaviour was experimentally determined up to 700 K which is well below the glass transition temperature of the glasses. The average thermal expansion coefficient (α_{av}) was evaluated for each glass from the plot of thermal expansion versus temperature. The α_{av} values vary from 7.1 to 19.8x10^{-6}/K for iron phosphate glass and cesium loaded iron phosphate glass which is shown as insert in Figure 1 and it exhibits a quadratic relation with mol % of Cs_2O. The non-existence of simple linear relation of thermal expansion behaviour with cesium content suggests that thermal

Table 1: Chemical composition of the iron phosphate glass glasses

Sample	Glass composition (mol %)		
	Fe_2O_3	P_2O_5	Cs_2O
IPG	40	60	0
IP9C1	37	57.5	5.5
IP8C2	34.5	53	12.5
IP7C3	33	46	21
IP6C4	29	44	27
IP5C5	26	38	36

expansion of these glasses strongly depends on the evolution of glass structure and is not simply an additive function of the constituents. The observed increase of thermal expansion of iron phosphate glass with cesium content is due to the characteristically large thermal expansion of the alkali metal-oxygen bond and increase in non-bridging oxygen content of the glass.

A heat flux type differential scanning calorimeter was used for the measurement of heat capacity (at constant pressure). The specific heat capacities (C_p) of iron phosphate glass and cesium

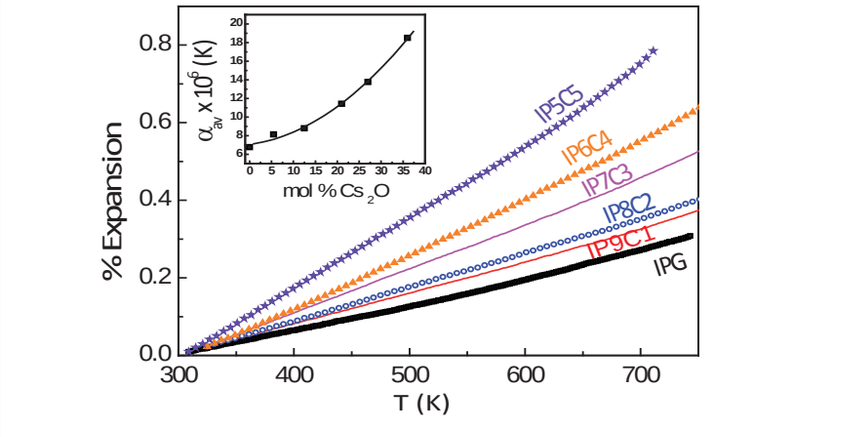

Fig. 1 *Linear thermal expansion of iron phosphate glass and Cs loaded iron phosphate glass*

loaded iron phosphate glass measured in this study are shown in Figure 2. The uncertainty in the present C_p data of the samples is ± 3 %. At a given temperature, the C_p values are found to decrease with increasing Cs_2O content. Higher the heat capacity, higher will be the bond strength and the stability of the material. The C_p was also estimated based on Neumann-Kopp (NK) additive rule using chemical composition of glasses and C_p data of corresponding oxides. The experimental data are much lower than the estimated value in all the glasses especially at temperatures above 400 K. Higher estimated C_p is due to the basic assumption of the NK rule that there is no heat capacity change during the formation of compound/glass i.e., the compound behaves ideally and that structural effects do not contribute to heat capacity, which may not be true in this case. At the lower temperature (< 400 K), experimental C_p matches with the estimated C_p especially for IP6C4 and IP5C5. Empirical NK rule is applicable for solid substances around ambient temperature (400 K) and especially in those cases where only lattice vibration and dilation of oxides contribute to the heat capacity.

From our earlier structural characterization studies, we have clear indication of the breakage of polymeric network of cesium loaded glasses beyond IP7C3. The far infrared spectrum of cesium loaded iron phosphate glass showed Cs ion vibration mode only for IP6C4 and IP5C5 glasses indicating that the incoming dopant (cesium) is no longer involved in cross linking but serves to terminate the linkage, thus decreasing the polymeric network. Thus, in iron phosphate glass and cesium loaded iron phosphate glass up to IP7C3, the glass network is predominant. In the case of IP6C4 and IP5C5, significant breakdown of the network structure is evident and only these two fairly obey the NK rule. However, at temperatures beyond 500 K, IP6C4 and IP5C5 also behave similar to other glasses. From the fitted C_p data, the enthalpy increments $H_T^0 - H_{298}^0$ were computed as a function of temperature.

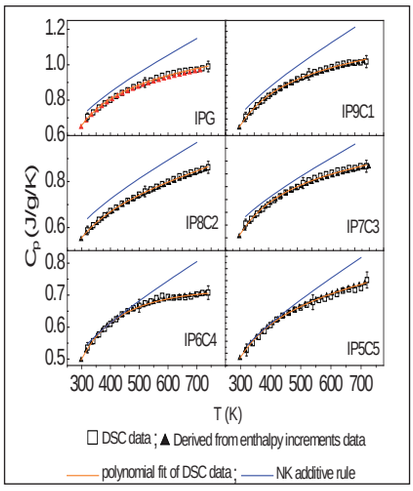

Fig. 2 Specific heat of iron phosphate glass and Cs loaded iron phosphate glass

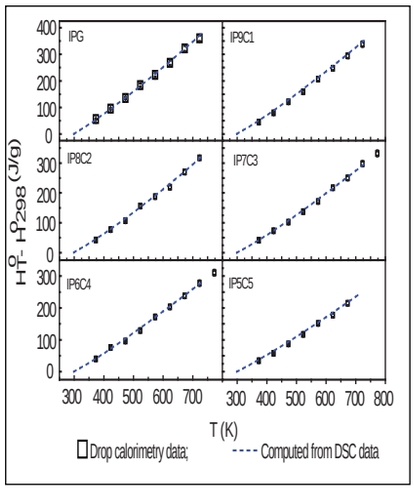

Fig. 3 Enthalpy increment data of iron phosphate glass type of glasses

The enthalpy increments of iron phosphate glass and cesium loaded iron phosphate glass were measured in the temperature range 373 to 723 K under static air atmosphere at intervals of 50 K as shown in Figure 3. The experimental enthalpy increment data were in good agreement with those derived from heat capacity data as shown in Figure 3. The fitted expressions of $H_T^0 - H_{298}^0$ were used to compute heat capacity of the glasses as a function of temperature. The computed heat capacity data from enthalpy increment measurements were found to be in excellent agreement with the measured heat capacity of the glasses by DSC as shown in Figure 2. This shows the inter-consistencies between the measured data. It needs to be emphasized that though the C_p measurements by DSC were carried out in argon atmosphere and drop calorimetric measurements in static air atmosphere, the enthalpy increment data agree well with each other. Generally, the thermogravimetric experiments of iron phosphate glass containing >10% of Fe^{2+} content in the glass show an increase in weight during heating. Iron phosphate glass and cesium loaded iron phosphate glass under present study contain much lower Fe^{2+} content, i.e., <5%. Nevertheless, in order to check the weight change of the glasses under study, thermogravimetric analyses were carried out in argon as well as in air. The TGA curves showed similar behaviour under both the atmospheric conditions and no weight change was observed in the temperature range of 300 to 750 K. The preponderance of Fe^{3+} in the glasses ensured their inertness in both the atmospheres. Thus, it is justifiable to compare the results of experiments carried out in argon with those in air. The above studies clearly indicated that the stability of iron phosphate glass decreases with cesium loading which needs to be further explored by assessing the glass forming ability and stability of these glasses.

V.14 Effect of Pressure on the Structural Stability of Iron Phosphate Glass: Role of Trace Water

Iron phosphate glasses-IPG, are being investigated as potential nuclear waste matrices. There is a paucity of work related to the structural stability of IPG under high pressures. One of the factors that plays a key role in qualifying these glasses as a nuclear waste matrix material is the detrimental effect of moisture on the structural stability of these glasses under pressure. Hence, the present study deals with the effect of high external pressure on the structural stability of both the amorphous and hydrated forms of IPG, using Raman and infrared spectroscopy.

Effect of pressure on anhydrous IPG samples

In-situ high pressure Raman measurements (Ambient to 24.2 GPa) were carried out on totally anhydrous binary iron phosphate glass chips of composition $40Fe_2O_3{:}60P_2O_5$ to look for changes in the phonon modes (Figure 1) signaling its structural stability. Raman measurements on samples under ambient conditions revealed the expected broad phonon features characteristic of disordered IPG. The Raman bands are not very sensitive responsive to initial increase in pressure upto ~3 GPa, while for higher pressures, the modes harden with a systematic loss in Raman intensity. The glass matrix is thus quite resilient to pressures upto a threshold value of ~3 GPa, beyond which one can observe significant positive pressure induced shifts in the mode frequencies. This corresponds to compression of bonds indicating densification of the glass matrix. For pressures greater than 19 GPa, the spectrum appears totally smeared and featureless with a total collapse of the Raman intensity suggesting increased disorder in the sample. This possibly implies the gradual breakdown of even the short range order that was originally present in the glass. The total collapse of the Raman intensity for pressures greater than 19 GPa could also arise due to the distortion of the PO_4 tetrahedra at very high pressures, leading to a lowering of the local site symmetry. It is interesting to note from the figure that the spectrum seems to recover back on decompression of the sample. This reversibility suggests that the phosphate chain length remains conserved throughout the entire pressure range. Further there seems to be no emergence of new bands on the application of pressure, ruling out the formation of new compounds or the possibility of the polymerising chains. Although a high degree of disorder is indeed observed to set in with increased pressure, the phosphate backbone still remains intact even for pressures as high as 24.2 GPa, i.e., the chains merely get

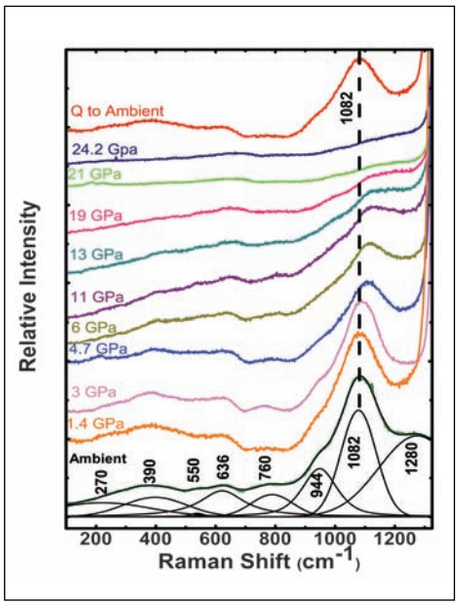

Fig. 1 Raman spectra of iron phosphate glass at various pressures

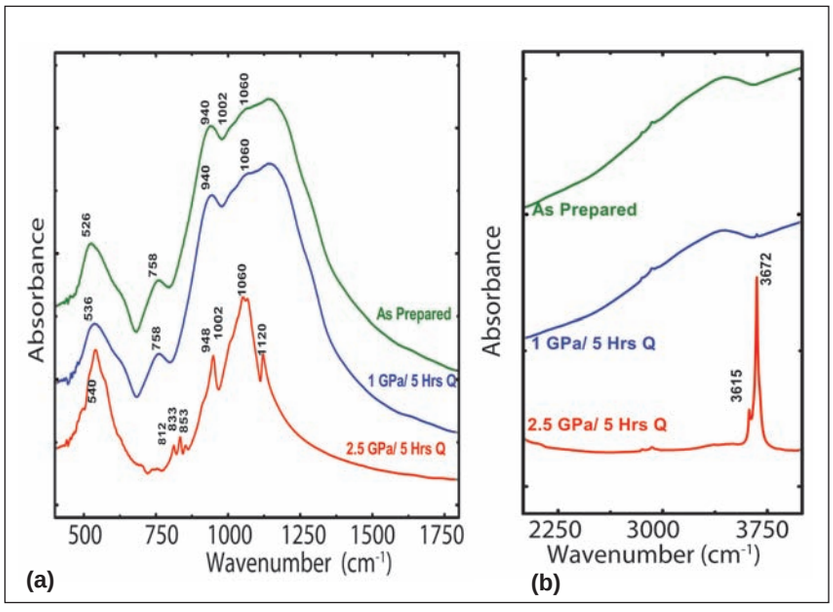

Fig. 2 IR spectra of pressure quenched IPG showing the effect of pressure on (a) Phonon modes corresponding to P-O vibrations in the region below 1800 cm^{-1} (b) Absorption features of liquid water In the 2000-4000 cm^{-1}region

compressed on pressurizing they neither break nor polymerise.

Effect of pressure on IPG samples with trapped water

IPG pellets which were identified to have trapped/adsorbed trace amount of water were soaked at 1 and 2.5 GPa for five hours at room temperature prior to quenching the sample to atmospheric pressure.

Room temperature mid infrared spectra of the as-received IPG sample along with the 1 and 2.5 GPa pressure quenched samples are shown in Figure 2. The mid infrared region (400-4000 cm^{-1}) has been split into two regions denoted by Figures 2a and 2b for clarity. Although the spectrum of the 1 GPa pressure treated sample remained unchanged as compared to the parent glass (Figures 2a and 2b), the 2.5 GPa pressure quenched sample showed dramatic sharpening of most of the phonon modes. The broad unresolved feature extending between 900-1500 cm^{-1} comprising the various P-O stretching modes of the phosphate linkages that make up the parent glass is also observed to collapse into three sharp features, a prominent feature centered at 1060 cm^{-1} indicative of the majority of the pyrophosphate linkages present in this glass along with well resolved shoulders on either side at 948 and 1120 cm^{-1} pointing to the presence of both ortho and metaphosphate units in the sample. This sharpening is indicative of the onset of ordering in the glass sample, possibly indicating de-vitrification of the IPG glass matrix under these conditions. Of particular interest are the changes that are observed in the broad 3000-4000 cm^{-1} region corresponding to the absorption features of water. This broad feature shows spectacular changes in the 2.5 GPa pressure treated sample with the emergence of two new sharp features centered at 3615 and

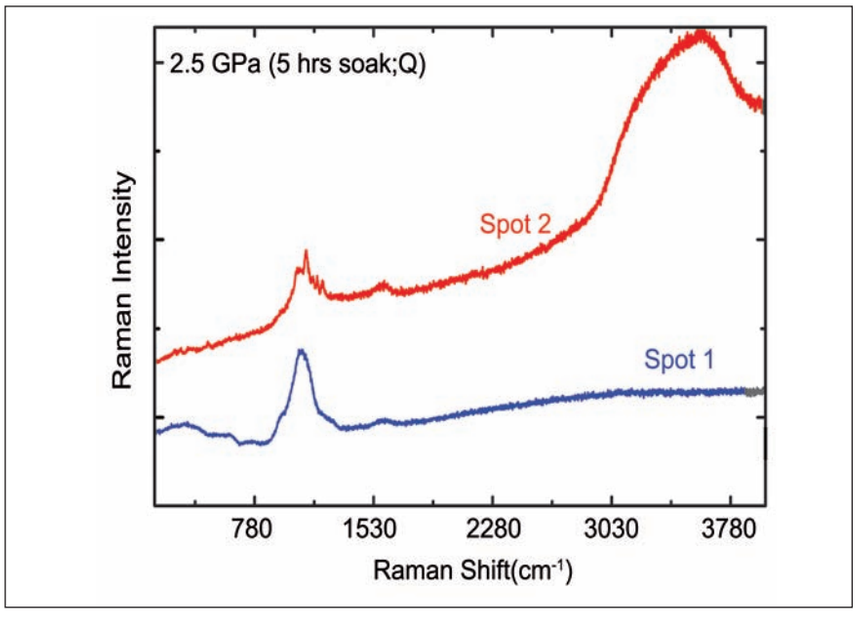

Fig. 3 *Raman spectra of pressure quenched IPG at different locations*

3672 cm^{-1}. These modes are known to be associated with isolated O-H stretch presumably arising due to the cleavage of the P-O-P bonds by the trapped water in the glass sample to form terminal P-O-H linkages. Water is known to weaken the glass structure by causing the rupture of the P-O-P linkages, leading to the formation of P-O-H groups. This rupture of the P-O linkages could decrease the viscosity of the parent glass thus rendering the required mobility that would serve to induce crystallization on pressurizing these glassy matrices. In addition, it is well known that pressure enhances the catalytic effects of water to induce crystallization in a glassy matrix and hence dramatically lowers the crystallization temperature. All the above factors and the inherently low thermal crystallization temperature in IPG makes the situation still more vulnerable to devitrification, thus causing the IPG matrix to devitrify at room temperature itself. Additional proof for the fact that the presence of water aids in crystallization of the glass matrix under pressure, is obtained from micro Raman measurements carried out on different spots on the 2.5 GPa pressure quenched IPG pellet (Figure 3). It is evident from the figure that grains that are devoid of water in the 3000-4000 cm^{-1} region remain unaffected, while the spot that shows huge absorption signals due to trapped water, show the emergence of sharp phonon features in the 800-1600 cm^{-1} region pointing to devitrification. These Raman measurements clearly bring out the role of water in inducing devitrification of IPG upon pressurizing.

The effect of external pressure on the local structure of both anhydrous and water trapped IPG pellets were studied using micro Raman and infrared spectroscopy. Thus, totally anhydrous IPG matrices retain their amorphous nature and are quite robust to high pressures of the order of 25 GPa. Presence of even trace quantities of water in the sample seems to be detrimental, leading to devitrification of the IPG matrix at pressures as low as 2.5 GPa. These results will have important bearing on the applications of iron phosphate glasses for radioactive waste immobilisation.

V.15 Development of Mixed Alkali Halides for Radiation Dosimetric Applications

Dosimetry using optically stimulated luminescence technique has emerged as a formidable alternate for dosimetry. A large number of materials like Al_2O_3:C, BeO, Mg_2SiO_4:Tb, $LiAlO_2$:Tb, Lithium magnesium phosphate, Lithium aluminium phosphate have been synthesized and studied for the optically stimulated luminescence dosimetric applications. Out of all the phosphors, mixed alkali halides doped with Europium has been found to be a very promising material due to its sensitivity and tolerable tissue equivalence.

There are several modes of stimulation and detection of light signals leading to varying terminology. Some of the common terms are CW-OSL (for continuous-wave optically stimulated luminescence), DOSL (for delayed optically stimulated luminescence), LM-OSL (for linearly modulated optically stimulated luminescence), POSL (for pulsed optically stimulated luminescence), PTOSL (for photo-transferred optically stimulated luminescence), and COSL (for cooled optically stimulated luminescence).

Though alkali halides doped with rare earths have tolerable tissue equivalence, the post-irradiation storage stability is very poor, since 50% of the signal is lost in 24 hours. Hence there is a need to modify the luminescence characteristic of this phosphor by suitably doping with co-dopants. Here, the development of mixed alkali halides doped with Europium and thermoluminescence and optically stimulated luminescence characteristics is presented.

Mixed fluorides of KF/NaF and MgF_2 (equimolar proportions) along with dopants (Eu 0.2 mol% and Ag 0.2 mol%) were mixed together and heated in argon atmosphere to 850° C for four hours and cooled slowly to room temperature. It crystallizes into cubic pervoskite structure. The X-ray diffraction pattern and the crystal structure of the synthesized phosphor shown in Figure 1.

The powder was ground well and irradiated to radiation from ^{90}Sr source and the thermoluminescence stimulated luminescence and optically stimulated luminescence were recorded using Riso thermoluminescence /optically

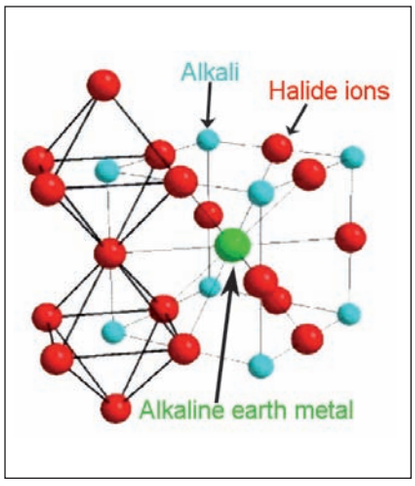

Fig. 1 *Structure of mixed alkali halides*

stimulated luminescence reader. For the measurement of optically stimulated luminescence, a blue LED source was used which has a peak emission wavelength at 470 nm. This exactly matches with excitation wavelength of $KMgF_3$:Eu,Ag (Figure 2). The optically stimulated luminescence decay in these phosphors was recorded in continuous wave mode using Blue LEDs as the stimulation source. The optically stimulated luminescence sensitivity was found to decrease with the addition of co-dopants however the stability of the signal has increased (less fading). Figures 3 and 4 below indicate that the optically

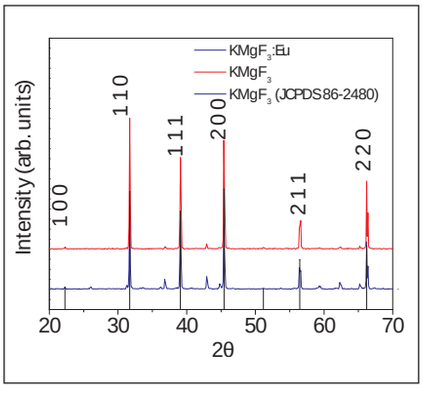

Fig. 2 *X-ray diffraction pattern of $KMgF_3$*

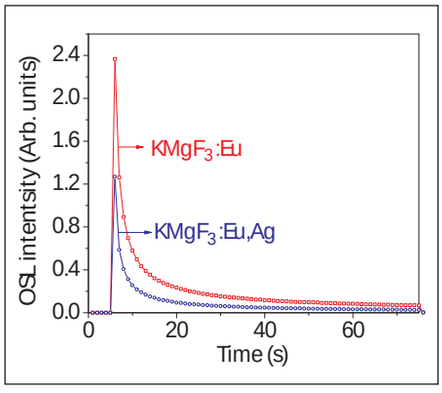

Fig. 3 *Optically stimulated luminescence decay curves of $KMgF_3$:Eu and $KMgF_3$:Eu,Ag*

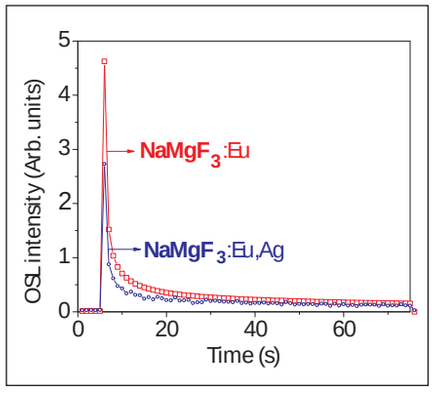

Fig. 4 *Optically stimulated luminescence decay curves of $NaMgF_3$:Eu and $NaMgF_3$:Eu,Ag $KMgF_3$:Eu,Ag*

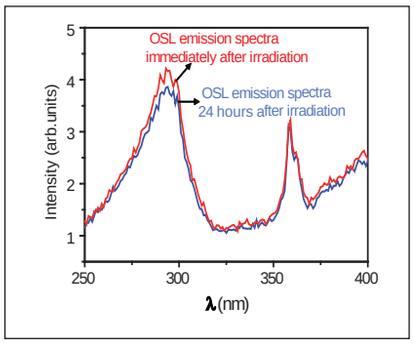

Fig. 5 Emission spectra after irradiation

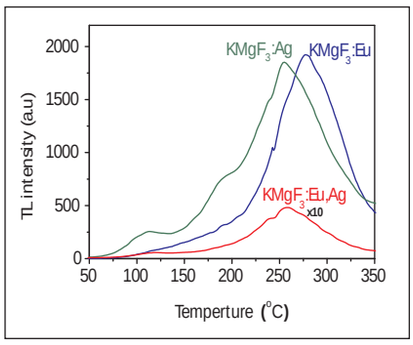

Fig. 6 Thermoluminescence glow curves of $KMgF_3$

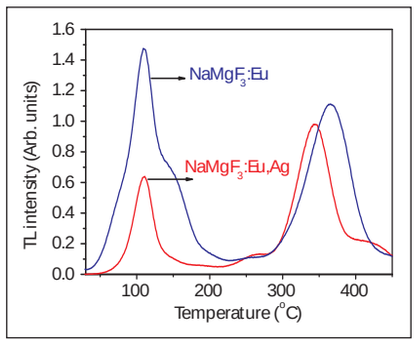

Fig. 7 Thermoluminescence glow curves of $NaMgF_3$

stimulated luminescence intensity of the irradiated sample shows negligible fading after a post-irradiation storage duration of 24 hours. The thermoluminescence stimulated luminescence peak of $KMgF_3$ doped with Eu as well as Eu, Ag were around 240°C, which is a desirable feature of any thermoluminescent dosimetric material. The sensitivity of the Ag co-doped phosphor is high compared to $KMgF_3$ doped with Eu alone. In the case of $NaMgF_3$ though the low temperature peak is high for the Eu doped sample, the high temperature peak intensities are comparable. The enhancement of its thermoluminescence sensitivity is possible by incorporating suitable amounts of Eu and Ag. Thus, from the point of view of stability, the Ag co-doped phosphors stands to be better choice of dosimetry material. The photoluminescence as well

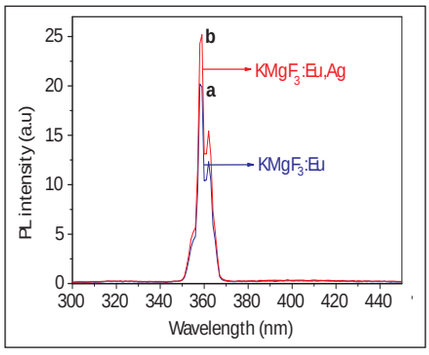

Fig. 8 Photoluminescence spectra of $KMgF_3$

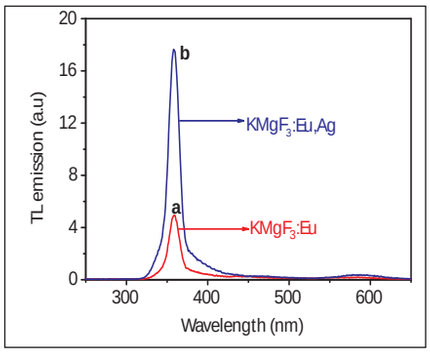

Fig. 9 Thermoluminescence emission spectra of $KMgF_3$

as thermoluminescence emission spectra showed characteristic wavelength of the rare earth dopant. The presence of the codopant Ag enhances the luminescence emission intensity (Figures 8 and 9). The enhancement in thermoluminescence intensity of $KMgF_3$:Eu,Ag can be explained on the basis of the Figures 5 to 7.

Luminescence studies in co-doped mixed alkali halide phosphors have shown that this attempt has resulted in the successful development of a new generation luminescent phosphor because of the fact that these materials are both thermally and optically stimulable with good sensitivity. By incorporating the monovalent dopant silver the post irradiation storage stability can be improved where by the utility of the phosphor for environmental dosimetry application is established.

V.16 Hybrid Signal Processing Approach for Enhanced Nondestructive Detection of Defects in Stainless Steel Plates

Eddy current non-destructive evaluation (NDE) is widely used for detection and sizing of defects in metallic materials. This technique works on the principles of electromagnetic induction and involves measurement of change in coil impedance that arises due to variations in electrical conductivity and magnetic permeability in material on which the sensing coil is placed. However, defect detection capability of this technique is influenced by lift-off (distance between coil and the material surface), surface roughness, geometry etc., which produce noise that degrades the detection sensitivity. Suppressing the noise without loosing the information demands the use of signal processing methods. In

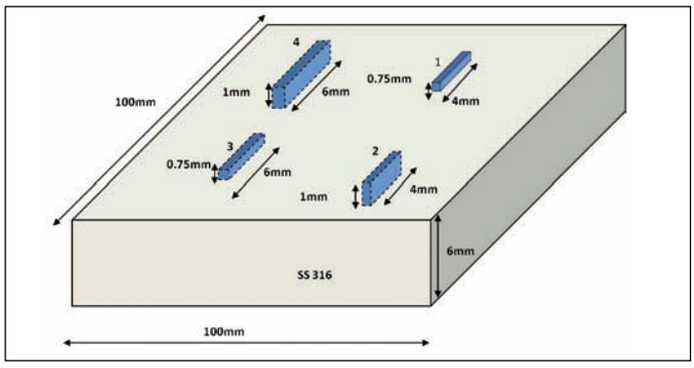

Fig. 1 *Details of four notches machined in a stainless steel plate*

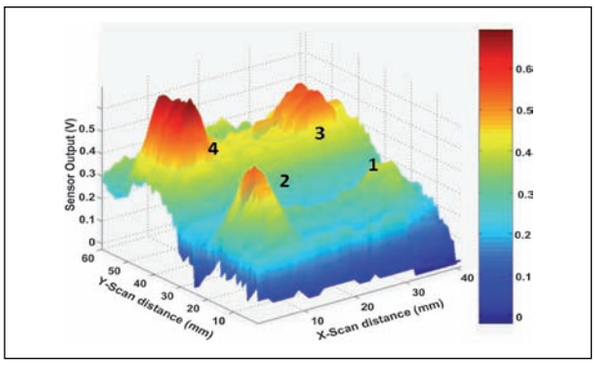

Fig. 2 *Eddy current image of real component of eddy current coil obtained from defects*

this regard, a hybrid approach that exploits the features of independent component analysis and wavelet packet analysis has been developed to separate the signals from lift-off variation during raster scanning on metallic plate having machined defects.

Eddy current images are obtained by scanning a 5 mm dia probe operating at 150 kHz (skin depth, δ = 1.2 mm) over an AISI type 316 stainless steel plate (100x100x6 mm^3) at a uniform speed of 5 mm/s using a computer interfaced X-Y scanner. Images corresponding to the real component of the eddy current signal are only considered as the probe wobble signal. The schematic of machined notches is given in Figure 1. Typical image obtained is shown in Figure 2. The image contains not only information related to notches but also the lift-off associated with surface roughness.

For eliminating undesired noise in eddy current images, independent component analysis that enables separation of statistically and mutually independent sources and wavelet packet analysis that enables separation of low and high frequency components of the signal, have been used. The performances of wavelet packet analysis, independent component analysis and hybrid approach are compared. Wavelet packet analysis retains the global information but some noised frequencies too while independent component analysis statistically de-correlate noise from useful signal but fails with the border effect. In order to maximize the benefits of both independent component analysis and wavelet packet analysis and minimize the drawbacks, hybrid approach is taken. The resultant image by independent component analysis (Figure 3) is able to discriminate the components related to lift-off noise and defect. The undulations in the edges are attributed to partial inclusion of noise components in the defect feature space during the reconstruction.

The independent component analysis image is passed through the wavelet packet analysis that consists of automated optimisation of wavelet filter and level of decomposition. The resulted output image from the wavelet packet analysis scheme (Figure 4) uses wavelet filter of Db5 (Daubechies 5).

A significant enhancement in signal to noise ratio (SNR) of 16.4 dB (notch No.1) with a drastic decrease in the lift-off noise has been observed by the proposed independent component analysis-wavelet packet analysis hybrid approach. This approach can be readily applied to austenetic stainless steel welds for detection of defects in the simultaneous presence of magnetic delta ferrite phase and surface roughness.

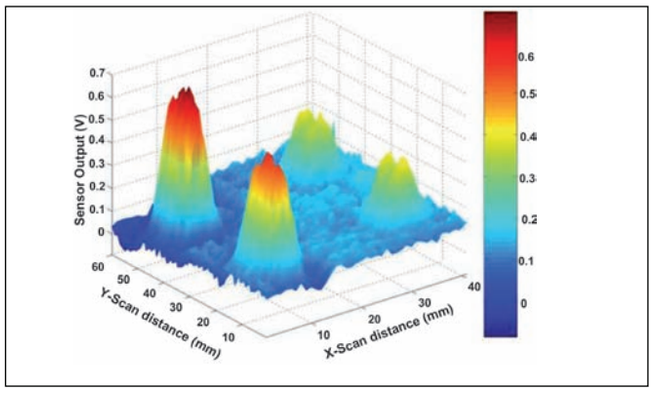

Fig. 3 *Independent component of measured data representing the defect information*

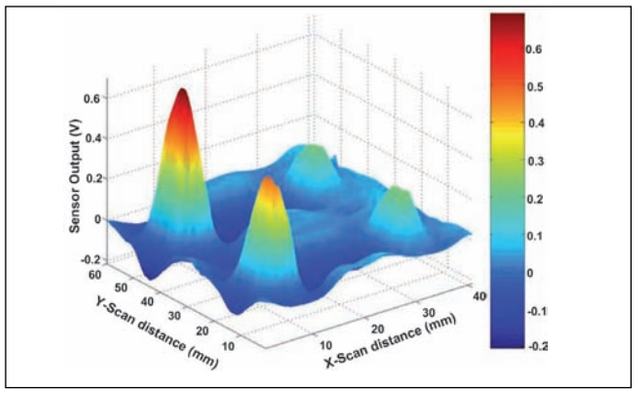

Fig. 4 *Eddy current image after the independent component analysis-wavelet packet analysis hybrid approach*

V.17 Thermogelling Properties of Triblock Copolymers in the Presence of Hydrophilic Fe_3O_4 Nanoparticles and Surfactants

Magnetic nanocomposites are stimuli-driven materials that have potential applications in dynamic seals, actuators, sensors etc. Understanding the mechanical properties of such nanocomposites and the optimal stoichiometry of particles to template sites under external magnetic field is a prerequisite for effective utilization of these materials for practical applications. In this context, the supra-molecular structure formed by thermo-gelation of a triblock polymer (F108) in presence of nanoparticles and surfactant has been probed by using rheometry and small angle X-ray scattering (SAXS). Triblock copolymers undergo self-aggregation which gives rise to micelles with a hydrophobic core surrounded by more hydrophilic shell. The repulsion between the monodisperse spherical micelles drives the formation of cubic phase that persists over macroscopic length scale. To explore the synergistic enhancement of physical properties at nanoscale, properties of nanocomposites and their supramolecular structure are studied.

Addition of Fe_3O_4 nanoparticles (size ~10nm), in a weak template of F108 (15 wt.%) leads to a decrease in the onset of gelation temperature and dramatic alteration in the viscoelastic moduli. The nanocomposite samples show a linear viscoelastic regime up to 5% strain. The SAXS measurements show that the intermicellar spacing of the supramolecular structure of pure F108 is ~16.5 nm (Figure 1). The nanoparticle clusters size distribution obtained from

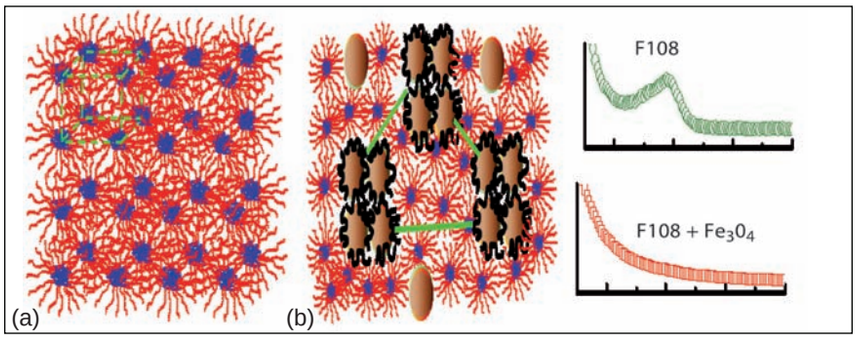

Fig. 1 *Schematic diagram of the micellar packing of pure pluronic F108 and with addition of nanoparticles along with the corresponding SAXS intensity as a function of scattering wave vector is shown (a) Cubic packing of F108 micelles and (b) The clustering of nanoparticle in F108 micellar templates*

SAXS is in good agreement with the microscopic image analysis. The sample with nanoparticle shows a gel-like behavior holding its weight on the inverted vial where as the sample without nanoparticles exhibits a fluid-like behavior (Figure 2). The addition of an anionic surfactant to nanocomposites leads to a dramatic reduction in the viscoelastic properties due to the formation of smaller size surfactant-rich complexes. These results unambiguously confirm that the thermogelation is due to the clustering of nanoparticles rather than the close packing of F108 micelles.

The addition of sodium dodecyl sulphate (SDS) in pluronics solution leads to a dramatic reduction in the viscoelastic properties while it remains almost unaffected with cationic and nonionic surfactants. The two orders of magnitude decrease in the elastic modulus in the presence of sodium dodecyl sulphate indicates a 'soft solid-like' microstructure formed by aggregating self assembled triblock polymers. Our results indicate strong electrostatic barrier imparted by the head group of SDS at the core-corona interface (that inhibits the formation of hexagonally packed layers of micelles) and the packing order. These results suggest that the microstructure and elastic properties of block copolymers micelles can be tuned by varying the concentrations of ionic surfactant that enhances their potential in applications as nano-carriers for drug delivery systems.

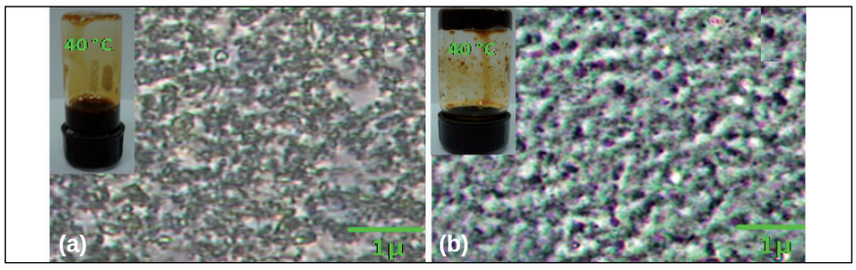

Fig. 2 *The optical microscopic images of 5 wt.% nanoparticle in (a) 15 wt.% and (b) 25 wt.% of pluronics F108 at 40ºC; inset shows the corresponding photographs of inverted sample vials*

V.18 Chemistry, Crystallography and Interfaces of Laves Phases in Relation to the Materials Performance

Laves phases are topologically close packed size-factor intermetallics with AB_2 stoichiometry. They mainly appear as precipitates in many metastable and nanostructured alloys after solidification and heat treatment. Ideally this compound should form at a particular radius ratio of 1.22 of the constituent atoms. But, significant variation from the ideal radius ratio value is frequently observed experimentally. Laves phases are of research interest because of their embrittling effect on structural materials such as steels in service. Laves phases also have useful electrical and magnetic properties and are potential hydrogen storage materials. Chemistry, interface structures and defects are believed to play a major role in determining their properties.

In the present work, stability of Laves phases has been assessed through basic alloy design approach in Ti-Cr alloy and the effect of the third element addition has been studied in V-Ti-Cr alloy systems. A model based thermodynamic approach (i.e., Miedema model) has been adopted to determine the phase stability in these alloy systems. In Miedema model, the formation enthalpy of the alloy system has been calculated as a function of the alloy composition range (Figure 1).

The total enthalpy of formation consists of the chemical, elastic and structural contributions of enthalpy which arise due to different types of interactions between the atoms of the constituting elements. The crystallography and chemistry of these tailor made alloys are investigated experimentally. In Ti-Cr system, Laves phase forms over a relatively narrow composition range and there is a cF24 to hP12 phase transformation at a higher temperature. Thermodynamic calculations show that faster cooling of the alloys for these composition ranges can lead to amorphous phase formation. It has been observed that as the kinetics of polytypic transformation is sluggish, higher temperature phases can easily be retained at room temperature. Often liquid fails to crystallize leading to a precipitation of crystalline Laves phase in an amorphous matrix. This is attributed to the Frank-Kasper polyhedral structure of Laves phases.

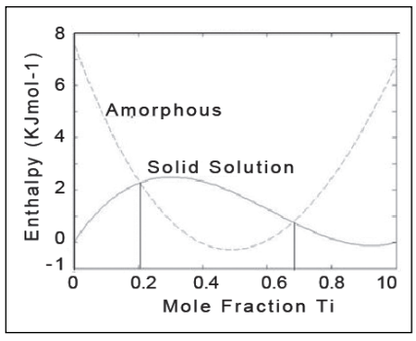

Fig. 1 *The Enthalpy- composition plot for the binary Ti-Cr system*

$TiCr_2$ alloy has been prepared using high purity Ti and Cr in a water-cooled vacuum arc melting system. X-ray diffraction (XRD) in the as melted condition shows that most peaks match the high temperature $TiCr_2$ Laves phases. However, a distinction between the hP12 and hP24 crystal structures cannot be made from XRD studies. Transmission electron microscopy studies of as melted Ti-Cr alloy were taken up to resolve this issue. Figure 2 is a typical bright-field image where the presence of all three polytypic structures with crystallite sizes ranging from very fine nanocrystallites to large grains are seen along with amorphous regions.

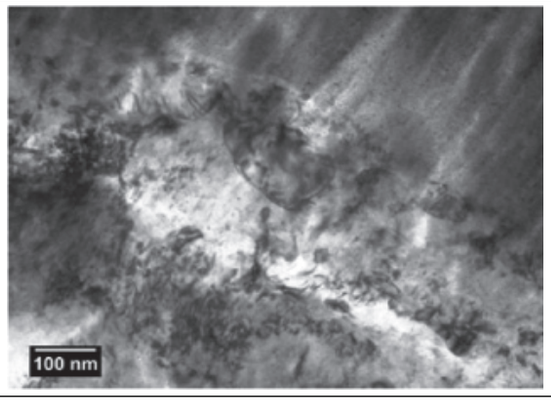

Fig. 2 *TEM bright field micrograph of as melted Ti-Cr alloy*

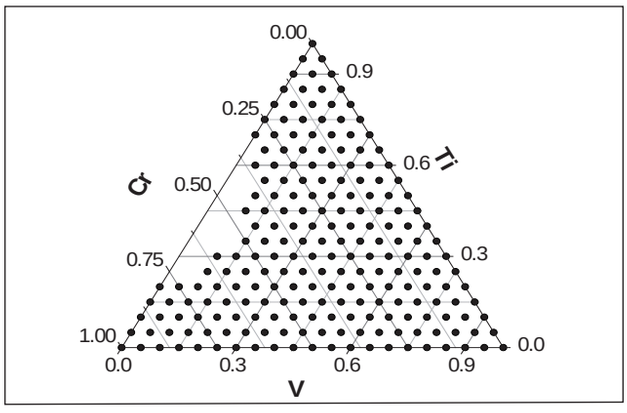

Fig. 3 *Effect of the vanadium addition a solid solution results for V concentration beyond 15 mole percent*

Thermodynamic calculations in V-Ti-Cr system show that ternary addition of V to the Ti-Cr Laves phase alloy is possible (Figure 3) though it leads to elastic distortion in the lattice. Structure of Laves phases can be considered to be an interpenetration of icosahedral clusters which ultimately build up super-tetrahedra. This establishes the possible link of icosahedral order in liquid, amorphous and some metastable alloys.

V.19 Implementation of Check Pointing and Restart as Fault Tolerant Mechanism in HPC Systems

Two HPC clusters, one with 128 nodes and another with 134 nodes, two blade clusters, one graphical processing units cluster with 12 graphical processing units cards and three independent symmetric multiprocessing(SMP) servers are available for computational applications.

Interprocess communication among nodes in the clusters takes place over the high speed Infiniband interconnect. These systems are commonly utilized by long-running scientific computing applications that employ MPI message passing model. The clusters use sun grid engine as a batch system for job scheduling.

In case of systems with a large number of components, failure rate also tends to be high. If the application running on such a system has to restart from beginning after a failure, it will result in the wastage of computing resources and time. Checkpointing is storing a snapshot of the current state of an application and using it for resuming the execution later. Checkpoint/restart provides many useful features for a high performance computing system, the first of it being fault tolerance. In a cluster environment, checkpointing and restarting a set of parallel processes that are part of a single application (gang scheduling) allows for flexible scheduling and higher total system utilization. Periodic checkpointing result in minimum loss of time and resources in case of unexpected failures, as job can be restarted from the latest checkpoint.

In Linux environment, checkpoint/restart may be implemented in three ways: by an application itself, through a library linked with the application (user level), or within the operating system kernel. A key issue to be considered during checkpoint/restart in a distributed system is to obtain a consistent state of the system. Checkpoint/restart techniques for parallel jobs can be broadly classified into three categories: uncoordinated, coordinated, and communication-induced.

Implementation of checkpoint/restart

In SMP servers, distributed multi threaded checkpointing, a user level checkpointing package for distributed applications was deployed for checkpoint/restart. It does not require any recompilation or relinking of user binaries. Computing intensive sequential codes such as 'DORT' and genetic algorithm applications and parallel MPI applications were successfully checkpointed and restarted.

For implementing a checkpoint/restart solution for IGCAR clusters, the following factors were taken into account

1) The ability to checkpoint and restart parallel applications
2) The presence of a batch system (sun grid engine) for job scheduling
3) The presence of Infiniband interconnect for interprocess communication among nodes and
4) The need to support various MPI libraries used by the parallel applications.

The system level checkpointing tool, Berkeley lab checkpoint/restart was integrated with MPI libraries and sun grid engine in the cluster. Parallel jobs using Open MPI were successfully checkpointed and restarted using Berkeley lab checkpoint/restart. For integrating Berkeley lab checkpoint/restart with sun grid engine, a checkpointing environment was configured with a checkpoint script for executing the checkpoint, a migration script which places a job to pending state so that it can be rescheduled later and a cleanup script for cleaning up Berkeley lab checkpoint/restart context files. With this checkpointing environment, sequential jobs running under sun grid engine were checkpointed and restarted.

V.20 Pressure Induced Metallization of $BaMn_2As_2$

The discovery of superconductivity in the FeAs compounds by chemical doping as well as by the application of pressure has provided impetus to search for superconductivity in compounds with similar structures. Among these classes of compounds $BaMn_2As_2$ is quite interesting as it occurs in G-type anti-ferromagnetic insulating ground state. Band structure calculations also indicate that $BaMn_2As_2$ is anti-ferromagnetic and has a semi conducting band gap of 0.2eV. It has been suggested that doping $BaMn_2As_2$ with carriers can induce large anti-ferromagnetic fluctuations in the metallic compound and can lead to an exotic superconducting ground state, with a larger T_C, as compared to that seen in $BaFe_2As_2$. With this in view, several transition metals were doped at the Mn site, but no metallicity could be obtained for substitutions with Cr, Fe, Co, Ni, Cu, Ru, Rh, Pd, Re and Pt at the Mn site nor Sb at As site. We, for the first time, provide a definitive evidence for metallization of single crystals of $BaMn_2As_2$ under the application of an external pressure of ~5 GPa using our low temperature resistivity measurements in a high pressure cell. Also associated with metallization at 5.8GPa is a sharp fall in resistivity, observed at ~17 K indicating the possibility of the occurrence of superconductivity in this compound. Further, from the measurements of room temperature lattice parameter variations as a function of pressure in the $BaMn_2As_2$ crystals, an anomalous change in the pressure volume curve is seen at the pressure at which metallization is observed in the resistivity data.

The single crystals of $BaMn_2As_2$ were synthesized using Ba chunks and pre-prepared MnAs powder taken in an alumina crucible and sealed in an evacuated quartz tube. The samples were then heated to 1473 K at a rate of 323 K per hour and held there for 24 hours and then cooled to 1073 K at a rate of 274.5 K per hour followed by a fast cooling at a rate of 323 K per hour down to room temperature. High pressure X-ray diffraction (HPXRD) experiments were carried out at room temperature using a Mao-Bell type diamond anvil cell (DAC) in an angle dispersive mode upto 10 GPa. High pressure resistivity measurements as a function of temperature in the 4.2 to 300 K temperature range, on a single crystal sample were performed in a home built, opposed anvil pressure-locked cell.

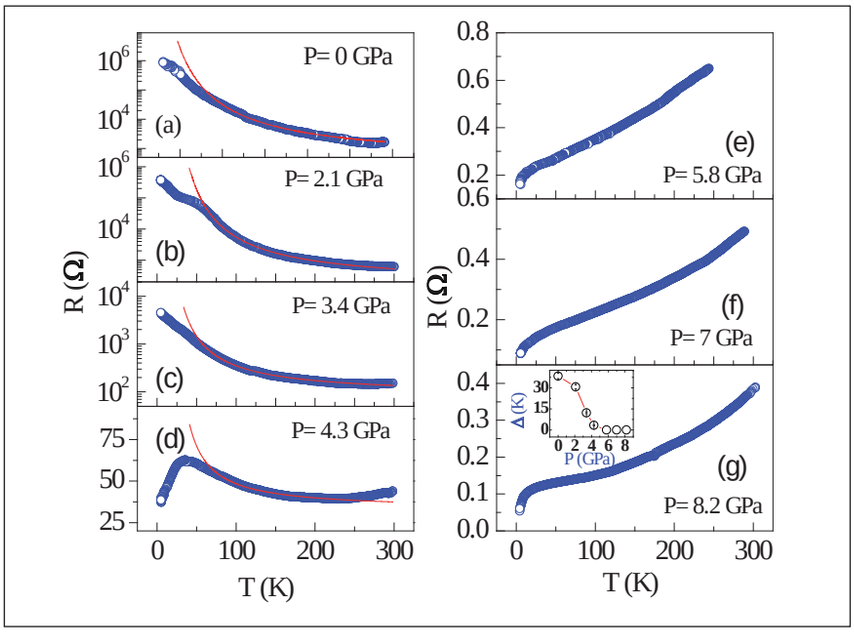

Fig. 1 *Resistance versus temperature for $BaMn_2As_2$ at different pressures between 0 to 8.2 GPa for representative pressures. Inset of Fig. 1g shows variation of energy gap with pressure*

Figure 1 shows the temperature variation of resistance from 4.2 K to 300 K for representative pressures between 0 to 8.2 GPa. At ambient pressure (Figure 1a) the resistance increases with decrease of temperature characteristic of a semiconductor. At a pressure of 0.8 GPa, the temperature dependent resistance (R(T)) again showed insulating behaviour in the 70 to 300 K temperature range, but a significant drop in resistance with respect to the ambient pressure data was seen at low temperature. With a further increase in applied pressures to 2.1 and 3.4 GPa (Figures 1b and 1c), the resistance at low temperature decreases, with a discernable two step variation of R(T). With a further increase in pressure to 4.3 GPa, the variation R(T) shows a change in sign at 36 K, indicating a metallic behaviour at low temperature. Thus, at this pressure, the crystal shows an insulator to metal transition as a function of temperature. At 5.8 GPa, R(T) shows a metallic behaviour in the whole temperature range of 4.2 to 300 K. With further increase of pressure from 5.8 to 8.2 GPa, the resistance further reduces at

all temperatures, while maintaining the metallic state. It is found that the resistance is reduced by seven orders of magnitude at 30 K, by five orders of magnitude at 50 K and by three orders of magnitude at 290 K with increase in pressure from 0 to 8 GPa.

The ambient pressure R(T) data fits to an activated behaviour in the 70 to 300 K temperature range. The activation energies obtained from fits of the R(T) data as a function of external pressure are shown in the inset of Figure 1g. It is evident from the figure that the activation energy systematically decreases with increase in applied pressure from 38.4±2 MeV at ambient pressure to 3.0±0.2 MeV at 4.3 GPa after which the crystal metallizes. In addition to the observation of metallization by the application of pressure at 5.8 GPa, a notable sharp fall in resistance was observed at temperatures ~17 K, which is visible in all graphs in the right panel of Figure 1. The magnitude of the fall in resistance increases with increase of pressure and it is more clearly seen in the R(T) measured at highest applied pressure of 8.2 GPa, indicating superconducting like transition for P≤ 5.8 GPa. In the light of the observation of metallization of $BaMn_2As_2$ (Figure 1), we have carried out high pressure powder X-ray diffraction measurements at room temperature, to investigate if the metallization is associated with a structural transition. The variation of the 'a' and 'c' lattice parameters as a function of external pressure are shown in Figure 2a. While both the lattice parameters, 'a' and 'c' decrease monotonically with increasing pressure, there is a distinct change in the pressure variation of lattice parameters, with a cross over region at ~ 5 GPa. The

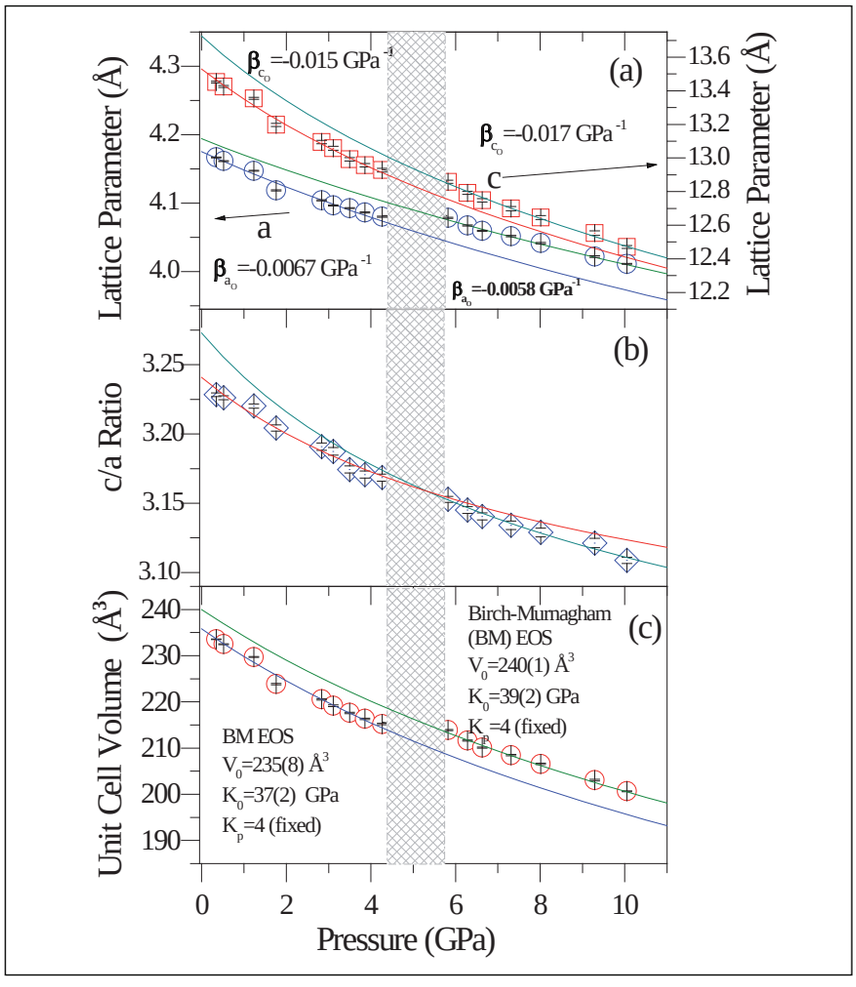

Fig. 2 *(a) The tetragonal lattice cell parameters of $BaMn_2As_2$, a and c, versus applied pressure. (b) The c/a ratio versus pressure plot (c) Unit cell volume versus pressure data. The solid lines are the third order fits Birch-Murnaghan equation of state fits to the data*

lattice parameter 'a' becomes less compressible at higher pressures, whereas, the compressibility of the lattice parameter 'c' shows a slight increase. The magnitude of c/a and its smooth variation with pressure (Figure 2b) indicates that the metallization observed in the present study is not associated with the collapsed tetragonal phase. Figure 2c shows the lattice volume versus pressure and the fits to the third order Birch-Murnaghan equation of state. The difference in the compressibility behaviour for the low pressure insulating phase and high pressure metallic phase can be clearly seen, with a cross over at 5 GPa. Thus, the insulator to metal transition (Figure 1), that is associated with an iso-structural transition (Figure 2) points to an electronic topological transition induced by pressure in this system.

In conclusion, we have demonstrated metallization of the G-type anti ferromagnetic $BaMn_2As_2$ under a application of pressure of ~5 GPa. High pressure XRD measurements at room temperature show that this insulator to metal transition is associated with an iso-structural electronic transition. The observed pressure induced metallization of $BaMn_2As_2$, would help in fine tuning the on-going efforts on metallization with chemical substitutions. The metallic phase has a sharp drop in resistance at 17 K, suggestive of a pressure induced superconducting transition in this system.

V.21 Tilt Rotation Distortion in Cubic Sesquioxide Dy_2O_3: a High Pressure X-ray Diffraction Study

Rare earth sesquioxides of the type Ln_2O_3 [Ln=rare earth] are in use in several industries and continues to attract research interest owing to their optical and dielectric properties among others. Presently there is also considerable interest in nano sized rare earth sesquioxides. Dy_2O_3 as a strong absorber of neutrons, has potential application in neutron-absorbing control rods in nuclear reactors.

The crystal structure of rare earth sesquioxides is believed to be governed by steric effects caused by the size of the rare earth ions and the directional nature of covalent bonding. At ambient conditions the sesquioxides have one of the three polymorps: type-A (hexagonal), type-C (cubic) and type-B (monoclinic). Polymorphism in these rare earth sesquioxides are extensively reported in literature. Surprisingly, the mechanism of the polymorphic phase transitions in these sesquioxides are not understood and their crystal structure data is scarce. Ab initio density functional theory calculations of these rare earth compounds are presently considered very challenging and density functional theory calculations reported in literature mainly concerns with the energy minimization of known polymorphs at different unit cell volumes. Clearly understanding these sesquioxides and their properties (e.g. variation of the bulk modulus with the size of the rare earth) entails detailed study of their crystal structures across the polymorphic transitions they exhibit.

High pressure (HP) has been used effectively to compress these sesquioxides to about 80% of the ambient pressure value and high pressure induced polymorphic transitions are known in several rare earth sesquioxides. Crystal structure evolutions with pressure of these sesquioxides (needed to understand the polymeric phase transitions) are however not known. A plausible reason could be that the loss of information due to increased peak overlap resulting from peak broadening in the high pressure diffraction data limits the extent to which reliable information can be extracted without sensible constraints.

We have collected angle dispersive X-ray diffraction (ADXRD) data of the sesquioxide: Dy_2O_3 upto a high pressure of 37 GPa using a Diamond Anvil Cell (DAC) at the B5.2R beamline of the ELETTRA synchrotron facility at Trieste. A polymorphic phase transition from the C-type cubic phase to the B-type monoclinic phase was observed at ~7 GPa and at even higher pressures, the A-type hexagonal polymorph was also observed. We have carried out detailed analysis of the data using advanced techniques like the distorted-polyhedra rigid-body constrained Rietveld refinements (Figure 1). Using these techniques we have found the presence of a tilt rotation distortion in the cubic (C-type) structure of Dy_2O_3 that explains the cubic C-type crystal structure and its evolution with pressure.

The cubic (C-type) crystal structure of rare earth sesquioxides can be completely described using two centrosymmetric octahedra. Furthermore, such a description allows carrying out equation of state (EOS) fits to the complete structure of the cubic sesquioxide (Figure 2).

Figure 3 shows the pressure evolution of the tilt rotation distortion and the thermal parameter. A decreasing value of tilt distortion and an increasing value of the thermal parameter with pressure is

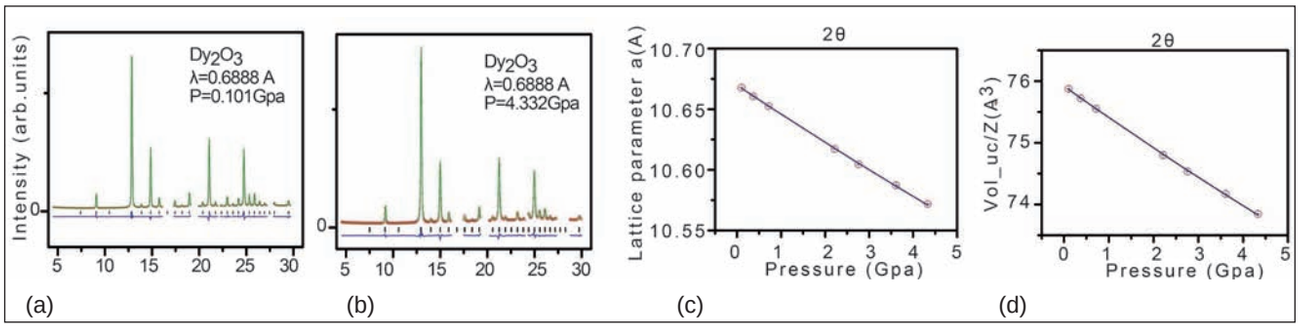

Fig. 1 *Rietveld refinemnet data of Dy_2O_3 at pressure of (a) 0.1 and (b) 4.3 GPa respectively. The observed, calculated and the difference plots are shown. A third order Birch-Murnaghan EOS fit to the lattice parameter (c) the volume (d) data is shown*

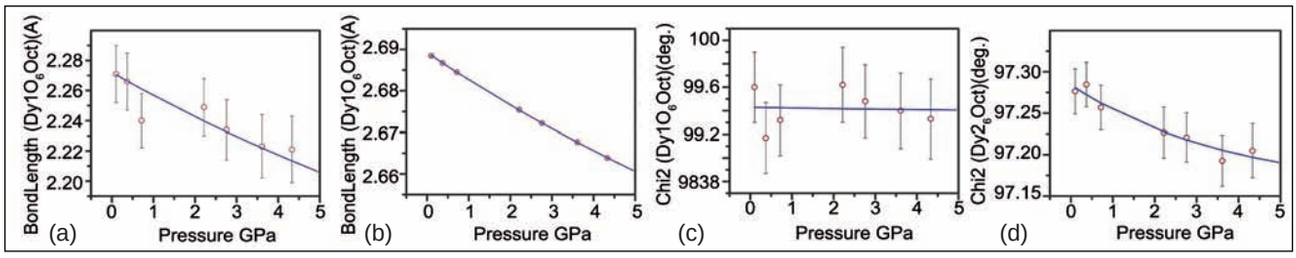

Fig. 2 *Pressure evolution of the octahedral bond length and angle (chi) of octahedra $Dy1O_6$ (a,c) and $Dy2_6$(b,d) respectively.*

indicative of the pressure limit of the stability of the cubic phase. Indeed the high pressure evolution of the cubic structure of Dy_2O_3 is defined by the Dy-O bond length and its compressibility. Similar analysis of other rare earth sesquioxides not only reveals the pressure limit of stability of the cubic phase but also their compressibility behavior.

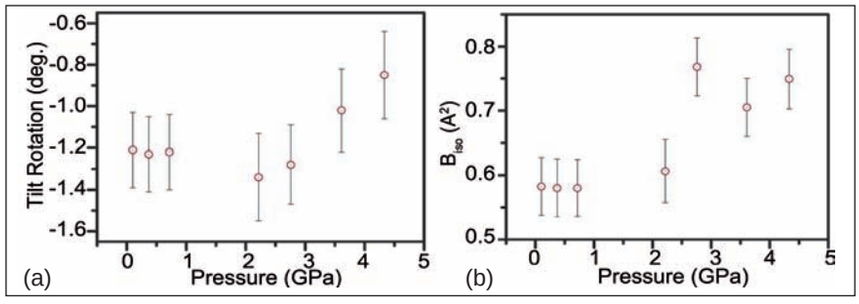

Fig. 3 *(a) Pressure evolution of the tilt rotation distortion of the cubic Dy_2O_3 structure (b) That of the overall isotropic thermal parameter*

V.22 Brillouin Spectroscopic Study of Central Peak in $NaNbO_3$ Single Crystal

Ferroelectric materials that belong to the perovskite family of compounds with general formula ABO_3 are studied with considerable interest not only from the fundamental point of view of understanding the phase transitions they exhibit but also for their applications in several fronts such as piezoelectric, electro-optic, high density optical data storage. $NaNbO_3$ based ferroelectric systems such as (Li, Na)NbO_3, (K, Na)NbO_3 with ultrahigh piezoelectric response has evoked considerable interest as next generation ecofriendly lead free piezoelectric ceramics required for various applications.

$NaNbO_3$ (NN) exhibits an unusually complex sequence of temperature driven anti-ferroelectric and ferroelectric phase transitions accompanied by the changes in the structure. The detailed mechanisms of these transitions are not well understood. Studies on the various aspects of phase transitions in $NaNbO_3$ have been carried out using a variety of experimental techniques such as X-ray absorption fine structure, electron and nuclear magnetic resonance techniques. Low frequency Raman studies on $NaNbO_3$ single crystal revealed the occurrence of a quasi-elastic peak across the anti-ferroelectric orthorhombic (D_{2h}^{11} Z=8) to anti- ferroelectric orthorhombic (D_{2h}^{13} Z=24) (P-R) phase and was attributed to a mechanism involving relaxing dipoles around off-center Nb ions. Based on the dielectric and extended X-ray absorption fine structure studies, an order-disorder nature of the phase transition was suggested for P-R transition.

Brillouin light scattering studies provides more detailed information on the dynamics of phase transition in the form of quasi-elastic scattering or central peak (CP). CP is the manifestation of the characteristic time scales of the order parameter (polarization in the present case) associated with the phase transition. Furthermore, high resolution of Fabry-Perot Interferometer yields accurate line-shape of CP. In the present work, we have carried out Brillouin scattering measurements over large free spectral range on $NaNbO_3$ single crystal over a wide temperature range to study dynamics of P-R phase transition.

Single crystals of NN grown by flux method are used in the present study. Brillouin spectra were measured in back-scattering geometry using a high-contrast

3+3-pass tandem Fabry-Perot Interferometer. For probing CP, the spectra were recorded with a large free spectral range (FSR) of 3300 GHz in order to cover a wide frequency range. Sample was excited using a single-mode diode diode-pumped solid state laser operating at 532 nm. The spectra were recorded from ambient to 773 K using

$$K = \int_a^b \frac{I(\omega)}{F(\omega,T)} d\omega$$

a commercially available heating stage with a temperature stability of ± 0.1 K. The measurements were performed at successively higher temperature during heating cycle. The spectra were fitted with sum of damped harmonic oscillators for phonons and a Debye type relaxation for CP with the assumption that it does not couple with the low frequency phonons.

Figure 1 shows the Brillouin spectra along with the fit for the phonons and CP at some selected temperatures. A broad CP together with optical phonons at 1500 GHz was found to appear above 493 K. Upon heating it became weak and vanished above 743 K. The integrated intensities of the central peak and the low frequency phonon modes are calculated using where a and b are the low and high frequency limits of the peak respectively. The plot of integrated intensities of CP as well as that of phonon mode-1 is shown in Figure 2. Upon heating, the integrated intensity of both CP and phonon mode-1 show gradual decrease up to 622 K and then exhibit dramatic increase as the temperature approaches T_c. The maxima for both the intensities occur at the same temperature that corresponds to the phase transition temperature T_c = 643 K. The two features exhibiting similar behaviour with temperature suggests that no intensity transfer occurs between the CP and phonon mode.

Figure 3 shows the temperature dependence of the relaxation time obtained for CP. One can see that the relaxation time remains constant up to 593 K and then increases rapidly (diverges) as the temperature approaches T_c. This can be attributed to a critical slowing down associated with the relaxation process of the order parameter. This arises due to the hopping process of off-centre Nb ions between equivalent positions within the oxygen octahedra. Therefore, the transition mechanism appears to be order-disorder type. On approaching T_c from above as well as below, rapid increase in the integrated intensities of CP and phonon mode suggest the increase in the correlations between the relaxing dipoles.

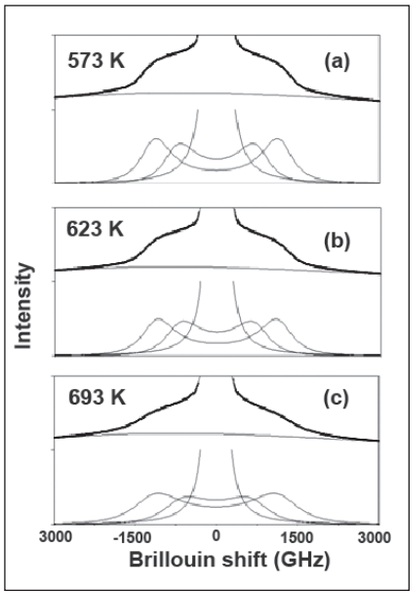

Fig. 1 *Brillouin spectra of $NaNbO_3$ measured with FSR of 3300 GHz at selected temperatures along with the fit for low frequency phonon and CP*

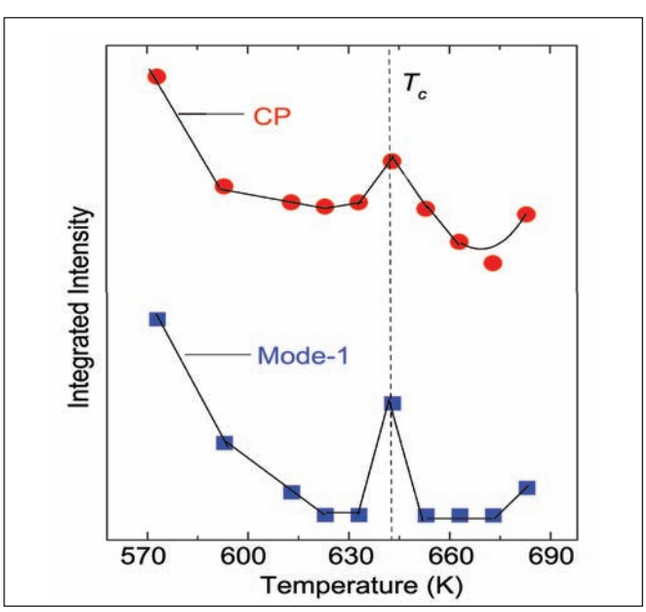

Fig. 2 *Integrated intensities of the CP and the phonon mode-1 as a function of temperature*

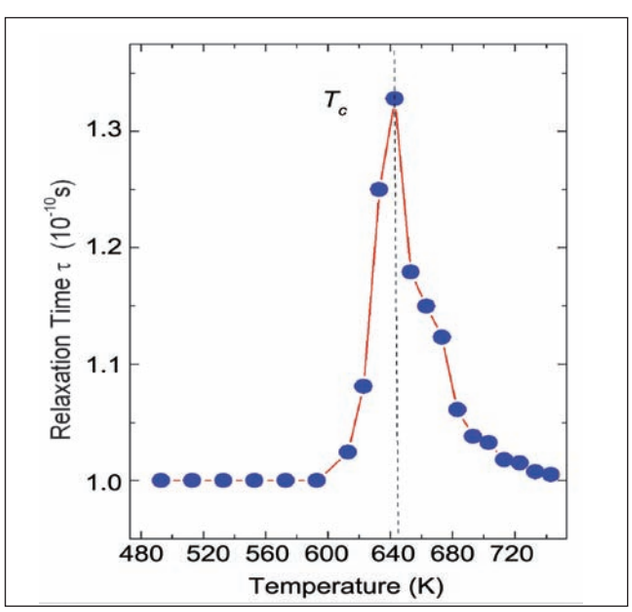

Fig. 3 *Temperature dependence of the relaxation time of CP*

V.23 Thermal Expansion and Structural Stability of $NaZr_2(PO_4)_3$ studied by Raman Spectroscopy, First Principles Calculations and X-ray Diffraction

$NaZr_2(PO_4)_3$ (NZP) is the prototype of a broad family of compounds with a framework structure that are highly stable and flexible. Corner sharing PO_4 tetrahedra and ZrO_6 octahedra form this framework, with the Na ions placed in the interstitial sites. $NaZr_2(PO_4)_3$ family of compounds are well known for their ultralow thermal expansion properties, superionic conductivity and they have also been considered as a host for nuclear waste immobilization due to their ability to accommodate most of the radioactive ions of widely different sizes at the interstitial Na-sites or at the octahedral Zr-sites. High temperature X-ray diffraction and differential thermal analysis on $NaZr_2(PO_4)_3$ showed the absence of phase transitions up to ~1000K. However, there are no reports of high pressure investigations of $NaZr_2(PO_4)_3$ in the literature.

$NaZr_2(PO_4)_3$ exhibits anisotropic thermal expansion, with $\alpha_c = 23.5 \times 10^{-6} K^{-1}$ and $\alpha_a = -5 \times 10^{-6} K^{-1}$, with an overall low positive thermal expansion coefficient $\alpha_{av} = 4.5 \times 10^{-6} K^{-1}$ from 293-1273 K. There are no previous studies of the phonons and vibrational modes responsible for this behaviour. This is a report on our recent investigations of the contribution of the various phonon modes to the thermal expansion of $NaZr_2(PO_4)_3$ through experiments, calculations using density functional theory and also its structural stability at high pressures.

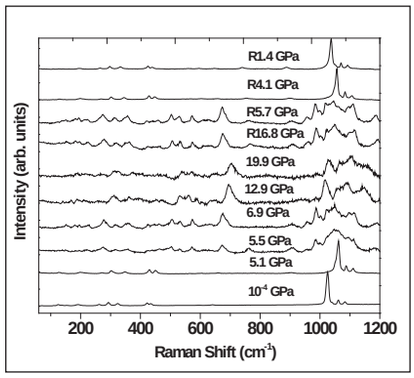

Fig. 1 *Raman Spectra of $NaZr_2(PO_4)_3$ at different pressures. The three spectra at the top are in the pressure reducing run*

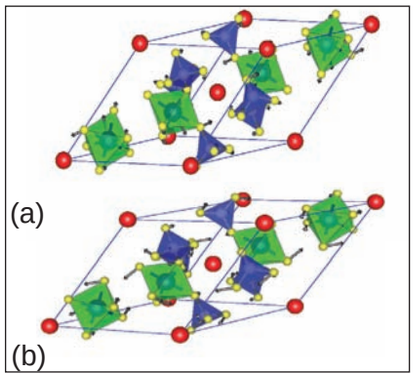

Fig. 2 *Atomic displacements of (a) The 113 cm^{-1} mode (b) The 127 cm^{-1} mode*

$NaZr_2(PO_4)_3$ was synthesized by a sol-gel technique. In situ high pressure Raman spectra were recorded up to 20 GPa from a symmetric diamond anvil cell (DAC), using a micro Raman spectrometer with 514 nm laser excitation. High pressure X-ray diffraction experiments were carried out at ambient temperature using a Mao-Bell type DAC in an angle dispersive mode at several pressures up to 19 GPa. The XRD patterns were indexed with POWD program. Theoretical calculation of phonon spectrum was carried out using VASP (Vienna Ab initio Simulation Package). To compute the phonon spectrum over the entire Brillouin zone and to carry out mode assignments, Phonopy program was used. Visual representations of the different phonon modes were obtained by plotting the eigen vectors of displacement of the various atoms in the unit cell using the VESTA visualization software.

$NaZr_2(PO_4)_3$ crystallizes in a rhombohedral structure with space group R-3c (D_{3d}^6) with six formula units in the crystallographic unit cell. Our group theoretical analysis predicts 25 Raman active and 27 IR active modes from $NaZr_2(PO_4)_3$. Raman spectrum of $NaZr_2(PO_4)_3$ at ambient conditions exhibits 17 distinct Raman bands (Figure 1), similar to that reported earlier. There is a dramatic change in the spectra at 5.5 GPa and the change is reversible on reducing the pressure Raman bands in the range 325-1084 cm^{-1} arise from the internal vibrations of phosphate ions. Lattice modes below 270 cm^{-1} arise from the translations of the Zr and the translations and librations of the PO_4 ions.

Atomic displacement plot -computed by density functional perturbation theory (DFPT)- of the lowest energy Raman active E_g mode at 113 cm^{-1} (Figure 2a) is seen to be a combination of the PO_4 librations and Zr translations that contribute negatively to thermal expansion–consistent with the present experimental and computational results. The E_g mode at 127 cm^{-1} (Figure 2b) seems to exhibit coupled rotation of PO_4 tetrahedra and ZrO_6 octahedra. The

Gruneisen parameter of this mode is experimentally determined to be negative.

From Raman spectroscopic measurements, it is seen that as the pressure is increased, the low energy bands at 72 and 112 cm^{-1} that arise from PO_4 librations and Zr translations soften. There are several distinct changes in the spectra above 5.5 GPa, giving clear indications of a structural phase transformation at about 6 GPa from rhombohedral to a new phase. There are no distinct changes in the spectra of the new phase up to 20 GPa. The mode Gruneisen parameters $\gamma_i = (B_0/\omega_i)(d\omega_i/dP)$, where B_0 is the bulk modulus for several internal modes are significantly positive which indicates that these modes contribute positively to thermal expansion. Negative contribution to thermal expansion is by the two low frequency modes at 72 and 112 cm^{-1} that correspond to librations of PO_4 tetrahedra and Zr translation respectively, reminiscent of other NTE systems such as $Zr(WO_4)_2$ and $Zn(CN)_2$.

The phonon spectrum was computed at a lower volume of 512.96 $Å^3$ (corresponding to 2.65 GPa) in addition to that at equilibrium volume. The Γ-point phonon frequencies at this volume and the equilibrium volume were employed to obtain the mode Gruneisen parameters. The γ_i for all 70 optical modes except the lowest energy Raman active E_g band ($\omega_{calculated}$=113cm^{-1},$\omega_{experimental}$=72cm^{-1}) mentioned above are positive. Using Einstein's specific heat equation for the various modes (i=1 to 70) the total specific heat C_V was obtained. Thermal expansion coefficient $\alpha=(\gamma_{av}C_V)/(3V_mB_0)$, where $\gamma_{av}=½\Sigma p_iC_i\gamma_i/C_V$, p_i are the degeneracies of the respective ω_i phonon branches at the Brillouin zone centre, V_m is the molar volume. The bulk modulus B_0 was computed by fitting the density functional theory-calculated energy versus volume data to the Vinet universal equation of state. Our calculations involve a set of seven energy-volume data and results in a B_0= 44.7 GPa.

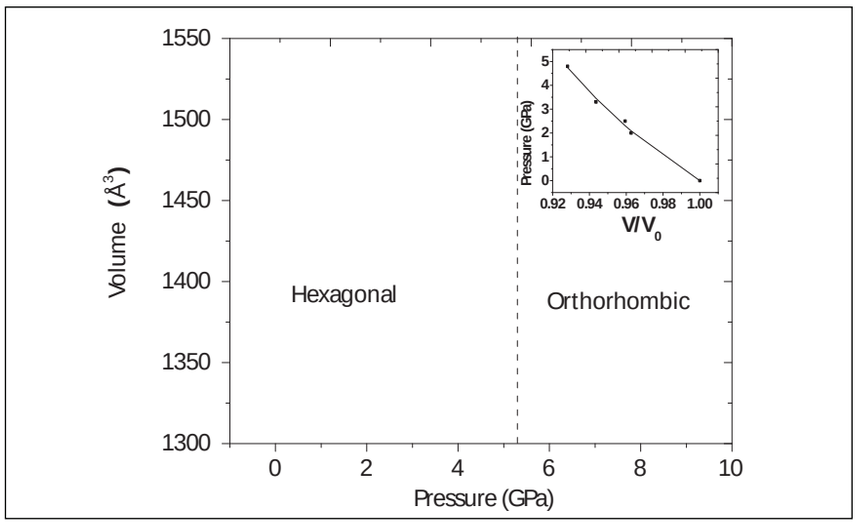

Fig. 3 *Pressure versus reduced volume of the hexagonal phase of $NaZr_2(PO_4)_3$ up to 5 GPa*

We also performed *in-situ* high pressure X-ray diffraction measurements on $NaZr_2(PO_4)_3$ to obtain the bulk modulus and to examine the phase transformation indicated by Raman spectroscopy. Up to 4.8 GPa the patterns could be indexed to a hexagonal structure R-3c with monotonically decreasing volume. Several new peaks (at 2θ = 9.8, 11.2, 15.1, 21.1°) emerge around 5.4 GPa, some old peaks (2θ = 16.1, 24.9) disappear and the pattern is quite different from the starting phase around 9.1 GPa. POWD analysis of these new patterns result in an orthorhombic structure, with a 5% reduction in volume around 5.4 GPa (Figure 3). When the P versus V in the hexagonal phase is fitted to third order Birch Murnaghan equation, a bulk modulus value B_0 of 47.5 GPa is obtained (inset Figure 3). This also validates the computed equation of state.

To conclude, we have investigated the thermal expansion behavior of $NaZr_2(PO_4)_3$ using Raman spectroscopy as a function of pressure at ambient temperature; the individual modes that make negative and positive contributions to thermal expansion in this material are identified, indicating that the PO_4 tetrahedral librations and Zr translations contribute to negative thermal expansion. Our X-ray diffraction measurements also show a reversible phase transformation around 6 GPa, in accordance with Raman spectroscopic observations. The new structure is found to remain stable up to 20 GPa, in contrast to other related framework structures that exhibit negative thermal expansion and pressure induced amorphization. Density functional perturbation theoretical calculations of phonon spectrum of $NaZr_2(PO_4)_3$ were carried out using VASP code. Mode assignments were carried out using Phonopy combined with VASP computed zone-centre phonon frequencies and eigen vectors. Thermal expansion coefficient ($7.5\times10^{-6}K^{-1}$) obtained from the computed quasi-harmonic mode frequencies is in good agreement with the reported experimental value.

V.24 Spin injection Effects in Superconductor Manganite Multilayer Structures

In general, ferromagnetism is known to be detrimental to superconductivity and therefore the coexistence of these two antagonistic phases is rarely seen in the bulk form. However, artificially fabricated thin film heterostructures have made it possible to bring the ferromagnetic phase in close proximity to the superconducting (SC) phase. The interplay of these two phases has resulted in exotic phenomena such as oscillation of superconducting transition temperature (T_c), domain wall superconductivity etc. These phenomena are interesting from the point of view of basic research to understand the mechanism of high temperature superconductivity (HTSC) and also offer the possibility of potential technological applications in the areas such as spintronics. In ferromagnetic/superconducting thin film heterostructures, superconductivity can be influenced mainly by two mechanisms: first is the direct proximity effect involving leakage of Cooper pairs inducing weak superconductivity across the interface and the second is the injection of quasiparticles into the superconducting layer which results in the suppression of the superconducting energy gap. Charge ordered (CO) manganite like $Pr_{0.5}Ca_{0.5}MnO_3$ (PCMO) can be used for the fabrication of such heterostructures in conjunction with high T_c superconductors (HTSC) like $YBa_2Cu_3O_7$ (YBCO) with a view to investigate such effects.

PCMO undergoes a phase transition from charge ordered antiferromagnetic insulating state to charge delocalized ferromagnetic metallic state under an external perturbation like magnetic field, electric field, substrate induced strain etc (schematic diagram in Figure 1a). This ferromagnetic state of PCMO can then be judiciously used as a source of spin injection into the HTSC. A variety of bilayer and trilayer thin film heterostructures of PCMO and YBCO have been fabricated on different substrates like MgO, $SrTiO_3$ (STO) and $LaAlO_3$ (LAO) to demonstrate the spin injection effect in these heterostructures. Measurement of magnetoresistance has been performed on PCMO/YBCO bilayer thin film (schematic diagram in Figure 1c) with different values of applied current (10μA to 40mA) and magnetic fields (0 to 12T). Applied current(I) has been used here as an external perturbation to induce localized clusters of ferromagnetic state inside the matrix of charge ordered PCMO layer. Based on the results of these measurements (shown in Figure 2a and 2b), it is inferred that the charge order melting is initiated in PCMO for I>1mA at H=0T leading to the formation of isolated tiny clusters of the ferromagnetic phase. The size of these ferromagnetic clusters increases with increase in the magnitude of applied current. The T_c of the underlying YBCO layer is thus suppressed by injection of quasi-particles emanating from the top PCMO layer.

T_c of the YBCO layer is decreased not only by the quasi-particle spin injection effects, but also by the direct proximity of the ferromagnetic phase; indeed the latter effect can play a crucial role in determining the overall behavior of the system. This fact can be cleverly used to control the T_c of the superconductor even without the direct electrical contact with the ferromagnetic phase. This behaviour has been demonstrated in another

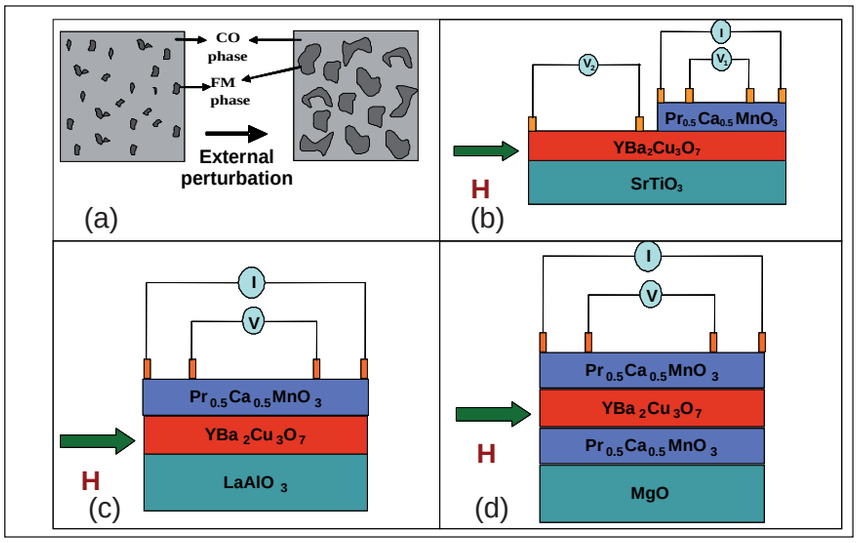

Fig. 1 *Schematic illustration of (a) Ferromagnetic clusters dispersed in a charge ordered matrix of the PCMO film expected to form under the application of external perturbations. (b) YBCO layer partly covered by a top PCMO by in-situ masking (c) YBCO/PCMO bilayer (d) PCMO/YBCO/PCMO trilayer*

experiment where magneto-resistance measurements have been performed on PCMO/YBCO bilayer deposited on STO substrate using an *in-situ* masking technique to cover ~ 50% area of the bottom YBCO layer by a top PCMO layer with a view to delineate the effects of spin injection and proximity effect of ferromagnetic layer on the superconducting properties (schematic diagram in Figure 1b). The T_c seems to be higher and the current induced decrease in T_c smaller on the YBCO portion not masked by PCMO, compared to the corresponding behavior observed for YBCO/ PCMO bilayer (Figure 3a). Flux pinning parameters of the YBCO film in the two regions were deduced from an analysis of the Arrhenius fit of R(T) versus 1/T using thermally activated flux flow model. The activation energy in the part of the YBCO film covered with PCMO was found to be higher compared to that for the part which is not covered by PCMO under applied current and magnetic field. The results clearly show that while T_c suppression effect is stronger in the part of the YBCO film under direct contact with PCMO, significant suppression of T_c is also achieved in the far away region of YBCO film which is not covered by PCMO.

Simultaneous use of multiple sources of external perturbation can enhance the nucleation of ferromagnetic clusters and thus can create a new possibility to effectively control the spin injection effect into the manganite/superconductor hetero-structure. Detailed investigations on PCMO/YBCO/ PCMO tri-layer heterostructures have been used to demonstrate this concept of simultaneous use of two or more external perturbations to influence the formation of ferromagnetic regions in PCMO.

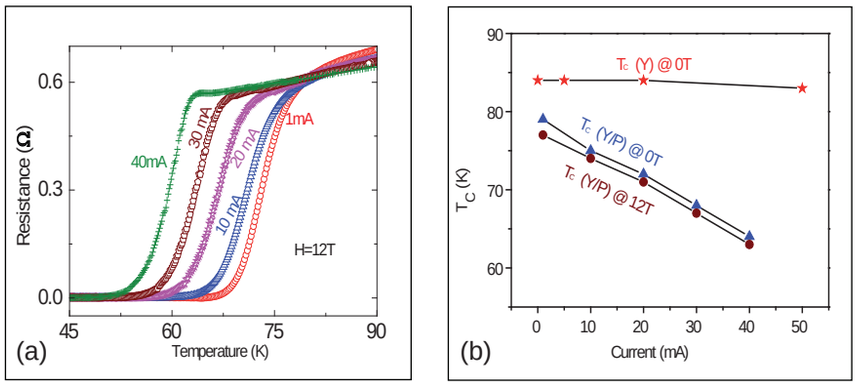

Fig. 2 *(a) Temperature dependent resistance at H=12T for different values of applied current ranging from 1mA to 40mA. (b) T_c vs applied current for a single layer YBCO (denoted as Y) and PCMO/YBCO bilayer (denoted as Y/P) for H=0T and H=12T field*

The trilayer was deposited on MgO substrate (schematic diagram in Figure 1d). There is a 9.2% lattice mismatch between the MgO and PCMO and thus PCMO film with thickness (~40nm) lower than a threshold experiences a substrate induced strain. This lattice strain can assist the formation of ferromagnetic clusters in PCMO. Magnetoresistance measurements have been performed on the trilayers using two different sets of current (1 and 5 mA) applied to the top PCMO layer. The investigations on the T_c for this trilayer for different values of applied magnetic fields and currents (Figure 3b) reveals that the suppression of T_c is much higher for the trilayer compared to that for the bilayer (where strain as a parameter was absent). The suppression of T_c due to the applied current has been measured to be ~ 0.8 K/mA for the trilayer whereas the value was only ~0.35 K/mA for the bilayer. Both substrate induced strain and electric field (current) are responsible for the nucleation of the ferromagnetic clusters in bottom and top PCMO layers respectively and this results in a higher quasiparticle spin injection effect as well as the direct proximity effect of ferromagnetic phase on the superconducting YBCO layer. These results demonstrate that strain can be used to control the formation of ferromagnetic clusters just like applied current.

These experimental results demonstrate the possibility of using controlled formation of ferromagnetic clusters in PCMO as a source of spin injection in YBCO and thereby control the T_c of the YBCO.

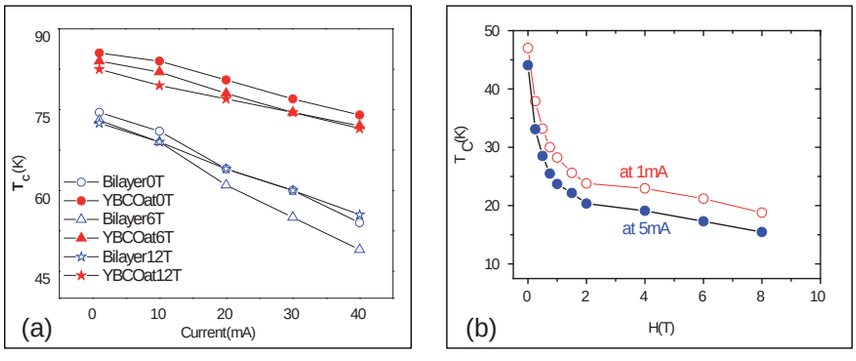

Fig. 3 *(a) Variation of T_c with applied current in masked bilayer heterostructure for the YBCO side not covered by PCMO and for the YBCO side covered by PCMO at H=0, 6 & 12T field and (b) Variation of T_c for trilayer heterostructure at applied currents of 1mA and 5mA*

V.25 Understanding Clear-Band Formation through Multi-scale Modeling of Dislocation Mechanisms

It is well-known that neutron irradiation of metals results in significant hardening, accompanied by ductility reduction. In the case of stainless steel, this is due to the formation of nanometer sized interstitial loops called "Frank Loops". Such deformed materials, under tensile loading, show a localization of these loops into several zones of defect-free regions called "clear bands". Understanding the formation of these clear-bands is of immense interest to the metallurgical community as it directly affects the strength of the material.

Plasticity is a classic case for employing the so-called "Mutliscale Modeling" paradigm where complementary modeling techniques are employed to understand physical phenomena occurring at different length and time-scales. The results obtained at a lower length scale are passed-above as input parameters to models applicable at the higher length-scales. Here, we report one such multiscale modeling effort aimed at understanding the formation of clear-bands in irradiated copper. Our goal in this work is to model irradiation-induced strain localization at the grain scale, using 3D dislocation dynamics (DD) simulations. The DD code used for the study is the edge-screw model called TRIDIS. In this framework, plastic strain is carried by dislocation lines discreticized into edge and screw segments, which glide on a discrete lattice.

In these DD simulations (Figure 1), Frank loops are modeled as prismatic loops, since the required Burgers vector of the loop and the stacking fault mechanisms are not available in TRIDIS. At the beginning of the simulation, the prismatic loops are frozen. When a possible dislocation reaction is detected between a mobile dislocation and a given prismatic loop, if the incoming dislocation is a screw, the loop segments are allowed to move according to the forces acting on them and if it is an edge, it is allowed to just shear the loop, if its resolved shear stress (RSS) is greater than 130 MPa.

With these mobility rules, a $0.60 \times 0.60 \times 0.72$ μm^3 simulation cell is considered. The applied stress tensor shear component is feedback controlled in order to impose a constant strain rate. As the loops are modeled as actual edge dislocations, there is a good deal of stress heterogeneity because of which cross-slip could not be accurately modeled and hence was switched off.

It can be seen from Figure 2 that the leading dislocations (i.e., those emitted first) are wavy and densely jogged: they clear the band first by loop absorption (local reaction) and then by sweeping the jogs towards the cell borders (unpinning mechanism). As a consequence, jogs and loop debris progressively accumulate in the cell borders. Trailing dislocations contain very few jogs since they glide in a region already cleared by the leading

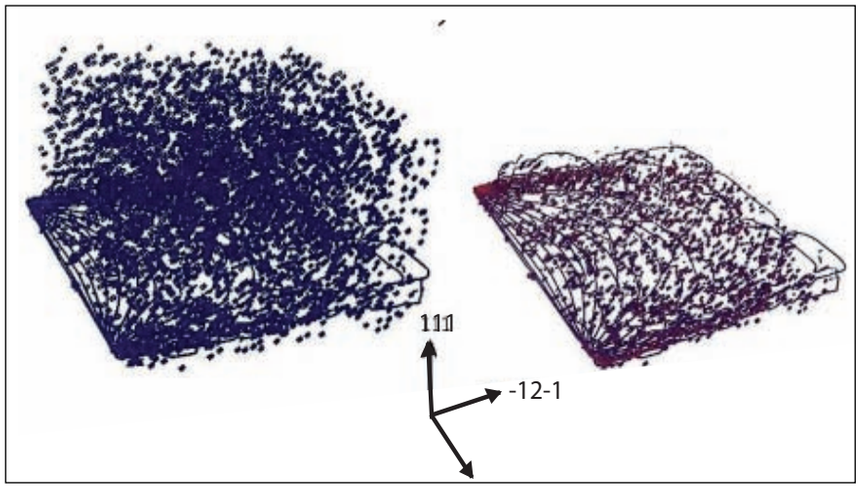

Fig. 1 *Snapshot of the DD simulation, involving the dislocation source and the prismatic loops, along with the zoom-over on the pile-up zone*

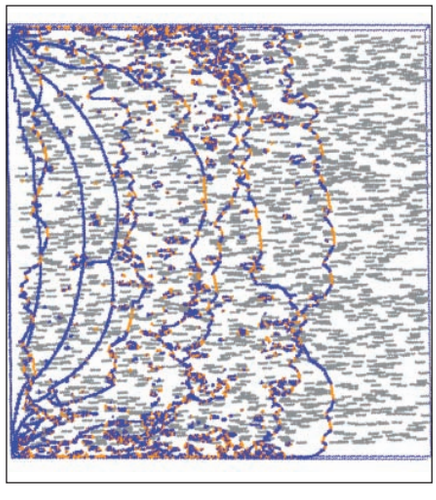

Fig. 2 *Dislocation pile up as seen along the (111) direction*

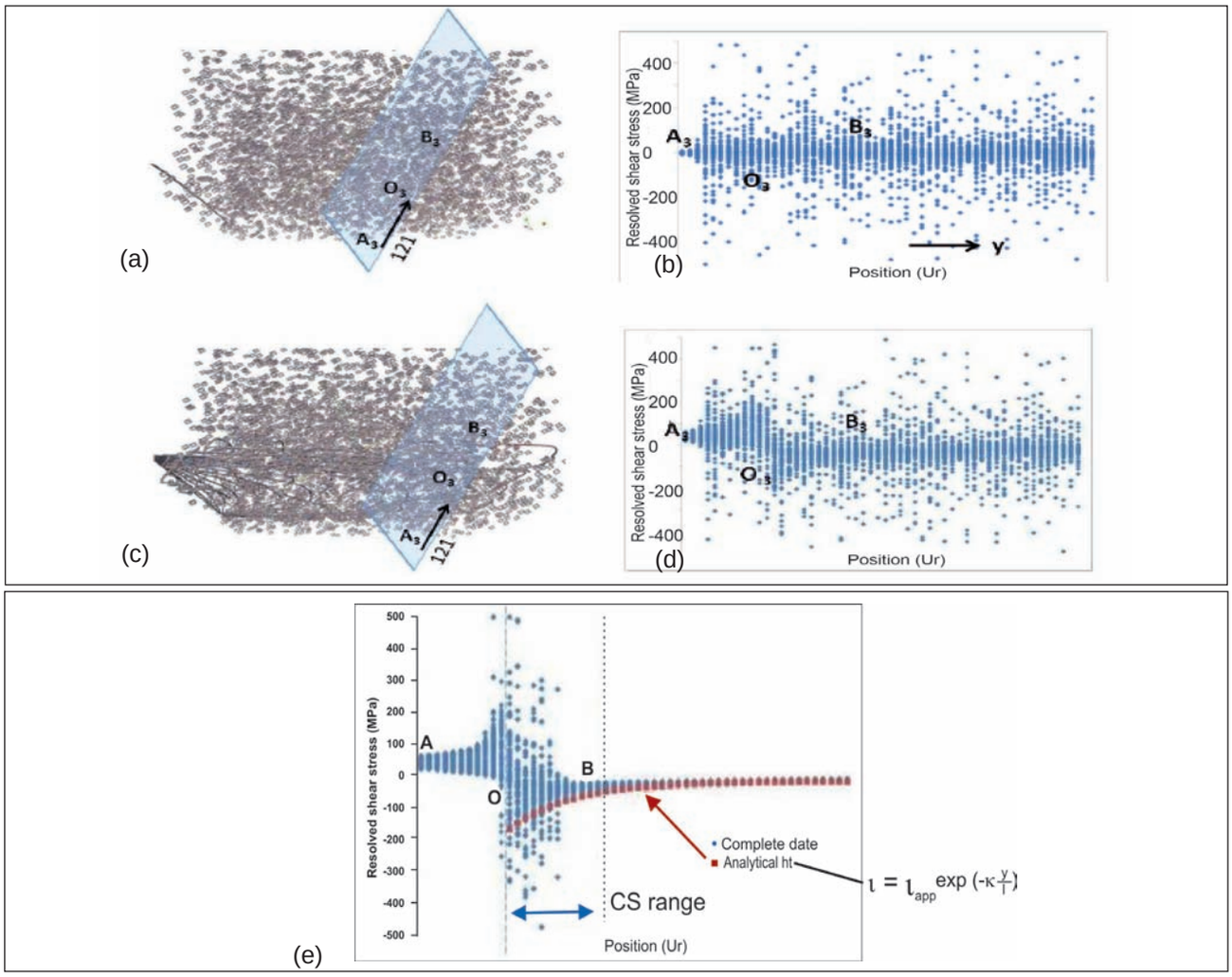

Fig. 3 *Stress profile along the cross-slip plane. (a) and (c) are the snapshots before and after the pile-up. (b) and (d) correspond to the stress profile along the (1,2,1) direction. The difference plot is between the stress values is shown in (e)*

dislocations. Trailing dislocations concentrate stress on leading dislocations by piling-up effect; until dislocation arm exchange and dislocation glide avalanches take place. The whole process gives rise to a finite thickness clear zone, band or channel.

An important effect of pile-up development that can be probed in DD simulations is the progressive accumulation of internal stress in the cross-slip system. For understanding this point further, a 2D mesh comprising 200×200 discrete points is generated parallel to the (1-11) cross-slip plane. The effective resolved shear stress (internal + applied) is calculated in each mesh point. Calculation is done before and after deformation, i.e. after clear band is generated, as shown in Figure 3a and 3c. Stress distribution exhibits a clear deformation-induced evolution in AOB region, with respect to un-deformed condition (compare (b) and (d) of Figure 3). This change is directly ascribed to structure development: shear loops, jogs and debris.

The stress polarized region extends over a certain distance on either side of position O. A clearer picture of deformation-induced changes can be obtained by subtracting after/before plots: stress contribution due to fixed loop is then filtered away. Between point A and point O, i.e. below the glide plane y = 0, stress polarity is positive and gradually increases, as $y \rightarrow 0$. Between point O and point B, i.e. above the glide plane y = 0, stress polarity is negative and gradually vanishes with increasing distance y > O. In any case, the positive stress branch (y < O) leads to acute cross-slip, while the negative stress branch (y > O) yields to obtuse cross-slip.

Since the dislocation induced internal shear stress decays with distance y to the slip plane, the shielding effect is limited to a distance d (with respect to the pile-up plane) above which the effective shear stress level comes down to the applied one. The stress profile along the cross-slip plane thus seems to give a good indication of the clear band width, without having to introduce any explicit cross-slip mechanism.

V.26 Development of an Embedded Atom Method Potential Required for the Study of Stability of Y_2O_3 Nano-particles in α-Fe by Molecular Dynamics and Monte-Carlo Simulations

Molecular dynamics simulation is a powerful tool for studying a variety of material characteristics. The reliability of the molecular dynamics simulation crucially rests on the reliability of the interatomic potential used in the simulations and hence the development of interatomic potential has acquired substantial attention. Study of stability of Y_2O_3 precipitates in α-Fe model alloys (α-Fe-Y-O) in the context of development of oxide dispersion strengthened steels is a current research program being pursued. The development of interatomic potential for α-Fe-Y-O is an important component of this program for studying its properties under radiation damage. The embedded atom method (EAM) is a widely used formalism for the interatomic potentials and it is adopted for the present requirement too. The EAM expresses the energy of the system as

$$E = \sum_i F_i(\rho_i) + \frac{1}{2}\sum_{i,j} \Phi_{ij}(r_{ij})$$

Here i,j represent individual atomic species, $F_i(\rho_i)$ is the embedding energy of i^{th} atom in a background electron density ρ_i, which is the total electron density at that site due to all other atoms. $\Phi_{ij}(r_{ij})$ is the pair potential between i^{th} and j^{th} atoms having interatomic separation r_{ij}.

The generation of the EAM potential for α-Fe-Y-O involves three steps. The first step is to generate the atomic charge densities of the constituent atoms and background electron density at the atomic sites of the relevant reference lattices at different volumes and configurations. The second step is to generate the embedding energy of the constituent atoms and Fe-Fe, Y-Y and O-O pair potentials. The third step is to generate the Fe-Y, Fe-O and Y-O cross-potentials. In order to achieve the goals of 2nd step, we use the ab-initio total energies of the reference lattices at different volumes and configurations in a fitting procedure along with suitable functional forms for the embedding energy and pair potentials. Suitable cut-off radii (r_c) for the evaluation of the background electron densities and pair potentials are used which takes into account all neighbours within r_c. The ab-initio total energies of the Fe, Y and O reference lattices are obtained using the VASP code, which is a state-of-the-art plane wave pseudopotential density functional code that reproduces the experimentally observed chemical behaviour.

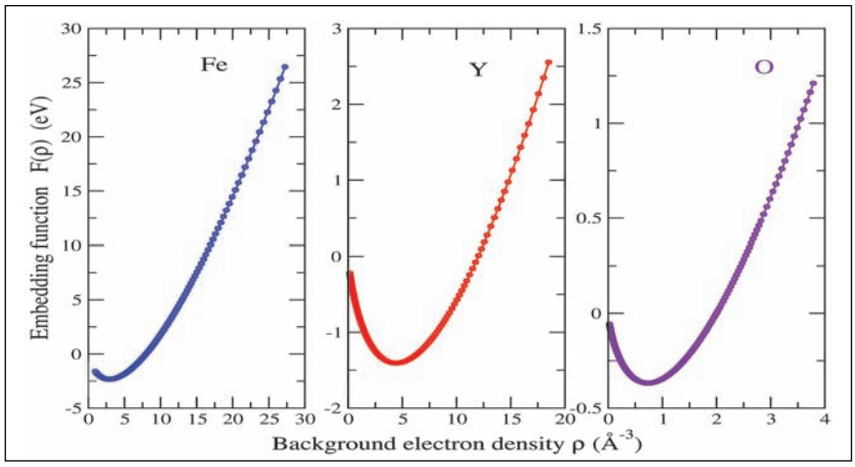

Fig. 1 *Embedding energy of the constituent atoms as a function of the background electron density*

In order to generate the cross-potentials, we consider the Y_2O_3, FeO and Fe_2Y lattices. The ab-initio total energies of these lattices at different volumes and configurations are obtained from VASP. The embedding energies and same species pair-potentials of these lattices at different cell volumes and configurations are generated using the results of the second step and subtracted from the ab-initio total energies to obtain the contribution of the cross-potentials. The interactions thus obtained are used in a fitting procedure to obtain the pair potential between the different species of atoms with the use of suitable functional forms. The r_c for fitting was taken as 5.6 Å so that all the required neighbours are included in the calculation. Thus we have developed the EAM interatomic potential for the α-Fe-Y-O system. The calculations involved in all these three steps, are carried out using the in-house developed computer codes and MINPACK library.

The functional form used for the embedding energy is ,

$$F_i(\rho_i) = AE_S\rho_i ln\rho_i$$

where, *A* is a constant determined by fitting and E_S is the negative of

sublimation energy. Pair potential is written as),

$$\Phi_{ij}(r_{ij}) = (r_{ij} - r_c)^2(C_{1,ij} + C_{2,ij}r_{ij} + C_{3,ij}r_{ij}^2)$$

where, r_c is the cutoff radius and $C_{1,ij}$, $C_{2,ij}$ and $C_{3,ij}$ are coefficients to be determined from fitting. Using these functional forms for the embedding energy and pair potential, we have carried out the fitting to obtain the parameters in the embedding function as well as those appearing in the pair potentials. In all, twenty one parameters required to describe the interatomic potential of α-Fe-Y-O system are determined. We have used the parameters obtained from our fitting to generate the embedding energies of the three atomic species as a function of the background electron density and the pair interaction between the different pairs of atoms as a function of interatomic separation. The embedding energy and pair potentials for α-Fe-Y-O are shown in Figures 1 and 2. The developed potential is applicable only to the α-Fe system and is not transferable.

The potential was used to generate the equilibrium lattice parameter, cohesive energy and vacancy, interstitial and Frenkel defect formation energies and elastic constants using LAMMPS molecular dynamics package and compared against the known values from literature. It was found that while lattice parameter, cohesive energy and elastic constants are reported accurately, the interstitial formation energy was not matching. As we need to study the dynamics of these particles and their stability under irradiation using molecular dynamics, it is necessary to start from a configuration where the Y_2O_3 precipitates are already formed. This is because the time scale of formation of the Y_2O_3 precipitates is very large (~hours) and thus

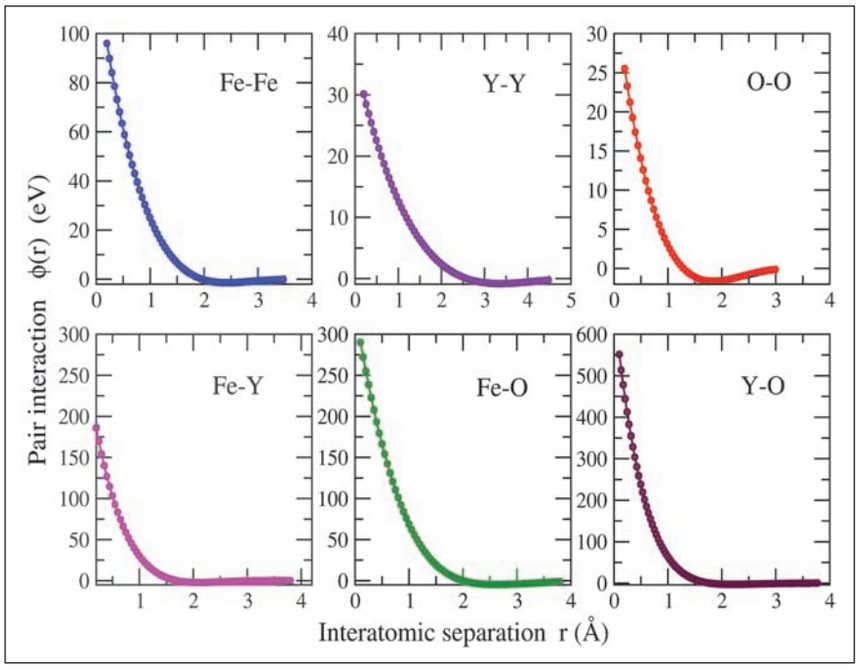

Fig. 2 *Pair potentials of the different pair of atoms as a function of the interatomic separation*

inaccessible to molecular dynamics, which is limited to nanometers and picoseconds in length and time scale. We have developed a lattice Monte-Carlo (MC) code to generate the possible configurations for the α-Fe-Y-O system. This is done by starting from a random mixture of Fe, Y and O atoms and swapping their positions depending on the probabilities determined by the interactions between them as given by our EAM potential. Configurations generated after 100,000 MC steps are taken as representative candidates for further molecular dynamics simulations. A typical α-Fe-Y-O configuration is shown in Figure 3. Average cluster size is ~1 nm, while minimum and maximum cluster sizes are 0.5 nm and > 2 nm.

The improvement of the potential is found to be necessary to achieve a better prediction of material characteristics. Improvement of the potential with the use of additional ab-initio data corresponding to defect lattices and more accurate functional forms for the embedding energy and pair potentials is in progress.

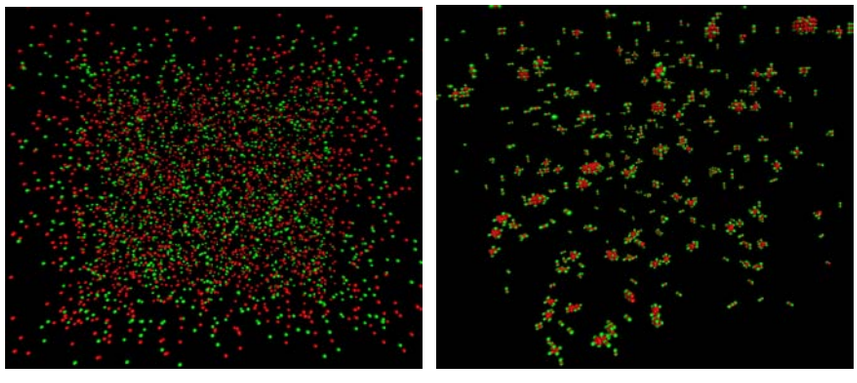

Fig. 3 *Configuration of Y_2O_3 nano-particles generated from MC. Only Y (red) and O (green) atoms are shown for clarity. Left panel shows the starting random configuration, while the right one corresponds to the configuration after 1 million MC swaps. The simulation is for 80×80×80 α-Fe unit cells (~1 million atomic sites), Y: 0.15 at%, O: 0.225 at% and T = 600 K*

V.27 STM Observation of Surface Transfer Doping Mechanism in 3 keV Nitrogen Ion Implanted UNCD Films

Diamond films have been extensively investigated for their application as electron field emitters owing to the negative electron affinity with low effective work function. Ultra nanocrystalline diamond (UNCD) is a fine grain material (3-5 nm) bounded with graphitic grain boundaries (1 nm) and smooth films can be prepared. The properties of UNCD films are found to depend on the grain size while the structure of the grain boundaries determines the electrical and optical characteristics. Electron field emission properties of UNCD are enhanced by doping the films with nitrogen. Two mechanisms of field emission in UNCD are proposed in literature and the suitable mechanism is still under debate. One is conducting channel mechanism where grain boundaries are the prominent electron emitters. Another mechanism is transfer-doping process where the grain boundaries can transfer electrons to the grains and make them semiconducting. We have used scanning tunneling microscopy (STM) and current imaging tunneling spectroscopy (CITS) in detail to understand the mechanisms controlling the field emission.

The UNCD films of ~ 300 nm thickness are grown on n-type Silicon substrates using a microwave plasma-enhanced chemical vapor deposition (MPECVD) process with IPLAS-Cyrannus reactor. Prior to the growth of UNCD films, the substrate was preseeded by ultrasonication in nanodiamond and Titanium powder and the films are grown in hydrocarbon plasma containing CH_4 /Ar in the ratio 1:99 at 1200 W and at 120 Torr for 3 hours. The films are implanted with 3 keV N^+ ions at fluences from $1x10^{14}$ to $5x10^{16}$ ions/cm^2 at room temperature from an indigenously built 30kV ion implanter which is installed recently. This has a hollow cathode ion source. Some of the films are implanted with 75 keV nitrogen ions from a 150 kV accelerator using RF ion source. SRIM2003 shows projected range of 5.4 and 110 nm and longitudinal straggling of 2.3 nm and 19 nm for 3 keV and 75 keV N ions respectively in diamond. Field emission measurements are carried out in a home built tuneable parallel plate capacitor setup. STM/STS/CITS measurements are done using a commercial UHV-STM operating in the range of 90-400 K and at a base pressure of 10^{-10} mbar.

Compared to pristine UNCD, enhancement in field emission is observed in both the 3 and 75 keV nitrogen implanted UNCD films. The turn on voltage decreases with increase in ion fluences. Figure 1a shows the STM image of pristine UNCD (a) and its corresponding CITS image (b) at a sample bias of -3.75V. STM shows grain sizes of 3 to 8 nm. Bright and dark regions in CITS image are visible with their shapes having similarity with the shapes of grain boundaries and grains which are marked 2 and 1 respectively. The CITS image (Figure 1b) shows clearly that the emission sites are mainly located along the grain boundaries. I-V curves are measured at more than twenty positions on the grain and grain boundaries and an average I-V curve is made. Figure 1c shows the variation of normalized conductance (dI/dV)/(I/V) against V which provides

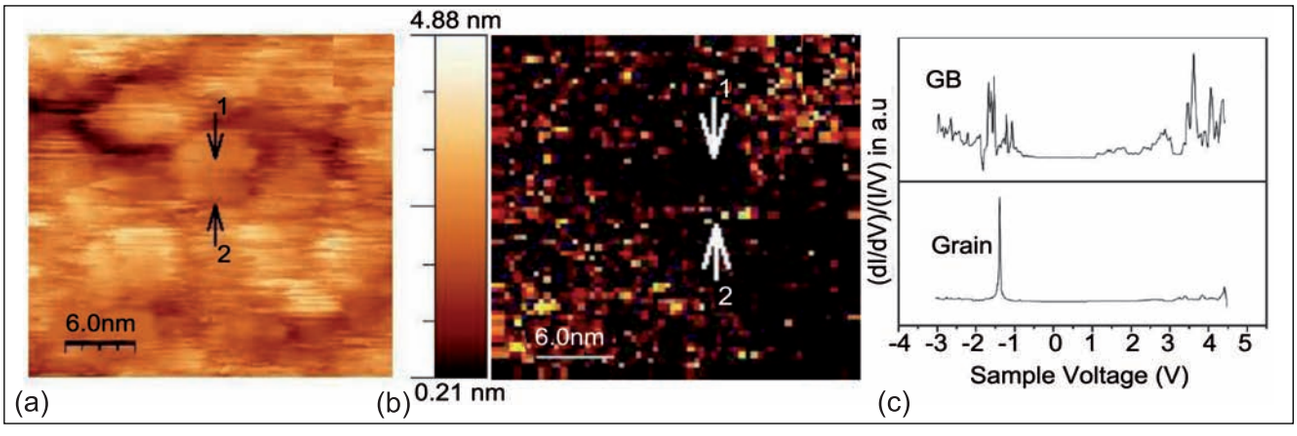

Fig. 1 *(a) STM image from pristine UNCD, (b) Its corresponding CITS image and (c) Variation of normalized conductance with (dI/dV)/(I/V) at grain and grain boundaries*

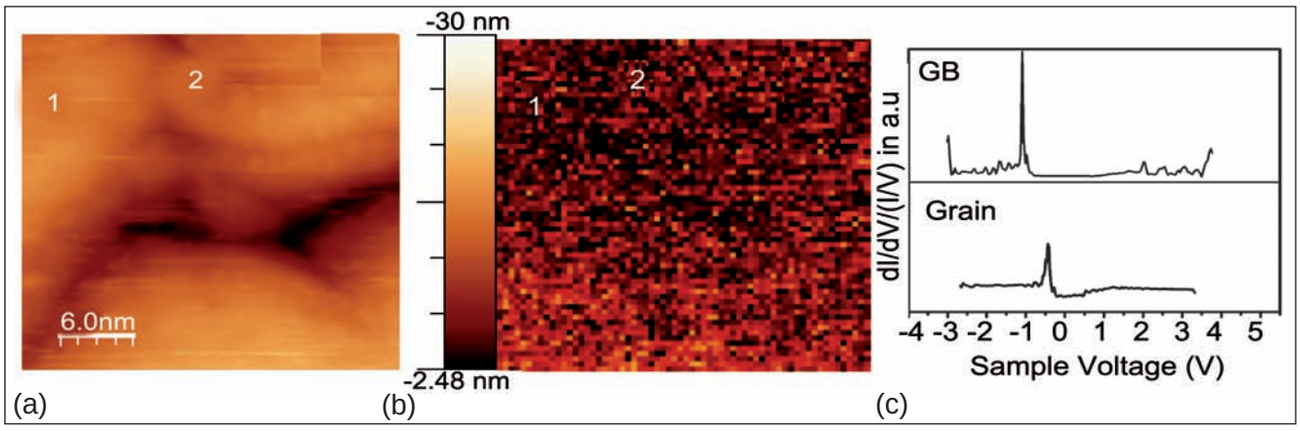

Fig. 2 *(a) STM image from 3 keV N+ implanted UNCD at a fluence of 5x10^{15} ions/cm^2 (b) Its corresponding CITS image and (c) Variation of Normalized conductance with (dI/dV)/(I/V) at grain and grain bound*

the information on the distribution of the surface density of states (DOS) and the bandgap of the materials. The band gap is measured to be 4.8 eV at the UNCD grain which is close to the theoretical value of 4.2 eV in nanodiamond and 3.8 eV at the grain boundary for as prepared UNCD. The singularity in the band gap region is removed by using an average value for I/V which is nonzero. Bandgap at grain boundary will be due to the presence of sp^2 and amorphous carbon. Density of states are not seen in the bandgap of grain. STM measurements of 75 keV nitrogen ion implanted UNCD also shows similar behavior like pristine UNCD with grain boundaries as dominant electron emitting sites but with proportionally smaller band gaps for both grain and grain boundaries.

Figure 2a shows the STM image of UNCD implanted with 3 keV nitrogen ions at a fluence of 5x10^{15} ions/cm^2 and its corresponding CITS Figure 2b at a sample bias of -4.18V. 6 to 30 nm size agglomerates are observed in STM images. CITS shows bright image from almost the whole surface except a smaller fraction of area resembling grain boundaries.

The agglomerates look like large diamond grains (marked 1) with facets which are bright. Thinner grain boundary like regions 2 (z-like) show poor emission and are in dark colour. Within the agglomerate, there appears to be some domains and domain boundaries. The domains are emitting electrons while the domain boundaries are not emitting. Contrast to this, in pristine and 75 keV nitrogen implanted UNCD only the grain boundaries emitted the electrons and they were the dominant emission sites. Some finer diamond grain structures are visible within the domain in STM image. It is likely that morphology of UNCD grains underlying the implanted layer is visible. But CITS is unable to resolve them further and shows brighter contrast. From Figure 2c, the band gap is measured to be 0.74 eV at the UNCD grain and 4.3 eV at the grain boundary for 3 keV nitrogen implanted UNCD consistent with CITS image. N-ions implanted at the surface will introduce some lattice defects and will convert a fraction of sp^3 in diamond grains to sp^2 phase and introduce density of states in the bandgap. This can enhance the conductivity and field emission properties. C1s XPS spectra (not shown) show sp^2 C=C, sp^3 C-C, C=N, C-N bonding components with binding energies 284.4, 285.1, 286.9 and 287 eV respectively. C=N is likely to be dominant at the grain boundaries where sp^2 bonded C is dominant and C-N is likely to be dominant in the grains where sp^3 bonded C is dominant. Among the relevant carbon–nitrogen bonding states, the largest effective negative charge on the nitrogen atoms is assigned to fragments with conjugated bonds (C=N). A conjugation leads to an increase of the effective negative charge on the nitrogen atoms. Consistent with charge transfer consideration, nitrogen ions residing at grain boundary can efficiently convert the UNCD grains into semiconducting via the transfer doping process, enhancing the electron field emission properties.

When N$^+$ ions are implanted at 3 keV, sp^2 carbon content at the surface of the grain will be more and there will be sufficient number density of C=N bonds at the UNCD grain surface as well as the grain boundaries and converting the grains into semiconducting by surface transfer doping process. In this case, diamond grain will be the dominant emitter. At 75 keV, nitrogen is buried deeper and C=N bonds and sp^2 C will be mostly at the grain boundaries and the field emission is dominated by conducting channel process and the grain boundaries will be the dominant emitters. The concentration of nitrogen and its depth profile appears to dictate the field emission mechanisms.

V.28 Recovery of Quantum Effects in Atom-Field Dynamics: Thermal Noise versus Photon-addition

Thermal radiation is a source of noise in the context of coherent signal. This source of noise is unavoidable at finite temperatures, making it necessary to understand its effects. Thermal radiation is characterized by the temperature of the source of photons, specifically, the average number of thermal photons is related to the temperature of the source. The photon-number distribution, which gives the probability of detecting the radiation in a given excited state, is a monotonically decreasing function. Higher the excited state smaller the probability of detection. A coherent state is another state of the electromagnetic field. A single mode coherent state is generated in the output of a laser operating well above the threshold. Since, finite temperature implies presence of thermal noise. It is important to know the effects of its presence. There are two distinct ways of incorporating thermal noise: superposition of coherent signal and thermal field and mixing of thermal radiation and coherent field. The former states are called displaced thermal states (DTS) and the latter are mixed thermal-coherent states (MTCS).

The simplest case to study is the system of a two-level atom interacting with a single mode electromagnetic field. The two-level system is modeled as an electric dipole. The interaction between the atom and the field leads to nontrivial evolution of the combined state of the field and atom. Two important features of the system are the atom-field entanglement and the population inversion in the two-level atom. Population inversion W(t) is defined as the difference between the probabilities for the atom to be in its excited and ground states. If population inversion is positive [respectively, negative], the probability to be in the excited state is higher [respectively, lower]. The temporal behaviour of W(t) has very distinct quantum features, if the electromagnetic field is in a coherent state prior to its interaction with the two-level system. The population inversion shows oscillations to begin with, collapses to zero and remains so for a duration. Then, it revives to attain nonzero values. This revival is a quantum feature. No classical stationary stochastic field can induce that type of revival.

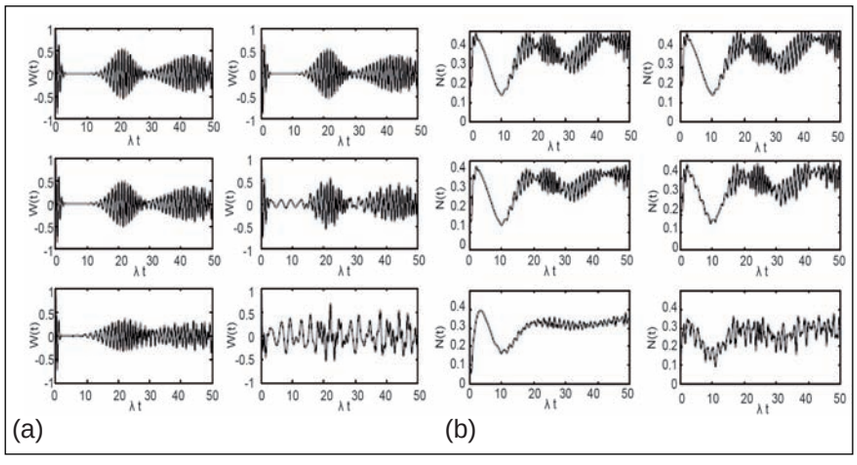

Fig. 1 *Dynamics of (a) Population inversion without photon-addition and (b) Entanglement without photon-addition*

If thermal noise is present, the "collapse-revival" phenomenon in the dynamics of W(t) is lessened or absent. Both mixing and superposing of thermal noise affect the collapse-revival of structures. Nevertheless, in the case of thermal noise superposition the effect of thermal noise is less pronounced (Figure 1a). In Figure, first column corresponds to DTS and the second corresponds to MTCS. First row is noise-free case, second row corresponds to one percent noise and the third row corresponds to ten percent noise.

Photon-addition is a way of adding energy to the field, by changing the contribution of different excited states to the state of the field. With the addition of a single-photon each to the coherent state and the thermal field, the dynamics between the field and the atom is drastically changed. If the initial field of the atom is the photon-added version of the noise-incorporated coherent state, the "collapse-revival" structures are preserved. In other world, the result of photon-addition is to mitigate the effects of thermal noise (Figure 1b). In essence, photon-addition has infused quantumness in the system as shown by the recovery of the collapse-revival structures in the dynamics of W(t).

Quantum theory, being a linear theory, allows for superpositions of states of the system. This leads to a peculiar feature of composite quantum systems made of two or more subsystems. The state of the composite system may not factor so as to identify the states of the subsystems (atom and that of the field are the subsystems in the present case). Such a state, wherein the subsystems do not

have a state of their own, though the composite system is in a well defined state is an example what is known as "entangled state". It is a unique feature of composite systems in quantum theory. It is possible to quantify the amount of entanglement in a composite system made of two subsystems. Interestingly, the time evolution of the entanglement also exhibits features similar to those of the population inversion. Presence of thermal noise affects these features. It turns out that photon-addition has the power to offset the effects of thermal noise and reintroduce the quantal features in the evolution of the atom-field entanglement.

V.29 Trihalomethanes Formation in Chlorinated Seawater

Chlorination is an important and widely used process adopted by almost all power plants over the world to control biofouling in the condenser cooling water system. Chlorine, in addition to its intended function, reacts with the natural organic matter (NOM) present in the water to form various chlorination byproducts (CBPs) in the chlorinated water. Trihalomethanes (THMs: $CHCl_3$, $CHCl_2Br$, $CHClBr_2$, $CHBr_3$) are ubiquitously present and are one of the dominant group formed among all CBPs. They are suspected to cause cancer, liver and kidney damage, retarded foetal growth, birth defects and possibly miscarriage. Formation of trihalomethane due to seawater chlorination and mixing of it into sea raises concern over the toxicity stress to the marine organism and consequently to human through food chain process. Formation of trihalomethane due to seawater chlorination was investigated.

Analytical setup was established for an accurate low level (ppb) determination of trihalomethane in aqueous matrix. Identification and quantification of trihalomethane was performed with GC equipped with an electron capture detector (^{63}Ni). As shown in Figure 1, the four trihalomethanes species, $CHCl_3$, $CHCl_2Br$, $CHClBr_2$ and $CHBr_3$ are well resolved under the adopted chromatographic conditions and the limit and sensitivity of detection for the present instrumental condition is in the following order $CHCl_2Br$ (0.01 µg/l)> $CHClBr_2$ (0.01 µg/l)> $CHBr_3$ (0.05 µg/l) > $CHCl_3$ (0.07 µg/l).

Effect of physico-chemical characteristics on formation of trihalomethanes

Trihalomethanes in the chlorinated seawater are found to form via a fast initial reaction. Bromoform was observed to be the main constituent (96-98%) of the trihalomethane in the chlorinated seawater in all experimental conditions (Figure 2). Significant amount of trihalomethane was formed within very short period of contact time and the rate of formation was observed to be subsided after five hours for all studied temperatures and chlorine doses. After five hours of reaction time the concentration of trihalomethane formed represented nearly 50% of the total yield for all applied chlorine dose. However, it was observed that trihalomethane were continued to form though a very lower rate even up to 168 hours of reaction time. The continuance of trihalomethane formation for such a long period also indicated the possible formation of trihalomethane due to transformation of initially formed long chain chlorinated organic

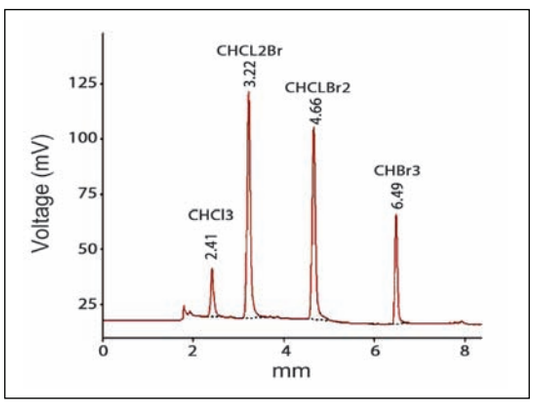

Fig. 1 *Separation of four trihalomethanes species*

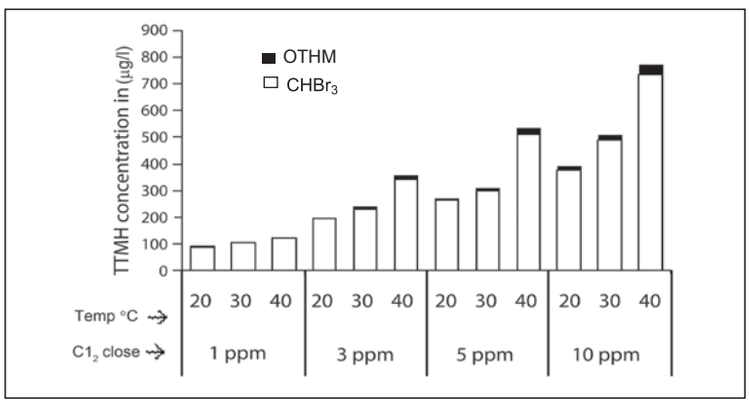

Fig. 2 *Distribution of trihalomethane species formed after 168 hours of reaction*

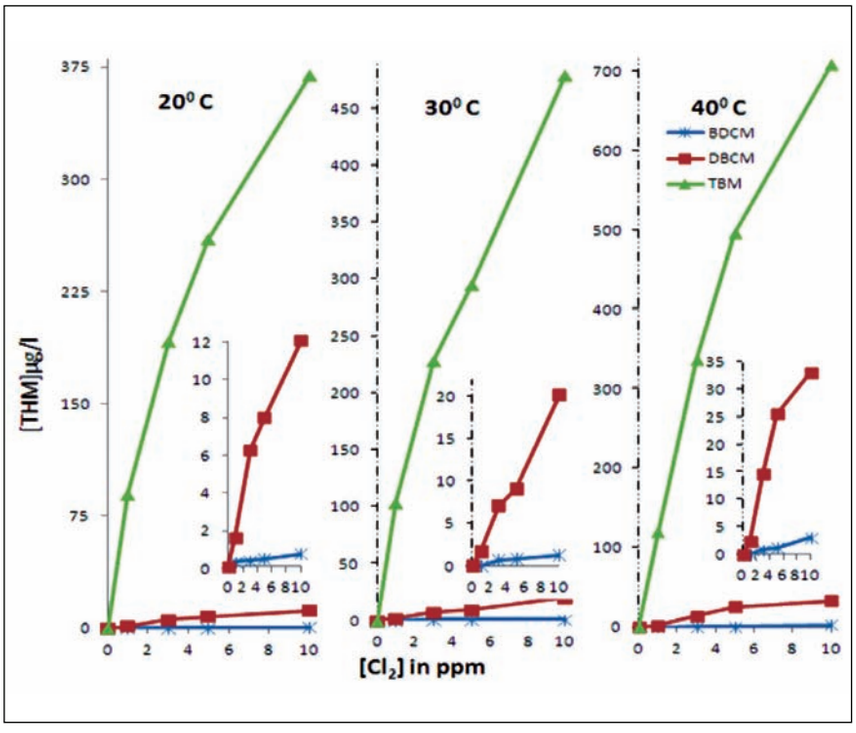

Fig. 3 *Formation kinetics of trihalomethane species at different conditions*

by-products. Higher chlorine dose and elevated temperature favored formation of trihalomethane, but fraction of halogen incorporation was observed to be gradually decreased with increasing chlorine dose from 1 to10 ppm. Elevated temperatures not only enhance the rate of formation of trihalomethanes but also increased the total yield. Load of trihalomethane found to be increased 80-90% more when temperature was increased from 20 to 40°C. The increase in the overall yield of trihalomethane was more significant when temperature was increased at higher range. natural organic matter fractions have become reactive at elevated temperatures which were otherwise inactive and became liable to react with the available oxidant forming more trihalomethane at higher temperature.

Speciation characteristic of Br-Trihalomethanes

The overall formation order of trihalomethane species at all experimental conditions was noted to be $CHCl_2Br < CHClBr_2 < CHBr_3$ and formation of $CHCl_3$ was not observed (Figure 3). Predominant formation of Bromoform is attributed to the formation of Hypobromous acid (HOBr) due to the reaction of HOCl and Br^- in seawater which contains ~65 ppm of Br. Bromoform was the only detected trihalomethane species at the very initial stage of the seawater chlorination, formation of $CHClBr_2$ and $CHCl_2Br$ was found to be favored by higher contact time, chlorine dose and temperature. Maximum concentrations of $CHCl_2Br$ and $CHClBr_2$ were found to be 3.15 µg/l and 33.16 µg/l respectively at 40°C with 10 ppm Cl_2 dose. Incessant formation of $CHCl_2Br$ and $CHClBr_2$ indicated the possibilities of some indirect reaction pathways for $CHCl_2Br$ and $CHClBr_2$ formation. Some mono- and di-chloro substituted natural organic matter might have formed at the very initial period of chlorination when HOCl molecule possibly coexisted with HOBr for a very short period, then the slow reactive mono- and di-chloro substituted natural organic matter fractions undergone bromination to produce the bromo-chloro species of trihalomethane at a longer contact time. However, due to the rare availability of adequate HOCl molecule at any time, successive chlorination of natural organic matter and formation of $CHCl_3$ was unfavorable in the chlorinated seawater.

Trihalomethanes in the MAPS cooling seawater discharge

Madras Atomic Power Station adopts continuous low dose chlorination of about 1 ppm so as to maintain a residual level of 0.1-0.2 ppm at the discharge outlet. Seawater samples from the MAPS cooling water discharge area were collected monthly, to investigate concentration and distributions of trihalomethanes species at the discharge cooling water outlet. The monthly average of total trihalomethane concentration in the discharge area were found to be vary between 12-41 µg/L during the study period, with Bromoform as the most dominant trihalomethanes species. Apart from Bromoform, negligible amount of $CHClBr_2$ was detected (< 1 ppb). Laboratory chlorination studies have shown that, concentration of trihalomethane formed within 5-15 min under laboratory chlorination of intake sea water with 1ppm Cl_2 dose at 30°C can be comparable with observed trihalomethanes in the discharge seawater of Madras Atomic Power Station. Observed trihalomethanes concentration in the discharged water always remained well below the WHO-2012 guideline values ($CHCl_3$<300, $CHCl_2Br$<100, $CHClBr_2$<60, $CHBr_3$<100 µg/L) and thus, do not pose any toxicological threat to marine organism.

V.30 Development of Radiation Response Biomarkers by Gene Expression Techniques

Quantitative-Polymerase Chain Reaction based assays that measure gene expression changes, mitochondrial DNA deletions and nuclear DNA mutations can be used as biodosimeters for accidental exposures of human to radiation. These molecular biomarkers provide robust approach for high-throughput minimally invasive radiation biodosimetry. Quantitative-polymerase chain reaction measurement of gene expression offers rapidity, sensitivity and reproducibility. Although this technique appears to evolve into a useful biodosimetry technique, validation from many laboratories on different ethnic communities is a likely prerequisite before it could find application in biodosimetry.

When cells are exposed to ionizing radiation, complex network of signal transduction pathways are activated to overcome the stress by regulation of genes involved in processes of signal transduction, cell cycle control, DNA repair and apoptosis. Up regulation or increased transcription of genes occurs due to the DNA damage caused either by direct hit of ionizing radiation exposure or indirectly by free radicals. *Growth arrest and DNA-damage-inducible 45 alpha* (*GADD45A*), cell cycle regulation and DNA repair gene and its expression is stimulated upon exposure to ionizing radiation. *GADD45A* is known to stimulate DNA excision repair and inhibiting entry of cells into S-phase of cell cycle. *GADD45A* interacts with *CDKN1A*, which mediates the p53-dependent cell cycle G_1 phase arrest in response to a variety of stress stimuli including exposure to radiation. Analyzing the level of expression pattern (transcription) of these genes in response to radiation by quantitative-polymerase chain reaction technique could serve as potential biological dosimeter. Towards this, e*x vivo* irradiation of whole blood obtained from healthy individuals has been used for relative gene expression analysis by quantitative-polymerase chain reaction technique.

Effects of gamma radiation on gene expression

Expression pattern changes of genes *GADD45A* and *CDKN1A* in human peripheral blood lymphocytes when irradiated with gamma radiation at dose rate (2.9 Gy/min) with total doses ranging from 0.5 to 4.0 Gy. *18S rRNA* was used as internal control gene. Relative fold change in expression changes of genes *GADD45A* and *CDKN1A* after irradiation at 24 hours and 48 hours were calculated from mean fold change in expression of the target gene using $2^{-\Delta\Delta Ct}$ method. Here, $\Delta\Delta Ct = (C_{t,target\ (GADD45A/CDKN1A)} - C_{t,\ 18SrRNA})$ irradiated after 24 hours / 48 hours - $(C_{t,target\ (GADD45A/CDKN1A)} - C_{t,\ 18SrRNA})$ non-irradiated after 24 hours / 48 hours. The C_t (cycle threshold) is defined as the number of cycles required for the fluorescent signal given by PCR amplified product to cross the threshold (i.e. exceeds background level). (Figure 1)

Expressions of both candidate genes were found to increase linearly with increasing doses at 24 hours. Genes *GADD45A* and *CDKN1A* exhibited 2 to 11 fold and 4 to 18 fold changes in expression levels respectively, with increasing radiation doses (Figure 2). Their expression levels returned to basal levels after 48 hours when compared to sham irradiated controls.

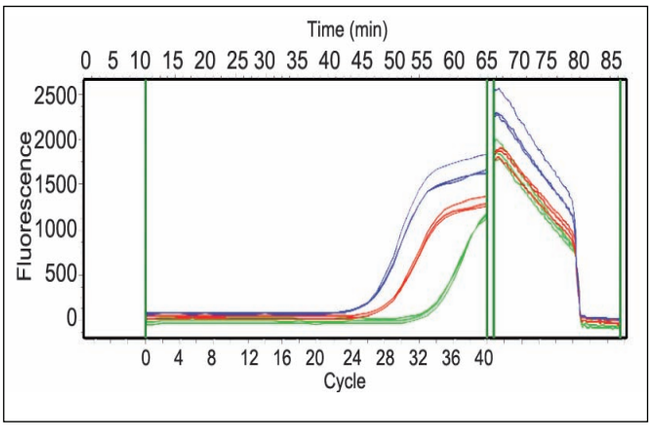

Fig. 1 *Real time PCR amplification plot showing C_t (cycle threshold) for three different samples for gene 18SrRNA*

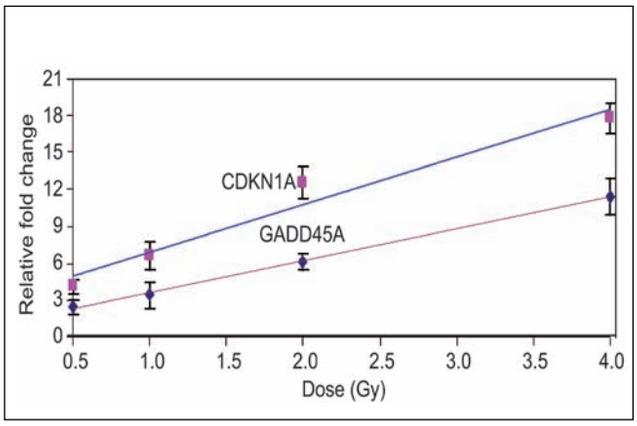

Fig. 2 *Relative expression of GADD45A and CDKN1A in irradiated human lymphocytes after 24 hours*

V.31 Zoo-plankton Dynamics and Imprint of Monsoonal Fish Assemblage in the Coastal Waters of Kalpakkam - A Seasonal Perspective

Zooplankton dynamics

Zooplankton is considered as the chief index of utilization of aquatic biotope at the secondary trophic level. Photographs of a few typical zooplankton species are given in Figure 1. As primary and secondary consumers, they account for about one tenth of the total marine biomass on which the whole class of fishery depends upon. Thus, their abundance is taken as one of the prime indices of the available fishery resources of water masses. Owing to such multi-faceted economic and ecological utility, zooplankton constituted a core subject of research in all marine biological investigations. Moreover, zooplankton study from this location is first of its kind and thus, a baseline data on zooplankton assemblage is of prime importance to evaluate the future impact. In view of this, study has been undertaken to assess the qualitative and quantitative aspects of zooplankton community in the coastal waters of Kalpakkam.

Zooplankton samples were collected using conical plankton net with mouth area 0.125 m^2 (mesh size-200 µm) fitted with flow meter (Hydrobios). The samples were brought to the laboratory and preserved with 5% buffered formalin for further analysis. Zooplankton biomass was measured by volume displacement method. The larger organisms of zooplankton community from both holo (whole life plankton) and meroplankton (larval plankton) were sorted out from the plankton mixture and counted separately. The residual

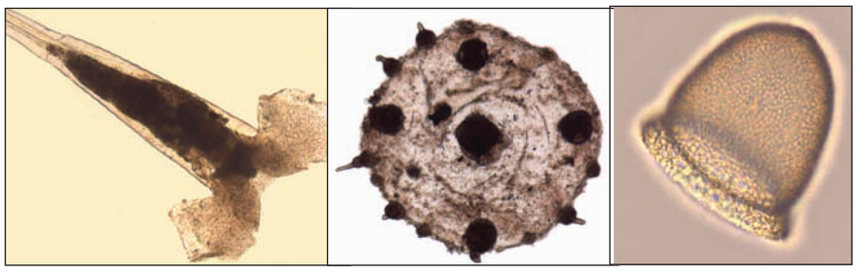

Fig. 1 *Few typical zooplanktons (a) Cresis acicula (b) Phialella quadrata and (c) Petalotricha ampulla*

mixture was then diluted to exactly 100 ml with folmaldehyde solution. One ml of this aliquot was transferred onto Sedgewick Rafter cell and examined under a stereo binocular research microscope for counting numerical density. The numerical density was expressed in terms of individuals 10 m^{-3}.

Results of qualitative aspects of the study period showed that in total, 255 species of mesozooplankton (size-0.2 – 20 mm) were found, of which, 22 were meroplankton, 198 holoplankton (Copepod – 123 and non-copepod holoplankton - 75) and the rest is unidentified species. The zooplankton community comprised of 12 phylums of holoplankton and 7 phylums of meroplankton. Qualitatively, this coastal region was found to be rich compared to other coastal waters of east coast (110) and west coast (138) of India. Copepod population was found to be predominated over the other groups in zooplankton community. During the study period (for the year 2012), the lowest (15) and highest (45) zooplankton species were observed in monsoon and post-monsoon seasons respectively.

The highest population density (7.1 x 10^5 Individuals $10m^{-3}$), qualitative number and biomass (0.40 g. dry $wt.^{-1}$) observed during post-monsoon/summer could be ascribed to the stable as well as optimal salinity, temperature, light, nutrient levels etc prevailed during these periods (Figure 2 and 3). However, the lowest number of species density (2.6 x 10^5 Individuals 10 m^{-3}) and biomass (0.22 g. dry $wt.^{-1}$) were found during

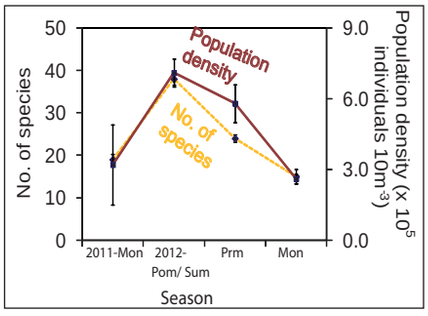

Fig. 2 *Seasonal variations in zooplankton population density and no. of species*

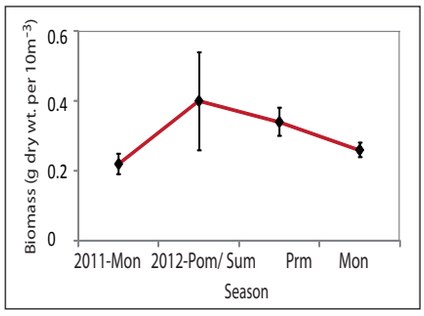

Fig. 3 *Seasonal variations in zooplankton biomass*

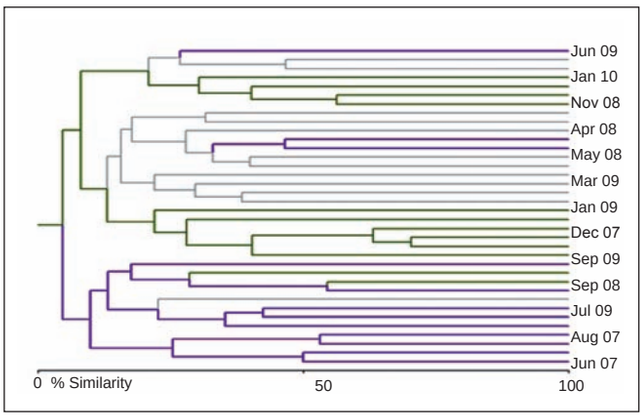

Fig. 4 Dendrogram showing seasonal diversity

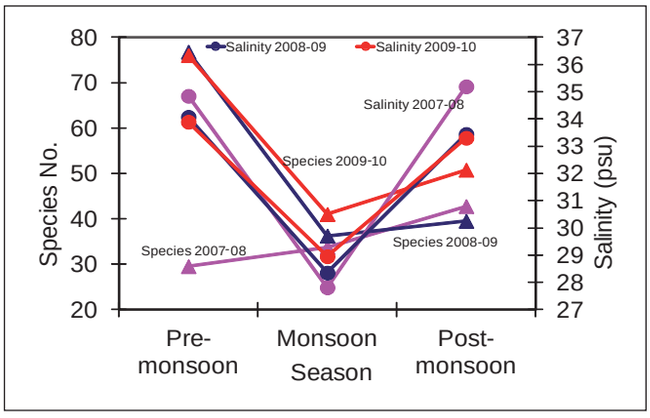

Fig. 5 Seasonal fluctuations in the species no. versus salinity

monsoon period, which coincided with the unfavorable environmental features prevailed during monsoon period and this did not support the zooplankton community survival and growth.

Fish assemblage on a temporal scale

A baseline study for piscean diversity was initiated to understand its spatio-temporal distribution along the coast of Kalpakkam.

Samples of fishes were collected at regular weekly intervals for a period of three years from landing centers of Pudupattinam and Sadras (12º33´N, 80º11´E) as well as from MAPS pump-house. So far, nearly 2546 marine fishes have been reported from Indian waters of which 569 species reported from south-east coast of India. During the ongoing study, we have discovered 342 species of marine fish from Kalpakkam coast, of which 281 species have been identified, representing 21 Orders, 97 Families and 187 Genera. Photographs of a few typical fish species from Kalpakkam coast are given in Figure 6. Over the period, the fish assemblage was dominated by the members of the Order Perciformes with 167 species (59.8 %) followed by Clupeiformes (6.45 %), Tetraodontiformes (5.73 %) and Pleuronectiformes (5.37 %). Out of these 281 species, 26 are new to the coast of Tamil Nadu, of which 15 are new to the East coast of India, of which 11 are new to the Indian coast. This also includes two cryptic species which are new to science.

In order to map the diversity on a temporal scale, a seasonal analysis of fish accumulation along Kalpakkam coast was conducted. Based on the local rainfall data, the annual climatic condition of Kalpakkam is divided into three seasons such as Pre-monsoon (June-September), Monsoon (October- January) and Post-monsoon (February-May). The maximum number of species was found during the pre-monsoon period, followed by post-monsoon and monsoon period. Distinct fish assemblage was observed during July and August. Seasonal changes within the community and association between species were investigated using the Jaccard similarity index. The dendrogram derived from the similarity coefficient calculated is shown in Figure 4. A clear separation among samples from different seasons was observed. Three major clusters emerged corresponding to three different seasons. The little deviations observed in some of the months can be explained either due to the coincidence with transition months or due to late arrival of monsoon in the particular year. In order to understand the effect of environmental factors on fish richness, a correlation analysis was done. (The result shows a positive correlation between phytoplankton, zooplankton and salinity). Moreover, a clear trend was observed between species number and salinity during all the three season (Figure 5). Hence, the increased freshwater discharge into the sea during this period and subsequent lowering of salinity could be a reason behind the poor species richness obtained during monsoon.

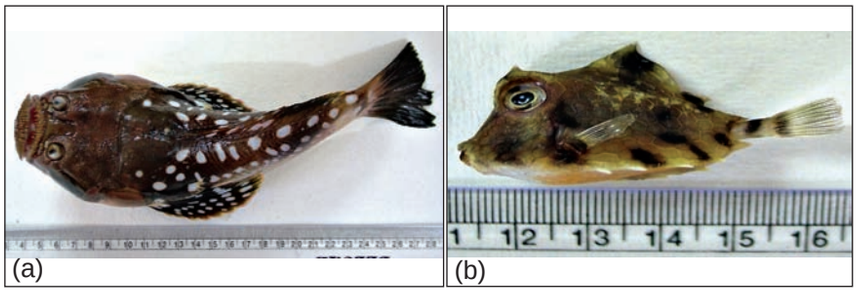

Fig. 6 Few typical fishes from Kalpakkam (a) Cresis acicula (b) Tetrosomus gibbosus

V.32 Ductility Behavior of Reinforced High Volume Flyash Concrete Beams

The ordinary portland cement is one of the main ingredients used for the production of concrete. The utilization of industrial waste like fly ash in eco friendly way along with cement, helps in preserving resources and also improves durability of concrete as it densifies the matrix. In this research ductility of reinforced flyash concrete beams is compared with reinforced ordinary portland cement concrete beams. Ductility is the capacity to undergo inelastic deformation and absorb energy. These include curvature, displacement and rotational ductility.

The materials used in the mix were ordinary portland cement, river sand, Fly Ash (F grade) and potable water. Beams were made with M30 grade concrete. Water-binder ratio of 0.45 and 0.75% conplast superplasticizer was used for ordinary portland cement reinforced concrete beams. Water-binder ratio of 0.45 and 1.3% conplast superplasticizer was used for fly ash concrete beams. Fe500 grade steel was used for longitudinal reinforcement and for stirrups.

The beam span was 2500 mm and cross section 150 x 250 mm.

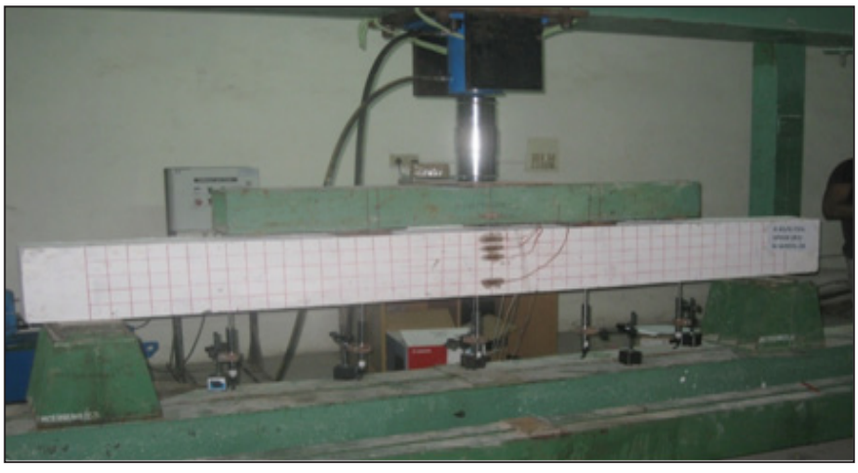

Fig. 1 *Test set-up*

The specimens were designed as per IS 456:2000. Out of the eight specimens tested, four specimens were cast without fly ash and the other four specimens were cast with 40% fly ash. Four specimens were tested at 28th day and four specimens were tested at 56th day from the date of casting.

The testing was carried out in a loading frame of 400 kN capacity. TML strain gauge was fixed at the mid span of the tension bar and then protected using coating tape to avoid accidental damage during pouring of concrete. Strain gauges were also attached to the concrete surface in the central region of the beam to measure the strain at different depths. The top surface of the beam was instrumented with strain gauge to measure the concrete compressive strains in the pure bending region. LVDTs were used for measuring deflections at several locations one at mid span, two directly below the loading points and two near the end supports. Strain gauges and LVDTs were connected to a data logger from which the readings were captured by a computer at every load intervals until failure of the beam occurred. The test was carried using a 400 kN hydraulic actuator and the beams were subjected to two-point loads under a load control mode (Figure 1). The developments of

Table 1: Performance details of fly ash concrete beams and OPC concrete beams

Beam designation	Max. Load (kN)	Deflection at max. Load (mm)	Max. Moment (KN.m)	Strain in concrete at max. load	Displace-ment ductility	Strain in steel	Load at first crack (kN)	Defle-ction at service loads (mm)	Max end rotation
B0% 1-28	186.8	21.0	68.49	0.0031	4.17	0.015	39.20	8.1	2.7
B40% 1-28	163.7	20.6	60.02	0.0029	4.12	0.019	30.90	8.2	2
B0% 1-56	189.7	25.0	69.56	0.0018	5.34	0.015	38.85	8.7	2.4
B40% 1-56	189.6	30.6	69.52	0.0033	4.61	0.006	36.40	8.0	2.1

cracks were observed and the crack widths were measured using a hand-held microscope with an optical magnification of X50 and a sensitivity of 0.02 mm.

Vertical flexural cracks were observed in the constant-moment region and final failure occurred due to crushing of the compression concrete with significant amount of ultimate deflection. When maximum load was reached, the concrete cover on the compression zone started to fall for both beams with and without fly ash. Crack formations were marked on the beam at every load interval at the tension steel level. It was noticed that the first crack always appeared close to the mid span of the beam. The cracks formed on the surface of the beams were mostly vertical, suggesting flexural failure in beams.

Displacement ductility is the ratio of ultimate to first yield deflection. In general high ductility ratios indicate that a structural member is capable of undergoing large deflections prior to failure. Table 1 shows the displacement ductility of beams, the moment-end rotation

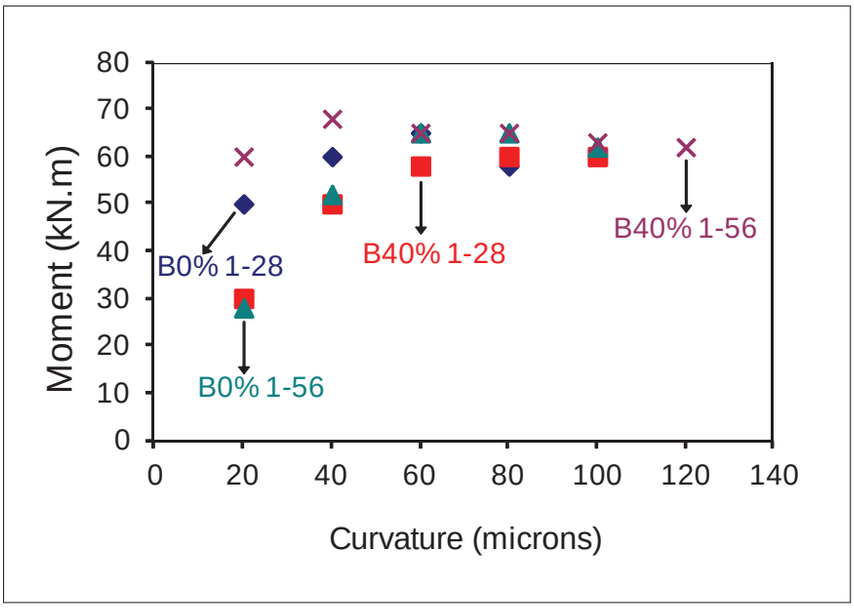

Fig. 2 *Moment curvature of beams at 28 and 56 days*

of fly ash concrete beams and ordinary portland cement concrete beams when tested at 28 and 56 days respectively. Moment-Curvature diagrams were generated for all the beams based on the concrete strain and steel strain. Figure 2 shows the moment-curvature of the beams at 28th and 56th day respectively. Thus the curvature and end rotation of the beams with fly ash is comparable with ordinary portland cement concrete beams. From the experimental investigation, it is generally observed that the flexural behavior of RC beams with 40% fly ash is comparable to that of ordinary portland cement concrete beams.

Fly ash concrete beams shows adequate displacement ductility and can be considered for structural members subjected to large displacement such as sudden forces caused by earthquake.

V.33 Innovative Application of Special Concrete in Tunnels/Trenches for Desired Performance - A Case Study

Ingress of ground water into tunnel/trenches is quite common especially in long spans since construction joints are unavoidable, affecting the functional performance of the structure. This is a serious concern when trenches are carrying pipe lines with radioactive materials. The leakage can be due to honey combs caused by improper placing and compaction of concrete either due to congestion in reinforcement or embedded parts. Development of self compacting concrete is found to be useful in such situations.

Self-compacting concrete is defined as a concrete, which is capable of self-consolidation without any external efforts like vibration, floating, poking and tamping etc. The mix is therefore required to have the attributes of passing ability and ability to fill all the space in the form by displacing the air without any segregation. Concrete is a heterogeneous material with ingredients having different specific gravity and hence it is difficult to achieve cohesive form especially when the

consistency is high i.e., flowable. The ingredients having higher specific gravity will tend to settle down transforming the mix from the intended cohesive concrete to a system of sedimentary layers of concrete ingredients. To overcome this, more amounts of fines and use of super-plasticizers become essential. Since super-plasticizers are high range water reducing agent, resulting concrete mix becomes very sensitive (mix may bleed) to the possible variations in the quality and quantity of the ingredients and may have potential to segregate. The last aspect is countered by the addition of viscosity modifying agent, which is added to ensure homogeneity. Viscosity modifying agent is a pseudo plastic agent, and keeps the mixture under suspension,even while providing segregation resistance capabilities. Underlying principle behind the development of self compacting concrete is that the sedimentation velocity of a particle is inversely proportional to the viscosity of the medium in which it is floating. The viscosity modifying agent offers high shear resistance to the ingredients at rest and relatively lesser shear resistance to those in motion, thus the coarser particles are maintained in suspension providing the required stability to self-compacting concrete (Figure 2).

Fig. 1 *Core cutting the top cover slab with drum type diamond core cutter*

Self compacting concrete technology was applied in IGCAR in an innovative manner for sealing leak in a trench.

An under-ground closed reinforced concrete tunnel of inner dimensions 750 X 330 mm for nearly 420 metres length and 2.5 metres below ground level for carrying stainless steel pipelines. From waste vault to waste tank form of demonstration fast reactor fuel reprocessing plant was constructed. The longest straight reach in this 420 metres length is 286 metres. It has a large stainless steel pipe laid inside the tunnel in which there are four stainless steel pipes of smaller diameter (pipe in pipe concept) that carry the liquid waste.

Before commissioning of this pipeline, there was an ingress of ground water into this particular tunnel and affecting the performance of the pipes (Figure 3). It was proposed to arrest this leakage by a viable procedure. The main root cause of leakage was both the horizontal and vertical construction joints along the length of the tunnel at few locations. Hence it was proposed to fill the space between the large stainless steel pipe and the outer walls of tunnel with self-compacting concrete and seal the leaky joints.

Fig. 2 *Pouring of self compacting concrete into the trench*

Fig. 3 *Tunnel before SCC*

V.34 Effect of Flyash on Biodeterioration of Concrete Exposed to Seawater Environment

Large number of concrete structures in the cooling water system of nuclear power plants exposed to seawater undergoes several deterioration reactions due to the aggressivity of the environment. The surface of concrete is the first line of defense against the marine environment protecting the reinforcements inside. Partial replacement of Portland cement by appropriate pozzollans like flyash are coming up to densify the matrix and making the concrete impermeable. Nuclear power plants with the new mandate of designing future power plants for 60 to 100 years are also looking for modified concrete to maintain the integrity for long time. The main objective of this work was to get a holistic idea about the behaviour of flyash concrete with respect to normal and superplasticizer modified concrete exposed to seawater environments. Three types of concrete mixes namely normal concrete, concrete with superplasticizer alone and concrete with flyash and superplasticizer (FA) were cast and immersed in Kalpakkam coastal water for a year. The compressive strength (CS), corrosion behaviour as indicated by half cell potential (HCP) and rapid chloride permeability (RCP) after the exposure are better for the FA concrete compared to those for normal concrete and superplasticizer (Table 1).

The important degradation parameter; the pH on the specimen surface, reduced from 12 to less than 7 on 250 days of exposure for normal concrete and superplasticizer compared to 360 days in FA. The biofilm on the FA concrete showed 2 order reduction

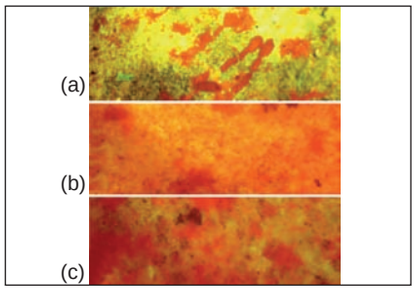

Fig. 1 *Epifluorescence micrographs*

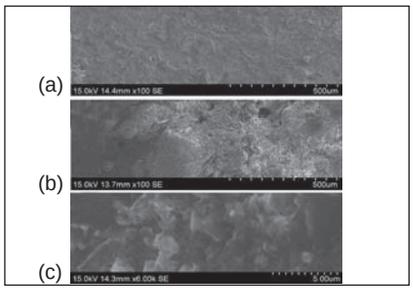

Fig. 2 *SEM micrographs*

in total aerobic bacterial density and three order reduction of anaerobic sulfate reducing bacteria compared to normal and superplasticizer concrete. Epifluorescence micrographs of biofilms on three types of specimens after 250 days of exposure (Figure 1) showed that streaks of viable biofilms (orange fluorescing) just appeared on FA (a) whereas dense biofilm is seen on normal concrete (b) and superplasticizer (c) .

Lock-in-Thermography studies revealed very little change in the phase angle and amplitude between one year seawater exposed and unexposed flyash modified concrete indicating least deterioration. Laser Raman spectroscopy (LRS) and X-ray diffraction (XRD) results confirmed that there is improvement of chemical composition with additional peaks of calcium silicates and more cementitious products on seawater exposed FA concrete. X-ray diffraction results showed additional peaks of calcium silicate hydroxide hydrate (36.5), calcium silicon sulfate hydroxide hydrate (39.5) and calcium silicon sulfate hydroxide hydrate (42.3) in exposed FA concrete. Raman spectra of unexposed FA concrete showed amorphous nature compared to the well defined Aragonite and silicate phases in normal concrete and superplasticizer concrete. However, the Raman intensities of sea water exposed FA concrete increased to a larger extent with aragonite, silicate and thaumasite phases and conversely Raman intensities decreased for normal concrete and superplasticizer concrete. It is inferred that, with time, Flyash chemically reacts with the byproduct calcium hydroxide released by the chemical reaction between cement and water to form additional cement products especially thaumasite which further acts as fillers of the voids and capillaries present in the concrete, leading to increased strength of the specimen. Thus, Laser raman spectroscopy and X-ray diffractionstudies established the reason of increase in compressive strength of exposed FA concrete as due to secondary hydration.

SEM micrographs (Figure 2) further confirmed absence of degradation in (a) FA concrete (b) the compared to normal concrete (c) superplasticizer. Thus FA concrete emerged far superior to normal concrete and superplasticizer concretes after a year exposure in seawater environments.

Table 1:Comparision study

Type	CS MPa	HCP mV	RCP Coulombs
N	49	–691	2730
SP	39	–683	2180
FA	82	–679	120

V.35 Extreme weather / Cyclone Predictions in the Bay of Bengal region Neighbouring Kalpakkam Coast

The Kalpakkam coastal site is prone to tropical cyclones in the pre-monsoon season in May and post-monsoon season in November-December. Accurate prediction of formation,movement and intensity of tropical cyclones is vital for disaster management. As the tropical cyclones are highly variable, dynamical models are required to forecast their movement.

A high resolution Numerical Weather Prediction Model called (WRF-ARW) based on non-hydrostatic dynamics is implemented operationally for obtaining quantitative forecasts of tropical cyclone related extreme weather for the Kalpakkam coast. This model includes complete equations of atmospheric motion, mass continuity, thermodynamic energy state, moisture conservation and parameterizations for sub-grid scale physical processes (convection, radiation, boundary layer turbulence and surface energy exchange). Two interactive nested domains of horizontal resolutions 27 km, 9 km and 35 vertical layers are used in the operational setup. The initial and boundary conditions are derived from the 50 km resolution National Centers for Environmental Prediction (NCEP) Global Forecasting System (GFS) analysis and forecasts. It is crucial to resolve the *in-situ* tropical cyclone circulation and the physical processes to obtain realistic forecasts with dynamical models. Hence the model was first subjected to rigorous evaluation considering 21 past cyclonic storms that formed in Bay of bengal region between 2000 to 2011.

Initially sensitivity experiments are conducted for 6 severe cyclonic storms (FANOOS, LAILA, NARGIS, SIDR, NISHA) with different physics. The numerical experiments indicated that Kain-Fritsch (KF) scheme gives best convection simulation with relatively higher convective warming in the upper troposphere and stronger vertical motion than the other parameterizations (Betts-Miller-Janjic, New Grell and the Grell-Devenyei ensemble schemes) (Figure 1). It is found that Kain-Fritsch scheme gives better simulations because of the inclusion of updrafts, downdrafts and shallow convection processes. The sensitivity tests with different boundary layer parameterizations indicated the non-local turbulence diffusion scheme (Hong-Pan) produced reasonable estimates of intensity and track due to better simulation of turbulent drag effects. The computed vector track distances and intensity agreed well with the observed best track parameters from India Meteorological Department (IMD) with the above identified physics.

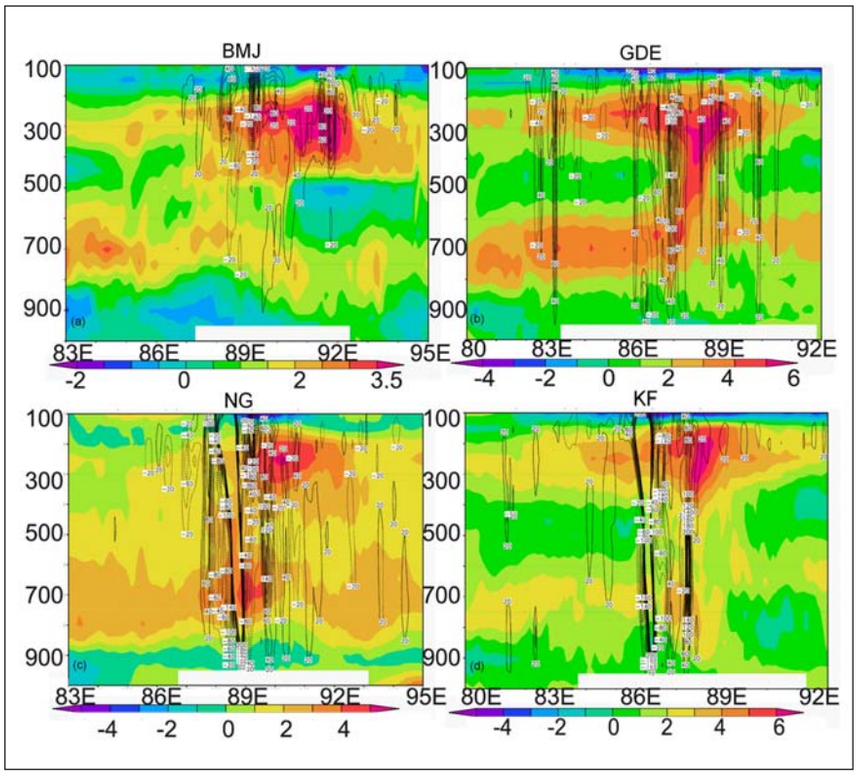

Fig. 1 *Vertical section of temperature anomaly and vertical winds (cm s^{-1}) with different convection schemes for SIDR cyclone corresponding to 21 UTC 11 November 2007*

Results of statistical analysis for the simulations using identified physics for 21 cyclones indicated that the model slightly overestimates the intensity of cyclones with a mean error of about –2 to 13 hPa for central pressure, –1 to –24 ms^{-1} for maximum sustained tangential winds (MSW) corresponding to 24 to 72 hours predictions. The mean errors in the predicted fields are found to vary as –1, 2, 13 and 10 hPa for central sea level pressure (CSLP), –5, –4, –24 and –18 ms^{-1} in MSW and 122,170, 244 and 250 km in vector track position corresponding to 12, 24, 48 and 72 hours of predictions.

These errors in predicted fields are smaller than the IMD operational cyclone (QLM) model forecast errors. About 67% of simulated cases have track errors within 135 km at land fall time. Further, the predictions are found better for northward moving cyclones followed by the northwestward, westward and northeastward moving cyclones which may be due to the control of β-parameter (increasing Coriolis force with latitude) in the model. Simulated and observed cyclone tracks for SIDR, NARGIS, NISHA, KAIMUK cyclones are presented in Figure 2 which illustrate the obtained low track position errors in the above three cases.

Simulated total cloud fractions (low, medium, and high) at landfall time for SIDR, KAIMUK cyclones along with their comparison with INSAT infrared imagery are presented in Figure 3. The model was able to reproduce the comma cloud pattern and their circular symmetry associated with each of the cyclones well. Satellite cloud imagery indicates dense convective cloud bands in all three cases and a well defined central eye region in the case of SIDR, KAIMUK which the model represented well. The cloud maximum reflectivity computed from the ARW hydrometeor fields also compared well with the Doppler Weather Radar reflectivity imagery indicating good simulations of hydrometeor fields and the rainfall bands around the respective storms.

Comparisons of simulated 24 hours rainfall with tropical rainfall measuring mission (TRMM) satellite data indicate slight under estimation in simulated rainfall amounts. However, the rainfall pattern matches closely in location and distribution. Further tests were conducted with assimilation of conventional (surface/ upper air) and satellite meteorological observations using the grid nudging and 3DVAR techniques. The nudging experiments indicated at least 18 to 24 hours of pre-forecast nudging and a nudging time scale of 1.0 e^{-4} (~3600 seconds) is required for surface observations to obtain impressive forecasts. These experiments conducted for a few cases of cyclones indicated impact of different observations on correcting the track errors as well as the overestimation of intensity parameters. A back-ground error covariance was generated for the 9 km resolution domain by running the ARW for two cyclone seasons in 2009, 2010 and the impact of surface/upper air observations with 3D-Variational data assimilation system was studied for 10 strong cyclones.

The model is operationally run to provide 3-day (72 hours) lead predictions. A 3D-Variational data assimilation system has been used to enhance the initial conditions with surface/upper air observations corresponding to 00 UTC (06 IST)

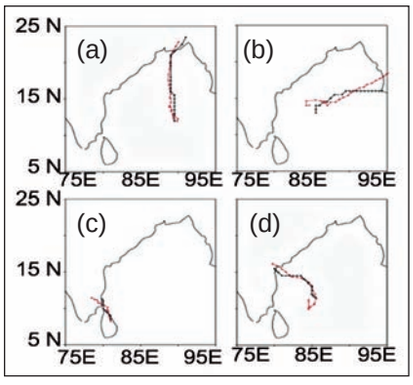

Fig. 2 *Simulated and observed cyclone tracks for (a) SIDR (b) NARGIS (c) NISHA and (d) KAIMUK*

on the start date of each simulation. The predictions with respect to winds, heavy rainfall have been provided to BHAVINI during the erection of inner vessel, main vessel components and to Cyclone Protection Committee during the cyclone season for site emergency preparedness. The predictions for NISHA (2008), JAL (2010) and THANE (2011), NILAM (2012) have been found to be very precise and practically effective in taking precautionary measures at the site.

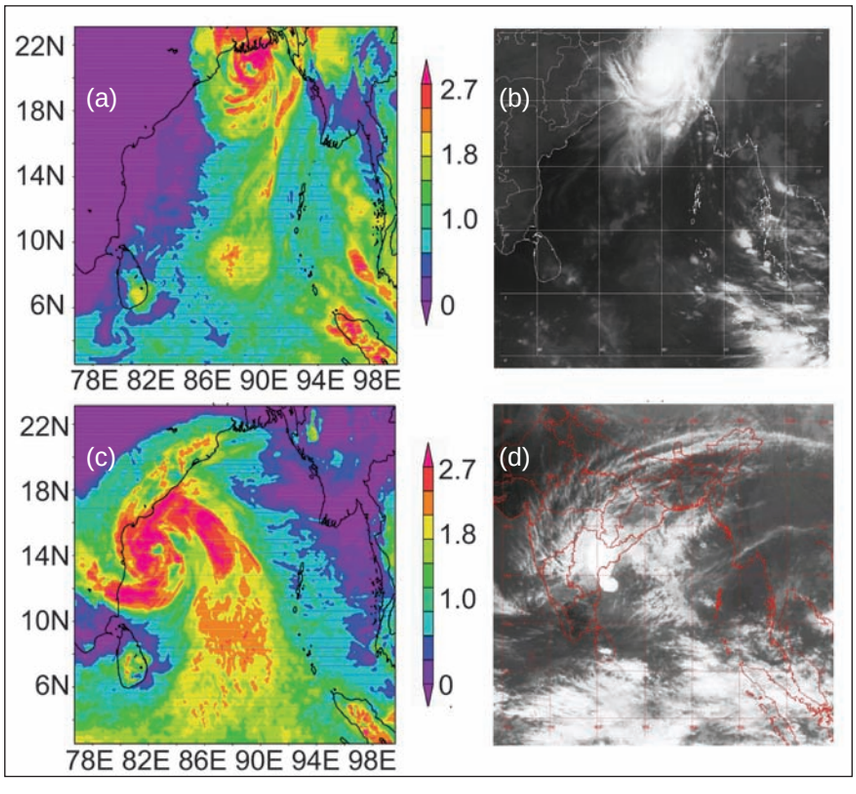

Fig. 3 *Cloud band structure of simulated storms SIDR, KAIMUK and their comparison*

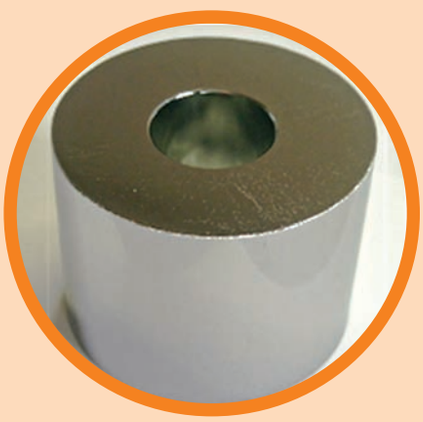

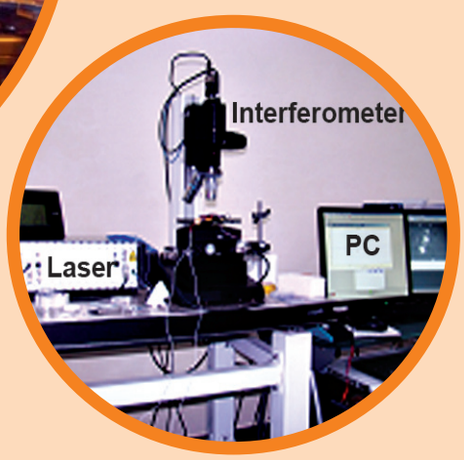

CHAPTER - VI

Infrastructure Facilities

VI.1 Repair of Hot Cell Equipment through Intrusive Techniques

The hot cells of radio metallurgy laboratory have completed twenty five years of service. The prudent philosophy adopted in the design of in-cell equipments facilitated their smooth functioning with minimum remote repairs using master slave manipulators (MSMs) in their first decade of service. It was followed by another decade where major contact repairs were done either through the cell rear door opening or the roof opening without direct man-entry into the hot cells. A minimally intrusive hot cell man entry system has been developed recently for contact repair of in-cell equipment.

Man-entry into the hot cell through the rear door is envisaged in design, but it posed several issues. Hence, the man entry system adopted entry through the roof opening and was designed for ensuring freedom of movement and safety of the crew minimizing the man-rem expenditure and spread of contamination. This system was successfully used for repairing the chain drive of the long travel motion of a crane which was neither visible through the shielding glass window nor accessible through the door/roof openings.

The man-entry system consists of three modules: a rigid bridge to be assembled over the roof opening, a central vertical box frame that hangs into the cell from the bridge with two foldable platforms hinged to its bottom end at 1.3 metres above the cell floor and a shuttle cage for emergency rescue of repair crew.

The man-entry system was qualified through mock-up trials outside the hot cell with detailed procedures and check lists. Necessary clearances were obtained from the hot cell operations review committee for executing the work.

The repair crew in the upper isolation area opened the roof cover plate and roof shielding plug of the hot cell after ensuring that the active materials in that cell are shifted to adjacent cells and that the cell atmosphere is converted from nitrogen to air. The radiation dose rate at the opening was 15.7 µGy/h. The continuous air monitor at upper isolation area close to the opening did not show any activity.

After placing the bridge over upper isolation area floor across the roof opening, the vertical box frame was lowered into the cell through it and bolted together (Figure 1). Two trained members of the repair crew in ventilated suit climbed down into the cell (Figure 2), with necessary tools, through the box frame. The platforms were made horizontal and hand rails were attached to them. Radiation dose rate at this level was measured as 51.3 µGy/h. Four persons wearing proper personal protective equipments assisted the repair work from the upper isolation area.

Examination of the drive chain of long travel motion of the crane revealed that one of its links was broken fully and that two more were partially broken. The repair crew inside the cell replaced the chain, as per the approved procedure. The time taken by the crew inside the cell for the investigations and repair was 1 hour 45 minutes. This excludes the time taken for preparatory works for establishing the support systems, safety and monitoring equipments.

Fig. 1 *Assembly of man entry system at upper isolation area*

The man-entry system was then disassembled and the bridge and box frame were taken to upper isolation area. The roof shielding block and roof cover were put back, and normalcy of the hot cell was restored. The entire operation was monitored and controlled through audio-visual aids from the operating area as well as the upper warm work area by the supervising crew.

This was the first time that a repair crew has entered an active hot cell in radiometallurgy laboratory and carried out equipment repair. Conceptualization of this minimally intrusive technique, obtaining safety clearances and execution of repair were completed in forty five days. Totally about twenty personnel were involved in the campaign. The total man-rem expenditure for the entire campaign was less than 0.2 pmSv.

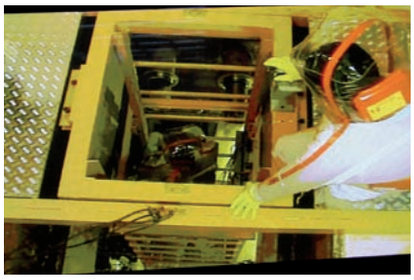

Fig. 2 *Repair crew in ventilated suit entering the cell*

VI.2 Erection and Commissioning of Ambient Temperature Electro Refiner Facility

Reprocessing of spent fuel from future metallic fuelled FBR's will be carried out by pyroprocessing method based on molten salt electrorefining. To develop the technology required for the associated pyroprocessing plants, engineering scale facilities are planned to be set up. First of such facilities called ambient temperature electro refiner facility has been setup in the low bay of augmented boron enrichment plant building of FRTG.

Electrorefining is the most important step of the pyroprocessing flowsheet where the separation of heavy metals from the fission products is achieved. In this process, the spent metal fuel is used as the anode of a molten salt electrorefining cell, molten LiCl-KCl eutectic salt as the electrolyte and a solid rod or molten cadmium as the cathode of an electrorefining cell operated at 773 K.

The ambient temperature electro refiner is a mock-up facility with the main objective of gaining operating experience with respect to remote handling and automation.

In ambient temperature electro refiner the electrorefining of copper will be done. This allows the facility to be operated at ambient temperature and without the need of argon atmosphere. Copper electrorefining does not simulate the thermodynamics and kinetics of the uranium electrorefining process. However, influence of the physical aspects of the electrorefiner such as the geometry, size, distance between the electrodes etc. on the rate of electro-deposition can be studied by copper electrorefining which would give reasonable indication of the suitable electrode configurations for uranium electrorefining. Hydraulic studies will also be carried out for improving the design of stirrer used for mixing the molten salt electrolyte. Both these studies are planned in ambient temperature electrorefiner facility.

Fig. 1 *Tilting station*

Fig. 2 *Assembly station and electrorefining station*

Fig. 3 *Scraping station*

The facility mainly consists of the electrorefining station, assembly station, tilting station and scraping station (Figures 1-3). The facility will have one anode and two cathodes which are held inside the electrorefining vessel by the respective subassemblies to which the electrodes are attached. The attaching/detaching of electrodes to the respective subassemblies is carried out at assembly station. The transfer of electrode subassemblies between assembly station and electrorefining station is done using a crane of two tonnes capacity. At tilting station any remaining copper pieces in the anode basket are removed. At scraping station the copper deposit is scraped and collected. Transfer of electrodes between the assembly station and scraping or tilting station is carried out using crane, electrode gripping mechanisms and electrode transfer basket. The facility is operated by programmable logic controller based system through process control panel. Provision also exists to operate and record data using SCADA. Assembly station and scraping station can be operated in auto mode as well as in manual mode through the SCADA system or control panel. The power supply to electrodes is provided through a separate panel but current and voltage data are recorded through the same SCADA system.

After erection of the steel structure on which the systems and components of the facility are supported, first the crane was erected, tested and commissioned followed by erection of other systems and components. Leak testing of the electrorefining vessel, performance testing of each station including motors, pneumatic drives and control panels has been completed.

The functioning of safety interlocks has also been checked. Remote operation of all the stations through SCADA has been demonstrated for the intended number of cycles. Integrated testing of the facility through remote operations is in progress. This will be followed by hydraulic studies for optimizing the design of stirrer for mixing the electrolyte followed by copper electrorefining studies as planned.

VI.3 Manufacture of Continuous Dissolver for Reprocessing

The continuous dissolver was designed by Reprocessing Group and manufactured at central workshop for reprocessing of spent fast reactor fuel. In order to achieve high dissolution capacities with ease of operation, maintenance and automation, a two stage continuous dissolver was made with low carbon grade austenitic stainless steel (AISI 304L). It consists of feeding cone, connection drums, oblique cone, dissolver drum, partition plates, cone plate, shaft, etc.

The partition plates have critical profiles with close geometrical and dimensional tolerances. In order to achieve the precision tolerances, CNC controlled machines, specially designed and fabricated fixtures were used. The oblique cones and dissolver drums were formed and fabricated from 1.6 and 3 mm thickness stainless steel sheets respectively. The assembly procedure was developed and fabricated cones, precisely machined components were assembled as shown in Figures 1 and 2. Sequence welding technique with controlled heat input and special fixtures were employed to control distortion during gas tungsten arc welding process. Subsequently liquid penetrant inspection was carried out to ensure the soundness of the weld joints. The assembly was surface treated with pickling and passivation. After successful functional test, it was commissioned in fume hood environment at Reprocessing Group. Manufacturing technology development of continuous dissolver was achieved with extensive planning, development of process and special fixtures.

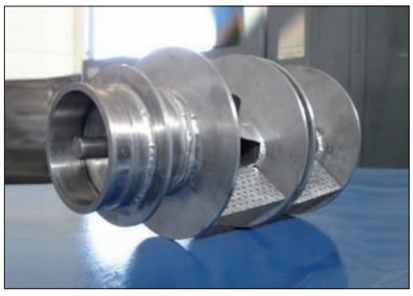

Fig. 1 *Internal assembly of continuous dissolver*

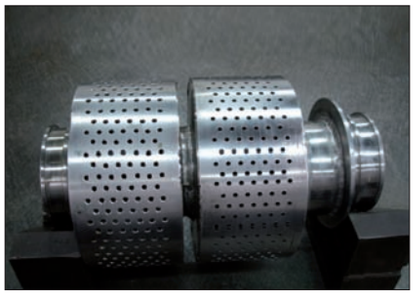

Fig. 2 *Continuous dissolver assembly*

VI.4 Intricacies Involved in Fabrication of NO_2 Generator

The NO_2 generator was manufactured for conditioning of feed solution to generate NO_2 gas in fuel reprocessing plant. The generator by construction have cylindrical shell of 2560 mm height and 950 mm diameter. The shell was joined by torispherical dished ends at both ends along with vane type mist eliminator mounted on the top dished end. It also consists of deep feed nozzles, air sparger, top and bottom instrument probes, thermo well, radar level probe, product gas nozzles, safety relief valve, drain nozzles etc. The low carbon grade austenitic stainless steel (AISI 304L) conforming to ASTM A 262 Practice C for inter granular corrosion was used as construction material.

The fabrication of NO_2 generator consisting of various components was a challenging task due to large size and huge weld metal deposition. The forming of dished ends, machining of nozzles and level probe components were critical due to the stringent

dimensional and geometrical tolerances. The torispherical dished ends were formed from 6 mm plates by progressive forming method and subjected to solution annealing heat treatment at 1050°C for stress relieving. The development of cylindrical shell was established based on actual dimension of the formed dished ends and required plates were cut in numerical control shearing machine and subsequently formed to cylindrical shape in plate bending machine. The required height of generator shell was achieved by joining two cylindrical shells using shielded metal arc welding /gas tungsten arc welding process. Sequence welding technique and mechanical spiders were used to control distortion. To ensure soundness of weld, the joints were subjected to liquid penetrant, ultrasonic and radiography examination. The generator was leak tested pneumatically at 3.9 bars (g). With expertise and adoption of best methodology at different stages, the NO_2 generator as shown in Figure 1 was successfully manufactured conforming to ASME Section VIII div I.

Fig. 1 *Nitrogen dioxide generator*

VI.5 Millimeter Sized Cantilever for Precise Mass Measurement

Cantilever is a simple structure, which is fixed at one end and free at other end. It is a harmonic oscillator, whose natural frequency depends on its mass. Natural frequency (f_1) of a cantilever is given by,

$$f_1 = \frac{1}{2\pi}\sqrt{\frac{k}{m^*}}$$

where k is spring constant and m^* is effective mass of the cantilever. When a mass (much smaller than the mass of the cantilever) is placed at the free end of the cantilever, the natural frequency decreases (f_2), and added mass Δm can be calculated using the formula, .

$$\Delta m = \frac{k}{4\pi^2}\left[\frac{1}{(f_1)^2} - \frac{1}{(f_2)^2}\right]$$

In fact, by reducing the dimensions of the cantilever, one can achieve sensitivities upto single molecule mass detection.

In the present work, a millimeter sized cantilever is explored as a precise mass sensor. Using this cantilever, mass of thin copper wire pieces were measured and are compared with theoretical values. Cantilever used in the present study is a piece of precisely cut single crystal n-type silicon wafer. Physical dimension of the cantilever are 8.3 mm (length) x 2.1 mm (width) x 0.43 mm (thickness). The Young's modulus and the density of the silicon wafer are 156 GPa and 1766 kgm^{-3} respectively. Natural frequency of the cantilever (with and without mass) was estimated using a laser interferometric vibrometer. The block diagram and the photograph of the experimental setup are shown in Figures 1a and1b. Cantilever was excited using a piezo actuator which was swept by a function generator. By varying the frequency of function generator, amplitude of vibration was recorded using the interferometer which in turn was interfaced to a PC. Now, resonance frequency was estimated from the peak of the plot of frequency versus amplitude

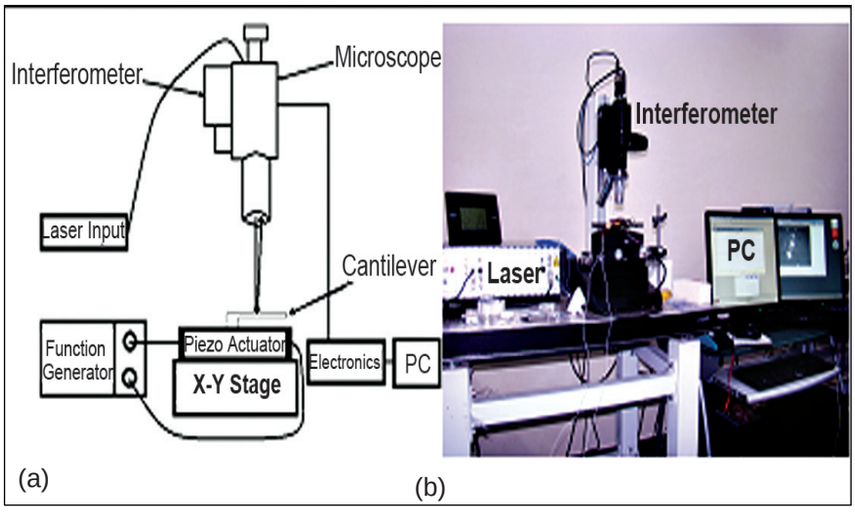

Fig. 1 *(a) Block diagram and (b) Photograph of the experimental setup used to measure the natural frequency of the cantilever using interferometer*

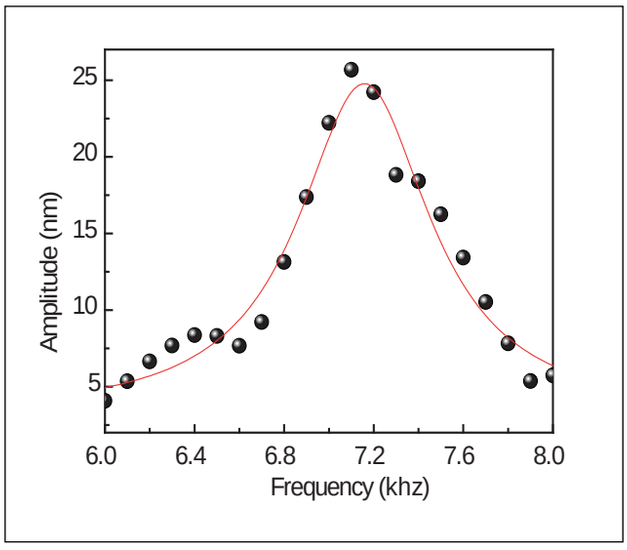

Fig. 2 *Resonance spectrum of the cantilever*

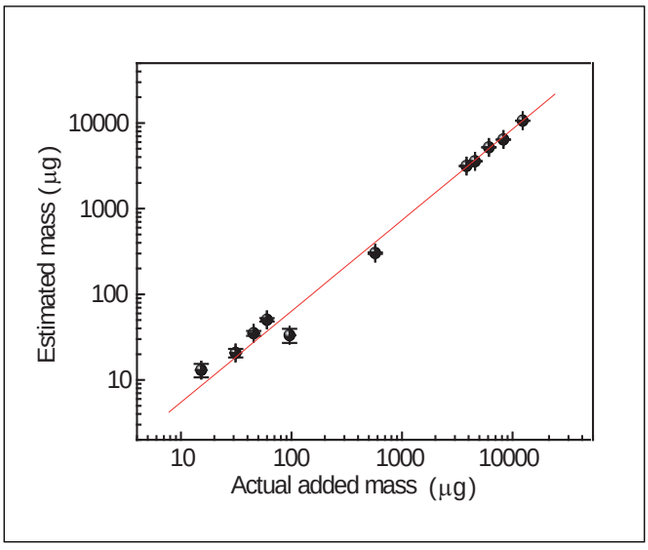

Fig. 3 *Actual added versus estimated mass of copper wire pieces*

(Figure 2). Experiment was repeated for various dimensions of copper wire pieces. Δm was estimated using the formula described above.

Figure 3 shows the graph betwen actual mass (calculated from volume and density of copper wire pieces) and estimated mass using the present setup. From the linear response of this graph, it is evident that millimeter sized cantilever can be effectively used as sensitive mass sensor over a wide dynamic range of 10 μg to 10 mg. Sensitivity of this sensor can further be enhanced by working at higher modes.

VI.6 The Parallel Computing Graphical Processing Units and Blade HPC Clusters

Multi-purpose parallel high-performance supercomputing cluster facility using graphical processing units servers and blade servers has been made operational to cater the diverse computational requirements of engineers and scientists of IGCAR.

Graphical processing units HPC cluster

The graphical processing units cluster consists of one master node with Dual CPU 6 core Xeon 5675 processor at 3.15 GHz and 48 GB RAM, four compute nodes with 12 NVIDIA Tesla M2090 GPGPU cards and a total of 288 GB RAM with 4 TB of storage, gigabit ethernet interconnect for monitoring and management of the cluster and low latency high bandwidth QDR infiniband interconnect for interprocess communication. Each Tesla card consists of 512 CUDA cores. In each graphical processing units 615 gigaflops of double-precision peak performance is possible. The graphical processing units memory optimizes performance and reduces data transfers by keeping large data sets in 6 GB of local memory that is attached directly to the graphical processing units. The high speed PCIe Gen 2.0 data transfer maximizes bandwidth between the compute node CPU and the Tesla graphical processing units processors. HPL in pack gives a peak performance of 3.9 Tera Flops (Figure 1).

The cluster nodes run on Red Hat Enterprise Linux 6.2 64-bit operating system and installed with NVIDIA drivers for graphical processing units functioning, OFED drivers for infiniband functioning, CUDA toolkit, CUDA SDK, GCC compilers with all relevant scientific and mathematical libraries. Workload manager tool PBSPro and cluster monitoring tool Ganglia are configured for smooth functioning of the cluster.

Graphical processing units computing is the use of a graphical processing units

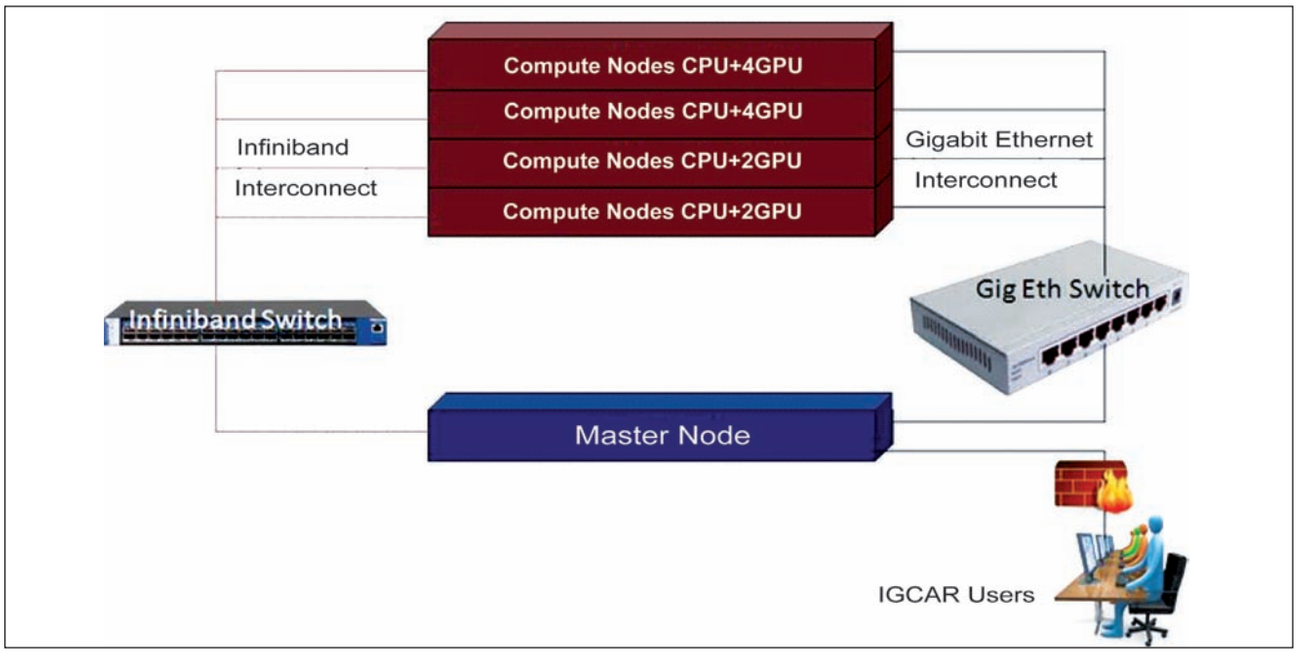

Fig. 1 *GPU cluster with four nodes*

together with a CPU to accelerate general-purpose scientific and engineering applications. CPU+graphical processing units is a powerful combination because CPUs consist of a few cores optimized for serial processing, while graphical processing units consist of thousands of smaller, more efficient cores designed for parallel performance. Serial portions of the code run on the CPU while parallel portions run on the graphical processing units. But to use the graphical processing units efficiently, application software should be CUDA enabled.

Blade HPC cluster

Two blade clusters (Figure 2) are installed each with a sustained HPLinpack benchmark of 1.08 TeraFlops. The master node is dual CPU 6 core X5675 at 3.06 GHz processor with 48 GB RAM, and 1.2 TB of storage and compute nodes are eight blade servers in one chassis with a total of 384 GB RAM. Each chassis consists of one internal infiniband switch, ethernet fabric switch and an intelligent platform management module that takes care of inter process communication, management and monitoring of the cluster respectively.

Advanced cluster distribution software ROCKS (ver 5.5) designed for massive scalability and performance has been installed and configured for building and managing blade servers cluster. ROCKS deploys, manages and upgrades the cluster. Using ROCKS, Red Hat Enterprise Linux 5.8 64-bit operating system was installed with GCC compilers and all relevant scientific and mathematical libraries. Using ROCKS cluster tools grid engine for resource, job management and ganglia for distributed cluster monitoring were configured for smooth functioning of the cluster.

The blade server based solutions offer modular design optimized to minimize the use of physical space and energy. A blade server is a server chassis housing multiple thin, modular electronic circuit boards, known as server blades or simply blades. Blade server based solutions give many potential advantages over traditional rack-mount servers like higher power and cooling efficiency, better serviceability, scalability, reliability and manageability, cable and space reduction and less total cost of ownership.

Applications

Graphical processing units and blade servers are particularly suitable for our user requirements where many sequential codes in reactor physics, computational fluid dynamics and finite element analysis should get better throughput along with linearly scalable parallel codes. Already highly compute-intensive scientific applications in the areas of computational molecular dynamics and weather modeling are ported into the clusters and are running successfully.

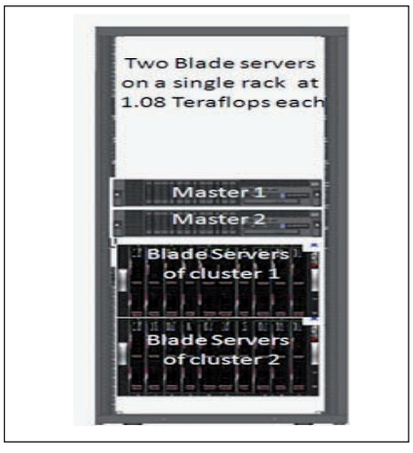

Fig. 2 *Blade clusters*

VI.7 Development of a Stand-alone Instrumentation and Control Device for Online Measurement of Absorbed Radiation Dose

Chemical dosimeters which work on the principle of radiation induced chemical changes are generally used for offline determination of absorbed dose levels. Restrictions imposed on extensive sample treatment and measurement procedures, with involved instrumentation for quantitative measurement of small changes come on their direct adaptation for online monitoring. A high resolution online conductivity measurement approach has been followed for circumventing these limitations.

Saturated solution of chloroform in water is used as chemical dosimeter. Its conductivity increases on exposure to gamma irradiation on account of generation of traces of highly conducting HCl. A high resolution fast response pulsating sensor based conductivity meter is deployed to measure small shift in conductivity due to production of HCl. A pair of electrodes, placed within a small volume of dosimeter solution in a mini cell, senses conductivity. This dosimeter cell constitutes a part of a specially designed logic gate oscillator circuit. With the change in solution conductance due to absorbed gamma radiation the digital pulse frequency of logic gate oscillator circuit changes. The digital pulses, which can be easily driven over a long distance from the irradiation site, are processed for frequency information at a desired sampling rate, thus enabling time dependent measurement of a conductivity related parameter. With highly successful results from many offline measurement campaigns as well as PC based online measurement campaigns a stand-alone instrumentation and control device has been developed and it is exclusively deployed for measurement and control of absorbed radiation dose.

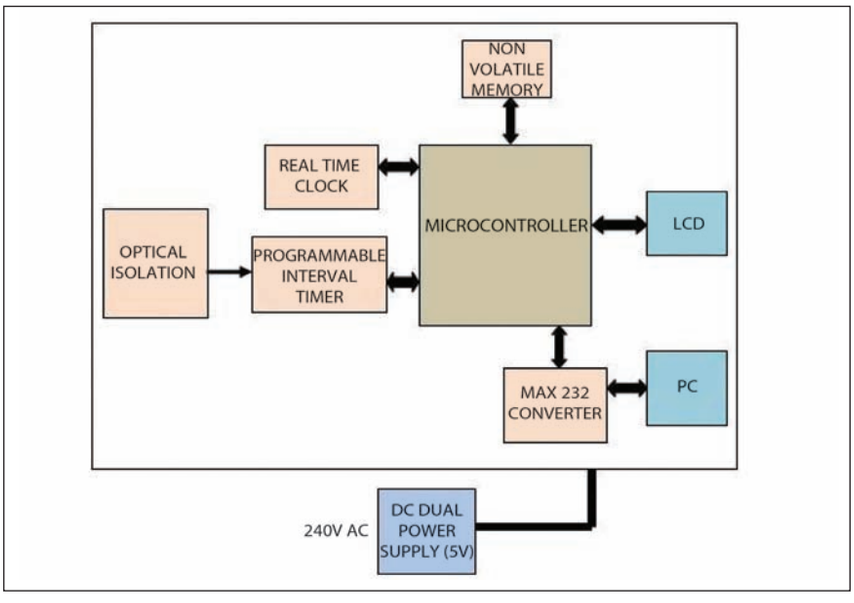

Fig. 1 *Block diagram of data acquisition cum control device*

Figure 1 shows the block diagram of data acquisition cum control device and Figure 2 shows the photograph of radiation dosimeter with all internal components used in designing this instrument.

The digital pulse from the conductivity cell is fed to programmable interval timer after optical isolation and signal shaping. The timer receives the isolated digital pulse frequency from the logic gate oscillator circuit in response to the change in conductivity of the chemical dosimeter. An 8051 family microcontroller AT89C55WD is the brain of the system which is interfaced with programmable interval timer, LCD, real time clock, EEPROM and serial transceiver. Counters in programmable interval timer is configured in mode 0 (interrupt on terminal count) and

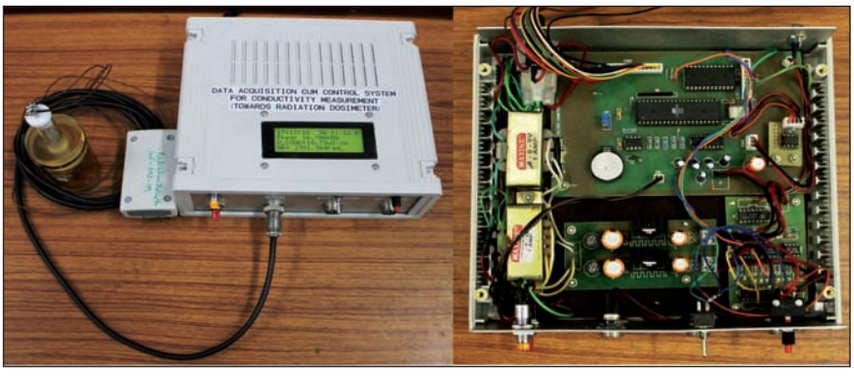

Fig. 2 *Photograph of radiation dosimeter with all internal components*

they count the input pulses for a desired time decided by the microcontroller. The output of programmable interval timer is processed by microcontroller to calculate pulse frequency. The absorbed dose of the chemical dosimeter is calculated from the pulse frequency using the pre-evaluated mathematical relation between pulse frequency and absorbed dose and displayed in LCD. Also this data is stored in an EEPROM with date and time stamp. The unit can be connected to PC via serial port to change counter configuration with new set of coefficients, set date and time and to read the saved data in memory into a notepad for further analysis. The firmware using Keil software is developed to convert frequency shift due to conductivity change in solution during irradiation which in turn converts it to radiation dose in appropriate unit.

The performance of the stand-alone radiation dosimeter has been tested in ^{60}Co Gamma chamber. The signal received from dosimeter cell kept inside the radiation chamber has been processed by the data acquisition system to give direct display of radiation dose with respect to time of exposure in radiation field. The absorbed dose increases linearly with increase in time of exposure. The pattern of such change in a typical measurement campaign for a duration of 2000 seconds is represented by $Y = 3.07507*X + 152.98385$ (R - square : 0.99986). Here Y:absorbed dose in rad and X:time of exposure in seconds. This approach of direct online measurement of absorbed radiation dose is the simplest approach with excellent reproducibility in measurement (RSD less than 1% from 1 to 100 Gy). This could be possible due to evolution of high resolution fast response pulsating conductivity meter.

VI.8 Comprehensive Centralized Surveillance System for Safe Operation of Radiological Laboratory

The ventilation system plays an important role in preventing the dispersal of radioactivity in radiological facilities. Radiation monitoring instruments installed in vantage points in the laboratory monitor whether ambient radiation level is within safe limits or more due to any dispersal. The ventilation system and the radiation monitoring instruments are expected to function effectively on all situations to provide safe and confident environment for the working personnel and hence the safe operation of the radiological laboratory. In Radiochemistry Laboratory, in order to preempt any malfunctioning or deviation of the operational parameters of the above systems, a customized surveillance system is installed. The system measures the critical operational parameters, logs them continuously, and displays them in gauges for the maintenance personnel to take preventive actions. The system also raises alarm, if any parameter deviates from the safe value, for the plant operator to make corrective action. The system also makes the data available to designated authorities through local area network (LAN) to recognize the tendency of the system performance.The system is running with class II power.

Hardware scheme

A customized microcontroller based remote terminal unit with TCP/IP connectivity is designed to condition a variety of signals from different kinds of instruments. The LAN is implemented using WIZNET module with 100 Base/TX connectivity provides 100 Mbps

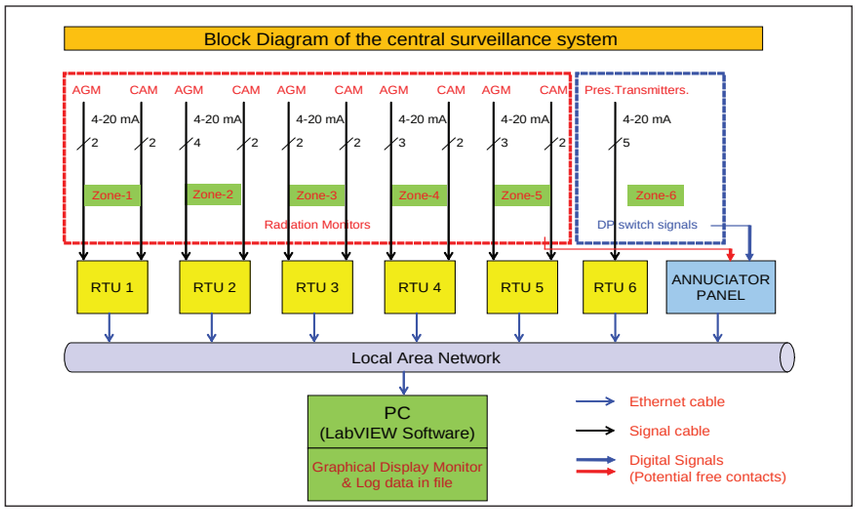

Fig. 1 *Overall block diagram of the system*

Fig. 2 Photograph of annunciator panel

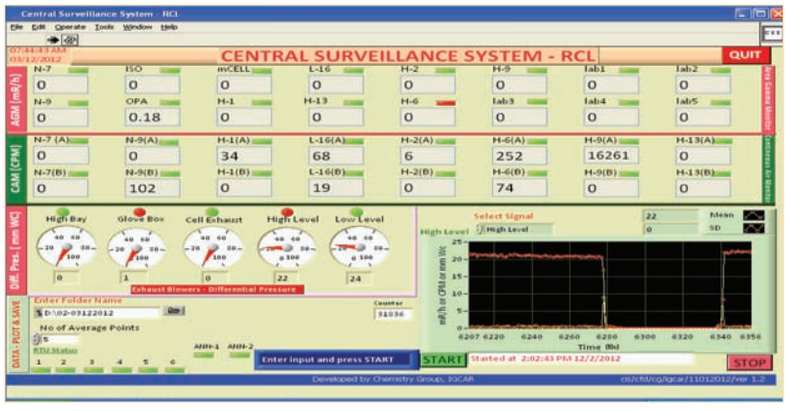

Fig. 3 Screen shot of running software

throughput in each direction with a maximum of 100 metres distance. Analog and digital signals from

a) Fourteen numbers of area gamma monitors

b) Ten numbers of alpha beta continuous air monitors

c) Differential pressure transmitters that measures the differential pressure level of HEPA filters of exhaust lines of different levels

d) Differential pressures witches across the exhaust filters are extended to the surveillance system.

The block diagram of the system is shown in the Figure 1. These remote terminal units are distributed all over the lab to accommodate the instruments depending on the population of the instruments in each zone. These remote terminal units are acting as local processors connected over (LAN) to central computer. The digital alarm levels of these instruments are extended to two numbers of annunciator panels. Each annunciator panel has thirty windows and the photograph is shown in Figure 2. The annunciator raises alarm whenever any of the signal parameters deviates away from the set threshold. The central PC acquires data from annunciator through modbus protocol using LAN. The annunciators transmit the signal through RS-232 ports of the annunciators to LAN. For this data exchange, a RS-232 to LAN converter is configured and adapted.

Software scheme

The conditioned analog and digital signals are acquired from different remote terminal units, processed and transmitted to the central computer through LAN. Computer based acquisition and processing software in LabVIEW is developed. One data point is generated every ten seconds (programmable) and used for displaying and logging in a file. The values are converted in their engineering units after proper calibration. The full scale value of the dose rate is 100 mR/hour, gamma/alpha count rate as measured by continuous air monitor is 50000 CPM and that of the differential pressure gauge is 100 mmwc. In the panel the data is displayed in gauges, text boxes and as an online graph. Online trend of selected signal can be investigated on the screen at any time during run time of the software. The online trend plot is done for both mean and standard deviation of the data under plot. The auto scale feature

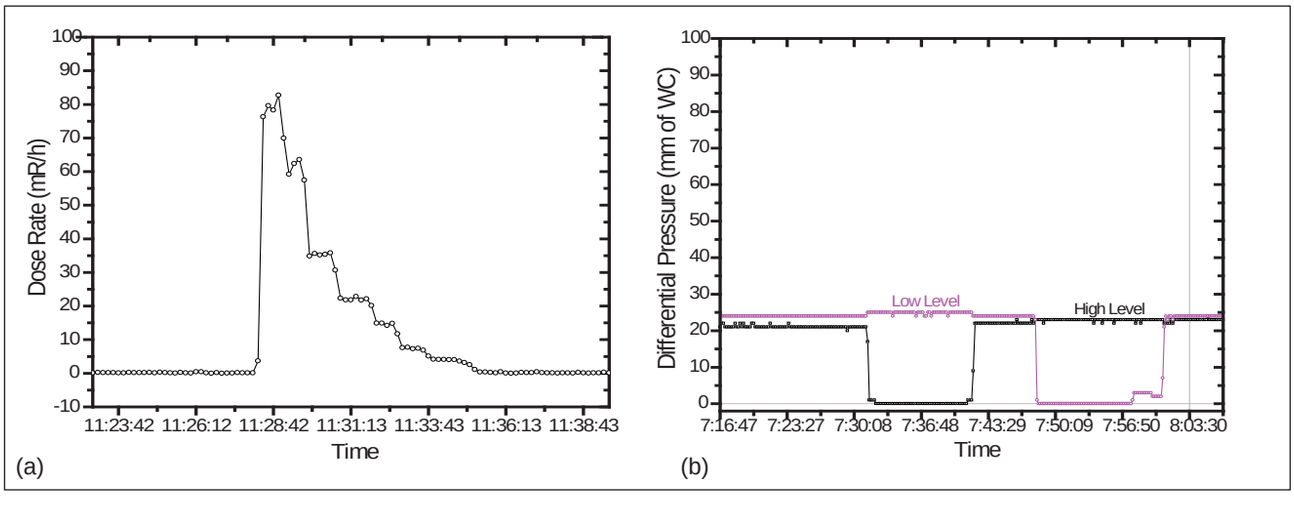

Fig. 4 (a) Recorded data for calibration of area gamma monitor and (b)Recorded ventilation data during changeover

is enabled to get the full scale value automatically as and when it changes to get the instantaneous profile of the past data and the present data. All signals are displayed in simple digital format along with the alarm signals in the form of square LEDs. Diagnostics display LEDs are also provided in the panel. The counter on the left side of the graph indicates the number of acquisitions done and also gives the running status of the acquisition. The actual screen shot of the panel is shown in the Figure 3.

Surveillance system as an event recorder and as monitoring logger

The centralized surveillance system provides recording of events happening in Radiochemistry Laboratory related to the ventilation system and background radiation level. The operation of ventilation system involves various events like change over of main to standby system and vice versa, status of modules running under class III power in the event of class IV power failure etc. Similarly, events like calibration of AGM, CAM, passage of radiation material around different zones and raise of radiation level are important to be noted. Some of the events logged in the recent past are shown in Figure 4. The Figure 4(a) shows the calibration of an area gamma monitor with ^{60}Co, 3 mCi source. The system has logged the dose rate as the calibrated distance of the source is moved away from the detector. The various values like 80, 65, 35, 22, 15, 9, and 5 mR/hour are clearly seen in the graph.

Similarly the change over event of blower system is recorded and shown in the Figure 4(b). The changes in the differential pressure values of the low level and high level exhaust system are observed to change from 20 mmwc to zero and back. The high level and then low level change over operation is observed in black and in magenta in sequence. The operation is over within a period of 10 minutes.

The remote terminal units are adaptable to different kind of analog signal like current, voltage and digital signals like frequency, TTL levels etc. The overall system is open to take in any future requirements.

VI.9 Digital Pulse Processor based Low Background Liquid Scintillation Counting System for Tritium Assay

Conventionally, pulse processing electronics for nuclear radiation detectors is in the analog domain spread out in different modules. Various operation parameters of these modules are to be optimized for concerted functioning of overall system to extract intended information. The convention demands field expertise to get the best results. Recently, due to the availability of high speed ADC, DSPs, the pulse processing electronics is practiced in digital domain with greater flexibility. The digital processors are adapted with much ease to realize the expected results. The processors offer comprehensive data output so that required information like time stamp of radiation event, energy, pulse shape, etc. can be retrieved in post analysis in customized software.

Configuration of liquid scintillation system

This article reports about a pulse processing method for liquid scintillation system for tritium assay using a commercially available digitizer, 100 MSPs (mega sample per second) four channel CAEN DT5724. The block diagram of the proposed liquid scintillation system is shown in Figure 1. The digitizer processes the preamplifier pulses to generate its arrival time and pulse height level information as binary data. Two of the four channels of the digitizer are adapted to process the preamplifier pulses from oppositely placed twin photomultiplier tubes (PMT). These PMTs are positioned suitably to monitor the scintillation pulses from tritium beta emitter in liquid scintillation cocktail. The

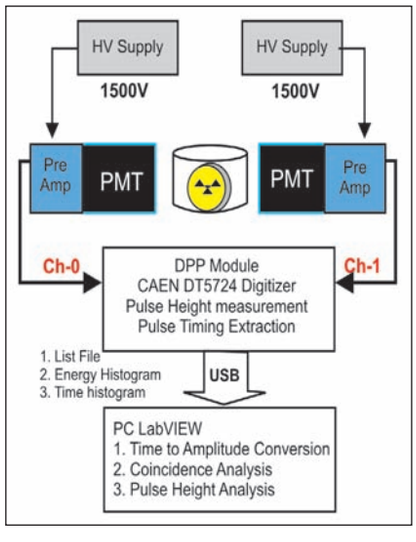

Fig. 1 *Block diagram of the system*

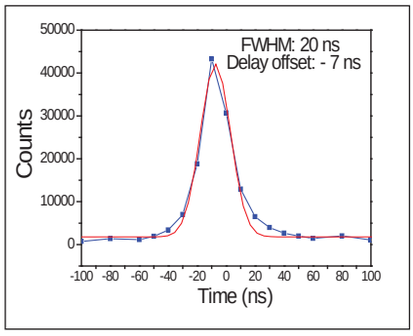

Fig. 2 *Coincidence spectrum extracted from the VI based TAC*

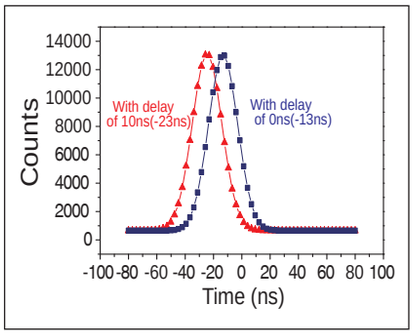

Fig. 3 *Calibration of digitiser using a delay of 10 nanoseconds in CH-0*

model ECIL BARC LSS4029 is adapted for this application. The digital data of both the channels are compared in offline software for time coincidence to infer coincidence counts for tritium along with energy spectrum. The coincidence of the beta pulses are looked at in order to discriminate the anti coincident noise pulses from the PMTs (block diagram of the system in Figure 1). This exercise is indispensable as the voltage discrimination is not feasible between the low energy tritium beta pulses and the noise pulses as they are comparable in their pulse heights.

Digital pulse processor

The two channel digitizer processes the preamplifier pulses from both the detectors independently and generates trigger pulses based on the user set threshold. It calculates the event time of the trigger from the start of the preset period using a kind of constant fraction discriminator technique. It processes the pulse using a trapezoidal filter technique and measures the pulse height using a 14-bit analog to digital converter. It stores the event time and the pulse height information of the pulses in a file in the same sequence in which they arrived for the entire preset period. The digitizer prepares a list of the time stamp of incoming pulses from both the channels along with their corresponding pulse height values. It is possible to invoke the file from LabVIEW and examine the list of time stamp data for both the channels for further timing analysis and corresponding pulse height data for energy analysis.

LabVIEW-VI routine to realize the time to amplitude converter

In conventional coincidence systems, the time spread between the actual event time and the machine time as measured by electronics and also the time delay between the channels show time distribution around a mean. Such a time spectrum can be generated by a combination of time to amplitude converter and multi channel analyzer modules. In digital domain, a VI routine in LabVIEW is developed to realize the virtual time to amplitude converter and multi channel analyzer combination effectively to generate the time distribution spectrum.

Keeping the first 'time stamp data' of one of the channels, say CH-0, as reference or 'start' event, the VI routine scans the list of time stamp data of the other channel, CH-1 to get a 'stop' event. If there is an event happened within ±100 nanoseconds then it increments the corresponding 10 nanoseconds bin or register depending on the value of time stamp. Then it terminates the scanning. Then, the VI routine moves to the second 'start' data of the CH-0 list, compares with the remaining data in CH-1 list and updates the bin contents accordingly.

After completion of the last data, (at end of preset period) the routine generates an array of XY data viz. number of coincidence pulses for the given preset period in different bins with a width of ten nanoseconds on either side ranging from -100 to +100 nanoseconds. Such a true coincidence spectrum plot, derived from the virtual time to amplitude converter is shown in the Figure 2. The blue curve is the actual plot and the red one is the Gaussian fitting for the blue. The preset period is 60 seconds. The FWHM is 20 nanoseconds. There is a delay offset in the CH-0 by about seven nanoseconds. The relevance of the deductions is as follows: the pulses from the CH-0 and CH-1 can be considered to be in coincidence for beta activity measurement if they are within twenty nanoseconds. The time period is known as the resolving time. The delay of seven nanoseconds is to be accounted in the software while scanning for coincidence.

Calibration of timing measurement

An experiment is conducted to verify the accuracy of the measurement of time stamp data. Hence, a standard calibrated delay unit ORTEC 425 A is introduced to delay the preamplifier pulses by a known period in one of the channels before the digitiser input. The time to amplitude converter spectrum drawn for this case is shown in the Figure 3. There are two spectrums in the figure. The blue one is drawn with the delay module included with zero nanoseconds set. There is a delay of thirteen nanoseconds because of the inherent minimum delay in the module, of the cables used and the delay between the channels. The red spectrum is drawn with ten nanoseconds delay set in the module 425 A. There is a shift of ten nanoseconds in addition

to the inherent delay. This confirms the accuracy of the time stamp measured by the digitizer.

LabVIEW-VI routine to generate energy spectrum

The pulse height data of the list is scanned for energy analysis. It increments the contents of the registers or channels corresponding to different pulse height values and creates an array of number of counts versus channel numbers. It plots the data as the pulse height histogram. The Figure 4 shows the pulse height spectrum of tritium beta pulses as received from CH-0 and CH-1.

LabVIEW-VI routine to count coincidence pulses

The VI routine examines the number of coincidence pulses in the CH-1 within ±10 nanoseconds with respect to the reference pulse in the CH-0. The offset correction is done in the software. The threshold set to generate time stamp is 10 LSB. The full scale pulse height value of the 14 bit analog to digital converter is set at 2.25 V. Hence the one LSB value is 0.137 mV. The threshold is effectively set at 1.37 mV.

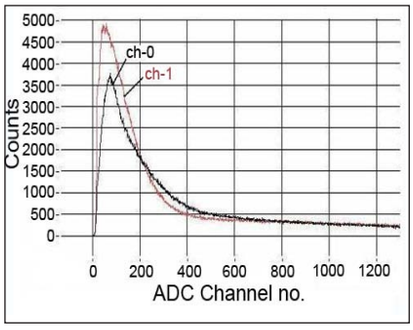

Fig. 4 *Energy spectrum of tritium beta pulses of both channels*

Typical results obtained for an experiment is shown in Table 1. Amersham Standard Tritium beta source vial is used.

Table 1: Typical results obtained for an experiment

Source	199400 DPM
Coincident beta counts	98911 CPM
Efficiency	49.6%
Background counts	10 CPM

The advantage of using digital pulse processing technique is illustrated in this report. A set of hardware modules and a lot of optimization procedures are spared by adapting digital approach.

The offline analysis paves the way for re-examining the data with different set of control parameters. A compact, developer and user friendly system is realized.

VI.10 Indigenous Charge Sensitive Pre-amplifier Design for Hyper Pure Germanium (HPGe) Detectors

High purity germanium detectors are used in almost all areas of the Nuclear Fuel Cycle. These detectors are currently being imported from non-tropical countries and given the ambient conditions in our country are prone to failure. Most of the failures relate to the pre-amplifier electronics. The indigenously developed resistive feedback type pre-amplifier for such detectors and the performance characteristics of a pre-amplifier unit with the detector are discussed.

HPGe based gamma spectroscopy system

Sophisticated instruments are used in nuclear installations for identifying, measuring and recording the parameters of the radio isotopes. Gamma spectroscopy system based on HPGe detectors plays a vital role in identifying the radio isotopes by detecting the gamma energy with higher energy resolution. The system consists of high purity germanium (HPGe) crystal as detector, charge sensitive pre-amplifier for amplifying the collected charge, spectroscopic amplifier for further amplification of signal and pulse shaping and multi-channel analyzer for plotting and analyzing the energy distribution of the pulses.

HPGe detector

A high reverse biased, vacuum sealed, super cooled (at liquid nitrogen (LN_2) temperature) semiconductor diode made of HPGe crystal performs the detection of gamma rays in the system (Figure 1). When a particle deposits energy in a semiconductor detector, equal number of electrons and holes are formed within a few

Fig. 1 *Photograph of high purity germanium detector crystal*

picoseconds along the particle track. This is proportion al to the energy deposited by the particle. As the electric field is present throughout the active volume, both charge carriers are attracted to the respective electrodes. The motion of these charge carriers constitutes a current that persists until those carriers are collected at the boundaries of the active volume.

Charge sensitive pre-amplifier

The main function of the pre-amplifier is to integrate the charge generated in the detector without losing the energy information required for the excellent resolution of the system. Pre-amplifiers are located close to the detector to reduce the noise interference that may appear due to long cables used. A field effect transistor, cooled up to LN_2 temperature, located inside the HPGe detector assembly connects the detector to the pre-amplifier (Figure 2). Keeping the field effect transistor in lower temperature ensures the minimum leakage current, which plays an important role in the energy resolution of the system. There are three types of pre-amplifiers used based on the feedback or reset technique implemented:

a. Resistor feedback

b. Transistor reset

c. Optical reset

Most of detectors employ resistor feedback type pre-amplifier. Transistor reset and optical reset are used where count rate is expected to be very high.

Pre-amplifier circuit using SMD components

Surface mount components are smaller in size compared to through-hole counterparts. These components can be placed on both sides of the circuit board. Thus compact size with more component

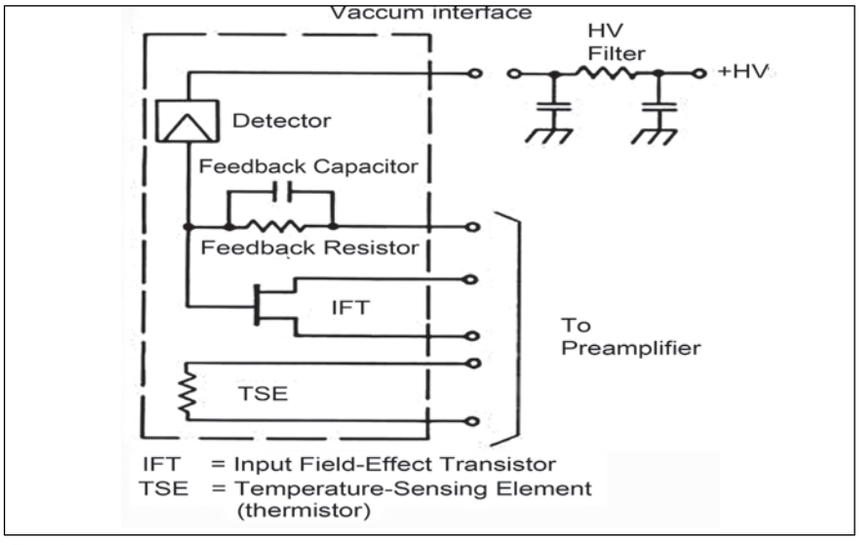

Fig. 2 *Simplified detector electronics diagram*

density can be achieved. The smaller package reduces the EMI in the circuit. It has very high resistance to mechanical shock and vibrations. These advantages of surface mount components over through-hole ones make them the perfect selections for the present pre-amplifier circuit design.

Design

The unmatched energy resolution of the instrument makes it as one of the superior as well as costlier instrument used in the nuclear industry. In India, lack of manufacturers and unavailability of high purity crystal manufacturing technique, added up the importance of the system. Now with such scenario of less number of manufacturers throughout the world and suppliers of the system, the procurement of a new system or servicing of the existing systems has become more critical and difficult also. In this crucial point, our Centre has constituted a task force in view to overcome the situation by servicing the existing non-working systems and develop HPGe based system indigenously by reverse engineering the existing detectors.

Observation shows that a number of detectors are not working because of the failure of pre-amplifier circuit. Most of the suppliers neither supply the circuit diagram of the

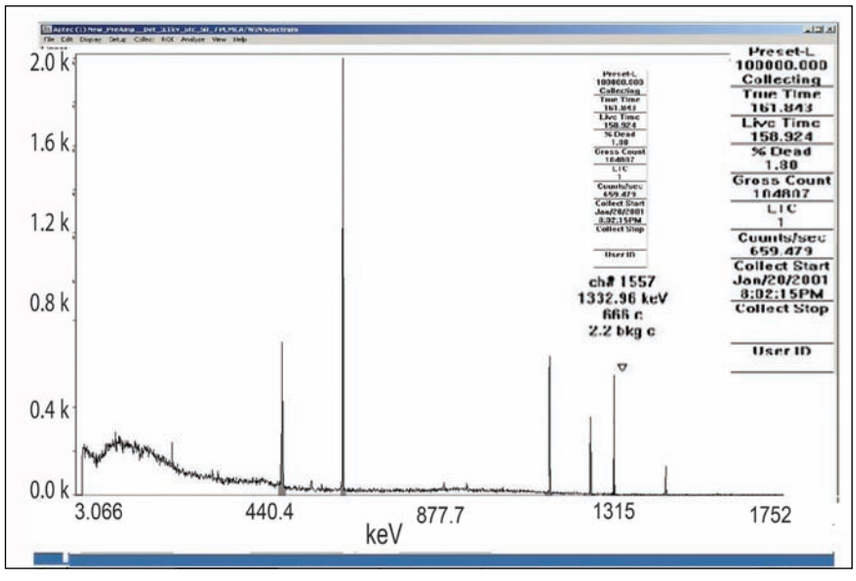

Fig. 3 *Energy spectrum acquired with the indigenous preamplifier mounted on one such faulty Eurisys measures detector*

pre-amplifier nor extend the service support to the system. Keeping these things in mind a task force is formed for designing indigenous detector electronics for their existing non functional detectors and succeeded in their approach.

In standard pulse height spectroscopy, it is necessary for the shaping times of the pulse processing electronics to be substantially larger than the longest rise time likely to be encountered from the detector if resolution loss due to ballistic deficit is to be avoided. To achieve this, pre-amplifier design consisting of drain current adjustment, pole zero compensation, DC offset adjustment, high count rate indicator, detector temperature sensing and high voltage shut down signal system has been evolved.

Performance of the indigenous HPGe pre-amplifier design

The indigenously designed pre-amplifier has been fitted into three nonfunctional detectors of Ortec, Eurisys Measures make. Proper tuning of drain current, pole zero cancellation and DC offset trim pots brought back the non functional detectors working well with an excellent energy resolution as brand new detectors.

One such acquired spectrum is shown in Figure 3 with a Eurisys Measures detector of 1.84 keV for ^{60}Co and 1.55 keV for ^{137}Cs were recorded. It shows an excellent energy resolution of the detector functionality with our indigenous pre-amplifier design.

The indigenous pre-amplifier designed and fabricated was fitted with a faulty Eurisys measures HPGe detector. An excellent energy resolution of 1.84 keV for ^{60}Co standard source, is achieved by proper tuning of the detector pre-amplifier electronics as shown in Figure 3.

VI.11 Challenges in Design and Construction of Building Housing 100 Tonnes Shake Table

The capacity of the seismic shake table is 100 MT, largest in India, with six degrees of freedom and necessary data acquisition for simulation of earthquake ground motions and analysis. The table is 6x6 metres with a central hole of 3.5 metres diameter. This special design gives the flexibility of testing large diameter vessels in hanging condition eliminating the requirement of stiff support structure reducing overall weight of pay load.

The building integrates the experimental areas along with control room, power pack area, other office area, etc., at the same time isolates the office structure from vibrations generated in the experimental area (Figure 1). The lab is a reinforced concrete framed structure of 20x40 metres and height 16.5 metres to facilitate tests of long components. Steel tubular roof truss is provided for flexibility of top loading of specimen if need arises. There are tall openings with sliding door and rolling shutter for truck entry. The power pack room is provided with acoustic wall paneling. The experimental hall is also provided with 20 MT capacity EOT crane for handling test components.

Foundation

In order to attenuate the transmitting vibration to around 0.01 grams at 10 metres from foundation the actuators (4 vertical and 4 horizontal) are placed on massive block foundation. Geotechnical investigations showed presence of weathered rock at four metres depth from natural ground level. Hence shake table is founded on massive block foundation on rock seven metres deep.

This required breaking of 1550 m^3 of rock using control blasting without exceeding the permitted peak particle velocity of

Fig. 1 *Structural dynamics laboratory*

8 mm/s. The procedure adopted for controlled blasting operation is line drilling method. The diameter of the blast hole was 32 mm with a depth ranging from 0.75 to 1.5 metres. Gelatin gel was used as a blast material. The charge factor was maintained approximately between 0.40 to 0.50 kg/m^3 of rock so as to make fragmentation only in the excavation pit. The peak particle velocity was measured near computer centre annexure 125 meter NW and Micro seismic station 70 metres SW of the laboratory.

The seismic block is provided with counter fort retaining wall to achieve

vibration isolation (Figure 2). The seismic mass block concrete is 1043 m^3 and cannot be done in single layer due to high heat of hydration. Hence concrete was placed in four pours with maximum single pour of 297 m^3 using temperature controlled concrete with a placement temperature of less than 23ºC.

In order to transfer the heavy axial and torsional reactions from powerful actuators a steel frame work with heavy embedded parts are also embedded well within concrete (Figure 3).

Fig. 2 *Top view of block foundation for shake tables*

Fig. 3 *Counter fort retaining wall and embedded frame structure*

A smaller shake table of 10 MT capacity will also be founded on the same block (Figure 2).

VI.12 Implementation of Fire Protection System (Mulsifyre System) for the Power Transformers at Central Switching Station

The maximum power demand of IGCAR including the other units BARCF, BHAVINI and GSO is about 23 MVA and is fed from central switching station (CSS) of IGCAR. The load is fed by two independent feeders of 25 MVA capacity each from MAPS switchyard. Considering the additional load requirement of upcoming projects such as FRFCF and two MGD desalination plant, the third feeder was commissioned from PFBR switchyard.

The power supply is further stepped down to 11 kV by means of three numbers of 20 MVA, 33/11 kV power transformers situated at CSS. As per the guidelines issued by Central Electricity Authority, it is mandatory to protect these transformers against any fire incident.

Hence it was decided to introduce “Mulsifyre System” for these transformers as part of fire protection system and mitigation of fire in case of exigencies. The system also can be used to cool the transformers to limit its operating temperature.

The note briefs about the design criteria of the state-of-art system and the major features introduced in the system.

Design features

The fire protection and detection system is based on the high velocity “Water spray system”. The minimum water velocity required is 10 m/s and the liquid shall have a flash point of more than 650°C.

The detection shall be by means of quartzoid bulbs and both detection and protection lines shall be supervised using pressure switch. In case of fire, the quartzoid bulb shall break resulting in pressure reduction in the detection line. The deluge valve gets opened automatically due to reduction in the pressure of the operating mechanism. The deluge valve can be opened either hydraulically by the pilot head detectors or manually. Wet pilot system is employed in the present case.

The three principles by which fire is extinguished are emulsification, cutting off oxygen, cooling and smothering. The system applies water in the form of conical spray consisting of droplets of water travelling at high velocity.

Detailed description of the system

The automatic high velocity water system (mulsifyre system) consists of pipes, deluge valve & trim kit assembly, isolating valve, strainer and spray nozzle.(Figure 1). The fire protection line is supervised using a pressure switch. The deluge valve can be automatically opened by using solenoid valve.

Wet pilot system is employed in this case (i.e.,) pressurised water is utilised for the detection system

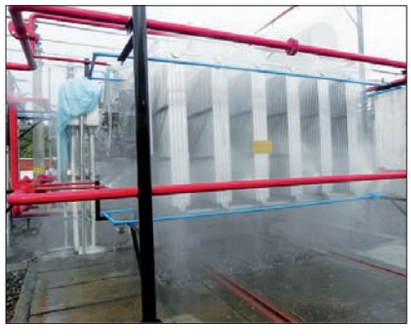

Fig. 1 *Fire protection system*

and reduction in pressure is sensed to initiate the actuation of mulsifyre system.

In case of fire, the quartzoid bulb shall break thereby reducing the water pressure in the detection network. The rapid rise in temperature will cause the liquid inside the fragile glass bulb (quartzoid bulb) to expand leading to breakage of the bulb. Due to reduction in operating pressure, deluge valve will open, thus allowing the water to be sprayed on the transformer through projectors in the form of a solid conical emulsifying spray.

The water demand is computed at an application rate of 10.2 lpm/m^2.

Implementation at CSS

The mulsifyre system is implemented for all the three 33/11 kV transformers at Central Switching Station. The system is connected to the IGCAR fire water system which is maintained at a pressure of 7 kg/cm^2. Three transformers have three independent systems and are capable of fighting the fire independently. The following additional features are introduced to the system.

- Dismantling spool pieces were introduced to facilitate removal of transformer in case need arises for the factory service
- Pylon support was provided for both fire detection and water spray lines with removable spool pieces for easy movement of transformer
- The number of nozzles and angle of spray is designed to cover the whole transformer with water spray
- The routing of pipe lines was carried out in such a way that the movement of operating and maintenance personnel is not hindered
- The location of detectors were selected in such a way that it is not affected by the routine operations and meeting the ISI standard
- The water flow equipment for each transformer is designed to be as 600 lpm and is achievable with the operation of fire water pump on actuation of fire alarm.

Testing and commissioning of the system

The erection of pipes, deluge valves, strainers and other isolation valves including supports were completed as per the layout. Provision is introduced to drain the system after each test. The instruments and other pressure switches were introduced and calibrated. The control panel was tested, negative sequence checked and control logic was checked.

Flushing of the system was carried out after bypassing the deluge valve before the spray nozzle and detectors were installed. During this flushing, leak check was conducted on all the flange joints. Pressure holdup test was conducted in the detector line by blanking the detector location to ensure the integrity of the system.

The detector line was pressurised by water pressure and hold up test was continued. Then the deluge valve was put into service. The valve operability on manual and auto modes was ensured.

The system was kept in poised state. The automatic operation of the system was actuated by depressurising the detector line. The effectiveness of spray line was monitored and photographed. Then the fire water system was pressurised to its rated pressure of 7 kg/cm^2 and the automatic actuation was simulated again.

The system was commissioned and tested to ensure its effectiveness to meet the mandatory requirement.

VI.13 Development of an Ion Mobility Spectrometer for Detection of Explosives

An Ion Mobility Spectrometer (IMS) is developed for use as an analytical tool and in particular, for the detection of species used as explosives. From the initial design based on literature and several optimization studies, a configuration is reached, which provides desired sensitivity with adequate resolution. A schematic representation of the optimized geometry of the ion mobility spectrometer is shown in Figure 1. About 10 mCi of ^{63}Ni is used as the ionization source. The electrodes are made of copper and are stacked using polytetrafluoroethylene (PTFE). This geometry is simple to fabricate, assemble and is of low cost.

On introduction of sample vapor (for instance TNT), the intensity of reactant ion peak (RIP) decreases

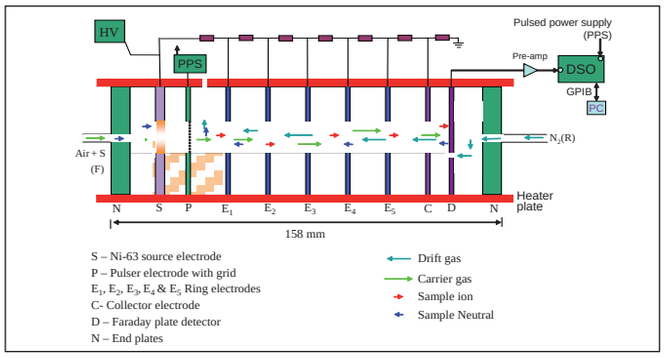

Fig. 1 *Schematic diagram of ion mobility spectrometer*

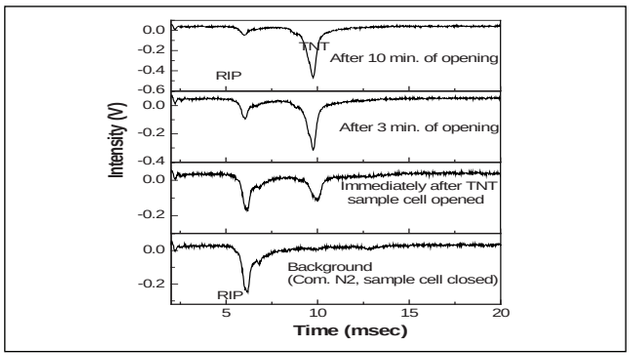

Fig. 2 *Mobility spectrum of TNT vapor*

and the intensity of the sample feature increases and these features are adequately separated in time as shown in Figure 2. The partial pressure of TNT corresponds to ~5 ppb by volume. The IMS cell has also been studied in the particulate mode. Typical mobility spectrum obtained using a particulate-sampler for a sample containing TNT and RDX is shown in Figure 3. The features appeared immediately after the sample introduction, and this spectrum was obtained within 10 seconds of sample introduction. These TNT and RDX features disappeared within 3 minutes of sample introduction. Further work will be carried out to improve the sensitivity and resolution.

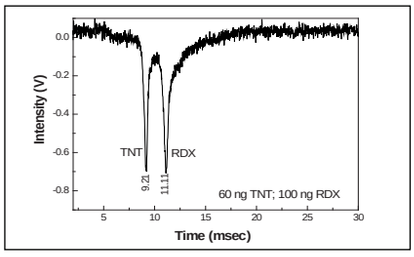

Fig. 3 *Mobility spectrum for TNT and RDX using swab (particulate) sample mode*

VI.14 New Aspects of Budget Monitoring in IGCAR

Budgetary allocation for various activities in our Centre, can be categorized into two types, viz., (a) capital budget and (b) revenue budget.

The capital budget is allocated to carry out the planned R&D projects or set up new facilities. The revenue budget is allocated for operation and maintenance of the existing facilities in the Centre. The expenditure is incurred mainly under the heads of accounts of materials and equipments (M&E), major/minor works (MW), supplies and materials (S&M), consultancy, office expenses, travel and salaries.

Financial growth of the centre

Since inception, the Centre has increased its multi-disciplinary activities which are evident from the phenomenal growth in its capital as well as revenue budget. The expenditure under capital and revenue budget for various five year plans are shown in Figure 1. There is an increase of about 149% under the capital budget expenditure from X plan to XI plan. Similarly the revenue budget has seen a rise of about 117% (Figure 1).

The growing expenditure is due to increase in the number of planned projects and operation/maintenance of various new facilities. During the XII plan there are eighty two planned projects (new as well as continuing from previous plan) which are to be monitored. Monitoring the large number of projects necessitates the effective use of information technology. The mechanisms adopted for monitoring the expenditure under capital budget and revenue budget heads are described below.

Capital budget monitoring mechanisms

During the formulation of capital projects, a unique project identification number (PIN) is assigned to each project. The following mechanisms are adopted for capital budget monitoring.

a) PIN-wise item list update: To monitor the expenditure in a project, it is necessary to track the projected and actual payments for each item

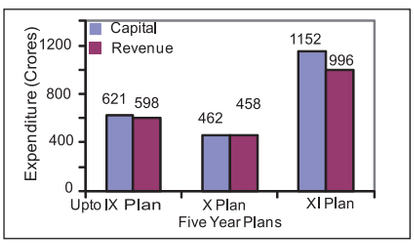

Fig. 1 *Budget outlay for IGCAR*

individually. The items under a project include the machinery and equipments to be purchased and the major/minor works to be carried out. Since the procedures and agencies to carry out these activities are different, a software module has been developed to enable the project and budget coordinators to keep track and update the items and also expenditure against each item under a project (Figure 2).

After an indent is released for procurement of the items, these items are added automatically by the system under the item list module of the particular PIN to update the projected and the actual expenditure against it. Other items like minor/major works can be added manually by the project coordinators under the same list.

Various reports are made available from the item list data updated by the project/budget coordinators for each project. These reports include project-wise expenditure details (annual, quarterly and monthly), sector-wise and also group-wise details. These reports also provide information towards estimating the revised budget of current year or budget for the next year.

b) MIS Reports: Various online reports are made available as part of management information system. These reports are based on the status of purchase data at various stages like, indent, tender, purchase order or payments. The following reports are made available to the users:

i. Tender enquiry to be issued
ii. Tenders opened/being opened shortly
iii. Purchase recommendation/ stores and purchase committee approval pending
iv. Purchase order to be released
v. Purchase orders released

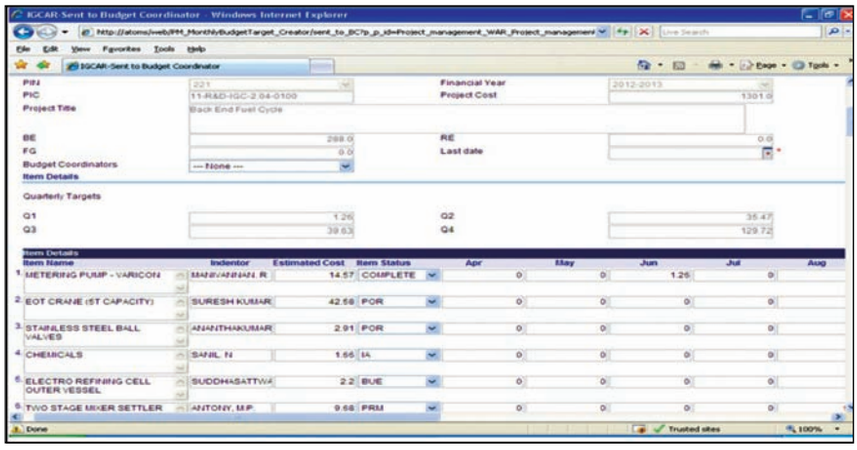

Fig. 2 *Screen shot of item list for a project*

vi. Expenditure details
vii. Balance Payments
viii. PO delivery date expired

c) Automation of Works Procedure: The major component of expenditure under capital and revenue budget is due to civil works and procurement of equipments. Presently the procurement procedure has been automated to a large extent starting from indent to payment stage. In order to automate the major/minor works procedures also in line with the procurement procedures, an initiative has been taken up to develop software modules for work requisition, technical sanction and work order. This will help in monitoring the physical and financial progress of the on-going works.

Revenue budget monitoring mechanism

The revenue budget is provided for operation and maintenance of the existing facilities/plants set up during the previous projects. The revenue budget is allocated to IGCAR annually. The allocated amount is distributed among the various Groups in IGCAR as per their requirements submitted through RB-5A and RB-17 forms. The form RB-5A is submitted to give the requirements under the object head of minor works and form RB-17 is submitted to give the requirements under the head of supplies and materials. The requirements under the other object heads are estimated by the accounts, IGCAR based on the expenditure incurred during the previous financial year.

To track the expenditure incurred by various groups under revenue budget, there is a need to evolve a mechanism to monitor the group-wise expenditure. For this purpose, the heads of accounts are further divided into various codes which identify the groups incurring the expenditure. These codes are known as PR-item codes in IGCAR. The PR-item codes are unique codes which identify the Group as well as the head of accounts including the object heads. While budget allocation as well as booking of expenditure, the PR-item codes need to be mentioned, which would ensure the group-wise monitoring of the expenditure against the allocated budget.

With the help of these mechanisms and online systems, the indenters and project coordinators are able to get updated information at their desktop which helps in effective monitoring of expenditure. These enable in meeting the budget targets in time and the inputs are useful in decision making.

VI.15 Enhancement of Infrastructure for Providing Effective Access to Information Resources

Scientific Information Resource Division (SIRD) takes untiring efforts to implement the state-of-art technology for its efficient services to the user community. The XI plan targets were successfully completed including virtualized high performance digital library architecture, CCTV based surveillance, advanced Radio Frequency Identification (RFID) based library management system, Live video streaming and enhanced e-resources based on the research requirements of the Centre.

SIRD Implemented server virtualization for providing maximum utilization of available servers. Server virtualization involves running more than one virtualized instance of a guest operating system on limited number of physical servers. Red Hat Enterprise Virtualization (RHEV) has been deployed at SIRD for hosting various applications. Live migration, high availability, scalability are the inherent benefits of virtualized environment. Prior to the implementation of virtualization in SIRD, there were about twelve numbers of servers each running separate applications and each being heterogeneous with different configurations. The digital infrastructure is migrated to virtualization based 3-tier model. The virtual machine, hypervisor and the virtual manager are configured on High Availability mode. This means if a hypervisor goes down due to some reason, the virtual machines that were running on that hypervisor get transferred to another running hypervisor, with no change in their state and loss of data. All the virtual machine images and data are stored in centralized IP based Storage Area Network (SAN) with RAID 60 based redundancy. Red Hat Virtual Resource Manger monitors the health of all virtual machines and in case of any failure, ensures the live migration of application from one machine to the other. Further the entire primary data centre is duplicated in a disaster recovery site located elsewhere to ensure the high availability of Digital Library services even during the contingencies (Figure 1).

The entire SIRD premises had been equipped with CCTV based surveillance cameras (Figure 2). About 48 cameras covering the entire user area are installed which can be accessed

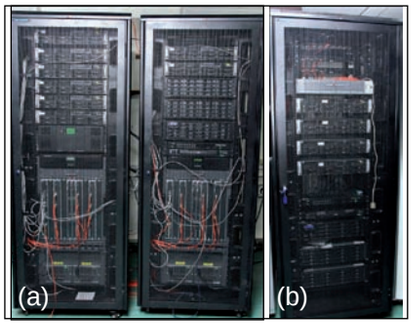

Fig. 1 *Virtualized server environment (a) Primary data centre and (b) Disaster recovery centre*

through the network. A centralized display has been put near the counter system for regularly monitoring various areas of SIRD.

The counter system has been refurbished to reflect the modern ambience with compact space and cabling. Book transactions were automated using the RFID based check-in/ check-out stations (Figure 3).

Beside these infrastructural changes, SIRD keeps building the e-collection regularly based on research needs of the centre. During this period, the complete archives of Nature and Scientific American, ICDD-PDF database, Bureau of Indian Standards and Indian patents are added to our collection.

Fig. 2 *CCTV display at SIRD*

Fig. 3 *Modernized counter at SIRD*

VI. 16 Enhancing Awareness in Neighbourhood

Kalpakkam is a unique site where in there are operating power plants, research reactor as well as a major power project under construction. The developmental activities in the site are also growing at a very fast pace with projected proposals for construction of additional reactors and associated closed fuel cycle facilities in the future. There is an urgent need to enlighten the public by conducting awareness programmes, especially the stake holders in the neighbourhood, in the wake of recent developments in the nuclear project sites, after the accident at Fukushima, Japan. The challenge in conducting the public awareness programmes lies in addressing the concerns and sensitivities of public at large, while countering misinformation and vested interest. The campaigns are to be conducted, in a systematic and demonstrative manner, professionally to make them successful. In the past, the issues of concern to public in nuclear energy have been on the economics and safety of nuclear power stations. A little more educated are concerned about the complex design and technology of nuclear plants. More importantly, post-fukushima, the recent upheavals in the public have been on issues of radiation safety, impact of radiation on environment and health and on issues relating to waste management which are directly related to their well being. Creating awareness about the programmes of the Department by educating the public, taking the neighbourhood to confidence and getting a positive feedback from media towards the programmes are essential. A mechanism has been established incorporating all the units of DAE at Kalpakkam to address the issues relating to public awareness, organizing awareness programmes and neighbourhood development in a concerted and efficient way. We have adopted a three pronged strategy to dispel the misconceptions of public, students and media.

Fig. 1 *Interactive session with students and teachers from Government School, Manamai*

Visit of students from schools in the neighbourhood were organized periodically in small groups (Figure 1). Senior colleagues made presentations on the activities

Fig. 2 *Interactive session with journalists and media*

and they also interacted with scientists and visited various facilities including reactors. The apprehensions of the students on the concepts of radiation and safety were also clarified by conducting demonstrations and experiments during the visit. In all about 470 students and 18 teachers in seven schools have benefitted by visiting our Centre, MAPS and BHAVINI in the last one year.

Media plays a vital role in connecting our organization to the public. To get a positive highlight to our activity in the media, an exclusive workshop for the journalists and the members from media was organized (Figure 2).Over seventy eight journalists from national and vernacular magazines participated in the workshop. There were presentations by senior colleagues, visits to various facilities of DAE units at Kalpakkam followed by a question answer session. The journalists had "Hands-on" experience with radiation safety equipments and gadgets.

Apart from organizing programmes in the near neighbourhood, awareness workshops were conducted in several academic institutions including Sathyabhama University, Science City, NEC College-Kovilpatti and OMIET-Justice Basheer Ahmed Sayeed College, Chennai were conducted for the benefit of the students. The workshops included scholarly presentations, posters, exhibits and demonstrations on various aspects relating to benefits of nuclear energy and our activities (Figure 3). Quizzes, speech, slogan and debate competitions were also conducted to lure active participation from the students. Many of the colleagues also have visited a number of institutions and have delivered lectures towards clearing the apprehensions in the minds of the public.

One important activity in public awareness is to improvise effective communication between the department and the public. Installation of FM radio is an effort in this direction for conveying messages to masses. The Kalpakkam Community Radio Station (Figure 4) is the first-of-its-kind launched in any of the Department of Atomic Energy (DAE) installations. The radio broadcasts at a frequency 90.8 MHz and covers all the thirty eight villages radially spread over

Fig. 3 *Demonstration during a workshop*

fifteen panchayats. The broadcasted programmes by and large focus on agriculture, culture, fishing, education, health, environment, women empowerment, music, history/archaeology, literary segment and emergency announcements during cyclone and other natural calamities, which is of relevance to immediate neighbourhood even while broadcasting lectures by eminent people on the advantages of nuclear energy. The facility also serves as a form of communicating information during emergencies like tsunami, cyclone etc.

The efforts would be enhanced to reach out to the public in the coming years by adopting innovative methods to bring the scientific facts and benefits of atomic energy to the public.

Fig. 4 *A programme organized by Kalpakkam community radio station*

CHAPTER-VII

Awards/Publications/ News & Events/ Organisation

Awards & Honours

Shri S. C. Chetal, Distinguished Scientist and Director, IGCAR has been conferred with "Lifetime Achievement Award by the Systems Society of India", in recognition of his illustrious career in systems theory and application and bringing the systems movement to its present day state through his life long contributions to the field.

Shri S.A.V. Satya Murty, Director, EI&RSG was awarded "INS Outstanding Service Award" for the year 2011, in recognition of his meritorious scientific and engineering achievements in the field of "Nuclear Reactor Technology, including Reactor Safety".

Shri E. Hemanth Rao, RDG, has received the "INS Young Engineer Award" for the year 2011 for his excellent contribution towards R&D on Sodium Cooled Fast Reactor Safety.

Dr. U. Kamachi Mudali was awarded "Vocational Excellence Award" for the year 2012 by Rotary Club of Chennai Port City, for his outstanding contributions to Nuclear Materials. He has also been elected as "Fellow of NACE" by National Association of Corrosion Engineers (NACE), USA for the year 2013 in view of his outstanding contributions to corrosion science, corrosion engineering and corrosion prevention.

Dr. M. Vijayalakshmi from MMG has been elected, 'Fellow of the Electron Microscopy Society of India' in recognition of her outstanding scientific contributions in the field of "Electron Microscopy".

HEPA Filter Test Facility at IGCAR has been accredited by National Accreditation Board for Testing and Calibration

Dr. K. Gireesan and Dr. T. S. Radhakrishnan from MSG and collaborators at CIPET-Chennai, have received the 2nd National Award (2011) for Technology Innovation under the category, Polymers in Public Health Care, instituted in various fields of Petrochemicals and Downstream Plastic Processing Industry by the Department of Chemicals and Petrochemicals, Government of India, for their work on the "Design and Development of Sensor array Hemet for whole Head Magnetoencephalography System".

DAE Awards & Honours

Department of Atomic Energy has instituted annual awards for excellence in Science, Engineering and Technology in order to identify best performers in the area of Research, Technology Development and Engineering in the constituent units (other than Public Sector Undertakings and Aided Institutions). The Young Scientist, Young Engineer, Young Technologist, Homi Bhabha Science and Technology Award and Scientific and Technical Excellence Award fall under this category. Group Achievement awards for recognition of major achievements by groups have also been instituted. They are the icons for young scientists and engineers to emulate. The awards consist of a memento, citation and cash prize.

The recipients of the Awards from IGCAR for the year 2012:

Homi Bhabha Science and Technology Award	: Dr. D.Ponraju, RDG
Scientific & Technical Excellence Award	: Dr. T.R Ravindran, MSG Shri K. Natesan, RDG
Young Scientist Award	: Dr. (Smt) S. Abhaya, MSG
Young Engineer Award	: Shri D. Naga Sivayya, RDG
Meritorious Award	: Shri J. Selvaraj, ROMG Shri P. Swaminathan, ROMG Shri M.K. Rajappan Achari, ROMG Shri M. Sambamurthi, FRTG Shri V.K. Parvadeesan, ESG Shri P.N. Madhavan, Accounts

Group Achievement Award:

Alpha Tight Transport of High Level Liquid Waste from Reprocessing of FBTR Fuel of 155 GWD/t Burn-up and Partitioning of Minor Actinide in Hot Cell

Dr. P. R. Vasudeva Rao, CG, Group Leader

Dr. M. P. Antony, Dr. N. Sivaraman, Shri K. A. Venkatesan, Smt. S. Rajeswari, Dr. R. Kumaresan, Shri R. Manivannan, Shri A. S. Suneesh, Smt. K. V. Syamala, Shri B. Robert Selvan, Smt. T. Prathibha, Shri R. Karunakaran, Shri T. Kalaiarasu, Shri A. Amalraj, Shri Tippana Bapuji, Shri M. Karunanidhi, Shri S. Sriram, Miss. S. Annapoorani, Shri J. S. Brahmaji Rao, Shri N. Ravi, Shri K. Thiruvengadam and Dr. T. G. Srinivasan, Raja Ramanna Fellow from CG, Shri T. Ravi from EIRSG, Shri A. Ravisankar, Shri V. Vijayakumar, Shri D. Natarajan, Shri Surajit Halder, Shri P. Varatharajan, Shri A. Palanivel, Shri S. Somasundaram, Shri P. Ramjee, Shri P. Rameshkumar, Shri K. K. Vinodkumar, Shri Apurba Kumar Majumder, Shri M. D. Mohauddin Ansari, Shri L. Yogananth and Shri Madhusudhana Rao from RpG. The award is also shared by Dr. T. Kumar from KARP, BARC(F).

Design and Development of PFBR Operator Training Simulator

Shri S. A. V. Satya Murty, EIRSG, Group Leader

Ms. T. Jayanthi, Shri K. K. Kuriakose, Shri N. Murali, Shri B. Sasidhar Rao, Dr. S. Srinivasan, Smt. H. Seetha, Shri K. R. S. Narayanan, Ms. Bindu Sankar, Ms. Rashmi Nawlakha, Smt. N. Jasmine, Shri Jaideep Chakraborty, Smt. Tadimeti Lakshmi Priyanka, Shri M. L. Jayalal, Shri R. Jehadeesan, Shri K. Vijayakumar, Smt. T. S. Kavithamani, Shri L. Sathishkumar, Shri G. Shanmugam and Shri B. Subbaraju from EIRSG, Shri P. Selvaraj, Shri K. Madhusoodhanan, Shri N. Theivarajan, Shri K. Natesan, Dr. K. Devan, Shri Jose Varghese, Shri M. Sivaramakrishna, Shri C. P. Nagaraj, Shri M. Sakthivel, Shri S. Athmalingam, Shri S. Raghupathy, Shri A. Venkatesan, Shri R. R. Ramanarayanan, Shri U. Parthasarathy, Shri Tanmay Vasal and Smt. T. Sathyasheela from RDG.

Thermal Shock Test Facility

Shri B. K. Sreedhar, FRTG, Group Leader

Shri Shiv Prakash Ruhela, Shri Sudheer Patri, Shri S. Chandramouli, Shri P. Madan Kumar, Shri Rakesh Kumar Mourya, Shri S. Ignatius Sundar Raj, Smt. S. Nagajothi, Shri R. Rajendra Prasad, Shri Nilayendra Chakraborty, Shri J. Prabhu, Shri A. Kolanjiappan, Shri R. Ramalingam, Shri R. Krishnnamurthy, Shri M. Sambamurthi, Shri P. Varadan, Shri R. Punniyamoorthy, Shri K. Karunakaran, Shri R. Shanmugam, Shri C. Adikesavan, Shri M. T. Janakiraman, Shri N. Mohan, Shri K. Arumugam, Shri Parmanand Kumar, Shri J. Prabhakaran, Shri P. C. V. Murugan, Shri N. Sreenivas, Shri L. Eagambaram, Shri P. R. Ashok Kumar, Shri M. Karthikeyan, Shri K. Ramesh, Shri V. Kumaraswamy, Shri Shaik Rafee, Shri K. Ganesh, Shri Ashish Tiwari, Shri L. Mohanasundaram, Shri L. Muthu, Shri T. V. Maran, Smt. J. I. Sylvia, Shri P. Vijayamohanarao, Shri M. Anbuchelian, Shri P. Bakthavatchalam, Shri C. Ambujakshan Nair, Shri A. Kulanthi, Smt. S. Narmadha, Shri G. Vijayakumar, Shri R. Iyappan, Shri Sarat Kumar Dash, Shri D. K. Saxena, Shri K. Radhakannan and Shri R. Parandaman from FRTG.

Development of Oxide Dispersion Strengthened 9Cr Ferritic-Martensitic Steel Cladding Tubes for Sodium Cooled Fast Breeder Reactors

Dr. T. Jayakumar, MMG, Group Leader

Dr. M. D. Mathew, Dr. Saroja Saibaba, Dr. K. Laha, Dr. B. P. C. Rao, Shri E. Mohandas, Dr. U. Kamachi Mudali, Dr. Divakar Ramachandran, Dr. N. Parvathavarthini, Dr. Arup Dasgupta, Dr. Anish Kumar, Dr. K. V. Rajkumar,

Smt. Diptimayee Samantaray, Shri Ram Kishor Gupta, Shri S. Thirunavukkarasu, Smt. K. S. Chandravathi, Shri M. Nandagopal, Shri G. V. Prasad Reddy, Shri Chanchal Ghosh and Shri Pradyumna Kumar Parida from MMG. The award is also shared by Shri B. Lakshmi Narayana, Shri B. Prahlad, Shri C. Phani Babu, Dr. Komal Kapoor, Shri S.K. Jha, Shri G. N. Ganesha, Shri L. Sudersanam, Shri Pranay Kumar Maity, Shri K. Umamaheswara Rao, Shri K. Ravikrishna, Shri Ch. Sampath Kumar Chary, Shri K. Somasekhar Reddy, Shri D. Sambasiva Rao, Shri P. Yadagiri, Shri G. Narayana Reddy and Shri M. A. Rasheed from NFC, Hyderabad.

Ferroboron as In-vessel Shield Material in Fast Breeder Reactors

Dr. R.S. Keshavamurthy, ROMG, Group Leader

Shri D. Sunil Kumar, Shri D. Venkata Subramanian, Shri Adish Haridas, Shri V. Rajan Babu and Shri S. Clement Ravi Chandar from RDG, Shri S. Raju, Shri Arun Kumar Rai, Dr. S. Murugan, Shri K. A. Gopal, Shri M. Muthu Ganesh, Shri Rajesh Saxena, Shri R. Ramesh, Shri C. N. Venkiteswaran, Shri D. Ganesan and Shri V. Anandaraj from MMG, Dr. S. Anthonysamy, Dr. K. Chandran, Dr. R. Sudha and Smt. P. R. Reshmi from CG, Dr. V. Ganesan from ROMG and Shri N. Vijayan Varier from TC&QCD.

Main Vessel - Roof Slab Weld Joint Mock up for PFBR Project

Shri R. Sritharan, RDG, Group Leader

Shri Gagan Gupta, Shri V. Rajan Babu, Shri Sriramchandra Aithal, Shri P. Puthiyavinayagam, Shri Abhishek Mitra, Shri C. Raghavendran, Shri Ravi Prakash Pandey, Shri Kulbir Singh, Shri V. Sebasti John, Shri S. Saravanan, Smt. P. Swetha, Shri G. Venkataiah, Shri S. K. Rajesh, Shri M. Babu Rao, Shri R. Manu, Shri V. Devaraj and Shri G. Soundararajan from RDG, Dr. B. Venkataraman, Shri P. Jagannathan, Shri B. Ananadapadmanaban, Shri G. Ramesh, Smt. Alka Kumari, Shri Shrikrishna Tripathi, Shri Sukumar Manna and Shri P. Narayana Rao from EIRSG and Dr. Shaju K. Albert and Shri Harish Chandra Dey from MMG.

Indigenous Repair and Servicing of HPGe Detectors

Shri J. Jayapandian, MSG, Group Leader

Shri C.R. Venkata Subramani, Shri G.Gunasekaran from CG, Shri R.Bhaskaran, Smt. O. K . Sheela, Shri A. V, Thanikai Arasu, Shri N.Chinnasamy from MSG, Shri G. Kempulraj, Shri P. Shanmugam, Shri P. Karruppasamy, Shri K. M. Natarajan and Shri N. Lakshimipathi from ESG(E&M), Shri R. Mathiyarasu, Shri M. K. Sundararajan, Shri Patil Sunil Waman from EIRSG and Shri P. C. Sandheep from RpG. The award is also shared by Dr. K. G. Bhushan, Dr. V. B. Chandratre, Dr. V. D. Srivastava, Shri Uday Sanjay Sule and Shri Sunil M. Rodrigues from BARC.

IGCAR Publications

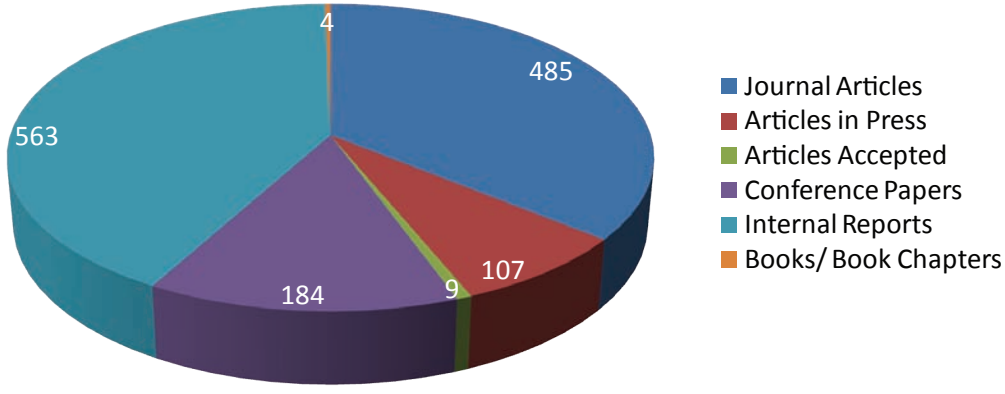

Special Lectures and Colloquia Series

1. "Fukushima Dailchi Nuclear Accidents by Prof. Balraj Sehgal, Royal Institute of Technology, Sweden, January 30, 2012.
2. "E-Tendering" by Shri T. U. Peter, January 30, 2012.
3. "Nanostructures via Thermal Spray: Processing, Properties and Modeling" by Prof. Christopher Berndt, President, ASM International, USA, February 15, 2012.
4. "SESAME experiments with European ROSETTA Mission" IGC Colloquium by Prof. W. Arnold, Germany, March 13, 2012.
5. "Designing Blue Print for Brain Building" by Dr. Shubha Tole, TIFR, Mumbai.
6. "Understanding Cancer and its Cause" by T.R. Rajkumar, Cancer Institute, Adyar, March 28, 2012.
7. "Evolving Nuclear Land Scope" Seaborg Memorial Lecture by Dr. S. Kailas, BARC, Mumbai, April 9, 2012.
8. "Prevention of Diabetes" by C. Snehalatha, Director, Research, India Diabetes Research Foundation (IDRF), June 26, 2012.
9. "Lessons from FUKUSHIMA" IGC Colloquium by Shri S. K. Chande, Vice-Chairman, AERB, July 18, 2012.
10. "Ionizing Radiation Harmful at any Dose" IANCAS colloquium by Prof. P.C. Kesavan, Distinguished Fellow, MSSRF, Chennai, August 13, 2012.
11. "Synthesis, Application and Characterization of Solvents and Diluents for Relevance to Reprocessing Applications" by Prof. J.B. Joshi, Homi Bhabha Chair, UICT, Mumbai, August 27, 2012.

Seminars, Workshops and Meetings

1. International Workshop on "New Horizons in Nuclear Reactor Thermal Hydraulics and Safety" during January 2-3, 2012.
2. Theme Meeting on "Novel and Innovative Measurements in Non Destructive Evaluation (NIM-NDE-2012)" during February 23-24, 2012.
3. Theme Meeting on "Role of Infra-Structural Engineers in the Development of Atomic Energy (RISE DAE)", February 24, 2012.
4. DAE-BRNS Theme Meeting on "Advanced Chemical Sensors and their Applications (ACSAP-2012)" during March 20-21, 2012.
5. Theme Meeting on "Robust I&C Systems for Nuclear Facilities", May 29, 2012.
6. Theme Meeting on "Technological Advancement in Production of Enriched Boron for the Control Rods of Fast Reactors", June 22, 2012.
7. "Electrochemistry and Corrosion Camp (ECC-2012)", September 28, 2012.
8. Theme Meeting on "Challenges and Issues in Surface Modification, Thin Films and Coatings" (STEM 2012) during November 5-6, 2012.
9. ATI/DAE Workshop on 'Right to Information Act' during November 15-16, 2012.
10. Workshop on "Publishing Connect" November 29, 2012.
11. Workshop on "Environmental Radioactivity Monitoring (WENRAM)" during December 10-11, 2012.

Nurturing Activities

1. "Hindi Workshop" for IGCAR Officials, March 21, May 23, October 11 and December 4, 2012.
2. "Summer Training Programme in Physics and Chemistry (STIPAC 2012)" during May 28 – July 06, 2012.
3. "BITS Pilani Practice School" during May 28 - July 13, 2012.
4. Graduation Function of the OCES 2011, 6th Batch of BARC Training School at IGCAR, July 31, 2012.
5. Annual Quality Circles Meet (CCQCM 2012) on August 24, 2012.
6. "Prof. Brahm Prakash Memorial Materials Quiz 2012" during September 14-15, 2012.
7. Celebration of "Hindi Week 2012" during September 14-21, 2012.
8. "Engineers Day 2012", September 24, 2012.
9. Hindi Vigyan Prashna Manch (South Zone) Quiz Competition, October 5, 2012.
10. Launching of KCRS 360 and Launching of Transmission of Employment News through Kalpakkam Community Radio Station (KCRS), December 22, 2012.

News and Events

MoU signed between IGCAR and Korea Atomic Energy Research Institute

January 28, 2012

Shri S. C. Chetal, Director, IGCAR and Dr. Yong Hwan Jeong, Director, Nuclear Materials Development Division, KAERI during the signing up of MoU with KAERI

Consequent to the Nuclear Cooperation Agreement signed on July 25, 2011 between Government of India and the Government of the Republic of Korea, Indira Gandhi Centre for Atomic Research and Korea Atomic Energy Research Institute (KAERI) entered into a Memorandum of Understanding (MoU) on January 28, 2012 at Kalpakkam. This MoU aims at mutually supportive research collaborations between IGCAR and KAERI in the fields of science and technology. The immediate areas of collaboration include high temperature mechanical properties, welding technology, high temperature design and life assessment.

BITS Practice School

May 21- July 13, 2012

Shri S. C. Chetal, Director, IGCAR interacting with the students from BITS Practice School

Twenty five students from BITS Pilani (Pilani, Hyderabad and Goa campuses) underwent BITS Practice School-I for six weeks at our Centre. Dr. P. R. Vasudeva Rao, Director, Chemistry Group inaugurated the Practice School at IGCAR on May 21, 2012. The BITS Practice School bridges the professional world with the educational world. The course aims at exposing the students to

industrial and research environments, on how the organizations work, to follow and maintain work ethics, study the core subjects and their application in the organization, participate in some of the assignments given to them in the form of projects. The students were from various engineering disciplines namely, Civil, Chemical, Computer Science, Electronics & Instrumentation, Electronics & Communication and Electrical & Electronics. Students carried out challenging projects in various Groups of the Centre in line with their discipline. During the period of their stay, they visited various facilities at IGCAR, BHAVINI and MAPS. Quiz, project work presentations, group discussions and report writing formed the practice school curriculum. Shri S. C. Chetal, Director, IGCAR had an interaction session with the students. The valedictory function was held on July 13, 2012 Shri S. A. V. Satya Murty, Director, Electronics, Instrumentation and Radiological Safety Group delivered the valedictory address and distributed the certificates to the students.

Summer Training in Physics and Chemistry-2012 (STIPAC - 2012)

May 28 - July 6, 2012

Participants of STIPAC-2012 with senior colleagues of the Centre

Summer Training Course in Physics and Chemistry (STIPAC), an annual event of IGCAR intended for the pre final year M.Sc. students was organised during the period May 28-July 6, 2012. The purpose of STIPAC is to provide opportunities for the selected students to participate in and become familiar with scientific research through lecture courses and hands-on laboratory experience in selected areas and eventually to motivate them to pursue a research career in science. The theme of this year's programme was "Computational Methods in Physics and Chemistry". A total of thirty six students, seventeen in physics and nineteen in chemistry discipline representing universities from several states across the country attended the programme this year. The selected students were provided a stipend of Rs.4000 per month and their travel expenses were reimbursed.

The event was flagged off on May 28, 2012 by Dr. S. K. Ghosh, Chemistry Group, BARC. Dr. P. R. Vasudeva Rao, Director, Chemistry Group and Dr. C. S. Sundar, Director, MSG in their inaugural address highlighted the genesis and evolution of Summer Training Course in Chemistry (STIC) and Summer Training Course in Physics (STIP) over the years and emphasized the need for such motivating programmes. The Chief Guest Dr. S. K. Ghosh, gave a lucid lecture on the "Concept of Density in Modeling Molecules and Materials at Different Length Scales".

During the six week period, the students underwent rigorous class room training in advanced areas of physics and chemistry with experts from different areas of specialisation delivering the lectures. The lectures offered in the STIP course included quantum mechanics, solid state physics, numerical methods, statistical mechanics, molecular dynamics, density functional theory, structure determination, refinement and transport properties, and in the STIC course on nuclear chemistry, solid state chemistry, thermochemistry, analytical chemistry, surface chemistry, electrochemistry, quantum chemistry, spectroscopy, actinide chemistry, coordination chemistry and computational chemistry. STIP students were involved in specific project work and the STIC students had practical sessions wherein they got the opportunity to work with some of the classical as well as state-of-the-art instruments. The areas of laboratory work in the STIC course included

nuclear chemistry, X-ray diffraction, thermal analysis, mass spectrometry, electroanalytical chemistry and infrared spectroscopy. In all, there were about 90 hours of classroom lectures and 90 hours of project/ practical work for both the physics and chemistry students. The students were very enthusiastic in their participation and showed a lot of interest and keenness in listening to various lectures.

Apart from these class room lectures, the students also had more informal "special evening lectures" delivered by senior scientists and speakers from IGCAR and other reputed institutes: Prof. E. Prasad, IIT Madras (Light Interaction with Matter); Dr. T. G. Srinivasan, Raja Ramanna Fellow, IGCAR (Advantages of Nuclear Energy); Prof R. Asokamani (Electronic Structure); Prof. Srinivas Hotha, IISER, Pune, (Development of Chemistry over the Last Century and Advantages of Becoming a Researcher); Shri T. N. Vaidyanathan, MAPS (Energy Scenario and Role of Nuclear Power); Dr. Prabhat Kumar, Chairman and Managing Director, BHAVINI (Managing Mega Projects), Dr. C. S. Sundar, Director, MSG (Superconductivity at 100); Prof. Anil Kumar, IIT Bombay (Magic and Science: The Art of "ACTIVE" Learning and Research); Dr. P. R. Vasudeva Rao, Director, CG (Science and Excitement); Dr. M. Sai Baba, AD, RMG (Improving Performance by Self Motivation) and Dr. Pankaj Mehta, Hindi Cell, IGCAR (Power of the Subconscious Mind).

The students also had the opportunity to visit various facilities at Kalpakkam such as FBTR, PFBR, MAPS and the UGC-DAE-CSR node. The concluding function was held on July 6, 2012. Prof. R. Murugavel, Head, Department of Chemistry, Indian Institute of Technology Bombay, delivered the valedictory address and also distributed the certificates to the students. He also delivered a technical lecture on "Recent Developments on Porous Solids".

Graduation Function of the Sixth Batch of Trainee Scientific Officers of BARC Training School at IGCAR

July 31, 2012

Dr. R. K. Sinha, Chairman, AEC and Secretary, DAE, Prof. Bhaskar Ramamurthi, Director, IITM, Chennai, Shri S.C.Chetal, Director, IGCAR, Dr. M. Sai Baba, Associate Director, RMG, Shri R. V. Subba Rao, Head, OCES-TS, RMG during the release of souvenir at the graduation function

The sixth batch of thirty five Trainee Scientific Officers from the BARC Training School at IGCAR have successfully completed their training and were graduated in a special ceremony that took place on July 31, 2012 in the Sarabhai Auditorium, Homi Bhabha Building, IGCAR. Prof. Bhaskar Ramamurthi, Director, Indian Institute of Technology Madras, Chennai was the Chief Guest. Dr. R. K. Sinha, Chairman, AEC and Secretary, DAE presided over the function. Dr. M. Sai Baba, Associate Director, RMG welcomed the gathering. Shri S. C. Chetal, Director, IGCAR gave an enlightening address to the gathering. Dr. R. K. Sinha released the souvenir featuring the training school programme in the academic year and Prof. Bhaskar Ramamurthi received the first copy. In his presidential address, Dr. R. K. Sinha gave a very inspiring and thought provoking lecture to the graduating TSOs. Prof. Bhaskar Ramamurthi gave away the prestigious 'Homi Bhabha Prize' comprising of a medallion and books worth Rs. 5000 to the meritorious toppers from all the disciplines. He also gave away the course completion certificates to all the graduates passing out. A few of the Trainee Scientific Officers passing out shared their experience, gave a feedback on the academic programmes and their stay at the hostel. Prof. Bhaskar Ramamurthi gave a very inspiring and motivational lecture to the students. Shri R. V. Subba Rao, Head, OCES-TS, RMG proposed the vote of thanks.

Sixth Batch of Graduates of BARC Training School at IGCAR with Dr. R. K. Sinha, Chairman, AEC and Secretary, DAE, Prof. Bhaskar Ramamurthi, Director, IITM, Chennai, Dr. Prabhat Kumar, Chairman and Managing Director, BHAVINI, Shri S. C. Chetal, Director, IGCAR and senior colleagues of the Centre

Annual Meet of Quality Circles - 2012

August 24, 2012

MOON QC receiving Dr. Placid Rodriguez Memorial Trophy (Mechanical and Manufacturing Category) from Shri G. Srinivasan, Director, ROMG

SAMURAI QC receiving Shri M. K. Ramamurthy Memorial Trophy (Plant Operation and Services Category) from Shri G. Srinivasan, Director, ROMG

Quality circle is a small group of employees doing similar or related work who meet regularly to identify, analyze and solve work related problems usually led by a senior team member. After completing their analysis, they present their solutions to management for implementation and to improve the performance of the organization. Thus, implemented correctly, quality circles can help the organization to reduce costs, increase productivity and improve employee morale.

At IGCAR, every year Annual Meet of Quality Circle is conducted and the case studies are presented by the Teams. The Quality Circle Meet–2012 was conducted on August 24, 2012 at Sarabhai Auditorium and Raja Ramanna Auditorium in parallel sessions. Welcome address was given by Shri G. Ravisankar, Project Engineer (Mech), DFMF & Head, CFD, Chemistry Group. The Presidential address was given by Shri R. Natarajan, Director, RpG and Director, ESG (Mechanical and Electrical). Inaugural Address was given by Shri B. Palaniappan, Chairman, QCFICC, Chennai and vote of thanks by Shri G. Kempulraj, Head, Central Workshop Division, ESG (Mechanical and Electrical).

About seventeen Quality Circles (about 200 members) from IGCAR presented their QC case studies in a wide spectrum of topics covering technical, research and development and services. Judges from Quality Circle Forum of India, Chennai chapter, adjudged the case study presentations. Under the 'Mechanical and Manufacturing' stream, the MOON QC Team of Fast Reactor Technology Group (FRTG) bagged 'Dr. Placid Rodriguez Memorial Trophy', while SAMURAI QC team of Engineering Services Group (ESG) won 'Shri M.K. Ramamurthy Memorial

Trophy' for plant operation and services category. Best maiden QC case study presentation trophy was won by PUREX QC team of Reprocessing Group.

During valedictory function, the events were summed up by Shri A. Jyothish Kumar, Associate Director, Engineering Services Group (Mechanical and Electrical). The programme concluded with the valedictory address and the prizes were distributed to the participants by Shri G. Srinivasan, Director, ROMG, IGCAR. Vote of thanks was proposed by Shri M. Krishnamoorthy, Member, Organising Committee.

Conference/Meeting Highlights

6th International Conference on Creep, Fatigue and Creep-Fatigue Interaction

January 22-25, 2012

Dr. T. Jayakumar, Director, Metallurgy and Materials Group and Chairman, Local Organising Committee, Shri S. C. Chetal, Director, IGCAR and Chairman, National Organising Committee, Dr. Farhad Tavassoli, Head, Fusion Materials Project, CEA, France and Dr. M. D. Mathew, Head, MMD, MMG, Convener, CF-6 on the dais during the inauguration

The 6th International Conference on Creep, Fatigue and Creep-Fatigue Interaction (CF-6) was held at Hotel Radisson Blu Resort Temple Bay, Mamallapuram during January 22-25, 2012. Shri S. C. Chetal, Director, IGCAR inaugurated the conference. Dr. Farhad Tavassoli, Head, Fusion Materials Project, CEA, France delivered the keynote talk on "Materials for Future Sources of Energy" as a part of the inaugural programme. CF-6 was organized by IGCAR jointly with the Metal Sciences Division and the Kalpakkam Chapter of the Indian Institute of Metals. The conference was sponsored by the Board of Research in Nuclear Sciences and co-sponsored by Society of Materials Science Japan, Korean Institute of Metals and Materials, Japan Society of Mechanical Engineers and Korean Society of Mechanical Engineers.

Forty three invited talks by eminent experts (twelve from India and thirty one from abroad) in the areas of creep, fatigue, creep fatigue interaction, materials development, and high temperature design and assessment were delivered in CF-6. One hundred and sixty contributory papers were also presented. More than three hundred fifty delegates including seventy five foreign delegates from fifteen countries attended CF-6. The technical programme was structured into twenty sessions which were held in two parallel sessions. Most of the contributory papers were presented as posters. The poster sessions were held on all the three conference days. There was also a separate category on student's posters. The best three posters in the general category and students' category were given awards. There were separate technical sessions on topics such as creep and fatigue deformation and damage, thermal and thermo-mechanical, fatigue, multi-axial and component testing, high temperature design and life assessment, materials for advanced nuclear reactors, oxide dispersion strengthened materials, materials for ultra super critical power plants, innovative testing techniques, deformation and damage modeling. Fifty eight academic and research institutions working in the areas of creep and fatigue were represented in CF-6.

Theme Meeting on Novel and Innovative Measurements in Non Destructive Evaluation (NIM-NDE-2012)

February 23-24, 2012

Dr. P. R. Vasudeva Rao, Director, Chemistry Group, IGCAR addressing the gathering after releasing the NIM-NDE-2012 Souvenir and handing over the copies to Dr. T. Jayakumar, Director MMG, Dr. C. Babu Rao, Head, UMA section and Dr. B.P.C. Rao, Head, RRHS & NDED

Shri S. C. Chetal, Director, IGCAR addressing the delegates attending the two day theme meeting

A two day theme meeting on 'Novel and Innovative Measurements in Non Destructive Evaluation (NIM-NDE-2012)' was organised jointly by IGCAR, Kalpakkam and BRNS, Mumbai at Convention Centre, Anupuram during February 23-24, 2012. The meeting started with welcome address by Dr. T. Jayakumar, Chairman, NIM-NDE-2012 and Director, Metallurgy and Materials Group, IGCAR. Dr. Jayakumar highlighted the need for a forum to discuss the recent advances in NDE sensors and measurement technologies for structural integrity assessment of components and welcomed the invited speakers and delegates. He lauded the three decades long novel research contributions of Dr. C. Babu Rao, Head, UMA Section, MMG who later delivered a keynote talk on "Development of novel sensors and NDE methodologies at IGCAR" in which he gave a detailed account of his research in fiber optic sensors, under sodium ultrasonics, eddy current sensor, XRF based zari analysis, medical diagnostics and societal applications. Shri S. C. Chetal, Director, IGCAR gave a special address during the theme meeting and highlighted the vital role of NDE techniques for in-service inspection of fast reactor components, especially main vessel, steam generator and reprocessing plant components. He stressed the need for developing high-temperature fiber optic sensors and NDE technologies for inspection of under-sodium components. Dr. P. R. Vasudeva Rao, Director, Chemistry Group released the souvenir and addressed the gathering. He highlighted the role of NDE technologies for ensuring safety and reliability of components. In the theme meeting, there were twenty eight invited talks by eminent professionals from IISc, IITM, BARC, SERC, CGCRI, NFC, Anna University, ISRO and IGCAR highlighting the advances in various NDE techniques. The meeting was attended by one hundred and forty delegates including thirty five graduate students and Ph.D. scholars pursuing studies in the area of NDE. There were very good scientific interactions during the technical sessions and poster sessions. During the valedictory function, the delegates lauded the efforts of the NIM-NDE-2012 organising committee and thanked the organisers for effectively conducting the theme meeting. Dr. B.P.C. Rao, Convener, NIM-NDE-2012 proposed a vote of thanks.

Indo-French Technical Meeting on Thermochemical Modelling

March 7-8, 2012

A two-day technical meeting on thermochemical modelling was held at IGCAR during March 7-8, 2012. Earlier, IGCAR and CEA, France had entered into an Implementation Agreement on "Thermodynamic Modelling of the Actinide Oxides and Oxy-Carbide Systems" under the existing CEA-DAE cooperation agreement in the field of basic research and modelling of physical phenomena. The objective of the present meeting is to exchange the views and

Dr. Jean-Paul Piron, French Correspondent and Dr. Jean-Christophe Dumas of Fuel Study Department, Nuclear Energy Directorate, CEA, Cadarache, France with Shri S. C. Chetal, Director, IGCAR and senior colleagues of the Centre

progress on the thermodynamic properties of actinide oxide and oxy-carbide systems and their modelling.

Dr. Jean-Paul Piron (Correspondent, France) and Dr. Jean-Christophe Dumas of Fuel Study Department, Nuclear Energy Directorate, CEA, Cadarache, France participated in the technical exchange meeting. The technical programme started after a brief meeting of the visitors with Director, IGCAR. Dr. P. R. Vasudeva Rao, Director, Chemistry Group made a presentation on fast reactor programme in India and discussed the scope of the agreement on thermochemical modelling.

Dr. S. Vana Varamban (Correspondent, India) of MCD, CG presented the progress made by IGCAR on thermochemical modelling of oxides and carbides of uranium and plutonium systems. Dr. Jean-Paul Piron and Dr. Jean-Christophe Dumas presented the progress made by CEA on thermochemical modelling of oxides of uranium, plutonium and americium systems and carbides of uranium, plutonium systems.

During discussions, several gaps in the current data, particularly in the carbide systems, were pointed out by the participants. Dr. Vasudeva Rao recommended a few benchmark problems to be solved by both countries and the results to be compared. Shri S. C. Chetal Director, IGCAR commented on the relevance of thermodynamics in fuel behaviour modelling.

Overall, the technical meeting helped exchange of views between CEA and IGCAR on the subject of thermochemical modelling of actinide oxide and carbide systems.

Theme Meeting on Severe Accident Analysis and Experiments

April 26-27, 2012

Panel members Shri H. G. Lele, RSD, BARC, Shri S. S. Bajaj, Chairman, AERB, Shri S. K. Mehta, Former Director, Reactor Group, BARC, Prof. K. Iyer, Mechanical Engineering Department, IIT Bombay, Dr. P. Chellapandi, Director, RDG, IGCAR and Shri P. K. Malhotra, NPCIL during the theme meeting

Shri S. K. Chande, Vice Chairman, AERB delivering the key note address

Following the Fukushima events, there is a need to review and re-assess the strategies adopted in various nuclear facilities for severe accident management. This is essential for evolving a robust accident mitigation and management guideline for all future nuclear reactors. A theme meeting was organized by SRI-AERB in collaboration with IGCAR, at Anupuram during April 26-27, 2012 with an aim to take a consolidated look at the current status of on-going analytical and experimental research work on various aspects of severe accident management, within the DAE units as well as at academic institutions. It is envisaged that the outcome of the deliberations would provide the necessary thrust and direction in focusing research activities in challenging areas and reorient collaborative research activities among the participating organizations. Shri S. S. Bajaj, Chairman, AERB, in his introductory remarks, indicated that events at Fukushima have changed the perspective of nuclear communities' in responding to such events and evolving mitigating measures. Shri S. K. Chande, Vice Chairman, AERB delivered the key note address highlighting the shift in focus and practices in safety subsequent to Fukushima. A total of twenty lectures were delivered by eminent invited speakers from various R&D organizations and academic institutions, on a wide range of issues relating to R&D on severe accidents in thermal as well as fast reactors. The theme meeting was concluded with a panel discussion chaired by Shri S. K. Mehta, Former Director, Reactor Group, BARC.

Theme Meeting on Robust Instrumentation and Control for Nuclear Facilities (RINF-2012)

May 29, 2012

Dr. P. R. Vasudeva Rao, Director, Chemistry Group, IGCAR inaugurating the theme meeting. Shri S. A. V. Satya Murty, Director, EI&RSG, IGCAR and Shri C. K. Pithawa, Head, Electronics Division, BARC are on the dias

A one day theme meeting on "Robust Instrumentation and Control for Nuclear Facilities" (RINF-2012) was organised at Sarabhai Auditorium, Kalpakkam on May 29, 2012. In his welcome address Shri S. A. V. Satya Murty, Convenor, RINF-2012 and Director, Electronics, Instrumentation and Radiological Safety Group, IGCAR, highlighted the importance of the theme meeting particularly in the context of development of robust instrumentation for nuclear facilities and welcomed the eminent speakers, delegates from IGCAR, BARCF, BHAVINI and MAPS.

Dr. P. R. Vasudeva Rao, Director, Chemistry Group inaugurated the theme meeting. He highlighted the vital role of instrumentation and control with respect to safety and availability of the nuclear reactor. He emphasized how important it is to provide robust and reliable instrumentation for nuclear facilities. He stressed the need for paying attention to design and the importance of redundancy. He mentioned the challenges faced because of fast developments in the field of electronics and computers and resultant obsolescence.

Shri C. K. Pithawa, Head, Electronics Division, BARC delivered the keynote address on 'Neutron detectors for Prototype Fast Breeder Reactor'. He explained the methodology followed in designing the neutron detectors to work at very high temperatures for fast reactors, the challenges faced and their solutions.

In the theme meeting, there were six invited talks by eminent professionals from IITM, Centre for Reliability, CEMILAC, BARC, ECIL and Ansh Technologies highlighting the various qualification methods to be followed in building robust instrumentation and control for nuclear facilities. The meeting was attended by more than one hundred and fifty delegates from IGCAR, MAPS, BHAVINI and BARC Facilities. Shri D. Thirugnana Murthy, EID, Secretary, RINF-2012 proposed the vote of thanks.

Theme Meeting on Technological Advancement in Production of Enriched Boron for the Control Rods of Fast Reactors

June 22, 2012

Shri S.C Chetal, Director, Indira Gandhi Centre for Atomic Research, presenting the inaugural address

A one day theme meeting on "Technological Advancement in Production of Enriched Boron for the Control Rods of Fast Reactors" was organized by IGCAR and BRNS at the Sarabahai Auditorium on June 22, 2012. The meeting started with the welcome address by Shri K. K. Rajan, Chairman, organizing committee and Director, Fast Reactor Technology Group. He highlighted the relevance of the theme meeting in the context of the Indian Fast Breeder Reactor programme and welcomed the invited speakers, delegates and guests. He lauded the efforts of Shri R.Subramaniam, Former Head of Chemical Technology Section at IGCAR who laid the foundation for the boron enrichment program at IGCAR and Dr. C. Anand Babu, Associate Director, Component Development Group for his contributions in leading the research and development programme for boron enrichment. Shri S.C Chetal, Director, IGCAR inaugurated the theme meeting and in his inaugural address outlined the importance of enriched boron carbide as absorber rod material for control of fast reactors. He also informed that boron carbide pellets to be used in the control rods of PFBR are ready for shipment at BARC. He reiterated that the development of this technology is a culmination of the combined efforts of BARC, IGCAR and Heavy Water Board. He stressed the need to initiate research and development for recycling the enriched boron carbide from the used control rods of fast reactors. During the meeting five kilograms of 90 percent enriched boric acid powder produced at the boron enrichment plants at IGCAR

was handed over to Shri K.Nagarajan, Associate Director, Chemistry Group for further processing. Dr. C. Anand Babu in his key note address detailed the road map of the boron enrichment in the country. He particularly recalled the uphill challenges and hurdles that were overcome in achieving the present level of technological maturity.

In the theme meeting there were eight invited lectures. The lectures were organized into three different technical sessions as process development for boron enrichment, technology development for conversion to enriched elemental boron and production and operating experience on absorber materials. The lectures were delivered by experts in this field from IGCAR, BARC and HWB. Engineers from the various groups of IGCAR, BHAVINI, BARC facilities, academic institutions and industries like THERMAX were the participants to this theme meeting. There were a total of 90 participants for the theme meeting. The scientific interactions during the technical sessions were beneficial and provided valuable inputs for the design, performance assessment and further improvement of the processes in the production of enriched boron for fast reactors. The meeting concluded with a vote of thanks by Dr. B. K. Sharma, Chairman, Techncial committee.

11th International Conference on High Nitrogen Steels and Interstitial Alloys (HNS 2012)

September 27–29, 2012

Shri S. C. Chetal, Prof. M. O. Speidel, Dr. Baldev Raj ,Prof. J.Foct and Dr. U. Kamachi Mudali during the release of souvenir

The 11th International Conference on High Nitrogen Steels and Interstitial Alloys (HNS 2012) was jointly organized by The Indian Institute of Metals, Kalpakkam Chapter and Ferrous and Metal Sciences Division, IIM with support from BRNS, Department of Atomic Energy, Mumbai, at GRT Grand, Chennai, India during September 27-29, 2012. HNS 2012 was cosponsored by Board of Research in Fusion Science & Technology, Gandhinagar, CSIR, New Delhi, DRDO, New Delhi, Jindal Stainless Limited, New Delhi, TATA Steel, Jamshedpur, Mishra Dhatu Nigam Limited, Hyderabad, Energietechnik Essen GmbH, Germany and Sandvik, Sweden.

The theme of HNS 2012 was 'High Nitrogen Steels and Interstitial Alloys – Developments and Challenges'. The objective of the conference was to provide a forum to discuss all the developments that have been made in high nitrogen steels and interstitial alloys with a view to identify the new challenges for the future development and applications. The presence of interstitial alloying elements in addition to nitrogen plays a major role in the structure, properties and application of various advanced steels including HNS alloys. The role of such interstitial alloying elements (hydrogen, oxygen, carbon and boron) along with nitrogen also affects the manufacturing, fabrication and application of conventional and advanced austenitic, ferritic, martensitic and duplex steels and stainless steels for a variety of applications in industries. In HNS 2012 these issues were addressed with a focus on automobile, chemical, marine, strategic, power and other important applications.

The conference was inaugurated on September 27, 2012 by Prof. Marcus O. Speidel senior member of International Scientific Committee on HNS from Swiss Academy of Materials Science, Switzerland. In his inaugural address he explained how nitrogen is gaining importance as an alloying element of stainless steels by making steels more austenitic, stronger, corrosion resistant, wear and fatigue resistant and one day it can replace the costly nickel in toto. Dr. Baldev Raj, President, INAE, President Research, PSG Institutions and Chairman, HNS 2012 who has presided over the function, stressed the importance of addressing the issues concerning the role of interstitial alloys along with nitrogen that affect manufacture,

fabrication and application of HNS and developing codes for engineering applications. Prof. Jacques Foct from University de Lille, France, the guest of honor, retraced the beginnings of HNS conference way back in 1988 at Lille, France and reiterated that the growing demand for these conferences confirm the importance of HNS emerging globally and wished the best for HNS 2012. Shri S. C. Chetal, Director, Indira Gandhi Centre for Atomic Research and Co-Chairman, HNS 2012 released the souvenir of HNS 2012 and delivered a key note lecture on "Application of Nitrogen Alloyed Steels for Indian Fast Reactor Programme". Dr. U. Kamachi Mudali, Convener, warmly welcomed the gathering, Dr. M. G. Pujar, Technical secretary, gave a brief overview of HNS 2012 and Dr. Rani P. George, Treasurer, proposed the vote of thanks.

Twenty four technical papers, fourteen invited lectures and two plenary lectures were presented by professionals from reputed academic and research institutions, suppliers, fabricators and user industries during the conference. About hundred delegates including leading experts from France, Switzerland, Russia, Austria, Germany, Czechoslovakia, Sweden, Poland and India participated in this important event. The delegates were mostly from industries such as steel, power generation, welding consumables, tube, pipe and valve manufacturing, commercial suppliers of steel products, equipment manufacturing, educational institutions and research and development organizations. About seventeen young delegates from academia and R&D put up posters displaying advances in high nitrogen steel research and had interesting interactions with peers and experts. Five best oral presentations and poster displays selected by eminent judges were presented with prizes.

HNS 2012 provided a platform for international experts and researchers on high nitrogen steels to address recent advances in production of HNS, alloy design, heat treatments, emerging trends in processing and application, surface modification and newer application of HNS. The conference definitely attracted wide participation from industry, research institutions, academia, end user companies and marketing personnel.

Theme Meeting on Structure and Thermodynamics of Emerging Materials (STEM-2012)

November 5-6, 2012

Participants of STEM-2012

The BRNS sponsored theme meeting, 'STEM-2012' focusing on "Challenges and Issues in Surface Modification, Thin Films and Coatings" was organized jointly by IGCAR and The IIM–Kalpakkam Chapter during November 5-6, 2012 at Convention Centre, Anupuram. During the inaugural session, Dr. M. Vijayalakshmi, Associate Director, PMG welcomed the gathering and Shri E. Mohandas, Convener, STEM-2012 briefed the participants about the STEM series. Plenary lecture on the topic "Magnetron Sputtering of Electronically Active and Passive Layers for Thin Film Solar Cells" was delivered by Dr. Klaus Ellmer of HZB, Germany in which he provided an excellent insight into the structure and various material choices available for fabricating thin film solar cells. The vote of thanks was proposed by Dr. C. Sudha, Secretary STEM 2012.

On the second day plenary lecture was delivered by Dr. H. Murakami of NIMS, Japan on "Effect of Iridium Addition on Oxidation Resistance of Coated Ni-based Single Crystal Superalloys". In addition, invited lectures were organized on various topics like sub-surface modification based on plasma based ion implantation and diffusion techniques, plasma assisted chemical vapour deposition, surface modification and thin film deposition using pulsed lasers, AFM/STM analysis of thin films and coatings and plasma sprayed thermal barrier coatings for molten chloride environment. The theme meeting was attended by around 120 delegates including eminent scientists and research scholars from IITs, NIT, IPR, Anna University and other Engineering/Science colleges and BARC and IGCAR. The technical program was appreciated by the participants and valuable inputs for future theme meetings were provided during the feedback session at the end of the theme meeting.

Theme Meeting on Supercritical Fluids

November 20, 2012

Dr. P. R. Vasudeva Rao, Director, CG addressing the gathering of theme meeting on supercritical fluids

The application of supercritical fluid is the subject of growing interest to nuclear and chemical industries, due to environmentally benign and fascinating properties of supercritical fluids. In this context, the southern regional chapter of Indian Association of Nuclear Chemists and Allied Scientists (IANCAS(SRC)), organized a one-day theme meeting on "Supercritical Fluids" on November 20, 2012 sponsored by BRNS at SRI convention Centre, Anupuram.

The theme meeting comprised invited lectures on theoretical aspects, physical properties, modelling, instrumentation and applications of supercritical fluids in nuclear and other industries. Dr. T. G. Srinivasan, President, IANCAS(SRC) inaugurated the meeting. The meeting had two sessions, with four lectures, chaired by Dr. P. R. Vasudeva Rao, Director, CG in the morning session and three lectures in the afternoon, chaired by Dr. T. G. Srinivasan. Eminent speakers from Bhabha Atomic Research Centre, Indian Institute of Science, CSIR and other National laboratories delivered invited lectures. About sixty delegates from various academic and research institutes including ten research fellows participated in the theme meeting. The theme meeting was well received by the delegates and provided good directions on the use of supercritical fluids in nuclear and other industries.

National Symposium on Radiation Physics

December 12-14, 2012

Indian Society for Radiation Physics (ISRP) organized a three day National Symposium on Radiation Physics (NSRP-19) during 12-14, December 2012 in the heritage town of Mamallapuram at Radisson Blu Temple Bay Resort. NSRP-19, with a focal theme of "Research and Applications of Radiation Physics: Perspective and Prospective", was supported by IGCAR, Kalpakkam, Indian Nuclear Society, Kalpakkam Branch, BRNS and AERB.

The inauguration function of the symposium was held on December 12, 2012, Dr. B. Venkatraman, President, ISRP and Associate Director, RSEG, IGCAR welcomed the gathering.

Dr. Prabhat Kumar, Chairman and Managing Director, BHAVINI presided over the inaugural function. During his presidential address, in addition to sharing his scientific and technical journey in DAE, he also urged nuclear physicists and design engineers to constantly strive for improvements in the design configuration, optimization of fuel performance and containment of radioactivity.

The symposium was inaugurated by Shri S. C. Chetal, Director, IGCAR. In his inaugural address he stressed the need for the balanced utilization of all forms of energy resources to meet the ever growing energy needs. He also highlighted the consequences of the conservative approach to the effects of ionizing radiation which has a bearing on the large safety margins and bias factors adopted in the design of safety related systems and suggested for effective optimization. He also insisted on the need to sharpen the communication skills to effectively reach out to the public at large about the facts and figures on nuclear power, safety, environmental releases and the biological effects.

Dr. K. S. Lakshmi, founder and Principal, Meenakshi College for Women, President, ISRP(K), released the souvenir and the proceedings of NSRP-19.

ISRP has instituted an Oration Award in the memory of Dr. A. K. Ganguly, former Director, Chemistry group, BARC, a doyen in the field of radiation physics and protection and a scientist of great eminence. The award is conferred on persons who have contributed significantly to the field of radiation physics and

Dr. Prabhat Kumar, Chairman and Managing Director, BHAVINI, Shri S. C. Chetal, Director, IGCAR, Dr. B. Venkataraman, AD, RSEG, Dr. K. S. Lakshmi, founder and Principal, Meenakshi College for Women, President, ISRP(K) and Shri S. Bala Sundar on the dais during the inaugural session

protection and presented to them during the NSRP conferences. The award for this year was conferred on Shri A. R. Sundararajan, former Director, Safety Research Institute, AERB, Kalpakkam for his outstanding contributions in the field of radiation safety.

As part of the conference, an exhibition displaying various radiation measurements and monitoring systems was also organized wherein leading companies from India and abroad participated. The exhibition was formally inaugurated by Shri S. C. Chetal, Director, IGCAR.

Followed by the inauguration the technical session started with key note talks by eminent scientists from DAE. Dr. S. Kailas, Director, Physics Group, BARC delivered key note address on “Accelerators as a tool for radiation physics and technologies”. Dr. D. V. Gopinath, Former Director, Health, Safety and Environment Group, BARC delivered key note address on “Some myths about radiation effects and nuclear energy”.

Plenary talks in the field of radiation in physics, chemistry, life sciences and agriculture by renowned scientists from DAE and other premier national institutes were also organized as part of technical sessions in the second day of programme. Prof. G. K. Rath, Chief, Dr. B.R.A Institute-Rotary Cancer Hospital, AIIMS gave a talk on role of ionizing radiation in health care. Shri S.A.V. Satyamurty, Outstanding Scientist, Director, EIRSG, IGCAR delivered a lecture on advances in Sensors and Instrumentation for Radiation Detection and Measurements. Shri A. R. Sundararajan, in his talk pointed out the challenges on assessment of internal exposure from plutonium. Prof. Rajarajan, Dean, Tamil Nadu Agriculture University, Coimbatore made elaborate presentation on research and applications of ionizing radiation in agriculture sciences. Dr. P. Mohanakrishnan, Former Associate Director, Reactor Physics Group, IGCAR dwelt upon the new research challenges in field of reactor physics and fuel cycle physics during his talk.

Followed by a series of plenary talks, there were twenty one technical sessions. To accommodate the oral presentations the sessions were held in parallel. Each session started with invited talks by eminent scientists from National Institutes and Universities. The main topics covered were: basic radiation processes, radiation transport theory and shielding, radiation related problems at accelerators and reactors, research reactors and AHWRs, Radiation detection and measurements, radioactivity transport in natural environment and radiation in space, radiation applications in industry, agriculture, food processing and medicine, radiation dosimetric techniques–solid state nuclear track detectors and luminescence and development of nano-phosphors.

A total of 189 scientific papers among various topics including, advanced radiation dosimetry, research reactors and applications of radiation in different areas which included agriculture and industries were presented during the conference. There were 109 oral presentations and 80 posters in the technical sessions. Awards for best three oral and poster papers and three young researchers were given away during valedictory on third day of conference. Additionally two more awards were also given to the two best experimental work papers dealing with detection and measurements of radioactivity, which were sponsored by M/s. Nucleonix Ltd, Hyderabad.

The participation by the student community, from basic science and engineering disciplines, in large numbers was one of the highlights of the symposium, which was highly encouraging as pointed out by Dr. D. V. Gopinath in his valedictory address The collective feedback from the participants was very good. The technical sessions, arrangements, accommodation and the local hospitality extended were highly appreciated by one and all.

Overall, this was a unique experience for all radiation physicists and a platform for the scientists, young researchers and students of Radiation Physics to share their work, knowledge and observations with each other. This also provided opportunity for the interaction between peer groups in forging collaborative studies.

Eminent Visitors To IGCAR

Dr. Barun Mukherjee, Honourable Member of Parliament from West Bengal with Shri S. C. Chetal, Director, IGCAR during his visit to the Fast Breeder Test Reactor

Dr. Barun Mukherjee, Honourable Member of Parliament (Rajya Sabha) from West Bengal visited the Centre on January 7, 2012. After a meeting with Shri S. C. Chetal, Director, IGCAR, Dr. Prabhat Kumar, Project Director, BHAVINI and Shri K. Ramamurthy, Station Director, Madras Atomic Power Station, Dr. Barun Mukherjee visited the Fast Breeder Test Reactor, Hot Cells and Non Destructive Evaluation Division, Facilities in Fast Reactor Technology Group, Chemistry Group, Structural Mechanics Laboratory, Sodium Fire Facility, Atmospheric Dispersion, Madras Atomic Power Station and the construction site of Prototype Fast Breeder Reactor.

Prof. Balraj Sehgal from Royal Institute of Technology, Sweden delivering IGC Colloquium on "Fukushima Daiichi Nuclear Accidents"

Prof. Balraj Sehgal from Royal Institute of Technology, Sweden, during his visit to the Centre on January 30, 2012 delivered the IGC Colloquium on "Fukushima Daiichi Nuclear Accidents".

Delegation from UK with Shri S.C. Chetal, Director, IGCAR and other senior colleagues of the Centre

A delegation of UK Academics comprising of **Prof. Chris Grovenor**, Head of Department, Materials Department, Oxford University and Co-Director, Bristol/Oxford Nuclear Research Centre, **Prof. Mike Fitzpatrick,** Head, Department of Materials Engineering at the Open University, Milton Keynes, UK and **Prof. P John Bouchard,** Professor in Materials for Energy, Materials Engineering at the Open University, visited IGCAR on February 13, 2012. They had in-depth discussions on the possible collaborations in the areas of life assessment and structural integrity; modelling and simulation, and severe accident and nuclear safety, to be funded by EPSRC, UK, under the Indo-UK civil nuclear collaboration. The meeting at Homi Bhabha building was chaired by Shri S. C. Chetal, Director, IGCAR, and involved presentations on areas of mutual interests by senior scientists of IGCAR. The UK delegation also visited the Metallurgy and Materials Science Groups and also the Structural Mechanics Laboratory.

Dr. Alexander Bychkov, Deputy Director General and Head of the Department of Nuclear Energy, IAEA and **Shri Viacheslav Gutkov** visited the Centre during February 23-26, 2012. During the meeting they were briefed about the Research and Development activities of the Centre by Shri S. C. Chetal, Director, IGCAR. After the meeting Dr. Alexander Bychkov and Mr. Viacheslav Gutkov visited the Fast Breeder Test Reactor & KAMINI, Hot Cells and Non Destructive Evaluation Division, Facilities in Fast Reactor Technology Group like Steam Generator Test Facility and SADHANA Loop, Sodium Chemistry Laboratories at Chemistry Group, Sodium Fire Facility, Madras Atomic Power Station and the construction site of Prototype Fast Breeder Reactor.

Dr. Alexander Bychkov, Deputy Director General and Head of the Department of Nuclear Energy, IAEA and Mr. Viacheslav Gutkov with Shri S. C. Chetal, Director, IGCAR and senior colleagues of the Centre

Shri V. Narayanasamy, Honourable Minister of State, Parliamentary Affairs Prime Minister's Office and Shri P. Viswanathan, Honourable Member of Parliament, representing the Kancheepuram Constituency with Shri S. C. Chetal, Director, IGCAR and senior colleagues of the Department during the meeting

Shri V. Narayanasamy, Honourable Minister of State for Parliamentary Affairs at Prime Minister's Office and **Shri P. Viswanathan**, Honourable Member of Parliament, representing the Kancheepuram Constituency visited the Centre on March 03, 2012. During the meeting they were briefed about the Research and Development activities of various DAE units at Kalpakkam by Shri S. C. Chetal, Director, IGCAR, Dr. Prabhat Kumar, Project Director, BHAVINI, Shri C. D. Rajput, Chief Superintendent, Madras Atomic Power Station and Shri S. Basu, Facility Director, BARC Facilities.

Prof. W. Arnold, Physikalisches Institut, University of Goettingen, and Department of Material Science and Technology, Saarland University delivering the IGC Colloquium

IGC Colloquium on "SESAME Experiments within the European ROSETTA Mission" was delivered by **Prof. W. Arnold**, Physikalisches Institut, University of Goettingen, and Department of Material Science and Technology, Saarland University, Saarbruecken, Germany on March 13, 2012, during his visit to the Centre.

Shri Dinkar Khullar, Ambassador and Permanent Representative of India, Vienna, Austria with senior colleagues of the Centre and the Department

Shri Dinkar Khullar, Ambassador and Permanent Representative of India, Vienna, Austria, visited the Centre during March 28-29, 2012. After meeting the senior colleagues of the Centre and the Department, Shri Dinkar Khullar visited the Fast Breeder Test Reactor, Hot Cells and Non-Destructive Evaluation Division, CORAL facility, Kalpakkam Reprocessing Plant, construction site of Prototype Fast Breeder Reactor and Madras Atomic Power Station.

Honorable Justice Shri S. Tamilvanan from Madras High Court and Prof. V. Manimozhi during their visit to the Fast Breeder Test Reactor

Honorable Justice **Shri S. Tamilvanan** from Madras High Court accompanied by his wife **Prof. V. Manimozhi** visited the Centre on April 14, 2012. During the meeting they were briefed about the challenges and opportunities of Atomic Energy by Dr. M. Sai Baba, Associate Director, Resources Management Group. After the meeting Honorable Justice Shri S. Tamilvanan and Prof. V. Manimozhi visited the Fast Breeder Test Reactor and Madras Atomic Power Station.

Shri S. K. Chande, Vice-Chairman, Atomic Energy Regulatory Board delivering IGC Colloquium on "Lessons from Fukushima"

Shri S. K. Chande, Vice-Chairman, Atomic Energy Regulatory Board during his visit to the Centre on July 18, 2012 delivered the IGC Colloquium on "Lessons from Fukushima".

Prof. Bala V Balachandran, Founder and Dean and Prof. S. Sriram, Executive Director from Great Lakes Institute of Management, Chennai with Shri S. C. Chetal, Director, IGCAR

Prof. Bala V Balachandran, Founder and Dean and **Prof. S. Sriram**, Executive Director, Great Lakes Institute of Management, visited the Centre on September 12, 2012. Prof. Bala V Balachandran and Prof. S. Sriram met Shri S. C. Chetal, Director, IGCAR and discussed on neighborhood development programmes and related issues.

A delegation from United States Nuclear Regulatory Commission led by **Ms. Kristine Svinicki,** Commissioner, US Nuclear Regulatory Commission visited the Centre during October 9-10, 2012. After a meeting with Shri S. C. Chetal, Director, IGCAR and senior colleagues, the delegation visited the Fast Breeder Test Reactor, facilities in Safety Engineering Group, Madras Atomic Power Station and construction site of Prototype Fast Breeder Reactor.

Delegation from United States Nuclear Regulatory Commission, USA with Shri S. C. Chetal, Director, IGCAR and senior colleagues of the Centre

Prof. Vijay Sazawal, Director of Government Programs at USEC, Inc, USA, with Shri S. C. Chetal, Director, IGCAR and Dr. P. R. Vasudeva Rao, Director, CG

Prof. Vijay Sazawal, Director of Government Programs at USEC Inc. USA, visited the Centre on December 10, 2012. During the meeting with Shri S. C. Chetal, Director, IGCAR and senior colleagues, he briefed about the "Progress in the U.S. Civil Nuclear Program". Prof. Vijay Sazawal then visited the Fast Breeder Test Reactor, Hot cells and Non-Destructive Evaluation Division, facilities in Fast Reactor Technology and Reactor Design Groups and construction site of Prototype Fast Breeder Reactor.

Shri Ashok Lavasa, IAS, Additional Secretary (Power), Ministry of Power accompanied by Shri T.S.Sundararajan, GM, NTPC, Shri K. Raj Kumar, Junior Engineer, NTPC and Shri Abhay Khanna, General Manager, ICF, visited the Centre on December 25, 2012. After a meeting with Dr. P. R. Vasudeva Rao, Director, Chemistry Group the delegates visited the Fast Breeder Test Reactor, Madras Atomic Power Station and Construction Site of PFBR.

Shri Ashok Lavasa, IAS, Additional Secretary (Power), Ministry of Power, Shri T. S. Sundararajan, General Manager, NTPC, Shri K. Raj Kumar, Junior Engineer, NTPC and Shri Abhay Khanna, General Manager, ICF, with Dr. P. R. Vasudeva Rao, Director, Chemistry Group during their visit to Fast Breeder Test Reactor

IGC COUNCIL

Chairman

Shri S.C. Chetal

Distinguished Scientist & Director, IGCAR

Shri S. C. Chetal graduated in Mechanical Engineering from Delhi College of Engineering in 1970. After graduating from the 14th Batch of BARC Training School, he joined in IGCAR in 1971. Since, then, he has been engaged in the field of Fast Reactor Engineering. At present, he is Distinguished Scientist and the Director of the Centre. He has made contributions towards design of FBTR sodium systems and components. He is the principal design engineer of PFBR. He has made outstanding contributions towards the material selection, manufacturing technology, R&D design and construction of 500 MWe Prototype Fast Breeder Reactor. He has enhanced the capabilities of the Indian industries to manufacture nuclear components with stringent tolerances. His contributions include the design and manufacturing of high temperature reduction retorts for zirconium and titanium sponge, design and technical specifications for the manufacture of the large size cryostat for ITER and materials development for advanced ultra supercritical plants. He is a member of many professional institutions and fellow of Indian National Academy of Engineering. He is a recipient of Indian Nuclear Society INS Award 2003 for contributions towards nuclear related high technology, National Design Award-2007 by Institution of Engineers, 2003 VASVIK Award, Agni Award for Excellence in self-reliance by DRDO for titanium sponge production, Certification of Appreciation by IAEA towards fast reactor technology and life time achievement award by System Society of India. His interests include pressure vessel and materials technology. He is on the Board of BHAVINI. He is also Director, General Services Organisation, managing the two townships with associated facilities of schools, hospitals, entertainment, sports and unique facility of zero solid waste in ensuring quality living.

Members

Shri Sekhar Basu, an engineering graduate from VJTI, Mumbai joined BARC Training School in 1974. Later he joined Reactor Engineering Division of BARC and completed the development of fuel for Boiling Water Reactors. He was shifted to Kalpakkam in 1988 and was responsible for commissioning of Land Based Nuclear Submarine Propulsion Plant. Subsequently, he was assigned the responsibility of Nuclear Recycle Programme and constructed reprocessing and waste management plants at Tarapur and Kalpakkam. Recently, he has also been involved in Fusion Reactor Programme, ITER, France. After taking over as Director, Bhabha Atomic Research Centre in 2012, Shri Basu is associated with research in basic and engineering sciences covering physics, chemistry, bio-medical, materials, etc. The work also involves development and application of technology for energy, health, food and agriculture sectors. Shri Basu has received awards from Indian Nuclear Society and Department of Atomic Energy for his significant contributions to Atomic Energy Programme. He is a fellow of Indian National Academy of Engineers and has a number of publications to his credit. Apart from pursuing programmes of BARC in various strategic areas, he is working towards major expansion programmes in activities of BARC in food and health sector.

Dr. P. Chellapandi is an Outstanding Scientist and Director, Reactor Design Group, IGCAR, Kalpakkam. He is from 22nd batch of BARC training school with first rank and joined IGCAR in 1979. He is responsible for the design and development of fast reactor power plant systems and components including core and shutdown and energy conversion systems. He is one of the key persons, who have been involved in the design and development activities of 500 MWe PFBR. His current activities focus on the development of innovative design features for the future fast breeder reactors beyond PFBR, planned by the Department. He has established two dedicated and unique laboratories at IGCAR: one for structural mechanics studies and another for safety engineering studies for the design validations. He has formulated many national collaborations with various reputed institutes and played a key role for establishing MoUs, particularly with IIT Madras, IIT Kanpur, IIT Kharagpur and IISc Bangaluru. He is the member of many important national and international committees including Project Design Safety Committee for PFBR (PDSC- PFBR), Apex Committee on Nuclear Power and Associated Fuel Cycle (AC-NP&AFC), Advisory Committee for Project Safety Review of Light Water Reactors ACPSR-LWR-2), Nuclear Fuel Complex Board of Management, Convener, Task Force for Conceptual Design of Future FBRs, Advisory Committee for Nuclear Reactors & Fuel Cycle Committee (NRFCC) of Board of Research in Nuclear Sciences (BRNS) and Safety Research Scientific Committee, DAE, International Atomic Energy Agency (IAEA) Technical Working Group on Fast Reactors (TWG-FR), during the period 2006-2011, the Chairman for the IAEA Technical Co-Operation Expert Mission for Codes and Standards for Sodium Cooled Fast Reactors. (NSR-1), coordinator from India in executing the implementing agreement under CEA-IGCAR Liquid Metal Fast Reactor Safety projects and an expert consultant for the conceptual design of an in-core sodium loop for high temperature multi sample, high dpa material experiments high flux reactor (JHR), CEA Cadrache. He has an outstanding academic record in Mechanical Engineering and a Gold Medal with perfect grade point average of 10 in his Master's Degree in the field of applied mechanics, from IIT Madras. He has guided more than ~120 M.Tech projects and more than ~300 B.E. Projects, all relevant to fast reactor design. He has a very impressive record of publications ~665 to his credit out of which 115 are in journals. He is a Fellow of Indian National Academy of Engineering. He has received the Homi Bhabha Science and Technology Award for the year 1997, Indian Nuclear Society Award and National Design Award in Mechanical Engineering in 2006, Agni Award for Excellence in Self-reliance – DRDO-2007, DAE Group Achievement Awards in 2006, 2007, 2008, 2009, 2010 and 2011 for design, manufacture and erection of PFBR reactor assembly components. He has been bestowed upon Distinguished Alumnus Award of the IIT Madras in 2010.

Dr. A. K. Ghosh, joined the Bhabha Atomic Research Centre in 1971 after graduating in Mechanical Engineering from Indian Institute of Technology, Kharagpur, India. He obtained his Ph.D from Indian Institute of Technology, Bombay. Currently, he is the Director, Health, Safety and Environment Group of BARC. Dr. Ghosh has been carrying out R&D work in the field of reactor safety and his area of work includes both thermal-hydraulic safety and structural safety. He has carried out some pioneering work on the hazards due to earthquakes and tsunamis. Presently, he is also associated with various programmes on radiation safety. He has published more than 100 papers in international journals and conferences. He is chairman/ member of various safety committees of BARC and Atomic Energy Regulatory Board (AERB) for Siting and Design Safety Review and has made significant contribution in the preparation of various safety codes and guides on these subjects.

Dr. P. D. Gupta, Distinguished Scientist is Director, Raja Ramanna Centre for Advanced Technology, Indore. Dr. Gupta is an internationally known laser-plasma physicist who has made pioneering research contributions to this area. He passed M.Sc. Hons (Physics) from Punjab University in 1972 and joined Bhabha Atomic Research Centre. He is a recipient of four gold medals for securing first rank in various university examinations. He joined BARC in August 1973 after passing out from 16th batch (1972-73) of Training School and was awarded Homi Bhabha Medal and Prize. He received his Ph.D. from Bombay University in 1984 and did his Post-doctoral work at the Department of Electrical Engineering, University of Alberta, Canada during 1984-86. He is recipient of Young Scientist Award of Indian National Science Academy (1984) and Young Associateship of Indian Academy of Sciences (1986-91) and became Fellow of the National Academy of Sciences, India, in 2004. As Director, Dr. Gupta is steering many R&D programmes in frontline areas of accelerators and lasers at RRCAT. These include synchrotron radiation sources and their utilization, development of superconducting radio-frequency cavities for high energy accelerators, proton linac spallation neutron source, cryogenics and magnet technology, ultra-intense laser-plasma

interaction, and lasers in research and industry. Dr. Gupta is a Senior Professor of Homi Bhabha National Institute (HBNI), Mumbai, and a member of the Academic Council. He has guided many young researchers for the award of Ph.D / M.Tech / M.Sc degrees. He has made ~ 350 research contributions of which 175 are published in international journals.

Dr. T. Jayakumar, B.Tech. (Metallurgy, REC Warangal), M.S (Metallurgy, IIT Madras), Ph.D (Engineering, University of Saarland, Germany) is currently an Outstanding Scientist and the Director, Metallurgy and Materials Group at IGCAR. Since 1978, he has been engaged in the field of Non-Destructive Evaluation. Over the years he has carried out and steered innovative research and development programmes in the areas of Non-Destructive Evolution, Failure Analysis and structural integrity of nuclear components specifically for the Fast Breeder Reactor. For the last few years he is actively coordinating and guiding research activities related to development of materials and manufacturing technologies for sodium cooled fast reactors, associated fuel cycle and Indian fusion programme. He is a Fellow of the Indian National Academy of Engineering. He has been a recipient of several awards such as National NDT Award from ISNT, Metallurgist of the Year award from IIM, Homi Bhabha Science and Technology Award from DAE, Outstanding Services Award from INS. He has co-authored three books, co-edited four books and has published over 270 papers in international journals. He also has six patents to his credit.

Shri P. V. Kumar joined the Training School of BARC in 1971 after graduation in Mechanical Engineering. He was involved in design, construction and commissioning of the Radiometallurgy Laboratory at IGCAR, Kalpakkam. He was a member of the KAMINI Reactor Commissioning Authority. He is presently Project Director of the Fast Reactor Fuel Cycle Facility that is planned to be established at Kalpakkam to close the fuel cycle of PFBR. He is a fellow of The Institution of Engineers (I) and Indian Institute of Welding.

Shri R. Natarajan, a Chemical Engineer is from the 19th batch of BARC training school and joined the Department of Atomic Energy in 1975. He is presently the Director of Reprocessing Group in IGCAR. Under his leadership, the CORAL facility, for establishing the process technology for the reprocessing of fast reactor fuels was designed, erected and commissioned. He led the team which has successfully completed the reprocessing of fast reactor spent fuel, with a burn-up of as high as 155 GWd/t of a plutonium rich fuel, which is an international benchmark. He is also responsible for the R&D activities of fast reactor fuel reprocessing and setting up of demonstration as well as the commercial PFBR fuel reprocessing plants. His specialization is in the design, development of process flow sheets and plant design. He has also experience in the design and operation of equipment for thorium-uranium cycles. He has participated in the irradiated thorium fuel reprocessing campaigns at the Reprocessing Development Laboratory and the uranium recovered is used as fuel for the reactor KAMINI. He has interest in solvent extraction process modeling, extraction equipment design, design of feed clarification systems of high active solutions, acid recovery systems, system designs of radioactive off-gas circuits and ventilation design of radioactive plants. He has over hundred technical presentations and publications to his credit. He has won the prestigious NOCIL Award for Excellence in Design and Development of Process Plant and Equipment for the year 2005 for his contribution in the development of fast reactor fuel reprocessing. He is also the recipient of Indian Nuclear Society's INS award for the year 2006 for his contributions to Nuclear Fuel Cycle technologies. He is a Fellow of the Indian National Academy of Engineering and Indian Institute of Chemical Engineers.

Dr. G. J. Prasad, Director, Nuclear Fuels Group, BARC graduated from BARC Training School in the 14th Batch (Metallurgy) after graduating in Metallurgical Engineering from NIT Rourkela and received Ph.D. (Technology) from University of Mumbai. His main area of work is in the development and fabrication of research and test reactor fuels and alloy fuels. He was responsible for the development and fabrication of U^{233} plate fuels for the KAMINI Reactor and currently LEU plate fuel for the modified core of APSARA reactor. His area of interest also includes fuels for thermal and fast reactors for generation of nuclear power. He is a designated Senior Professor of HBNI in Engineering Science. He has received the Prime Minister's Award in 1998, MRSI Medal in 2001 and DAE Special Contribution Award in 2006.

Dr. Prabhat Kumar, Distinguished Scientist and Chairman and Managing Director, BHAVINI is responsible for construction and commissioning of India's first Prototype Fast Breeder Reactor which has been designed indigenously and launched as a precursor to commercial exploitation on a large scale. This advanced technology reactor requires understanding of various disciplines of science, multidisciplinary capability of engineering and management skills to achieve the success. In his career, he has worked on nuclear system and component design, indigenisation of critical nuclear equipment, participated in erection of the equipment and their commissioning. He has headed Quality Assurance Group of Kudankulam project during its formative years, later he worked for coolant channel life management, remote tooling for reactor inspection, maintenance and started the R&D centre for NPCIL. He has steered many programmes of vital importance for Indian nuclear power plants and has broad vision of the issues involved. With a large exposure on Pressurized Heavy Water Reactor and Pressurized Water Reactor technologies, he has been chosen to construct India's prestigious Prototype Fast Breeder Reactor, PFBR. He has lead a multi disciplinary team from NPCIL and IGCAR directed towards ensuring a robust construction of PFBR.

Shri K. K. Rajan is from 24th batch of BARC Training School and joined IGCAR, Kalpakkam in 1981. He is a graduate in Electrical Engineering from NIT, Calicut. His initial contributions were purification, transportation and charging of sodium required for FBTR, Calibration of FBTR sodium flowmeters and other sodium experiments in support of FBTR. He has been steering a multidisciplinary program in the area of Sodium Technology. He has made substantial contributions towards testing of PBFR model steam generator in SGTF and PFBR fuel handling machines at reactor operating conditions in LCTR. He was also involved in the development of permanent magnet flowmeters and special type of heaters required for FBR sodium systems. He has played a key role in the receipt and safe transfer of 1750 tonnes of nuclear grade liquid sodium to PFBR storage tanks. He is also responsible for design, construction, commissioning, safe operation and maintenance of high temperature experimental sodium facilities and conducting sodium experiments in support of FBRs. He is a member of Indian Nuclear Society and a fellow of Institution of Engineers (India). He has more than 120 publications in both national and international journals to his credit. He is presently Outstanding Scientist and Director of the Fast Reactor Technology Group.

Shri Rajnish Prakash, Chairman and Chief Executive, Heavy Water Board, has graduated in Chemical Engineering from University of Roorkee (presently I.I.T. Roorkee) in 1974. He has done post graduate course DIIT in Chemical Reaction Engineering from I.I.T. Delhi. Shri Prakash has worked in most of the Heavy Water Plants in various capacities. Shri Prakash played an important role in setting up and commissioning of India's first ammonia based Heavy Water Plant at Baroda and later in new generation plants. He also worked in the area of process development of ammonia-water exchange process which included pilot plant studies and development of efficient column internals. He is credited with indigenous development of catalyst for ammonia based Heavy Water Plants. Shri Prakash has been instrumental in process development for production of various stable isotopes like Oxygen 18 and is instrumental in promoting the non nuclear applications of Deuterium in the country through collaboration with academics and industry. Shri Prakash was also involved in design and implementation of various modifications and ENCON schemes at the plants which resulted in substantial saving of energy and reduction in cost of production. Shri Prakash was elevated to the post of Associate Director (Operation) at Heavy Water Board (Corporate Office) in April 2005. Later he was elevated to the post of Director (Technical) in January 2008. He was also working as Technical Advisor to Chief Executive, HWB, looking after Corporate / Strategic Planning, diversification & growth strategies, export of heavy water and alternate applications of heavy water. Shri Prakash coordinated the first export of Heavy Water to South Korea; a proud moment for DAE and the country. Later his efforts led to further export of heavy water to South Korea, China and USA. Besides being a technocrat par excellence, he has been a good sportsman and has represented his college in many events. Even today, he is a good swimmer and good player of badminton/Table Tennis/Chess, etc. Shri Prakash is a recipient of many awards including Group Achievement Award of DAE for the year 2010 for his excellent contribution in "Indigenous Development of 2nd Stage Cylinder Body of High Pressure Synthesis Gas Compressor at HWP (Baroda)".

Shri N. Saibaba is a Gold medalist from Andhra University. He joined the 19th batch of Training School, Mumbai and is the recipient of Bhabha Award for topping the batch. He developed expertise in the manufacture of seamless tubes in a variety of strategic and exotic materials employing hot and cold deformation processes for meeting critical requirements of Atomic Energy, Space and Defence. He has made several pioneering contributions in the manufacture of critical core components of Power Reactors, some of which were developed for the first time in the country. He was responsible for the development of seamless calandria tubes for Pressurized Heavy Water Reactors and specially shaped pressure tubes for Advanced Heavy Water Reactors, development of hexagonal channels for Prototype Fast Breeder Reactors and square channels for Boiling Water Reactors through pilger route, development of pressure tubes by heat treated and strengthened route and establishment of process technology for manufacture of double clad tubes with zirconium lining. He is presently engaged as Director on the Boards of UCIL & IREL and IGCAR Council. Presently, he is the Chairman of Indian Institute of Metals (IIM), Hyderabad Chapter and Chairman for Indian Society for Non-Destructive Testing (ISNT), Hyderabad Chapter He is appointed as Chairman for Center of Plant Engineering Services (CoPES). He received DAE Award for Group contribution as Group Leader - 2006, 2009, 2010 & 2011,INS Award for contributions in the field of Nuclear Fuel Cycle Technologies – 2008, Annual NFC Award for Meritorious contribution – 2005, 2006 & 2007, Outstanding contribution from NFC Management – 1993 & 1998 and Gold Medal from Andhra University for securing First Rank – 1975. He is a Fellow of Andhra Pradesh Akademi of Sciences, Life Member of IIM, ISNT and INS.

Shri S. A. V. Satya Murty did his B.Tech. from Jawaharlal Nehru Technological University in 1977. He was a University Gold Medalist in his B.Tech. Later, he joined one year orientation course in Nuclear Science & Engineering (21st Batch) at BARC. He was awarded Homi Bhabha prize for getting 1st rank. In the initial years, he was working in the Central Data Processing System Section of FBTR. In 1981, he joined Computer Division and played a key role in the establishment of Mainframe Computer System for IGCAR. He is instrumental in establishing internet and E-Mail facilities, Network Security Systems, IGCAR Campus network etc. He also played an important role in the installation and development of High Performance Computing Facility, Intra DAE VSAT Network (Anunet), Grid Computing facility, PFBR Simulator, Advanced Visualization Centre, Wireless Sensor Networks lab etc., He has more than 110 Journal Publications / Conference Papers and edited two International Conference Proceedings. Currently he is the Director of EIRSG and is responsible for the development of robust I&C systems for PFBR.

Shri G. Srinivasan is a Mechanical Engineer from the 18th batch of BARC Training School. He joined FBTR project as a designer in 1975, and participated in the design, fabrication and installation of Reactor Assembly Components. He moved over to O&M in 1983. After holding the positions of Senior Engineer (Planning) & Senior Engineer (Technical), he took over as Technical Services Superintendent and later as AD (O&M). He is Director, ROMG since September 2008.

Shri Gyan Prakash Srivastava is currently the Director, Electronics and Instrumentation Group of BARC. Born on 25th February 1949, he obtained the degree of M.Sc. (Tech) in Electronics and Radio Engineering in 1969 and joined BARC in 13th batch of Training School. He has worked in the areas of Control Engineering and Advanced Instrumentation for Nuclear Reactors, Antenna controls, Non Destructive Testing and Nuclear Security. He has been the Chairman and Managing Director of Electronics Corporation of India Ltd. Hyderabad during 2003-06. He is a fellow of Indian National Academy of Engineers and Indian Electronics and Telecommunication Engineers. Currently, he is also the Chairman of BARC Safety Council, Project Director, Global Centre for Nuclear Energy Partnership, Haryana: and Chairman, Project Implementation Committee, BARC-Vizag. He is a member of Advisory Committee on Nuclear Security at IAEA and Chairman, Advisory Committee on Nuclear Security, AERB. He is a recipient of Vasvik award, INS award and Special Contribution Award of DAE.

Dr. C. S. Sundar, obtained his Masters degree in Physics from the University of Delhi in 1973, and Ph.D in Physics from the University of Madras in 1983. He heads the Materials Science Group at IGCAR with a comprehensive research programme on basic research in materials science. He is also a Senior Professor at the Homi Bhabha National Institute. Dr. Sundar's research contributions, spanning over three decades, has been on the investigation of structure, defects and phase transitions in novel materials that include high temperature superconductors, fullerenes, strongly correlated systems and colossal magnetoresistive manganites using the techniques of positron annihilation and infrared spectroscopy. He has over 100 journal publications. He is a recipient of the Materials Research Society of India Medal, 1994, the Young Research award, IUMRS, ICA the MRSI-ICSC superconductivity and Materials Research Annual Prize 2007 and the Tamil Nadu Scientist (TANSA) award, 2008. He is a Fellow of the Indian Academy of Sciences, Bengaluru, National Academy of Sciences, Allahabad and has recently been elected as a Fellow of the Indian National Science Academy, New Delhi. Dr. Sundar is a member of the Nano Science Advisory Group of Department of Science and Technology, Research Council of the National Physical laboratory, New Dehi, and UGC-DAE CSR, Indore. He is on the Editorial Board of Solid State Communications and is an Associate Editor, Bulletin of Materials Science.

Dr. P. R. Vasudeva Rao, is a Distinguished Scientist and presently Director of Chemistry Group in IGCAR. He obtained his Doctorate degree in Inorganic Chemistry from Bombay University in 1979. He has played an active role in shaping the Radiochemistry Programme of IGCAR to its current status. His research interests cover a wide range of areas such as development of alternate extractants and resins for actinide recovery, solvent extraction, third phase formation, thermodynamics, applications of ionic liquids and supercritical fluid extraction in actinide separations, development of pyrochemical and other non-aqueous processes for recovery of actinides and rare earths, thermochemical studies on nuclear materials, fuel behaviour in reactors and high performance liquid chromatography. He has published more than 200 papers in reputed international journals apart from guiding several research scholars for their doctorate degrees. He is also a Fellow of Tamil Nadu Academy of Sciences. He was awarded the MRSI Medal in 1998 and the INS award for the year 2007. He was also selected for the Chemical Research Society of India Silver medal - 2011 and MRSI-ICSC Superconductivity and Materials Science Senior Award - 2011

Shri K. K. Vaze obtained his B.Tech. degree in Mechanical Engineering from IIT, Bombay in 1973 and thereafter joined 17th batch of BARC Training School. After graduation from BARC Training School in 1974, he joined the Nuclear Systems Division of Indira Gandhi Centre for Atomic Research, Kalpakkam where he worked in the area of structural analysis and design of fast reactor components. In 1989, he joined the Reactor Safety Division of Bhabha Atomic Research Centre, Mumbai. His current fields of work include design & detailed engineering of Advanced Heavy Water Reactor, reactor safety, earthquake engineering, fatigue and fracture analysis, experimental stress analysis, fitness-for-purpose evaluation, residual life estimation and life extension. At present he holds the post of Director, Reactor Design & Development Group in Bhabha Atomic Research Centre. He is a fellow of Indian National Academy of Engineering and recipient of Indian Nuclear Society Award: Nuclear Reactor Technology, including Reactor Safety in 2007 for his contributions in the area of structural analysis and design related to reactor safety. He has also received DAE Special Contributions Award in the year 2007 and Group Achievement Award 2010.

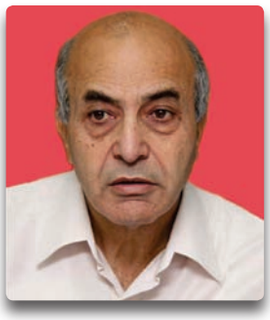

Shri P. K. Wattal is a Graduate in Chemical Engineering and joined Bhabha Atomic Research Centre (BARC), Trombay after completing 18th Batch of Orientation Programme of BARC Training School. Since then, he has been involved with the R&D activities in the area of back-end of nuclear fuel cycle. Presently, as Director, Nuclear Recycle Group, BARC, he is heading the Reprocessing & Waste Management Programmes at the back-end of Nuclear Fuel Cycle at Trombay and holding the responsibility of setting up and operation of Reprocessing and Waste Management Plants. Shri Wattal has participated in a number of international technical meetings on preparation of documents pertaining to waste management. Presently he is leading Indo-French Bilateral Programme on waste management. He is also Chairman of Working Group for Test Blanket Programme on Radwaste, International Thermonuclear Experimental Reactor (ITER), Cadarache, France and a Member of Technical Working Group on Nuclear Fuel Cycle Options and Spent Fuel Management (TWGNFCO) of International Atomic Energy Agency (IAEA), Vienna.

Organisation and Activities of Various Groups

Chairman

Shri S. C. Chetal
Director, IGCAR

Chemistry Group

Dr. P. R. Vasudeva Rao
Director, CG

Dr. K. Nagarajan
AD, FChG & Head, FChD

Dr. K. V. Govindan Kutty
Head, MCD

Shri G. Ravishankar
Head, CFD

The Chemistry Group is responsible for carrying out R&D to provide inputs with respect to all the chemistry aspects of the fast reactor and its fuel cycle. Besides the R&D activities, the Chemistry Group also provides extensive analytical support using a wide range of analytical techniques to all the programmes at Kalpakkam. The areas of R&D in Chemistry Group include sodium chemistry, chemistry of un-irradiated as well as irradiated fuel materials, development of fuel cycle, high temperature chemistry, analytical chemistry, spectroscopy and boron chemistry. Chemistry Group also has been developing instrumentation and facilities in support of the R&D programme. Development of sensors for PFBR and sensors for environmental applications, development of radionuclide traps for PFBR, development of cleaning and decontamination techniques for fast reactor components, development of technology for production of plutonium rich fuels and minor actinide containing fuels through sol-gel route, development of sodium bonding for metallic fuels and pyroprocessing are some of the R&D programmes on the anvil. Recent achievements include the fabrication of test fuel pins containing microspheres of $(U,Pu)O_2$ for irradiation in FBTR, demonstration of uranium recovery from U-Zr slugs by electrorefining, determination of burn-up of MOX(PFBR) test fuel by HPLC and development of unsymmetrical diglyoclamides as candidate extractants for minor actinide partitioning.

Electronics, Instrumentation and Radiological Safety Group

Shri S. A. V. Satya Murty
Director, EIRSG

Shri N. Murali
AD, ICG & Head, RTSD

Shri B. Venkatraman
AD, RSEG & Head, RSD

Shri B. Ananthapadmanaban
Head, QAD

Shri K. K. Kuriakose
Head, CD

Dr. K. K. Satpathy
Head, E&SD

Shri D. Thirugnanamurthy
Head, EID

The Electronics, Instrumentation and Radiological Safety Group is actively involved in the development of Instrumentation & Control for the 500 MWe Prototype Fast Breeder Reactor. Towards this the I&C systems are designed with safety and availability of the reactor as the guiding requirements through redundant systems and also keeping in mind the simplicity of design and maintainability. A judicious combination of hardwired and computer based I&C systems, state-of-the-art design, manufacturing processes and testing were employed in the design of I&C systems. The systems developed include safety critical, safety related and non safety I&C systems. The Prototype systems were qualified after rigorous environmental, EMI/EMC and seismic testing. The application software developed was subjected to thorough Verification & Validation procedures. The Group is also developing a full scope replica type Operator Training Simulator for PFBR. An advanced visualization centre was established and various PFBR systems are modeled for visualization in 3D and walkthrough. R&D activities in the areas of innovative instrumentation using pulsating sensors, Wireless Sensor Networks for use in future reactors, computational intelligence, knowledge management etc. are in progress. State-of-the-art computational facilities with a total processing power of about 30 tera FLOPS and data communication facilities are being provided. To take care of the security challenges the security electronics systems are constantly deployed and upgraded.

The Group is also responsible for providing quality assurance/quality control services for all the major projects being undertaken by IGCAR through the ISO 9001-2008 certified Quality Assurance Division. The Radiological Safety Division of the Group is responsible for R&D activities in the areas of radioactivity transport and improving the radiation detection and measurements through advanced techniques. This Division provides health physics and radiation safety services for the radioactive facilities in IGCAR. Environmental and Industrial Safety Division provides industrial safety services to all the facilities at IGCAR. This Division also carries out R&D in the domain of aquatic and terrestrial biodiversity and sediment characterization. The Group organizes public awareness programs on radiation safety and nuclear energy in addition to training and awareness programs on industrial, radiation and fire safety to occupational workers.

Engineering Services Group (Civil)

Shri P. V. Kumar
Director, ESG(C)

Shri C. Sivathanu Pillai
AD, CEG

Engineering Services Group (Civil) is responsible for providing quality services pertaining to civil engineering activities. The group has a mandate to establish additional infrastructure requirements so as to meet design, R&D and operational objectives of IGCAR. The group has expert teams with capability to design, engineer and execute systems under their jurisdiction.The nature of work involves interaction with several State Government and Central Government Organisations.

Engineering Services Group (Mechanical & Electrical)

Shri R. Natarajan
Director, ESG(M&E)

Shri A. Jyothish Kumar
AD, ESG &Head, ESD

Shri C. Chandran
Head, AC & VSD

Shri G. Kempulraj
Head, CWD

The Engineering Services Group is responsible for providing quality services and activities pertaining to Electrical Engineering, Voice Communication Systems, Air-conditioning and Ventilation Systems, Material Handling Equipments and Central Workshop activities. The group also coordinates the telecommunication requirements of the Centre. The group has a mandate to establish additional infrastructure requirements so as to meet Design, R&D and operational objectives of IGCAR. The group has expert teams with capability to design, engineer and execute systems under their jurisdiction. Electricity, quality-air and other services including services from Central Workshop are being extended to other units of DAE located at Kalpakkam. The nature of work involves interaction with several State Government and Central Government Organisations. AC&VSD is responsible for providing reliable air-conditioning and ventilation services to various radioactive laboratories and R&D facilities of the Centre, operation and maintenance of Central Water Chilling Plant to supply un-interrupted chilled water to various active and research facilities, design, procurement, installation, testing and commissioning of air-conditioning projects for new facilities at IGCAR and design and execution of active ventilation systems procurement, erection, testing and installation of Material Handling Equipments.

Fast Reactor Technology Group

Shri K. K. Rajan
Director, FRTG

Shri B. Babu
Head, IDSD

Shri B. K. Nashine
Head, DDRSD

Shri G. Padmakumar
Head, SEHD & CTD

Shri V. Prakash
Head, VDD

The Fast Reactor Technology Group (FRTG) has the mandate of development and testing of FBR components and is actively involved in testing of PFBR components in air, water and sodium. Design validation of critical components of FBR is achieved through experiments in sodium and water using full scale/scaled down models. FRTG has expertise in the development of sensors such as EM flow meters, level probes and other devices such as electromagnetic pumps for sodium application. Process development for enrichment of boron, based on ion exchange chromatography has been successfully demonstrated by the group and 91% enriched boron required for FBTR was produced for the first time. Engineering development towards scaling up of pyro processing techniques from laboratory to engineering scale also is the responsibility of group. The group has developed expertise in sodium handling and in the design, construction, commissioning and operation of high temperature sodium systems. The major sodium test facilities of FRTG include 5.5 MWt Steam Generator Test Facility (SGTF) for testing the model SG of PFBR, SADHANA loop for experimentally demonstrating natural convection based safety grade decay heat removal system of PFBR, Large Component Test Rig (LCTR) for testing critical full scale PFBR components, In Sodium Test facility (INSOT) for creep and fatigue testing and Sodium Water Reaction Test (SOWART) facility to study self wastage and impingement wastage of SG tubes. Recent achievements of FRTG towards PFBR include sodium testing of PR & PTM of Inclined Fuel Transfer Machine (IFTM), development and sodium calibration of PFBR mutual inductance type level probes and qualification of PFBR shut down mechanism in air and sodium. Testing of Eddy Current Position Sensor (ECPS) for DSRDM, development and qualification of high temperature ultrasonic transducers for Under Sodium Ultrasonic Scanner (USUSS) of PFBR, manufacture and sodium calibration of eddy current flow sensors for primary sodium pumps of PFBR were also completed successfully.

Materials Science Group

Dr. C. S. Sundar
Director, MSG

Dr. G. Amarendra
Head, MPD

Shri M. P. Janawadkar
Head, CMPD

Dr. A. K. Tyagi
Head, SND

The Materials Science Group, comprising of three Divisions, has the mandate of pursuing high quality basic research on topical problems in Materials Science, to work towards ion beam and computer simulation of radiation damage and to pursue research on innovative sensors accruing from basic research in superconductivity and nanomaterials. The Condensed Matter Physics Division focuses on the

investigation of physical properties of novel materials under temperature, pressure and magnetic fields. Active research programs on Raman spectroscopy studies of vibrational properties, Dynamic light scattering and Confocal Microscopy studies of soft condensed matter, Laser heated diamond anvil cell facility for synthesis and study of materials under high pressure and high temperature and investigation of material properties at low temperatures under high magnetic fields and pressures are being pursued. The indigenously built SQUID sensors and control electronics have been translated into SQUID based measuring systems such as a high field magnetometer, a SQUID based set-up for Non-Destructive Evaluation (NDE), and SQUID based Magnetoencephalography (MEG). The activities of Materials Physics Division pertain to studies on Ion beam simulation of radiation damage using a 1.7 MV tandem accelerator; in depth studies on defects using Positron Annihilation Spectroscopy and Computer simulation of material properties. The Surface and Nanoscience Division focuses on studies on thin films using a variety of techniques such as Secondary Ion Mass Spectrometry and Scanning Probe Microscopy. Studies on controlled growth of nanometric multi-layer films for increased hardness and exploration of nanomaterials micromachined cantilevers and MEMS as sensors are being actively pursued.

Metallurgy and Materials Group

Dr. T. Jayakumar
Director, MMG

Dr. A. K. Bhaduri
AD, MDTG

Dr. U. Kamachi Mudali
AD, CSTG

Dr. S. Venugopal
AD, GRIP & Head, RIRD

Dr. M. Vijayalakshmi
AD, PMG

Shri Jojo Joseph
Head, PIED

Dr. M. D. Mathew
Head, MMD

Shri E. Mohandas
Head, MSCD

Dr. B. Purna Chandra Rao
Head, NDED

Dr. Saroja Saibaba
Head, MTPD

Dr. Shaju K. Albert
Head, MTD

The Metallurgy and Materials Group has been primarily engaged in a broad spectrum of activities that span Research, Development and Deployment (RD&D) of solutions to a variety of materials related issues of fast reactors and associated fuel cycle facilities. The activities concern the design and accelerated field realization of new materials and process modifications to meet the high reliability of materials performance required in advanced reactor and reprocessing concepts. Accordingly, over the years, the MMG has specialized in spearheading novel and directed cross-disciplinary basic research under various themes: design of newer variants of candidate, structural materials, novel functionally effective neutron shielding materials, indigenization of materials development for advanced ultrasupercritical technology to name a few. MMG houses a very elaborate in-house and state of the art materials characterization and testing facilities, including those required for post-irradiation examination of nuclear materials. The human resource expertise of MMG has ever since its inception been an exquisite blend of experienced and energetic talents, which specialize in almost all branches of theoretical and experimental aspects of materials science and technology.

Reactor Operations and Maintenance Group

Shri G. Srinivasan
Director, ROMG

Dr. V. Ganesan
PM, DFMF

Shri K. V. Suresh Kumar
Head, ROD

Shri B. Ananthapadmanaban
Head, RMD

Shri N. Kasinathan
Head, RAD

Dr. R. S. Keshavamurthy
Head, RPD

Shri P. R. Swaminathan
Head, PPD

Ms. S. Usha
Head, TSD

Reaction Operation Maintenance Group is responsible for safe operation of Fast Breeder Test Reactor (FBTR) and KAMINI reactor within the limits given in technical specification documents. The group also takes part in the operational safety review of PFBR Project documents. The Training section of the group is responsible for training the O&M staff of PFBR and future FBRs besides training O&M staff of FBTR and KAMINI. Progressive modifications in FBTR to increase its availability and for gaining newer experience in operation, utilizing the reactor for irradiation of advanced fuels and materials for fast reactors and conducting safety related experiments form a major part of ROMG's activities.

Reprocessing Group

Shri R. Natarajan
Director, RpG

Shri A. Ravishankar
AD, RPOG

Shri V. Sundararaman
AD, PDCG & Head, FRPD

Shri B. M. Anandarao
Head, RPDD

Dr. U. Kamachi Mudali
Head, RRDD

Shri V. Vijayakumar
Head, RPOD

The success of Indian Fast Breeder Reactor (FBR) programme depends on closing the fuel cycle within a short period so that the inventory of fissile material outside the reactor can be as small as possible. The Reprocessing Group (RpG) of IGCAR is responsible for achieving this objective. Various activities with regard to the fast reactor fuel reprocessing technology such as the design, construction and operation of the reprocessing plants are being undertaken by this group. There are facilities to carry on extensive engineering scale testing of equipment and systems before installation in radioactive hot cells. Chopper, dissolver, feed clarification equipment, centrifugal extractors and different types of pulse columns are a few important equipment that are

being developed for deployment in fast reactor fuel reprocessing plants. Apart from equipment development, research is towards understanding and solving various process, chemistry and analytical problems of fast reactor fuel reprocessing such as, process flow sheet studies to improve the plant performance for higher recoveries and reduced waste generation, mathematical modeling of solvent extraction of the complex U-Pu system, solvent management, development of alternate solvent-diluent systems, development of online monitoring of Pu for process control, liquid flow metering in high radioactive fields, development of material handling equipment inside the hot cells etc. In one of the hot cell facilities, uranium was recovered from irradiated thorium rods using THOREX process which is used as fuel in KAMINI reactor and in FBTR (as PFBR test fuel). The other hot cell facility, called CORAL (Compact facility for Reprocessing Advanced fuels in Lead cells) commissioned in 2003, is being deployed as a versatile test bed for validating the process flow sheet and scaling up of equipment designs for fast reactor fuel reprocessing, by processing the FBTR spent fuel. This experimental facility has been used for reprocessing several batches of mixed carbide fuels irradiated in FBTR with 25, 50, 100 and 155 GWd/t burn-ups. This has provided valuable experience to the design of Demonstration Fast Reactor Fuel Reprocessing Plant in which all the types of FBTR fuels, such as the mixed carbide and oxide of different compositions, will be reprocessed on a regular basis. DFRP is also designed to reprocess PFBR fuel subassemblies also for demonstrating the reprocessing of irradiated PFBR oxide fuels. In addition to these activities, RpG is also carrying out the design of the reprocessing plant, for reprocessing spent fuels of PFBR on commercial basis.

Reactor Design Group

Dr. P. Chellapandi
Director, RDG

Shri K. Madhusoodanan
AD, PPG & Head, I&CD

Shri P. Puthiyavinayagam
AD, CDG

Shri P. Selvaraj
AD, RAG

Shri V. Balasubramaniyan
Head, RCD

Dr. K. Devan
Head, RND

Shri A. John Arul
Head, RSDD

Shri B. K. Nashine
Head, SED

Shri S. Raghupathy
Head, CH & MD

Shri N. Theivarajan
Head, PPCD

Dr. K. Velusamy
Head, MHD

Reactor Design Group is responsible for analysis of FBR power plant systems and design and development of components including core, shutdown and handling mechanisms and balance of plant. The group is responsible for getting safety clearance from Atomic Energy Regulatory Board (AERB). The group comprises of Core Design Group (CDG), Reactor Analysis Group (RAG), Power Plant Group (PPG), Reactor Components Division (RCD) and Component Handling & Mechanism Division (CHMD). The group also executes R&D in the domain of structural mechanics, thermal hydraulics and safety engineering, involving national and international institutions. It provides design support to the construction and commissioning of 500 MWe Prototype Fast Breeder Reactor (PFBR), which is under construction at Kalpakkam. It also provides analytical support to other

groups in the Centre including Fast Breeder Test Reactor (FBTR) as well as for other strategic and high end technologies in the country. The responsibility of group includes developing high quality human resource for the design and analysis of SFRs in the country. It is currently engaged in conceptualizing as well as detailing the innovative reactor components for the reactor assembly of future SFRs. The group has about 145 scientists and engineers, who are relatively younger consisting of three groups and two divisions and two laboratories. These apart, it has a modern design office with many advanced modeling and analysis softwares, Structural Mechanics Laboratory (SML) having state-of-the-art facilities for carrying out tests on large components, high temperature structural integrity and seismic tests with large size shake tables and safety research laboratory (SRL) for carrying out tests in the domain of severe accidents and to study the science & technology of sodium fires and fire extinguishers. This group has high quality expertise in the domain of design of mechanisms operating in sodium, mechanical design and analysis of components as per the American (ASME) and French (RCC-MR) design codes, thermal hydraulics of liquid metal, plant dynamics etc.

Fast Reactor Fuel Cycle Facility

Shri P. V. Kumar
Project Director
FRFCF

Fast Reactor Fuel Cycle Facility is entrusted with the work of planning, designing and constructing the Fast Reactor Fuel Cycle Facility to close the fuel cycle of PFBR. FRFCF is a multi unit project involving BARC, IGCAR and NFC. IGCAR is piloting the work on this project. The Group interacts with the participating groups from different units of DAE . Coordination of activities related to design of the facility, obtaining regulatory and statutory approvals for the project, preparation of the detailed project report, processing for obtaining financial sanction and development of infrastructure at the project site, is the mandate of this group.

Resources Management Group

Dr. M. Sai Baba
Head, SIRD/SPHRDD
& AD, RMG

Resources Management Group (RMG) comprises of the Scientific Information Resource Division, Strategic Planning and Human Resources Development Division and OCES-Training Section. The significant activities of the group include strategic planning and human resource management, conducting the academic programmes of BARC Training school at IGCAR, formulating and monitoring capital projects towards budget planning and management including providing necessary reports and proposals to DAE, automation and integration of activities pertaining to administration, accounts, stores, budget and procurement on a single platform, coordinating the visits of important dignitaries and delegations to the Centre, formulating and facilitating collaborations and MoU, providing technical coordination with various agencies and conducting public awareness programmes for the benefit of public and media, providing information resources through conventional library and the library on the desktop by digital networking with special emphasis to cater to the needs of students and young scholars and publishing important documents of the Centre like IGC Newsletter, Annual Report, Benchmarks, preparation of Annual Reports and plan related documents.

Technical Co-ordination & Quality Control Division

Shri N. Vijayan Varier
Head, TC&QCD

Technical Co-ordination & Quality Control Division is primarily responsible for quality control of several critical equipments for IGCAR in the western region. TC&QCD has also been providing technical co ordination services for various activities of PFBR. TC&QCD also participates in a number of R&D activities which are being carried out at BARC towards meeting the mandate of IGCAR and PFBR. Staff of TC&QCD completed the QA support for manufacture of the balance six reactors for the Titanium sponge plant commissioned at KMML, Kerala. TC&QCD participated in the R&D activities for development of high temperature fission chambers, neutron detectors for PFBR along with various divisions of BARC, under sodium ultrasonic scanner, for PFBR including manufacture of scanner, participation in task force for the reactor worthy scanner and spare scanner, ISI vehicle development at BARC and now at IGCAR and sputter ion pump development at BARC and inspection. TC&QCD participated in the inspection activities for the major components of welded grid plate technology development, inner vessel sector model, tri-junction forging, motors for centrifugal extractors, safety grade decay heat exchanger and air heat exchanger models, integrated cold traps for purification of Na, sodium to air heat exchanger, PFBR-Neutron Detector Assembly and retorts for titanium sponge production.

Madras Regional Purchase Unit

Shri A. S. L. K. Rao
RD, MRPU

Material Management activities for IGCAR and GSO are taken care of by Madras Regional Purchase Unit (MRPU) which comes under Directorate of Purchase & Stores of Department of Atomic Energy. Procurement and payment to suppliers are carried out at Chennai and inventory and accounting are carried out by Central Stores at Kalpakkam. MRPU was the first DAE unit to introduce E-Tendering and more than 25% of files were processed by E-Tendering mode. MRPU processed 4700 indents with an estimated cost of 334 crores during the year 2012.

Administration and Accounts

Shri O. K. Sathian
Chief Administrative Officer

Shri N. K. V. Sharma
Joint Controller (Finance & Accounts)

Shri K. R. Sethuraman
AO(R&SR) & Secretary, IGCSC

LIST OF IMPORTANT ABBREVIATIONS

AC&VSD	Air Conditioning and Ventilation System Division
AERB	Atomic Energy Regulatory Board
BARC	Bhabha Atomic Research Centre
BARCF	Bhabha Atomic Research Centre Facilities
BHAVINI	Bharatiya Nabhikiya Vidyut Nigam Limited
CD	Computer Division
CDG	Core Design Group
CED	Civil Engineering Division
CEG	Civil Engineering Group
CERMON	Continuous Environmental Radiation Monitoring Network
CFD	Chemical Facilities Division
CG	Chemistry Group
CTD	Chemical Technology Division
CH&MD	Components Handling & Mechanism Division
CMPD	Condensed Matter Physics Division
CORAL	Compact facility for Reprocessing Advanced fuels in Lead cell
CSTG	Corrosion Science & Technology Group
CT&VDD	Chemical Technology and Vibration Diagnostics Division
CWD	Central Workshop Division
DDRSD	Device Development and Rig Services Division
EID	Electronics and Instrumentation Division
EIRSG	Electronics and Instrumentation and Radiological Safety Group
E&SD	Environmental & Safety Division
ESD	Electrical Services Division
ESG	Engineering Services Group
FBR	Fast Breeder Reactor
FBTR	Fast Breeder Test Reactor
FChD	Fuel Chemistry Division
FChG	Fuel Chemistry Group
FRFCF	Fast Reactor Fuel Cycle Facility
FRPD	Fuel Reprocessing Process Division
FRTG	Fast Reactor Technology Group
GRIP	Group for Remote Handling, Robotics, Irradiation Experiments and PIE
GSO	General Services Organisation
HWB	Heavy Water Board
IAEA	International Atomic Energy Agency
IIT	Indian Institute of Technology
ID&SD	Instrumentation Development & Services Division
IMSc	Institute of Mathematical Sciences
I&CD	Instrumentation & Control Division
ICG	Instrumentation & Control Group
LMFBR	Liquid Metal Cooled Fast Breeder Reactor
LM&SCD	Liquid Metals and Structural Chemistry Division
MAPS	Madras Atomic Power Station
MCD	Materials Chemistry Division
MCG	Materials Chemistry Group
MDTG	Materials Development and Technology Group
MFTR	Metal Fuel Test Reactor
MHD	Mechanics & Hydraulics Division
MMD	Mechanical and Metallurgy Division
MMG	Metallurgy and Materials Group
MPD	Materials Physics Division
MRPU	Madras Regional Purchase Unit
MSG	Materials Science Group
MSSCD	Materials Synthesis & Structural Characterization Division
MTD	Materials Technology Division
MTPD	Microscopy & Thermo-Physical Property Division
NDED	Non-Destructive Evaluation Division
NFC	Nuclear Fuel Complex
NICB	Nuclear Island Connected Building
NPCIL	Nuclear Power Corporation of India Ltd.
PDCG	Process Design & Commissioning Group
PFBR	Prototype Fast Breeder Reactor
PHWR	Pressurized Heavy Water Reactor
PIED	Post Irradiation Examination Division
PMG	Physical Metallurgy Group
PPCD	Power Plant Control Division
PPD	Project Planning Division
PPG	Power Plant Group
PDCG	Process Design & Commissioning Group
QAD	Quality Assurance Division
RAD	Reactor Analysis Division
RAG	Reactor Analysis Group
RCD	Reactor Components Division
REG	Reactor Engineering Group
RIRD	Remote Handling, Irradiation Experiments and Robotics Division
RMD	Reactor Maintenance Division
RMG	Resources Management Group
RND	Reactor Neutronics Division
ROD	Reactor Operation Division
ROMG	Reactor Operation and Maintenance Group
RPDD	Reprocessing Plant Design Division
RpG	Reprocessing Group
RPOD	Reprocessing Plant Operations Division
RPOG	Reprocessing Projects & Operation Group
RRDD	Reprocessing Research and Development Division
RSD	Radiological Safety Division
RSDD	Reactor Shielding and Data Division
RSEG	Radiological Safety & Environmental Group
RTSD	Real Time Systems Division
SED	Safety Engineering Division
SE&HD	Sodium Experiments & Hydraulics Division
SGTF	Steam Generator Test Facility
SIRD	Scientific Information and Resource Division
SND	Surface and Nanoscience Division
SOWART	Sodium Water Reaction Test facility
SP&HRDD	Strategic Planning & Human Resource Development Division
TC&QCD	Technical Coordination & Quality Control Division
TSD	Technical Services Division
VDD	Vibration Diagnostics Division

INDIRA GANDHI CENTRE FOR ATOMIC RESEARCH

Shri S. C. CHETAL
DIRECTOR, IGCAR

- IGC COUNCIL
- IGC SCIENTIFIC COMMITTEE [IGCSC]
- DIRECTOR'S ADVISORY COMMITTEE [DAC]
- **Dr. P. R. VASUDEVA RAO** — DIRECTOR, CHEMISTRY GROUP
- **Dr. C. S. SUNDAR** — DIRECTOR, MATERIALS SCIENCE GROUP
- **Shri S. A.V. SATYA MURTY** — DIRECTOR, ELECTRONICS, INSTRUMENTATION AND RADIOLOGICAL SAFETY GROUP
- **Dr. T. JAYAKUMAR** — DIRECTOR, METALLURGY & MATERIALS GROUP
- **Shri R. NATARAJAN** — DIRECTOR, ENGINEERING SERVICES GROUP (MECHANICAL & ELECTRICAL)
- **Dr. P. CHELLAPANDI** — DIRECTOR, REACTOR DESIGN GROUP
- **Shri P. V. KUMAR** — DIRECTOR, ENGINEERING SERVICES GROUP (CIVIL)
- **Shri G. SRINIVASAN** — DIRECTOR, REACTOR OPERATIONS & MAINTENANCE GROUP
- **Shri K. K. RAJAN** — DIRECTOR, FAST REACTOR TECHNOLOGY GROUP
- **Shri. R. NATARAJAN** — DIRECTOR, REPROCESSING GROUP
- **Shri P. V. KUMAR** — PROJECT DIRECTOR, FAST REACTOR FUEL CYCLE FACILITY
- **Dr. M. SAI BABA** — ASSOCIATE DIRECTOR, RESOURCES MANAGEMENT GROUP
- **Shri N. Vijayan Varier** — TECHNICAL CO-ORDINATION & QUALITY CONTROL DIVISION
- **Shri N. K. V. SHARMA** — JOINT CONTROLLER (FINANCE & ACCOUNTS)
- **Shri O. K. SATHIAN** — CHIEF ADMINISTRATIVE OFFICER

Groups / Divisions / Heads

Chemistry Group

Dr. P. R. VASUDEVA RAO — DIRECTOR

- Dr. K. NAGARAJAN — ASSOCIATE DIRECTOR, FUEL CHEMISTRY GROUP
- Dr. K. NAGARAJAN — FUEL CHEMISTRY DIVISION
- Dr. K. V. GOVINDAN KUTTY — MATERIALS CHEMISTRY DIVISION
- Shri G. RAVISHANKAR — CHEMICAL FACILITIES DIVISION

Electronics, Instrumentation and Radiological Safety Group

Shri S.A.V. SATYA MURTY — DIRECTOR

- Shri N. MURALI — ASSOCIATE DIRECTOR, INSTRUMENTATION & CONTROL GROUP
- Shri N. MURALI — REAL TIME SYSTEMS DIVISION
- Shri D. THIRUGNANAMURTHY — ELECTRONICS & INSTRUMENTATION DIVISION
- Shri K. K. KURIAKOSE — COMPUTER DIVISION
- Dr. B. VENKATARAMAN — ASSOCIATE DIRECTOR, RADIOLOGICAL SAFETY & ENVIRONMENTAL GROUP
- Dr. B. VENKATARAMAN — RADIOLOGICAL SAFETY DIVISION
- Shri B. ANANTHAPADMANABAN — QUALITY ASSURANCE DIVISION
- Dr. K. K. SATPATHY — ENVIRONMENTAL & SAFETY DIVISION

Resources Management Group

Dr. M. SAI BABA — ASSOCIATE DIRECTOR, RESOURCES MANAGEMENT GROUP

- Dr. M. SAI BABA — STRATEGIC PLANNING & HUMAN RESOURCE DEVELOPMENT DIVISION
- Dr. M. SAI BABA — SCIENTIFIC INFORMATION RESOURCE DIVISION

Administration

Shri O. K. SATHIAN — CHIEF ADMINISTRATIVE OFFICER

- Shri K. R. SETHURAMAN — ADMINISTRATIVE OFFICER (R&SR)
- Shri S. S. BHOOPATHY — ADMINISTRATIVE OFFICER (P)

Accounts

Shri N. K. V. SHARMA — JOINT CONTROLLER (F&A)

- Shri T. M. G. KUTTY — DEPUTY CONTROLLER ACCOUNTS
- Shri P. N. MADHAVAN — Sr. ACCOUNTS OFFICER

Groups / Divisions / Heads

Engineering Services Group (Mechanical & Electrical)

- **Shri. R. NATARAJAN** — DIRECTOR
  - Shri A. JYOTHISHKUMAR — ASSOCIATE DIRECTOR, ENGINEERING SERVICES GROUP
    - Shri A. JYOTHISHKUMAR — ELECTRICAL SERVICES DIVISION
    - Shri G. KEMPULRAJ — CENTRAL WORKSHOP DIVISION
    - Shri C. CHANDRAN — AIR-CONDITIONING & VENTILATION SYSTEM DIVISION

Engineering Services Group (Civil)

- **Shri P. V. KUMAR** — DIRECTOR
  - Shri C. SIVATHANU PILLAI — ASSOCIATE DIRECTOR, CIVIL ENGINEERING GROUP

Fast Reactor Technology Group

- **Shri K. K. RAJAN** — DIRECTOR
  - Shri V. PRAKASH — VIBRATION DIAGNOSTICS DIVISION
  - Shri G. PADMAKUMAR — CHEMICAL TECHNOLOGY DIVISION
  - Shri B. K. NASHINE — DEVICE DEVELOPMENT & RIG SERVICES DIVISION
  - Shri G. PADMAKUMAR — SODIUM EXPERIMENTS & HYDRAULICS DIVISION
  - Shri B. BABU — INSTRUMENTATION DEVELOPMENT & SERVICES DIVISION

Metallurgy & Materials Group

- **Dr. T. JAYAKUMAR** — DIRECTOR
  - Dr. S. VENUGOPAL — ASSOCIATE DIRECTOR, GROUP FOR REMOTE HANDLING, ROBOTICS, IRRADIATION EXPERIMENTS AND PIE
    - Shri JOJO JOSEPH — POST IRRADIATION EXAMINATION DIVISION
    - Dr. S. VENUGOPAL — REMOTE HANDLING, IRRADIATION EXPERIMENTS AND ROBOTICS DIVISION
    - Dr. U. KAMACHI MUDALI — ASSOCIATE DIRECTOR, CORROSION SCIENCE & TECHNOLOGY GROUP
    - Dr. B. PURNA CHANDRA RAO — NON-DESTRUCTIVE EVALUATION DIVISION
  - Dr. A. K. BHADURI — ASSOCIATE DIRECTOR, MATERIALS DEVELOPMENT AND TECHNOLOGY GROUP
    - Dr. M. D. MATHEW — MECHANICAL METALLURGY DIVISION
    - Dr. SHAJU K. ALBERT — MATERIALS TECHNOLOGY DIVISION
    - Dr. M. VIJAYALAKSHMI — ASSOCIATE DIRECTOR, PHYSICAL METALLURGY GROUP
    - Shri E. MOHANDAS — MATERIALS SYNTHESIS & STRUCTURAL CHARACTERIZATION DIVISION
    - Dr. SAROJA SAIBABA — MICROSCOPY & THERMO-PHYSICAL PROPERTY DIVISION

Materials Science Group

- **Dr. C. S. SUNDAR** — DIRECTOR
  - Shri M. P. JANAWADKAR — CONDENSED MATTER PHYSICS DIVISION
  - Dr. G. AMARENDRA — MATERIALS PHYSICS DIVISION
  - Dr. A. K. TYAGI — SURFACE & NANOSCIENCE DIVISION

Groups / Divisions / Heads

Reactor Design Group

- **Dr. P. CHELLAPANDI** — DIRECTOR
  - Shri P. PUTHIYAVINAYAGAM — ASSOCIATE DIRECTOR, CORE DESIGN GROUP
    - DR. K. DEVAN — REACTOR NEUTRONICS DIVISION
    - Shri A. JOHN ARUL — REACTOR SHIELDING AND DATA DIVISION
  - Shri V. BALASUBRAMANIYAN — REACTOR COMPONENTS DIVISION
  - Shri S. RAGHUPATHY — COMPONENTS HANDLING & MECHANISM DIVISION
  - Shri K. MADHUSOODANAN — ASSOCIATE DIRECTOR, POWER PLANT GROUP
    - Shri K. MADHUSOODANAN — INSTRUMENTATION & CONTROL DIVISION
    - Shri N. THEIVARAJAN — POWER PLANT CONTROL DIVISION
  - Shri P. SELVARAJ — ASSOCIATE DIRECTOR, REACTOR ANALYSIS GROUP
    - Dr. K. VELUSAMY — MECHANICS & HYDRAULICS DIVISION
    - Shri B. K. NASHINE — SAFETY ENGINEERING DIVISION

Reactor Operation and Maintenance Group

- **Shri G. SRINIVASAN** — DIRECTOR
  - Shri K. V. SURESH KUMAR — REACTOR OPERATION DIVISION
  - Shri B. ANANTHAPADMANABAN — REACTOR MAINTENANCE DIVISION
  - Miss. S. USHA — TECHNICAL SERVICES DIVISION
  - Shri P. R. SWAMINATHAN — PROJECT PLANNING DIVISION
  - Dr. R. S. KESHAVAMURTHY — REACTOR PHYSICS DIVISION
  - Shri N. KASINATHAN — REACTOR ANALYSIS DIVISION
  - Dr. V. GANESAN — PROJECT MANAGER DFMF

Reprocessing Group

- **Shri R. NATARAJAN** — DIRECTOR
  - Shri V. SUNDARARAMAN — ASSOCIATE DIRECTOR, PROCESS DESIGN &COMMISSIONING GROUP
    - Shri V. SUNDARARAMAN — FUEL REPROCESSING PROCESS DIVISION
    - Dr. U. KAMACHI MUDALI — REPROCESSING RESEARCH & DEVELOPMENT DIVISION
  - Shri A. RAVISHANKAR — ASSOCIATE DIRECTOR REPROCESSING PROJECTS & OPERATION GROUP
    - Shri V. VIJAYAKUMAR — REPROCESSING PLANT OPERATIONS DIVISION
    - Shri B. M. ANANDARAO — REPROCESSING PLANT DESIGN DIVISION


Fast Breeder Reactors
Towards Energy
Security for the Nation